

Dissertation

Surface Science Investigations of Catalytic Alloys on Metal Surfaces by XPS, PM-IRAS, TPD, LEED, and STM

ausgeführt zum Zwecke der Erlangung des akademischen Grades eines
Doktors der technischen Wissenschaften unter der Leitung von

Univ.Prof. Mag.rer.nat. Dr.rer.nat. Günther Rupprechter

Institut für Materialchemie E165

eingereicht an der Technischen Universität Wien

Fakultät für Technische Chemie

von

Dipl.-Ing. Harald Helmuth Holzapfel

Matrikelnummer: e9525592

Jörgerstraße 3/39

1170 Wien

Wien, am 6.3.2015

eigenhändige Unterschrift

Zusammenfassung

Das Hauptziel dieser Arbeit war die Untersuchung der Eigenschaften und des katalytischen Verhaltens von Modellkatalysatoren unter verschiedenen Bedingungen. Die Bedingungen erstreckten sich dabei über den Bereich des Ultrahochvakuums (UHV) bis hin zu Messungen nahe des Umgebungsdrucks und schließen damit die „Lücke“ zwischen der reinen Modellkatalyse im UHV und der angewandten Katalyse im mehr relevanten Bereich höherer Drücke.

Dabei wurde zunächst die Bildung und Stabilität der verwendeten PdZn Katalysatoren untersucht. Das Verhalten bei der Adsorption und Desorption von CO und die Reaktionen mit Methanol und D₂O wurden mittels verschiedener oberflächenanalytischen Verfahren untersucht. Dabei wurden Temperatur-programmierte Desorption (Temperature Programmed Desorption, TPD) Röntgenphotoelektronenspektroskopie (X-ray Photoelectron Spectroscopy, XPS), Polarisations Modulierte Infrarot-Reflexions-Absorptions-Spektroskopie (Polarization Modulation Infrared Reflection Absorption Spectroscopy, PM-IRAS), Beugung niederenergetischer Elektronen an Oberflächen (Low Energy Electron Diffraction, LEED) und Rastertunnelmikroskopie (Scanning Tunneling Microscopy, STM) eingesetzt. PM-IRAS ist eine oberflächensensitive Untersuchungsmethode, welche den Bereich von UHV bis Umgebungsdruck abdeckt. Mit dieser Methode kann man simultan die an der Oberfläche adsorbierten Moleküle und die in der Gasphase vorhandenen Reaktionsprodukte aufzeichnen. XPS, TPD, LEED und STM dienen zur Charakterisierung der Proben im UHV.

PdZn/Pd(111) Oberflächenlegierungen repräsentieren ideale Modellsysteme, z.B. für den industriellen Prozess der Methanol Dampfreformierung (Methanol Steam Reforming, MSR). Dies ist ein wichtiger Schritt zur Förderung alternativer Energieformen. Die Eigenschaften wurden ebenso an intermetallischen PdZn Sinterkristallen untersucht und mit denen der Oberflächenlegierungen verglichen.

PdZn/Pd(111) Oberflächenlegierungen werden durch Aufdampfen von Zn auf Pd(111) Einkristallen und Erhitzen auf die entsprechende Legierungstemperatur hergestellt. Dabei zeigte sich, im Einklang mit bisherigen Untersuchungen, dass die Legierungsbildung bei ca. 473 K beginnt und sich aber bei Temperaturen über 673 K zu zersetzen beginnt. In diesem Temperaturbereich bildet sich eine stabile 1:1 Oberflächenlegierung. Diese beginnt sich bei

weiterer Temperaturerhöhung zu zersetzen. Schlussendlich kann die ursprüngliche Pd(111) Oberfläche bei Temperaturen von über 900 K wiederhergestellt werden. Mittels PM-IRAS konnte gezeigt werden, dass an den so hergestellten PdZn/Pd(111) Oberflächen CO ausschließlich „on-top“ auf Pd-Atomen adsorbiert wird. Der vollständige Bedeckungsgrad wurde mittels TPD bestimmt und beträgt $\frac{1}{2}$ Monolage. Dies steht im Widerspruch zum gängigen Modell einer Pd/Zn „row structure“. DFT Berechnungen zufolge könnte damit maximal eine Bedeckung von $\frac{1}{3}$ Monolage erreicht werden. Die hier präsentierten Ergebnisse unterstützen daher das Modell einer Umordnung zu einer Pd/Zn „ZickZack“ Anordnung an der Oberfläche in Gegenwart von CO. Dies zeigt die, bislang wenig untersuchte, Komplexität des Verhaltens bimetallischer Systeme unter Einfluss eines Adsorbats auf.

TPD und IR Spektren zeigen, dass die Umsetzung von Methanol auf Pd(111) zu einer beträchtlichen Bildung des Katalysatorgifts CO führt, wohingegen bei der Umsetzung auf PdZn/Pd(111) ein anderer Reaktionsweg unter Vermeidung der Entstehung von CO eingeschlagen wird. Ebenso konnte auf PdZn/Pd(111) mittels XPS keine Kontaminierung der Oberfläche mit CH_x Spezies festgestellt werden, während auf Pd(111) eine rasche CH_x Kontaminierung beobachtet wurde.

Die Eigenschaften von Modellsystemen können deutlich von den Systemen der angewandten Katalyse abweichen. Daher wurden neben den PdZn/Pd(111) Oberflächenlegierungen auch intermetallische PdZn Sinterkristalle (hergestellt mittels „Spark Plasma Sintern“) untersucht. Die Adsorption und Desorption von CO wurden auch hier mittels XPS, TPD und PM-IRAS untersucht. Dabei konnten mittels TPD dieselben Desorptionsspeaks wie für PdZn/Pd(111) beobachtet werden, zusätzlich aber auch weitere Desorptionismuster. Dies lässt den Schluss zu, dass es, neben den für die Oberflächenlegierung typischen Adsorptionsplätzen, noch weitere Adsorptionsmöglichkeiten auf den Sinterkristallen gibt.

Abstract

The primary objective of this work was the investigation of properties and catalytic behavior of well-defined model catalysts. This work covers the wide scope of conditions from ultra high vacuum (UHV) to ambient pressure to close the gap between pure model systems and more relevant systems for applied catalysis. PdZn/Pd(111) surface alloys have been prepared and characterized under the well-defined conditions of ultra high vacuum.

The formation, stability, and structure of Pd(111) and PdZn/Pd(111) surface alloys and their interaction with CO, methanol and D₂O were studied by applying a combination of complementary techniques such as Temperature Programmed Desorption (TPD), X-ray Photoelectron Spectroscopy (XPS), Polarization Modulation Infrared Reflection Absorption Spectroscopy (PM-IRAS), Low Energy Electron Diffraction (LEED), and Scanning Tunneling Microscopy (STM). PdZn surface alloys represent well-suited model systems for modern Methanol Steam Reforming (MSR) catalysts. The goal is use this as an environmentally beneficial renewable energy source. The properties were also investigated on sintered PdZn bulk intermetallics and compared to the results on surface alloys.

PM-IRAS is a surface sensitive method which can be applied from UHV up to atmospheric pressure. It allows simultaneous monitoring of reaction intermediates adsorbed on the catalyst surface and of products in the gas phase. Thus, PM-IRAS is well-suited as an in-situ method to study catalytic reactions. XPS, LEED, and STM have been applied for characterization of the model systems in UHV.

PdZn surface alloys on Pd(111) were prepared by Zn deposition on Pd(111) at or below room temperature. This procedure covers the surface with non-interacting Zn layers. Subsequent annealing to temperatures above 473 K leads to the formation of PdZn surface alloys. At annealing temperatures above approximately 623 K the surface alloy starts to decompose, finally restoring the clean Pd(111) surface at temperatures above 900 K. It was shown by PM-IRAS that even at mbar pressure CO adsorbed exclusively on-top of single Pd atoms on the alloy layer, giving rise to a characteristic IR band at 2070 cm⁻¹. PM-IRAS also proved that the PdZn alloy is structurally very homogeneous. The CO saturation coverage was found to be ½ ML by TPD. To the contrary, on a surface with conventional, bulk-like geometric arrangement of Pd and Zn atoms in rows, CO adsorption on bridge sites with saturation

coverage of $\sim 1/3$ ML was predicted by DFT calculations. These experiments are supporting a suggested reconstruction of PdZn/Pd(111) to a “zigzag”-rearrangement of the atomic components on the surface in the presence of CO. This investigation provides new insights in the complexity of bimetallic systems.

TPD and IR spectra reveal that methanol was decomposing to a significant amount on Pd(111), yielding CO and CH_x, which did not happen on the PdZn surface alloys. No carbonaceous deposits were detectable with XPS, which is in great contrast to pure Pd where rapid carbon formation was observed. This difference is of great relevance in explaining the improved catalytic properties of PdZn catalysts for MSR. One explanation might be the lack of adsorption sites for bridge bound formaldehyde species which are a likely precursor for C-O bond cleavage.

To identify possible differences between the surface alloy “models” and “real” system, a comparative study between the adsorption properties of well-defined PdZn/Pd(111) surface alloys and bulk intermetallic ZnPd sinter „single“ crystals was performed. The corresponding intermetallic PdZn bulk material was prepared by powder metallurgical means and subsequent spark-plasma-sintering. The adsorption/desorption properties of CO as probe molecule on intermetallic ZnPd were studied by XPS, TPD, and PM-IRAS. For TPD, the same desorption features as observed on PdZn/Pd(111) could also be identified in the spectra obtained on the bulk PdZn crystal. This indicates the presence of the same kind of adsorption sites on both systems. However, on the PdZn bulk crystal additional desorption features were observed in TPD spectra. In PM-IRAS additional bands of multiple bound CO species were observed. This suggests the presence of a new kind of adsorption sites on the bulk PdZn crystal which was not observed on the surface alloys.

Danksagung

Meinen besonderen Dank möchte ich aussprechen an:

Prof. Günther Rupprechter für seine fortwährende Unterstützung, die Möglichkeit diese Dissertation in seiner Arbeitsgruppe durchzuführen und die Möglichkeit, meine Ergebnisse bei zahlreichen nationalen und internationalen Konferenzen zu präsentieren;

Prof. Josef Redinger für seine Bereitschaft als Zweitgutachter und Zweitprüfer zu fungieren;

Christian Weilach und Christoph Rameshan für die exzellente Betreuung bei der Durchführung meiner Arbeit;

den Mitgliedern der Arbeitsgruppen Oberflächenchemie und Katalyse für eine wissenschaftlich interessante und ausgesprochen angenehme Arbeitsatmosphäre in Forschung und Lehre;

Rainald, Johannes und Rupert für all die technische Unterstützung;

Andrey vom Boreskov Institute of Catalysis in Novosibirsk für die Unterstützung bei den STM Messungen

den Kollegen von Institut für angewandte Physik (AG Prof. Diebold, Prof. Schmid und Prof. Redinger) für Organisation zahlreicher interessanter Seminare;

Prof. Marc Armbrüster für die Zurverfügungstellung eines ZnPd Sinterkristalls und dessen metallographische Untersuchung;

Sergey Kozlov und Konstantin Neyman vom Institut de Química Teòrica i Computacional und Institució Catalana de Recerca i Estudis Avançats in Barcelona für die DFT Berechnungen der Oberflächenstruktur;

Joachim Schnadt, Jan Knudsen und Niclas Johansson vom Max-lab Synchrotron in Lund für die technische Unterstützung bei der Durchführung der HP-XPS Messungen.

all meinen Freunden und Kollegen, die hier nicht namentlich genannt wurden.

Der größte Dank gilt jedoch meiner Familie, meinen Eltern, die mir das Studium erst ermöglicht und mich bei meinen Entscheidungen immer unterstützt haben.

Table of Contents:

1	INTRODUCTION	11
2	EXPERIMENTAL	17
2.1	BASIC SETUP	19
2.1.1	XPS and PM-IRAS Chamber.....	19
2.1.1.1	Transfer to a new location	23
2.1.2	STM Chamber.....	25
2.1.2.1	Sample Mounting and Transfer	26
2.2	POLARIZATION MODULATION INFRARED REFLECTION ADSORPTION SPECTROSCOPY (PM-IRAS)	29
2.2.1	Principles.....	30
2.2.2	Data Processing and Acquisition.....	37
2.3	X-RAY PHOTOELECTRON SPECTROSCOPY (XPS)	38
2.3.1	Theory.....	38
2.3.2	Quantification	46
2.3.3	Analyzer and detector	46
2.3.4	Synchrotron (Maxlab II) and High Pressure XPS.....	51
2.3.4.1	High Pressure Cell.....	55
2.3.5	Data Processing and Acquisition.....	56
2.4	AUGER ELECTRON SPECTROSCOPY (AES)	59
2.4.1	Principles.....	59
2.4.2	Data Processing and Acquisition.....	62
2.5	LOW ENERGY ELECTRON DIFFRACTION (LEED)	63
2.5.1	Principles.....	63
2.5.2	Data Processing and Acquisition.....	66
2.6	TEMPERATURE PROGRAMMED DESORPTION (TPD)	68
2.6.1	Principles.....	68
2.6.2	Data Processing and Acquisition.....	70
2.7	SCANNING TUNNELING MICROSCOPY (STM).....	73
2.7.1	Principles.....	75
2.7.1.1	Electron tunneling	75
2.7.1.2	STM tips.....	79
2.7.1.3	Piezoelectric actuators	81
2.7.1.4	STM imaging modes	83
2.7.1.5	Vibration isolation.....	85
2.7.2	Data Processing and Acquisition.....	86
2.8	ADDITIONAL COMPONENTS.....	88
2.8.1	Sputter Gun.....	88
2.8.2	Evaporator.....	89
2.8.3	Thickness monitoring / Microbalance.....	90
2.8.4	Electron Beam Heater.....	91
2.8.5	Spot Welding	93

2.8.6	<i>Spark Plasma Sintering</i>	94
2.9	ULTRA HIGH VACUUM TECHNOLOGY	95
2.9.1	<i>Theory</i>	95
2.9.2	<i>Practical</i>	100
2.9.3	<i>Vacuum components</i>	103
2.9.3.1	Materials for Vacuum Technology	103
2.9.3.2	Vacuum pumps.....	106
2.9.3.3	Pressure measurement	115
2.10	ADSORPTION OF MOLECULES IN VACUUM	121
2.10.1	<i>Adsorption of CO on metal surfaces</i>	122
2.10.2	<i>Adsorbate-induced reconstruction of surfaces</i>	123
2.11	DFT CALCULATIONS	124
3	PD(111) AND PDZN/PD(111) SURFACE ALLOYS	126
3.1	SAMPLE PREPARATION	126
3.2	CO ADSORPTION ON Pd(111).....	127
3.2.1	<i>Adsorption geometries</i>	127
3.2.2	<i>LEED</i>	128
3.2.3	<i>XPS</i>	131
3.2.4	<i>PM-IRAS</i>	132
3.2.5	<i>TPD</i>	133
3.3	METHANOL DEHYDROGENATION ON Pd(111)	135
3.3.1	<i>TPD</i>	135
3.3.2	<i>PM-IRAS</i>	139
3.3.3	<i>XPS</i>	142
3.4	PREPARATION OF PdZn/Pd(111)	153
3.5	CO ADSORPTION ON PdZn/Pd(111).....	157
3.5.1	<i>PM-IRAS</i>	157
3.5.2	<i>TPD</i>	162
3.6	STM MEASUREMENTS ON Pd(111) AND PdZn/(111)	171
3.6.1	<i>Pd(111)/PdZn surface alloys</i>	176
3.7	SURFACE REARRANGEMENT INDUCED BY CO ADSORPTION	180
3.8	METHANOL DEHYDROGENATION ON PdZn/Pd(111).....	199
3.8.1	<i>TPD measurements</i>	199
3.8.2	<i>PM-IRAS measurements</i>	202
3.8.3	<i>XPS measurements</i>	207
3.9	METHANOL DECOMPOSITION AND OXIDATION ON Pd(111) BY HP-XPS	210
3.9.1	<i>Introduction</i>	210
3.9.2	<i>Setup and sample preparation</i>	212
3.9.3	<i>Measurement plan</i>	214
3.9.4	<i>Summary</i>	215

4	ZNPD BULK INTERMETALLICS	226
4.1	INTRODUCTION.....	226
4.2	TETRAGONAL ZNPD.....	230
4.2.1	Preparation.....	230
4.2.2	CO and D ₂ O adsorption on ZnPd bulk sinter crystals	236
4.2.3	MeOH desorption on ZnPd.....	254
4.3	PD ₂ ZN.....	257
4.3.1	Summary.....	263
5	OTHER SURFACE SCIENCE AND CATALYSIS PROJECTS.....	264
5.1	CARBON NANOTUBES	264
5.1.1	Sample preparation for XPS	264
5.1.1.1	XP Spectra of C 1s	265
5.1.1.2	XP Spectra of Al.....	269
5.1.1.3	XPS binding energies	270
5.1.1.4	Discussion	271
6	CONCLUSIONS.....	272
7	APPENDIX	275
7.1	XPS/PM-IRAS SYSTEM.....	276
7.1.1	Overview	276
7.1.2	Manipulator	278
7.1.3	X-Ray source	279
7.1.4	Analyzer	285
7.1.5	Triple Evaporator	286
7.1.6	Auger-LEED unit	287
7.1.7	STM-System.....	288
7.1.8	System overview	288
7.1.9	Manipulator	289
7.1.10	STM unit.....	290
7.2	MAXLAB-SYNCHROTRON DATA.....	292
7.2.1	Overview	292
7.2.2	Technical data.....	293
7.2.3	Sample mounting.....	294
7.2.4	Pressure monitoring.....	296
7.2.5	Beam flux calibration.....	298
7.3	MEAN FREE PATH	301
7.4	INFRARED SPECTRA IN GAS PHASE.....	303
7.5	INFRARED SPECTRA ON A Pd(111) SURFACE	307
7.6	VACUUM SYMBOLS	308
7.7	LIST OF SYMBOLS	309
7.8	LIST OF ABBREVIATIONS	310
7.9	LIST OF FIGURES.....	312

7.10	LIST OF TABLES	323
8	PUBLICATIONS	324
9	CURRICULUM VITAE	329
10	REFERENCES	331

1 Introduction

In heterogeneous catalysis, model catalysts are a fundamental part of research efforts since decades. Gerhard ERTL has been awarded in 2007 with the Nobel Prize in chemistry “for his studies of chemical processes on solid surfaces” [1]. Heterogeneous catalysts are typically very complex multifunctional systems and difficult to understand and to investigate with conventional techniques. Therefore, model systems are used to understand catalytic processes on an atomic level by simplifying the catalyst system. Catalytic processes are essential to produce liquid fuels in the amount and quality necessary for the world’s societal development. Catalysts are also necessary to eliminate pollutants associated to these primary energy sources, i.e., to allow a sustainable development.

The most simplified models in surface science and model catalysis are well-defined metal single crystals with, even on an atomic level, flat surfaces and only few defect sites (e.g. steps). They are prepared and investigated under controlled ultrahigh vacuum (UHV) conditions [2-6]. Single crystals have been utilized to address activity of different facets [7-9] and the interaction of molecules with specific surface sites [10-13]. The basic idea behind single crystal models is that, in the end, the sum of the properties of all different sites and facets should represent a real catalyst nanoparticle used in an industrial process. On the other hand, a model system may be oversimplified, and therefore miss some of the functionalities of a real catalyst. For example, a single crystal cannot model dynamic interactions between different facets and it neglects possible effects of the support material used to disperse noble metal particles.

The interest of catalytic reactions using methanol as a chemical storage molecule (e.g. onboard hydrogen source for fuel cells) for energy is currently increasing. Methanol can be industrially produced from syngas (gas- or coal derived) and from CO_2 by hydrogenation (“ CO_2 -neutral”) [14]; also mature technologies for biomass gasification are being used for methanol production (e.g. woody biomass can be gasified to water gas, a hydrogen-rich syngas). Methanol has a high hydrogen to carbon ratio and no C-C bond which needs to be broken. Several catalytic reactions to produce hydrogen from methanol are available:

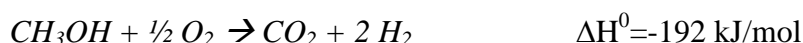
Methanol decomposition (MD):



Methanol steam reforming (MSR):

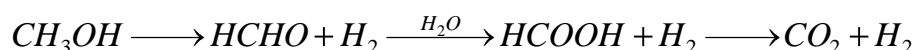


Methanol oxidation:



Methanol steam reforming seems to be the most attractive way as it produces the highest hydrogen amount, runs at relatively low temperatures (500 – 600 K), and does not directly produce *CO*. MSR is endothermic but much less energy is needed than steam reforming of other hydrocarbons [15].

Several reaction mechanisms are described for MSR, via full dehydrogenation of methanol to *CO*, followed by partial conversion of *CO* with water to *CO*₂ or the intermediate formaldehyde species would directly react with water:



A good catalyst for MSR requires:

- High selectivity to *CO*₂ and avoid *CO* formation
- Activity at low temperatures
- Components and preparation should be low cost
- Stable at extended time and towards changes in reaction conditions (e.g. production of hydrogen on demand)

Pd particles are for example active in the methanol decomposition reaction that converts methanol to *CO/CO*₂ and *H*₂. Regrettably their activity at lower temperatures (< 500 K) is not sufficient and in many cases catalyst poisoning occurs. Published results are sometimes controversial and the reason for the Pd catalyst imperfectness is still not clear [16-20]. This part of the thesis deals with the examination of the mechanism of MeOH decomposition and oxidation under UHV and ambient pressure conditions.

The commercial Cu/ZnO industrial catalyst used in chemical reactions such as MSR, suffers in low sintering stability and pyrophoricity. Once Cu catalysts have lost their activity from either sintering or oxidation, they cannot be regenerated. A comparison of loss of reactivity over time between a conventional Cu catalyst and Pd/ZnO/Al₂O₃ catalyst is shown in Fig. 1-1.

Selectivity is a key issue since CO is an unwanted by-product (catalyst poison). On unalloyed Pd surfaces CO production is favored. Studies of the MSR activity of other metals of the groups VIII to X and different support materials were performed by Iwasa et al [21].

The values obtained for the Pd-based catalysts are listed in Tab. 1-1. Although for Pd (and Pt) supported on In₂O₃ or Ga₂O₃ the formation of alloy phases under reaction conditions also occurred, the Pd/ZnO system is the most active and selective for MSR. PdZn alloys selectively produce hydrogen and CO₂ and, contrary to Pd alone, avoid CO formation. The activity and CO selectivity of Pd/ZnO (circles) and an industrial Cu/ZnO catalyst is shown in Fig. 1-2

Tab. 1-1: Steam reforming of methanol over various supported Pd catalysts. Reprinted from [22].

		CO ₂	CO	DME		
Pd/ZnO	54.2	99.2	0.8	0	2.2	0.497
Pd/In ₂ O ₃ ^c	28.3	95.5	4.5	0	2.1	0.291
Pd/Ga ₂ O ₃	21.2	94.6	5.4	0	2.6	0.177
Pd/SiO ₂	15.7	0	100	0	9.0	0.021
Pd/Al ₂ O ₃	58.9	0	69.6	30.4	14.0	0.036
Pd/MgO	41.0	6.6	93.4	0	10.4	0.053
Pd/ZrO ₂	64.3	18.4	81.6	0	6.6	0.139
Pd/CeO ₂	62.4	22.7	77.3	0	36.2	0.025
Pd/A.C.	2.3	0	100	0	–	–
Pd/Ta ₂ O ₅	6.0	0	100	0	–	–
Pd/HfO ₂	13.6	0	100	0	–	–
Pd black	10.9	0	100	0	2.1	0.0071
Cu/ZnO	19.3	100	0	0	1.0	0.300

Note: Reaction conditions: reaction temperature = 493 K, inlet partial pressures of methanol = 10.1 kPa, inlet partial pressures of water = 10.1 kPa.

^aPd loading = 10 wt%.

^bTurnover frequency for H₂ formation.

^cReduction temperature is 523 K.

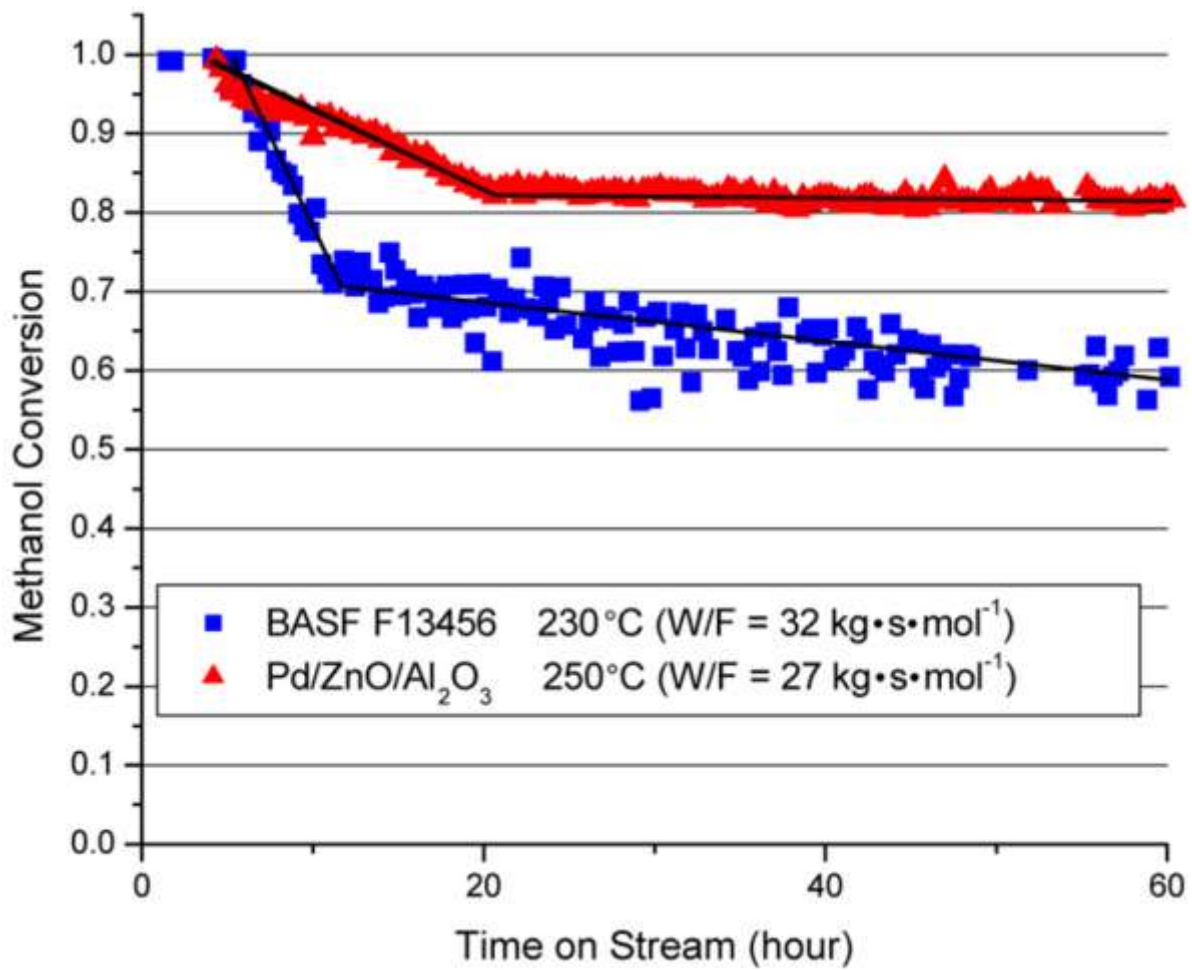


Fig. 1-1: The comparison of loss of reactivity over time between a conventional Cu catalyst (BASF F13456) and Pd/ZnO/Al₂O₃. The Cu-based catalyst suffers from fast deactivation, whereas the Pd-based catalyst deactivates to a lesser extent. Reprinted from [23]

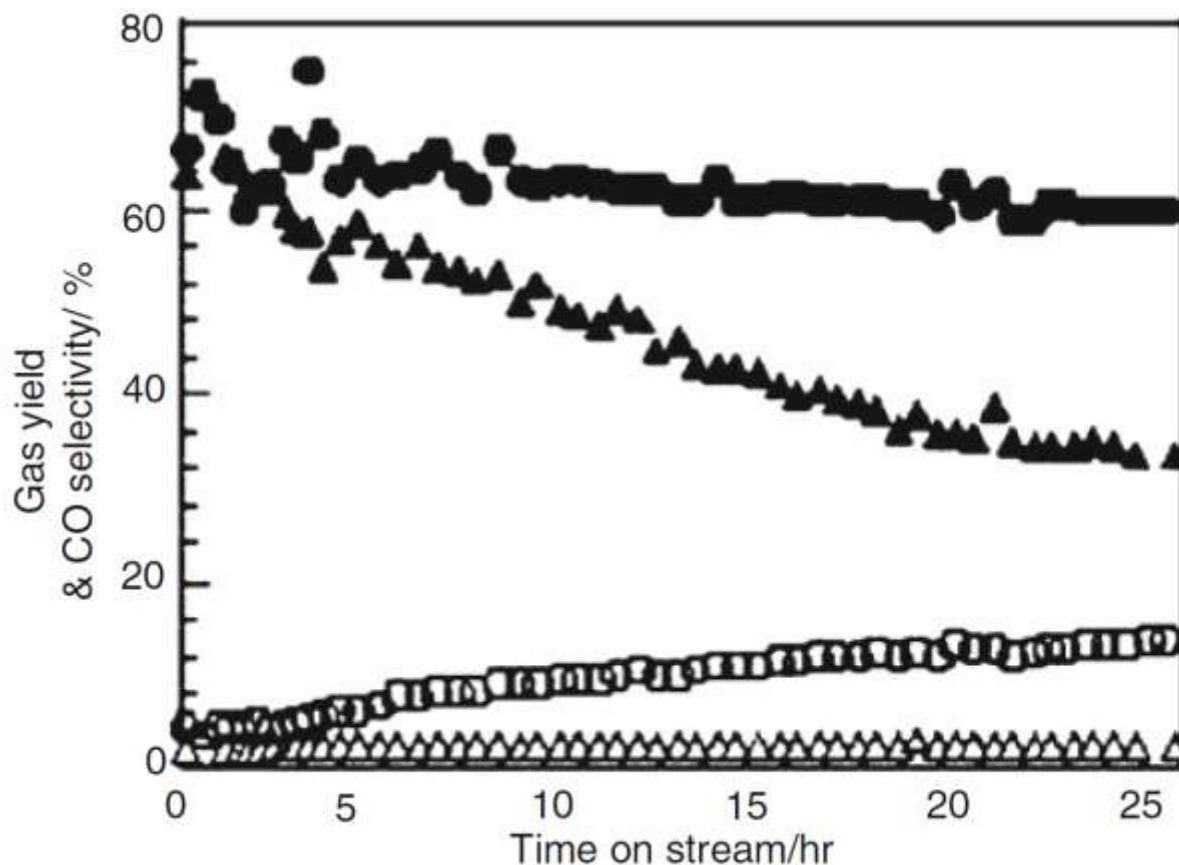


Fig. 1-2: Activity (solid symbols) and CO selectivity (open symbols) of Pd/ZnO (circles) and an industrial Cu/ZnO catalyst (triangles). Reprinted from [24].

Per definition, catalysis is a process that increases the rate of a reaction (without modifying the overall standard Gibbs energy) due to the participation of a substance called a catalyst, but, unlike other reagents, a catalyst is not consumed by the reaction itself. Physico-chemical changes of catalysts, e.g. during catalytic cycles, are often regarded as unwanted because they usually decrease the catalytic performance. But in some cases this may lead to improvements in catalytic properties or stability. The manner of rearrangement needs to be understood at an atomic level to get the possibility to control them [25]. We found the evidence that sample preparation under *CO* atmosphere can change the surface arrangement of the Pd/Zn system. To the best of our knowledge, modification of elemental arrangement in the presence of adsorbates and its influence on adsorptive properties have not been reported before.

This work presents a valuable insight to the mechanism of MSR on PdZn/Pd(111) and highlights interesting properties that were revealed in this work on the model systems, because a model system may not satisfactorily represent the real catalyst. A comparative study between the adsorption properties of well-defined PdZn/Pd(111) surface alloys and bulk ZnPd intermetallic sinter “single crystals” was performed to identify possible differences between the surface alloy “models” and “real” system [24, 26-28].

2 Experimental

This chapter gives an introduction to the background of the necessary experimental techniques applied in this thesis. Initially, the setup of the UHV system in which most of the experiments were performed, will be introduced. All experiments described below were carried out in an ultrahigh vacuum (UHV) chamber with base pressure of 5×10^{-10} mbar (XPS/PM-IRAS chamber, see 2.1.1) and 1×10^{-10} mbar (STM chamber, see 2.1.2), respectively.

For all experiments and sample preparations, high purity gases from Messer Austria were used. For argon, oxygen, helium, hydrogen and nitrogen the purity was 5.0 (99.9990 %), for CO 4.7 (99.997 %), and for CO₂ 4.5 (99.995 %). Some care has to be taken for CO cleanliness. To prevent contamination from Ni- or Fe-carbonyls (the gasline is made of stainless steel), the impurities were removed by passing CO over a carbonyl absorber cartridge. Also, the gasline should be rinsed with Ar after using CO. Methanol (> 99.9 %, University distillation plant) and D₂O (99.99 atom %, Sigma-Aldrich) were purified using repeated freeze-pump-thaw cycles. In addition, methanol was stored over a 3 Å molecular sieve.

To clean the Pd(111) substrate, the Pd single crystal was sputtered in 5×10^{-6} mbar Ar at 1 kV for 45 min at 300 K followed by annealing for 15 min at 1200 K. The sample was then cooled in 5×10^{-7} mbar O₂ down to 650 K to remove residual carbon. Finally, the single crystal was flashed to 1200 K in UHV. Sample cleanliness was checked by XPS and LEED.

PdZn surface alloys (“surface intermetallic phases”) were prepared by physical vapor deposition of Zn (high purity Zn-wire, 99.98%, GoodFellow) out of a Ta crucible mounted in an Omicron e-beam evaporator (EFM 3). The deposited amount of Zn (nominal thickness reported in ML) was calibrated using a quartz microbalance. The Zn flux during evaporation was additionally controlled via an internal flux monitor. In this respect, one Monolayer is always referred to 1.53×10^{15} atoms/cm², i.e. the value of a close packed (111) crystal plane in bulk Pd. It has been shown by Kratzer et al. [29] that when using a quartz microbalance to calibrate the amount of Zn deposited, great care has to be taken due to the lowered sticking coefficient of Zn on the “dirty” surface of the quartz crystal microbalance. To overcome this

problem we have deposited several ML of Zn on the quartz surface directly before calibration of the flux.

Carbon monoxide is a common probe molecule which should not modify the properties of the investigated surface (the validity of this will be reassessed later in this work [30]). Although it is an ideal adsorbate for surface science, *CO* is very poisonous and needs precaution if used. It is an odorless and colorless gas. The main reason of its toxicity is the inhibition of hemoglobin which is then not able to transport oxygen. The affinity of *CO* to Fe^{2+} under physiological conditions is 250 times higher than the affinity of oxygen to Fe^{2+} . The density is similar to air; it will not accumulate on the floor like CO_2 and can easily diffuse through walls. This is a reason why living spaces over car garages are not allowed. The heaviness of intoxication depends on the amount of inhibited hemoglobin (HbCO), *not* directly on the concentration in the air. At HbCO < 20%, first symptoms are headache, tiredness, and dizziness. At 20-30% HbCO, declining strength of purpose often blocks the ability of the endangered person to get to a safe place (though the physical ability still exists). At HbCO > 30% the awareness dwindles, the breath becomes shallow and it leads to an acirculatory collapse. An HbCO level of more than 50% is potentially lethal and at more than 70% HbCO death results within some minutes, characteristic is the cherry-red color of the skin. Subacute intoxication is a result of accumulated consumption of air with a *CO* concentration between 500 and 2000 ppm for some hours. A concentration of more than 10000 ppm in the air leads to death within a few minutes. Intoxicated persons have to be brought to a safe place and supplied with artificial respiration of 100% oxygen [31]. In Austria, the MAK-value (“Maximale Arbeitsplatzkonzentration”; threshold limit value, TLV) is 30 ppm, which is not dangerous to adult, healthy persons [32].

Because of the high dangerousness of this gas the lab is equipped with gas sensors to prevent a serious accident if the gas line starts leaking for any reason. Two types of sensors are in use, one stationary sensor (*CO* warning and low oxygen warning) and a mobile sensor (Dräger PAC 5500). One should note that the sensor responds also on reducing gases like hydrogen. Outside the lab we have a gas mask with *CO* active filter to close the main valve of the gas bottle.

2.1 Basic setup

2.1.1 XPS and PM-IRAS Chamber

All XPS/PM-IRAS experiments presented in this thesis were performed in a customized ultrahigh vacuum (UHV) system, which combines the advantages of surface science methods with the possibility to investigate catalytic gas phase reactions up to atmospheric pressure with in-situ IR spectroscopy. The system was originally designed by Prof. Günther RUPPRECHTER at the Fritz Haber Institute of the Max Planck Society in Berlin (based on a previous design of an SFG high pressure cell [33-35]). The UHV chamber setup was extended later by XPS spectroscopy by Dr. O. Rodriguez DE LA FUENTE and Dr. M. BORASIO [36-38]. Then it was transferred and extended to a new location in Vienna by my former supervisor Dr. Christian WEILACH [39]. During my work on this thesis, the chamber was modified and transferred to another location in Vienna (see chapter 2.1.1.1). Basically, the UHV system consists of two parts, a “preparation” chamber (upper part) mainly used for sample preparation and XPS/LEED/TPD characterization, and a high pressure (HP) cell (lower part) to perform and study catalytic reactions with PM-IRAS, see detailed descriptions in the following chapters. See Appendix for more detailed drawings of the system.

The preparation chamber is equipped with an Ar⁺ sputter gun for sample cleaning and a triple electron beam metal evaporator to deposit nanoparticles or films of various metals by Physical Vapor Deposition (PVD). Calibration of the metal flux is done by using a quartz microbalance which can be moved to the exact sample position. The evaporation process settings are controlled via an internal flux monitor. The surface structure, composition and cleanliness of the sample can be controlled by LEED and XPS, respectively [39].

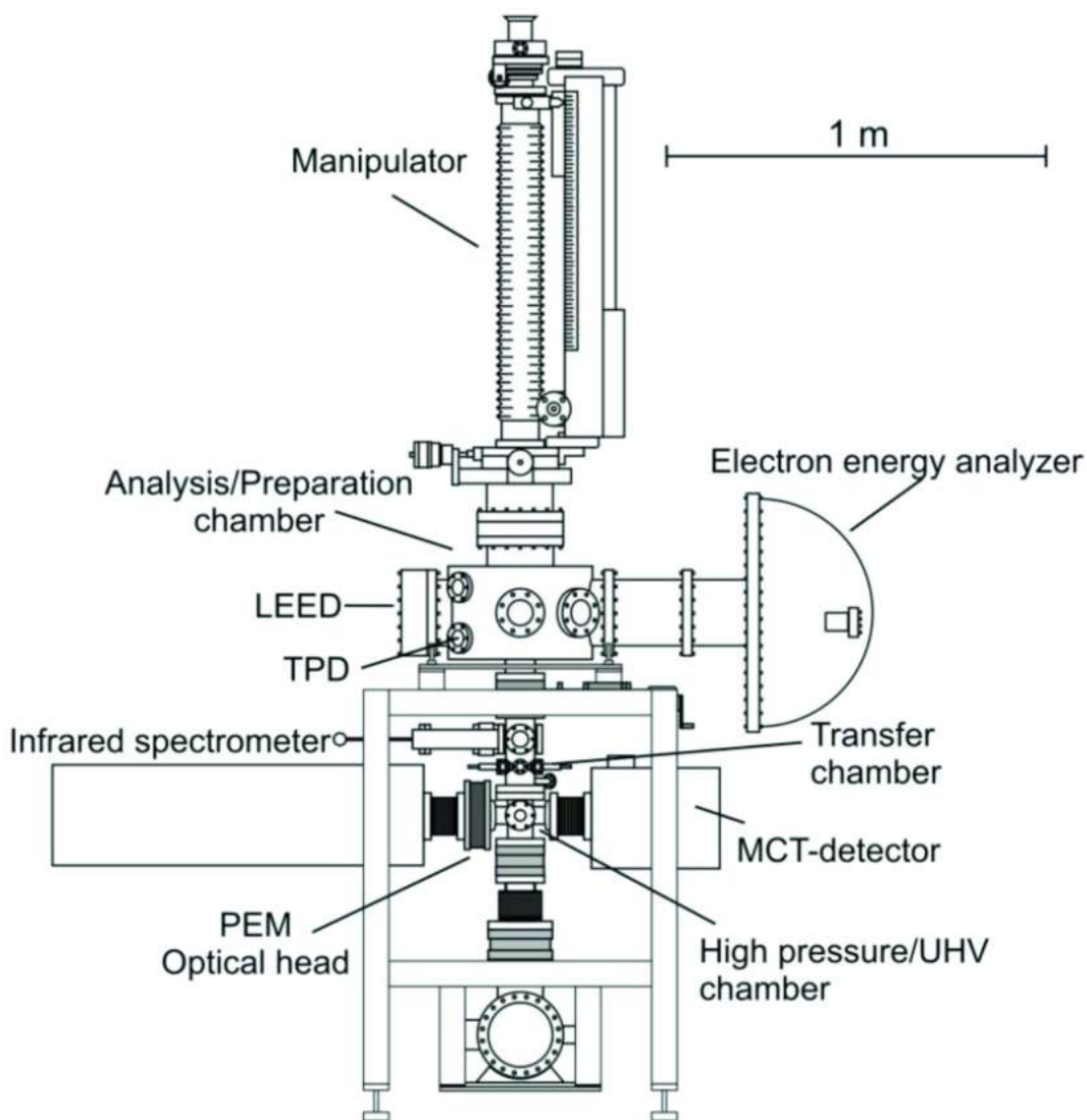


Fig. 2-1: Overview of the XPS/PM-IRAS system and its components.

Samples, usually disc shaped, polished single crystals (with a groove at the edge for easy mounting) are fixed with tantalum wires (Advent Research Materials Ltd., 99.9% purity) onto two molybdenum current feedthroughs of a customized cold finger which is mounted on a VG Omniax MX manipulator (x,y,z , 360° rotation). The samples can be resistively heated to about 1300 K or cooled with liquid nitrogen to about 80 K using the cold finger (Fig. 2-2). Temperature readout and control is done by an Eurotherm controller. The K-type thermocouple wires (Omega Engineering Inc., \varnothing 0.13 mm) were spot welded to the backside of the crystal [39].

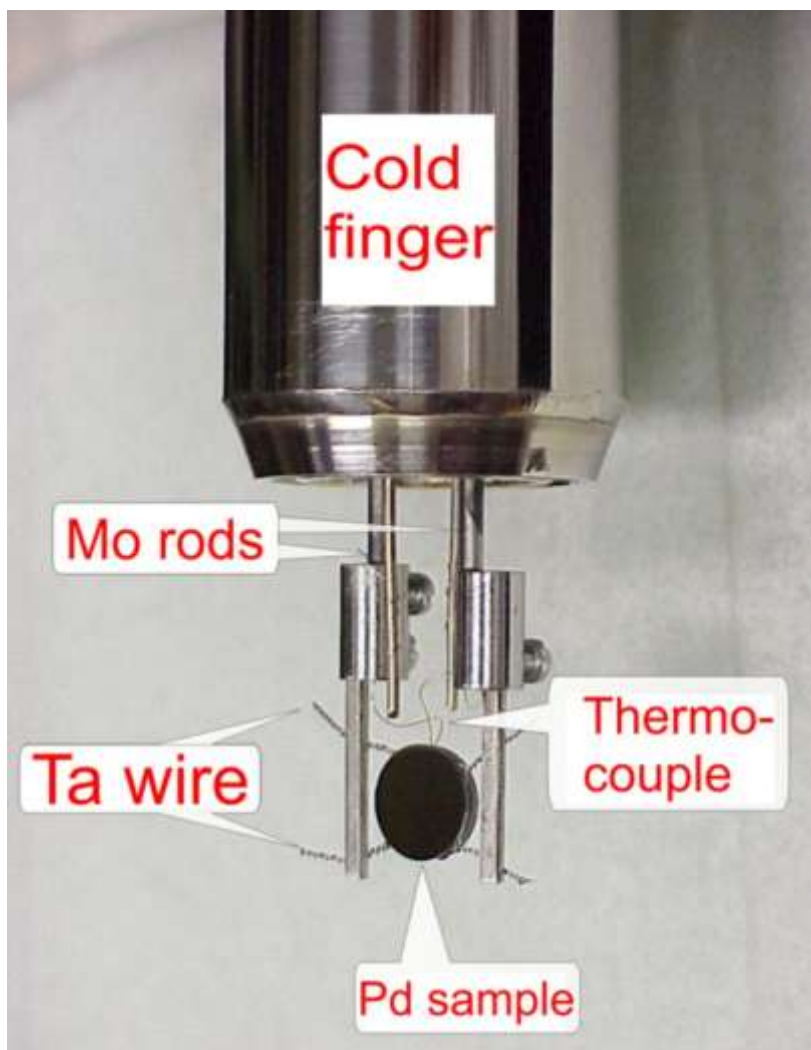


Fig. 2-2: Cold finger with a mounted single crystal (attached on Mo rods). The Alumel/Chromel wires are spot welded on the backside of the sample and connected to the thermocouple rods.

The sample will be moved from the preparation chamber to the reaction cell with the manipulator and enters a differentially pumped arrangement of spring loaded Teflon seals. This separates the UHV part from the high pressure cell [33, 40]. The reaction cell can be operated at pressures from UHV up to atmospheric pressure (adding an inert gas like He or Ar to get a total pressure of ~1 bar). To avoid wall reactions the inner side of the reaction cell is gold-coated. The cell can be pumped down in a short time after experiments at elevated pressure with a turbo molecular pump.

The XPS-system is equipped with a SPECS XR50 non-monochromatic Al/Mg dual anode X-Ray source (maximum Al $K\alpha$ 400 W and Mg $K\alpha$ 300 W) and a SPECS PHOIBOS EA 150 hemispherical analyzer. See Appendix 7.1.3 and 7.1.4 for detailed drawings and a data sheet

of analyzer and X-Ray source. Unless otherwise noted, all XP spectra presented in this work were acquired using Al K α radiation.

TPD spectra were collected by a differentially pumped MKS eVision+ quadrupole mass spectrometer. The temperature ramping was performed by a Eurotherm 3208 PID controller. To minimize contributions of residual gases and molecules desorbing from the sample holder, and from the back side and edges of the crystal, the nozzle of the mass spectrometer was placed in front of the single crystal (< 1 mm distance).

The PM-IRAS spectra were acquired on a Bruker IFS66v/S spectrometer, polarization modulation was performed by a Hinds-PEM-90 ZnSe photoelastic modulator.

To close the gap between model and real catalysis [41], PM-IRAS can be applied from UHV up to ambient pressure and provides surface vibrational spectra of adsorbed species, based on subtraction of gas phase contributions [38, 42, 43]. A detailed description of the PM-IRAS system and related theory is given in chapter 2.2.

2.1.1.1 Transfer to a new location

During the (long time) construction of a new chemistry building on the main place of the chemistry department of the University of Technology, Vienna on the Getreidemarkt (6th district of Vienna), the Institute of Materials Chemistry was housed in a building of the University of Veterinary Medicine, Vienna (“VetMed”) for some years. The first part of this thesis was done at this location. After the new building had been finished, the complete equipment was transferred to the new building, called “Lehartrakt” on the Getreidemarkt. Due to a huge delay in finishing the basic indoor installations (water, gas, electricity, and ventilation), the transfer and re-setup took much longer than expected. Also, we and the new building experienced a lot of growing pains which further increased the delay in getting scientific results on the new location. The (old) setup of the equipment in the VetMed is shown in Fig. 2-3.

We used the opportunity for some slight improvements in handling and also replaced some components but the main system remained unchanged. This new setup of the system is shown in Fig. 2-4.

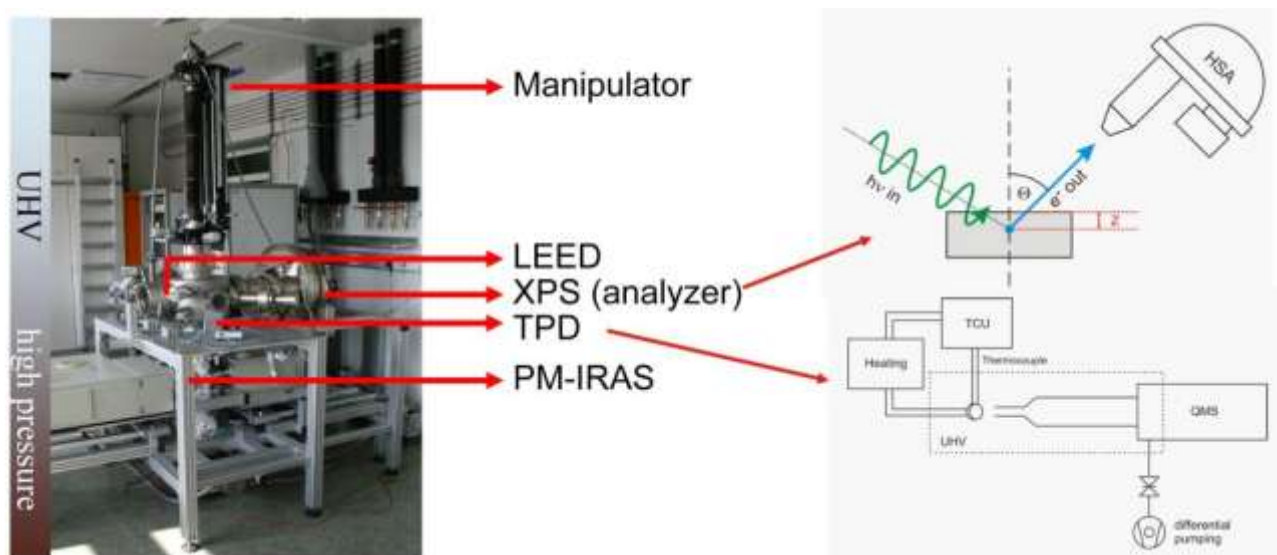


Fig. 2-3: Picture of the XPS and PM-IRAS setup located at VetMed (left side) and scheme of the components (right side).

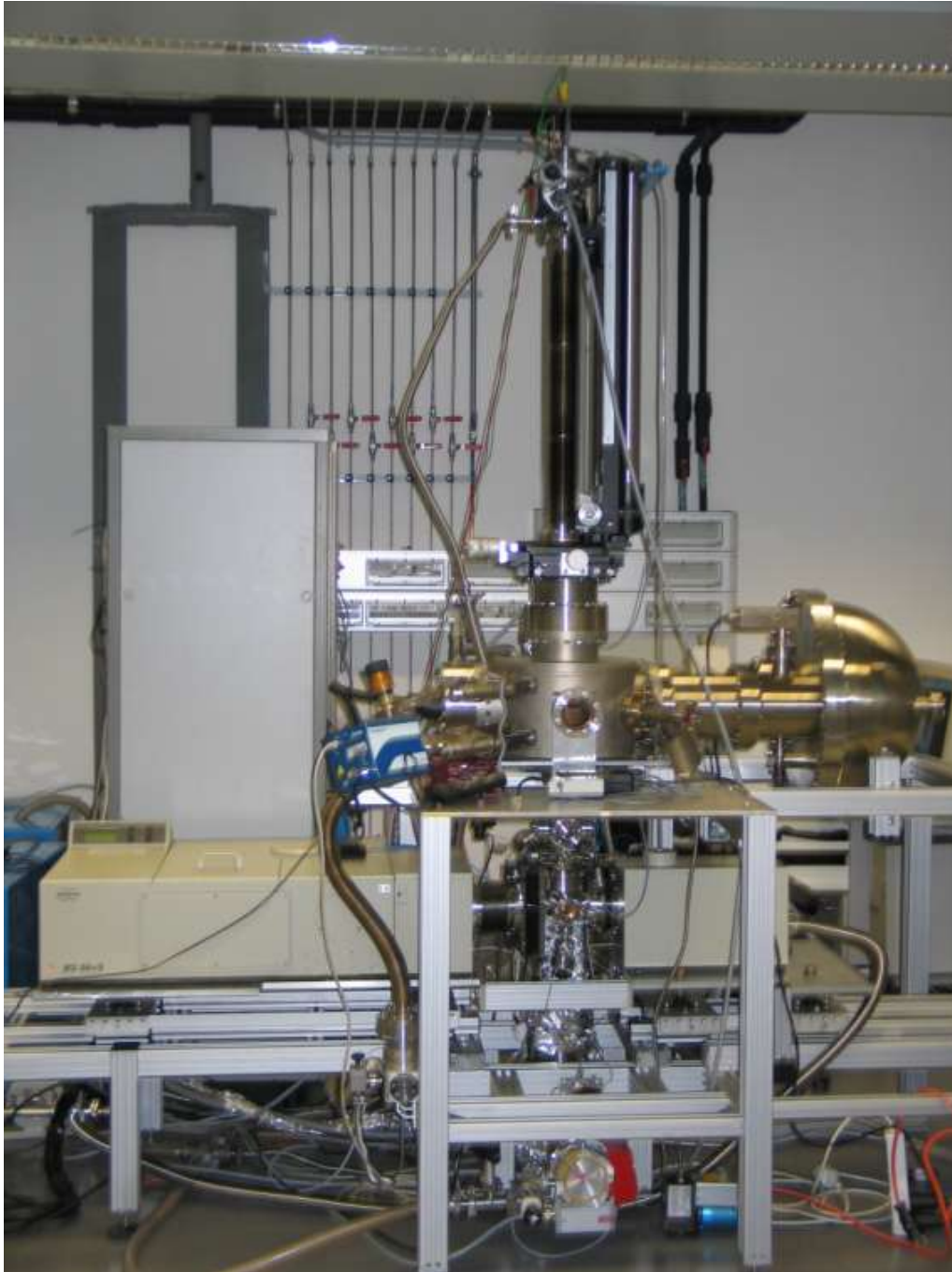


Fig. 2-4: New XPS and PM-IRAS setup located at Getreidemarkt/Lehartrakt after relocation.

2.1.2 STM Chamber

The new Specs STM system (see Fig. 2-5) was delivered as a complete system with load-lock chamber, preparation chamber and STM chamber. The system is equipped with an ErLEED 150 Auger-unit, a sputter gun, a sample stage with e-beam heating and a HT STM 150 Aarhus microscope. The preparation chamber is pumped with a turbomolecular pump using a scroll pump as backing pump. The STM chamber is pumped with a titan sublimation pump and an ion getter pump (Varian Vaclon Plus 300 Starcell). The system is equipped with magnetic coupled transfer rods for sample motion. We extended the system with an evaporator, a microbalance, a mass spectrometer, and a self-made doser.

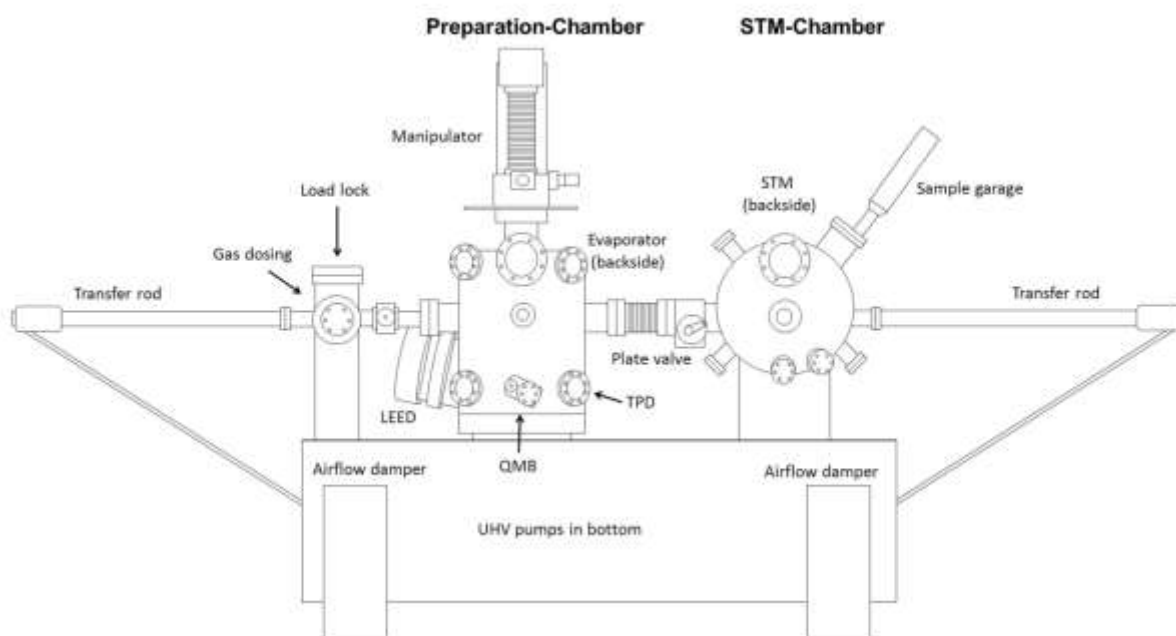


Fig. 2-5: General scheme of the STM system before the preparation chamber was changed for the installation of a X-Ray source [44].

Due to special needs in sample types and sample preparation, it was necessary to modify some of the standard parts. With the original setup it was not possible to achieve high temperature (>1200 K) for a longer time in a reliable way. We had to change the position of the e-beam filament and some details on the sample stage (see Fig. 2-51). Also the screws and the tungsten spider (Fig. 2-6 and Fig. 2-7) of the high temperature sample plate were loosened after some heating cycles; this caused vibrations on the sample during STM measurement which made it impossible to get atomic resolution. The grounding of the sample stage was unreliable and had also been fixed to get the LEED/Auger unit working.

2.1.2.1 Sample Mounting and Transfer

In the original design thick samples (e.g. head-shaped single crystals as used in this work) were fixed on the sample holder with a spacer ring and a tungsten spider (see Fig. 2-6). The upper and lower sample plates were screwed together using bolt spacers (all materials are made of molybdenum). Assembling was made much easier by a mold, designed by our technician Johannes Frank. As mentioned in the previous chapter, this design has some major disadvantages and therefore was responsible for a significant loosed time for practical measurements. Thermal and electrical contact of the crystal to the sample plates caused heating up the whole sample plates (and also the sample stage). The tungsten spider agglomerated on the back side of the sample, which made it necessary to intensive mechanical cleaning of the sample back side after every sample-mounting (and also wasting a spider for each sample, even though they are a low cost consumable supply). Additionally, temperature reading by the installed type K thermocouple was not reliable, which had to be redesigned and controlled by a pyrometer.

Using a ceramic washer between the sample lower plate and a ceramic plate with a hole (see Fig. 2-9) between the sample and upper plate was the improvement to get stable high temperatures for a longer time and preserving the stage. Here, the sample was grounded with a thermocouple wire to the plate to get the necessary conductivity for STM measurements. Unreliable temperature reading could be solved by redesigning the thermocouple contact from sample plate to the stage (see Fig. 2-8) using an Alumel/Chromel foil. This fixed also the problem of rebending the thermocouple contact what was necessary after a few times of transferring the sample in/out of the stage. But this design needs also some more improvement because of limited space in the STM stage.

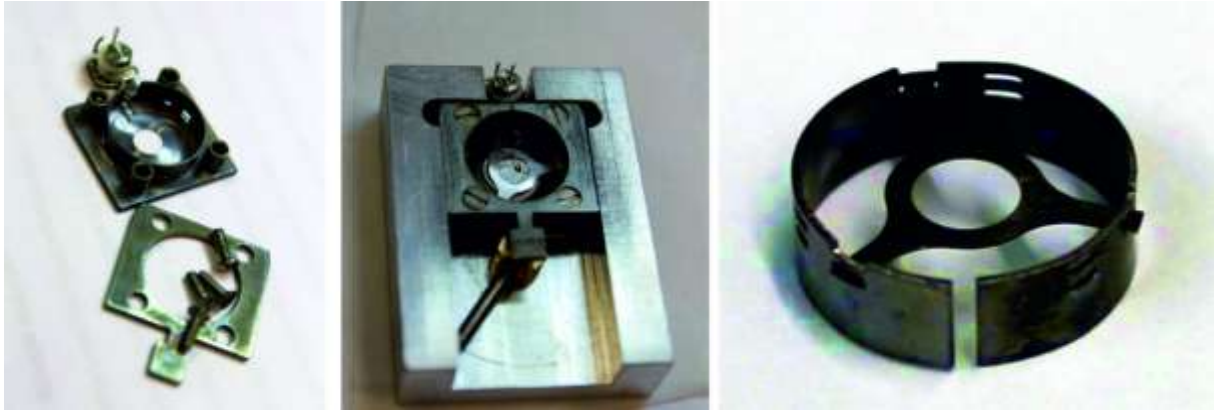


Fig. 2-6: Assembling parts of the original sample plate for thick head-shaped crystals. The sample is clamped with a “spider” (picture on the right side). The mold for sample plate assembling (picture in the middle) is a self-made design by our technician.

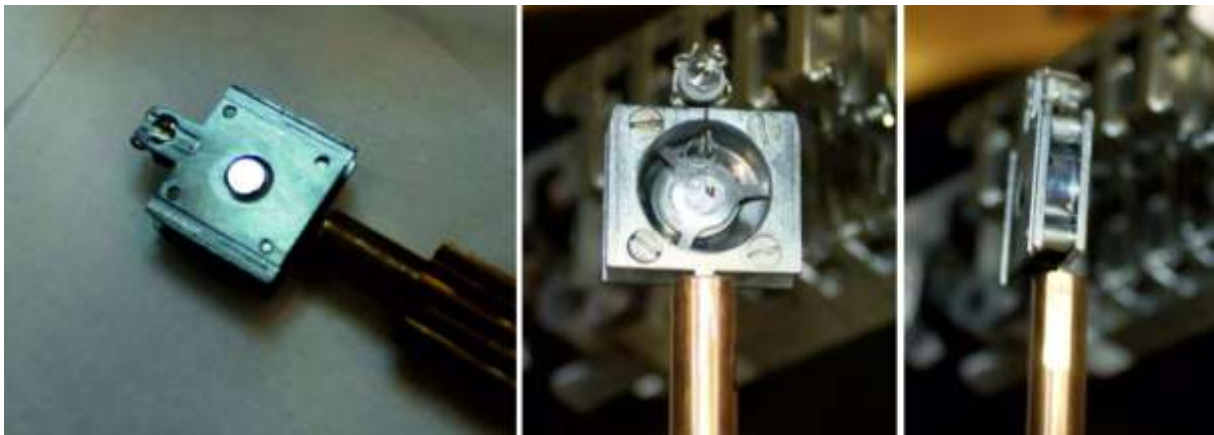


Fig. 2-7: Original sample plate for thick head-shaped crystals. The missing thermal/electrical insulation of the sample to the sample plate makes it impossible to reach stable high temperatures, as needed for sample preparation.

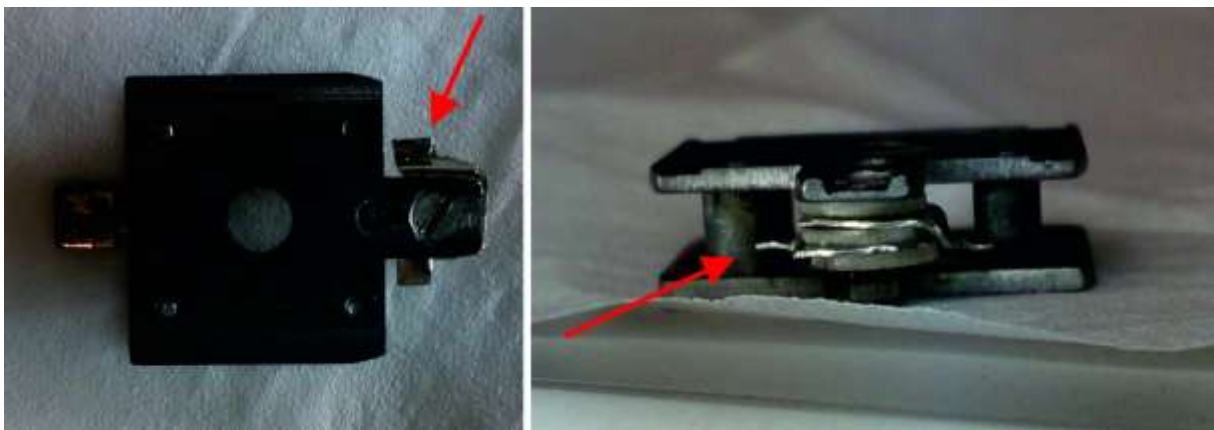


Fig. 2-8: New design of the K type thermocouple contact (sample holder to stage).

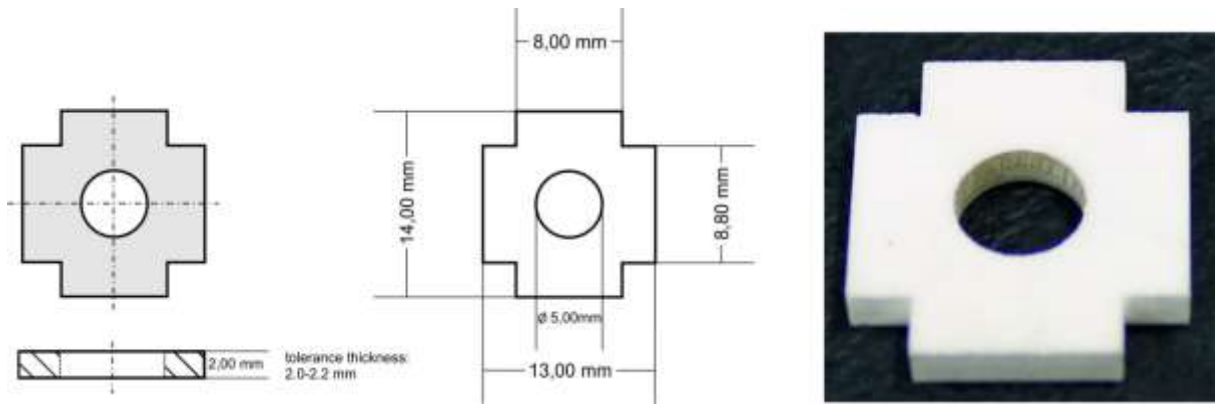


Fig. 2-9: Custom made ceramic plate (Al_2O_3) to cover and insulate the single crystal in the sample holder.

2.2 Polarization Modulation Infrared Reflection Adsorption Spectroscopy (PM-IRAS)

Infrared (IR) spectroscopy is a widely used and effective spectroscopic method in surface science [45]. IR spectroscopy for the study of adsorbed species on metal surfaces was used since the 1960s. This approach, using single reflection of an IR beam at grazing incidence, is called IRAS (sometimes abbreviated with IRRAS). It allows obtaining information of chemical identity, geometry and adsorption sites of adsorbed species over a wide spectral range. IRAS is not restricted to high vacuum (contrary to most other surface sensitive methods) and is also applicable to more realistic samples like metal nanoparticles supported on oxides. Thus, IRAS can bridge the gap between model catalysts and “real” catalysts. IRAS and Electron Energy Loss Spectroscopy (EELS) offer excellent sensitivity (0.1 to 0.01 % of a monolayer), and can be applied to a broad spectral range. EELS is restricted to highly ordered surfaces, limited to a maximum operating pressure of about 1×10^{-6} mbar and has a rather poor spectral resolution (about of 5 to 30 cm^{-1}) [39, 46-48]. Vibration frequency is characteristic for the adsorbed species and its chemical environment.

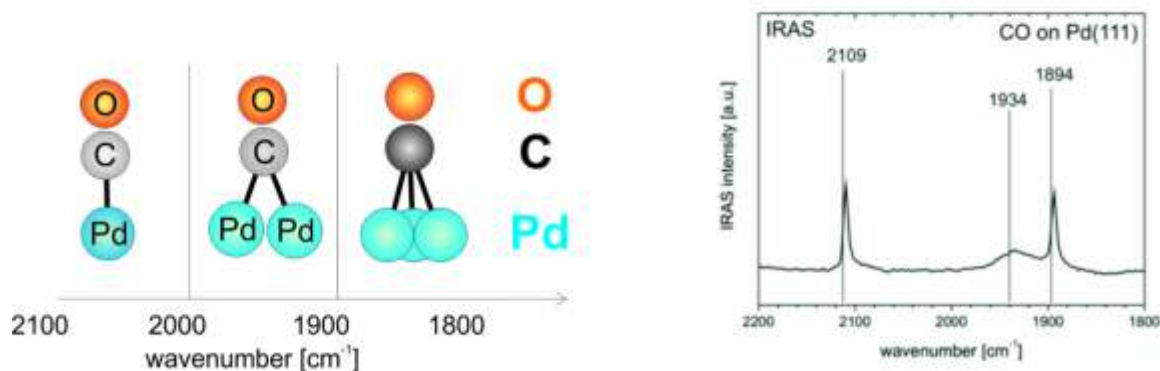


Fig. 2-10: Scheme of CO bonding (on-top, bridge, three-fold hollow) on Pd (left) with the corresponding IRAS spectrum (right).

Tab. 2-1: Molecular orbital description of CO-bonding.

CO-Bonding			
	M(σ) \leftarrow CO(5σ) σ -Donator WW „Hinbindung“	M(π) \leftarrow CO(1π) π -Donator WW „Hinbindung“	M(π) \rightarrow CO(2π) π -Akzeptor WW „Rückbindung“
M-C	increase \uparrow	increase \uparrow	increase \uparrow
C-O	increase \uparrow	decrease \downarrow	decrease \downarrow
ν_{CO}	increase \uparrow	decrease \downarrow	decrease \downarrow

General details about CO bonding on metal surfaces can be found in chapter 2.10.1.

2.2.1 Principles

IR spectroscopy in transmission or diffuse reflectance (Diffuse Reflectance Infrared Fourier Transform Spectroscopy, DRIFTS) mode is one of the most important techniques to study the adsorption properties of powder catalysts. Thus, IRAS more or less allows transferring the understanding between model systems and “real” (industrial grade) catalysts. The whole IR range from Far-infrared (FIR) to Near-infrared (NIR) is accessible, with a main principle resolution below 1 cm^{-1} [39].

Transmission IR spectroscopy cannot be performed on nontransparent samples. Therefore, one has to operate in reflection mode (i.e. the sample itself acts as a mirror for the incident IR beam). Besides the regular IR selection rules ($\Delta\nu = \pm 1$, $\Delta J = \pm 1$), on metallic samples, the so-called metal surface selection rule applies [49].

The main consequences of this selection rule are:

- Vibrations on metallic surfaces can only be excited if the incident IR beam possesses a p-polarized component
- Only molecular vibrations with a dynamic dipole moment perpendicular to the metal surface can be excited

A reason for this is the formation of so-called image dipoles below the metal surface, created by the electrons of the substrate, as shown in Fig. 2-11 for a diatomic molecule. The image dipole of molecules which are parallel adsorbed to the surface is exactly in opposite to the molecules dipole

moment. Therefore, the total dipole moment vanishes and the vibration is inactive for IR spectroscopy. Vibrations perpendicular to the surface may even be enhanced because the p-component of the electric field is amplified under the condition of grazing incidence [50].

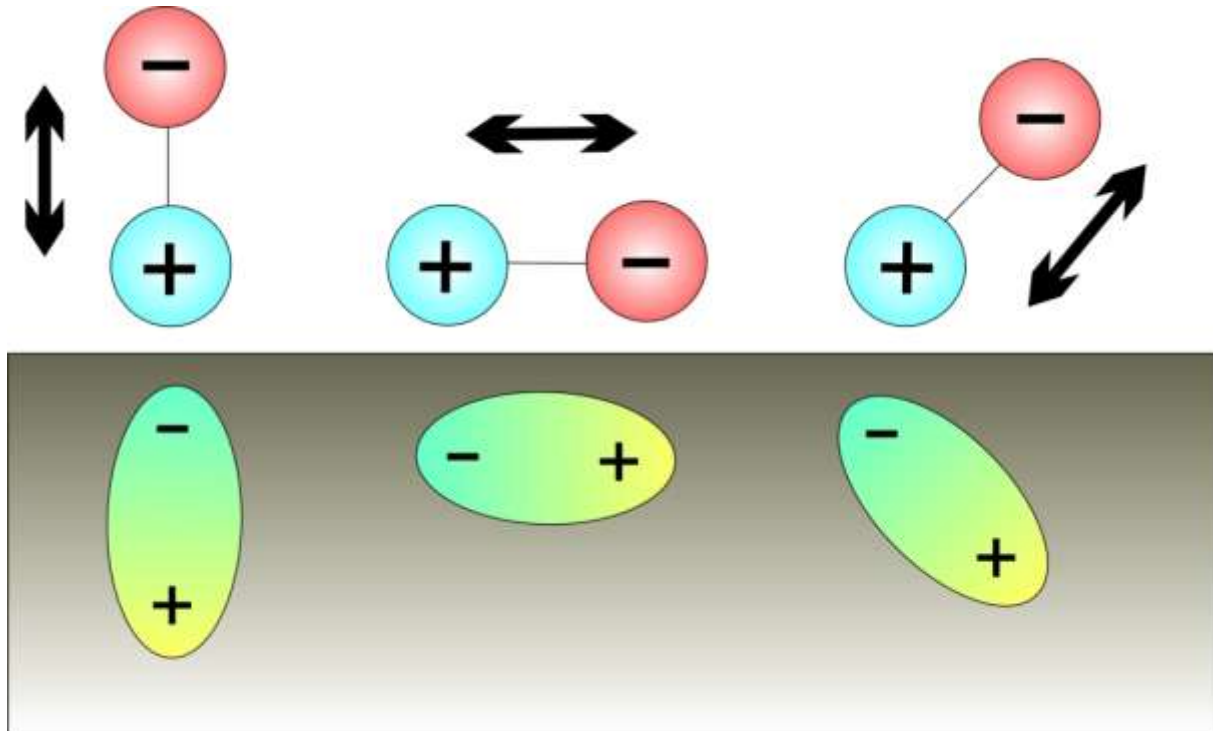


Fig. 2-11: Dipoles of a bi-atomic molecule.

The second part of the metal surface selection rule can be explained as shown in Fig. 2-12. The incoming wave strikes the surface under a certain angle of incidence Φ (angle between incoming wave and surface normal; see Fig. 2-12), and is reflected from the surface at the same angle.

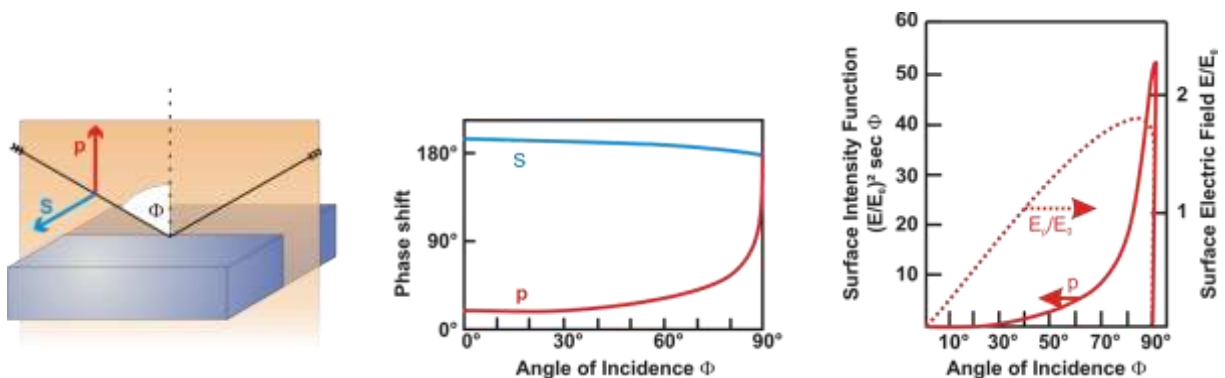


Fig. 2-12: Reflection of an IR beam on a metal surface. a) Polarization planes and angle of incidence. b) Phase shift upon reflection. c) Surface Electric field and Intensity of p-polarized light vs. angle of incidence [39, 48].

If the polarization vector of the incident wave is parallel to the plane created by the incoming and outgoing beam, it is called p-polarized (from the German word “parallel”), and if the polarization vector is perpendicular to this plane as s-polarized (from the German word “senkrecht”). E_p and E_s are the corresponding electric field components.

The electromagnetic wave endures a phase shift depending on the angle of incidence. This phase shift has an almost constant value of 180° for the s-polarized component and therefore the electric field is vanished by destructive interference (see Fig. 2-12). In contrast, the phase shift for a p-polarized component depends strongly on the angle of incident. It is low for small and medium values of Φ but finally increases to 180° as soon as the angle of incidence approaches 90° . Under the condition of grazing incidence a large electric field is set up on the surface. Fig. 2-12 shows the resulting electric field E_p versus Φ .

Assuming that the total absorption intensity depends on the square of the surface electric field and the number of molecules, one can derive a function $E_p^2 \sec(\Phi)$ [51]. The amplitude of this surface intensity function shows a strong narrow maximum at approximately 88° , i.e. grazing incidence. This leads to the experimental necessity to do IRAS measurements at or close to grazing incidence.

One can resolve the electric field vector of IR light into s-polarized (incident plane) and p-polarized components (perpendicular to the incident plane).

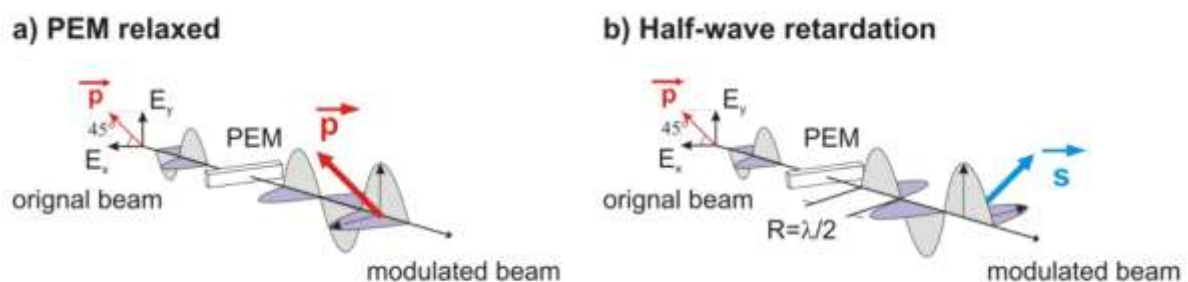


Fig. 2-13: Principle of polarization modulation with a PEM a) relaxed and b) half-wave retardation respectively.

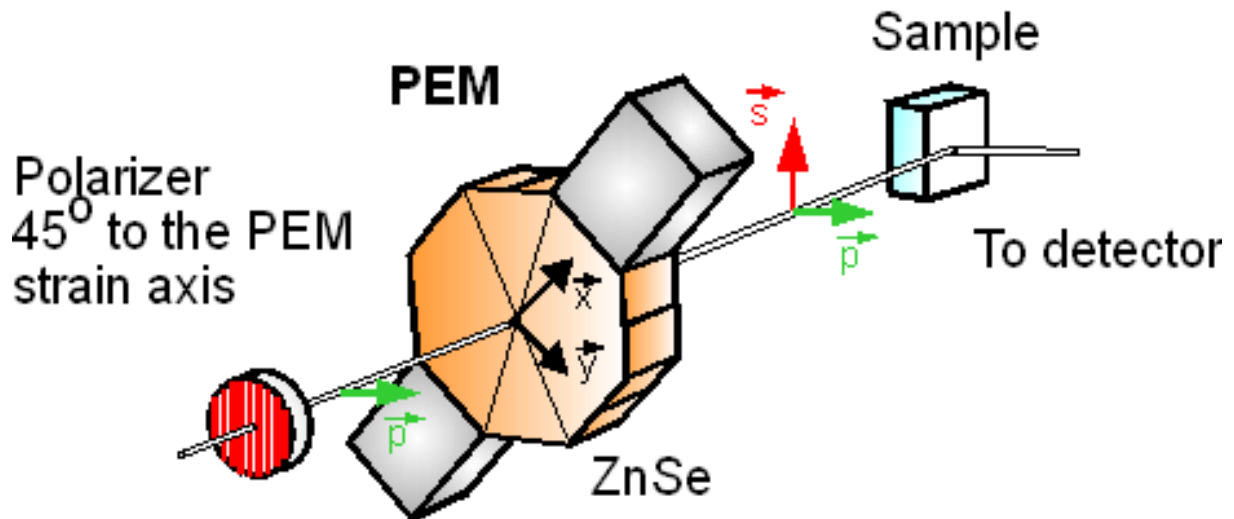


Fig. 2-14: Polarizer and ZnSe-photoelastic modulator used for PM-IRAS.

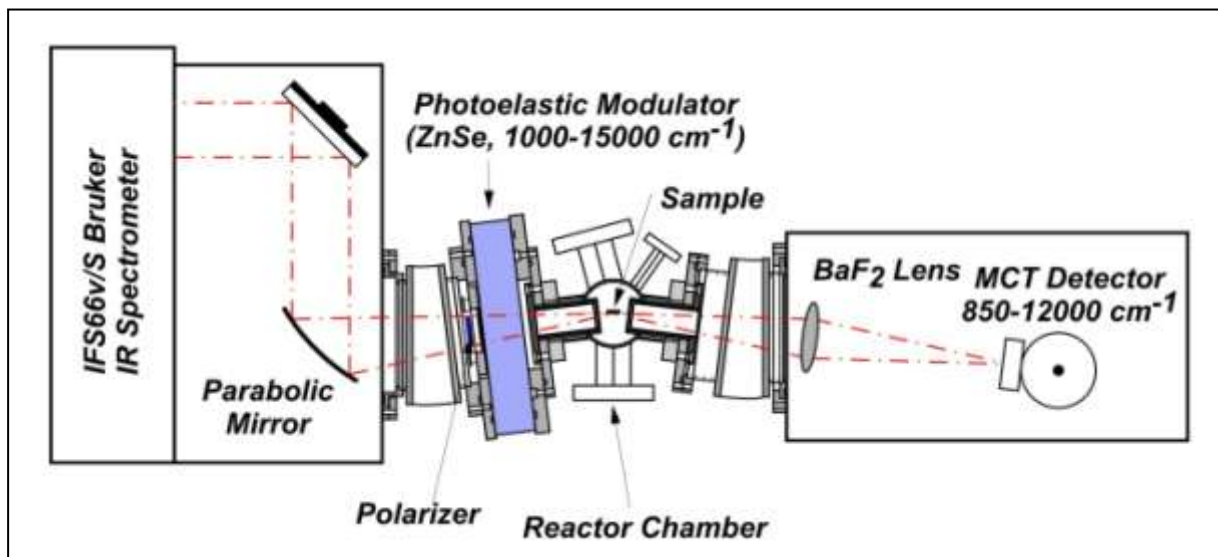


Fig. 2-15: Sketch of the PM-IRAS setup in our lab.

Second order Bessel function:

The PM-IRAS spectrum, also called differential reflectance spectrum ($\Delta R/R$), is then calculated from the two simultaneously acquired spectra by equation (1.1.1) [52].

$$\frac{\Delta R}{R} \approx \left[\frac{1 - \cos \varphi_0}{2} - \frac{2 \cdot I_p - I_s}{I_p + I_s} \times \frac{\sin^2 \varphi_0}{8} \right] \times \frac{2 \cdot I_p - I_s}{I_p + I_s} \quad (1.1.1)$$

According to Barner and Hipps [52, 53] this can be modified to equation (1.1.2):

$$\frac{\Delta R}{R} \approx J_2 \varphi_0 \cdot \frac{R_p - R_s}{R_p + R_s} \quad (1.1.2)$$

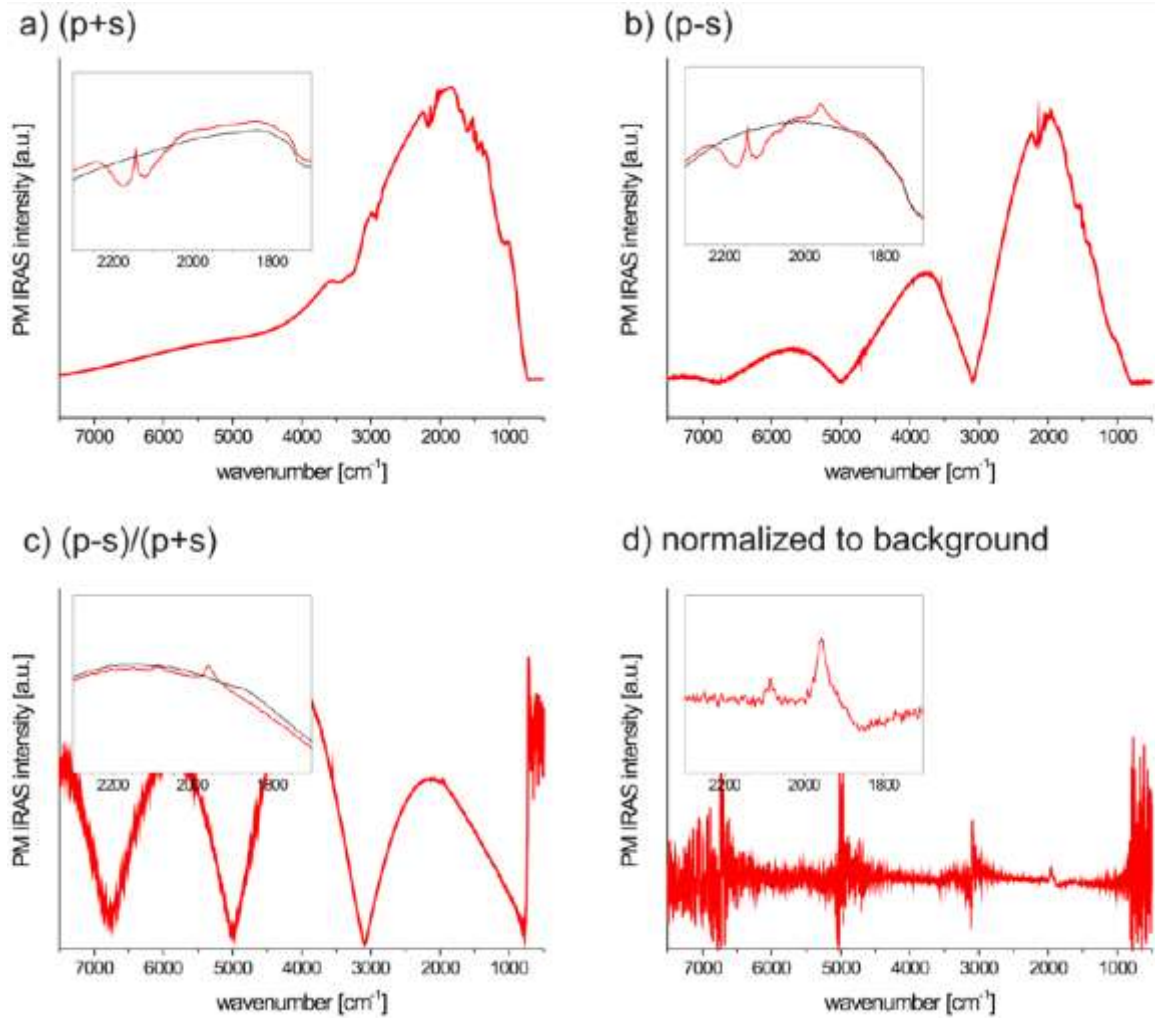


Fig. 2-16: Data processing in PM-IRAS using CO adsorption on Pd(111) as example: a) average spectrum, b) modulated difference spectrum, c) differential reflectance spectrum (to the spectrum of the clean Pd(111) surface) and d) final PM-IRAS spectrum after normalizing. The inserts show magnifications of the range between 2300 cm^{-1} and 1700 cm^{-1} . The black curves in the inserts represent the corresponding background spectra of the empty surface.

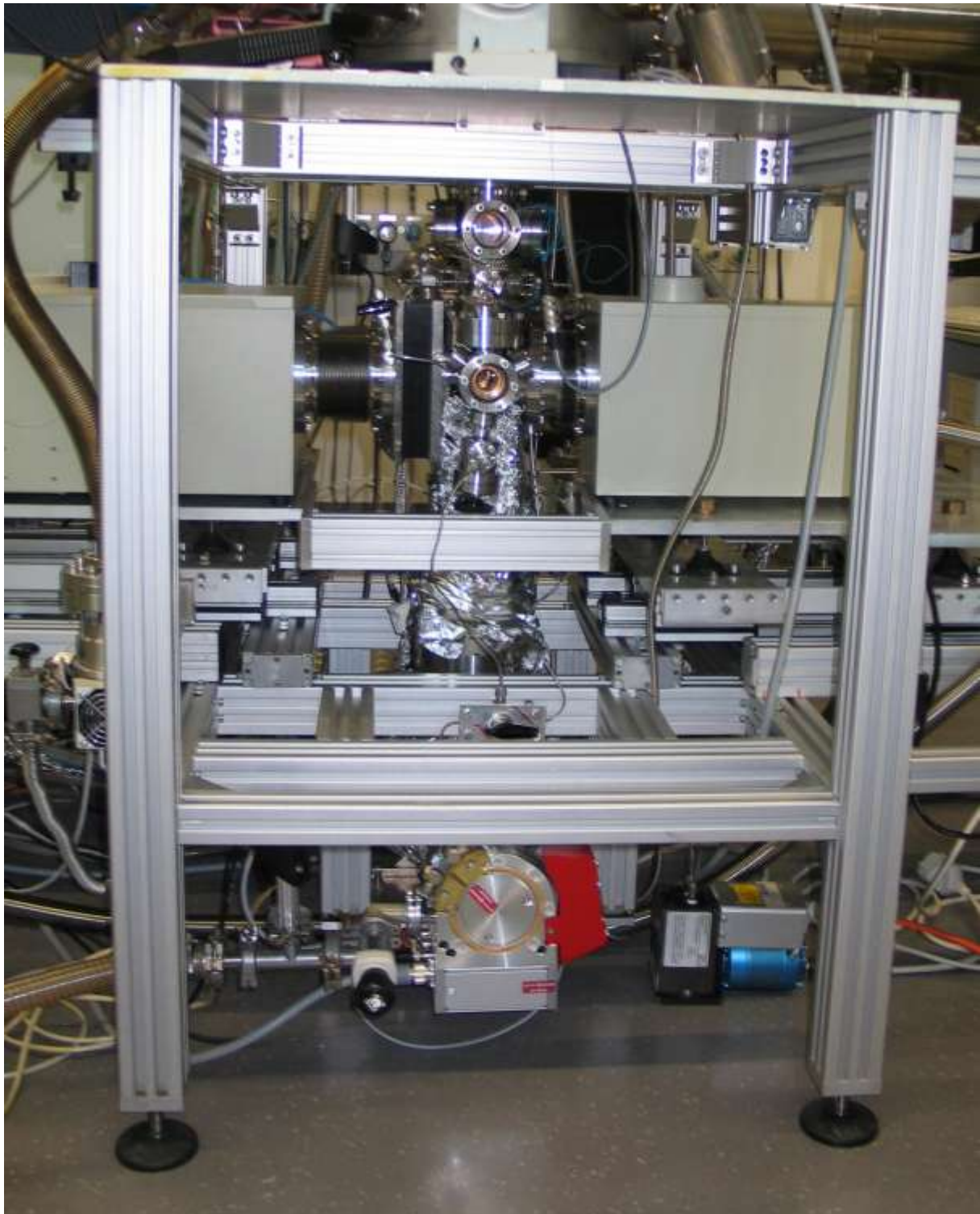


Fig. 2-17: PM-IRAS setup (left side: IR modulator, middle: high pressure chamber, right side: detector).

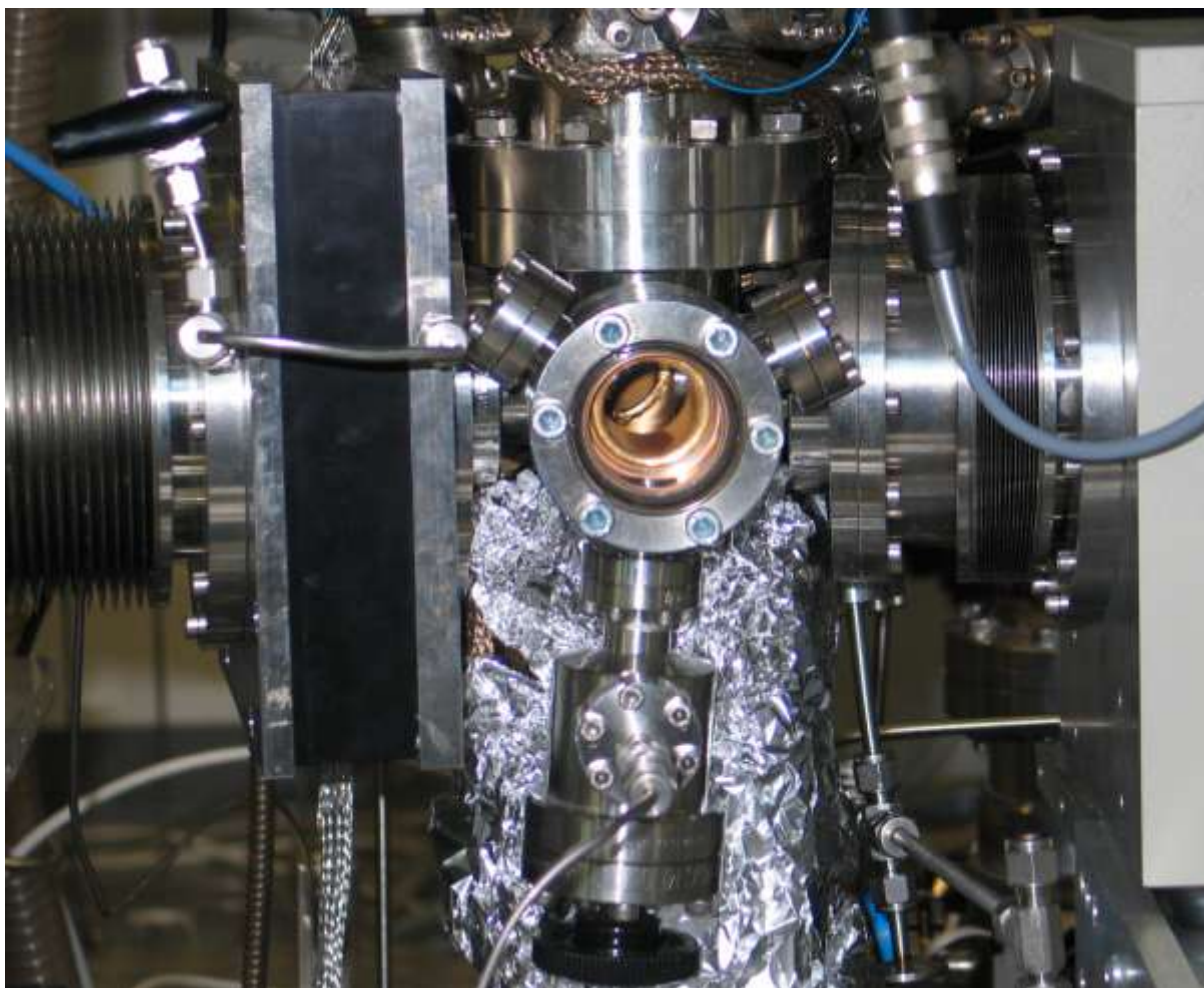


Fig. 2-18: PM-IRAS Setup. Detailed view of the high pressure cell.

MCT Detector:

The two main types of IR detectors are thermal and photonic (photodetectors). The thermal effects of the incident IR radiation can be followed through many temperature dependent phenomena. Bolometers and microbolometers are based on changes in resistance. Thermocouples and thermopiles use the thermoelectric effect. In IR spectrometers the pyroelectric detectors are the most widespread. The response time and sensitivity of photonic detectors is usually much higher, but these have to be cooled to cut thermal noise.

Mercury cadmium telluride (HgCdTe, MCT) is a common material for photodetectors used in Fourier transform infrared spectrometers. HgCdTe is a zincblende II-VI ternary alloy of CdTe and HgTe with a tunable bandgap spanning the shortwave infrared to the very long wave infrared regions. The amount of cadmium (Cd) in the alloy (the alloy composition) can be chosen so as to tune the optical absorption of the material to the desired infrared wavelength. CdTe is a semiconductor with a bandgap of approximately 1.5 eV at room temperature. HgTe is a semi-metal, hence its bandgap energy is zero. Mixing these two substances allows one to

obtain any bandgap between 0 and 1.5 eV. The detection occurs when an infrared photon of sufficient energy kicks an electron from the valence band to the conduction band. Such an electron is collected by a suitable external readout integrated circuits (ROIC) and transformed into an electric signal. The main limitation of MCT detectors is that they need cooling to temperatures near that of liquid nitrogen (77K), to reduce noise due to thermally excited current carriers. On the other side, MCT features high detection speed sensitivity. The spectral range is 12500-400 cm^{-1} [54, 55].

2.2.2 Data Processing and Acquisition

Most of data processing was first done by the very powerful (but not always user-friendly) software OPUS 4, which was provided by the manufacturer (Bruker), and exported as simple text files, readable for OriginPro and MS Excel for further data preparation and presentation.

2.3 X-Ray photoelectron Spectroscopy (XPS)

The photoelectric effect was experimentally observed by Heinrich HERTZ and Wilhelm HALLWACHS [56, 57] and explained by Albert EINSTEIN in 1905 who was awarded with the Nobel prize in physics [58, 59]. He used the concept of a light quantum (photon) to describe the process of photoemission from the surface. The ejection of an electron requires more energy than the work function of the material. Increasing the intensity of the photons increases the number of ejected electrons, but not the energy that each electron possesses. The time lag between the incidence of radiation and the ejection of the electron is small ($< 10^{-9}$ s). The energy of the photoelectrons emitted is exactly the energy of the incident photon minus the work function of the material, which makes it possible to use this effect as an analytical instrument.

Photoelectron spectroscopy (PES) was developed beginning in 1960 by Kai Manne Börje SIEGBAHN at the University of Uppsala for which he was awarded for Nobel prize [60-62]. It is a powerful tool to study the energy levels of atomic core electrons.

2.3.1 Theory

PES has been segmented into ultraviolet photoelectron spectroscopy (UPS) and X-ray photoelectron spectroscopy (XPS), according to the source of radiation.

In UPS, valence electrons ($E < 40$ eV) are emitted from the sample by using an UV-light source for irradiation, while in XPS core level electrons ($E > 40$ eV) are excited using an X-ray gun ($AlK\alpha$, $MgK\alpha$) or synchrotron radiation.

Although the penetration depth of X-Rays is in the μm range, the escape depth of photoelectrons out of the sample is about 3-30 Å, depending on the radiation energy and the angle to the detector.

The principle of the photoemission process is shown in Fig. 2-19. The conducting sample needs to be in electrical contact with the spectrometer so both have a reference for measuring the electron energy called *Fermi level* (E_{fermi}). XPS is a relatively nondestructive method for many materials because only the ejection of electrons is required for analysis. The detection limit is about 0.1% of a monolayer [63].

X-Ray photoelectron spectral peaks are named according to the orbitals ($l=1, 2, 3\dots$) and the spin ($s=\pm 1/2$) of the core level from which the electrons are ejected (example: Pd $3p=1 - 1/2 = 1/2$ and $1 + 1/2 = 3/2$). XPS is sensitive to all elements except of hydrogen and helium - H and He within solids are not detectable by XPS because their photoelectron cross sections (yields) are below XPS detection limits. This arises from two effects, the photoelectron cross-sections decrease with decreasing atomic number and XPS is not highly sensitive to valence electrons (hydrogen and helium only have valence electrons, while XPS analysis is optimized toward core electrons).

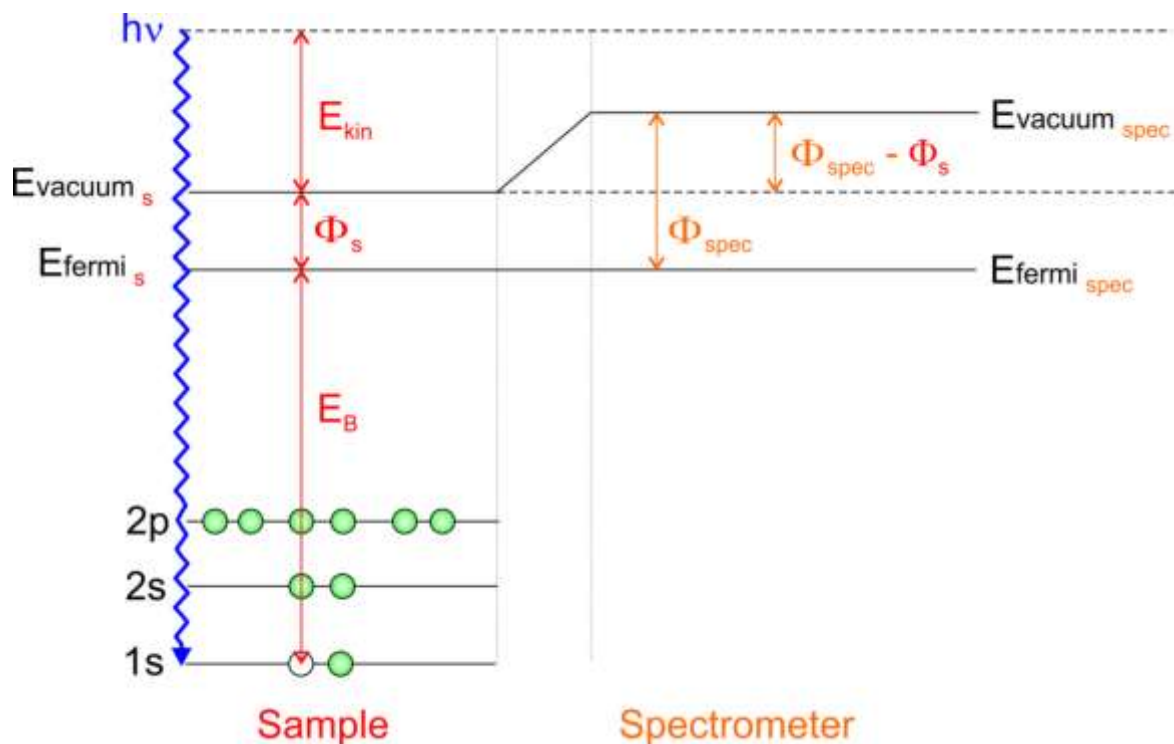


Fig. 2-19: Scheme of the energy levels in XPS. The ejection of an electron requires more energy than the work function of the material.

$$E_{kin} = h\nu - E_B - \Phi_{spec} \quad (1.1.3)$$

(E_{kin} =kinetic energy at the sample surface, E_b =binding energy, Φ_{spec} =work function of the spectrometer)

The work function is the required energy to remove the electron from the fermi level to the vacuum level. The work function of the sample Φ_s is not directly involved in the measurement of the kinetic energy that is seen by the spectrometer. The binding energy can be calculated from the measured kinetic energy with Eq. (1.1.3).

Secondary processes:

Photoionization is accompanied by two other secondary emission processes (see Fig. 2-20). In x-ray fluorescence (XRF), after removal of an electron of the inner orbitals by radiation, electrons from higher orbitals can fill the hole left behind. The released energy in form of a photon is equal to the energy difference of the two orbitals involved and thus characteristic to the atoms present. The other process is the emission of an Auger-electron (see chapter 2.4.).

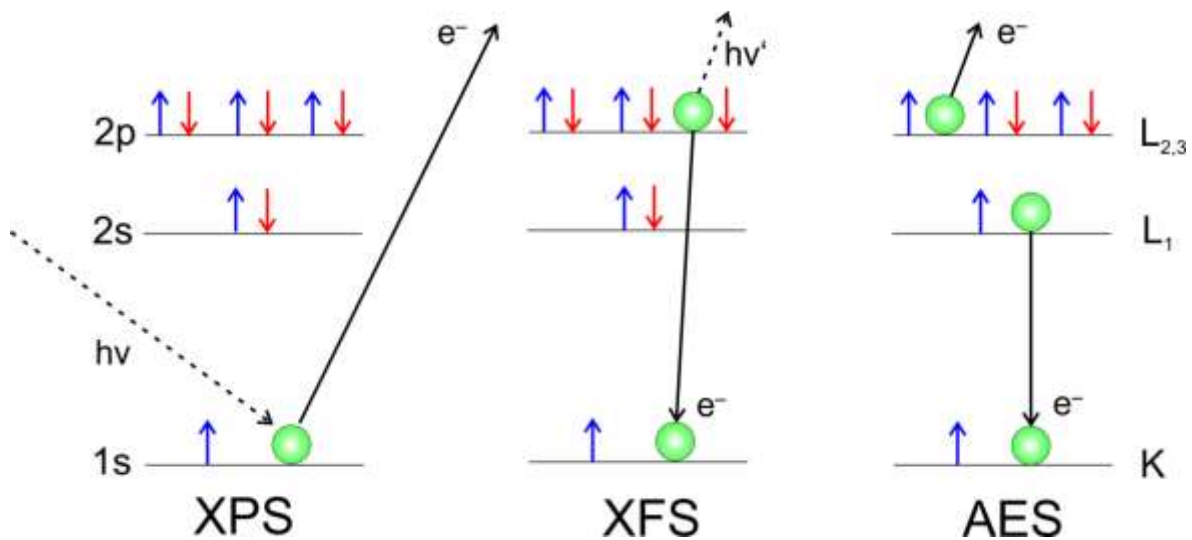


Fig. 2-20: Photoemission for XPS and secondary processes (X-Ray fluorescence and Auger electron spectroscopy).

XFS is dominated at higher photon energies (~10 kV) and therefore the effect is negligible in lab-based XPS systems due to the relatively low photon energy of common X-ray sources (AlK α =1486.6 eV, MgK α =1253.6 eV). On the contrary, Auger excitations commonly appear in XP spectra [63, 64].

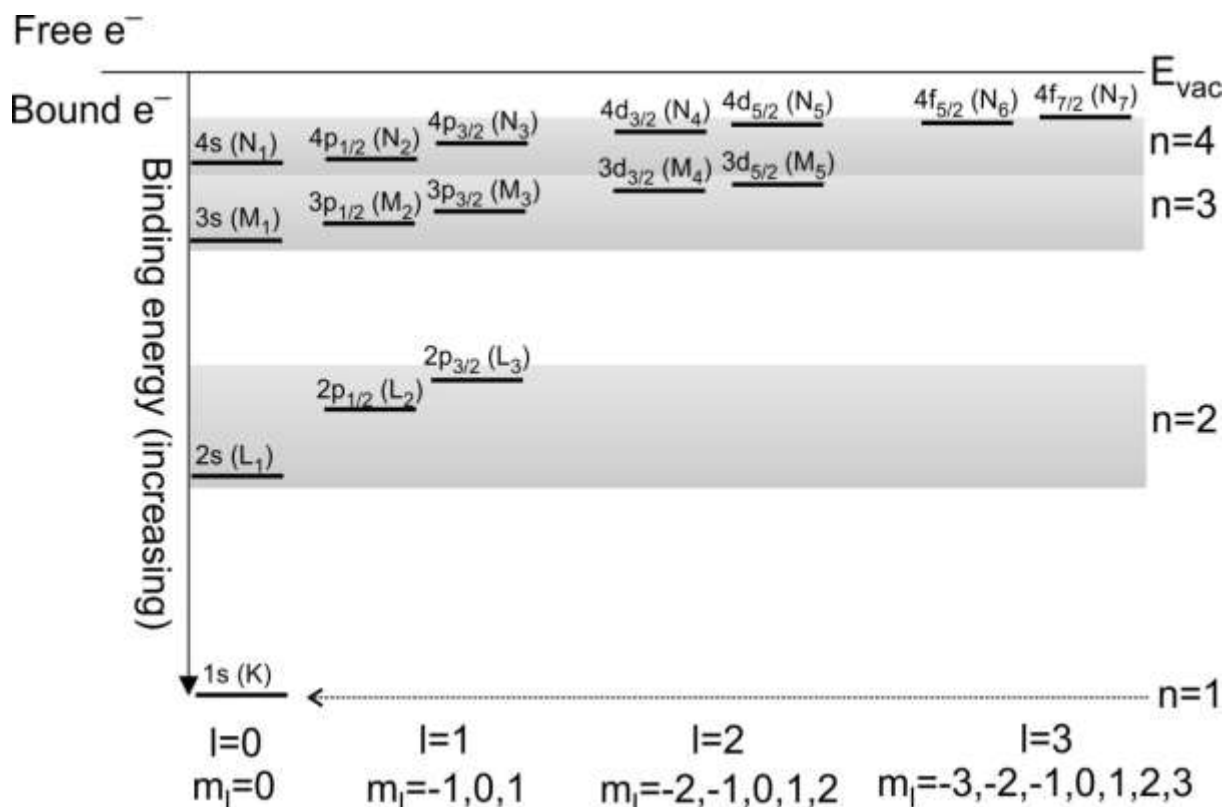


Fig. 2-21: Scheme of available stationary states (not to scale). These starts to merge with increasing n , that is, as E_{Fermi} is approached. Spectroscopic notation is describing these levels is shown above and X-ray notation is shown in brackets.

Nomenclature:

There are two types of nomenclature used to describe the stationary states in an atom, irrespective of whether they are occupied or not. Both describe the same thing, and are directly related to the quantum numbers (see Fig. 2-21). The spectroscopic notation was developed by chemists, while X-ray notation was developed by physicists. As a result, in XPS, which was developed by chemists, spectroscopic notation is used, while AES (and also XRF and EELS), which were developed by physicists, use X-ray notation.

Spectroscopic notation uses a specific integer followed by a specific letter to define a particular stationary state. The number used is the same as the principal quantum number of the electron that occupies this level. The letter relates to the angular quantum number. An s orbital (*sharp*) describes the stationary state occupied by electrons with the angular momentum quantum number $l=0$. A p orbital (*principle*) describes the stationary state occupied by electrons with $l=1$. A d orbital (*diffuse*) describes the stationary state occupied by electrons with $l=2$ and an f orbital (*fundamental*) describes the stationary state occupied by electrons with $l=3$.

A variation in the energy of a stationary state containing electrons with the same n and l quantum numbers can occur if spin orbit splitting is in effect. The energy levels resulting from this splitting are labeled by the quantum number j presented in subscript form following the principle and angular momentum designation. As an example, the 2p level has two energetically distinct levels arising from spin orbit splitting that are referred to as the $2p_{1/2}$ and $2p_{3/2}$ levels. All p , d , and f orbitals split into doublets described by the respective j values.

X-ray notation uses capital letters K, L, M, N, O, \dots to denote the principal quantum number, starting with K for electrons with $n=1$. Levels in the valence region, close to vacuum level, can become indistinguishable in energy and are often assigned the letter V (valence). Sublevels are designated by an integer value as a subscript (1 is used for the level with highest binding energy of the electrons, e.g. the 2s level is represented as L_1 , and the $2p_{1/2}$ and $2p_{3/2}$ levels are referred to as the L_2 and L_3).

To give an example, the creation of a 1s core hole in an aluminum atom followed by the transition of a $2p_{3/2}$ electron to fill this core can be described in full spectroscopic notation as follows:

- The creation of the hole: $1s^2 2s^2 2p^6 3s^2 3p^1 \rightarrow 1s^1 2s^2 2p^6 3s^2 3p^1$
- And the transition: $1s^1 2s^2 2p^6 3s^2 3p^1 \rightarrow 1s^2 2s^2 2p^5 3s^2 3p^1$

In X-ray notation the transition is denoted as a KL_3 transition. Such transitions result in either Auger electron emission or X-ray emission, the X-ray notation is favored. The Auger process (assuming the emitted electron is from the $2p_{1/2}$) is referred as KL_3L_2 . For fluorescence, the emission is referred to as a KL_3 X-ray, or in the Siegbahn X-ray convention as a $K\alpha_1$ X-ray. In this notation, the Greek letter denotes allowed transitions from stationary states of the next principal quantum number (the order being $\alpha, \beta \dots$) and the subscribed number refers to the relative intensity (1=most intense) [65, 66].

Background of the XP spectra:

The high binding energy side has a higher background (see Fig. 2-22) due to the partial loss of kinetic energy of the ejected electron because of inelastic collisions on the way through the material. Counts from these energy losses have a reduced kinetic energy and show a higher binding energy as one can see from Eq. (1.1.3). The high background at more than 900 eV is due to bremsstrahlung (generated from the X-Ray source).

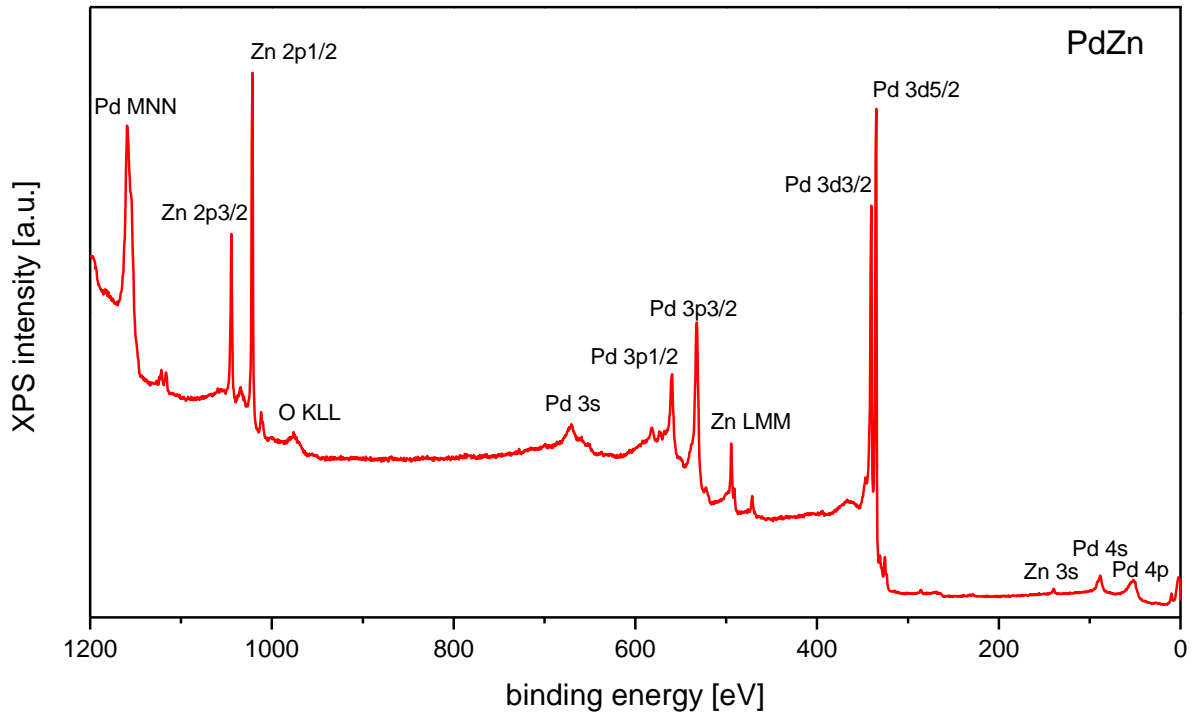


Fig. 2-22: XPS survey scan of a Pd(111) sample evaporated with 3 ML Zn. XPS and Auger signals are visible.

For performing spectroscopy, the photoelectrons have to escape from the probe surface into the vacuum level and then they have to be detected by the analyzer.

Measuring conditions:

Ultrahigh vacuum (UHV, see Chapter 2.9 for details) is necessary for XPS measurements. First, pressures below $\sim 10^{-6}$ mbar are required to operate filaments and anode without damage of the X-Ray source (in our system the interlock is set to $5 \cdot 10^{-6}$ mbar). Second, high vacuum is required for a sufficient inelastic mean free path (IMFP) for the photoelectrons to reach the detector. The concept of the mean free path for a photoelectron is analogous to the mean free path of a molecule in kinetic theory of gases. Another reason why UHV is needed, for all surface science experiments, is the minimization of surface contaminations. The exposure of 10^{-6} mbar during one second corresponds to 1 L (Langmuir). The exposure of a surface can be mathematically described as fluence, the number of particles per area (Φ) is the flux (J_N) integrated over time, see Eq. (1.1.4).

$$\Phi = \int J_N dt \quad (1.1.4)$$

And, derived from kinetic energy, J_N can be expressed in Eq. (1.1.5):

$$J_N = p \cdot \sqrt{\frac{1}{2\pi \cdot k \cdot T \cdot m}} \quad (1.1.5)$$

(p =pressure, k =Boltzman constant, T =temperature, and m =mass of a given molecule)

Assuming a sticking coefficient of 1.0, one L leads to the adsorption of one monolayer of an adsorbate. The sticking coefficient describes the ratio of the number of molecules that adsorb on the surface to the total number of molecules impinging on the surface during exposure [63, 67].

Experiments desired under higher pressures needs equipment like presented in chapter 0.

Radiation sources:

There are several requirements to make an X-ray source suitable for useful XPS. These are the energy resolution of radiation, the photon energy, and the ease of application of the anode material. For example, Y M γ ($h\nu=132.3$ eV, $fwhm=0.45$ eV) has a very narrow line width but too low photon energy for most elements to be analyzed. Cu K α ($h\nu=8048$ eV, $fwhm=2.5$ eV) has a very large excitation line, but the natural line width too large, this would limit to a poor spectral resolution. Si K α ($h\nu=1739.5$ eV, $fwhm=1.00$ eV) has both, sufficient photon energy and narrow line width; difficulties applying Si as anode material makes it impractical. Commercial lab systems usually uses a dual anode with Al K α ($h\nu=1486.6$ eV, $fwhm=0.85$ eV) and Mg K α ($h\nu=1253.6$ eV, $fwhm=0.70$ eV), both are fulfilling all technical requirements [68].

Though Al and Mg sources are named as “K α ”, this X-ray lines are a unresolved doublet (K $\alpha_{1,2}$) and have *satellite features*, K $\alpha_{3,4}$ and K β , this excitations are appearing as satellites and can lead to spectral misinterpretation. K $\alpha_{3,4}$ are about 10 eV on the low binding energy side with a tenth of intensity. K β excitations appear about 70 eV on the lower binding side, see also Tab. 2-2. These satellite peaks can be removed by using a monochromatized X-ray source. In nonmonochromatized systems the satellite intensities can be reduced by a thin aluminum foil X-ray window to reduce the bremsstrahlung from the X-ray source. Due to the large amount of energy used for radiation generation (13 kV, 300 W), the X-ray source needs sufficient water cooling [63].

Tab. 2-2: X-Ray satellites for Al and Mg sources: separation from main peak ($K\alpha_{1,2}$) and relative intensity.

Source	Al $K\alpha_{1,2}$	Al $K\alpha_3$	Al $K\alpha_4$	Al $K\alpha_5$	Al $K\alpha_6$	Al $K\beta$
Separation	0	9.8	11.8	20.1	23.4	69.7
Intensity	100	6.4	3.2	0.4	0.3	0.6
Source	Mg $K\alpha_{1,2}$	Mg $K\alpha_3$	Mg $K\alpha_4$	Mg $K\alpha_5$	Mg $K\alpha_6$	Mg $K\beta$
Separation	0	8.4	10.0	17.3	20.5	48.0
Intensity	100	9.2	5.1	0.8	0.5	2.0

A drawback of discrete line sources that some photoionization will be at minimum, others are at maximum for the same line energy. Tunable radiation is available from synchrotron sources as described in chapter 2.3.4.

Plasmon loss peaks are extrinsic plasmons with the origin in collective oscillations of an electron gas excited by interactions with electrons of sufficient kinetic energy. Intrinsic plasmons are excited by interaction of the emitted electron with the core hole. An example for plasmon excitation in PdZn is given in chapter 3.4.

Shake-up, shake-off, and multiplet splitting: the rearrangement of electrons after photoemission often results in an excited state some eV above the ground state. The photoelectron endures a loss in kinetic energy that raises a peak at the higher binding energy side of the main peak. For transition metals and rare earth metals these satellite peaks can be quite strong. Interaction of photoelectrons with valence band electrons cause *shake-off* lines. Photoelectrons in metals with a high electron density near the Fermi endure an energy loss by excitations in empty states above the Fermi edge, and, instead of discrete losses, a tail on the low kinetic energy side of the core level peak appears. This results in the typical asymmetric peak shape of many metals. Due to unpaired electrons in the valence band (or core levels near the valence band), an exchange interaction can occur during an s-electron emission because the remaining s-electron is also unpaired, giving rise to a doublet of the s-peak [69].

Chemical shift: the observed spectral characteristics (binding energy, peak width and shape, and sometimes bonding satellites) are also depending on the bonding state of an atom. Chemical bonding in a compound has an influence on the binding energy compared to bonding in the pure element, this is called “chemical shift”. If an atom is bonded to another one, a charge transfer to the atom with higher electronegativity occurs and the effective charge of the former becomes positive, thus increasing the binding energy and vice versa. Therefore, metal oxides typically show a shift of the metal XPS peaks to higher binding energies. In practice, listed data from handbooks [70] and online databases [71] are used for

interpretation of the observed chemical shift. The full theory of chemical shift includes also screening and relaxation effects, but this will not be discussed here in detail [50, 70, 72].

2.3.2 Quantification

The basis of XPS (and AES) quantification is the determination of the intensity of a characteristic signal from a measured spectrum. The most common method is comparison of the signal intensity using the elemental *relative sensitivity factor (RSF)*, which is independent of the excitation intensity. It is assumed that for a specific instrument (and constant instrument parameters) every pure element sample shows up with certain intensity. When measuring a sample with two or more components, the ratio of the peak areas, corrected with the RSF, are thought to be equal to the mole fraction of elements. The RSF values are listed in the operators manual of the instrument [65, 73, 74].

2.3.3 Analyzer and detector

The resolution of the energy analyzer needs to be sufficiently high to resolve peaks from different oxidation states and should be relatively constant for all transitions. A relative resolution, R , is required to match line widths by the absolute resolution at the highest radiation energies (see Eq. (1.1.6)).

$$R = \frac{\Delta E}{E_0} \quad (1.1.6)$$

(R =relative resolution of the detector, ΔE =absolute resolution defined by fwhm, E_0 =kinetic energy of peak position)

Using a $MgK\alpha$ source (fwhm=0.70 eV, $h\nu=1253.6$), a relative resolution of $6 \cdot 10^{-4}$ would be required. Attaining this resolution would suffer from enormous losses of sensitivity. Therefore the kinetic energy of the incoming photoelectrons is retarded to constant preselected pass energy of the analyzer. Using the example of a $MgK\alpha$ source from above, for a pass energy of 50 eV a relative resolution of $1 \cdot 10^{-2}$ is necessary. This can be achieved with acceptable loss of energy [63].

Sample charging is a result of accumulation of positive charge. Grounding the sample restores electrical neutrality. On nonconducting surfaces (e.g. oxides), ejected electrons are faster lost than new electrons can return to compensate charging. Thus Photoelectrons are ejected with a decreased kinetic energy. As a result peakshifts to higher binding energies and peak broadening can be observed in the spectra. Charging correction can be achieved using a reference peak or with an electron flood gun.

The hemispherical analyzer (HSA; also referred to Concentric Hemispherical Analyzer, CHA) consists of two concentric 180°-hemispheres, of radius R_1 and R_2 (see Fig. 2-23). Analyzed area and detector are situated in that way, that the path of electrons coming from the sample and arriving at the detector forms lines tangential to the average of R_1 and R_2 at both ends of the hemispheres. Applying specific potentials to these hemispheres, results in the deflection of electrons of a specific energy to the detector.

The most common operation mode works with acceleration/deceleration of the electrons to a constant energy value (pass energy) before entering the HSA (constant analyzer energy, CAE or fixed analyzer transmission, FAT mode). In this operation mode, the energy resolution remains independent of kinetic energy. A lower pass energy results in an improved resolution, but at the cost of sensitivity [75].

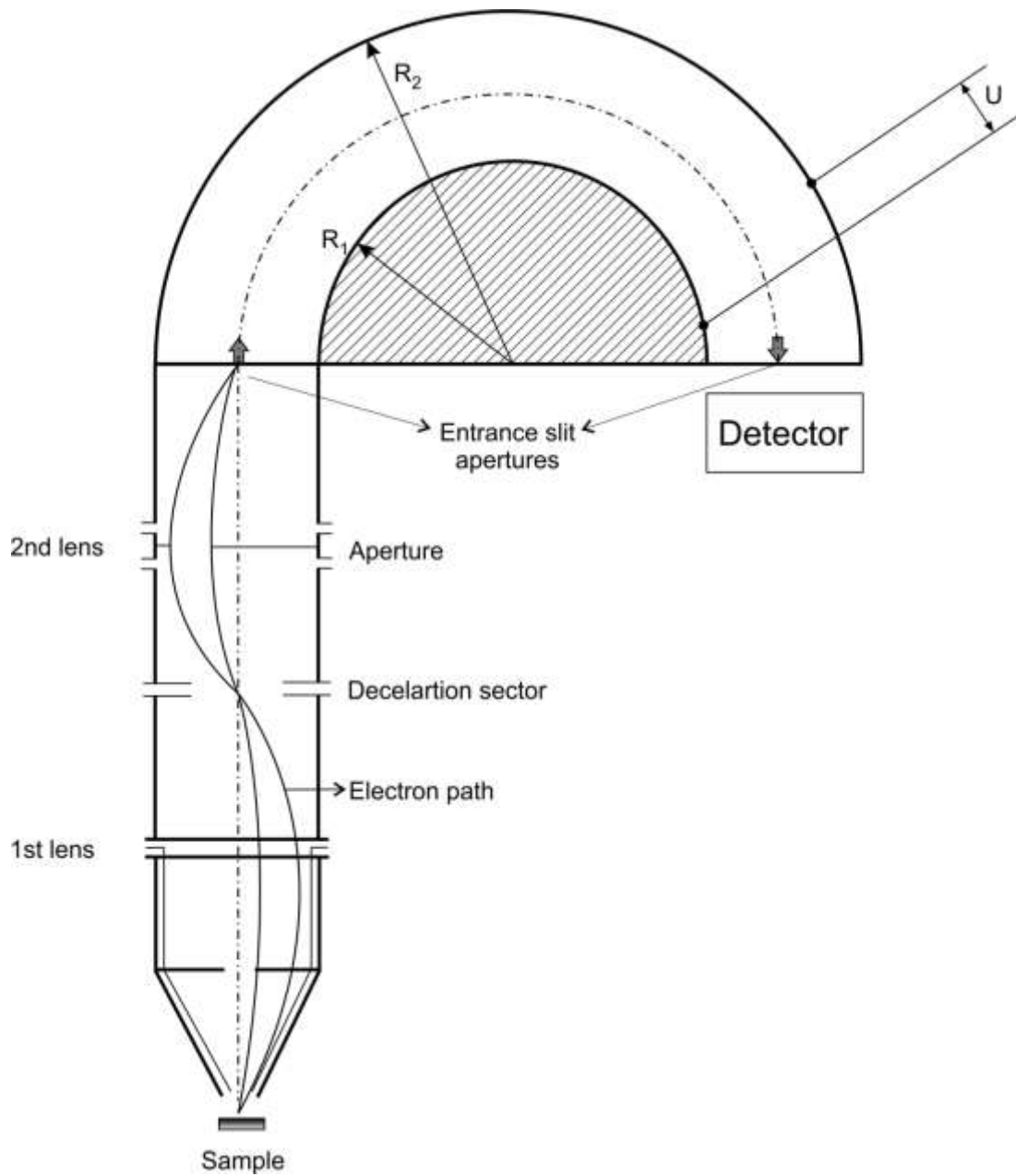


Fig. 2-23: Sketch and basic principle of a hemispherical analyzer (HSA).

The electric field \mathcal{E} of a sphere is proportional to the square of the radius:

$$\mathcal{E} = \frac{q}{4\pi\epsilon_0 r^2} \quad (1.1.7)$$

(ϵ =electric field; q =point charge; ϵ_0 =permittivity of free space; r =radius)

And therefore, the potential difference between inner and outer sphere is:

$$U = \int_{R_1}^{R_2} \frac{q}{4\pi\epsilon_0 r^2} dr = \frac{q}{4\pi\epsilon_0} \left(\frac{1}{R_1} - \frac{1}{R_2} \right) = \frac{q}{4\pi\epsilon_0} \cdot \frac{R_2 - R_1}{R_1 R_2} \quad (1.1.8)$$

(U =potential difference, R_1, R_2 =radii of inner and outer sphere)

The basic trajectory is given by the balance between centripetal and electrostatic force:

$$\frac{mv_0^2}{r_0} = -e\mathcal{E} = \frac{eU}{r_0^2} \frac{R_2 R_1}{R_2 - R_1} \quad (1.1.9)$$

(m =mass, v =tangential speed; r =radius of curvature; e =elementary electric charge)

From this it follows the pass energy:

$$E_0 = \frac{mv_0^2}{2} = \frac{eU}{2r_0^2} \cdot \frac{R_2 R_1}{R_2 - R_1} = \frac{eU}{2 \frac{R_1 + R_2}{2}} \cdot \frac{R_1 R_2}{R_2 - R_1} = eU \frac{R_1 R_2}{R_2^2 - R_1^2} = \frac{eU}{\frac{R_2}{R_1} - \frac{R_1}{R_2}} \quad (1.1.10)$$

The energy resolution in XPS (ΔE) can be defined as result from three parameters, the FWHM of the source (ΔE_p), the line width of the photoelectron emission (ΔE_n), and the energy resolution of the energy analyzer (ΔE_a)

Assuming that all components exhibit a Gaussian line shape, ΔE can be expressed as:

$$\Delta E = \left[\Delta E_p^2 + \Delta E_n^2 + \Delta E_a^2 \right]^{1/2} \quad (1.1.11)$$

The intrinsic line width of the photoelectron emission (ΔE_n) vary over a large range from <0.1 to >1.0 eV, arising from several factors including the irreducible line width (from the

core hole lifetime) and line broadening introduced by phonons (lattice vibrations). This results in a Gaussian–Lorentzian line shape [65, 76].

To obtain the best possible sensitivity, the detector must be capable of recording individual electrons (pulse counting mode). This signal is recorded in units of current (A), which are then represented in units of counts per second (also referred as intensity).

The current represents the passage of electrons across a fixed point in space per second. The passage of this single electron per second gives 1.602×10^{-19} A. The sensitivity of conventional pulse counting electronics is in the range of 10^{-15} A. Therefore, to record individual electrons, the detector used must exhibit a gain (multiplication factor of the original signal) of at least 10000. An electron multiplier (EM) consists of a group of detectors that operate by amplifying the signal generated by an electron impinging on the outermost surface of the EM exposed to the incoming electron beam. This configuration can be achieved by channeltron (CEM) or microchannel plate (MCP) detectors.

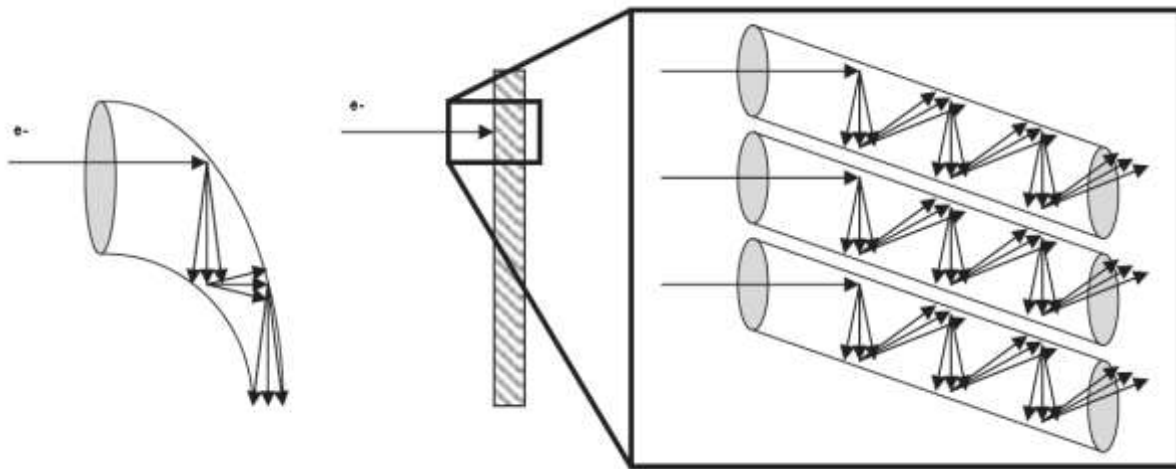


Fig. 2-24: Sketch of a channeltron detector (left) and microchannel plate detector (right)

A channeltron (see Fig. 2-24) is a continuous dynode structure, coated with an electron-emissive material (e.g. PbO). An electron thus creates an electron cascade.

A microchannel plate is in some manner an extension of a 1-D channeltron array consisting of a 2-D array of parallel capillaries, which are internally coated with an electron-emissive material to create an electron cascade [65].

2.3.4 Synchrotron (Maxlab II) and High Pressure XPS

For thermodynamic and/or kinetic reasons, the catalyst's chemical state observed under vacuum conditions is not necessarily the same as that of a catalyst under realistic operating pressures. Therefore, investigations of catalysts should ideally be performed under reaction conditions in the presence of a gas or gas mixtures. Using a differentially pumped analyzer separated by small apertures, XPS can be operated at pressures of up to 1 Torr, and with a recently developed differentially pumped lens system, the pressure limit has been raised to about 5 mbar. Here, we describe the technical aspects of high-pressure XPS and discuss recent applications of this technique to oxidation and heterogeneous catalytic reactions on metal surfaces.

For all High Pressure XPS measurements presented in this work, we had the opportunity to perform these experiments at the MAX-lab II synchrotron, endstation I511.

MAX II is MAX-labs largest and most used storage ring of the Maxlab synchrotron in Lund (until Max IV will be opened in 2015). It has a circumference of 90 meter and is today fully extended. MAX II is a third generation synchrotron source and was started 1996. MAX II has an emittance of 9 nmrad and has seven insertion devices.

The electrons from the injector have an energy of 400 MeV when they are injected in MAX II. Then they are accelerated inside the storage ring until they reach an energy of 1500 MeV. By this energy the electrons have a speed of 99.99999% of the speed of light and their mass is almost 3000 times higher than their resting mass. MAX II has the highest electron energy of MAX-labs storage rings. MAX II was initially designed for synchrotron light within the ultraviolet and soft X-ray area but with help from superconductive insertion devices it is also possible to produce synchrotron light within the hard X-ray area.

MAX II is filled with electrons once or twice a day and the ring has at its most a current of 300 milliamperes. With a circumference of 90 meters and an electron speed close to the speed of light it means that 500 billion electrons are circulating in the ring when it is in use [77-79].

Tab. 2-3: Technical data of Max II, from Maxlab webpage [79].

Circumference (m)	90
Injection energy (MeV)	400
Operating energy (MeV)	1500
Maximum stored current (mA)	300
Electron beam life-time (Ah)	4@5% coupling
Horizontal emittance (nm rad)	9
Coupling (%)	0.5-1
Nr of straight sections	10

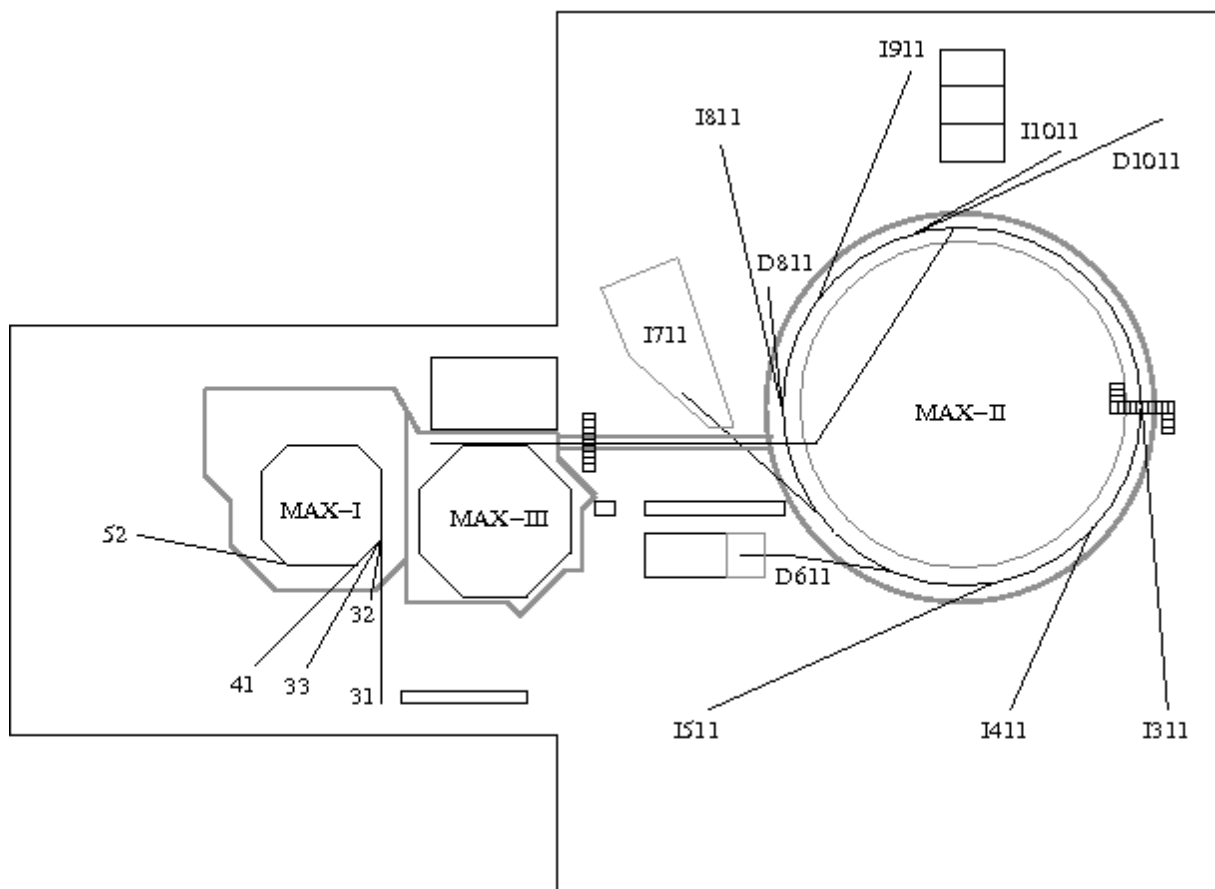


Fig. 2-25: Overview of the whole Maxlab hall and beamlines (including I511), from Maxlab information folder.



Fig. 2-26: Maxlab III storage ring (left) and beamline I511 (right).

Beamline I511 is an undulator based VUV (Vacuum Ultraviolet) soft X-ray beamline aimed at high resolution High Pressure X-ray Photoemission Spectroscopy (HP-XPS), X-ray Absorption Spectroscopy (XAS) and X-ray Emission Spectroscopy (XES). The beamline has two branch lines, I511-1 and I511-3 with a flip-mirror placed immediately after the exit slit to direct the radiation alternately into these two stations.

The I511-1 experimental station (HP-XPS) is equipped with analyzers for XPS and XAS on surfaces under UHV and up to near-ambient pressure conditions.

The HP-XPS is aimed at surface studies under near-ambient pressure conditions (up to 1 mbar) conditions. The endstation consists of separate analysis and preparation chambers with two manipulators: one for UHV measurements and one for high pressure measurements (HP cell). The preparation chamber includes the usual equipment for preparation and characterization of surfaces (Ar^+ ion sputter gun, LEED optics) as well as a load lock for sample transfer into the chamber. The analysis chamber is equipped with a SPECS Phoibos 150 NAP hemispherical analyzer for XPS and an x-ray tube for offline measurements. The high pressure cell is connected to the analysis chamber via a separate load lock. The system is connected to a gas system which allows the storage and mixing of up to 6 different gasses.

Beamline I511 was closed on March 24, 2013. The beamline will be rebuilt as the improved SPECIES beamline with a new undulator capable of elliptical polarization over a photon range of 27-1500 eV, a new RIXS endstation that e.g. will be able to measure liquid jet samples, and an HP-XPS endstation with improved flux and resolution [77-79].

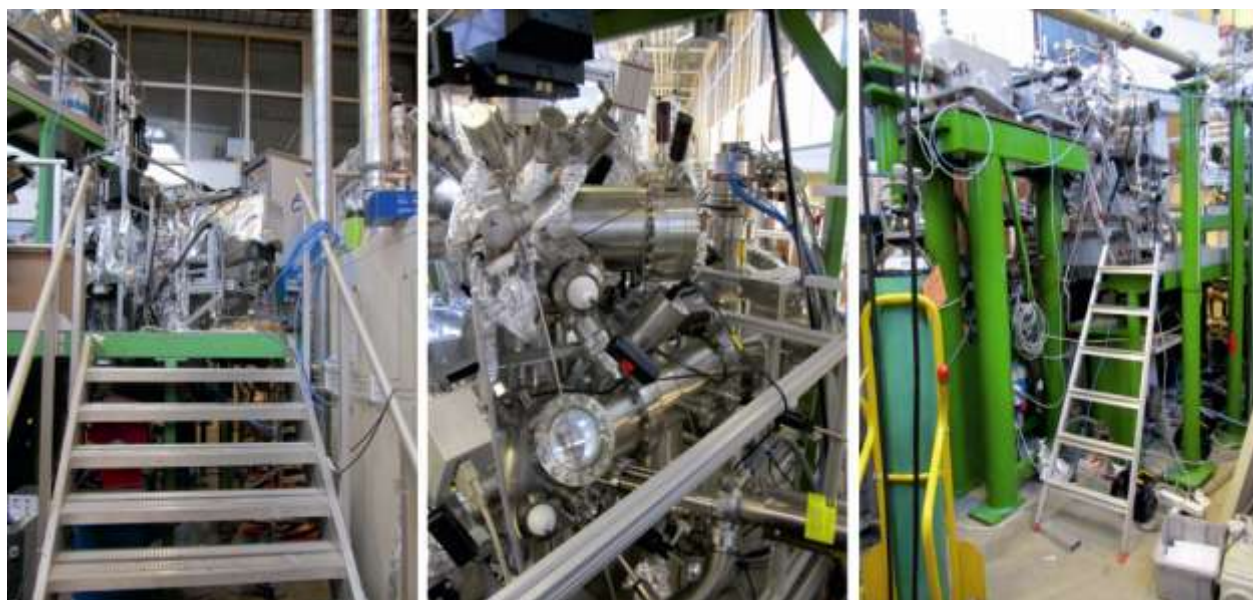


Fig. 2-27: Maxlab III HP-XPS endstation (beamline I511)

2.3.4.1 High Pressure Cell

In the high pressure cell, a sample can be investigated in situ at gas pressures up to 2 mbar. The synchrotron light enters the cell via a Si_3N_4 membrane window while the electrons escape to the analyzer through a 1 mm aperture situated some millimeters in front of the sample. The sample can be loaded into the high pressure cell directly from the UHV manipulator, without breaking vacuum. This gives the possibility to prepare clean surfaces under UHV conditions, characterize them using LEED or XPS and then study their reactivity or catalytic processes in situ in the high pressure cell. The sample can be heated up to 600 K and cooled down to 150 K in the high pressure cell [78, 79].



Fig. 2-28: HP-XPS cell. On the left side with open bayonet coupling to the analyzer, in the middle open sample inlet and on the right side ready for measurement.

2.3.5 Data Processing and Acquisition

In general the interpretation of XP spectra starts with the identification of the major lines and associated weaker lines and lastly with the identification of remaining minor lines. C 1s, O 1s, and O KLL are usually present in almost any spectrum (bearing in mind, that small “unidentifiable” lines can be ghost lines). The most intense photoelectron lines are relatively symmetric and typically the narrowest lines observed. These lines can be a little bit asymmetric for pure metal samples due to coupling with conduction electrons. Less intense photoelectron lines at higher binding energies are typically broader than lines at lower energy. The identification of chemical states primarily needs accurate determination of the line energies and therefore the voltage scale of the instrument needs to be precisely calibrated [80].

Peak-fitting of XP spectra is not simple procedure and needs some experience. One should be careful using only parameters which are automatically suggested by any software as this often yields in incorrect results. The parameters for the best fitted spectrum is not always the final answer (with enough peaks one can always fit a spectrum). Peak fitting can only be a help to verify of a model.

Before starting the peak-fit and calculating the peak areas, the background of the spectra has to be subtracted (after setting the region limits). A common method is the *Shirley background*. In XPS (and in AES), the background at the lower energy side of a peak is usually higher than at the higher kinetic energy side. It is assumed that the background at a given kinetic energy in the spectrum should be proportional to the total number of electrons above this energy.

Therefore, in the Shirley model, the peak spectrum is decomposed in N channels between the limiting high kinetic energy and low kinetic energy point. The calculation from spectral data is an iterative procedure. All backgrounds calculated for this work are from the Shirley-type. Therefore other background methods, like *linear* or *Tougaard* background are not discussed here. If necessary a region shift has to be added (e.g. to compensate charging effects). After adding a peak some parameters needs to be set. Depending on the software the peak type (i.e. orbital: s, p, d, f) has to be selected. For p-, d-, and f-type peaks this combines the two splitting peaks (FWHM is the same for both the splitting peaks). In some cases it is also possible to use two s-type peaks for a splitting peak. The idealized line-shape of XPS peaks is a convolution of a Gaussian and Lorentzian function. To put it roughly, the the Gaussian function describes the measurement process and the Lorentzian function models the natural lifetime broadening (uncertainty principle). This sometimes includes asymmetry in the peaks. Each peak in the Gaussian-Lorentzian product function has four parameters (peak position, Area, FWHM, and the Gaussian-Lorentzian parameter) which can be set by the software. Asymmetric line shapes are difficult for quantification as the asymmetric tail moves the intensity away from the peak maximum. A simple integration of the line-shape can move the energy region outside the region of the defined background limits [80, 81].

Two different programs where used in this work. The first program is “XPSpeak”, a freeware program XPS spectra analysis written by Raymund Kwok. This software offers a lot of functions for background and peak fitting. Unfortunately the author seems no longer supporting this software and the program runs buggy under newer Windows versions (7 and 8). Also, the import of vms (vamas) files from the SpecsLab data acquisition is not possible. It is needed to split the original data file into ASCII files for every region. Another problem is the poor export functions for processed files.

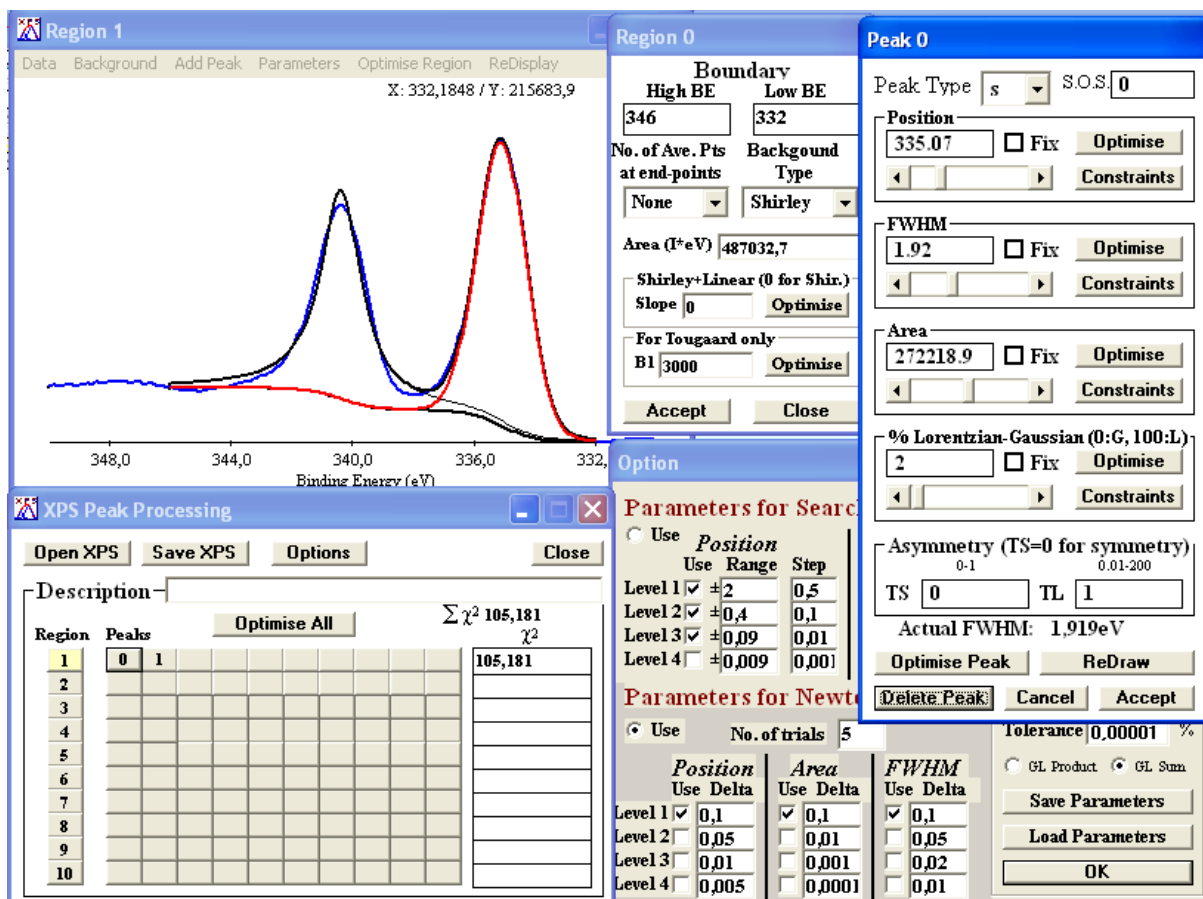


Fig. 2-29: Screenshot of the programm XPSpeak processing a Pd3d peak as example.

CasaXPS (© 2009 Casa Software Ltd) is powerful processing software for XPS and AES and has better import and export functions than XPSpeak. For beginners there are “too much” information/features on a short place. The tools seem to be very comfortable, but one has to be careful, not every peak that the software automatically “suggests” makes sense. In my opinion, the used time for peak fitting is the same as in XPSpeak. In the first program one has to set the parameters manually, in the latter program one has to correct the automatically set parameters manually.

Also some other programs where tested but these two programs where the most usefull at this time.

2.4 Auger Electron Spectroscopy (AES)

The Auger effect was first described by the Austrian physicist Lise MEITNER in 1922 [82] and independent by Pierre AUGER in 1925 [83]. Though Meitner was the first who discovered and reported this effect, usually only Pierre AUGER is credited with the discovery.

Auger excitations are a secondary process of X-ray photoemission and also commonly appear in XP spectra. AES is highly surface sensitive and element specific.

2.4.1 Principles

Auger electrons have only a small mean free path in solids, compared to X-Rays. A nonradiative relaxation to an inner shell can take place by having one electron from a less tightly bound orbital occupy the hole, while a second electron is ejected into vacuum (see Fig. 2-20). The energy is equal to the difference in total energies of the initial and final states. For Auger emissions one can observe a transition between an inner and an outer shell. The binding energy of the inner shell gives evidence about the investigated element. A second situation is to have transitions between two inner shells, the net result of the Auger process is the ejection of an inner shell electron. Thus, ejected electrons will feel the potential of the valence shell just as in the case of photoionization, and the chemical shift can be observed in Auger spectroscopy of inner shells. The study of chemical shifts of core electrons by Auger spectroscopy is hindered by the broadening effect due to the larger natural widths of the more deeply lying atomic levels. AES is sensitive to the lighter elements, and unlike X-ray fluorescence and can be detected for elements as light as lithium ($Z = 3$). Lithium represents the lower limit for AES sensitivity since the Auger effect is a 3-state event necessitating at least three electrons. Neither H nor He can be detected with this technique. [84-86].

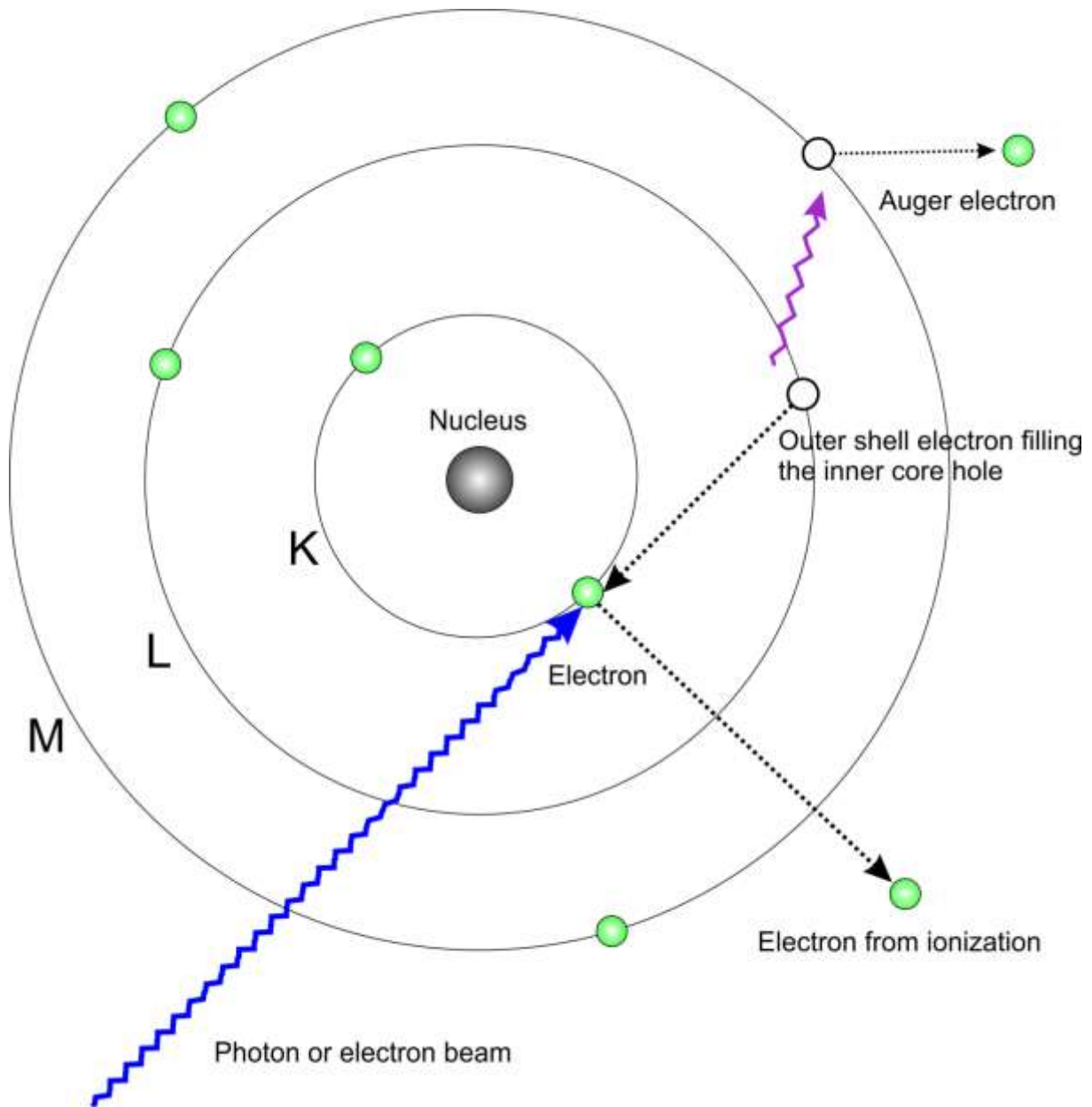


Fig. 2-30: Scheme of an KLM Auger process. A core electron can be removed by an photon or electron beam, leaving behind a hole. This core hole is then filled by an outer shell electron. The loss of energy is equal to the difference in orbital energies. This energy is coupled to a second outer shell electron, that will be emitted from the atom.

Nomenclature:

Spectral lines are named In X-ray nomenclature (see chapter 2.3.1). Regarding that the orbital angular momentum (quantum number: l) and spin (spin quantum number: s) of the electrons has to be coupled to obtain splitting of the energy levels.

For *single electron systems*, the levels are termed with $n=K$ ($=1$), L ($=2$), M ($=3$),...; the suffix numbers the separate energy levels 1 ($l=0$), 2 ($l=1, j=1/2$), 3 ($l=1, j=3/2$), 4 ($l=2, j=3/2$), 5 ($l=2, j=5/2$), ...

Multi electron systems are more complicated due to various coupling options. Elements with low atomic numbers ($Z < 20$) are first coupling \vec{l} to a total orbital angular momentum \vec{L} and \vec{s} to a total spin \vec{S} and both to a total angular momentum \vec{J} (Russell-Saunders-coupling or *L-S* coupling).

For heavy elements ($Z > 75$) \vec{l} and \vec{s} are coupling each to a total orbital quantum number \vec{j} and a total angular momentum \vec{J} (*j-j* coupling).

For elements with ($20 > Z > 75$) both coupling types are mixing to an intermediate coupling.

Quantification:

Auger peak intensities are depending on the excitation source and therefore Auger element libraries must include relative sensitivity factors for the specific electron gun energy used to excite the surface material. Historically Auger spectra are measured using a fixed retard ratio mode for the analyzer. This mode records the number of electrons reaching the detector as the kinetic energy of the ejected electrons is stepped such that the ratio of the initial kinetic energy of the electron to the pass energy of the analyzer is maintained as a constant during the acquisition. Electron yield depends on several critical parameters such as electron-impact cross-section and fluorescence yield. Auger data are more difficult to quantify, the method to quantify Auger spectra is to measure the intensity of a transition using a differentiated spectrum, determining the peak intensity by the difference in the positive and negative going derivative peak heights. This must be numerically differentiated to provide the data in a form suitable for quantification in terms of peak to peak intensities [71, 84, 87, 88].

$$I_A = i_p \cdot 1 + R \cdot Q \cdot Y \cdot \int_0^{\infty} n(z) \cdot e^{\left(\frac{-z}{\lambda \cos \theta}\right)} dz \quad (1.1.12)$$

(i_A =Auger electron current; i_p =primary electron current; R =Background scattering factor; Q =ionization probability; Y =probability of Auger decay; $n(z)$ = concentration of the element at depth z ; λ =inelastic mean free path of the Auger electron; θ =take-off angle of the Auger electron measured from the surface normal)

As shown in Fig. 7-12 (appendix), the Specs ErLeed unit in the STM chamber is dual system for AES and LEED.

2.4.2 Data Processing and Acquisition

Auger spectra are recorded with the Specs software RFA-PC 4.20 which is also used for controlling the LEED unit in the STM system. Quantification and data processing was done with CasaXPS as also used for XP spectra. LEED pictures were recorded by an external reflex camera.

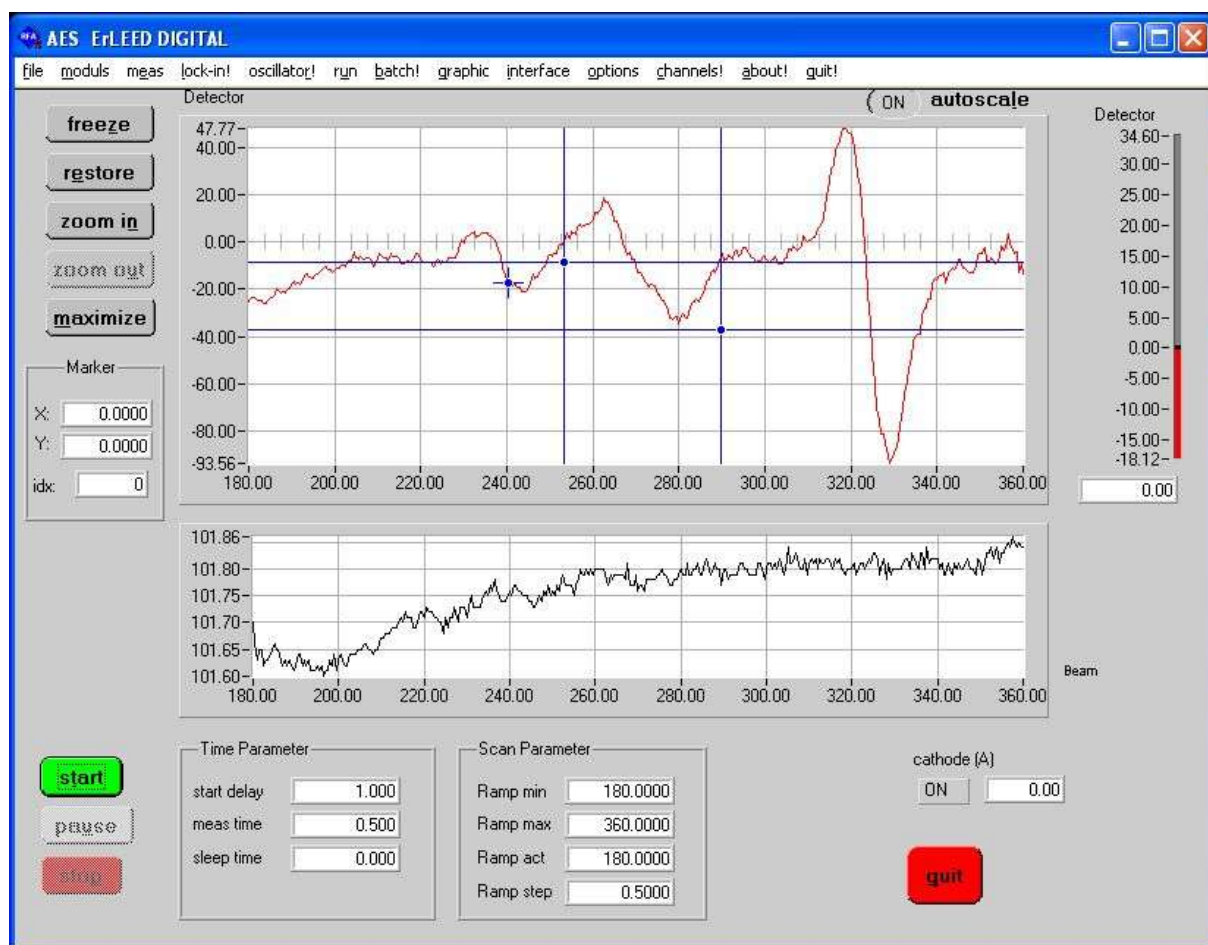


Fig. 2-31: Screenshot of RFA-PC recording a Pd(111) sample. This software is used for AES measurement and for the LEED settings.

2.5 Low Energy Electron Diffraction (LEED)

LEED is a very suitable tool to study the long range periodicity of a surface. In 1924, Louis DE BROGLIE proposed the wavelike nature of all particles by wave mechanics. Clinton DAVISSON and Lester GERMER confirmed this hypothesis experimentally in the Bell Labs in 1927. Low Energy Electron Diffraction became a popular surface analysis method not until the early 1960s, since ultra-high vacuum and preparation methods for clean and well-structured metal surfaces became widely available [89, 90]. It still accounts for most of the described surface structure determinations. Its key feature utilizes the long-range periodic order of a sample surface to process elastically scattered electrons into distinct diffracted beams.

2.5.1 Principles

An electron beam (typical energy: 50 to 300 eV) hits on the surface of a single crystal and is scattered. The de Broglie wavelength of electrons is in the same range as the surface lattice parameters (some Ångströms). The diffraction pattern, generated by elastically scattered electrons, is displayed on a fluorescent screen. Surface extended X-ray absorption fine structure (SEXAFS) and backscattering photoelectron diffraction (PED) are two techniques that also exploits the same phenomenon of coherent interference of elastically scattered electrons (Fig. 2-32). In both methods, the electron source is not from outside like in LEED - the photoelectrons are emitted from a core level of an atom. In that case, the signal includes the sum of the directly emitted photoelectrons and components from electrons elastically scattered by atoms [91].

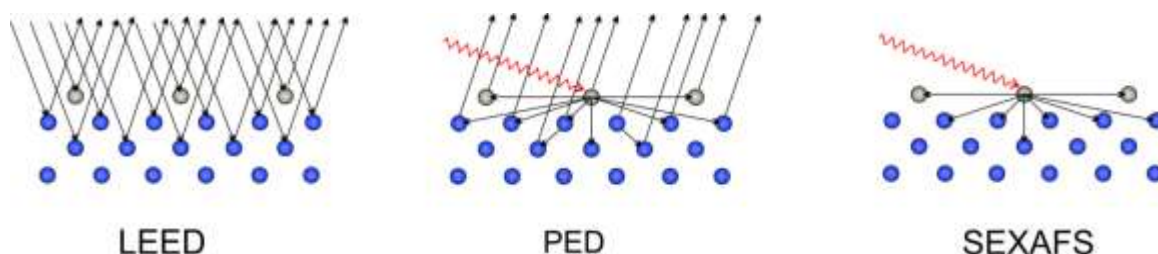


Fig. 2-32: Comparison of low energy electron diffraction (LEED), backscattering photoelectron diffraction (PED), and surface extended X-ray absorption fine structure (SEXAFS).

The electrons cannot penetrate deeper than $\sim 10 \text{ \AA}$ into the crystal, due to their short mean free path (depending on the kinetic energy of the electrons). The diffraction pattern is therefore ruled by the 2-dimensional surface periodicity [50, 92]. The incident beam currents are typically in the range of $1 \mu\text{A}$ into an area of $< 1 \text{ mm}^2$. In this range, radiation damage can be a problem for fragile surfaces and adsorbates.

In one dimension constructive interference, i.e. a reflection spot in the diffraction pattern is only observed at angles for which the path difference between two waves (electrons) is an integer multiple of the wavelength. In the case of a two dimensional surface, the diffraction pattern observed by LEED represents the reciprocal lattice of the surface. The unit cell itself is defined by the lattice vectors a_1 and a_2 , the reciprocal lattice is made up by the reciprocal lattice vectors a_1^* and a_2^* [50, 93].

$$\begin{aligned} a_1 \cdot a_2^* &= a_2 \cdot a_1^* = 0 \\ a_1 \cdot a_1^* &= a_2 \cdot a_2^* = 1 \end{aligned} \quad (1.1.13)$$

The length of the reciprocal lattice vector is given by Equation (1.1.14) where γ is the angle between the two base vectors a_1 and a_2 [39, 50, 92].

$$|a_1^*| = \frac{1}{|a_1| \cdot \sin \gamma} \quad (1.1.14)$$

In case of a cubic lattice, $\gamma=90^\circ$ and consequently $\sin \gamma=1$, following Equation (1.1.15).

$$|a_1^*| = \frac{1}{|a_1|} \quad (1.1.15)$$

A schematic drawing of a rectangular surface lattice and the resulting diffraction pattern after transformation into reciprocal space is shown in Fig. 2-33. The LEED pattern itself does not give information about the absolute position of the atoms but it reflects the surface periodicity. The observed LEED pattern may not even represent the true periodicity, since it can be a superposition of various surface domains [94].

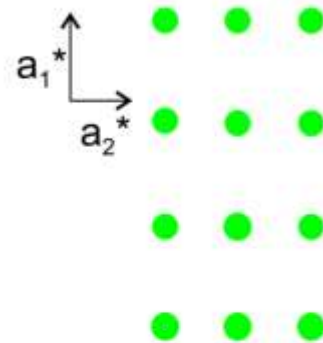
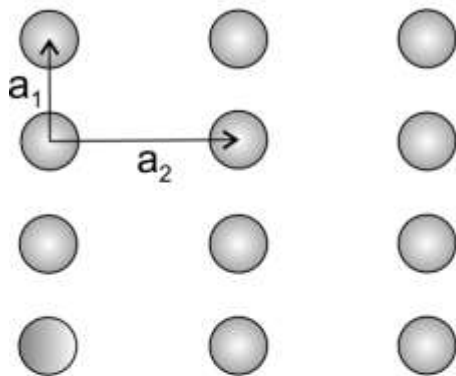
Quantitative LEED pattern analysis of the 3-dimensional surface structure is possible by obtaining an I - V curve (I =intensity of a selected single diffraction spot; V =primary electron

beam energy). This requires extremely precise optical alignment of the sample with respect to the LEED optics and therefore in this work only qualitative analysis of the recorded LEED diffraction pattern will be discussed.

SURFACE LATTICE (real space)

LEED PATTERN (reciprocal space)

rectangular



2 x 2 super structure

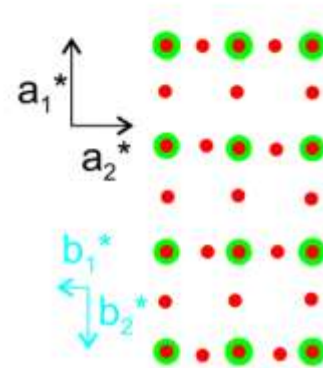
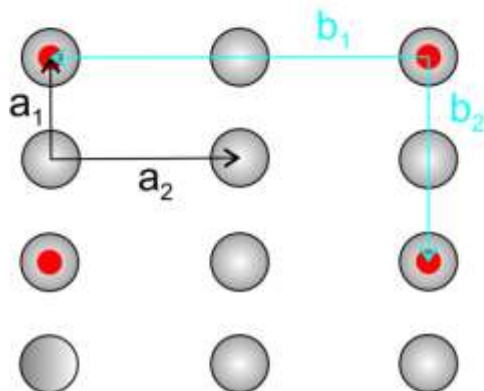


Fig. 2-33: Schematic representation of a rectangular surface lattice and the corresponding LEED pattern. In the lower picture, a primitive 2x2 overlayer of e.g. adsorbate molecules is superimposed on the surface principal lattice [39].

2.5.2 Data Processing and Acquisition

The principle of a LEED system is shown in Fig. 2-34. The main element is a so-called Retarding Field Analyzer (RFA). It consists of the fluorescent screen and usually 4 grids in front of it. For displaying the diffraction pattern a high voltage between sample and fluorescent screen is applied. Inelastically scattered electrons can be filtered off by a variable negative voltage which is applied to the grids.

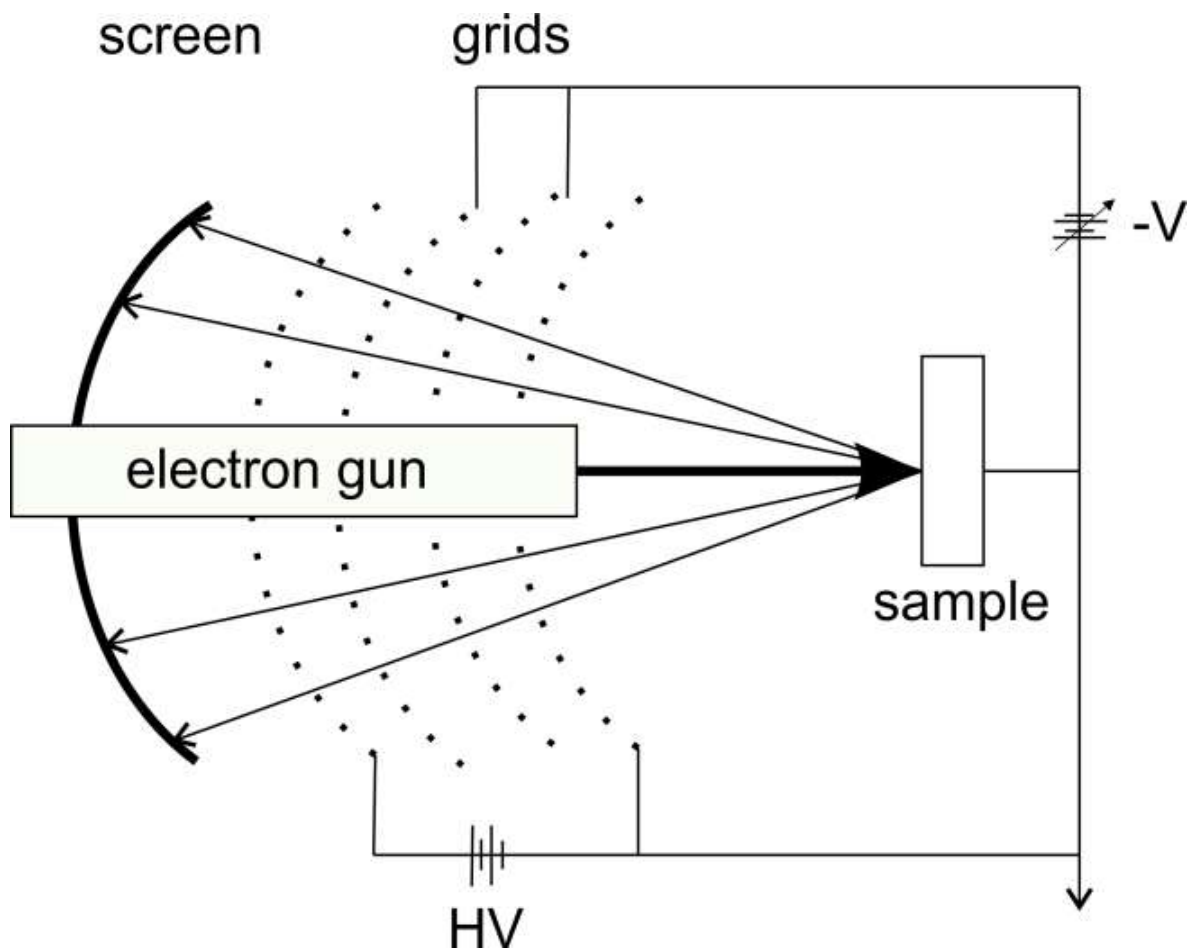


Fig. 2-34: Scheme and principle of a LEED system.

As an example, a LEED pattern of a clean hexagonal Pd(111) surface is shown in Fig. 2-35.

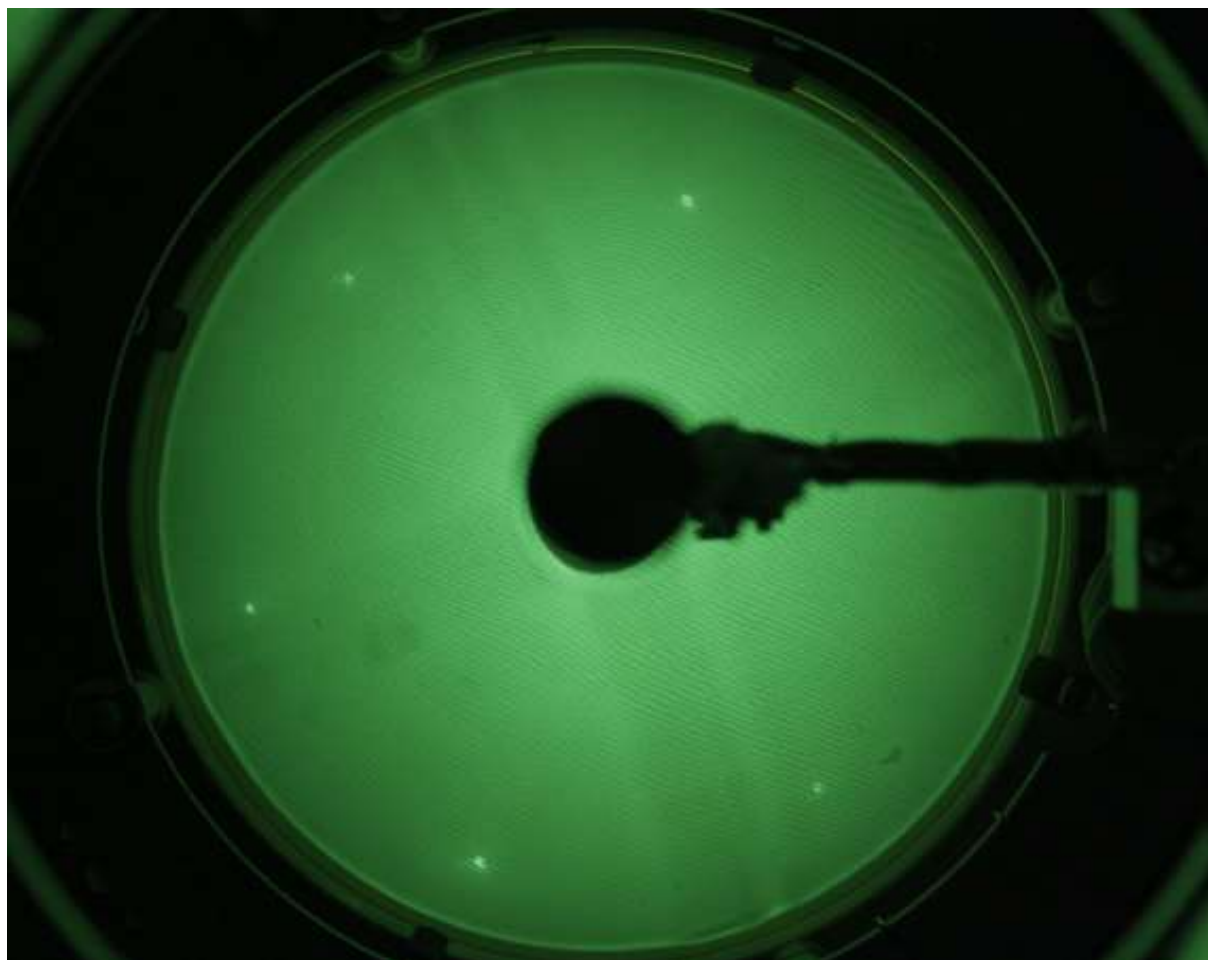


Fig. 2-35: LEED pattern of a Pd(111) single crystal surface at 100 eV.

Details regarding the diffraction patterns of metal single crystals and adsorbed species will be discussed later in the experimental part, chapter 3.2.2.

2.6 Temperature Programmed Desorption (TPD)

Temperature Programmed Desorption (TPD), sometimes called Thermal Desorption Spectroscopy (TDS), is based on desorption of molecules adsorbed on a surface. It is a suitable tool to study adsorption and desorption processes and can be used for single crystals, but also for foils or powder materials [46, 50, 95, 96].

2.6.1 Principles

The sample is heated with a constant heating rate (typically in the range from 30 to 90 K per minute) and the species desorbing from the surface are monitored with e.g. a line-of-sight Quadrupole Mass spectrometer (QMS). Our setup is shown in Fig. 2-36. The temperature control unit (TCU) indicates the feedback loop which measures the temperature of the sample and tunes the heating power to operate with the desired linear heating ramp. The nozzle in front of the sample is designed as a mechanical shield to minimize contributions of residual gases from the UHV system to the TPD spectrum. The QMS is differentially pumped to provide sufficient gas flow towards the mass spectrometer near the sample. This avoids re-adsorption of molecules.

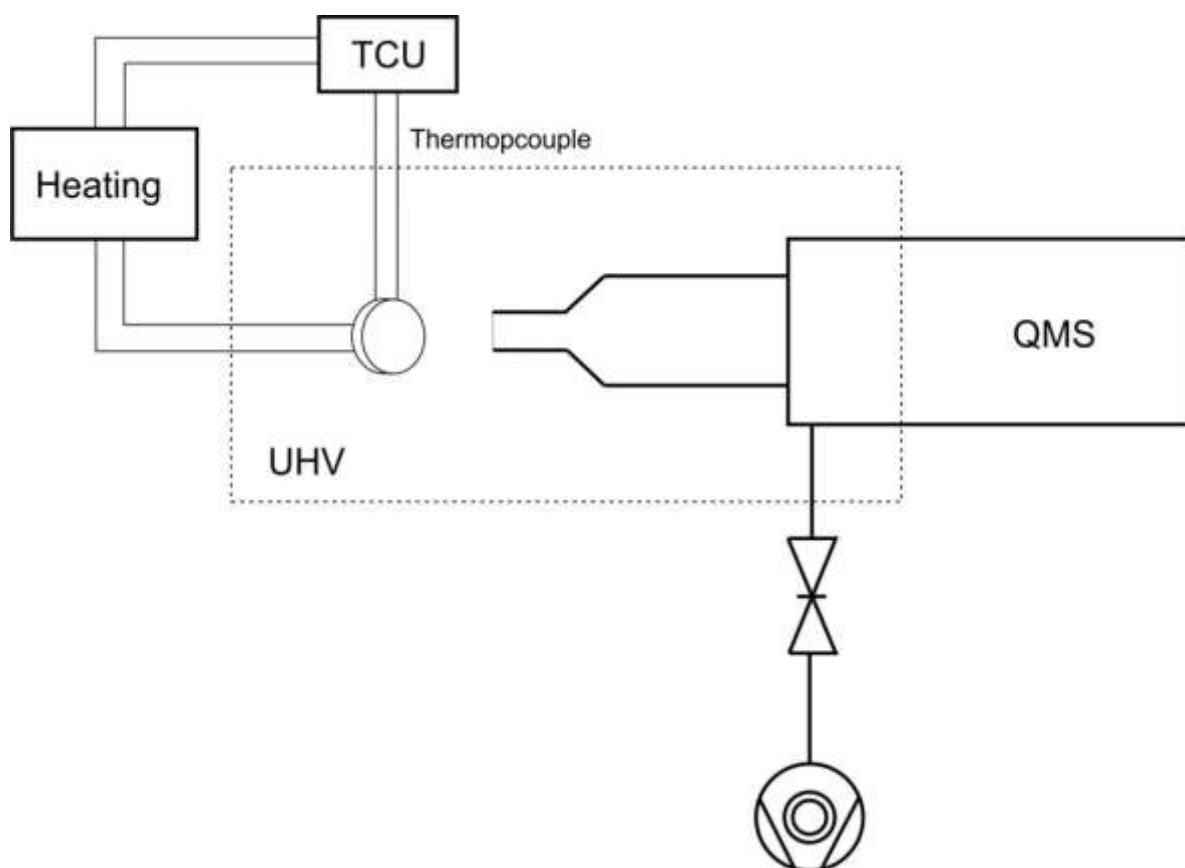


Fig. 2-36: Schematic TPD setup. TCU=Temperature Control Unit; QMS=Quadrupole Mass Spectrometer.

The most important information obtained from a TPD spectrum is the surface coverage θ , the activation energy for desorption E_{des} and the frequency factor of desorption ν , which reflects the desorption mechanism. The activation energy of desorption provides information about the bond strength between a molecule and the surface and therefore drawing conclusions about the available binding sites. From the coverage dependency of TPD spectra it is even possible to draw conclusions on the lateral interactions between the adsorbed molecules [39].

2.6.2 Data Processing and Acquisition

The complete analysis of TPD spectra is complicated and time consuming, as simplified methods are often used such as the Redhead method [97, 98].

In this work, the simplified equation (1.1.16) was used for yielding E_{des} .

$$E_{des} = RT_{max} \left[\ln \left(\frac{\nu T_{max}}{\beta} \right) - 3,46 \right] \quad (1.1.16)$$

(E_{des} =desorption energy of the adsorbate, T_{max} =temperature of the peak maximum and β =heating rate, R =gas constant)

One difficulty of the Redhead method is that the value for ν has to be known or estimated. This may be problematic, because ν can change with coverage [39]. The practical application of this equation for Pd(111) is discussed later in the experimental part of this work (chapter 3.2.5 and 3.3.1).

An outstanding way to detect desorbed species under UHV conditions is using a quadrupole mass spectrometer. It can quantitatively record the desired species. The system is limited to the detection speed of mass spectrometer. Measuring a wide range of masses (fragments of the desorbed species) can slow down the detection and may be not fast enough for the desorption rate. This was an experimental limitation for the MKS eVision+ quadrupole mass spectrometer (QMS) with the corresponding EasyView software which was used in the XPS chamber.

A quadrupole mass spectrometer is used for filtering sample ions, based on their mass/charge ratio. The filter part consists of four cylindrical metal rods as shown in Fig. 2-37. The rods are used as electrodes; each opposite pair is electrically connected. One pair is connected to the positive pole, the other one to the negative pole of the electric power source (DC).

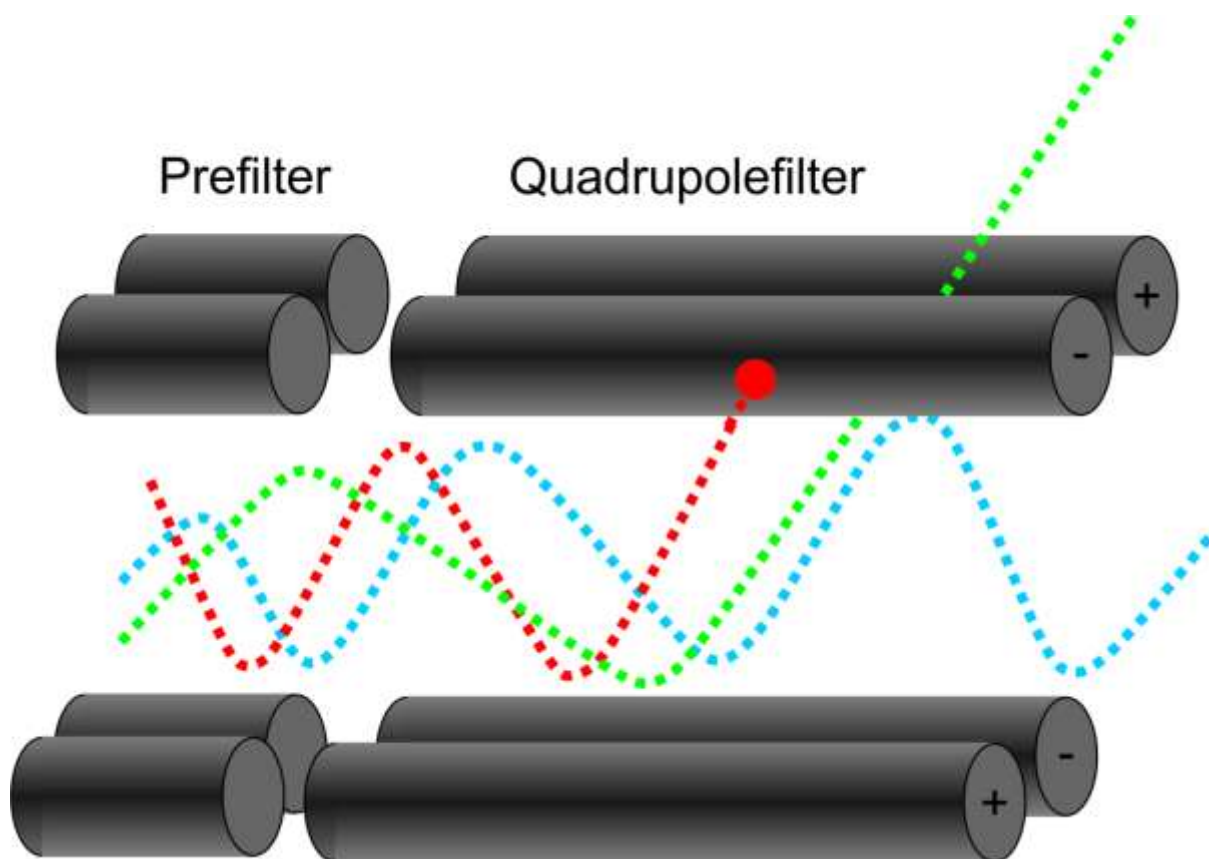


Fig. 2-37: Basic principle of a Quadrupole Mass Spectrometer for filtering sample ions, based on their mass/charge ratio.

The molecules will be ionized by electron impact ionization. The electrons are produced by heating a filament (thermoionic emission) and then accelerated into a beam moving to a trap electrode. The following ionization process can be used to obtain structural information of the molecule. The so produced ion fragments are then directed to the analyzer with a repeller electrode.

A radio frequency voltage with a superimposed direct current voltage is applied. The ions are moving between the rods and the current or the frequency is set that only ions with a certain desired mass/charge ratio will reach the detector.

$$u(t) = U + V \cos \omega t \quad (1.1.17)$$

(U =direct voltage, $u(t)$ =time-varying voltage, V =voltage of the alternating part, ω =frequency)

In absence of a direct current potential, the ions between the rods are moving to the middle during positive alternating current half-phase and branch off during negative alternating current half-phase. If an ion hits a rod during the negative half-phase, it will be neutralized

and “removed” from the vacuum. In case of superimposing the alternating current potential with a positive direct current potential the moment of inertia of ions with equal kinetic energy is proportional to the square root of the mass. An ion with high mass in a high frequency current field will not significantly change its trajectory; it is mostly influenced by the direct current field. This ion will move between the rods with high probability. Ions with low mass in a low frequency field can be eliminated by collision with the rod during the negative half-phase. Therefore, the pair of rods with the positive potential acts as a high-pass mass filter for ions. The pair of rods with the negative potential will collect all positive ions in absence of an alternating potential. Low mass ions can compensate this during the positive half-phase of alternating current and therefore the rods are acting as low-pass mass filter for ions. Only ions in a narrow mass/charge range are able to pass the quadrupole [99].

The passing ions are detected by a Faraday cup for high pressures and an electron multiplier for low pressures and high sensitivity. A Faraday cup is a metal cup which is connected to the circuit. The ions are acting as charge carrier and the resulting electrical current can be measured. An electron multiplier can even detect single electrons. By the secondary emission process on an emissive metal plate, one electron can induce the emission of a few electrons. These electrons will be accelerated to the next metal plate by applying a potential. By repeating this process, one electron can trigger the emission of many electrons, which are collected by a metal anode.

2.7 Scanning Tunneling Microscopy (STM)

Scanning tunneling microscopy was invented in 1981 by Gerd BINNIG and Heinrich ROHRER (at IBM Zürich), and was awarded with the Nobel Prize in Physics in 1986 [100]. In 1982 they obtained the first atomic resolution picture of a Si(111) 7x7 surface. Atomic resolution capability is the most important feature of STM.

This method requires very clean surfaces, atomic sharp tips, vibration control, and sophisticated electronics. The resolution of a good system is considered to be 0.1 nm lateral resolution and 0.01 nm depth and therefore individual atoms can be imaged and manipulated [101]. An atomic sharp tip is brought to a small distance to the sample surface using a piezo electric drive (Fig. 2-38).

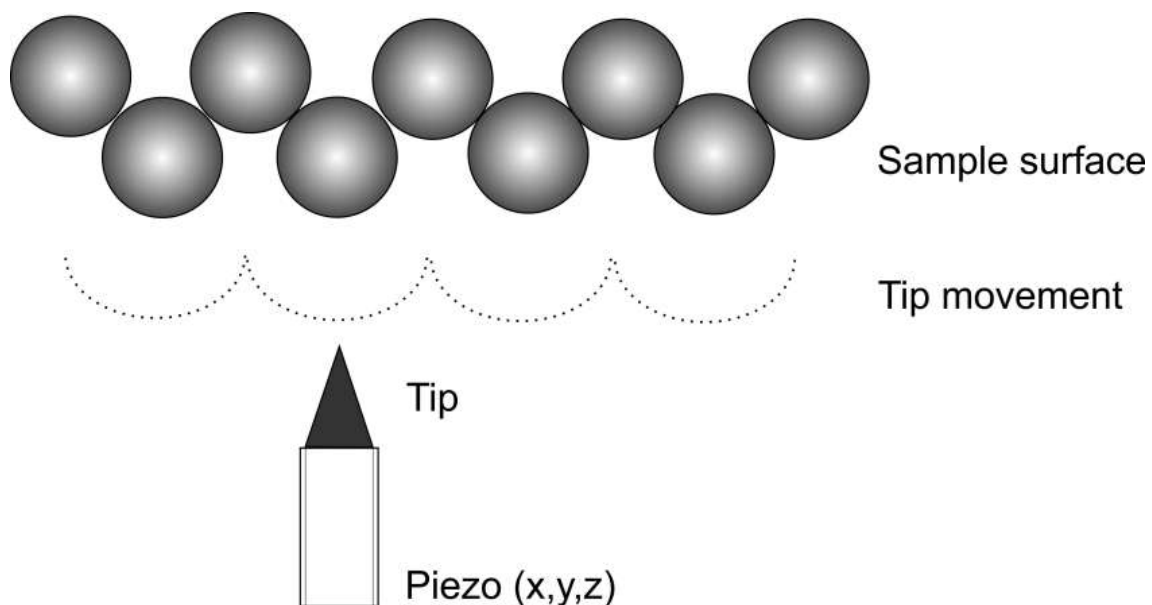


Fig. 2-38: STM piezomotor controlled tip movement over a solid surface.

A tunneling current will flow between sample and tip if a bias voltage has been applied due to the tunneling effect. Depending on the polarity of the applied voltage, the current can be from the tip to the surface or contrary. The tunneling current depends exponentially on the tip separation. Therefore it can be used to control the distance between the front of the tip and the conductive sample surface and can be kept constant (the most used STM operation mode) during the scanning process over the sample surface.

The electronic feedback can be traced by the tip to get a “topographic image” of the sample surface. Furthermore, the tunneling current contains information of the local electronic properties of the sample surface. It is often a misunderstanding that STM is an electronic probe of the surface, though images tempt to the impression of “seeing” atoms [102].

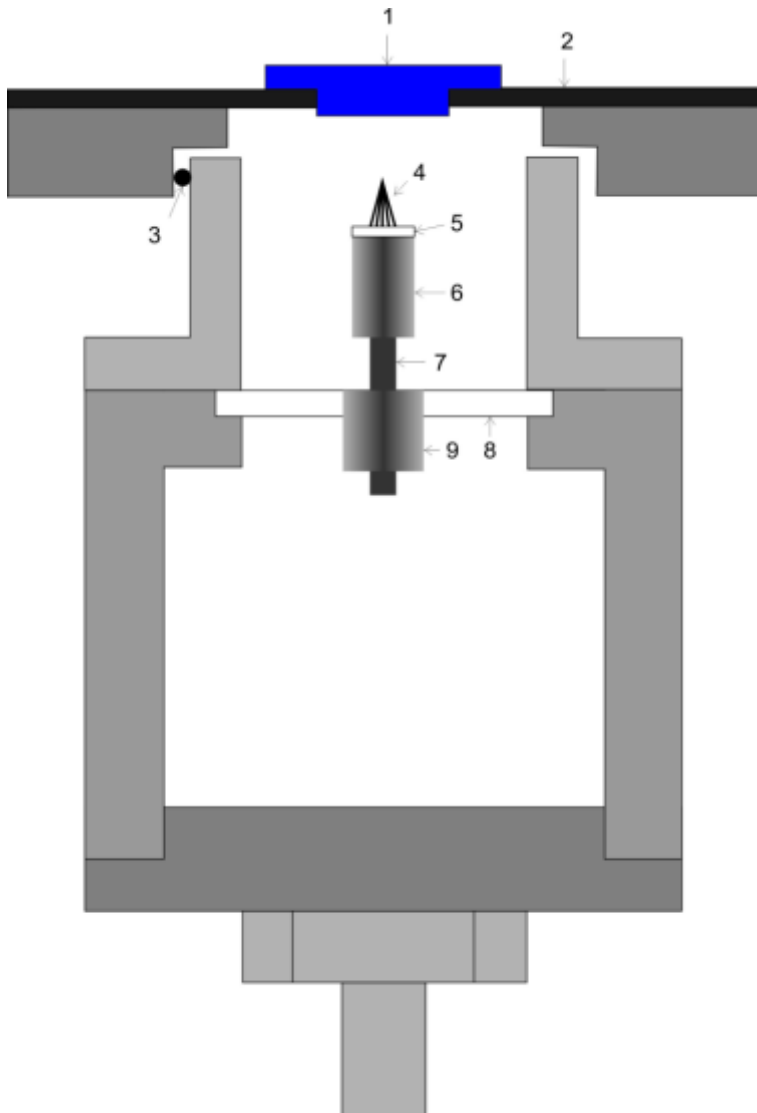


Fig. 2-39: Sketch of the Aarhus STM system. 1=sample, 2=holder, 3=quartz balls, 4=tip, 5=macor[®] holder, 6=scanner tube, 7=rod, 8=macor ring, 9=piezo tube [103].

In the Aarhus system, the sample is placed in a holder which is fixed by springs. The top plate is thermally and electrically insulated from the body by quartz balls. The tip is held by a macor¹ holder which is glued to the scanner tube. The piezo tube forms a small inchworm motor. A positive voltage to an electrode will clamp that electrode to the rod, whereas a negative voltage will free that electrode from the rod [103].

¹ Machinable glass ceramic.

2.7.1 Principles

2.7.1.1 Electron tunneling

Tunneling is the quantum mechanical phenomenon where a particle (i.e. electron) tunnels through a barrier (in STM the barrier is a gap of about 1 nm) that it could not overcome in classical physics. In quantum mechanics, particles can, with a very small probability, tunnel to the other side. The Heisenberg uncertainty principle implies that there are no solutions with a probability of exactly zero. Therefore, the probability of the existence of a particle on the other side of a barrier is non-zero. Such particles will appear on the opposite side with a frequency proportional to this probability. The particle “borrows” energy from its surrounding to tunnel through the wall and paying it back by making the reflected electrons more energetic than they otherwise would have been.

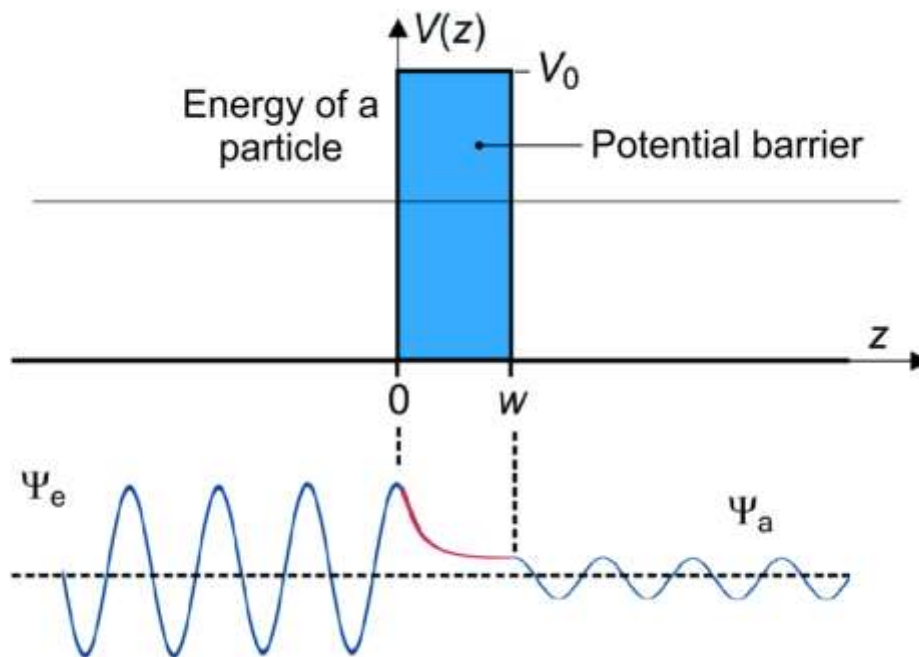


Fig. 2-40: Tunneling through a potential wall. The energy of the tunneled particle ($E < V_0$) is the same but the amplitude is lower, proportional to the tunneling probability. Ψ_e =penetrating wave, Ψ_a =transmitted wave.

The measured tunneling current is usually in the range of 1 nA and the distance from the tip to the surface is about 0.5 nm [104]. The behavior of the electrons from the surface through a vacuum barrier to the surface can be described as a one-dimensional potential wall:

$$V(z) = \begin{cases} V_0, & 0 < z < w \\ 0 & \text{elsewhere} \end{cases} \quad (1.1.18)$$

($V(z)$ =potential barrier, w =thickness of the potential barrier, z =direction of tunneling current, Ψ_e =penetrating wave, Ψ_a =transmitted wave)

This is a common quantum mechanics calculation which can be found in standard textbooks about quantum mechanics [105, 106]. The time-independent one-dimensional Schrödinger equation is given in equation (1.1.19) and (1.1.20) and is used for calculating the wave function $\Psi(z)$.

$$\left(-\frac{\hbar^2}{2m} \frac{d^2}{dz^2} + V(z) \right) \Psi(z) = E \Psi(z) \quad (1.1.19)$$

($V(z)$ =tunneling current, m =mass of the tunneling particle, z =direction of tunneling current, $\Psi(z)$ =wave function, E =energy of the particle)

$$\Psi(z) = \begin{cases} ae^{ikz} + be^{-ikz}, & z < 0 \\ ce^{\kappa z} + de^{-\kappa z}, & 0 < z < w \\ ge^{ikz} + he^{-ikz}, & z > w \end{cases} \quad (1.1.20)$$

($\Psi(z)$ =wave function, a, b, c, d, g, h =coefficients described in equation (1.1.21))

Using the wave numbers $k = \frac{\sqrt{2mE}}{\hbar}$ and $\kappa = \frac{\sqrt{2m(V_0-E)}}{\hbar}$, the behavior of the tunneling electrons through the potential barrier can be calculated. For $\Psi(z)$, the limit of the barrier is assumed as continuously differentiable; its first derivation gives the coefficients a , b , c , d , and h ; see equation (1.1.21).

$$\begin{aligned}
a &= g \left(\cosh \kappa w + \frac{i}{2} \frac{\kappa - k}{k \kappa} \sinh \kappa w \right) e^{ikw} \\
b &= \frac{1}{2} g \left(-i \left(\frac{\kappa}{k} + \frac{k}{\kappa} \right) \right) \sinh \kappa w e^{ikw} \\
c &= \frac{1}{2} g \left(1 + \frac{1k}{\kappa} \right) e^{-\kappa + ik w} \\
d &= \frac{1}{2} g \left(1 - \frac{1k}{\kappa} \right) e^{\kappa + ik w} \\
h &= 0
\end{aligned} \tag{1.1.21}$$

These coefficients can be used to calculate the tunneling probability $|T E|^2$ as shown in equation (1.1.22).

$$|T E|^2 = \left| \frac{g}{a} \right|^2 = \frac{1}{1 + \left(1 + \frac{\kappa - k}{4} \right) \sinh^2 \kappa w} \tag{1.1.22}$$

This can be simplified for $\kappa w \gg 1$ with $\sinh^2 \kappa w \approx e^{2\kappa w}$ to equation (1.1.23)

$$|T E|^2 \approx e^{-\frac{2\sqrt{2m(V_0-E)} w}{\hbar}} \tag{1.1.23}$$

Using $\kappa = \frac{\sqrt{2m(V_0-E)}}{\hbar}$, the function of tunneling current through a potential barrier can be written as:

$$I = I_0 e^{-2\kappa z} \tag{1.1.24}$$

(I =tunneling current, I_0 =function of the applied voltage between tip and surface and local density of states, $z=w$ =thickness of the potential barrier, $\kappa = \frac{\sqrt{2m\Phi}}{\hbar}$, Φ =work function)

The tunneling current I is an exponential function which is monotonically increasing with decreasing distance [107, 108]. The theory of a time-dependent treatment of tunneling probability in a three dimensional case would go beyond the scope of this work. Details can be found in [109].

Estimation how much time is needed for the tunneling process are between zero and $5 \cdot 10^{-16}$ s. Recent experiments at ETH Zürich clarifies a maximum time requirement of $3,4 \cdot 10^{-17}$ s (measuring accuracy of the their setup) [110].

2.7.1.2 STM tips

There are some general requirements for a good STM tip. First, to get atomic resolution on flat samples, the tip must be terminated in a single atom. Also the macroscopic shape has some importance. The tunneling current depends exponentially on the tip separation. The closest atom to the surface gives the main contribution. The contribution of atoms on the tip with just a few Å more distance is very low and can usually be neglected. However, it can lead to multiple image artifacts if two or more atoms on the tip front have almost the same distance.

For topographic studies on larger scales, the macroscopic shape becomes more important. A broad tip cannot penetrate into narrow groves, this leads to smoothing effects of the STM imaging. Also the chemical composition of the tip is important. Contamination layers like oxides can significantly reduce the vacuum tunneling which can lead to a mechanical contact between tip and sample surface. The kind of atoms and orbitals on the tip-end (which dominates the tunneling current) has influence on atomic corrugation amplitudes [109].

There are two common types of tips:

Tungsten tips needs to be etched before they can be used. Depending on the equipment this can be done inside or outside the UHV chamber. However, tungsten will be easily oxidized. Therefore, the tip has to be sputtered with Ar to remove the oxide from time to time. It is not possible to sharpen a crashed tip by sputtering. This type of tips cannot be used under air or poor vacuum conditions.

Pt/Ir tips can be quite easy prepared by mechanically cutting a wire with a plier to get a tip suitable for atomic resolution. This preparation method and the unreactivity of Pt/Ir prevent oxide layers on the tip. It can be used for measurements outside of UHV conditions without getting oxidized. A special Pt/Ir alloy is used to increase the hardness because relatively soft tip can be easily damaged in case of mechanical contact.

Another point is the shape of the tip; small asperities can usually guarantee atomic resolution on flat surfaces. But the macroscopic radius of a tip is big and irregularly shaped, which makes it difficult to get useful images of very rough surfaces. Other tip materials like very hard tips (e.g. titanium carbide single crystals) or magnetic tips (e.g. CoCr or CrO₂) are rarely used for some special applications [109].

Originally our system was equipped with a tungsten tip. A disadvantage of our system is that we have to open the chamber when changing the tip. The only way to definitely check the quality of the tip for atomic resolution is to do a STM measurement on a suitable sample. It is useful to check a sample which is easy to prepare, like HOPG². It is not possible to do this with tungsten on air, due to the mentioned reason. In case of using tungsten tips we need to open the chamber, change the tip, remount the STM, and pump the system at least to high vacuum. When the tip is not good enough we have to do this procedure again.

This was one of the main reasons that we switched to Pt/Ir tips because we can check the quality of the tip on air before remounting the STM (see Fig. 2-32). One other reason was that we do not have the equipment to etch tungsten tips in our lab, but it takes just a few minutes to cut a new Pt/Ir tip.

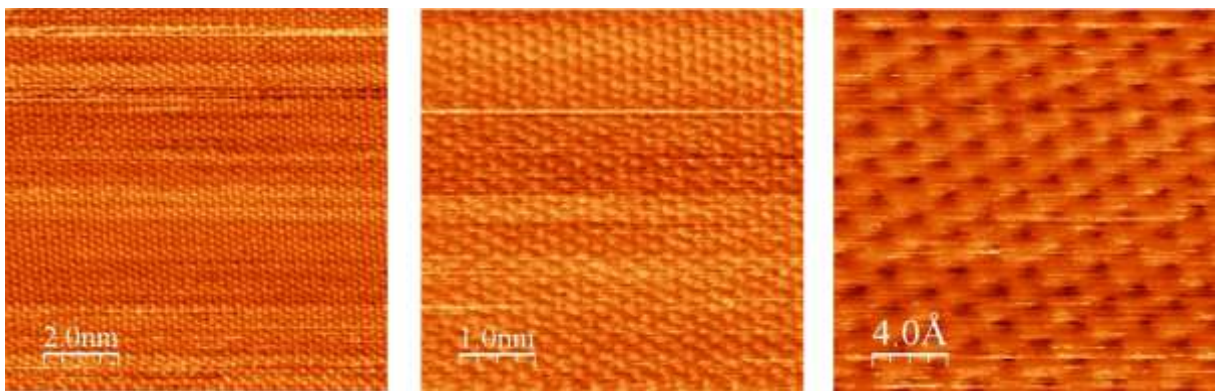


Fig. 2-41: Test pictures of HOPG with a Pt/Ir tip on air.

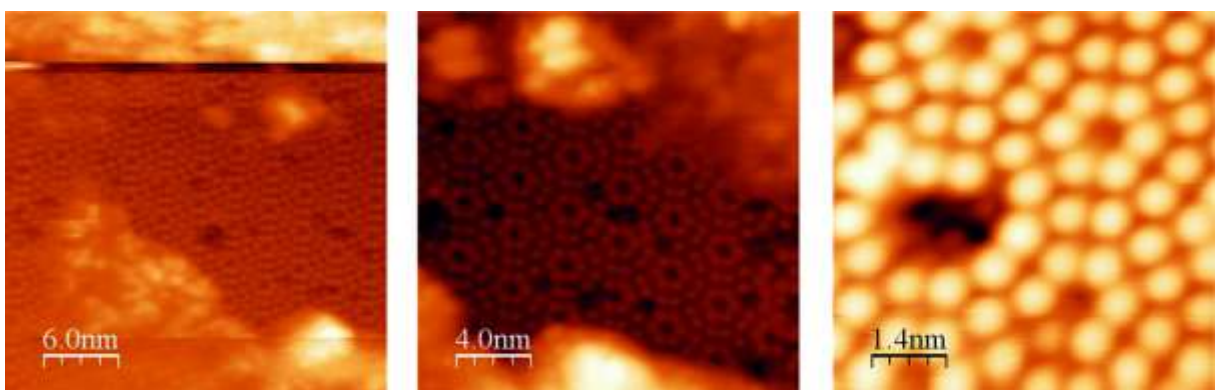


Fig. 2-42: Test pictures of a Si(111) 7x7 reconstructed surface in UHV (W-tip).

² Highly Ordered Pyrolytic Graphite with a renewable and extreme smooth surface.

2.7.1.3 Piezoelectric actuators

It is necessary to allow 3-dimensional movement of the tip which is achieved by piezoelectric drives. The first clamping-type piezo motor (inchworm motor) was realized in 1974. Fig. 2-34 shows the basic principle. The moving process is a cyclical process using a sequenced activation of three piezo elements. The two outer piezo actuators, number 1 and 3 in Fig. 2-34, are activated independently to clamp the sliders.

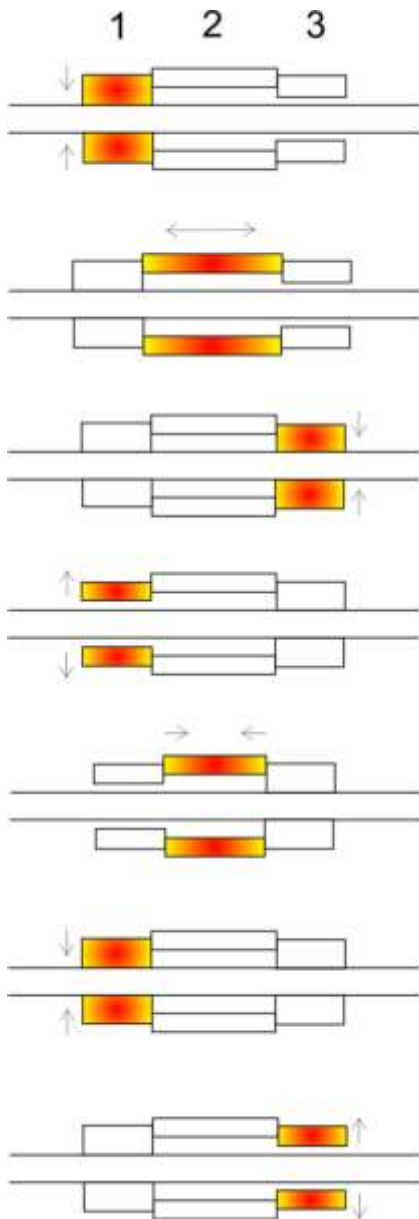


Fig. 2-43: Working principle of a clamping-type piezo motor (inchworm).

The sensitivity of tubes, compared to bar with the same size, is higher due to the smaller wall thickness. A combination of three tubes allows tip movement in three directions. Alternatively one can use one tube in which the outer electrode is divided in four parts. Exciting two opposite electrodes allows movement in all three directions due to bending the piezo tube. Piezo elements are very sensitive against electrical influences, characteristically in the pressure range between 1 and 10^{-4} mbar (“corona range”). They can be destroyed if it will be used under these conditions. So, we are limited to a lower (HV to UHV) or higher (usually on air) pressures during the STM measurement.

2.7.1.4 STM imaging modes

The tip is moved across the sample surface in the x,y direction, the changes in surface height and density of states cause changes in current. The change of z -position (height) of the tip at a constant current can be measured or the current with respect to position.

Constant current mode is the first and most used operation mode by Binnig and Rohrer. The tunneling current between sample and tip is kept constant. The height (z direction) is controlled by the voltage applied to the z drive (U_z). The recorded signal U_z and (U_x, U_y) for the lateral movement is converted into a topographic map (see Fig. 2-44). Although the principle seems to be simple, the interpretation of the topographic map is not trivial. Usually (and also in this work) it is called “topographic image”, not only the arrangement of the atoms determines the x,y,z result. For interpretation of the contours it is necessary to evaluate contributions of the tip and sample properties.

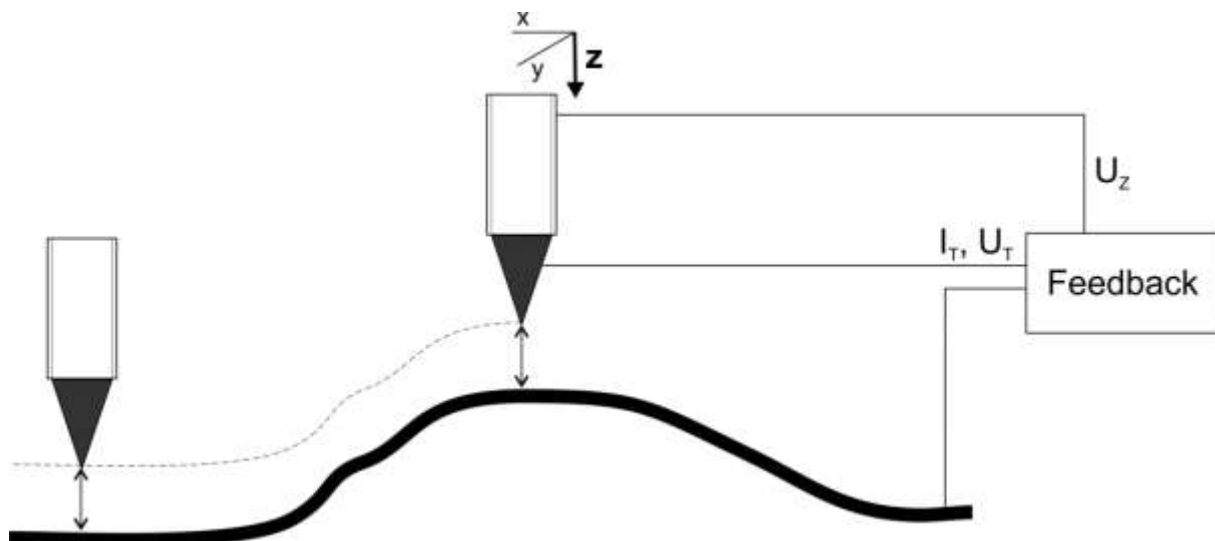


Fig. 2-44: Constant current mode. U_z =Voltage applied to the piezo drive for z movement (height).

The tunneling current is determined by the overlap of the tails of the wave functions from surface and tip. The scanning speed is limited by the feedback control unit and not fast enough for fast scanning like video-STM.

Constant height mode uses a pre-defined height profile; the height is kept constant and will not be adjusted (see Fig. 2-36). This method can prevent artifacts of the feedback loop. The scan speed is not limited to the response time of the feedback, but by the read-out of the tunneling current (the piezoelectric drive needs more time to register the height change than the change of the current). This mode can be used to observe real-time dynamic processes on atomic scale. A disadvantage is the higher requirement on long-time stability of the scan unit and the higher probability of a tip crash on larger structures.

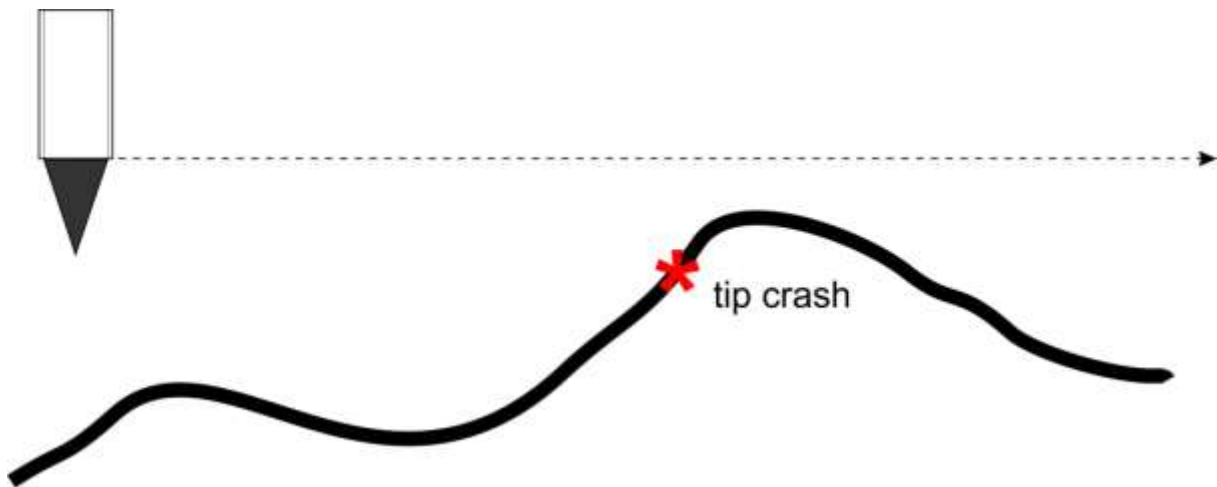


Fig. 2-45: Constant height mode. Large structures can cause a tip crash.

STM images are basically in grayscale, colors can be added in post-processing to highlight features [102].

2.7.1.5 Vibration isolation

The elimination of vibrations is an important step for a successfully operating STM system. The vibration can be a result of vibrations of the building (traffic outside the building, other running machines, air condition, vacuum pumps, and acoustic noises. In our case important problems were also vibrations from the sample plate (see also chapter 2.1.2). Another source of noises can be from the electrical installation).

Passive damping can be achieved with viscoelastic materials like Viton³ (against high-frequency vibrations and large amplitude shocks) and metal springs (against lower frequency vibrations). Metal springs are not very effective against vibrations and have to be used in combination with viscoelastic materials [109].



Fig. 2-46: Active anti-vibration system (air buffer) in our STM system.

To eliminate mechanical vibrations we used an anti-vibration device from Newport (active damping with air buffer working with air-flow), mounted on the whole system (Fig. 2-46). All

³ Fluoropolymer elastomer.

mechanical vacuum pumps need to be switched off. The STM device itself is using a metal spring core combined with Viton as an additional damper.

2.7.2 Data Processing and Acquisition

The STM system is controlled and data were recorded using the manufacturer's software "SPECsProbeUSB".

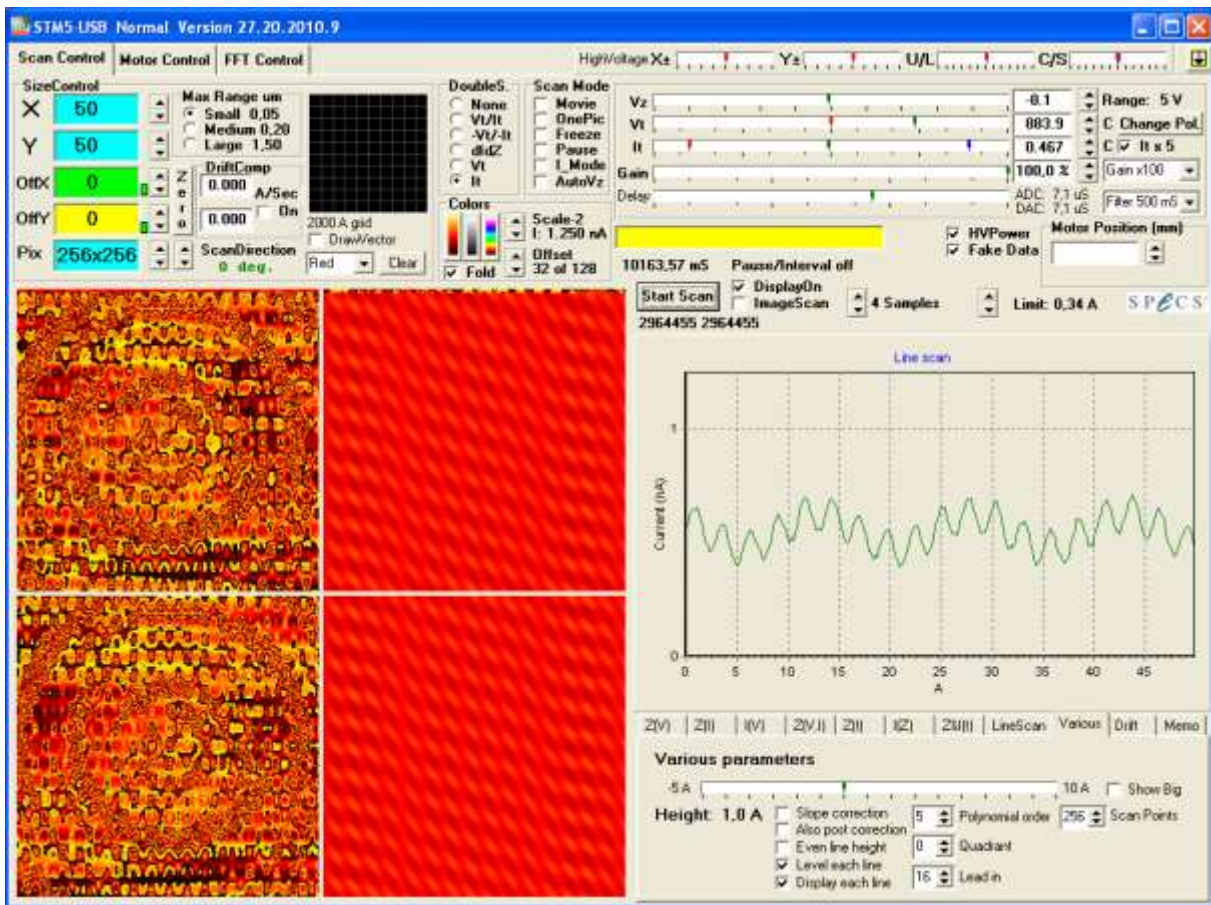


Fig. 2-47: Screenshot of "SPECsProbeUSB".

STM pictures processed with "STM Image Analysis" provided by the manufacturer Specs (which offers only some rudimentary features, but is useful for a quick view) and "WSxM" software from nanotec [111]. WSxM is basically designed for Nanotec AFM systems, however it is provided as a free application and is working with the files of our system and one of the most powerful programs available for this purpose. Also "Gwyddion" [112] is a powerful free (and open source) software, but finally we preferred WSxM.

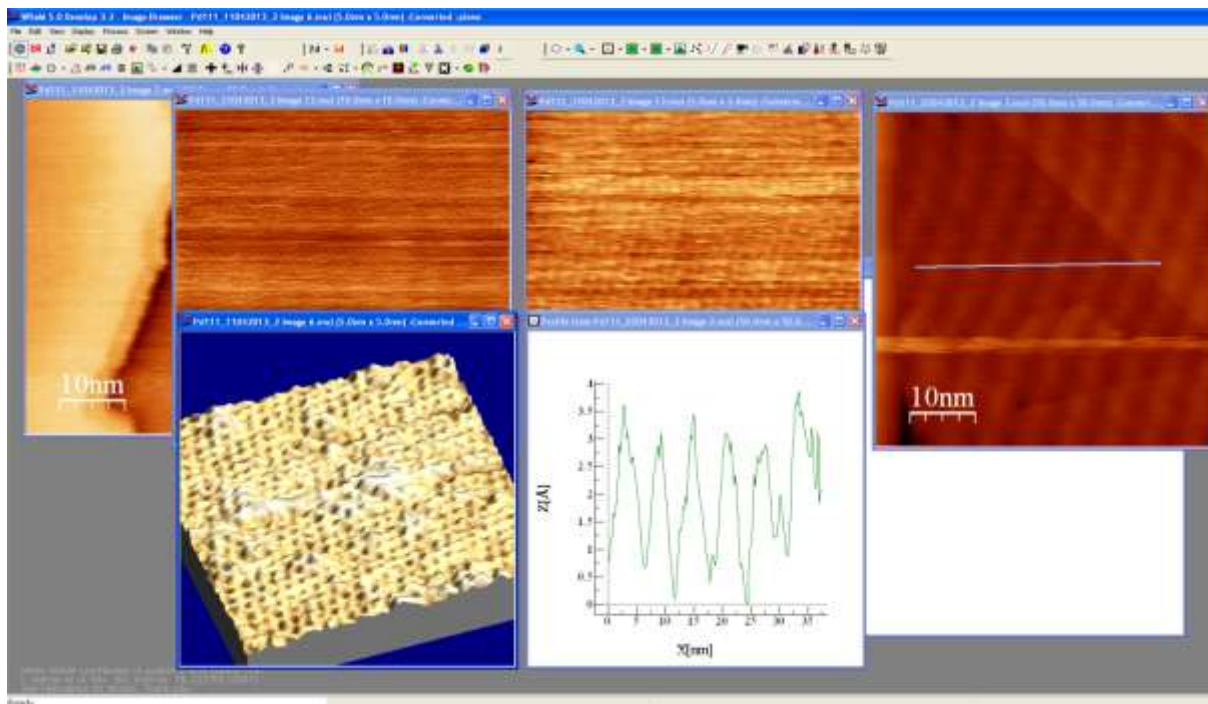


Fig. 2-48: Screenshot of WSxM software processing Pd(111) STM data.

2.8 Additional Components

2.8.1 Sputter Gun

For energetic ions with energies from a few hundred eV to some keV, surface atoms or adsorbed species can be ejected. The ions (e.g. Ar^+) are generated by electron impact within the filament of the sputter source and are then focused at the target (in our lab 1-3 kV are used). Impurities of the ion beam can be minimized with an optimized filament geometry. This is called “sputtering” process is used in surface cleaning and the same principle can also be exploited for ion pumps. With some modifications a sputter gun can also be used to deposit metal atoms on a surface.

The impact of such an ion on a surface stops its momentum energy which is transferred rapidly into a small region. The impacting ion loses some incoming energy which is then distributed to a sequence of collisions. The ion can be neutralized by acquiring an electron. The ejection of a target atom needs an outwardly directed momentum with sufficient energy. The sputtered particles come from the surface layer which is therefore roughened. The surface can get healed afterwards by annealing to appropriate temperatures [113].

2.8.2 Evaporator

The evaporant can be either evaporated from a bar, from a rod or from a crucible. This is achieved by electron bombardment heating. The first step is a heating process of a filament. The hot filament will produce an electron beam that is excited due to heating. Electrons are accelerated towards the evaporant by a high voltage. The bombarding electron beam induces a temperature rise of the evaporation material causing evaporation (the kinetic energy of the electrons is converted into thermal energy). The resulting vapor is then used to cover the surface of the sample. A crucible can only be used for easy to evaporate materials (e.g. low melting point like Zn as used for this thesis).

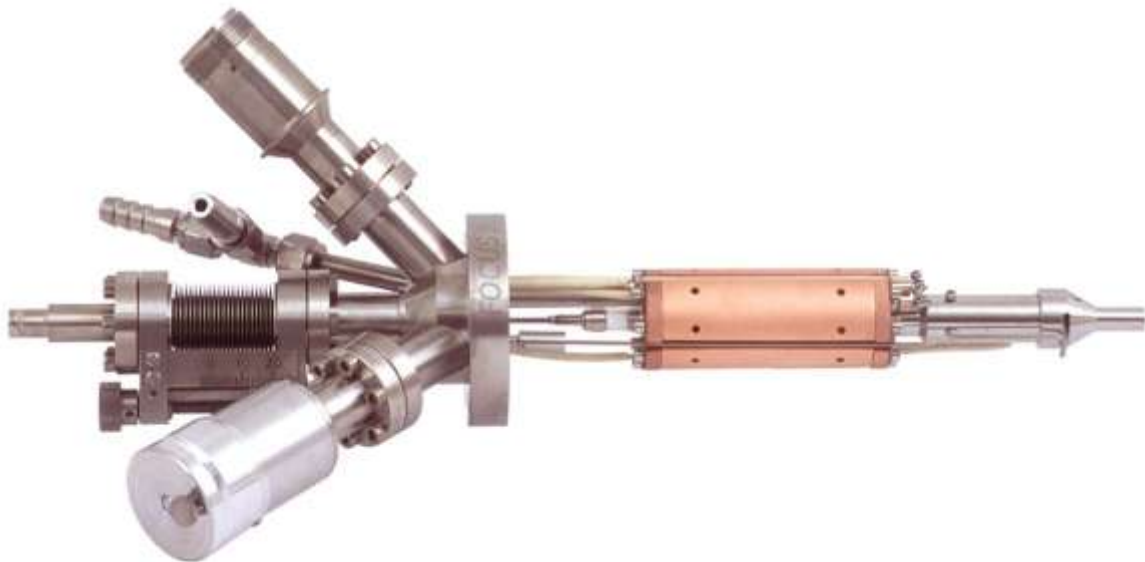


Fig. 2-49: Picture of an Omicron EFM 3 evaporator as used in our lab. The instrument is designed for high precision sub-mono-layer up to multi-layer deposition of a wide variety of evaporants including highly refractory materials.

The evaporation cell (a drawing is shown in Fig. 7-11, Appendix) is enclosed in a water-cooled copper cylinder. This, and the fact that just a restricted region of the evaporant is heated, facilitates to keep the background pressure during evaporation in the range of 10^{-9} mbar. The beam exit column contains an ion collector which serves as a flux monitor. At a given electron emission current and e-beam energy the ion flux measured there is directly proportional to the flux of evaporated atoms [114].

2.8.3 Thickness monitoring / Microbalance

A quartz crystal microbalance (QCM) measures a mass per unit area by measuring the change in frequency of a quartz crystal resonator. The core piece of the QCM is a piezoelectric quartz crystal sandwiched between a pair of electrodes. When the electrodes are connected to an oscillator and an AC voltage is applied over the electrodes the quartz crystal starts to oscillate at its resonance frequency due to the piezoelectric effect. The resonance is disturbed by the addition of a small mass at the surface of the acoustic resonator. Frequency measurements are easily made to high precision; hence, it is easy to measure very low mass densities [115].

The high sensitivity and the real-time monitoring of mass changes on the sensor crystal make QCM's very attractive technique for a large range of applications, e.g. for monitoring the rate of deposition in thin film deposition systems under vacuum.

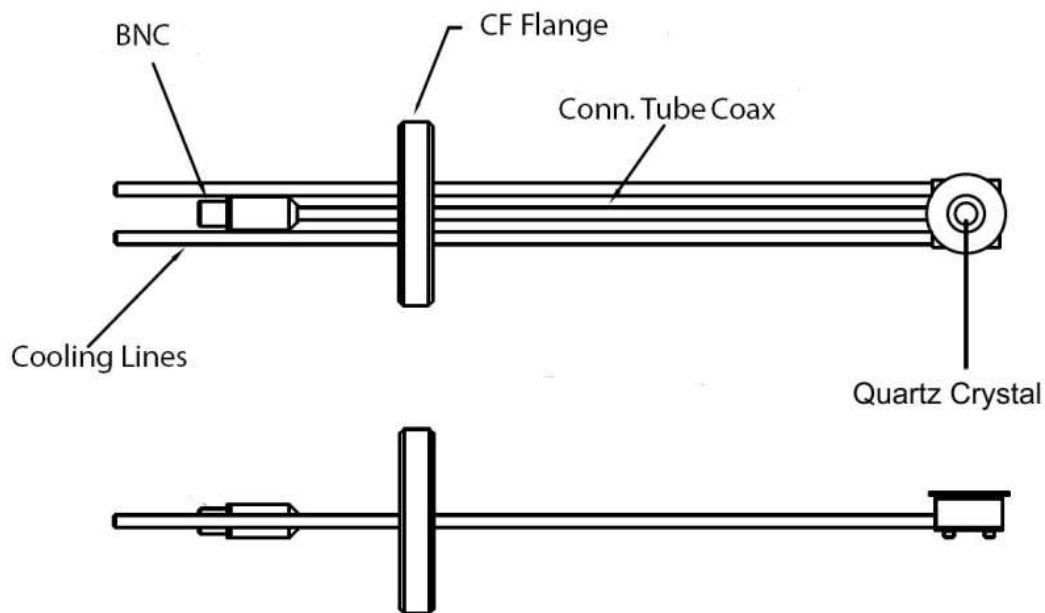


Fig. 2-50: Scheme of an Inficon microbalance as was used in our UHV-system.

2.8.4 Electron Beam Heater

In vacuum, free electrons can be easily influenced by electric and magnetic fields to form a sharp beam. At the spot of collision, the electron beam transfers kinetic energy to solid-state matter into heat. This offers the possibility of very fast localized precisely controlled heating. In our system, the filament consist of a thoriated tungsten wire [116]. Thoriated filaments are discovered in 1914 and made useable by Irving LANGMUIR in 1923 [117]. Thoriation increases the thermoionic emission. Thorium atoms are diffusing to the filament surface along grain boundaries and spreads over the surface by migration, this forms the emissive layer. This forms a monolayer and electropositive dipole effects are further reducing the work function from 4.5 eV (pure tungsten) to 2.6 eV (thorium itself has a work function of 3.3 eV). Heating in a hydrocarbon atmosphere carburizes the surface and stabilizes the emissive layer. This type of filaments is very stable and resistant to high voltages, because thorium atoms are continually diffusing to the surface and are renewing the layer [117-119].

The filament current is supplied with a potential between 600 and 1000 V with respect to the earth. The power through the heater can be either controlled manually or by a eurotherm temperature controller. The temperature on the sample can be measured via thermocouples. Although the design seems to be easy, a lot of care has to be taken, especially at high temperatures. The necessary sample holder setup and serious problems which can appear is described in chapter 3.6.

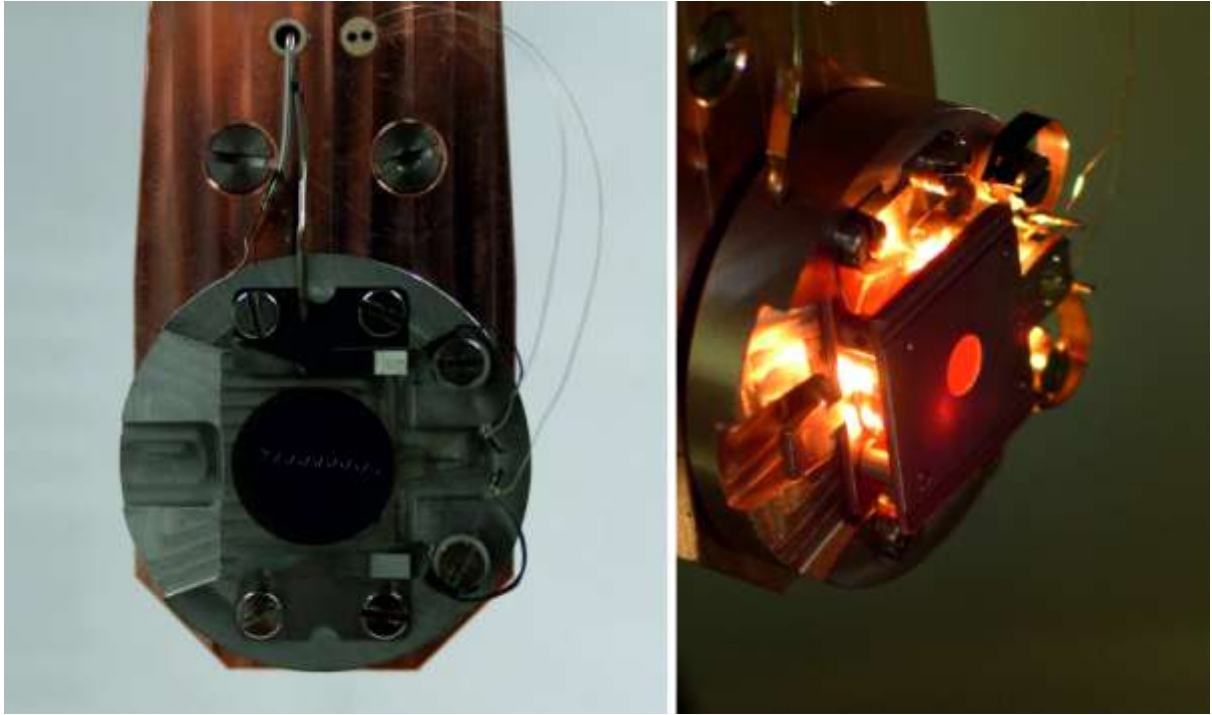


Fig. 2-51: E-beam heater of the STM system. Left: filament; right: glowing filament with sample.

2.8.5 Spot Welding

The heat obtained by the resistance to electric current of two metal parts in contact to each other can be used to weld these two parts together on a small spot. With two copper alloy electrodes, the metal sheets are clamped together on a small spot. A large current melts the metal and forms the weld. The advantage is that a big amount of energy (determined by the resistance between the electrodes, the magnitude and time of the applied current) can be concentrated on a small spot for a very short time. The amount of heat can be adapted to materials properties, their thickness and the electrodes. Usually a double pulse is used to get a better contact (the first pulse soften the metals and the electrodes can come closer for the second pulse).

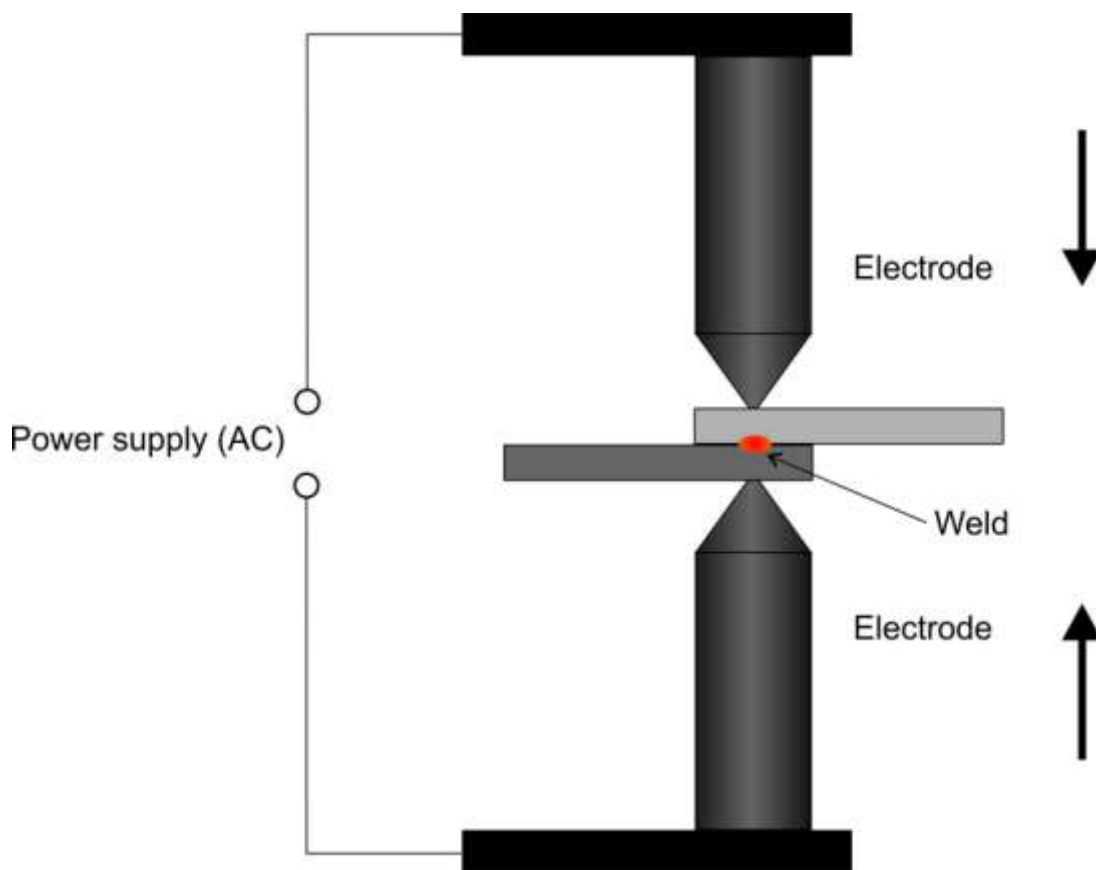


Fig. 2-52: Scheme of spot welding. A high current melts the metal and forms the weld.

2.8.6 Spark Plasma Sintering

By sintering, objects can be made of metal powders. In general, the material is heated up to temperatures below the melting point for some hours. The bonding of the atoms takes place by diffusion.

Spark plasma sintering (SPS) needs only a few minutes due to much higher heating rates. By application of both, temperature and high pressure, the temperatures can be lower than for conventional sintering. In this technique, high densities and nano-sized structures can be achieved and coarsening and grain growth is avoided [120, 121].

Contrary to the name, usually no spark or plasma occurs in this process. The DC current (~30 V, >600 A) passes through a graphite die where the powder is fed into. The SPS chamber is operated under argon atmosphere or in vacuum. An axial pressure is simultaneously applied during heating.

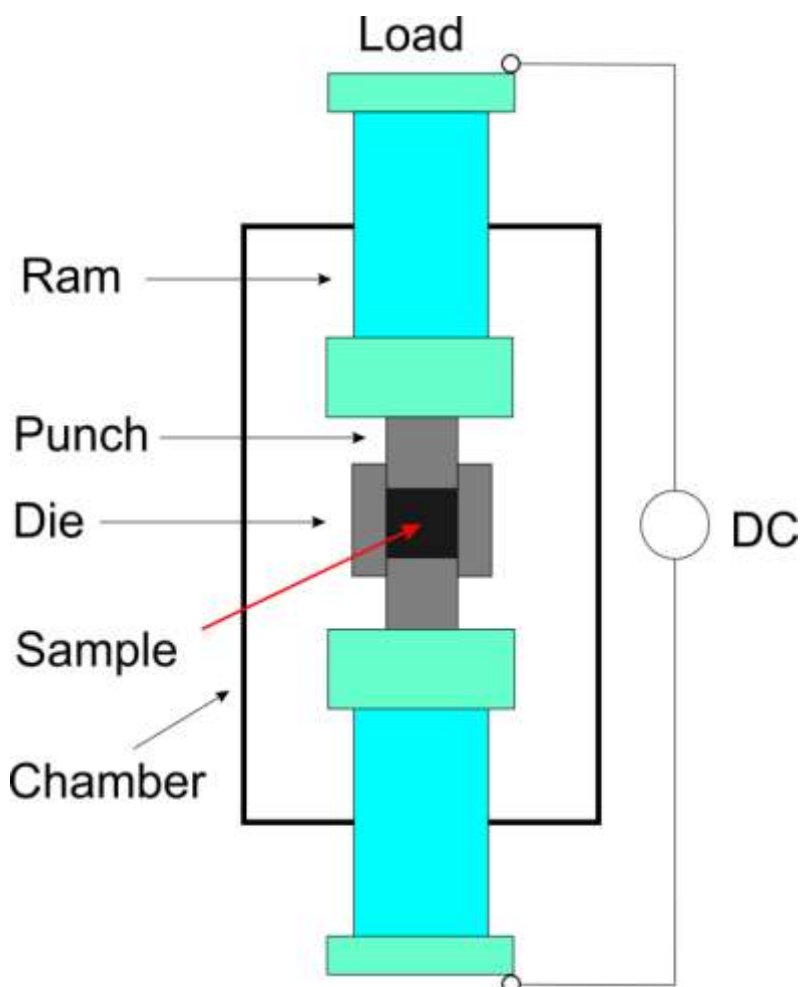


Fig. 2-53: Scheme of spark plasma sintering.

2.9 Ultra High Vacuum technology

2.9.1 Theory

Maxwell–Boltzmann distribution describes particle speed in gases. N particles in the volume V are in thermal nondirectional movement. For a given temperature, the speed of one particle is selected randomly from nearly zero to high values, but the probability is different. The number of particles in thermodynamic equilibrium with a velocity vector between v and dv can be expressed by equation (1.1.25).

$$dN = N \cdot \left(\frac{m_0}{2\pi kT} \right)^{3/2} \cdot e^{-\left\{ \frac{m_0 \cdot v_x^2 + v_y^2 + v_z^2}{2kT} \right\}} dv_x dv_y dv_z \quad (1.1.25)$$

(m_0 is the mean mass of one gas particle; the second and third factor of equation (1.1.25) can be explained as the probability $w(v)$ to find a particle with a speed between v and dv)

This leads to equation (1.1.26) [122].

$$dN = N \cdot w(v) dv_x dv_y dv_z \quad (1.1.26)$$

and

$$w(v) = \left(\frac{m_0}{2\pi kT} \right)^{3/2} \cdot e^{-\left\{ \frac{m_0 \cdot v_x^2 + v_y^2 + v_z^2}{2kT} \right\}} \quad (1.1.27)$$

In thermodynamic equilibrium, the *mean value of the velocity* vector is zero. On the other hand, the *velocity magnitude* has a non-zero value:

$$\bar{v} = \int_0^\infty \int_0^\infty \int_0^\infty v \cdot w(v) dv_x dv_y dv_z \quad (1.1.28)$$

For calculation one can make the assumption that the tips of all vectors with a quantity between v and dv are standing on the spherical shell ($4\pi v^2 dv$).

$$\bar{v} = \int_0^{\infty} 4\pi v^3 \left(\frac{m_0}{2\pi kT} \right)^{3/2} \cdot e^{\left\{ \frac{m_0 v^2}{2kT} \right\}} dv \quad (1.1.29)$$

This leads to the following integral:

$$\int_0^{\infty} v^3 e^{-av^2} dv \quad (1.1.30)$$

And the *velocity magnitude* can be calculated by

$$\bar{v} = \sqrt{\frac{8kT}{\pi m_0}} \quad (1.1.31)$$

One should note, that the *mean value of the velocity square* is not the square of the mean value of the velocity magnitude, it can be calculated by Equation (1.1.32) and (1.1.33).

$$\overline{v^2} = \int_0^{\infty} 4\pi v^4 \left(\frac{m_0}{2\pi kT} \right)^{3/2} \cdot e^{\left\{ \frac{m_0 v^2}{2kT} \right\}} dv \quad (1.1.32)$$

$$\overline{v^2} = \frac{3kT}{m_0} \quad (1.1.33)$$

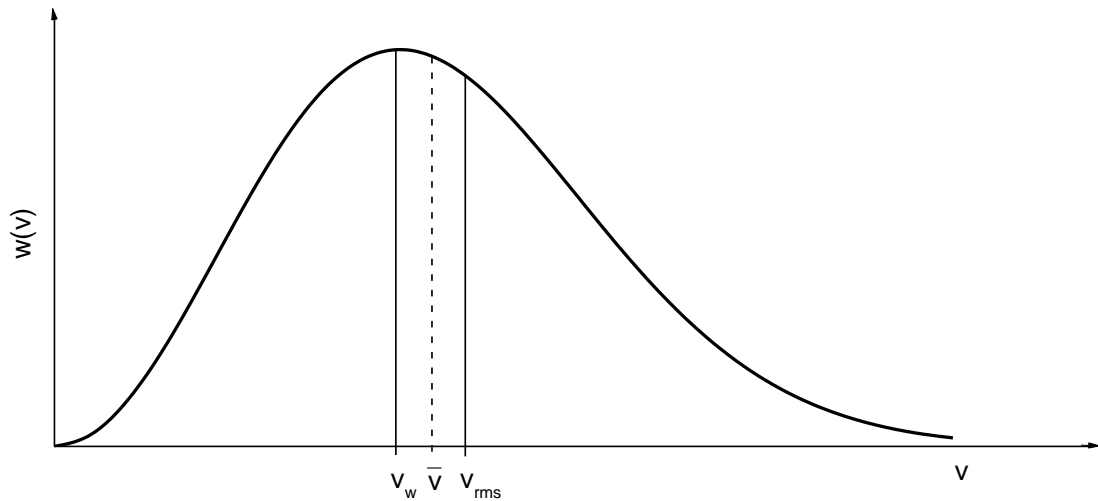


Fig. 2-54: Velocity distribution.

First, the velocity distribution increases (starting with zero at $v=0$) almost quadratically, then it reaches the maximum value at the most probable velocity v_w and finally decreases exponentially. The curve is not symmetric due to the factor v^2 , this means that higher velocities are more favored than lower (v_{rms} =velocity mean root square).

$$\begin{aligned}
 v_w &= \sqrt{\frac{2kT}{m_0}} \\
 \bar{v} &= \sqrt{\frac{8kT}{\pi m_0}} \\
 v_{rms} &= \sqrt{\overline{v^2}} = \sqrt{\frac{3kT}{m_0}} \\
 v_w &< \bar{v} < \sqrt{\overline{v^2}}
 \end{aligned}
 \tag{1.1.34}$$

The mean velocities of some different gases can be found in

Tab. 2-4: Mean velocities of gases at room temperature [122].

Gas/vapor	\bar{v} [m/s]
Apiezon ⁴	135
Argon	397
Oxygen	425
Nitrogen	454
Water	566
Helium	1256
Hydrogen	1757

Mean collision rate:

The number of collisions per time unit and volume among gas particles is called collision rate. In a simple model the gas particles are assumed as spherically. Their radii can be measured by collision experiments and are therefore indicated as gas kinetic collision radii.

Assumed, a gas particle (with a collision radius r_1 and a mean thermic velocity \bar{v}) moves through a gas with a collision radius r_2 . It collides in the time dt with all particles which are present in the cylindrical volume with the length $\bar{v} \cdot dt$ and the cross section $\pi \cdot (r_1 + r_2)^2$. This leads to equation (1.1.35).

$$dZ = n \cdot \pi \cdot (r_1 + r_2)^2 \cdot \bar{v} \cdot dt \quad (1.1.35)$$

and

$$v_V = \frac{dZ}{dt} = n \cdot \pi \cdot (r_1 + r_2)^2 \cdot \bar{v} \quad (1.1.36)$$

⁴ A silicon free hydrocarbon based ultra high vacuum grease.

Equation (1.1.36) can only be applied if exclusively the gas particle with r_1 is moving. With a view to also moving gas particles with r_2 , one cannot use the mean velocity of the colliding particle. The relative movement of the particles has to be used. Equation (1.1.36) needs to be modified to equation (1.1.37).

$$v_v = \frac{dZ}{dt} = \sqrt{2} \cdot n \cdot \pi \cdot (r_1 + r_2)^2 \cdot \bar{v} \quad (1.1.37)$$

Mean free path:

The distance which a gas particle can move without a collision is called mean free path Λ . It can be calculated by the assumption that a particle covers a distance s with the velocity \bar{v} per time dt .

$$s = \bar{v} \cdot dt \quad (1.1.38)$$

Here, $v_v \cdot dt$ collisions are taking place.

$$\Lambda = \frac{\bar{v} \cdot dt}{v_v \cdot dt} = \frac{1}{\sqrt{2} \cdot n \cdot \pi \cdot (r_1 + r_2)^2} \quad (1.1.39)$$

If $n=p/kT$ is used, Eq. (1.1.40) is obtained⁵:

$$\Lambda = \frac{kT}{\sqrt{2} \cdot p \cdot \pi \cdot (r_1 + r_2)^2} \quad (1.1.40)$$

This means, the mean free path is inversely proportional to the pressure [122].

⁵ By momentum transfer of all gas particles to a wall with an area A and an angle of incidence \mathcal{A} .e. all particles in a cylindrical volume with the area A and the length $v \cdot \cos \mathcal{A} dt$. Integration over the on the wall reflected part and the angle \mathcal{A} results: $p=F/A=nkT$.

2.9.2 Practical

Practical vacuum technology suffers from outgassing. Inner materials can release gas continuously in a small rate. To achieve ultra high vacuum special procedures are needed. A surface that has been exposed to air (from manufacturing process or from opening the chamber) will be in equilibrium with the gas. It will be covered with components of the air. Also, adsorbed gases from outside the chamber can permeate in a very small rate. Water from atmospheric pressure is dominating the adsorbed phase. Adsorbed gases near to the surface are tending to desorb under vacuum conditions. Permeation through the sealings has a significant contribution to the outgassing. Most of the free gas in the pumped chamber is soon removed, pressures in the range of 10^{-3} mbar can be achieved in some minutes, and, after starting turbo molecular pumps, pressures in the range of 10^{-6} mbar can be achieved in a few hours. At this pressures, the gas load from outgassing increases [113].

The binding energy of multilayer water molecules is 41 kJ/mol. When this weakly bonded molecules have been removed, the binding energy on typical materials for vacuum technology is in the range of 85 – 90 kJ/mol. Weakly adsorbed gases are quickly pumped away and gases with a high desorption energy (>100 kJ/mol) have a very small, neglectible contribution to the pressure in the chamber. Molecules between this desorption energies (e.g. ~ 80 kJ/mol for water) have a high and long lasting contribution [113].

Desorption rates are depending on the temperature, therefore it is possible to increase the desorption process dramatically at higher wall temperatures of the vacuum chamber. This procedure, heating up the system with continual pumping, is called bake-out. After venting the chamber (less water is absorbed when venting with dry inert gases, e.g. nitrogen) or after experiments with gases that are difficult to remove from the chamber, the system needs a bake-out. The vacuum system will be heated up to temperatures $>100^{\circ}\text{C}$ for several hours or days. The maximum bake-out temperature of the system is limited by sensitive parts of the system (e.g. piezos) or Viton⁶ gaskets, if used. The adsorbed gas is removed at a much higher rate than at room temperature, and gas from the bulk diffuses to the surface at a much higher rate. The surface of the wall is depleted of gas particles, and after cooling to room temperature the outgassing rate is dramatically reduced.

⁶ Fluoropolymer elastomer.

After bake-out all filaments have to be degased. In an UHV system, the permeation of hydrogen and helium from the atmosphere through the chamber wall material at room temperature becomes relevant, even though the atmospheric concentration of these gases is about 500 ppb (H) and 5 ppm (He) [123], respectively. Hydrogen permeates stainless steel and helium permeates glass. The permeation of other gases is usually not significant [113].

Tab. 2-5: Overview of properties in different ranges of vacuum [124, 125].

	Low vacuum	Medium vacuum	High vacuum (HV)	Ultra High vacuum (UHV)
Pumps	Rotary vane pump, membrane pump, scroll pump	Rotary vane pump	Turbo pump	Turbo pump, ion getter pump, cryo pump
Pressure range [mbar]	1000 - 1	1 - 10^{-3}	10^{-3} - 10^{-7}	$< 10^{-7}$
Mean free path [cm]	10^{-5} - 10^{-2}	10^{-2} - 10	10 - 10^4	$> 10^4$
Knudsen number $K=\lambda/D$	$< 10^{-2}$	10^{-2} - 0.5	0.5 - 10	> 10
Type of flow	viscous (laminar)	Knudsen range	molecular	Flow of single molecules
Particles per cm^3	10^{19} - 10^{16}	10^{16} - 10^{13}	10^{13} - 10^9	10^9 - 10^4

Tab. 2-6: Overview of vacuum in industry and nature [124, 125].

	Pressure [mbar]	Mean free path	Particles per cm³
Vacuum cleaner	ca. 800	70 nm	10^{19}
Light bulb	0,1 - 0,01	1 mm - 1cm	$10^{15} - 10^{14}$
Thermos flask	0,01 - 0,0001	1 cm - 1m	$10^{14} - 10^{12}$
Electronic tube	$10^{-7} - 10^{-9}$	1 - 1000 km	$10^9 - 10^6$
Satellite orbit	$10^{-7} - 10^{-8}$	ca. 2 km	$10^9 - 10^8$
Pressure on the moon	10^{-11}	10000 km	$4 \cdot 10^5$
Interplanetary space	$< 10^{-18}$	$\sim 10^{11}$ km	(10)
Interstellar space			(1)
Intergalactic space			(10^{-6})

2.9.3 Vacuum components

2.9.3.1 Materials for Vacuum Technology

All gases for experiments from this work were supplied by stainless steel pipes connected with Swagelok® tube fittings (Fig. 2-55). For reliable connection the tube (with ferrules as shown in Fig. 2-55) has to be fully inserted into the fitting and the nut rotated finger-tight and further tightened until the tube will not turn by hand. For final mounting the nut needs to be tightened by one and one quarter turns with a wrench (while holding the fitting body steady). To control the tightness a leak check has to be done using slightly overpressure and soap water (bubbles are indicating a leak).

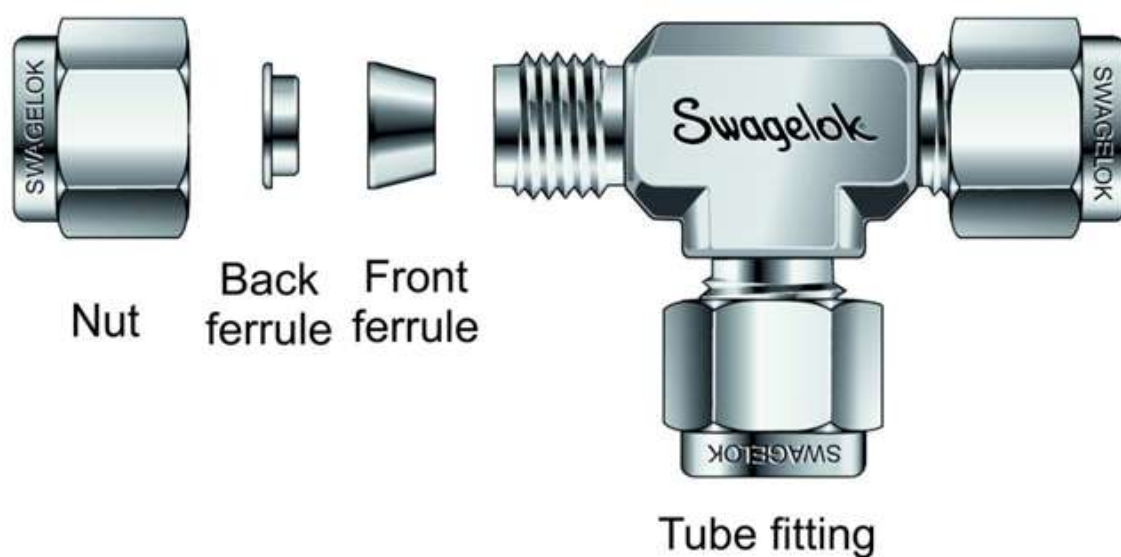


Fig. 2-55: Swagelok® fitting for connecting gasline tubes [Swagelok product catalogue].

Kleinflange (KF) constitutes an economical system of reusable interfacing stainless steel vacuum fittings and components standardized for DN10KF, DN16KF, DN25KF, DN40KF, and DN50KF. Assemblies are usable to 10^{-8} mbar. Maximum temperature for sustained use is $\sim 150^{\circ}\text{C}$. They are ideal for vacuum systems requiring regular assembly and disassembly. The KF flanges seal is made by compression of a Viton®-(or sometimes Nitrile)-O-ring between mating flanges. The seal is made in seconds by finger-closure of a wing nut on the circular

clamp (see Fig. 2-56). A metal carrier is designed that it stops the o-ring distorting when the seal is made, that means that it is impossible to over tighten the o-ring.

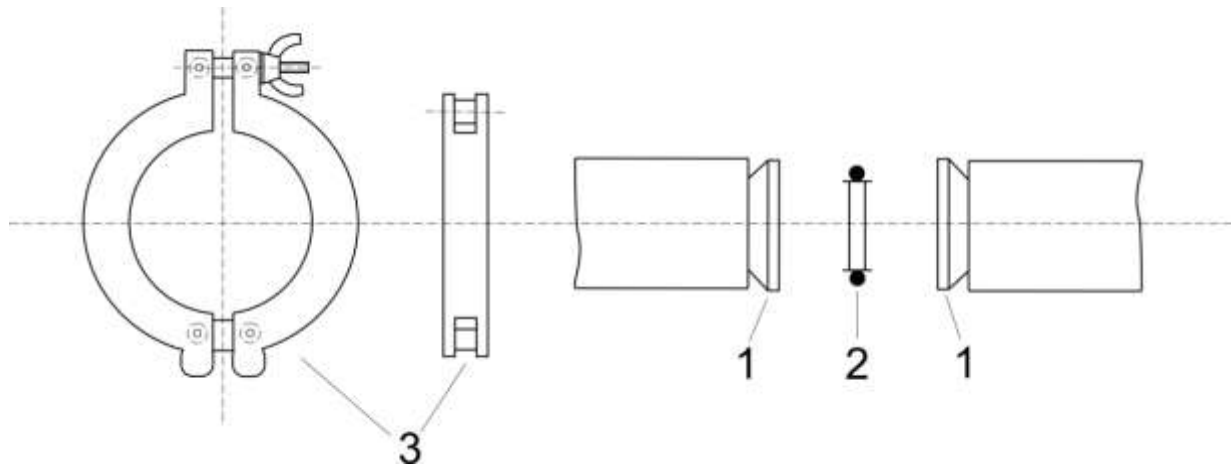


Fig. 2-56: Scheme of a Kleinflange (KF). 1=Kleinflange, 2=centering ring, 3=clamping ring.

*Conflat*⁷ (CF) flanges (see Fig. 2-57) are using copper gaskets and knife-edges to achieve an UHV seal. Each face end of a CF flange has a knife edge which cuts into the softer metal gasket, providing an extremely leak-tight, metal-to-metal seal. Bolting the flanges together causes the CF knife-edges to deform the gasket. The knife edge is recessed in a groove to hold the gasket in place and to reduce gasket expansion during bake out.

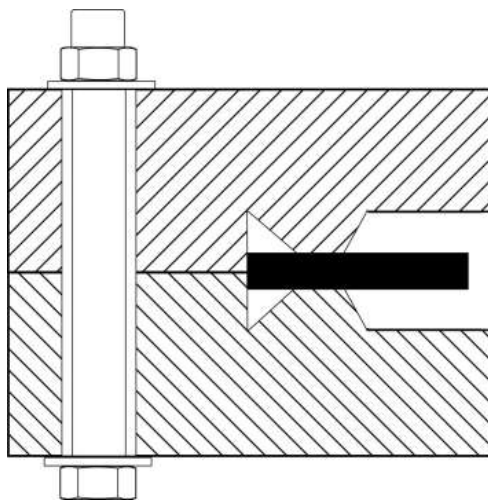


Fig. 2-57: Scheme of a CF flange. Aa knife edge cuts into the copper gasket (black), providing an extremely leak-tight, metal-to-metal seal.

⁷ The name Conflat was registered by Varian Inc. (now part of Agilent Technologies), so usually the name CF is used by other manufacturers.

The maximum bake out temperature is limited by the gasket material. A copper gasket is bakeable up to 450°C but can only be used once. If the flange has to be opened very often, a Viton[®] gasket can be used, but the bake out temperature is limited to 120°C and the reachable vacuum is not as good as when using copper. For fragile flanged components it is recommended to use annealed copper gaskets which are softer.

A *vacuum feedthrough* is a flange that contains a vacuum-tight electrical or mechanical connection to the vacuum chamber. An electrical feedthrough allows voltages to be applied to components inside the vacuum chamber. A mechanical feedthrough is used for translation (x,y,z) and rotation of components. A wobble stick is a mechanical feedthrough system for picking up and manipulate objects inside the vacuum chamber. Another type of transfer mechanism is a rod using a stiff high flux magnetic coupling. This removes the need for bellows or sliding seals and is compatible with UHV environments.

Vacuum grease is a lubricant with very low volatility for applications in vacuum conditions. A higher volatile compound like in common lubricants would evaporate, which makes it impossible to get a good vacuum, also it would not be present to provide lubrication. Special hydrocarbon based vacuum sealants, greases and lubricants (like Apiezon[®]) can be used in the range of 10^{-9} mbar at room temperature [126, 127].

2.9.3.2 Vacuum pumps

There is no pump which can be used in the whole range from low vacuum up to UHV for its own. Common pumps for low vacuum (called pre-vacuum in an UHV system) are rotary vane pumps, diaphragm pumps and scroll pumps.

The types of pumps that are available to meet these needs can be classified in:

- positive displacement pumps, gas is manipulated using repetitive mechanical movements of driven parts and synchronized valve actions that displace it from the inlet to the outlet in discrete amounts (e.g. rotary vane pumps). These pumps can operate mostly in the range from atmospheric pressure down to 10^{-3} mbar.
- momentum transfer pumps, incoming gas molecules interact with very fast-moving blade that add a directed impulse to their motion and transfer them continuously to an outlet at a pressure much below the atmospheric pressure (e.g. turbomolecular pumps).
- In capture pumps, molecules are removed from the gas phase by being trapped on surfaces by the physical or chemical processes of condensation and adsorption, there is no pump outlet (e.g. cryopumps, sublimation pumps, and ion getter pumps).

Tab. 2-7: Short overview of vacuum pumps [124].

Gas transfer pumps						Gas-binding pumps
Gas displacement pumps			Kinetic pumps			
Oscillation displacement pumps	Double rotor displacement pumps	Single rotor displacement pumps	Mechanical kinetic pumps	Propellant pumps	Ion transfer pump	Adsorption pumps
Diaphragm pump	Roots pump	Liquid ring pump	Gas ring pump	Propellant jet pump		Ion getter pump
Piston pump	Screw pump	Rotary vane pump	Turbomolecular pump	Diffusion pump		Sublimation vaporization pump
Scroll pump	Claw-type piston pump	Rotary piston pump				Cryopump

Rotatory vane pumps (s. Fig. 2-58) are the most common pumps for creating pre-vacuum in UHV systems. Due to the very simple and highly reliable design, this type of pumps provides excellent vacuum performance, high pumping stability and a long operating life.

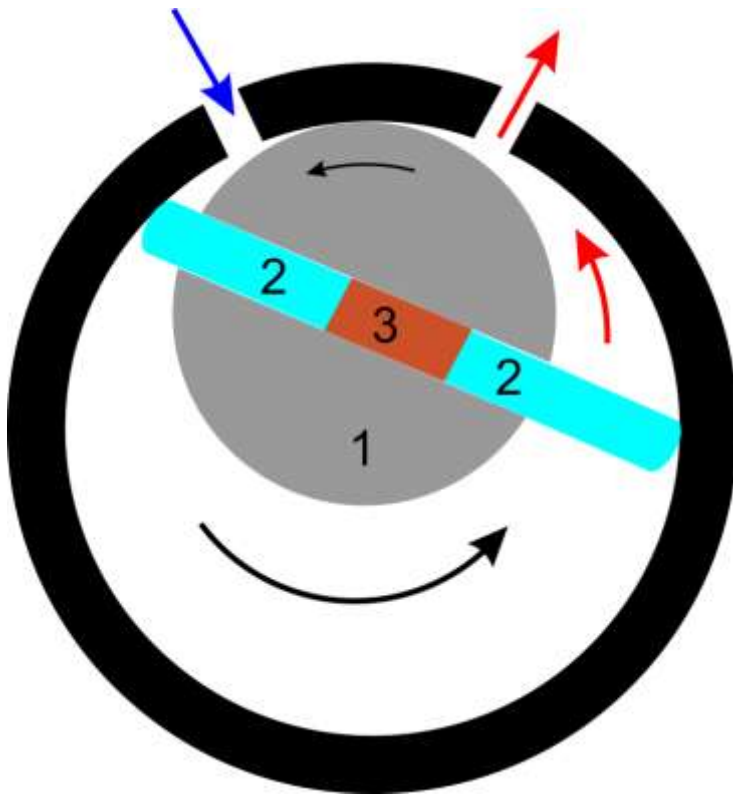


Fig. 2-58: Principle of a rotary vane pump, 1=rotor; 2=vanes; 3=pushrod/spring [128].

A rotor is rotating eccentrically inside the circular pump housing and is sealed into the cam by two side-plates. As the rotor rotates and fluid enters the pump, centrifugal force, hydraulic pressure, and pushrods push the vanes to the walls of the housing. The tight seal among the vanes, rotor, cam, and sideplate is the key to the good suction characteristics common to the vane pumping principle. This creates vane chambers with different volumes. On the inlet, the volume expands. On the outlet side, the volume will be compressed and then exhausted with every full rotation. To improve the performance, rotary vane pumps can be operated as multiple stage pump system. A pressure down to 10^{-3} mbar can be achieved. Backstreaming of oil can be a serious problem in case of an electricity blackout. Oil backstreaming can be reduced by an anti-suckback valve or an oil mist separator to prevent oil contamination of the vacuum system when the pump is switched off (manually by a mistake or in case of power fail). However, there is always a very small oil backstreaming into the UHV chamber which can be a problem in highly sensitive systems during long-time operation (e.g. STM). In those cases an oil-free pre-vacuum system should be considered.

In case of pumping condensable gases at corresponding temperatures (i.e. organic solvents), the pumps needs operate in gas ballast mode. The outlet valve opens before the vapor

condenses. Vapor and ballast gas are discharged together. This corrupts the attainable vacuum but prevents condensation of vapor in the lubricating oil [124, 129].

The *scroll pump* uses two interleaving scrolls to pump gases (it can be also used as compressor). One scroll is fixed, the other one moves eccentrically (but not rotating). To prevent abrasion, a Teflon gasket is used as lubricant. On advantage is that the pump needs no oil. Disadvantages are the lower performance then rotary vane pumps and, when it's used in continuous operation, the Teflon ring has to be replaced every few month.



Fig. 2-59: Mechanism of a scroll pump



Fig. 2-60: Scroll pump orbiting (left side) and Teflon sealing (right side).

Turbomolecular pump:

The principle of the *molecular pump* is that the gas particles to be pumped receive, through impact with the rapidly moving surfaces (rotor blades), a momentum in a designed flow direction. The surfaces of the rotor blade form, with the stationary surfaces of a stator, intervening spaces in which the gas is transported to the backing port. A pumping effect can be only attained when the circumferential velocity (at the outside rim) of the rotor blades reaches the order of magnitude of the average thermal velocity of the molecules which are to be pumped. The mean thermal velocity depends on the type of gas as a function of molar mass.

In modern *turbomolecular pumps* the momentum transferring surfaces are the inclined surfaces created by machining angled slots radially inwards from the edge of a circular disc to form a bladed rotor that resembles the multiple-bladed structure of an axial flow turbine. The rotors turn at speeds sufficient to give their outer parts velocities comparable with molecular velocities. Each rotor is paired with a similar set of stationary stator blades. The flow direction is axial, and although the structure resembles a turbine arrangement, the pump operates in the molecular flow range. The basics of the pumping action is that the inclined blades, in moving at high speed through the gas, intercept more molecules on their downward facing side than if they were stationary and tend to project them in an axial direction. This action is duplicated by the stator blades that receive molecules that have gained a velocity increment in rebounding from the rotor [113, 130].



Fig. 2-61: 3D model of a turbomolecular pump [131].

A cut through a turbomolecular pump model. The different rotor sizes and grain sizes can clearly be seen in Fig. 2-61.

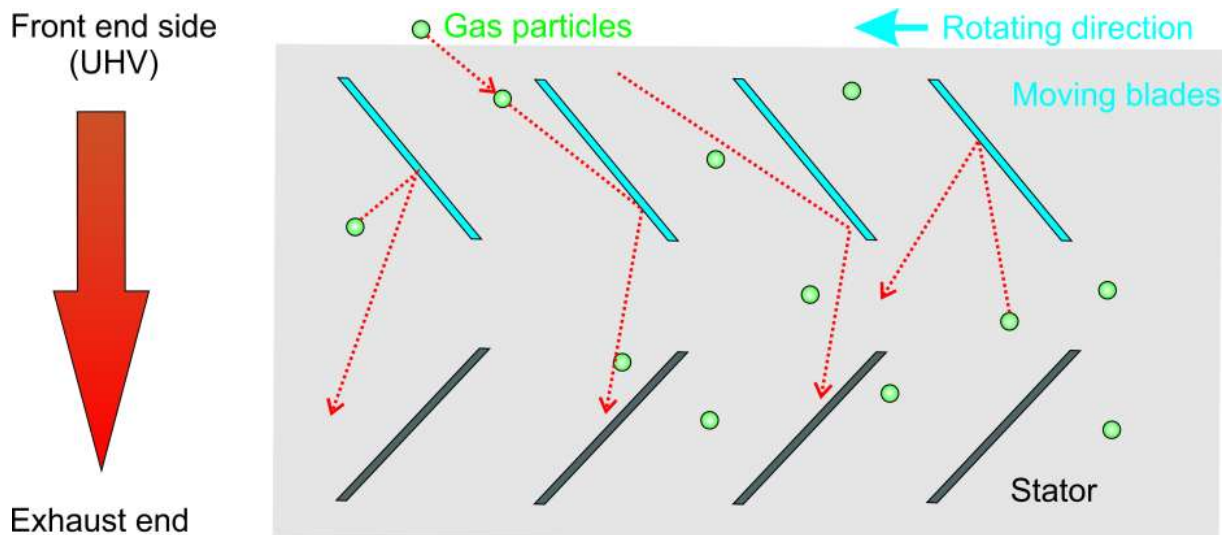


Fig. 2-62: Momentum transfer in a turbopump.

The bearings can be oil- or grease-lubricated, or magnetic. Water or air cooling is required to cool bearings and motor especially with high throughput and high inlet pressures.

Pumps with magnetic bearings use a combination of the fields of permanent magnets and electromagnets to levitate the rotor assembly and control the motion. They held vibrations to a minimum and are free from contamination and therefore ultraclean, but much more expensive.

To operate a turbo molecular pump, a backing pump (usually a rotary vane pump or scroll pump is used) is required to exhaust the turbo pump to the atmosphere and must be of adequate size for roughing out the pump and the chamber.

The *titanium sublimation pump* is used to augment pumping in some UHV applications. It works by capturing molecules by chemisorption on freshly deposited surfaces of titanium film, forming stable surface compounds such as titanium (e.g. titanium hydride, titanium oxide, titanium nitride ...). Freshly deposited, titanium has a highly reactive surface, gettering most gases (except noble gases and some other inert molecules). The pump is designed that titanium sublimates from the surface of a filament made of titanium or a titanium alloy (85% Ti, 15% Mo). The filament is resistively heated by passing a current ~40 A through it. Usually three filaments are mounted on a flange (see Fig. 2-63). Current to the supporting electrodes is supplied via electrical feedthroughs in the flange. The filaments get thinner with use and have to be replaced from time to time. Cooling down (with liquid nitrogen) the surfaces onto which titanium is deposited can improve the capture rate (see Tab. 2-8).

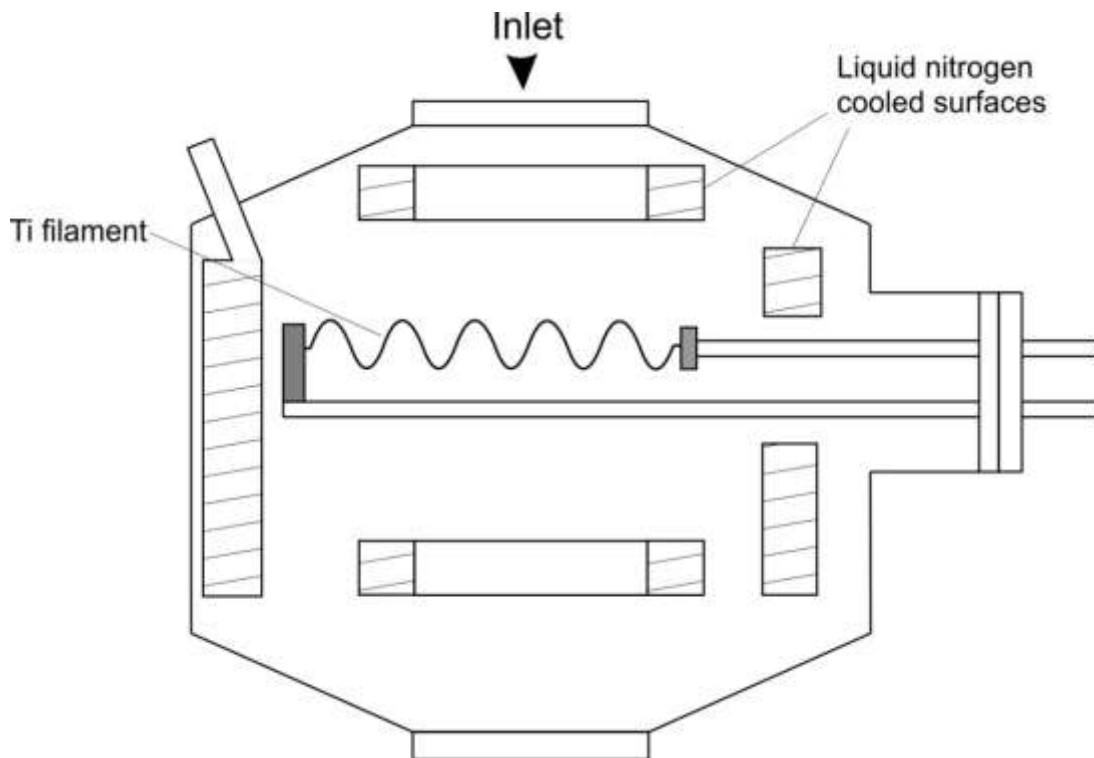


Fig. 2-63: Scheme of a titanium sublimation pump.

Tab. 2-8: Measured TSP pumping speeds for some gases (in $l\ s^{-1}\ cm^{-2}$) [113].

Gas	H ₂	N ₂	O ₂	CO	H ₂ O
295 K	3	4	9	8	3
77 K	10	10	11	9	14

Operation does not need to be continuous for long periods; the fresh surface is created by depositing titanium only periodically when the deposited layer becomes saturated. The highest pressure for operation is in the range of $\sim 10^{-5}$ mbar. At low pressures, the time to saturation is longer [113].

Ion-getter pumps are using the effect of ionization of gas molecules and getting them in titanium. The basic principle is the ejection of a number of atoms from a surface due to the impact of a single energetic particle such as an ion accelerated in an electric field (see Fig. 2-64). The basic element is a diode consisting of a short cylindrical tube anode (A), made of thin stainless steel, and two cathode plates (K1/K2) made of titanium whose planes are perpendicular to the cylinder axis. A strong magnetic field (~ 0.15 T) from permanent magnets external to the stainless steel pump casing is directed parallel to the cylinder axis. The cathodes are earthed and the anode is at a potential 3–7 kV. The discharge is initiated by the

creation of an electron due to field emission at a cathode. Its acceleration to the anode is prevented by the presence of the strong magnetic field that causes it to spiral around a magnetic field line. The electrons follow long spiral trajectories around field lines back and forth between the cathodes [113].

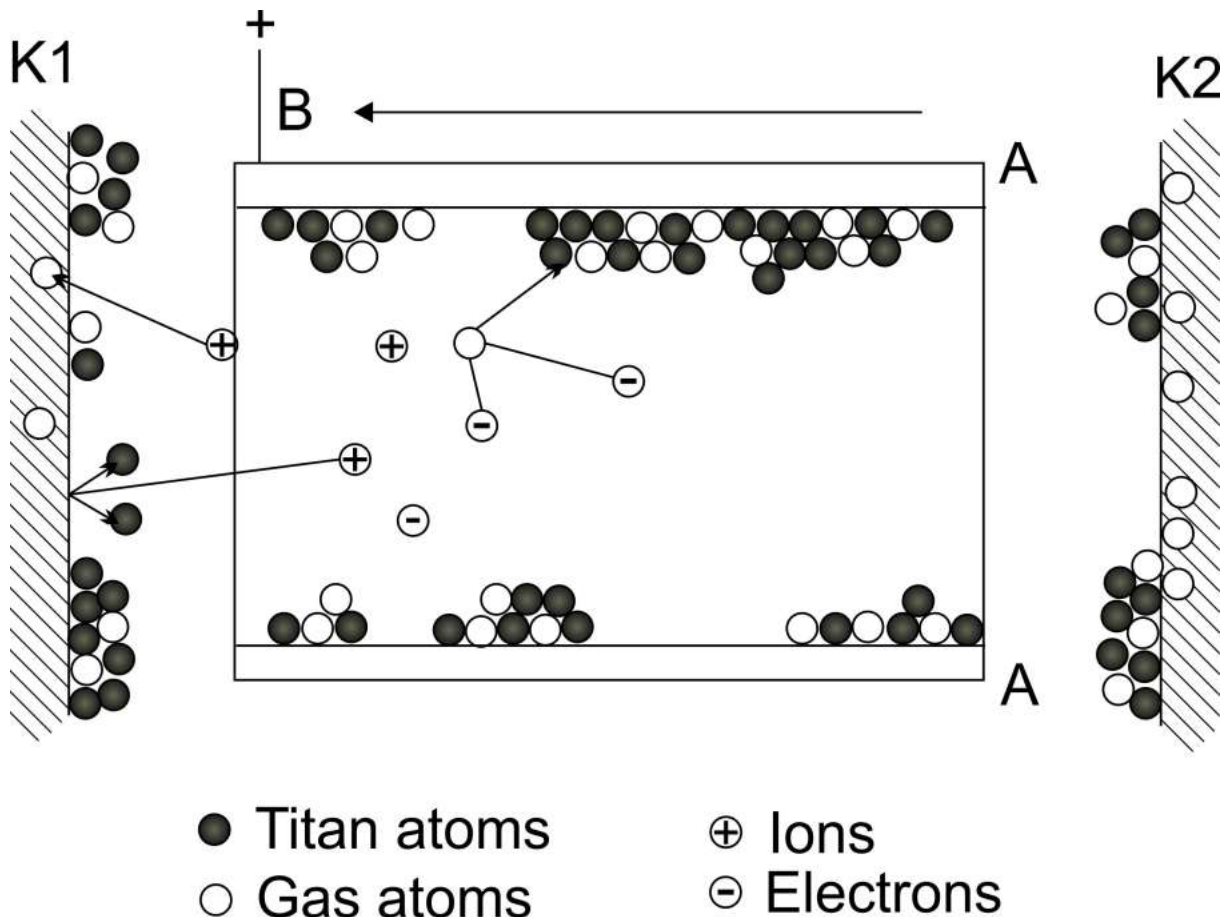


Fig. 2-64: Getter pump: schematic drawing of the pumping effect of an adsorption pump. *K1, K2* getter cathode plates (Ti); *A* anode cylinder; *B* magnetic field; on *A* and outlying area of *K1* and *K2* gas particles covered with getter material (Ti); implanted gas particles in the inner area of *K1* and *K2* [125].

The presence of the large negative space charge causes the potential along the cylinder axis in the central region between the cathodes to be slightly below cathode potential. Therefore, the electric field within the cylinder is radial and perpendicular to the magnetic field. Outside the cylindrical space charge region, the electric field becomes increasingly axial.

Implantation of ions: The ions are moving almost straight to the cathode. Contrary to electrons, the magnetic field has only a low influence on the ions because of the higher mass. The penetration depth of the ion is in the range of 10 atom layers (“implantation”). This gettering effect acts on all gas atoms and molecules, even noble gases (even though He is very

difficult to pump, but the small size of helium atoms enables easy diffusion). Very large molecules cannot penetrate, but fragments of the impact on the cathode can be captured.

Cathode evaporation: The impact of ions on the cathode surface can remove some atoms from the getter material away to other surfaces in the surrounding. This develops a getter film on the anode and on the outlying area of the cathode. This pumping effect depends strongly from the type of gas.

Implantation of neutral particles: Ions, particularly from noble gases, can be reflected from the cathode surface if they will get neutralized on the metal surface. They will be implanted on another place due to the high kinetic energy.

The freshly deposited titanium surfaces pump the neutral molecules of active gases (e.g. N₂, CO, ...) by chemisorption as in the TSP. The pumping is enhanced for dissociated molecules. The other mechanism buries the molecules into the cathodes to become buried as stable trapped compounds. However, depending on how deep the molecules were buried, some may be later released by resputtering. This is particularly the case for argon atoms.

The operation conditions are limited to high vacuum. This has to be kept in mind when dosing gases in the vacuum chamber. In our STM-system the ion getter pump is located in the STM chamber and separated from the preparation chamber (except for sample transfer).

Pumping speeds are a maximum in the region of $\sim 10^{-7}$ mbar, falling off at lower pressure. They provide a very clean ultrahigh vacuum environment, which is necessary for many applications (e.g. STM) [113, 122].

2.9.3.3 Pressure measurement

The vacuum measured in this work span a range of at least 13 orders of magnitude, from atmospheric pressures down to 10^{-10} mbar and below. No single type of measuring device can cover this range. Those that measure force directly are restricted to higher pressures. Determination of lower pressures requires the measurement of other phenomena in the vacuum that depend on the number density n . Effects that can be used are thermal conduction, viscosity and ionization, these methods are described as indirect, and calibration is in most cases required. In most vacuum systems the usage of a rough vacuum pump is required to operate other types of pumps to attain high vacuum and ultrahigh vacuum. Therefore, more than just one type of gauge is usually needed to span the range of operation, monitoring the pump-down process and the finally achieved pressure.

Capacitance Diaphragm Gauge (“Baratron”)

Gauges that rely on a change in capacitances are often referred to as *Baratron gauges*. When the flexure of a diaphragm is sensed electrically rather than mechanically, greater sensitivity and precision are possible. The basic principle measuring a vacuum is that the pressure-induced displacement of a metallic diaphragm with respect to a fixed partner electrode close to it causes a change in their mutual capacitance, which is converted to a pressure reading. The deflection of the diaphragm is measured as the change in capacitance of a plate capacitor. One electrode is fixed; the other is formed by the diaphragm. When the diaphragm is deflected, the distance between the electrodes and thus capacitance of the capacitor is altered (see Fig. 2-65). The sensitivity and measuring range depends on the stiffness of the diaphragm. For a device with a nominal range of 0–1000 mbar the high pressure must move the diaphragm close to electrode without touching it, and a relatively stiff diaphragm is required. For a version designed for lower pressure maxima, a weaker diaphragm is used. The pressure can be measured with the sensors to an accuracy of about 10^3 . Therefore, typical devices are 1000 to 1 mbar, 100 to 10^{-1} mbar, 10 to 10^{-2} mbar, and 1 to 10^{-3} mbar. Typical accuracies are better than $\pm 1\%$ in the upper three decades of operation with reduced accuracy at lower pressures. The capacitance diaphragm gauge represents the only absolute pressure measuring instrument that is independent of the type of gas and designed for pressures lower than 1 mbar [129, 130].

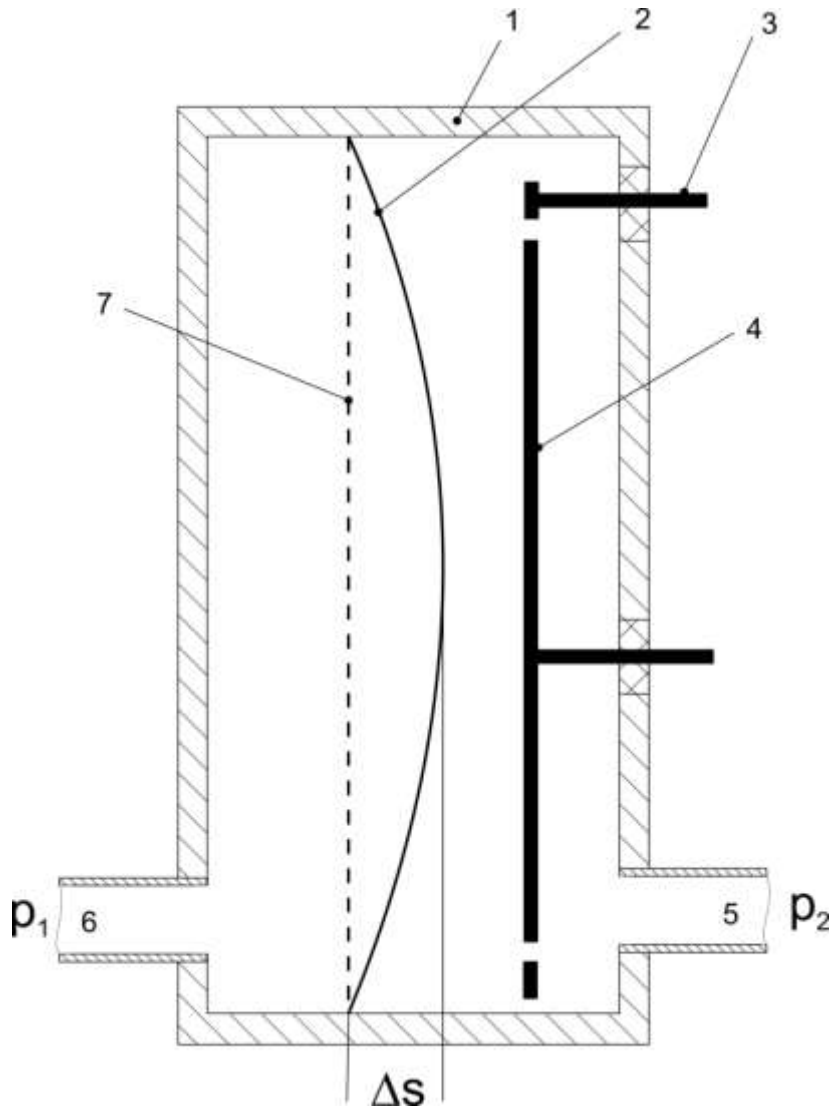


Fig. 2-65: Baratron gauge. 1=housing; 2=membrane; 3=feedthrough capacitor ring, 4=capacitor ring; 5=gas inlet (reference pressure p_2); 6=connection to vacuum chamber with pressure p_1 to be measured; 7=membrane zero position, Δs =membrane displacement [125].

Pirani gauge:

The basic arrangement is that the filament (with the electrical resistance RF), is incorporated into a *Wheatstone* bridge circuit. A DC power source (with the voltage V) sends current through branches $(RF+R1)$ and $(RC+R2)$. The current through the former maintains the filament with resistance RF at a designated temperature of about 100–150 K above room temperature. The branch $(RC+R2)$ contains a compensating resistor (to allow changes in ambient temperature that would cause bridge unbalance). The detector D senses out-of-balance current. The bridge is balanced at good vacuum where the heat loss due to gaseous conduction is negligible in comparison with the small heat loss due to thermal radiation.

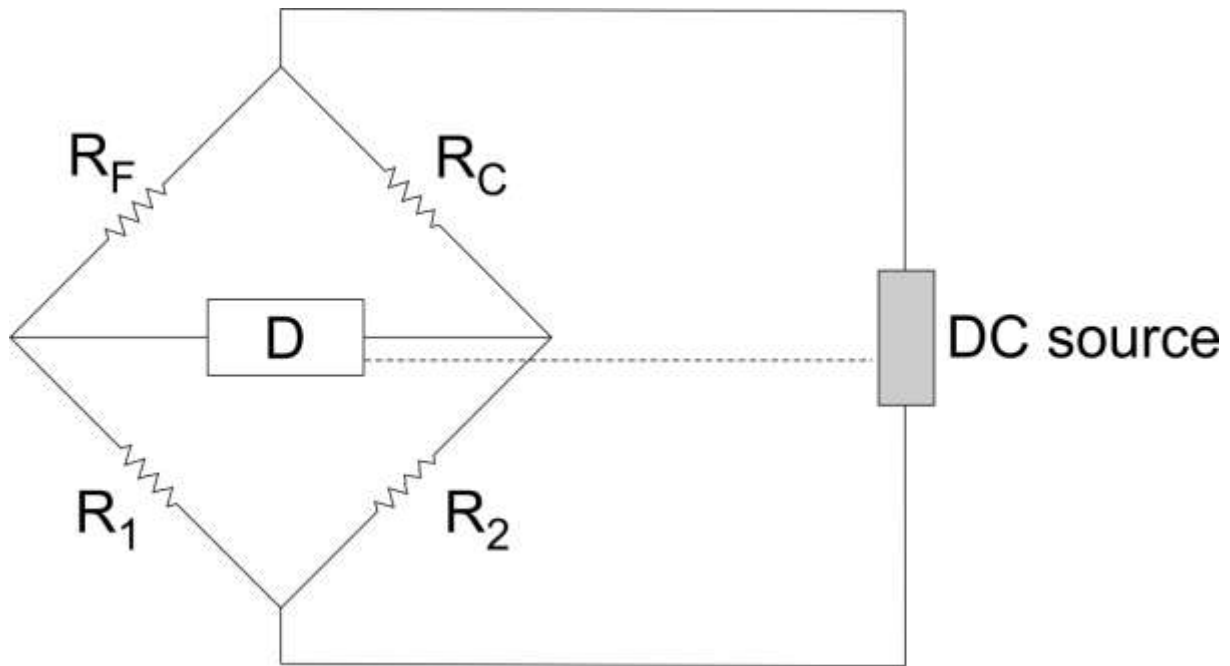


Fig. 2-66: Scheme of a Pirani gauge. R_F =electrical resistance of the filament, R_C =compensation, R_1, R_2 =resistance of the branches, D =detector.

These determine a threshold level in the range of $\sim 10^{-3}$ mbar. The gauge is not sensitive at lower pressures. At higher pressures, due to the conduction through the gas cools down the filament and therefore resistance. This is unbalancing the *Wheatstone* bridge and its output signal gives a measure of pressure. Filaments are usually made of tungsten (the electrical resistance depends strongly on temperature). Modern electronic control can measure in the range up to 1000 mbar. The gauge measures the total pressure for gases and vapors and its response can considerably from the gas species. The gauges are usually calibrated for nitrogen [113].

Ion gauge:

The routine measurement of high and ultrahigh vacuum is possible only using ion gauges. Gauges using mechanical, viscous, or thermal effects have inadequate sensitivity at pressures in the UHV range. There are of two basic types. In the hot cathode ionization gauge, a current of electrons, released thermionically from a filament, is accelerated to ionize some of the gas molecules, creating positive ions. The rate of ionization is proportional to the number density of molecules and hence the pressure. The current of ions is collected and affords a measure of pressure (see Fig. 2-67, Fig. 2-68, and Fig. 2-69).

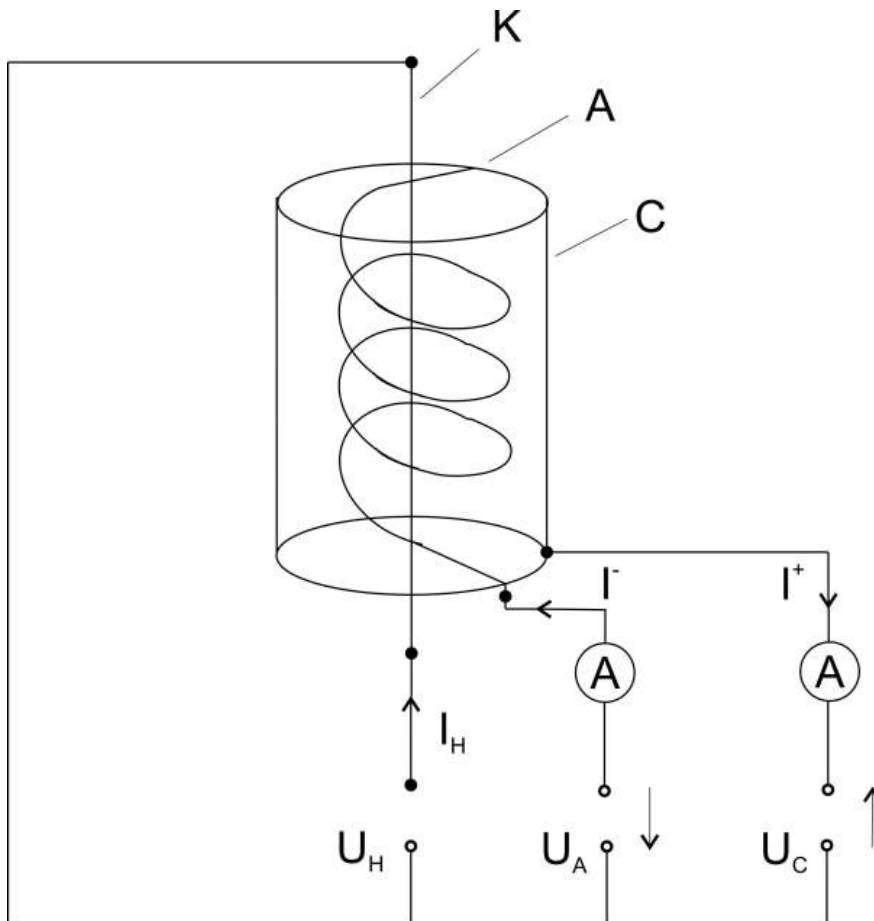


Fig. 2-67: Ion gauge. U_H =Filament voltage; U_A = Anode potential (acceleration voltage); I_H = Filament current of glow anode; I^- =Electron current to anode; i^+ =Electron current to collector; K=Cathode; A=Anode; C=Collector.

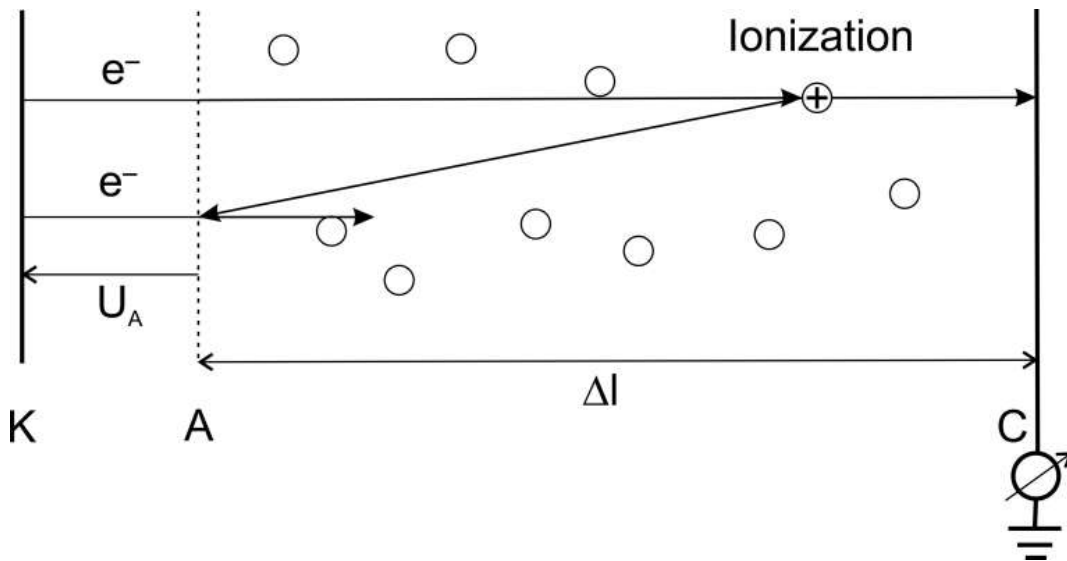


Fig. 2-68: Ion gauge. U_A = Anode potential, acceleration voltage; K=Cathode; A=Anode; C=Collector.

The probability of ionization, and hence the associated current, depends on the identity of a gas, therefore ion gauges are usually calibrated for nitrogen. Other gas pressures can be calculated by using sensitivity factors according to the manual [130].

On the path Δl through a gas with a number density of molecules n , N^- electrons are colliding with gas particles.

$$\Delta N^- = N^- \cdot n\sigma \cdot \Delta l \quad (1.1.41)$$

In this case, $\Delta N^- = \Delta N^+$ ions are formed. Here, σ is the cross section of ionization (depending on the gas species and the energy of the colliding electrons). The factor $n\sigma$ is the number of formed ions per electron and path length.

Divided by time, the electron current induces an ion current given in equation (1.1.42) and (1.1.43).

$$I^+ = I_C \cdot n\sigma \cdot \Delta l \quad (1.1.42)$$

$$\Delta N^- = I_C \cdot \frac{\sigma \cdot \Delta l}{kT} p = I_C \cdot S \cdot P \quad (1.1.43)$$

Here, S is the sensitivity constant of the gauge. S mainly depends on the gas species and on the geometry of the system. It has to be estimated by calibration. To be exactly, S can be only defined for one gas species, the composition residual gas is usually unknown. Therefore S has to be defined by equation (1.1.44), where I_0 is the ion current of the residual gas [122].

$$S = \frac{I^+ - I_0}{I_C \cdot p - p_0} \quad (1.1.44)$$

The electrode potentials and electron emission currents in ion gauges are regulated electronically by an associated control unit. Emission currents typically can be set at 100 μ A, 1 mA, or 10 mA by increase of the filament heating current. The highest value is appropriate at the lowest pressures in order to maximize the ion current.

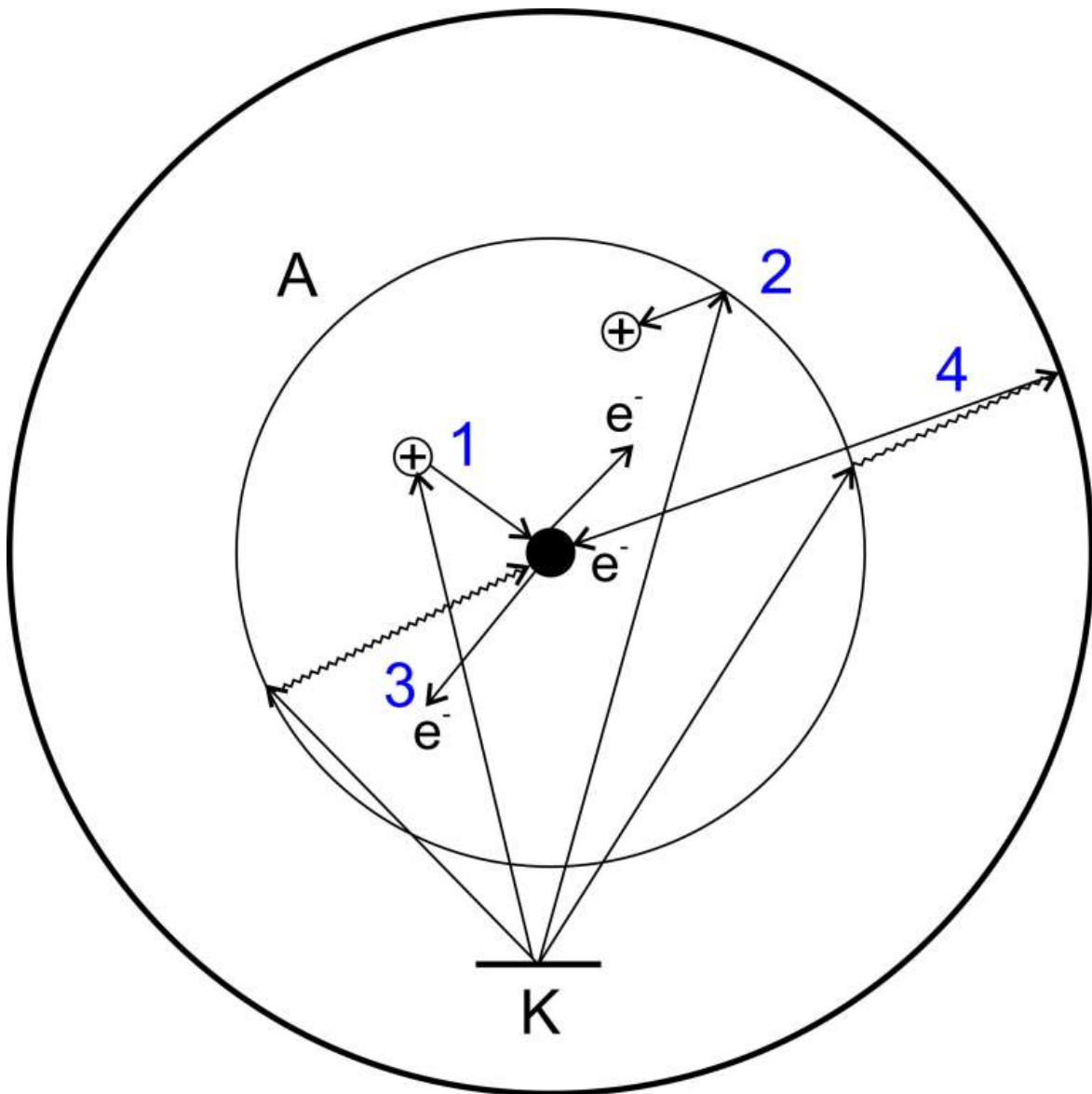


Fig. 2-69: Schematic drawing. 1=Ionization of a gas particle by an electron and following emission of a secondary electron due to collision of the ion with the collector; 2=electron stimulated ion desorption; 3=X-ray effect; inverse X-ray effect (electron emission from the wall). When electrons are hitting the grid, there is a probability for the emission of photoelectrons which are producing photoelectric interferences in the ion collector. This limits the range of ion gauges but can be prevented with improved configuration of collector and cathode. The inverse X-ray effect is generated by X-ray stimulated photoelectrons from the gauge casing in the opposite direction but less intense. [122, 125].

2.10 Adsorption of molecules in vacuum

Under the assumption of an atomic clean surface, gas particles can be reflected or getting a thermodynamic equilibrium with the surface and stick on it. This general adsorption process can involve a chemical reaction between the surface and the adsorbate (chemisorption) or the fundamental interacting force comes from the van der Waals force (physisorption). In case of physisorption, the adsorption energy is in the range of 4 to 40 kJ/mol, the overlap of the wave functions of molecule and surface is small and no major change of the electronic structure occurs.

The attracting forces between gas particle and surface can be organized into van der Waals forces, electrostatic forces and valence forces.

Van der Waals forces are the weakest and have a short range of distance. These are interacting forces between two neutral molecules. Every atom or molecule can be interpreted as an oscillating dipole. In the time average, the dipole moment is approximated zero. By approaching, electrostatic forces between this two oscillating dipoles becoming active, proportionally to $1/r^7$ [132].

Electrostatic forces between particles with the same electrically charge are retracting, oppositely poled particles are attracting. Here, Coulombs law (forces proportional to $1/r^2$) has to be used. If an ion comes closer to the surface, freely movable charges will be displaced and in the interior of the metal so-called image charges with the oppositely pole are formed. The distance between the interfaces in the interior of the metal to the surface is the same as the distance from the surface to the gas particle and the attracting force is proportionally to $1/r^2$. Under the influence of electric fields, neutral particles can act as dipoles.

Valence forces are the strongest forces between two molecules. They appear when two electron shells passing through. This means that the range of distance is very small.

Statistically reflected, the adsorption/desorption equilibrium is achieved after infinite time. This equilibrium depends on temperature, pressure, gas species, material and structure of the surface. On an idealized homogenous surface, the adsorption energy is a function of the distance r and the same for every place on the surface. Adsorbates can desorb if they have a sufficient energy [133].

2.10.1 Adsorption of CO on metal surfaces

Carbon monoxide is one of the most popular probe molecule in surface science. Bonding of CO on metal surfaces can occur in on-top, bridge, and three- or four-fold hollow coordination sites (s. Fig. 2-10).

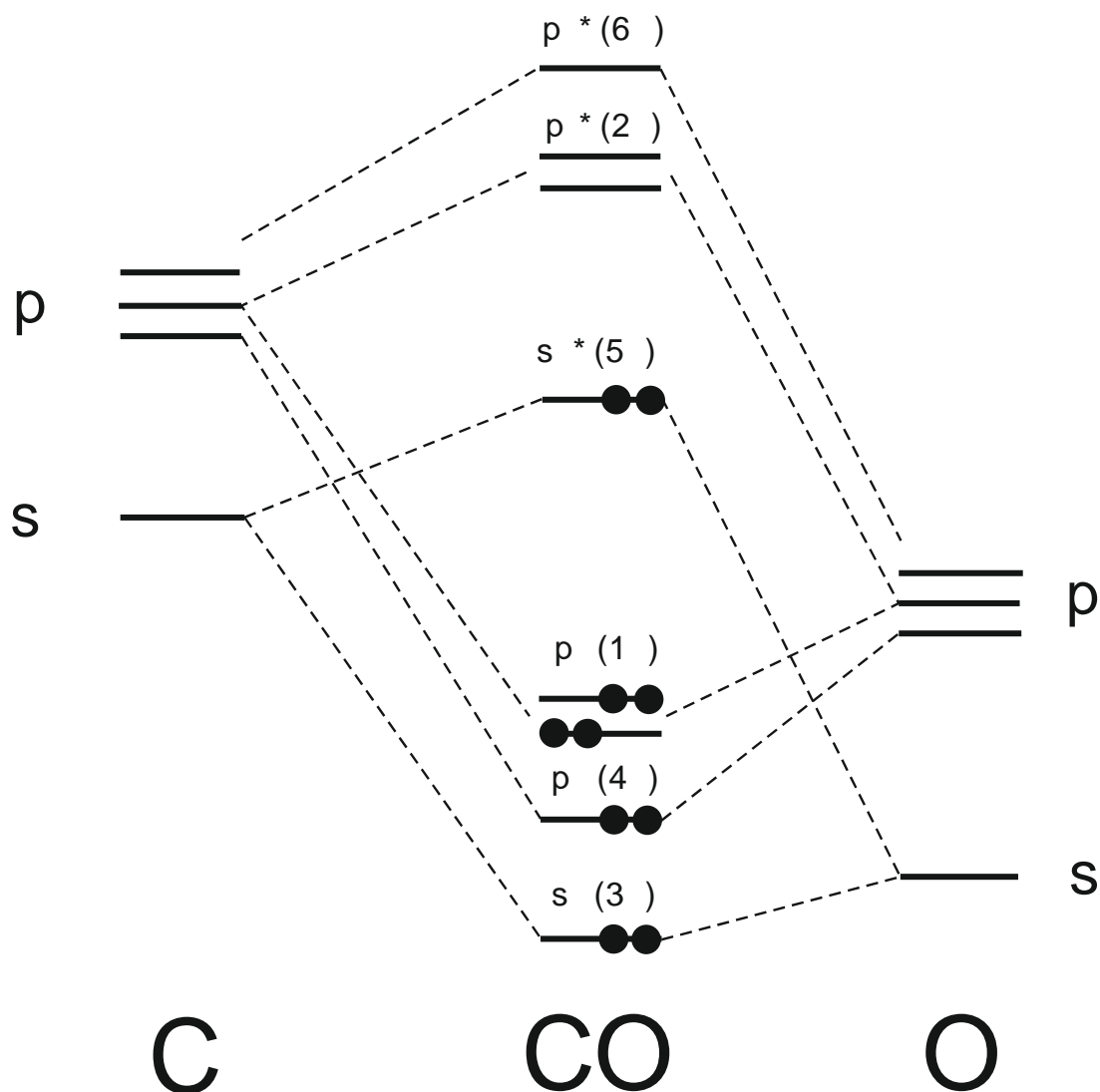


Fig. 2-70: Scheme of CO molecular orbitals.

2.10.2 Adsorbate-induced reconstruction of surfaces

Adsorbates modified by the surface are the basis of heterogeneous catalysis. In some cases also the adsorbate can modify the surface in a very subtle way. A simple example is the modification of the relaxation of surface layers. As a consequence of the termination of the bulk, typically the spacing of surface layer differs from underlying layers. Typically the surface layer spacing is contracted. The amplitude of this relaxation damps very fast with depth. These relaxations can change if an adsorbate is added and in some cases larger changes can occur. An example is the adsorption of atomic oxygen on Ni(100). If covered with 0.5 ML oxygen, an ordered $c(2 \times 2)$ phase is formed in which O-atoms are sitting in alternate hollow sites. In the second layer half of the Ni-atoms have an O-atom directly above, the other half not. Ni-atoms which are occupied with an O-atom directly above are 0.035 \AA lower than the other Ni-atoms in this layer. [91, 134-136].

A part of this work is to investigate a possible reconstruction of bimetallic surfaces induced by CO.

2.11 DFT calculations

All DFT calculations presented in this work were kindly provided by Konstantin M. NEYMAN and Sergey M. KOZLOV from the Departament de Química Física and Institut de Química Teòrica i Computacional, Universitat de Barcelona, Martí i Franquès, 1, 08028 Barcelona, Spain.

Spin-restricted periodic DFT calculations were performed with the VASP package with a revised Perdew–Burke–Ernzerhof (RPBE) exchange–correlation functional, which yields adsorption energies for CO on Pd(111) [137-140] close to the experimental values [141]. Plane-wave basis set with cutoff energy of 415 eV was used to calculate eigenstates of valence electrons; core electrons were modeled with projector augmented wave (PAW) technique [142]. The first Brillouin zone was sampled by Monkhorst–Pack $3\times 3\times 1$ mesh of k-points, and the Methfessel–Paxton smearing [143, 144] of 0.1 eV was applied to Kohn–Sham eigenstates during geometry optimization. The total energies were extrapolated to 0 smearing. DOS were calculated by use of a denser $5\times 7\times 1$ k-points mesh and the smearing of 0.3 eV [134]. PdZn surface alloys on Pd(111) were modeled by a six-layer thick $p(4\times 3)$ supercell, which allowed us to consider CO coverage as low as $1/12$ ML. Depending on the thickness of surface alloy under consideration, the top four layers of the slab consisted of either stoichiometric PdZn alloy or pure Pd and were relaxed (together with adsorbed CO molecules). The two bottom layers of the slab consisted only of Pd atoms and were fixed at bulk-derived positions with the experimental interatomic Pd–Pd distance of 275 pm. Geometry optimization was performed until all forces acting on atoms became less than $0.1 \text{ eV}\cdot\text{nm}^{-1}$ [134].

Vienna Ab initio Simulation Package (VASP): a simulation package program for atomic scale materials modelling, e.g. electronic structure calculations and quantum-mechanical molecular dynamics, from first principles developed by the Computational Materials Physics Group at the Vienna University.

For insulators, the DOS (density of states) goes to zero before the gap and the integration of a smooth function usually does not cause problems. At nonzero temperatures occupancies of metals are no longer discontinuous. For metals functions needs first to be multiplied by a sharp Fermi occupation, this makes their resolution in planewaves very hard. One needs to

extend the DFT model to a finite temperature DFT in which case the bands are smeared in energy. For metallic systems unoccupied bands must be included. Bands need to be smeared (artificial smearing²⁷) in energy so that the occupancies become continuous. The additional entropic contribution must be calculated by approximating this term with a smooth operator. Numerical integration methods are requiring a very fine reciprocal space mesh (k-mesh) inside the Brillouin zone (unit cell also in reciprocal space beyond which repeats itself. It is defined by the area surrounded by the planes that are perpendicular bisectors of the vectors from the origin to the reciprocal lattice points). *Methfessel–Paxton smearing* expands the delta function in a set of orthogonal Hermite polynomials and the entropic contribution due to this smearing can be calculated very accurately, which makes it desirable for calculations with metallic systems. Usually a smearing width of 0.1 eV is used [144]. The kinetic energy poses also problems, the kinetic energy operator contains a derivative term, and one can't write it in terms of the electron density since it is impossible to collect the wavefunction and its conjugate as a single norm square. To tackle the kinetic energy, it is assumed that the density can be written as the sum norm squares of a collection of single-particle non interacting orbitals which are called *Kohn-Sham orbitals*. These equations have the form of a single-particle Schrödinger equation, but the difference is that the effective potential operator, which yields the orbitals that determine the density, depends on the density itself. This system must be solved self-consistently, this is resorted by set of algorithms (“mixing algorithms”) [145].

A problem with DFT is that the exact functionals for exchange and correlation are not known (except for the free electron gas). Approximations exist to enable calculations of certain physical quantities quite accurately. A widely used approximation is the local-density approximation (LDA), where the functional depends only on the density at the coordinate where the functional is evaluated. The generalized gradient approximations (GGA) use exchange functionals including the first-order gradients and are an improvement over LDA for bond energies. In molecular calculations, more complex functionals are needed, and a huge variety of exchange-correlation functionals have been developed. The most common used functional is the revised *Perdew–Burke–Ernzerhof* (RPBE) exchange model (a direct generalized-gradient parameterization of the free electron gas with no free parameters) [146, 147].

Special points (depending on the symmetry) are chosen for skillful integration of the smooth function. A general method, proposed by *Monkhorst and Pack*, is widely used because it leads to a set of points calculated by a simple formula which is valid for all crystals [143, 148].

3 Pd(111) and PdZn/Pd(111) Surface Alloys

3.1 Sample preparation

To clean the Pd(111) substrate, the Pd single crystal was sputtered in 5×10^{-6} mbar Ar at 1 kV for 45 min at room temperature followed by annealing for 10 - 15 min at 1200 K. The sample was then cooled in 5×10^{-7} mbar O_2 down to 600 K to remove residual carbon. Finally, the single crystal was flashed to 1200 K in UHV. STM studies have shown that annealing temperatures below 600 K is not enough to fully anneal all defects [149]. Sample cleanliness was checked by XPS (see Fig. 3-1) and LEED (see Fig. 3-3). The XPS contains always some small impurities of carbon, oxygen and molybdenum (rods). The C 1s region should look like in the example: The peak at 285.5 eV (CO) has to be of the same, or better, lower intensity than the one at 292 eV (satellite). When the result is not satisfying, the procedure has to be repeated again (at least some oxygen/annealing cycles). In case of a very dirty surface also sputtering time and Ar pressure can be increased. LEED cannot detect small amounts of impurities on the surface, but can check the surface reconstruction after sputtering/healing the surface.

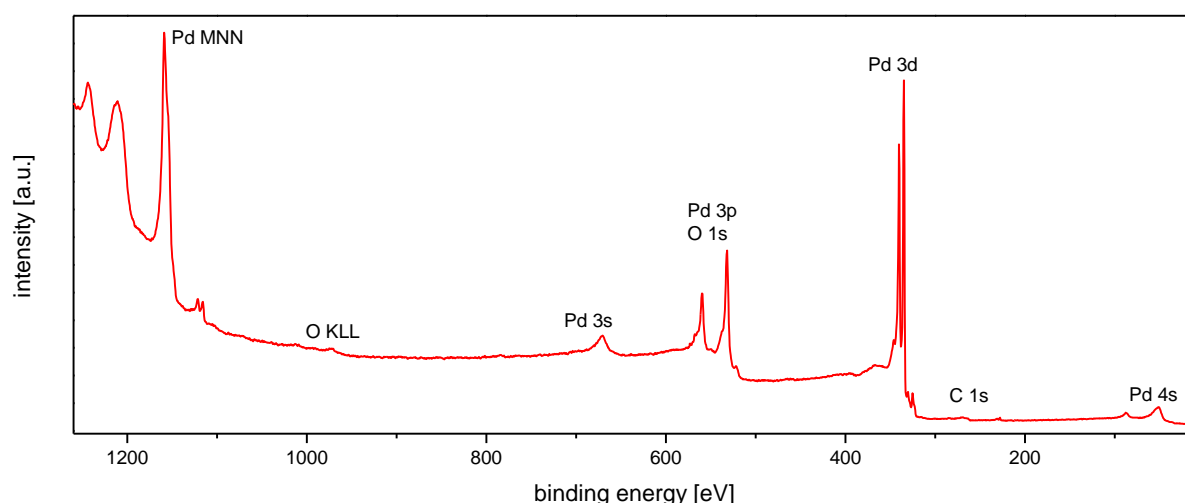


Fig. 3-1: AlK α XPS spectra of a clean Pd(111) surface.

3.2 CO adsorption on Pd(111)

3.2.1 Adsorption geometries

The adsorption of *CO* on metal surfaces is one of the most studied model system in surface science with various different surface science techniques. *CO* is a very suitable spectator molecule to characterize the different binding sites on catalytic surfaces [30, 48, 134, 150-154].

In general, *CO* can adsorb on metal surfaces in three different geometries, linearly on-top of a single metal atom, bridge-bonded to two metal atoms, and 3-fold bridged in fcc or hcp hollow sites (see Fig. 3-4). These different binding geometries can be distinguished by IR spectroscopy via the frequency of the internal *C-O* stretching vibration. The frequency range for linear bonded *CO* is from 2000 to 2100 cm^{-1} ; for bridge-bonded from 1900 to 2000 cm^{-1} ; and for 3-fold hollow bonded from 1800 to 1900 cm^{-1} [48], see also chapter 2.2 and 2.10.

The exact values are depending on the amount of backbonding from the metal *d*-electrons into the antibonding $2\pi^*$ orbital of the *CO* molecule [155, 156]. As described in the next chapter, also Coverage affects the observed vibration frequencies. Intermolecular dipole interactions between neighboring molecules are increasing with increasing coverage. This effect is described in literature as dynamic dipole-dipole coupling and typically induces a frequency shift towards higher wavenumbers, which indicates strengthened internal *C-O* bond. Another effect is the reduction of backbonding from the metal *d*-electrons to the *CO* molecules with increasing coverage. This leads to a weakened metal-*CO* bond and a strengthened internal *C-O* bond, this results again in a shift to higher wavenumbers [33]. A sketch of bonding types of *CO* on Pd(111) is shown in Fig. 2-10 in the chapter before.

A *CO* saturated surface can be easily prepared by cooling down in *CO* atmosphere (5×10^{-6} mbar) to 90 K with liquid nitrogen.

3.2.2 LEED

The hexagonal LEED pattern of a clean Pd(111) surface, prepared as discussed above is shown in Fig. 3-3.

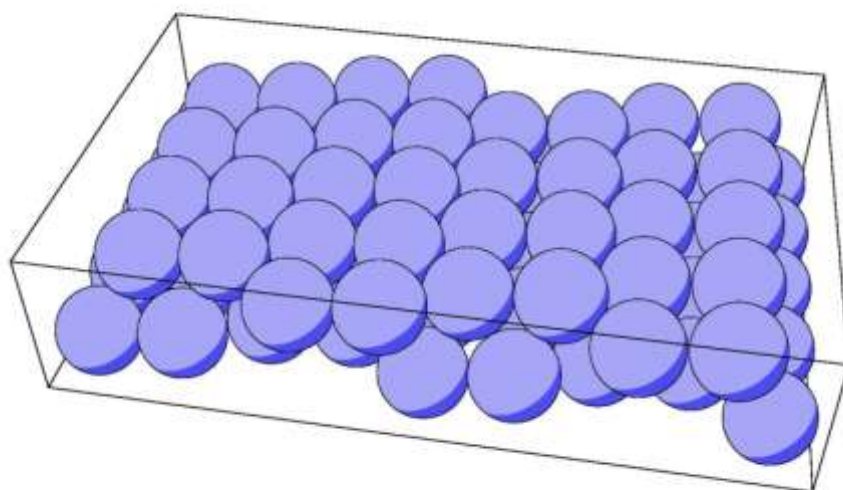


Fig. 3-2: Pd(111) hexagonal surface generated using BALSAC (web application) [157].

..

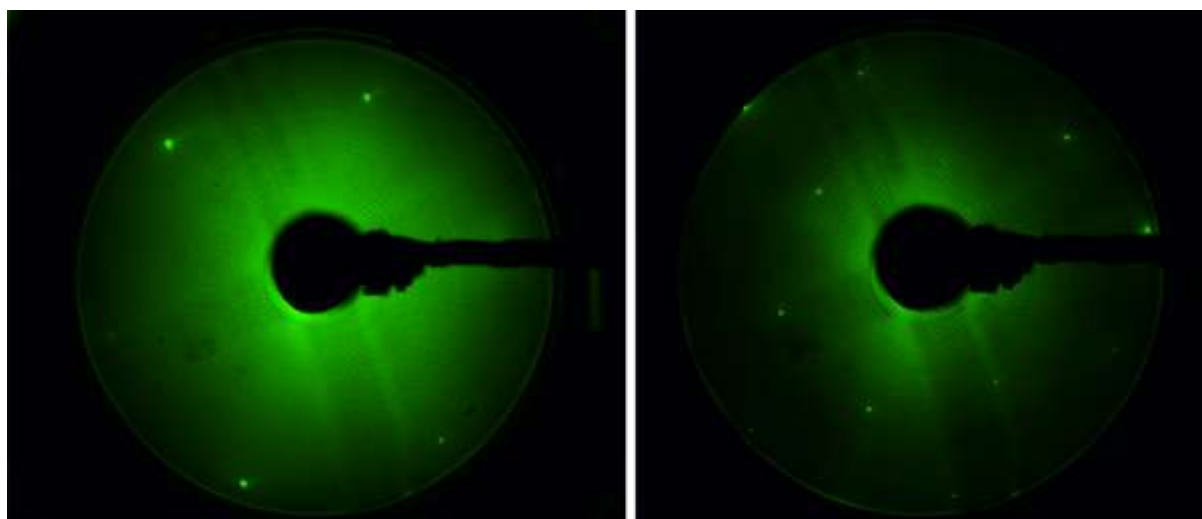


Fig. 3-3: LEED of a hexagonal Pd(111) surface at 100 eV (left) and 225 eV (right), respectively.

The adsorption of *CO* on Pd(111) at low temperature has been the subject of several earlier studies. An overview can be found in [158]. *CO* adsorbs exclusively on 3-fold hollow sites in a $(\sqrt{3}\times\sqrt{3})R30^\circ$ surface structure at a coverage of $\frac{1}{3}$ ML. At a $\frac{1}{2}$ ML coverage, the unit cell

changes to a $c(4 \times 2)$ structure and, at the saturation coverage (0.75 ML) an ordered (2×2) -3 CO structure can be observed. At the saturation coverage, CO occupies on-top sites and 3-fold hollow sites in a ratio of 1:2 with 3 CO molecules per unit cell [39, 141]. The Lattice model of CO on $Pd(111)$ at full coverage is shown in Fig. 3-4.

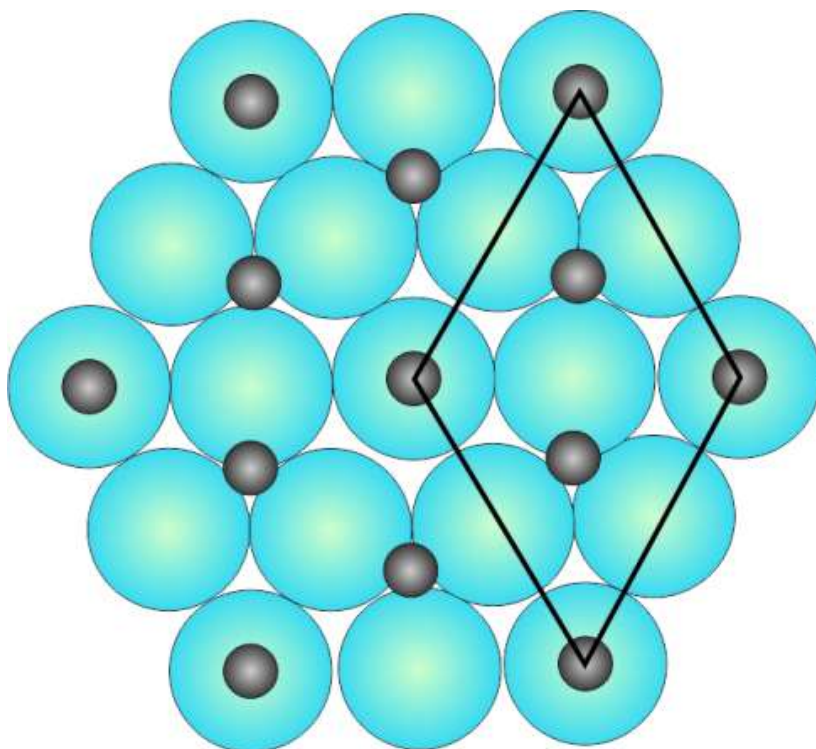


Fig. 3-4: Lattice model of CO on $Pd(111)$ at saturation coverage (0.75 ML) [39].

With LEED experiments, seventeen distinct ordered structures ranging in coverage from $\frac{1}{3}$ to 0.75 ML have been identified. For details see [159]. In Fig. 3-5, LEED images at low and saturation CO coverage on $Pd(111)$ are shown.

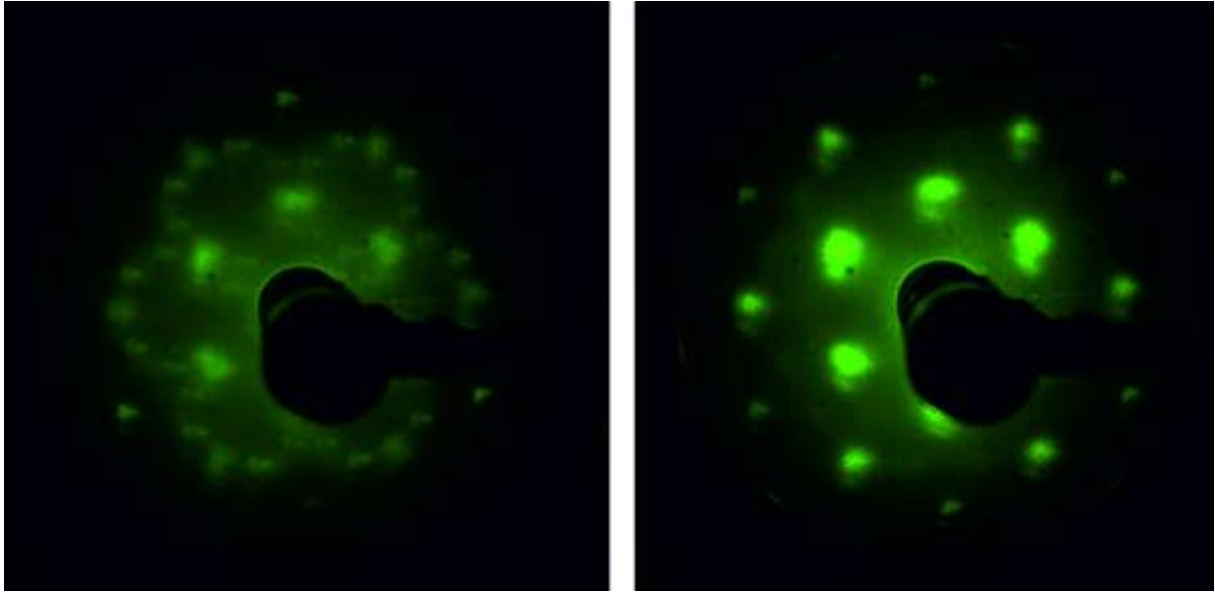


Fig. 3-5: LEED of CO on Pd(111). Low CO coverage (left) and saturation coverage (right), respectively.

3.2.3 XPS

With XPS one can detect components of the first few layers and their chemical bonding state. Physically adsorbed species do not influence the peak position, but the intensity of the substrate. Adsorbed carbon monoxide can be observed at a binding energy of 285.5 eV (see Fig. 3-6). The peak positions of Pd are discussed in chapter 3.4.

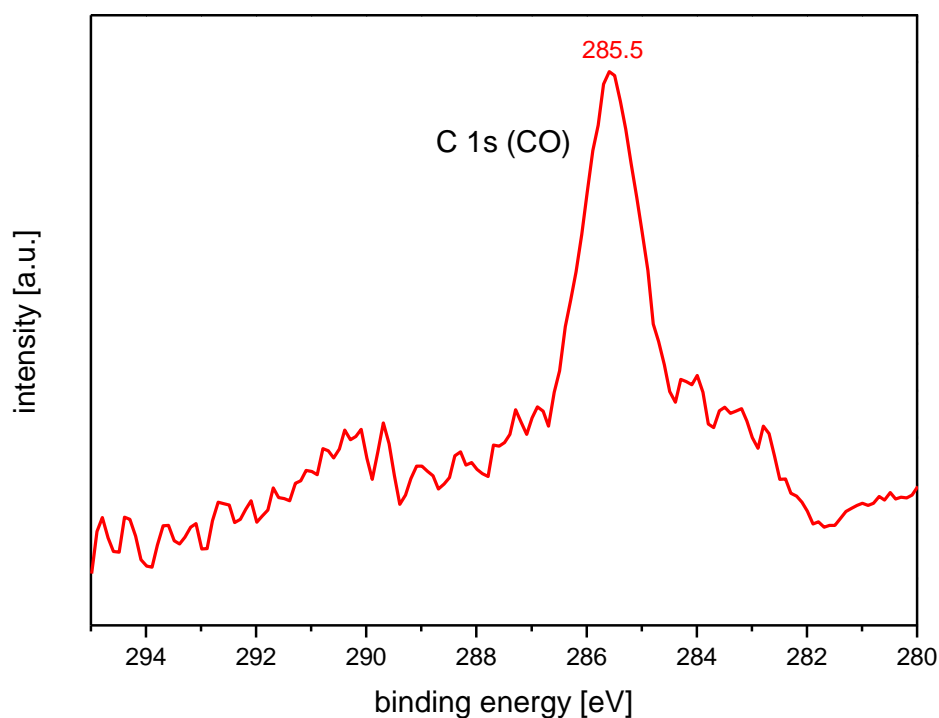


Fig. 3-6: Carbon monoxide adsorbed on Pd(111) at saturation coverage (285.5 eV).

After transferring the complete system to the new location in the Lehartrakt (see 0), XPS (and also TPD and PM-IRAS) experiments with Pd(111) and PdZn/Pd(111) on clean and with adsorbates covered surfaces were repeated and compared with the old results from the old location (“VetMed”). As expected, the new spectra contained the same features, binding energies and intensities (between the error margins).

3.2.4 PM-IRAS

Vibrational frequencies of the $C-O$ bond stretching are depending on the different adsorption sites of CO on Pd(111). PM-IRAS spectra in Fig. 3-7 show the frequency shift of the $C-O$ stretching band depending on the pressure exposed.

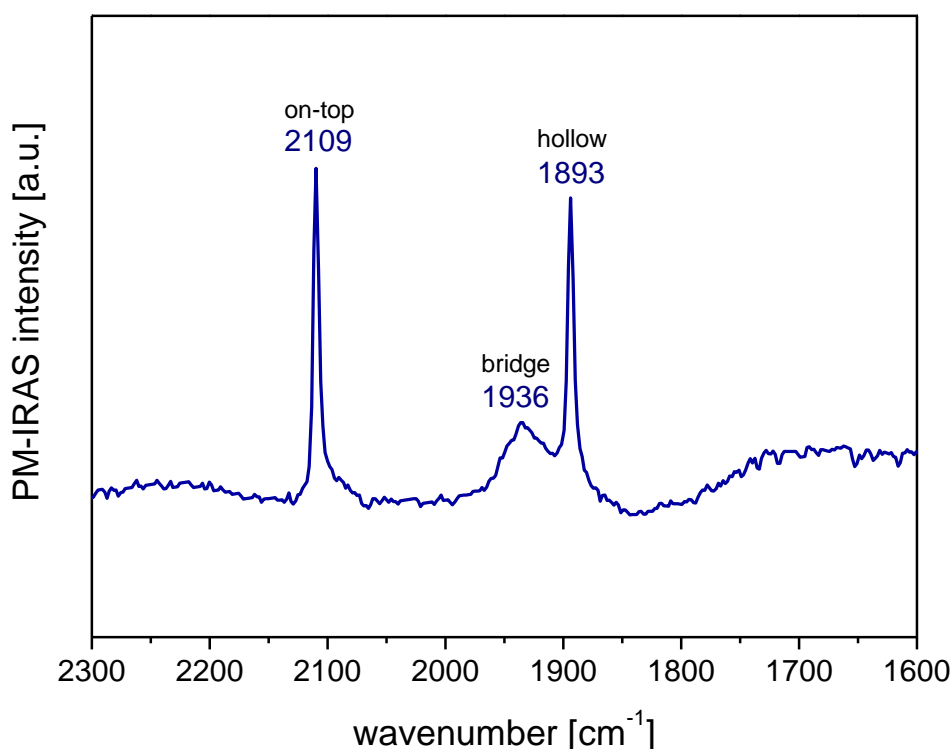


Fig. 3-7: PM-IRAS spectra of CO on Pd(111) recorded at 200 K in 10^{-6} mbar CO . Three different adsorption sites (on-top, bridge, hollow bonded) are clearly visible.

At 10^{-6} mbar exposure, bridge sites (1936 cm^{-1}), on-top sites (2109 cm^{-1}) and hollow bonded (1893 cm^{-1}) CO is visible. The CO mobility at low temperatures is low and thus CO adsorbs in less ordered structures [160]. The sample was heated up to 500 K and then cooled down in 10^{-6} mbar CO . The presence of water in high pressure experiments plays a role during long time exposures at low temperatures. It was observed that co-adsorbed water induces a shift of the on-top CO frequency [30, 35]. High pressure experiments should therefore be carried out above the desorption temperature of water ($\sim 170\text{ K}$ for Pd).

3.2.5 TPD

As discussed before, the maximum coverage for the (2×2) -3 CO saturation structure is 0.75 ML. This value was also used to calibrate the TPD setup used in this thesis. The schematic TPD setup was already described in chapter 2.6. TPD measurements are starting from 90 K using a heating rate 60 K per minute (also heating rates of 30, 90, and 120 K per minute were tried giving the same results). To avoid background signals, the nozzle of the mass spectrometers has to be moved as close as possible to the surface without touching it. A typical TPD spectrum is shown in Fig. 3-8. It exhibited a quite sharp peak at 146 K and a broad peak with an absolute maximum at 448 K and a shoulder at about 350 K. The first small feature at about 100 K (“heating peak”) belongs to CO desorbed from the sample holder inside the chamber (molybdenum rods, tantalum and thermocouple wires).

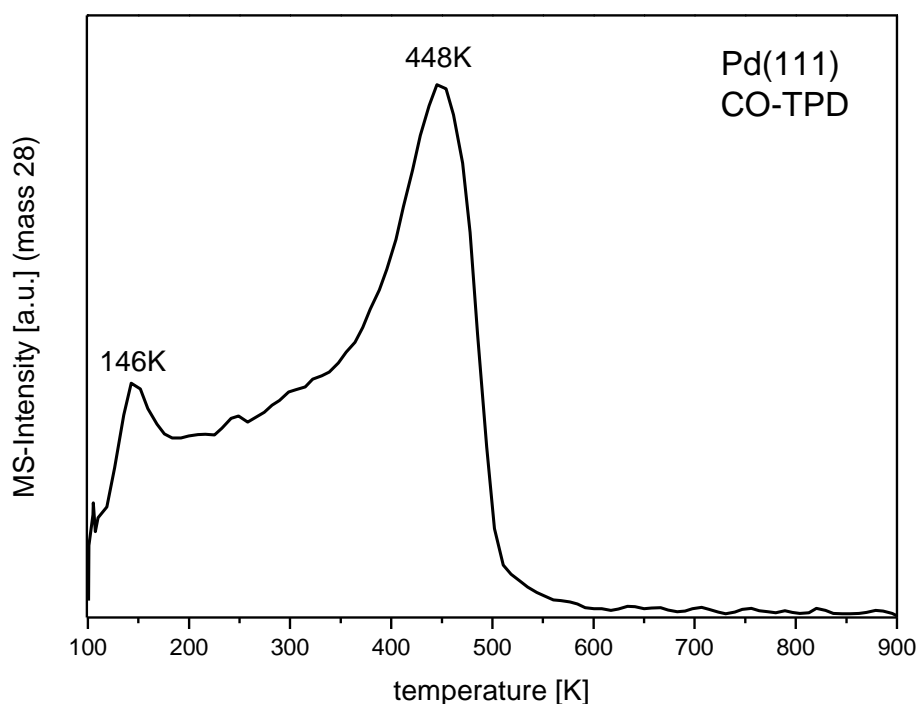


Fig. 3-8: CO TPD of a saturated Pd(111) surface. A sharp peak at 146 K and a broad peak with an absolute maximum at 448 K and a shoulder at about 350 K can be observed. The broad band probably indicates heterogeneity of surface sites [28].

The peak at low desorption temperature can be assigned to CO desorbing from on-top sites during a phase transition from the well-ordered (2×2) -3 CO structure to a less dense structure

with *CO* now sitting on bridge and on-top sites [150, 158]. The absolute desorption maximum of 448 K corresponds to *CO* molecules desorbing from 3-fold hollow in good agreement with the literature [141]. Most of the initially adsorbed *CO* was already desorbed at this temperature.

Applying the Redhead method (see chapter 0) and assuming a preexponential factor for desorption of $\nu=10^{15.3} \text{ s}^{-1}$, which is in good agreement with available data for desorption for *CO* on pristine Pd(111) [141], the desorption temperature of 448 K corresponds to an adsorption energy of 140.9 kJ/mol (reported in literature between 140.7 to 148.5 kJ/mol [161-163]).

3.3 Methanol dehydrogenation on Pd(111)

Decomposition and oxidation of methanol on noble metals are prototypical reactions in surface science and catalysis for using these reactions as models for the interaction of alcohols (e.g. from biofuels) and other small organic molecules with catalysts [164-168]. Methanol dehydrogenation can provide a valuable source of hydrogen (e.g. for direct methanol fuel cells (DMFCs) or of syngas), but the catalyst poison *CO* needs to be removed (carbon deposition can suppress *C-O* bond scission [16, 19, 169-171]). Methanol oxidation can be used as a test case to improve the total oxidation of volatile organic compounds (VOC), in waste removal [172].

In this chapter methanol decomposition and oxidation on Pd(111) single crystals will be investigated by XPS, TPD and PM-IRAS. The setup in this chapter allows only investigations of methanol adsorption/desorption under UHV conditions up to a methanol pressure of 10^{-6} mbar. To gain further insight into these processes, the $\text{CH}_3\text{OH}/\text{Pd}(111)$ system was revisited using a combination of XPS, PM-IRAS, and TPD. XPS investigations with ambient pressure-XPS are discussed in chapter 3.9.

3.3.1 TPD

Fig. 3-9 shows TPD spectra of desorption and decomposition of methanol on Pd(111). Initially 10 L (1 Langmuir = 1.33×10^{-6} mbar) of methanol (a correction factor of 1.9, according to the manual, was considered for the ion gauge) was dosed. It was shown that this is sufficient to cover the surface with a multilayer of adsorbant [36]. A heating rate of 90 K per minute (as also used for the *CO*-TPD's in this work) was used. A pronounced sharp desorption peak for CH_3OH was found at 150 K (the M28 and M30 peaks at this temperature are fragments of the MS ionization process). Regrettably it was not possible to resolve multilayer and monolayer methanol. A pronounced tailing desorption peak of *CO* desorption was found at 458 K (see Fig. 3-9).

Desorption of formaldehyde (a possible intermediate during methanol decomposition) was not observed.

The desorption energy for this *CO* feature was calculated to be 142 kJ/mol. It is clearly visible that methanol was partially dehydrogenated to *CO* on Pd(111), this is in good agreement with some previous studies. [36, 173-175]. By comparing the peak areas, it was estimated that

about 41% of the adsorbed CH_3OH dehydrogenates, resulting in CO desorption which is also in good agreement with earlier studies by Demirci and Winkler [175]. The same experiment was then carried out on PdZn/Pd(111) (see chapter 3.8) and on sintered PdZn bulk crystals (see chapter 4), no CO production was observed on PdZn/Pd(111) which will be discussed later.

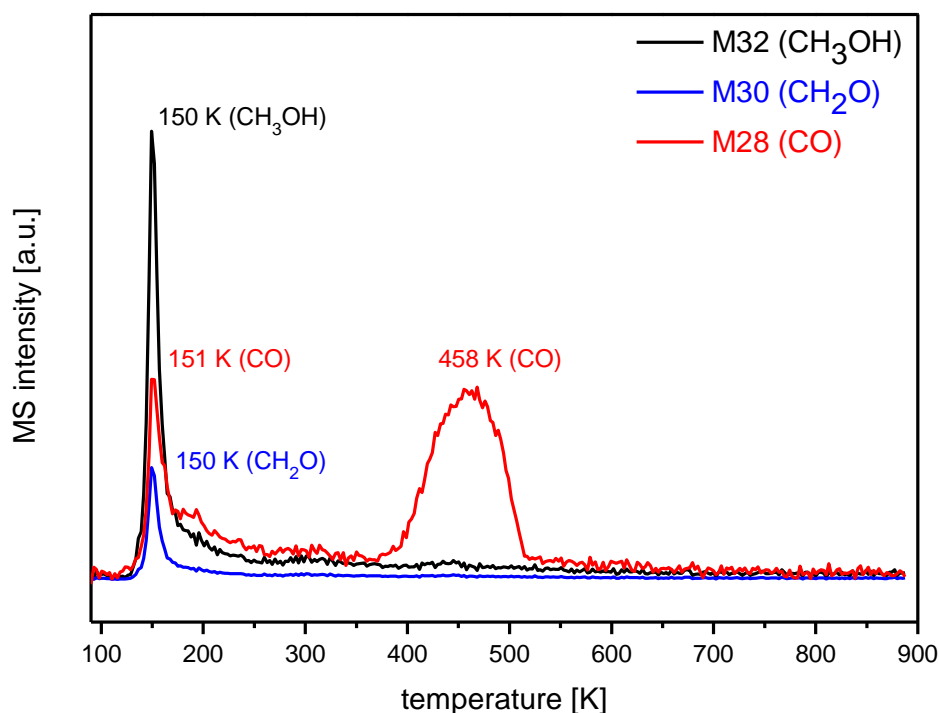


Fig. 3-9: TPD spectra for CO , CH_2O , and CH_3OH after dosing 10 L MeOH at 90 K on Pd(111). At 150 K a pronounced sharp desorption peak for CH_3OH can be detected (the M28 and M30 peaks at this temperature are fragments of the MS ionization process). A pronounced tailing desorption peak of CO desorption was found at 458 K.

To mimic the methanol steam reforming process [30, 176-178] we have dosed both, methanol and D_2O (D_2O , to distinguish dosed water from “background-water”). First we dosed 10 L methanol and immediately following we dosed 10 L D_2O on the Pd(111) sample. D_2O desorbed with a single peak at 159 K and the desorption peak for methanol was at 156 K. CO desorption was monitored at 461 K (see Fig. 3-10). There were no differences observed when D_2O was dosed first in the experiment. It is suggested that the reaction proceeds via full dehydrogenation of methanol to CO , followed by partial conversion to CO_2 via water gas shift reaction), whereas on PdZn the intermediate formaldehyde directly reacts with the OH group from decomposed water. The desorption energy was calculated to be 143 kJ/mol and about

40% of the adsorbed methanol dehydrogenates, resulting in CO desorption. This is very similar to the methanol TPD experiment without D_2O shown in Fig. 3-9. No CO desorption was observed when carrying out the experiment on PdZn/Pd(111), see chapter 3.8. D_2O , dosed on Pd(111) desorbs at 166 K, slightly higher than with methanol co-dosing, see Fig. 3-11.

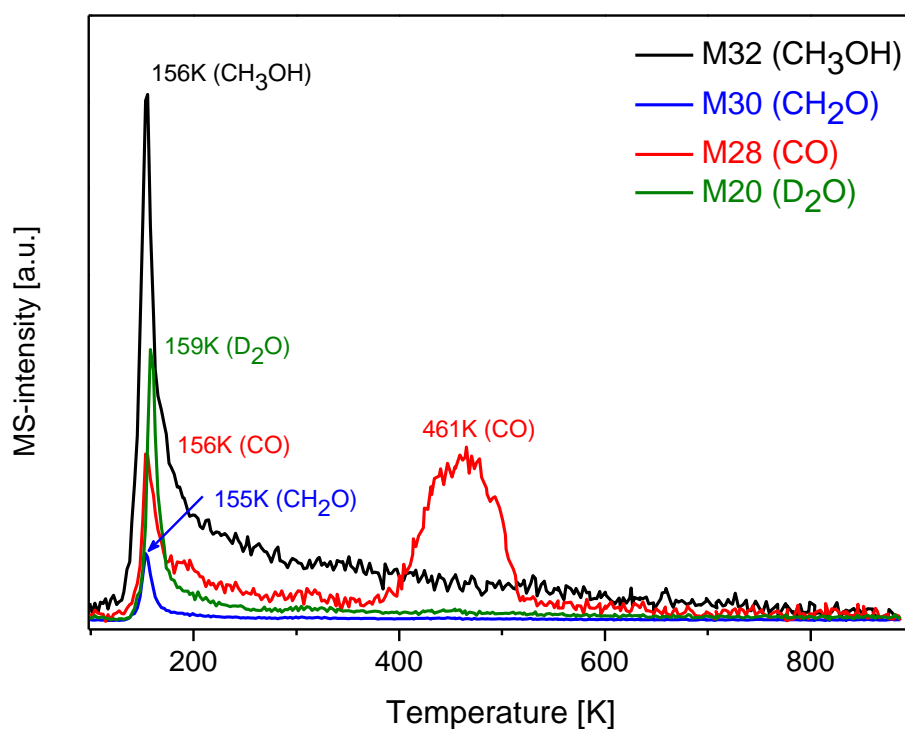


Fig. 3-10: TPD spectra for D_2O (159 K), CO (461 K), CH_2O (155 K), and CH_3OH (156 K) after dosing each 10 L $MeOH$ and D_2O at 90 K on Pd(111).

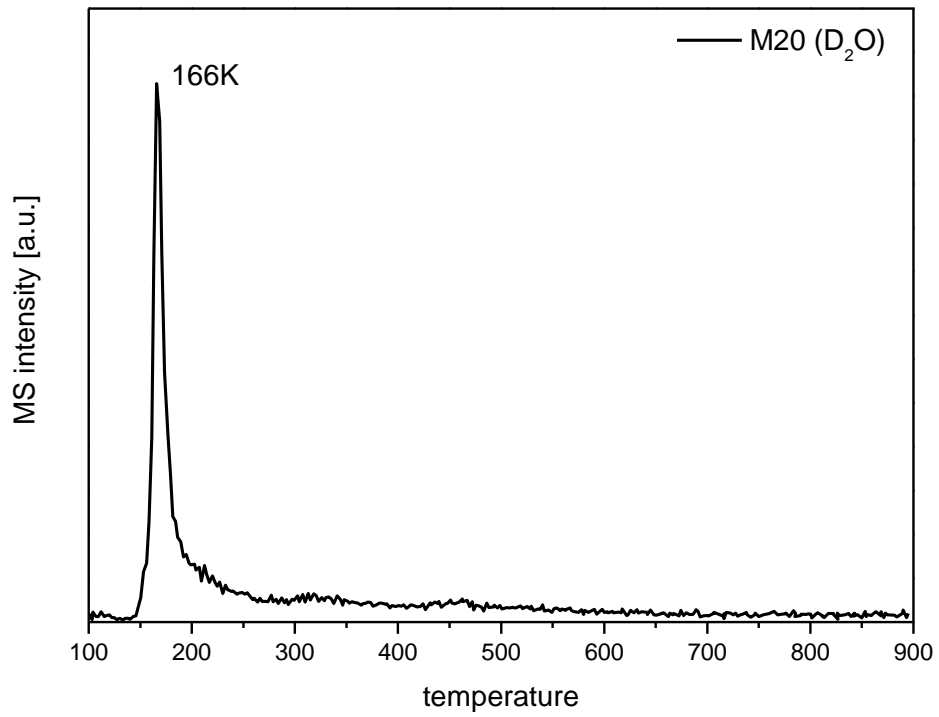


Fig. 3-11: TPD spectrum for D_2O after dosing 10 L D_2O at 90 K on Pd(111). D_2O desorbs at 166 K, slightly higher than with methanol co-dosing.

3.3.2 PM-IRAS

Winograd et. al [165, 179] suggested that a critical methanol coverage obtained by an exposure of 1 L at 100 K supports bimolecular interactions and promotes C-O bond cleavage.

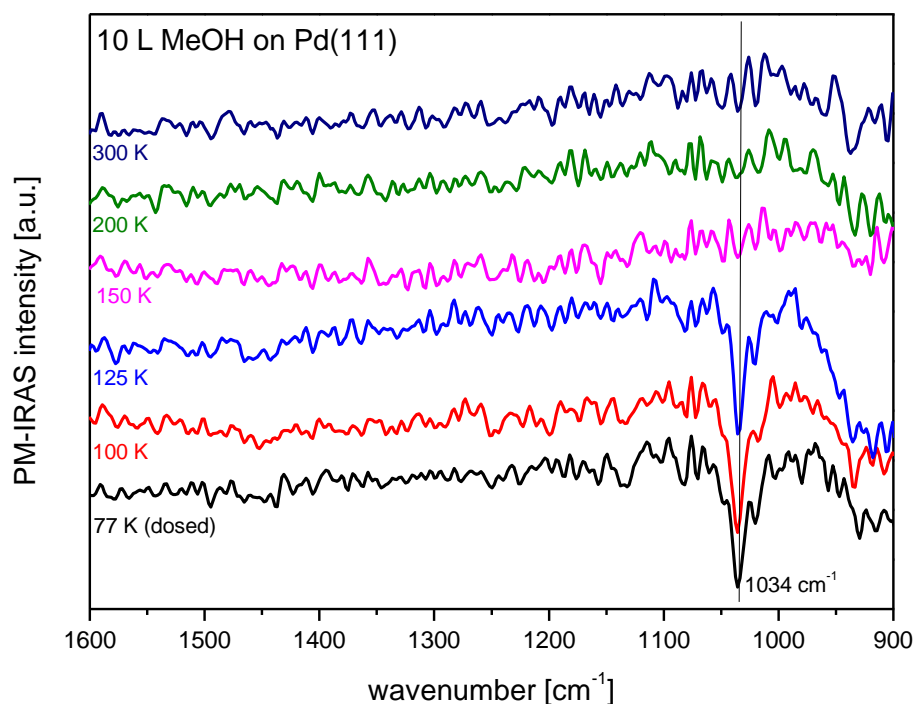


Fig. 3-12: PM-IRAS surface spectra measured after dosing 10 L methanol on Pd(111) at different temperatures. Range 1600 – 900 cm⁻¹. The IR band at ~1034 cm⁻¹ can be assigned to $\nu(\text{CO})$.

With our XPS setup we cannot fully differentiate between CH_3OH , CH_xO and CO species on the surface. Therefore PM-IRAS experiments were carried out at different reaction conditions. In Fig. 3-12 - Fig. 3-14, 10 L methanol was adsorbed on Pd(111) at 77 K. The sample was then subsequently heated up to 300 K. The formation of CH_x could not be observed (or was below the detection limit) under these conditions. The signal in Fig. 3-12 at ~1034 cm⁻¹ belongs to CO from methanol decomposition. The weak band in Fig. 3-13 at ~1700 cm⁻¹ indicates the formation of surface intermediates, bonding via oxygen). In Fig. 3-14 bands for high coverage MeOH (~3300 cm⁻¹) and – with increasing temperatures - low coverage MeOH (~3550 cm⁻¹) are visible [180].

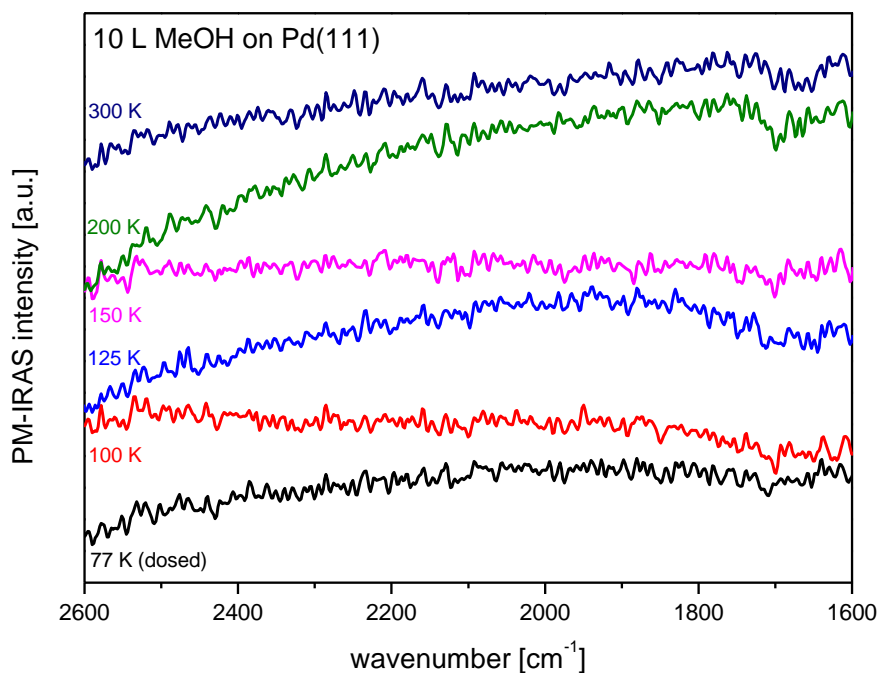


Fig. 3-13: PM-IRAS surface spectra measured after dosing 10 L methanol on Pd(111) at different temperatures. Range 2600 – 1600 cm^{-1} . The weak band at $\sim 1700 \text{ cm}^{-1}$ can be assigned to $\nu(\text{CO})$ from H_2CO .

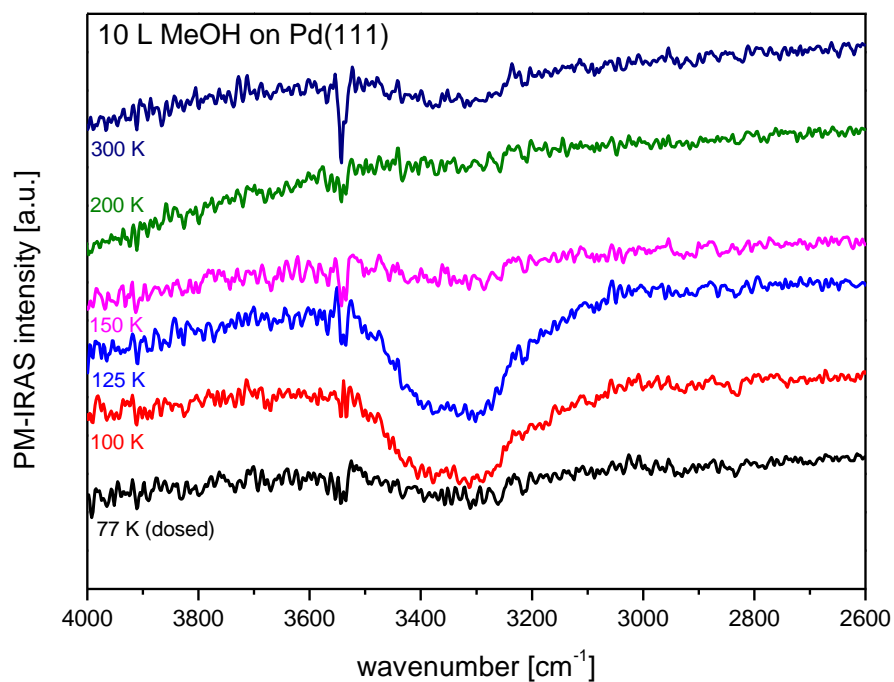


Fig. 3-14: PM-IRAS surface spectra measured after dosing 10 L methanol on Pd(111) at different temperatures. Range 4000 – 2600 cm^{-1} . The broad band at $\sim 3300 \text{ cm}^{-1}$ can be assigned to $\nu(\text{OH})$ for high coverage MeOH and the narrow band at $\sim 3550 \text{ cm}^{-1}$ to low coverage MeOH.

Fig. 3-15 shows PM-IRAS spectra at different methanol pressures. The features at 1226 and 1319 cm^{-1} belongs to formaldehyde (from dehydrogenation of methanol via methoxy, formaldehyde and formyl to CO) at different binding geometries [181]. The broad band at $\sim 1900 \text{ cm}^{-1}$ belongs to 3-fold-hollow bonded CO.

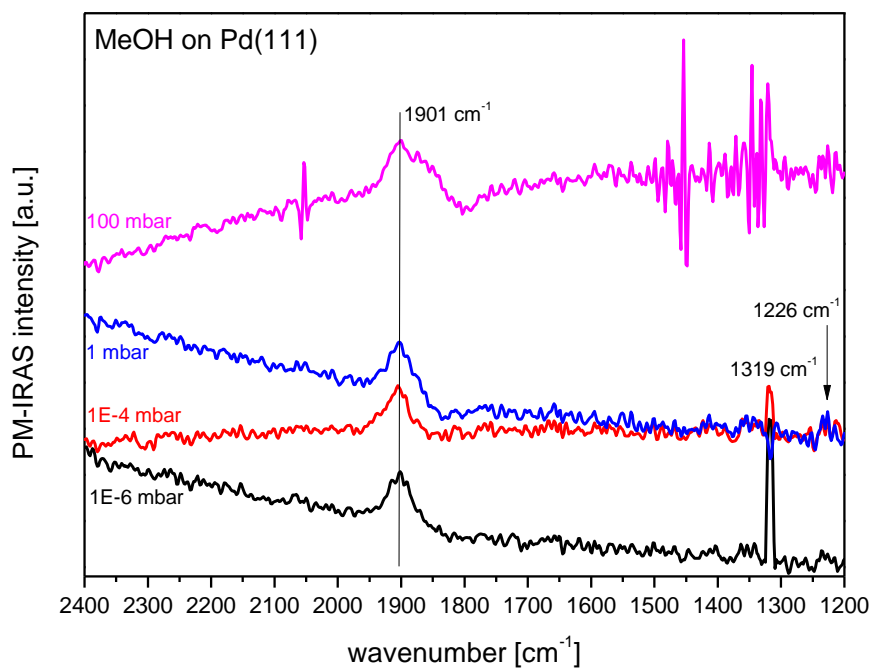


Fig. 3-15: PM-IRAS surface spectra, MeOH on Pd(111) depending on the pressure (at RT). The IR bands at 1226 cm^{-1} and 1319 cm^{-1} can be assigned to formaldehyde and at $\sim 1900 \text{ cm}^{-1}$ to CO.

3.3.3 XPS

Fig. 3-16 shows C 1s XPS spectra of Pd(111) after exposure of 10 L methanol, acquired between 100 and 600 K. At 100 K the a pronounced C 1s signal can be observed at 286.8 eV. Increasing the temperature leads to a decreasing C 1s signal and a shift to lower binding energies. At 600 K carbon species are completely desorbed from the surface or dissolved in the bulk.

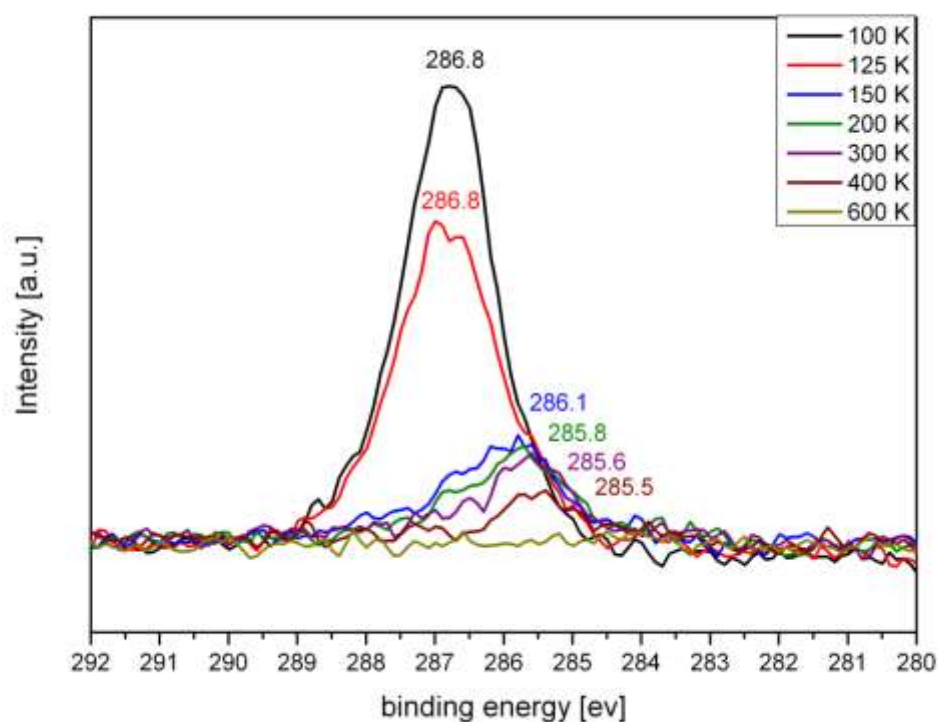


Fig. 3-16: XPS C1s spectra: evolution of carbonaceous species on Pd(111) after 10L MeOH exposure with increasing temperatures from 100-600K. The C 1s signal shifts from 286.8 eV (100 K) to 285.5 eV (400 K) and vanishes at 600 K completely.

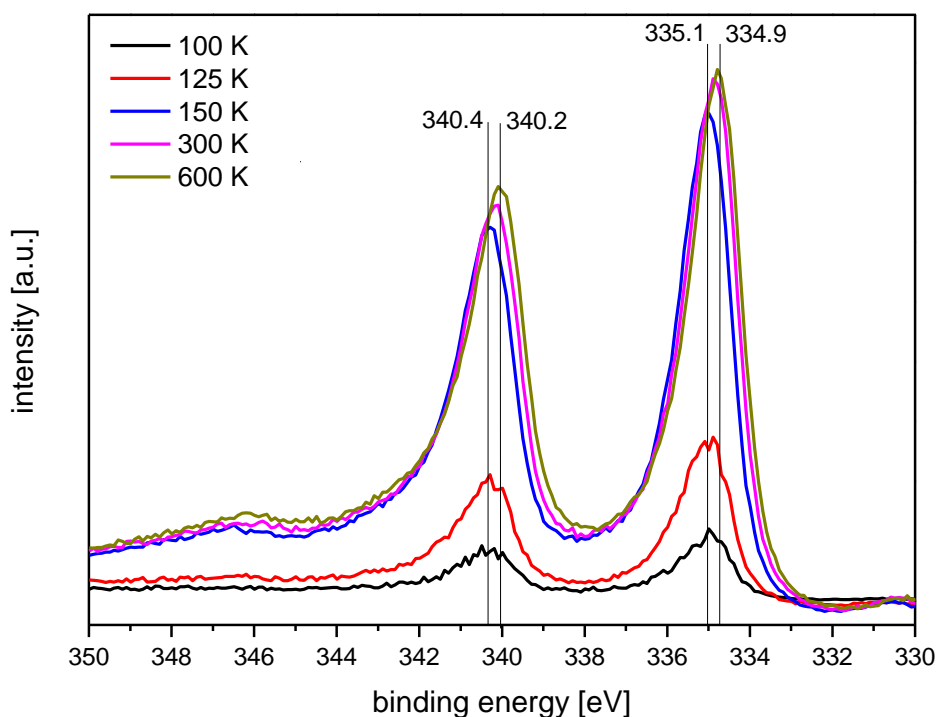


Fig. 3-17: XPS Pd 3d spectra: evolution of the Pd 3d signal after 10L MeOH exposure with increasing temperatures from 100-600K. The Pd 3d_{3/2} shifts slightly from 340.4 eV (100 K) to 340.2 eV (600 K). The Pd 3d_{5/2} signal shifts from 335.1 eV (100 K) to 334.9 eV (600 K). At 100 and 125 K a thick methanol overlayer dampens the Pd 3d signal almost completely.

The interpretation of the spectra was aided by temperature programmed desorption (TPD) shown in chapter 3.3.1. TPD indicated desorption maxima at ~150 K for CH_3OH desorption (multilayer desorption cannot be distinguished from monolayer desorption in our experiments, see also [30, 182]).

The feature at a binding energy of ~286 eV originates from CH_3OH , CH_xO ($x = 1-3$) and CO (see chapter 3.2). The methanol multilayer is present at low temperatures (100 K in Fig. 3-16), producing a single C1s peak with a binding energy of 286.8 eV. The thick methanol overlayer dampens the Pd3d signal almost completely (Fig. 3-17). At 125 K, the multilayer partially desorbed, indicated by the decrease of intensity of the C1s signal, but the Pd3d signal is still very low. At 150 K, the methanol multilayer desorbed and the C1s intensity decreased dramatically, the signal shifted to 286.1 eV and the Pd3d signal was clearly visible.

Further increasing of the temperature reduced the C1s signal slightly and the binding energy was shifted to 285.8 eV (200 K) and 285.6 (300 K), respectively. Based on other studies (e.g. secondary ion mass spectrometry (SIMS) studies [168, 182], this could indicate the onset of CH_3O (methoxy) formation by $O-H$ bond scission. In the temperature range between 200 K and 400 K, methanol desorption, dehydrogenation of CH_3O via CH_xO to CO , and partial desorption of CO occurs. The 285.6 eV peak at 300 K results from CH_xO and/or CO . HREELS studies detected only CO at 300 K and CH_3O -related peaks appeared at 200 – 250 K [183-186].

Due to CO desorption almost no C1s could be observed at 500 K (not shown) and finally at 600 K the signal is completely below the detection limit.

C1s signals at a binding energy of 284-284.5 eV are typical for hydrocarbon species (CH_x ; $x=1-3$) and may be used to examine a possible $C-O$ bond scission, but cannot be clearly seen in Fig. 3-16. This indicates that no (or below the detection limit) carbonaceous species were produced which further conclude that $C-O$ bond scission is absent (or very limited) under this conditions and therefore methanol desorption is the dominating process. Winograd et al. [179, 182] suggested that a critical methanol coverage obtained by an exposure of 1 L methanol at 100 K promotes $C-O$ bond cleavage (due to bimolecular interactions). Higher or lower exposures did not produce carbonaceous species under these conditions. Therefore, we investigated a series of different methanol exposures from 0.5 – 5 L at 100 K and subsequently heated to 300 K. No CH_x formation could be observed under these conditions (see Fig. 3-18).

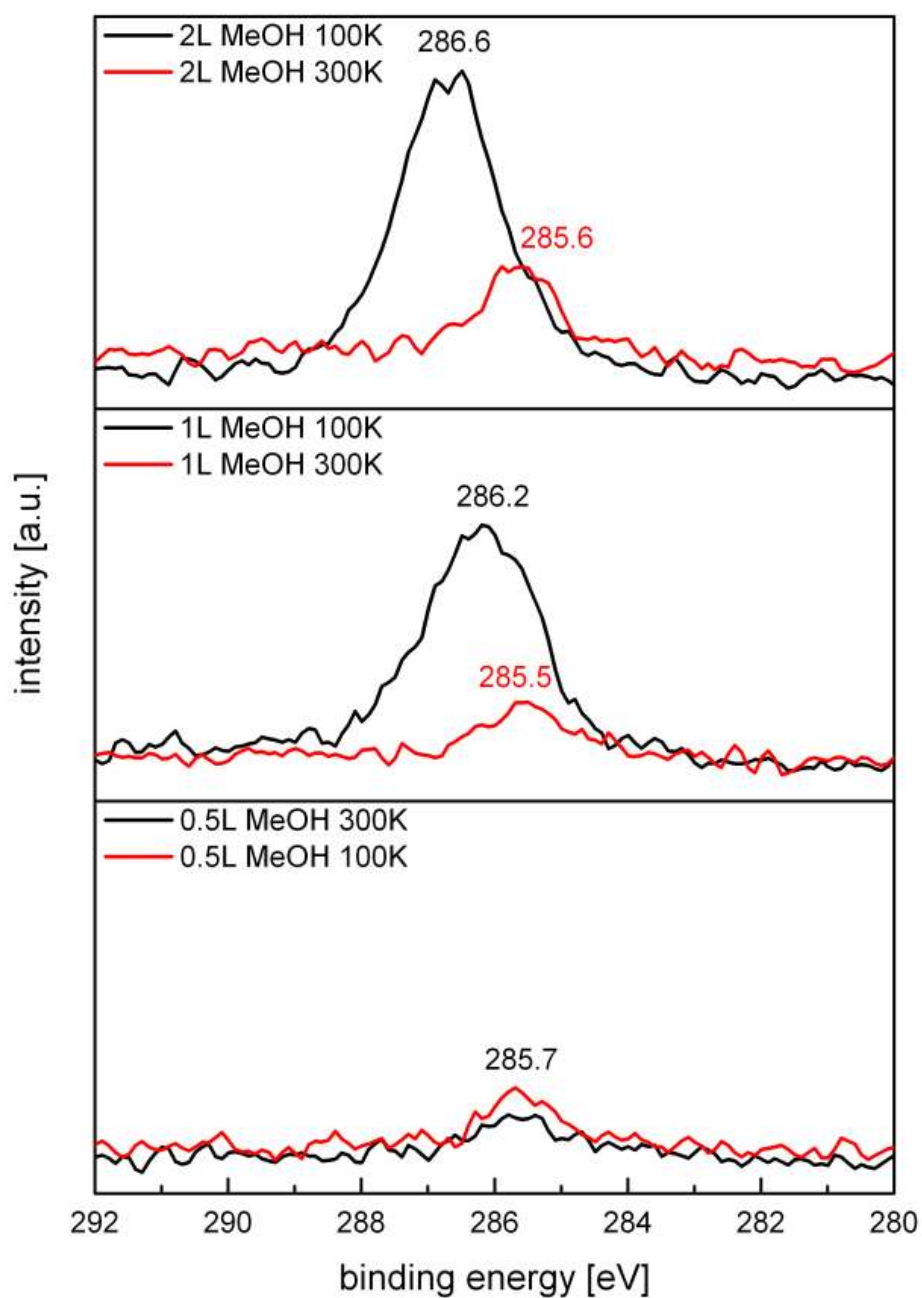


Fig. 3-18: XPS C1s spectra of different methanol exposures on Pd(111) at 100 and 300 K. After exposure of >1 L methanol at 100 K a clear C 1s signal at ~286 eV is present.

XPS cannot fully differentiate between CH_3OH , CH_xO and CO with our setup; therefore also experiments using PM-IRAS were performed (discussed and compared with methanol adsorption/desorption on PdZn, see chapter 3.8).

The probability of methanol dehydrogenation and *C-O* bond scission under UHV conditions is quite small due to fast methanol desorption (before the reaction onset temperature). Therefore we carried out experiments under a methanol pressure of 10^{-6} mbar (using the sensitivity factor for the ion gauges) to provide a sufficient surface coverage.

Fig. 3-19 and Fig. 3-20 shows XP spectra after an exposure of 10^{-6} mbar methanol (5 min to 9 h) at 300 K and 450 K, respectively.

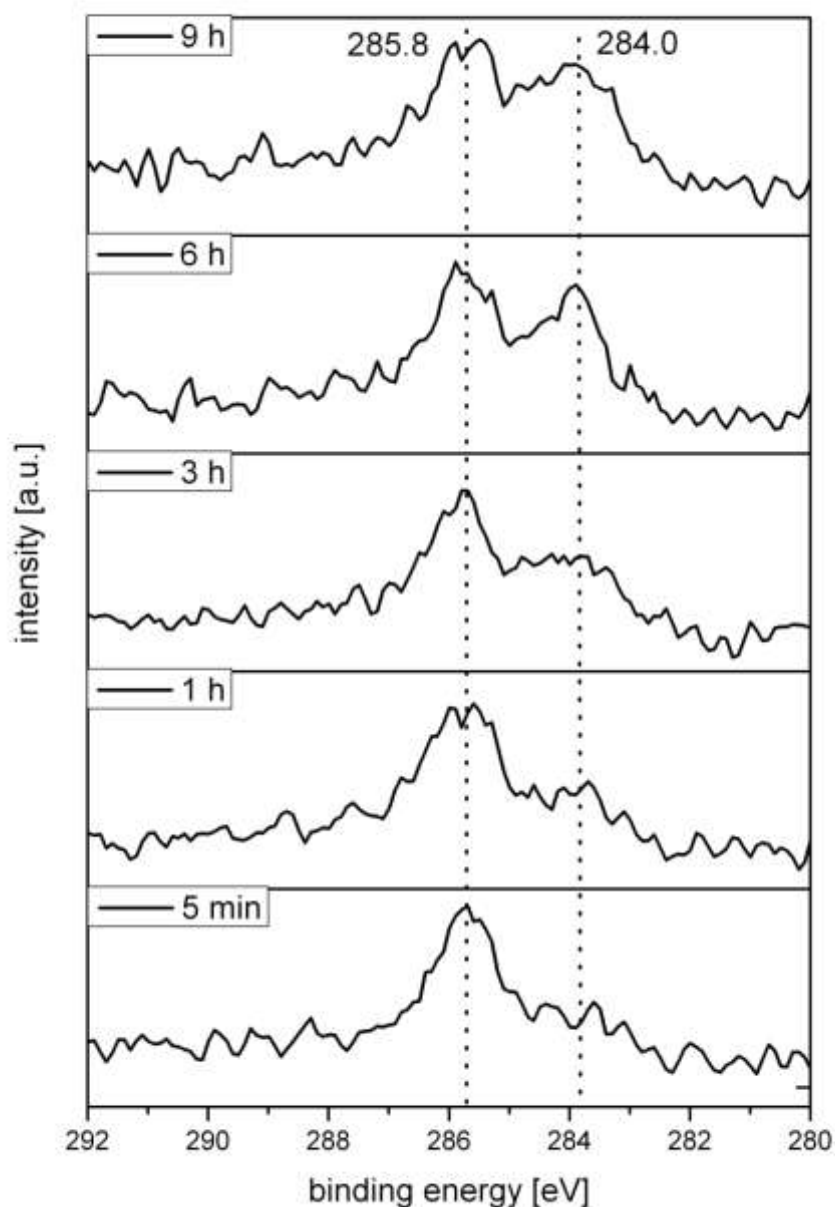


Fig. 3-19: C1s XP spectra measured during 10^{-6} mbar methanol exposure on Pd(111) at 300 K. The C 1s signal at 285.8 eV can be assigned to *CO* and the signal at ~ 284.0 eV can be assigned to carbonaceous species.

At 300 K two signals were observed, *CO* at a binding energy of 285.8 eV and carbonaceous species at about 284.0 eV (Fig. 3-19).

Under these conditions dehydrogenation as well as *C-O* bond scission takes place. The growth rate of the CH_x species starts rapidly, is then slowing down and approaches saturation values after about 4 hours. As expected, the CH_x formation rate is faster and the final concentration is higher at 450 K (see Fig. 3-21). The initial CH_x deposition rate is high for both temperatures, the carbon coverage increases and less free sites are available, resulting in a decrease of the rate.

The *CO* formation closely correlates with the CH_x formation. At 300 K, after a fast initial *CO* growth, there is a slight decay and finally a constant *CO* coverage is reached. For the sample at 450 K the initial development is similar and then again the *CO* coverage stays constant, but with lower concentration. Obviously the lower the *CO* coverage, the faster is the CH_x formation rate and the higher is finally the CH_x coverage. It seems that higher temperatures favor the endothermic methanolic *C-O* bond scission. But also the partial blocking of Pd sites on the surface with a high *CO* coverage at lower temperatures is also a barrier for this process. After 4 hours 0.3 ML *CO* and 0.4 ML CH_x were observed on the surface at a temperature of 300 K. At 450 K, only about 0.15 ML *CO* and about 0.8 ML CH_x are detected.

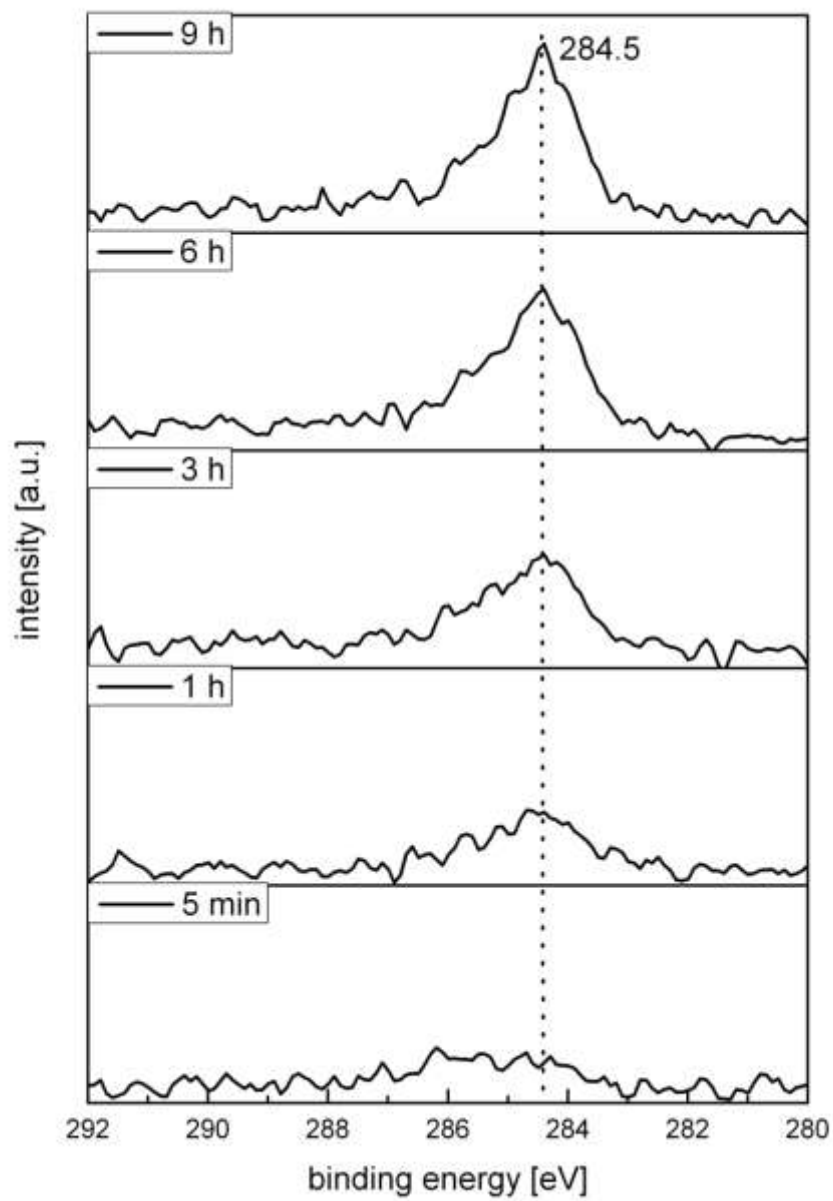


Fig. 3-20: C1s XP spectra measured during 10^{-6} mbar methanol exposure on Pd(111) at 450 K. The CH_x formation rate (~ 284.5 eV) is faster than at 300 K.

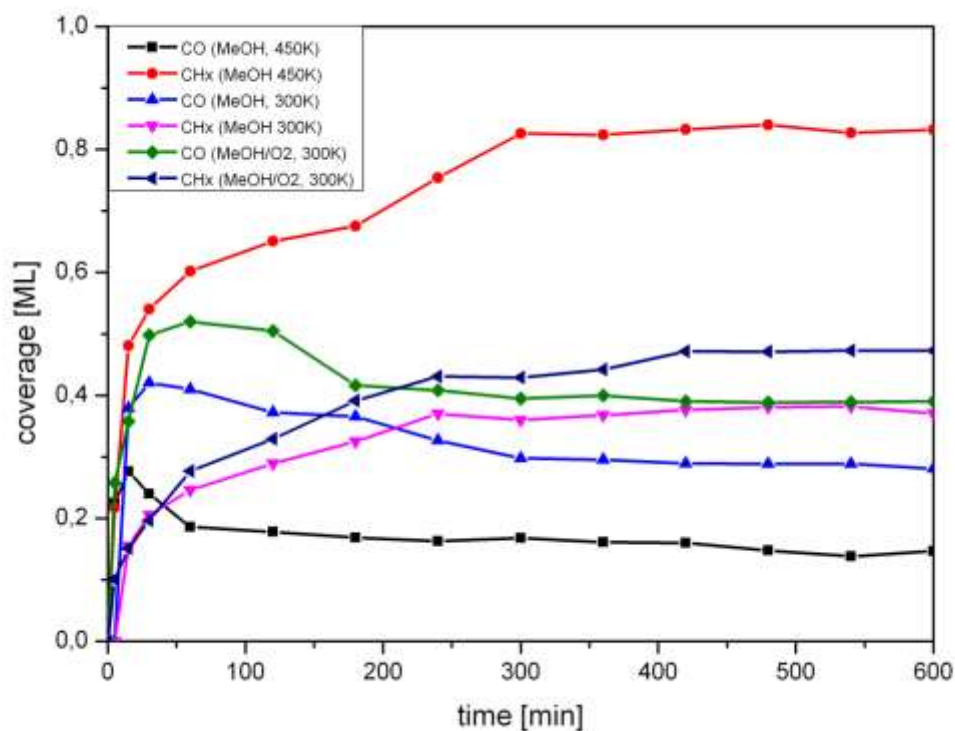


Fig. 3-21: Evolution with time of carbon species. Relative amounts of CO and CH_x species (estimated by comparing XPS C1s to Pd 3d peak area using the well-known (2x2)CO saturation coverage as reference).

Fig. 3-22 shows the evolution of the CH_x binding energies of the carbonaceous species with time for 300 and 450 K. At 300 K, the binding energy shifts from initially 383.6 eV to 284.1 eV. Rodriguez et al. [187] interpreted this as a transition from isolated carbon atoms to carbon islands. The formation of carbon islands is different at 450 K. First, the formation is very fast and then after a slight decay, the measured CH_x binding energy reaches a constant value around 284.4 eV. This suggests that higher temperatures induce a different kind of carbon island formation [30].

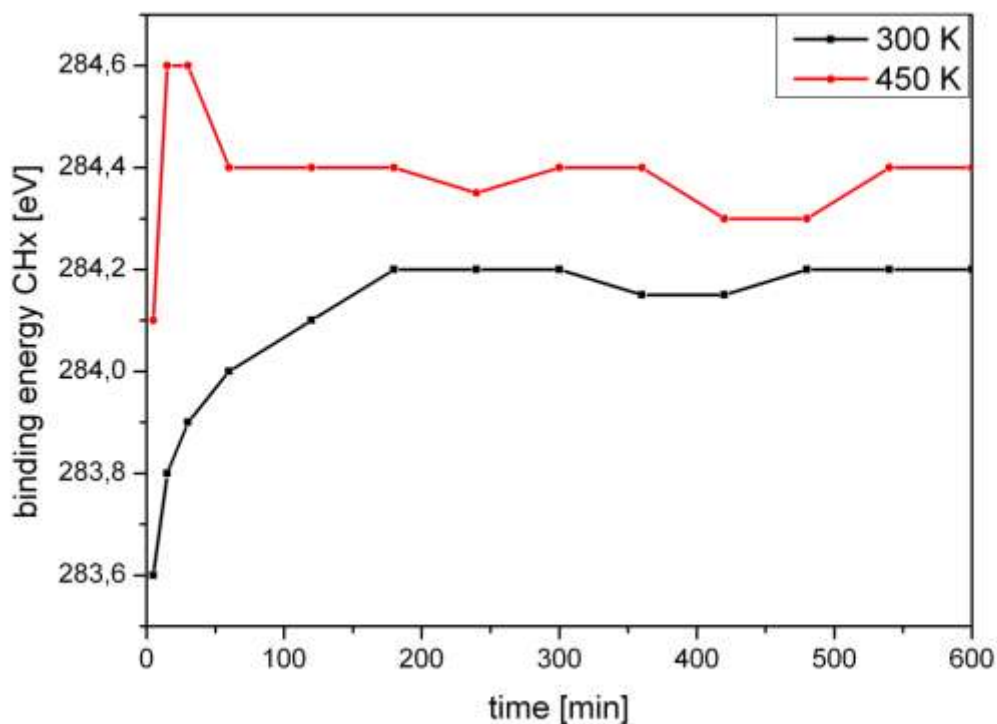


Fig. 3-22: Evolution of the binding energy of the carbonaceous species (XPS C1s spectra). At 300 K, the binding energy shifts from initially 383.6 eV to 284.1 eV. At 450 K, the CH_x formation is very fast and finally reaches a constant value around 284.4 eV

Methanol oxidation on Pd(111) was studied by measuring XPS and PM-IRAS with time at 10^{-6} mbar CH_3OH/O_2 1:1 pressure. The influence of carbonaceous adlayers present during reaction will be investigated. The presence of carbon species may not only act as poison, but can also influence the selectivity for methanol oxidation [38].

At the beginning a strong C1s signal at 285.8 eV was observed by XPS (see Fig. 3-23). After a small increase of the amount of adsorbed CO at the beginning, the coverage was constant at 0.4 ML after about 2 h. During reaction the CH_x signal increased up to saturation coverage of about 0.45 ML (see Fig. 3-21). As expected, the binding energy of the Pd3d was constant which indicates that the Pd(111) single crystal surface remained metallic during methanol oxidation under this conditions (a full oxidation to PdO would result in a shift of the binding energy shifts of approximately +1.5 eV).

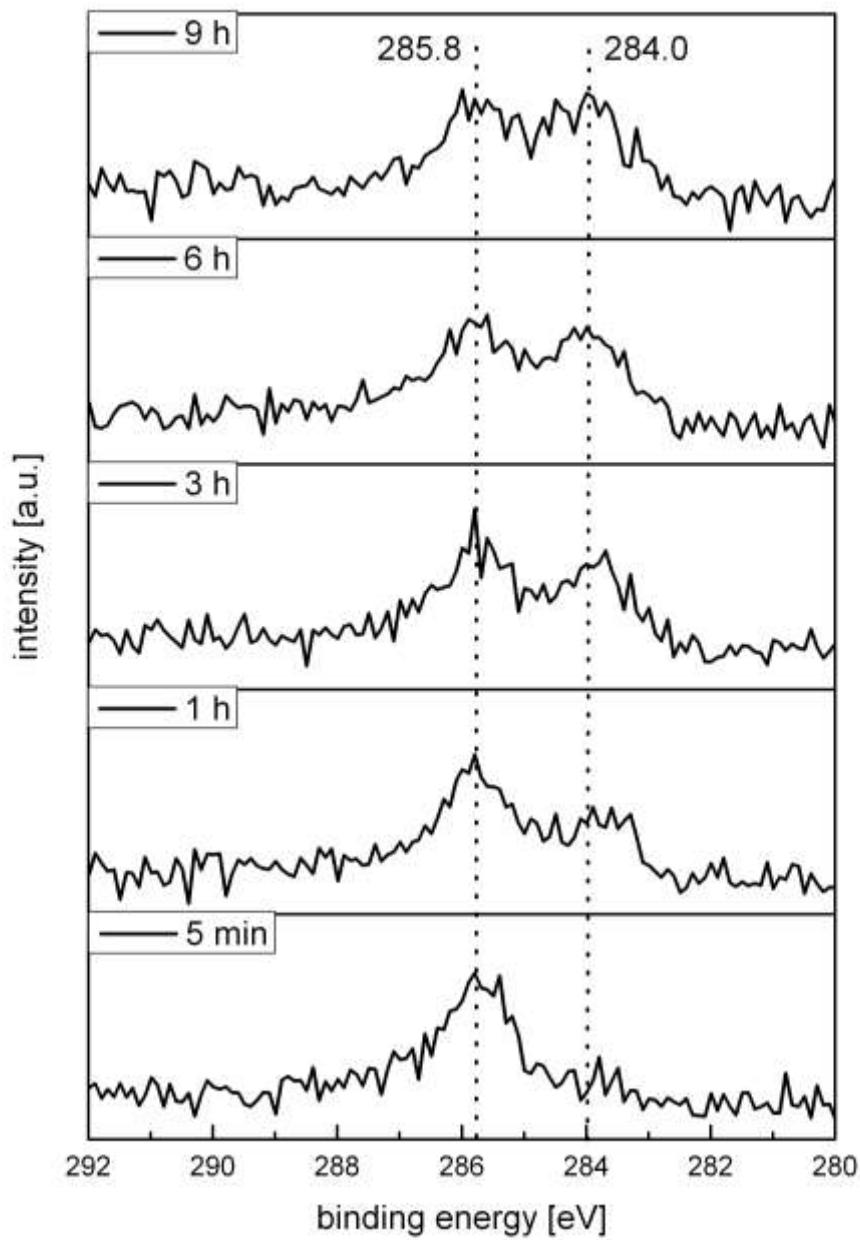


Fig. 3-23: Evolution of the binding energy of the carbonaceous species on Pd(111) at 300 K and a pressure of 10^{-6} mbar $\text{CH}_3\text{OH}/\text{O}_2$. The CH_x signal (~ 284 eV) increased during reaction.

Previous studies of CH_3OH decomposition on Pd(111) [6, 36, 164, 165, 168, 179, 183-197] reported activity for dehydrogenation while $C-O$ bond scission activity was typically very small (or absent). Dehydrogenation of methanol to CO and H_2 occurs via CH_3O (methoxy) as first intermediate, and is followed by stepwise hydrogen abstraction to CH_2O , CHO and CO [183-186, 188, 190, 193, 195, 197, 198] which is in general acceptance. Methanol first adsorbs as methoxy group, and is bounded via the oxygen atom to 3-fold hollow sites at the surface. The cleavage of the $C-O$ bond may occur, resulting in the formation of CH_x species, as detected by XPS (see Fig. 3-21) but the mechanism and probability of $C-O$ bond scission has still some controversy.

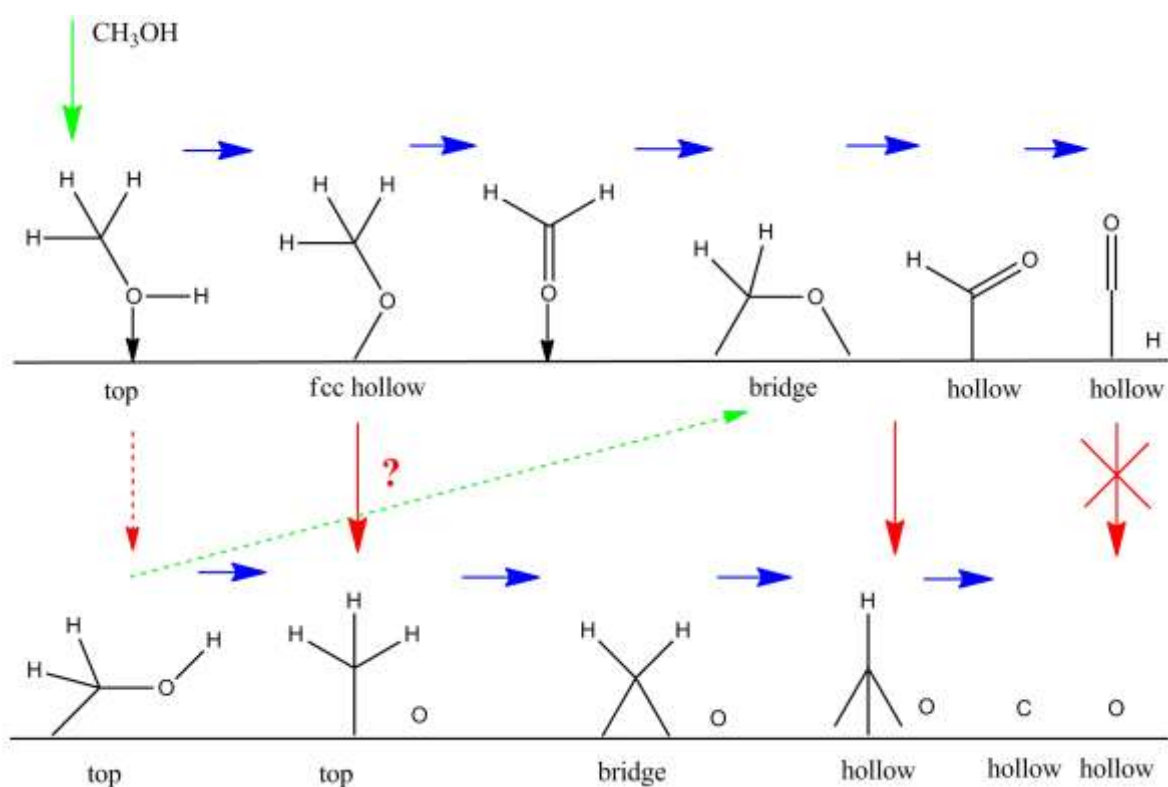


Fig. 3-24: Reaction mechanism of the methanol decomposition on Pd(111) [39].

3.4 Preparation of PdZn/Pd(111)

The cleaning procedure for the Pd(111) substrate was the same as described in chapter 3.1 (sputtering in 5×10^{-6} mbar Ar at 1 kV for 45 min at room temperature, followed by annealing for 15 min at 1200 K and then cooling down in 5×10^{-7} mbar O₂ to 600 K and finally, the flashing to 1200 K in UHV). The sample cleanliness was checked by XPS and LEED.

PdZn surface alloys were prepared by physical vapor deposition of Zn (high-purity Zn wire, 99.98%, GoodFellow) out of a Ta crucible mounted in an Omicron e-beam evaporator. The deposited amount of Zn was calibrated by use of a quartz microbalance with the Zn flux during evaporation being additionally controlled via an internal flux monitor. In this respect, one monolayer (ML) is always referred to 1.53×10^{15} atoms/cm². This is the value of a close-packed (111) crystal plane in bulk Pd. It has been shown by Kratzer et al. [199] that great care has to be taken when using a quartz microbalance to calibrate the amount of deposited Zn due to the lowered sticking coefficient of Zn on the contaminated surface of the quartz crystal. To overcome this problem we have deposited several monolayers of Zn on the quartz surface immediately before the flux calibration. Upon annealing of the deposited Zn layers, a well-ordered LEED pattern was obtained under UHV, suggesting the coexistence of three rotational domains of a (2×1) structure consisting of alternating rows of Pd and Zn atoms, what is in agreement with recent STM studies [199, 200]. The observation of a “(2x2)” LEED pattern is somewhat misleading at first because the stable (111) surface of a PdZn 1:1 alloy has a (2×1) periodicity. However, considering the six fold symmetry of the hexagonal (111) surface, the observation of a “(2x2)” LEED pattern can actually be explained as a superposition of the diffraction pattern of three (2x1) surface domains with different rotational orientation (rotated by 60°).

The deposition of 1 ML Zn results in the formation of two layers of a PdZn 1:1 surface alloy. For submonolayer amounts of Zn, bilayer growth of the surface alloy was observed in agreement with simulations [199, 201, 202] and thus, a deposition of 0.5 ML Zn results in the formation of two-monolayer-high islands of PdZn layers, rather than one complete PdZn layer. To ensure the formation of complete alloy surface layers, we have experimentally studied model systems after deposition of 1 ML Zn (=2 ML PdZn) and 3 ML Zn (>4 ML PdZn).

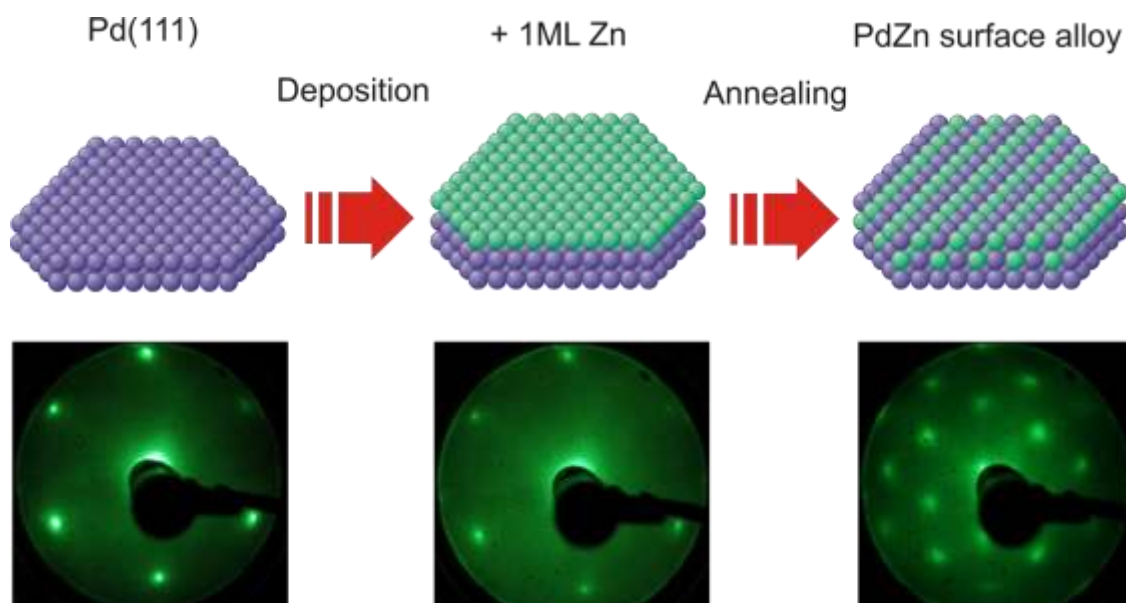


Fig. 3-25: Preparation of a PdZn surface alloy with corresponding LEED pictures. The surface is covered with a Zn-layer after evaporation. Annealing leads to the formation of a Pd:Zn 1:1 surface alloy [39, 203].

It was previously shown by Low Energy Ion Scattering (LEIS) and DFT calculations that PdZn surface alloys show different surface corrugation depending on the number of alloy layers (i.e. alloy thickness) [204, 205], which has a strong influence on the catalytic behavior of the system for MSR [206, 207]. This work will mainly deal with multilayer PdZn alloys.

The preparation of the PdZn surface alloys could also be monitored by XPS by following the changes in the Pd 3d (Fig. 3-26) and Zn 2p region (Fig. 3-27). Compared to the black trace of clean Pd(111) in Fig. 3-26, after deposition of 3 ML Zn at 90 K the intensity of the Pd 3d signal (grey trace) was significantly reduced (about 40%) and the peak shape was slightly asymmetric towards higher binding energy. Nevertheless, the peak maximum remained at the same binding energy of 335.0 eV, i.e. at the value of bulk Pd [30, 80]. After 5 min annealing at 550 K (red trace) the intensity of the Pd signal increased (by 28%) with a shift of the peak maximum of 0.3 eV towards higher binding energy. Contrary to the Pd 3d peaks, the intensity of the Zn 2p_{3/2} signal decreased (about 15%) upon annealing and the peak maximum was shifted from 1021.5 eV after deposition to 1020.9 eV. The observed peak shifts are well in line with a predicted redistribution of charge between Pd and Zn [208-210].

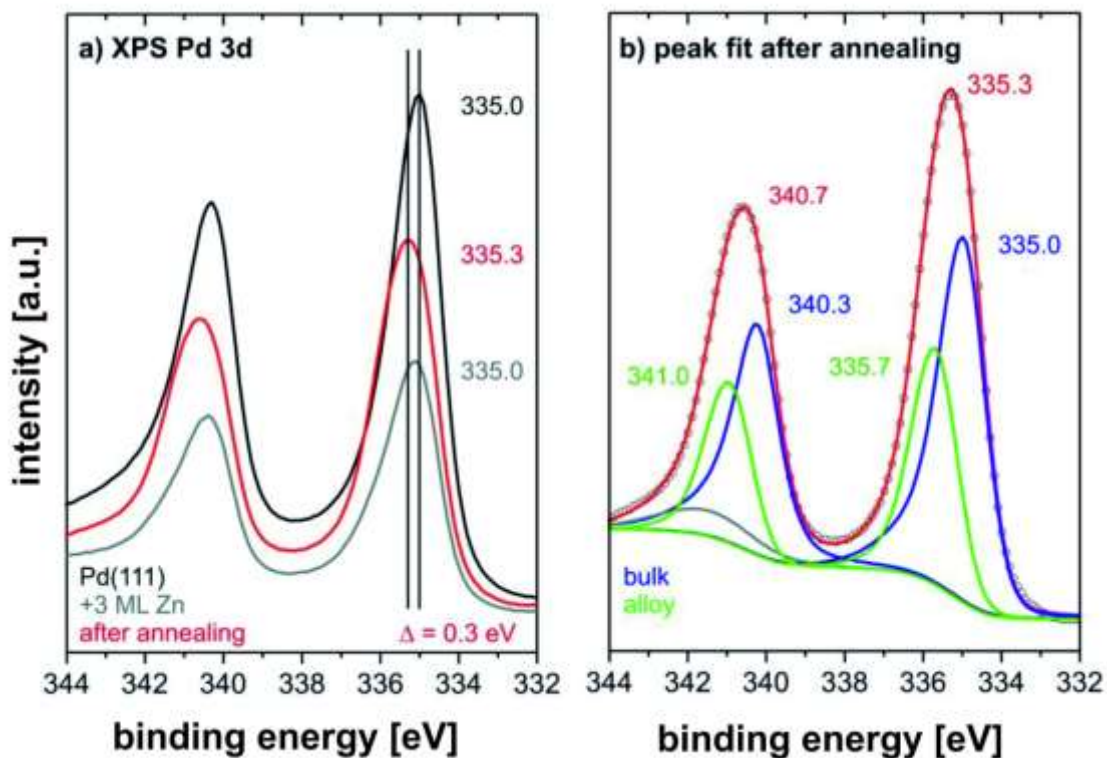


Fig. 3-26: XPS Pd 3d region: a) Evolution of the Pd signal during alloy formation with 3 ML Zn initially deposited on Pd(111) at room temperature. b) Peak fit of the Pd 3d region after annealing 550 K (i.e. of red trace in a)).

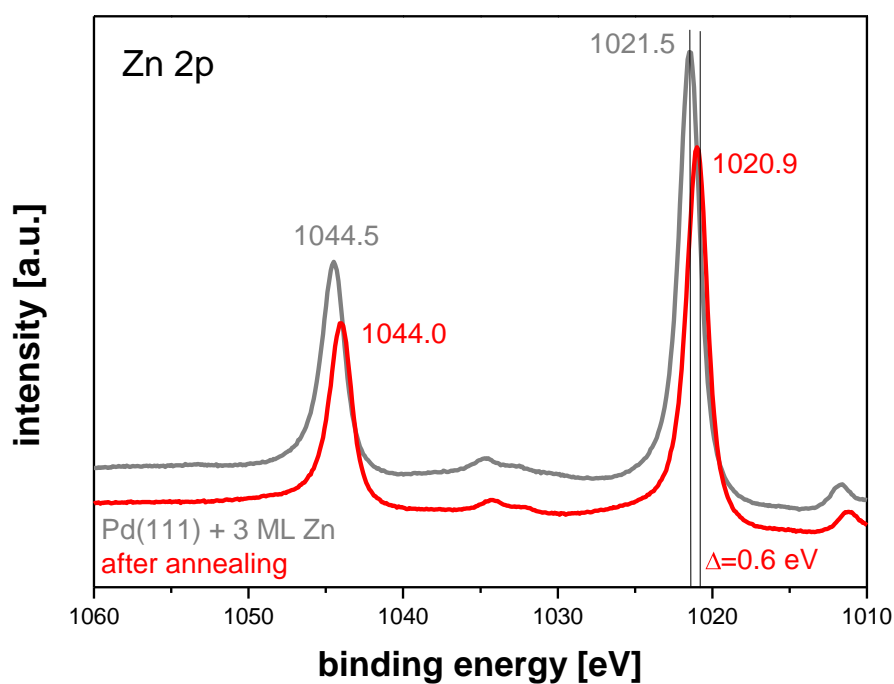


Fig. 3-27: XPS Zn 2p region: Evolution of the Zn signal during alloy formation with 3 ML Zn initially deposited on Pd(111) at room temperature (grey trace) and after annealing 550 K (red trace).

Several groups have used this approach to prepare PdZn surface alloys to be used as planar model catalysts but, nevertheless, some open questions still remained. One topic debated was the onset temperature of alloy formation. Some groups stated that alloy formation occurs spontaneously directly upon Zn deposition at room temperature [200], while other studies pointed out the necessity of annealing to elevated temperature [203, 205, 211]. Thus, the alloy formation was observed by TPD and PM-IRAS utilizing CO as probe molecule. This will be discussed in the next chapter 0.

3.5 CO adsorption on PdZn/Pd(111)

TPD and PM-IRAS measurements were performed utilizing CO as a probe molecule to study the available adsorption sites available on the PdZn/Pd(111) surface alloy. CO is also an unwanted by-product in the methanol steam reforming reaction.

Because CO adsorption on Zn atoms can be excluded under these conditions [206, 212, 213], the observed features in TPD and IR could be assigned to CO bound on Pd atoms in the PdZn surface layers.

3.5.1 PM-IRAS

The occupied adsorption sites on PdZn/Pd(111) were studied by PM-IRAS and in the following chapter with TPD. After sample preparation, a PM-IRAS spectrum was acquired at 90 K in 10^{-6} mbar CO. The sample was then heated in 10^{-6} mbar CO atmosphere to 300 K, cooled once more to 90 K and the next IR spectrum was recorded. This procedure was repeated successively increasing the annealing temperature up to 900 K (Fig. 3-28).

Starting at 273 K, no CO adsorption can be observed for annealing temperatures up to 423 K. As CO does not significantly adsorb on Zn (as mentioned before) under these conditions, the absence of CO adsorption clearly shows that the Zn layers are intact and not yet alloyed with palladium. After annealing to 473 K, CO adsorption can be observed in the spectra. At first, an IR band at 2059 cm^{-1} is detected, which gains intensity upon further increasing the annealing temperature, and shifts to higher wavenumbers due to increasing CO coverage. Higher coverage increases the intermolecular dipole interactions between neighboring CO molecules (dynamic dipole-dipole coupling), which induces a frequency shift to higher wavenumbers. Additionally, increasing coverage reduces the amount of back bonding from the metal d-electrons to the CO molecules, weakening the metal-CO bond and again resulting in a blue shift of the internal C-O stretch [30].

The maximum intensity of this band is obtained after heating the sample to 573 K (at a wavenumber of 2074 cm^{-1}) and it is attributed to CO linear bound on (surface) Pd atoms in the PdZn alloy. The strong increase of the CO signal between 473 K and 573 K can be explained by two facts:

- the ongoing alloying process between these two temperatures
- a reconstruction of the PdZn surface layer that leads to higher CO-coverage; see chapter 3.7 and [134]. At this coverage every Pd atom on the surface is occupied by a CO molecule with on top geometry. IR absorption bands at about 2070 cm^{-1} for linear bonded CO on PdZn surfaces were also observed by Föttinger et. al. [214] and Conant et. al. [23] for PdZn nanoparticles supported by ZnO in technological catalysts. This confirms that the examined PdZn surface alloys represent well-suited model systems for PdZn nanoparticles in MSR catalysts (excluding interface effects related to the ZnO support).

Upon annealing to 673 K the intensity of the on-top band was clearly reduced and a signal for bridge-bonded CO appeared at 1943 cm^{-1} . This signal indicates the onset of alloy decomposition since bridge-bonded CO requires patches of 3 or more Pd atoms at the surface, not present in the PdZn(111) 2x1 surface periodicity. Alloy degeneration starts by Zn diffusion into the Pd bulk and Zn desorption from PdZn surfaces was reported to occur at temperatures above 900 K [200, 215]. Finally, in the spectrum obtained after heating the sample to 900 K two IR bands at 2087 cm^{-1} (on-top CO) and at 1954 cm^{-1} (bridge-bonded CO) can be observed. This spectrum very closely resembles the one for CO on clean Pd(111) under the same conditions. TPD measurements (chapter 3.5.2) are leading to the same conclusions.

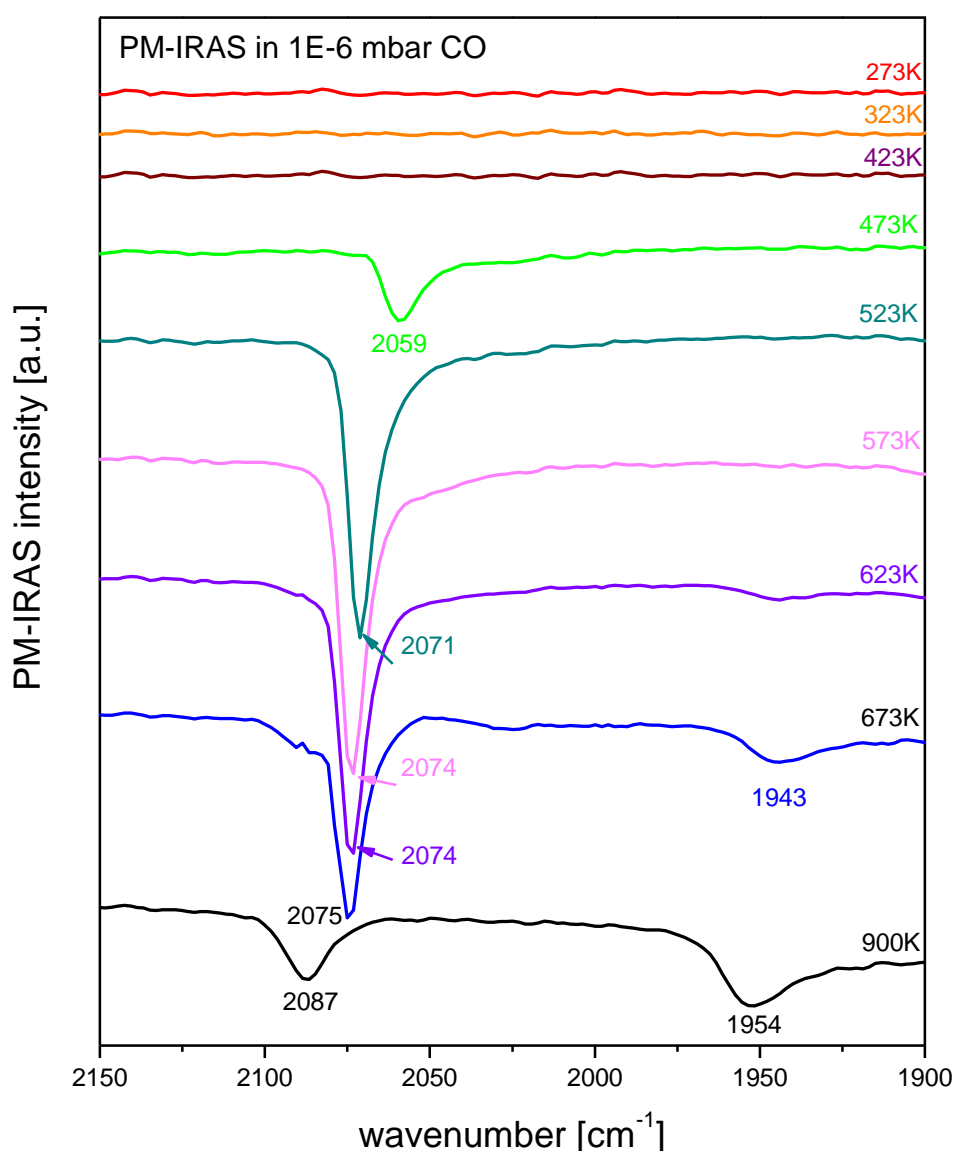


Fig. 3-28: PM-IRAS spectra characterizing the PdZn/Pd(111) alloy formation (1 ML Zn evaporated) at successively higher annealing temperatures (spectra acquired after cooling to 90 K after annealing in $1 \cdot 10^{-6}$ mbar CO). The signal at $\sim 2070 \text{ cm}^{-1}$ can be assigned to on-top CO. After decomposition of the surface alloy (900 K) two IR bands at 2087 cm^{-1} (on-top CO) and at 1954 cm^{-1} (bridge-bonded CO) can be observed.

Previous PM-IRAS studies [205, 206, 213] have shown that on well-defined PdZn/Pd(111) surface alloys exclusively on-top sites were occupied by adsorbed CO molecules, irrespective of alloy thickness. PdZn surface alloys could be characterized by a sharp, characteristic band for on-top CO at $\sim 2070 \text{ cm}^{-1}$ in IR experiments performed in a CO background (= high coverage). Similar spectra are obtained on oxide-supported PdZn nanoparticles [214]. Multiple bound CO species were only observed upon annealing to temperatures above 623 K,

when partial alloy decomposition started (Fig. 3-28). The DFT-calculated stretching frequencies of *CO* on top of Pd atoms are 2024–2035 cm^{-1} at low coverage and 2059–2083 cm^{-1} at saturation coverage. Calculations for *CO* adsorbed on bridge sites gives frequencies of 1883–1894 cm^{-1} at low coverage and 1966–1995 cm^{-1} at high *CO* coverage. The calculated *CO* stretching frequencies do not significantly depend on the alloy thickness.

Fig. 3-29 shows coverage-dependent IR spectra. Upon a *CO* dose of 0.1 Langmuir, a broad band at 2048 cm^{-1} and a sharper, less intense band at 2068 cm^{-1} could be distinguished in the spectrum. Subsequently increasing the *CO* dose resulted in an intensity increase of the band at 2068 cm^{-1} accompanied by a decrease of the 2048 cm^{-1} band until the latter finally vanished from the spectrum after a *CO* dose of 10 L. The appearance of two IR bands corresponds to two different *CO* species on the surface. One can differentiate between *CO* that does not have other *CO* molecules at adjacent adsorption sites (dominates at low coverage) and those that have *CO* neighbors (dominates at high coverage) [30]. Their frequencies are different because increasing dipole–dipole interactions and reduced back bonding from the metal at higher coverage result in a spectral blue shift of the C–O stretching vibration. Positions of experimental bands at 2048 and 2068 cm^{-1} are in agreement with calculated frequencies for a reconstructed structure (this will be discussed later in chapter 3.7).

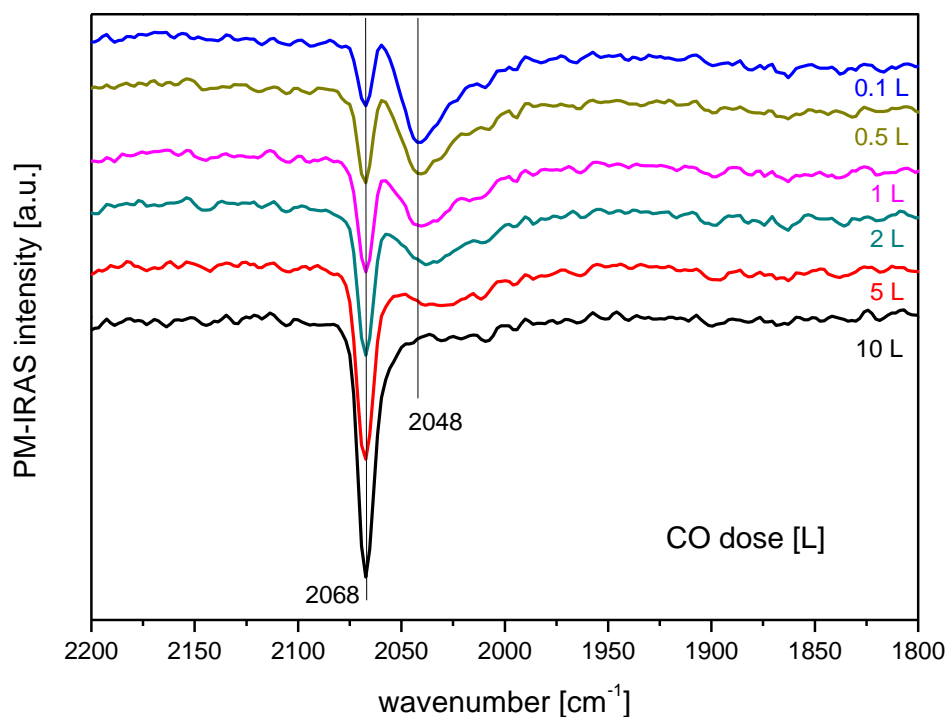


Fig. 3-29: Coverage-dependent PM-IRAS spectra of *CO* adsorption on >4 ML PdZn/Pd(111) at 100 K. Two types of *CO* can be observed. *CO* that does not have other *CO* molecules at adjacent adsorption sites (low coverage) and those that have *CO* neighbors (high coverage). These two species can be distinguished by IR. The band at 2068 cm^{-1} (increasing with coverage) can be assigned to neighboring *CO*.

Different from the results presented above, Jeroro et al. [216, 217] could not observe *CO* adsorption after deposition and annealing of 1 ML Zn. An explanation could be the low dose of *CO* used in their experiments (0.5 L at 100 K) which may be not enough to saturate the PdZn surface. It was shown by Tamtögl et al. [218] that exposures of a least 5 L *CO* were required to saturate the surface with *CO*. In addition, from a comparing the presented LEED pattern in [216] it is probable that Jeroro et al. strongly underestimated the actual Zn coverage.

3.5.2 TPD

To determine the saturation CO coverage on PdZn/Pd(111) and to investigate alloy formation and decomposition in more detail, TPD measurements were performed to monitor CO adsorption and desorption depending on the PdZn surface alloy thickness, annealing temperature, and CO dosage/pressure.

Starting from an unalloyed sample (1 or 3 ML Zn deposited at liquid N₂ temperature on Pd(111) substrate), the sample was first heated to 273 K and cooled down in $1 \cdot 10^{-6}$ mbar CO to 90 K to saturate the surface with CO. After that, repeated TPD runs were performed to consecutively higher end temperatures (each of which was kept for 5 min to anneal the layers at this temperature). The results are shown in Fig. 3-30 and Fig. 3-31. The temperatures are indicating the annealing temperature before the TPD run. After one run was finished, the sample was saturated again with CO during cooling before the next TPD spectrum was acquired. All measurements were repeated 3 times with a heating rate of 60 K/min (also heating rates between 30 and 120 K/min. were tested with no significant difference).

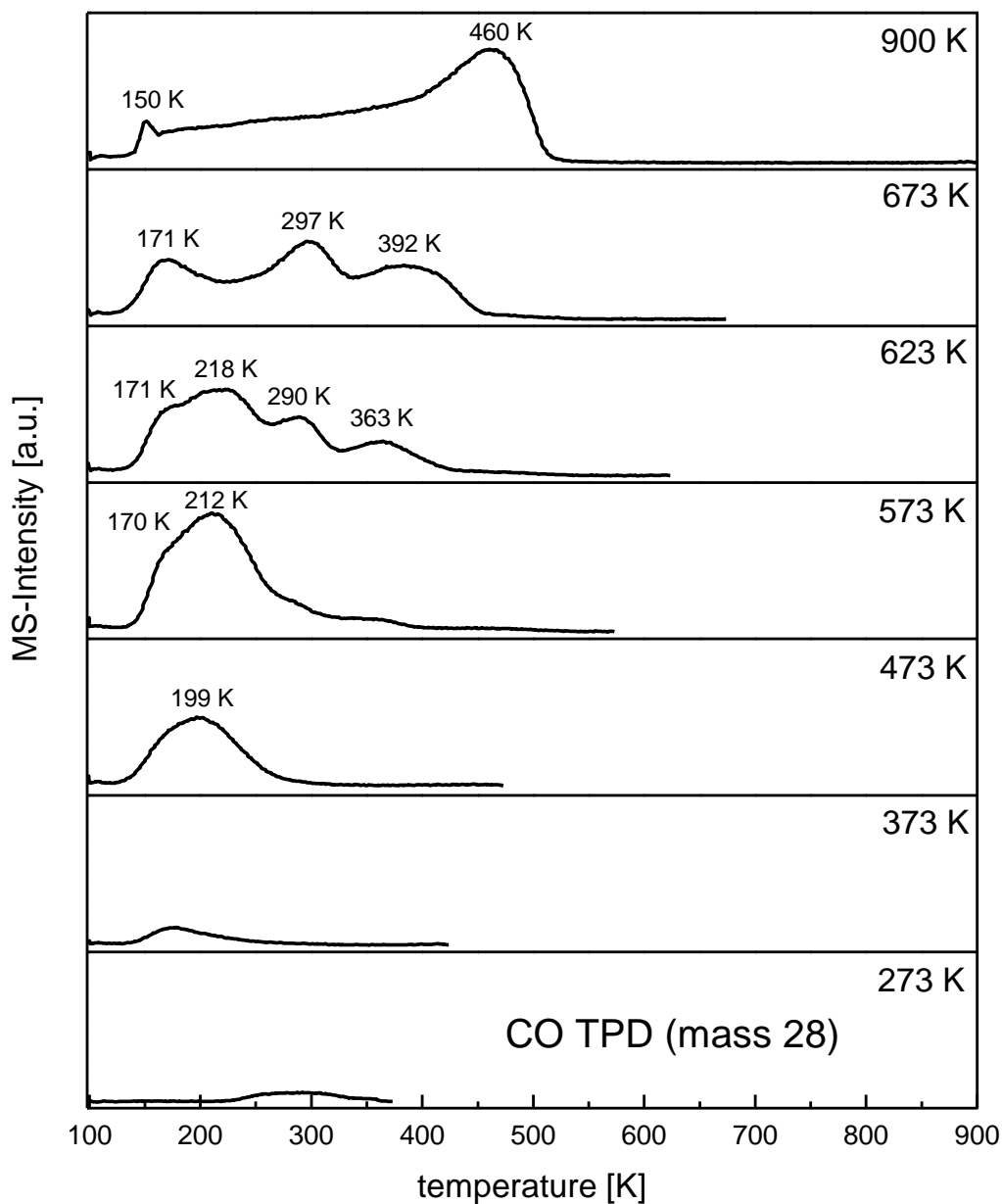


Fig. 3-30: CO TPD spectra from a 2 ML PdZn/Pd(111) alloy depending on annealing temperature. After an annealing temperature of 473 K a clear CO desorption peak at 199 K appeared. The desorption peak reached its maximum intensity (“ideal” PdZn alloy) after an annealing temperature of 573 K. Multiple desorption peaks after an annealing temperature of 623 K are an indication for alloy decomposition.

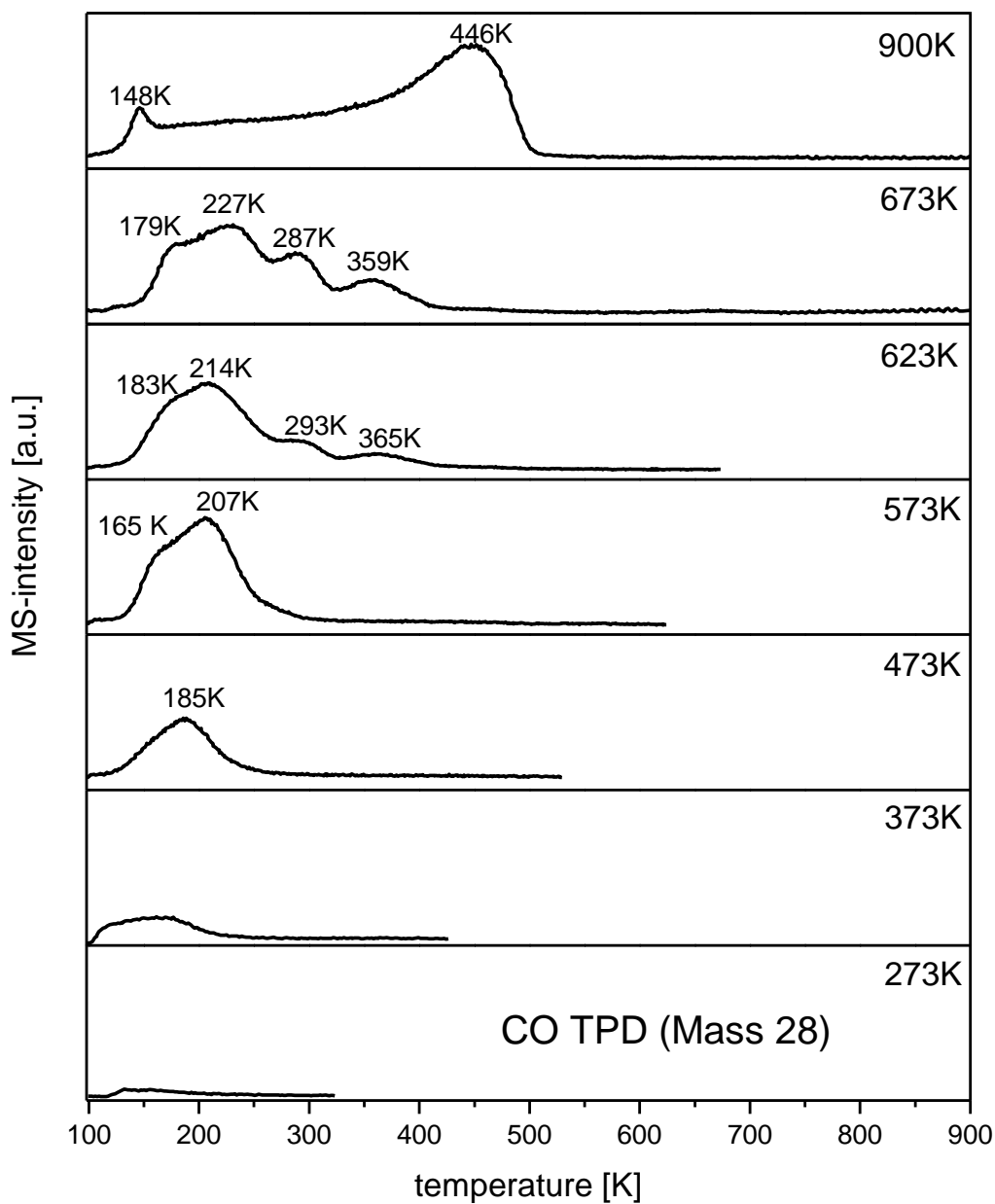


Fig. 3-31: CO TPD spectra from a >4 ML PdZn/Pd(111) alloy depending on annealing temperature. After an annealing temperature of 473 K a clear CO desorption peak at 185 K appeared. The desorption peak reached its maximum intensity (“ideal” PdZn alloy) after an annealing temperature of 573 K. Multiple desorption peaks after an annealing temperature of 623 K are an indication for alloy decomposition.

Mainly three regimes can be differentiated:

- Up to the annealing temperature of 373 K, basically no *CO* desorption was observed, in good agreement with the previously reported absence of *CO* adsorption in PM-IRAS, see chapter 3.5.1 and [205]. In this regime, the deposited Zn layers are not yet alloyed with the Pd substrate. Only trace amounts of *CO* were detected by mass spectrometry, most probably due to *CO* desorbing from the heating wires holding the crystal or from the crystal edges.
- After heating to 473 K, alloy formation starts, a clear *CO* desorption peak could be observed, which can be attributed to *CO* desorbing from alloyed PdZn layers. After annealing to 573 K, this peak reached its maximum intensity (“ideal” PdZn alloy) and was made up from two desorption features: a shoulder at ~170 K and the peak maximum at ~210 K.
- Further annealing above 623 K resulted in the appearance of additional desorption features at higher desorption temperature, indicating the onset of alloy degradation via Zn dissolution in the bulk and the reappearance of Pd patches at the surface. Finally, after annealing to 900 K, the PdZn alloy was completely decomposed and the surface had transformed back to clean Pd(111). The acquired TPD and PM-IRAS spectra closely resemble the spectra obtained upon *CO* desorption from Pd(111), see chapter 3.2 and [158]. The degradation of the alloy takes place via Zn dissolution in the Pd bulk and Zn desorption into the gas phase was detected to start at more than 900 K [200, 215], as mentioned in chapter 3.5.1.

In the TPD spectra shown in Fig. 3-30 and Fig. 3-31, only minor difference can be seen between 2 ML and >4 ML PdZn/Pd(111) (at temperatures when alloys are stable), indicating that *CO* desorption was not really affected by the thickness of the underlying PdZn layer.

While the general trend was the same for both PdZn systems, some small differences in the TPD spectra could be observed. In the “transformation regime” (>573 K), the spectra suggests that the transformation back to Pd(111) proceeded faster and more easily on the thinner alloy, meaning that lower temperatures were required for the thinner alloy to reach the same surface state. And also it seems that presence of an effect of subsurface Zn on the *CO* adsorption on Pd(111). When the TPD spectra, acquired after annealing to 900 K, are compared, the *CO* desorption maximum was shifted by more than 10 K to lower temperatures for the system with higher Zn content. This finding is in agreement with results of recent DFT studies that

showed lowering of *CO* adsorption energies on Pd(111) if Zn atoms are present in the subsurface region [30, 134, 211].

For the “ideal” PdZn alloys (annealing to 573 K), we have estimated the adsorption energy by applying the Redhead equation and using a pre-exponential factor for desorption of $10^{15.3} \text{ s}^{-1}$. This was already discussed in chapter 3.2.5. The desorption energies, estimated from TPD, are calculated to $E_{TPD}=0.66 \text{ eV}$ (2 ML) and $E_{TPD}=0.64 \text{ eV}$ (>4 ML), this will be further discussed in chapter 3.7.

By integrating the peak areas and taking the well-known 0.75 ML coverage of the (2×2) *CO* saturation structure on Pd(111) as a reference (this well-defined structure *CO* occupies on top and 3-fold hollow sites, as characterized by various methods) [158], the *CO* coverage for each TPD spectrum was calculated (see Fig. 3-32 and Fig. 3-33).

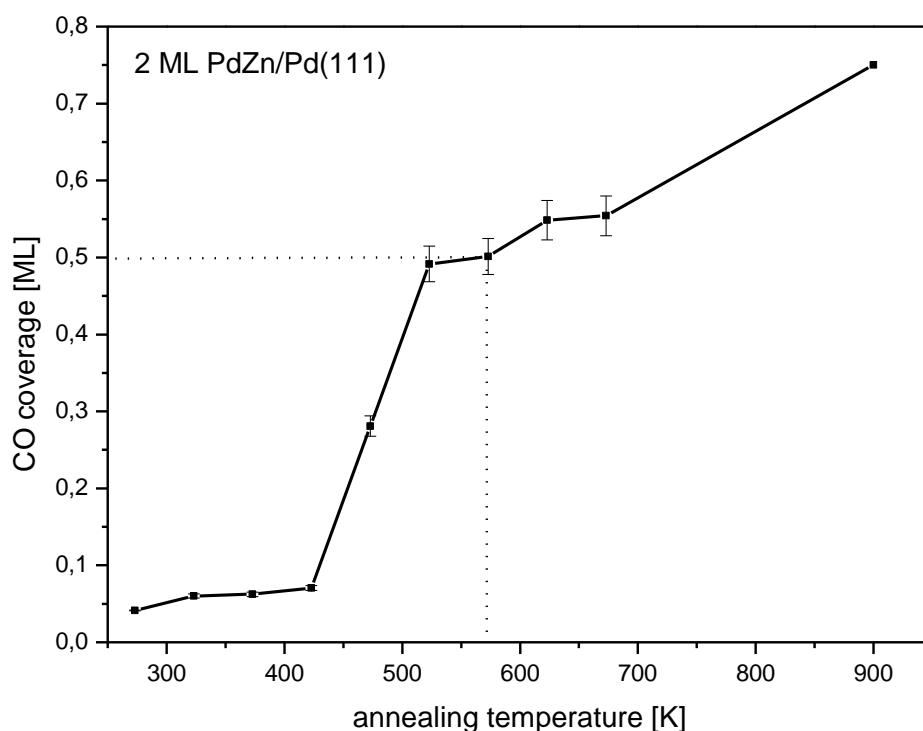


Fig. 3-32: CO coverage as deduced from the TPD spectra versus annealing temperature. The dashed line indicates saturation coverage on the “perfect” alloy. Error bars were derived from three repeated measurements. The saturation coverage of CO on Pd(111) is 0.75 ML.

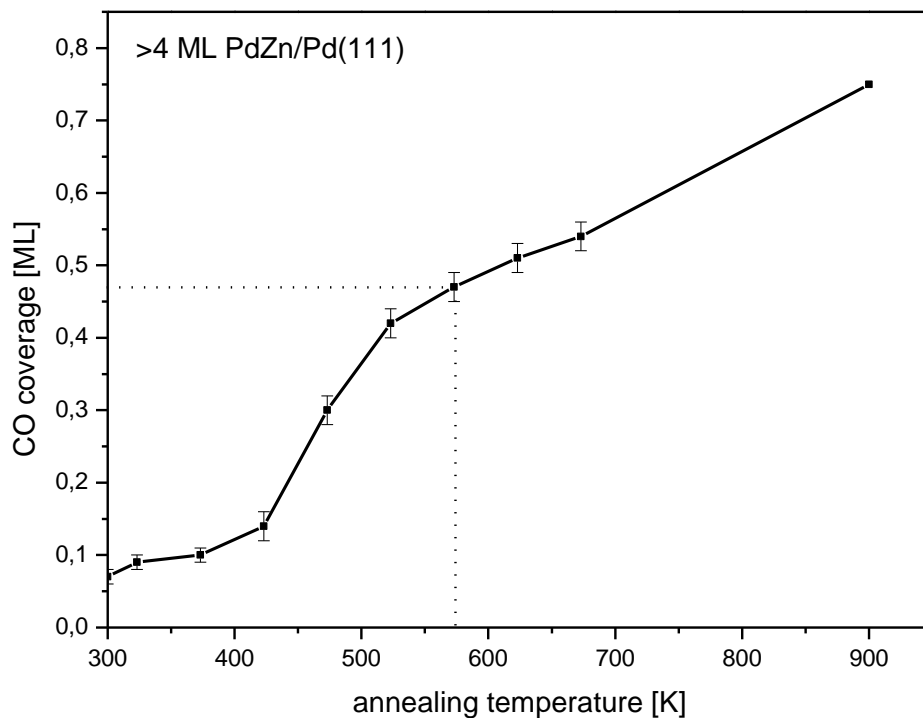


Fig. 3-33: *CO* coverage as deduced from the TPD spectra versus annealing temperature. The dashed line indicates saturation coverage on the “perfect” alloy. Error bars were derived from three repeated measurements. The saturation coverage of *CO* on Pd(111) is 0.75 ML.

After annealing of both systems to 573 K – at this temperature the alloy-related TPD and PMIRAS features were most pronounced – the *CO* coverage was 0.50 ± 0.02 ML for the 2 ML PdZn/ Pd(111) system and only slightly lower, 0.47 ± 0.02 ML, for the >4 ML PdZn system. This is in good agreement with similarly prepared systems [218].

As already mentioned, the Pd:Zn ratio is 1:1 in a PdZn alloy surface layer. This indicates, that every surface Pd atom is occupied by a single *CO* molecule. This gives some indication about the surface arrangement and will be discussed in chapter 3.7.

To investigate this in more detail, a number of TPD spectra were acquired upon increasing the initial CO dose from 0.5 L to saturation coverage, similar to the PM-IRAS spectra in Fig. 3-29. The TPD spectra are shown in Fig. 3-34 and Fig. 3-35 for the systems of 2 ML and >4 ML PdZn/Pd(111). Two CO desorption regimes can be distinguished, desorption from the PdZn surface alloy below 300 K and desorption areas above 400 K.

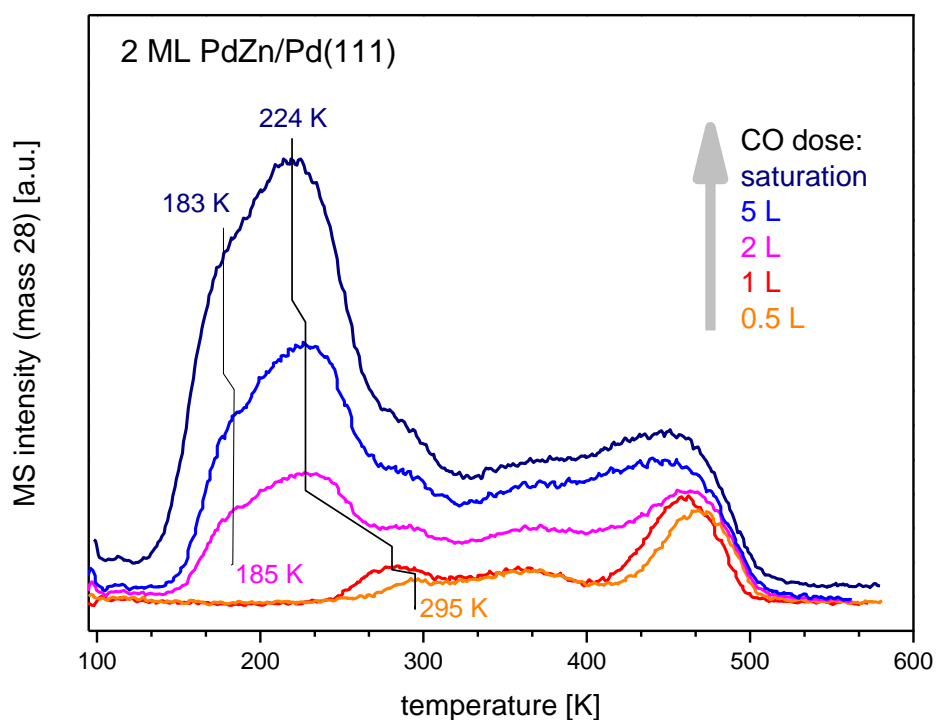


Fig. 3-34: Coverage-dependent CO TPD spectra for 2 ML Zn/Pd(111). For each series the CO dose at 90 K was subsequently increased from 0.5 to 5 Langmuir. Saturation coverage (sat.) was achieved by cooling the system in $1 \cdot 10^{-6}$ mbar CO to 90 K.

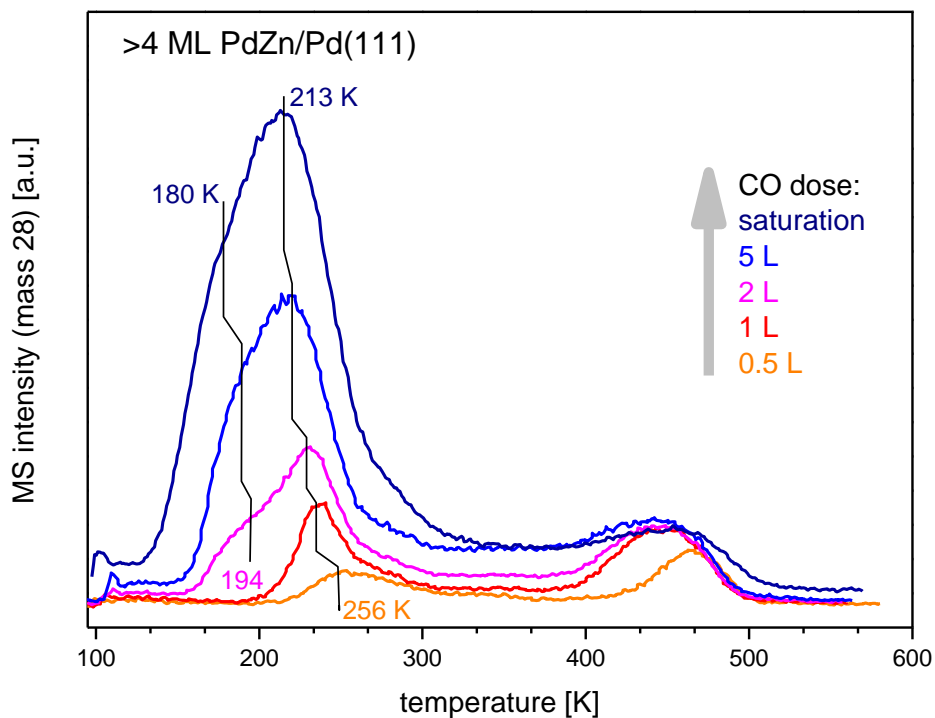


Fig. 3-35: Coverage-dependent *CO* TPD spectra for >4 ML Zn/Pd(111). For each series the *CO* dose at 90 K was subsequently increased from 0.5 to 5 Langmuir. Saturation coverage (sat.) was achieved by cooling the system in $1 \cdot 10^{-6}$ mbar *CO* to 90 K.

After the smallest dosage of 0.5 L *CO* onto the 2 ML PdZn system, a small desorption feature was observed with a maximum at 295 K, this can be attributed to desorption from the alloy. With increasing dosage, desorption maximum of the <300 K regime gradually shifts to lower temperatures (see

Tab. 3-1). Upon dosage of 2 L *CO*, another desorption feature appeared as a shoulder near 183 K. The signal increased in intensity at higher dosage but basically did not alter the position of the desorption maximum. The third feature around 295 K was also detected in the spectra after elevated doses, which might tentatively be attributed to *CO* desorbing from imperfect areas of the surface.

Tab. 3-1: CO Desorption maxima for the <300 K regime for 2 and >4 ML PdZn/Pd(111) surface layers at different CO dosage. See also Fig. 3-34 and Fig. 3-35.

Desorption maximum temperature / CO dosage	0.5 L	1 L	2 L	5 L	Saturation coverage
2 ML PdZn/Pd(111)	295 K	285 K	185 K/227 K	183 K/226 K	183 K/224 K
>4 ML PdZn/Pd(111)	256 K	236 K	194 K/231 K	193 K/218 K	180 K/213 K

For the >4 ML surface, the general trend was similar (Fig. 3-35), but alloy-related features were more pronounced (see also Fig. 3-30 and Fig. 3-31). This is an indication about the surface arrangement and will be discussed in chapter 3.7.

3.6 STM measurements on Pd(111) and PdZn/(111)

The first step was to check and optimize the preparation procedure for this application. In STM the system is measuring only on the first layer. Even if the prepared sample seems to be perfect when controlled by LEED or XPS, it is possible that the first atomic layer is not completely ordered and flat (the information depth of LEED is a few atomic layers) or adsorbates (below the XPS detection limit) cover the metal surface. In these cases it is difficult or impossible to get the expected information by this method. The second issue is a stable (noise-free/vibration-free) system to get atomic resolution.

It has turned out that the preparation conditions as used in the XPS/PM-IRAS system (see chapter 3.1) are also working for STM when using two or three cleaning cycles more.

Unfortunately on many days sensible STM measurements were not possible due to an unstable system (sometimes the noises were a few hundred times higher than on “good days”). Possible reasons for these noises were maybe construction works and unauthorized test drillings on the area Getreidemarkt, but even after finishing of these construction works undefinable noises influenced the measurements very often. Other possible sources of noises are wastewater treatment (below the lab room) and ventilation systems, but this cannot really explain why on some day conditions are good and sometimes not. Furthermore, it seems that this depends not mainly on the time of day, also late at the evening (when most people went home) the problem exists. However, if it is not possible to stabilize the system, one has to wait for the next day. Due to the high sensitivity for contaminations the sample has to be prepared again but the intensity of noises remains unclear until the STM measurements starts.

So it is possible that the surface was on some days – in principle – perfect for the STM but the STM not ready.

Fig. 3-36 shows a small area of a clean Pd(111) surface, single atoms are noisy but clearly visible. A large area scan (Fig. 3-37 and its 3D representation Fig. 3-38) reveals a flat surface with some steps. At this time the surface looked very clean but after ~1 h some adsorbates were visible (see Fig. 3-39) that means the time frame for measurements on a good surface is quite short for Pd(111).

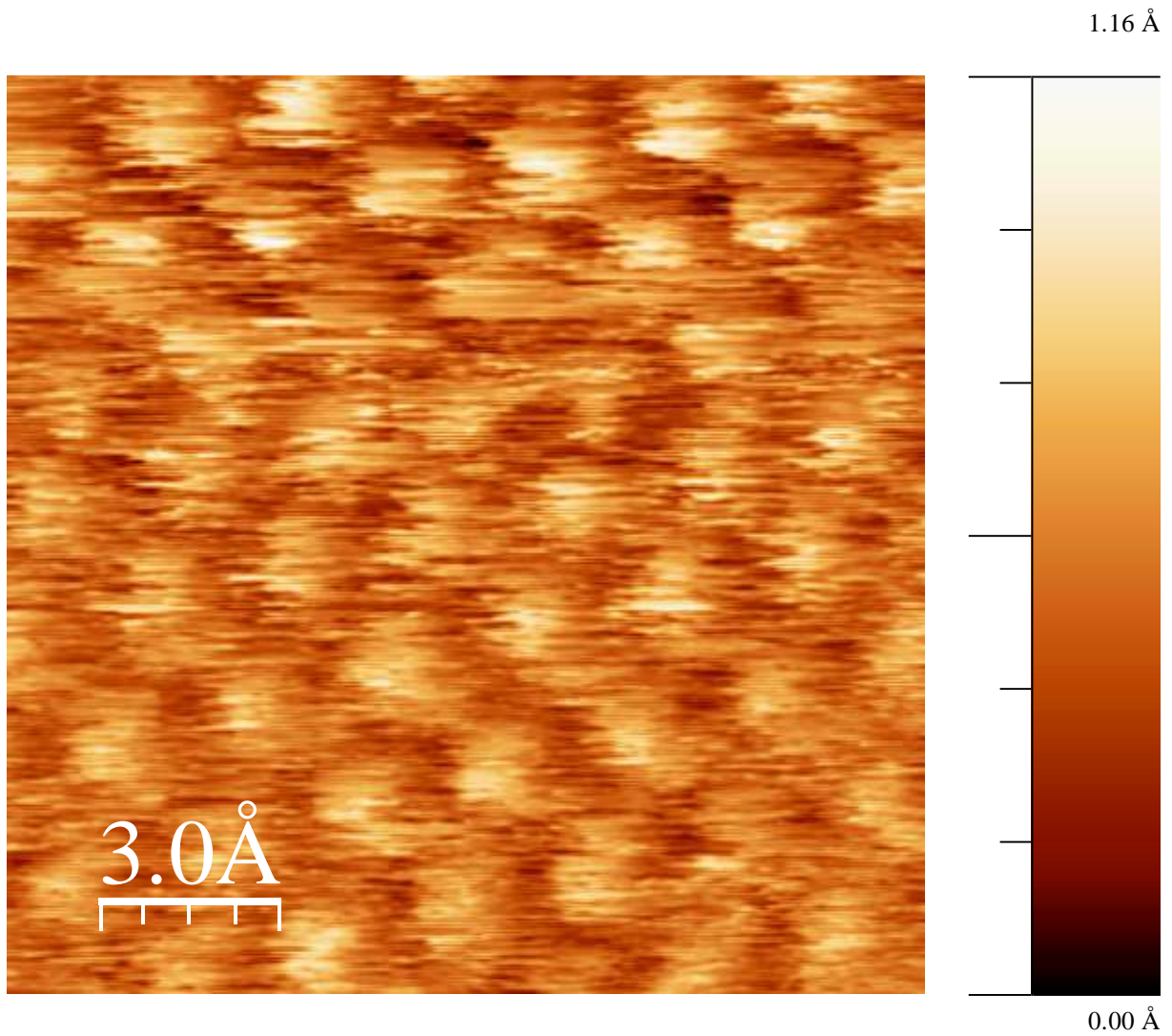


Fig. 3-36: Atomic resolution on a Pd(111) surface ($15 \times 15 \text{ \AA} \times \text{ \AA}$, tunneling current I_t : 0.440 nA, tunneling voltage V_t : 371.7 mV).

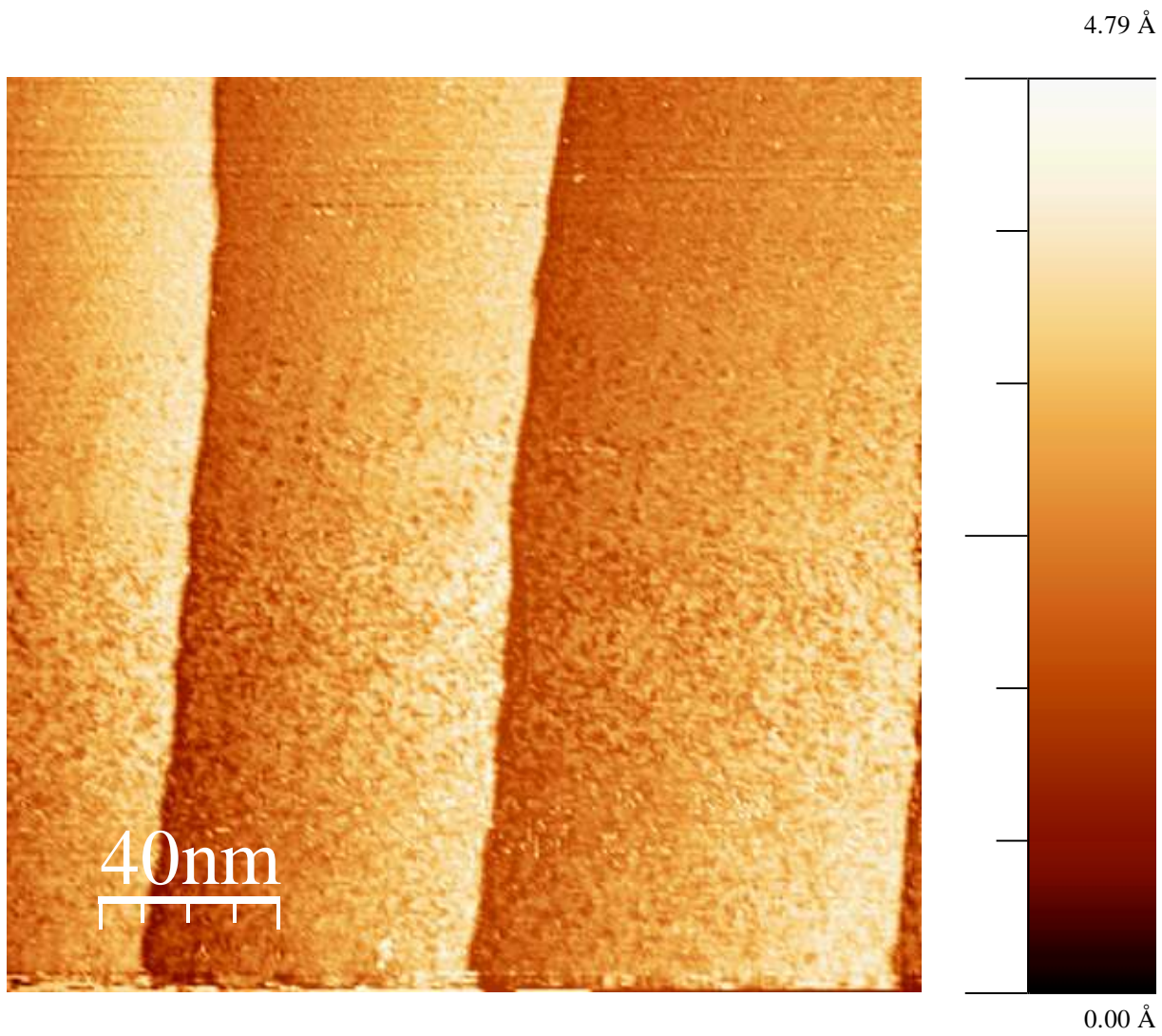


Fig. 3-37: Steps on a clean Pd(111) surface (large area scan; 2000x2000 ÅxÅ, It: 0.370 nA, Vt: 441.9 mV).

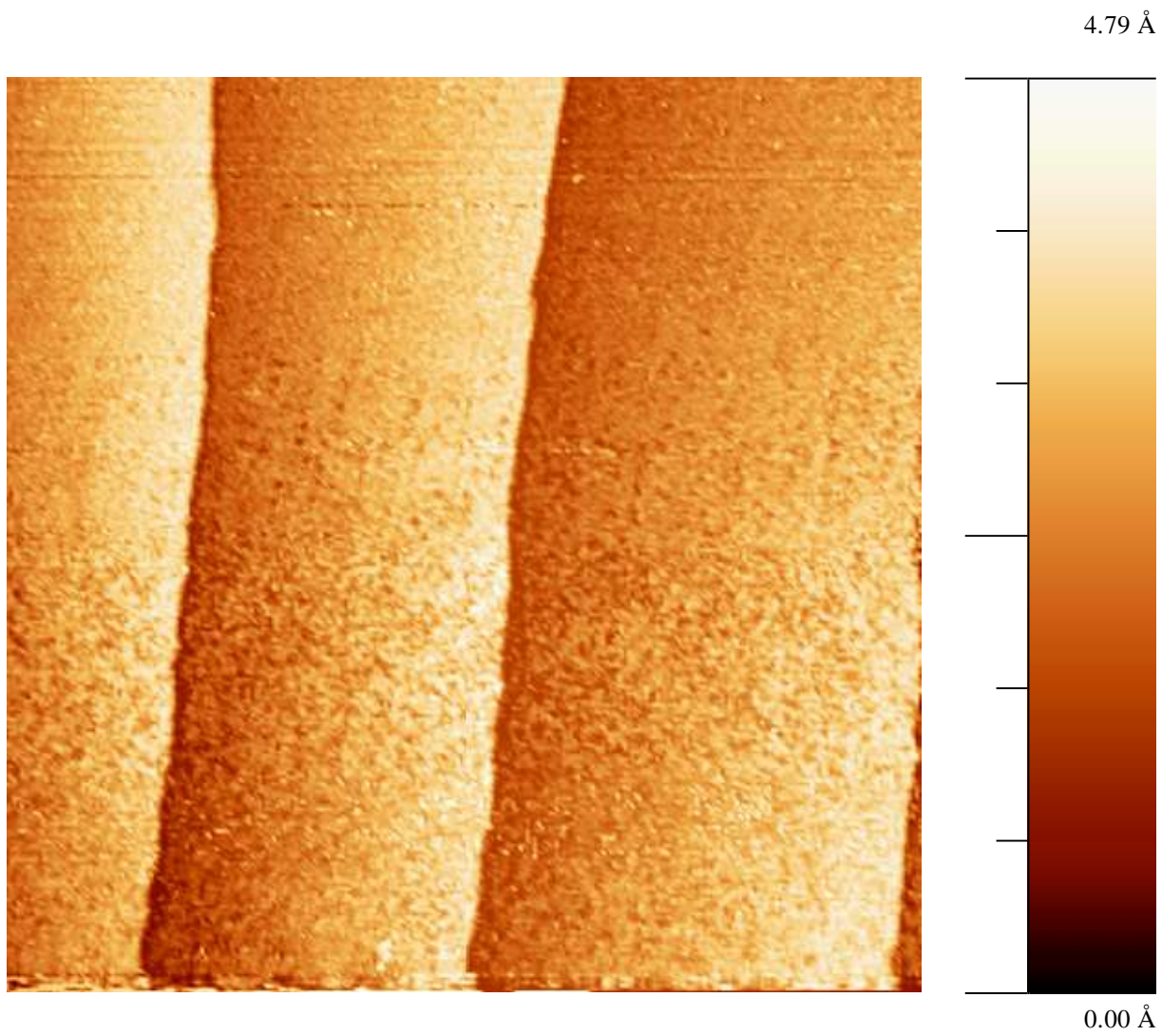


Fig. 3-38: 3D visualization of the steps on Pd(111) shown in Fig. 3-37.

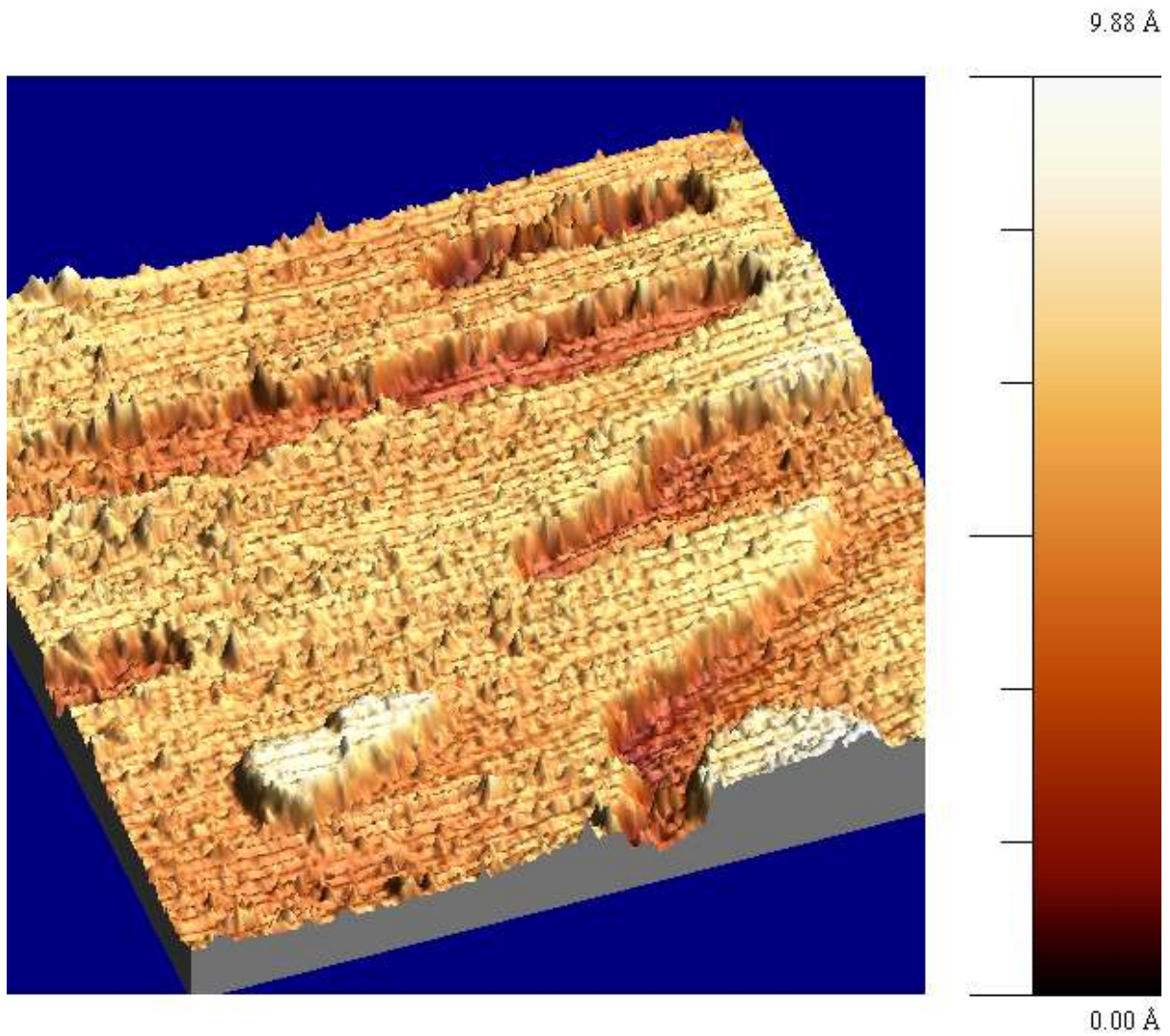


Fig. 3-39: 3D visualization of adsorbates on Pd(111) (.500x500 ÅxÅ, It: 0.760 nA, Vt: 1486.5 mV). The adsorbate in the left lower corner is about 100x40 ÅxÅ and 3 Å in height.

3.6.1 Pd(111)/PdZn surface alloys

The Pd(111) sample was cleaned and prepared as described in the chapter before and controlled by LEED. After transferring to the STM chamber and stabilizing the system (shutting off all pumps, activating the air dampers and waiting for 3 h) a quite good Pd(111) surface STM image was recorded (see Fig. 3-41).

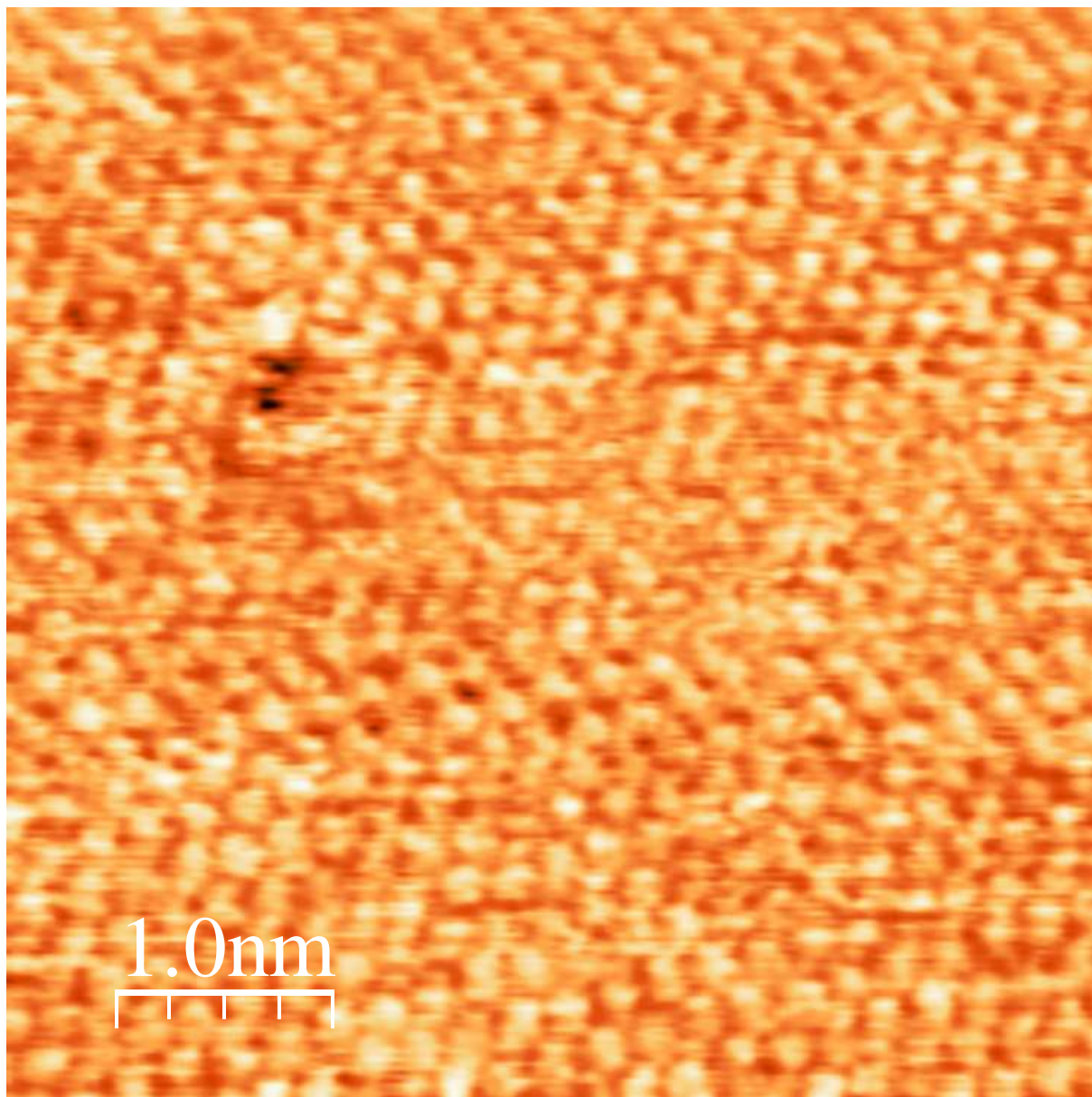


Fig. 3-40: STM image of a Pd(111) surface ($V_t=371$ mV; $I_t=0.530$ nA; $100 \times 100 \text{ \AA} \times \text{ \AA}$) prepared for evaporating with Zn.

The sample was then transferred back to the preparation chamber, 3 ML Zn were evaporated on the surface and finally alloyed at 573 K in a $5 \cdot 10^{-6}$ mbar CO atmosphere for 5 minutes. In the middle of the image a Pd(111) patch is visible. The rest of the picture is quite noisy and shows no atomic resolution. Scans on other positions are similar – no (or just patches of a few atoms) atomic resolution can be observed. This may have two reasons. First, the pyrometer for temperature measurements has a temperature range of 300°C – 1300°C, the lower limit is close to the stability limit of the surface alloy (see chapter 3.4). As result the surface may be (at least partly) decomposed and no ideal alloy position was found by STM. A second possibility is that the alloy formation was not finished at this time and the Pd(111) patches are a reason of an incomplete evaporated Zn layer. This is unlikely because 3 ML Zn should cover the whole surface. In addition, the sample was transferred back to the preparation chamber and the alloying procedure was repeated. STM images recorded after that did not show useful details. No atomic resolution was possible and more and more adsorbates on the surface where also interfering the measurement. This indicates that the surface was not well ordered at this time.

The alloy formation on a well ordered Pd(111) surface was repeated with a slightly lower emission current of the e-beam heater (compared to the emission current when the pyrometer starts recording at 300°C) to avoid temperatures higher than the decomposition temperature of the alloy. Anyway, it was not possible to get atomic resolution of the surface alloy until now. Reasons can be a non-uniform temperature distribution of the heating system or too much adsorbates on the surface.

In future sample heating and temperature reading needs to be improved and source of noises needs to be eliminated.

Fig. 3-41: STM image after evaporating 3 ML Zn and alloying at 573 K in $5 \cdot 10^{-6}$ mbar CO ($V_t=371$ mV; $I_t=5.170$ nA; $100 \times 100 \text{ \AA} \times \text{ \AA}$). A Pd(111) patch can be seen in the middle. In the surrounding no atomic resolution was possible.

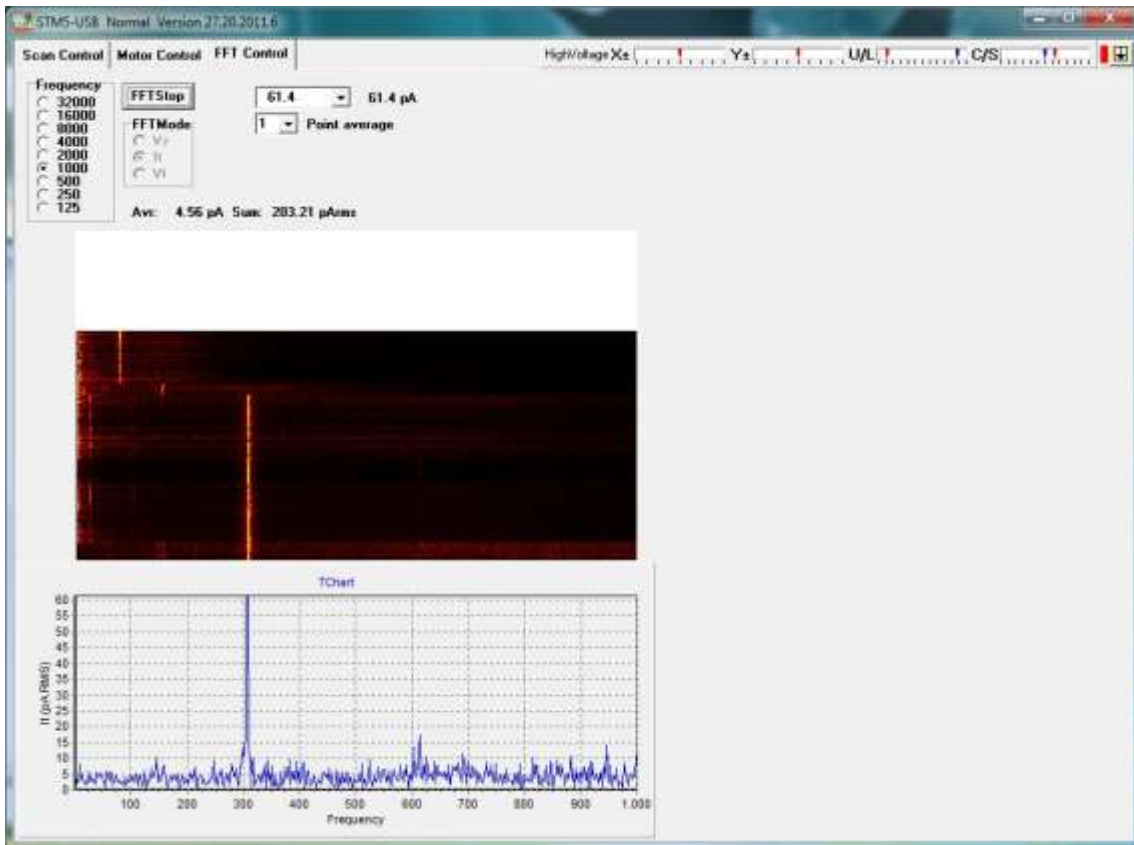


Fig. 3-42: Not identified both noises at the STM system, probably due to construction work near the building recorded as Hz/A spectrum. The noise at 300 Hz is much higher than noises after installation.

3.7 Surface rearrangement induced by CO adsorption

We have found that the results of TPD and PM-IRAS experiments performed in this work are not compatible with the CO adsorption calculated on conventional structure of PdZn/Pd(111). To resolve this discrepancy between experimental and theoretical results, a revised surface structure with Pd and Zn atoms arranged in zigzags is proposed. Structure and reactivity of a catalyst are well-known to change in the presence of certain adsorbates [219-222]. However, this topic seldom becomes a subject of investigation, even for very chemically potent adsorbates as spectator species [223-226]. Some experiments suggest that reconstruction of bimetallic $Co/Re/\gamma Al_2O_3$ and $LaNi_{10}$ catalysts may occur even in the presence of CO, a common probe molecule, which should not modify the properties of the investigated surface [227]. The reason for these complications is the structural complexity of the alloys, which yields additional degrees of freedom, such as surface segregation (changes in the amount of one component on the surface) and geometric arrangement (change in relative order of components without changing the relative amount on the surface), the latter will be discussed in this chapter. Surface segregation recently attracted a lot of attention [228-232]. Component rearrangement was actually neither sufficiently studied experimentally nor theoretically [134, 201, 233-237].

The arrangement affects:

- elemental composition of adsorption sites present on the surface
- distances between atoms in the surface
- surface corrugation
- relative stability of an adsorbate on various sites and its saturation coverage

Computational:

The computational part presented in this work were performed by our collaboration partners, Sergey M. KOZLOV and Konstantin M. NEYMAN at the Departament de Química Física and Institut de Química Teòrica i Computacional, Universitat de Barcelona, Martí i Franquès, 1, 08028 Barcelona, Spain.

The used DFT model and parameters are summarized in chapter 2.11 and will not be further discussed here.

The average adsorption energies of CO at the coverage $\theta = N/12$ ML, where N is the number of CO molecules present in the supercell, were calculated from the total energies E of systems X , $E[X]$, in the following way [134]:

$$E_{ads} \theta = E_{PdZn/Pd} + NE[CO_{gas}] - E[CO_N / PdZn / Pd] / N \quad (1.1.45)$$

according to which positive values of E_{ads} mean stabilization. Harmonic vibrational frequencies were calculated by displacing C and O atoms by 2 pm in all three Cartesian directions. Estimated contributions of harmonic vibrations to adsorption energy are 0.06 eV per CO molecule at 0 K (zero point energy corrections) and only 0.014 eV per CO molecule at 200 K. Because of their rather small magnitude, these corrections are not included into consideration. The calculated harmonic vibrational frequency of a gas-phase CO molecule, 2120 cm^{-1} , underestimates experimental harmonic frequency of CO stretching by 50 cm^{-1} and is by 23 cm^{-1} lower than experimental anharmonic frequency [238]. Thus, for better comparison of (anharmonic) frequencies yielded by PM-IRAS experiments with calculated frequencies, the latter are shifted by 23 cm^{-1} to higher values [134].

Experimental:

The first section describes the model of PdZn/Pd(111) surface with modified elemental arrangement and the properties of reconstructed surface in the absence and in the presence of CO. The obtained PM-IRAS and TPD results will then be compared with observables calculated for the conventional and reconstructed surface structures.

Stability of the system:

Under UHV conditions (in the absence of CO), the elemental arrangement on the surface of PdZn/Pd(111) was determined to be alternating rows of Pd and Zn atoms [202, 215] (see Fig. 3-43 and Fig. 3-44, left side) and was even visualized [200]. In the following this is referred as “row” structure. The modified elemental arrangement on the surface was modeled by “zigzag” structure (see Fig. 3-43 and Fig. 3-44, right side), which is constructed from the row structure by shifting laterally one row of 2 Pd and 2 Zn atoms along itself for 275 pm, that is experimental Pd-Pd distance or $\frac{1}{4}$ of the respective supercell dimension. This model may not match exactly the actual elemental arrangement, which may have an intractably big periodically repeated cell or even be aperiodic. In this thesis no other plausible arrangements are considered for two main reasons. First, in the absence of experimental input (i.e., supercell

size) it is impossible to reliably predict the exact arrangement of atoms by periodic DFT methods. Second (unlike the conventional row structure), the present model is sufficient to reconcile results of PM-IRAS and TPD experiments with those obtained by DFT.

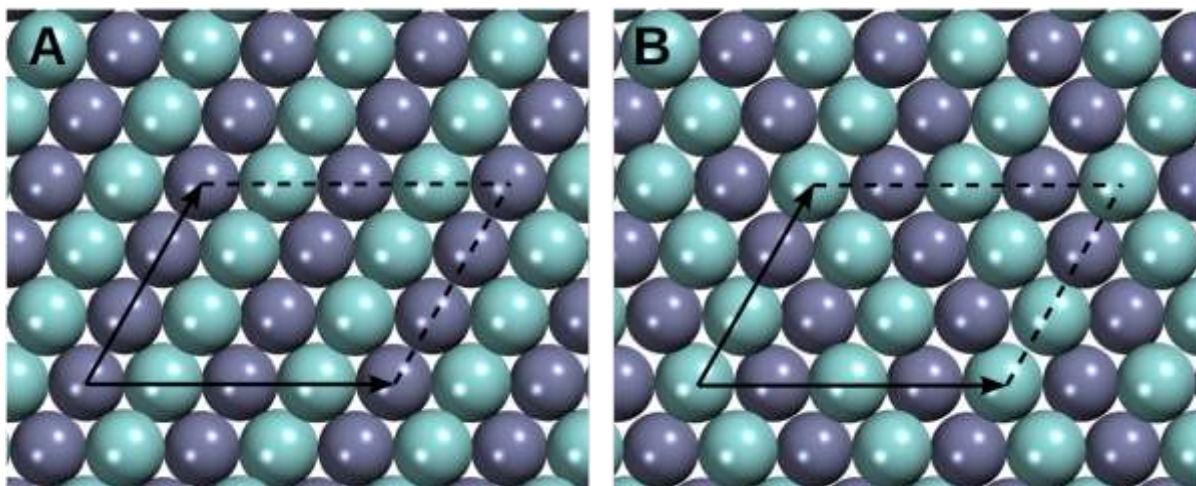


Fig. 3-43: PdZn surface alloy on Pd(111) with row structure and reconstructed zigzag structure. Pd atoms are displayed in cyan, Zn atoms are displayed in grey [134].

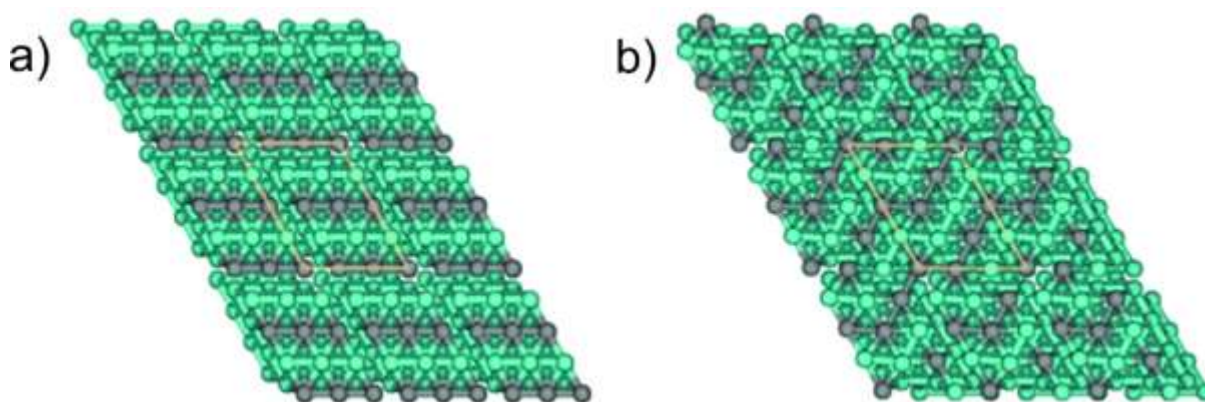


Fig. 3-44: 3D model of PdZn surface alloy on Pd(111) with row structure (left) and reconstructed zigzag structure (right). Pd atoms are displayed in cyan, Zn atoms are displayed in grey [239].

Fig. 3-45 shows the relative stability of the PdZn/Pd(111) surface alloys of various thicknesses in the absence and in the presence of CO adsorbed on the most stable adsorption sites, which have one or more layers arranged in zigzags, with respect to the alloy of the same thickness but structured in rows.

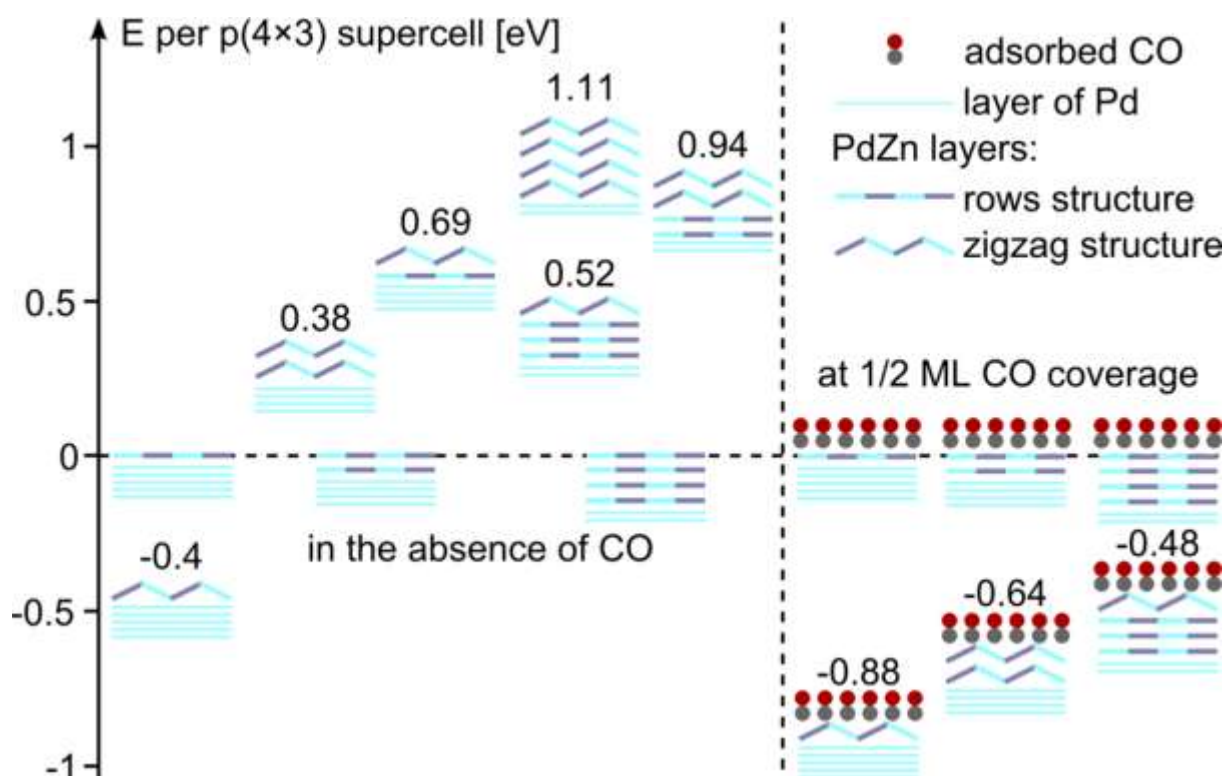


Fig. 3-45: Relative stability (eV) of reconstructed zigzag structure of PdZn/Pd(111) with respect to row structure depending on number of layers arranged in zigzag fashion and CO coverage. Values are calculated for p(4×3) supercell that has 12 atoms in each layer [134].

Obviously, in the absence of adsorbates, a monolayer PdZn surface alloy is by 0.4 eV per p(4×3) supercell more stable with the zigzag structure. For multilayer surface alloys the row structure is the most stable one. A 1 ML PdZn surface alloy needs to be prepared by evaporating 0.5 ML Zn on Pd(111). The annealing process may also lead to 2 ML PdZn patches instead of a complete 1 ML PdZn surface [39]. Due to these experimental limitations, the structure of a 1 ML PdZn/Pd(111) surface will not be further discussed in this work.

The second most stable structure with adsorbed CO is that with two top layers arranged in zigzags in the case of bilayer alloy, and only one zigzag layer in the case of four-layer alloy. The adsorption of CO at a surface coverage of 1/2 ML (one CO molecule per Pd atom on the surface), which has been experimentally observed (see Fig. 3-32 and Fig. 3-33), stabilizes zigzag structures of multilayer alloys by ~1 eV, turning them into the most stable configuration. The relative stability of monolayer PdZn surface alloy with zigzag structure is further increased by ~0.5 eV.

As already mentioned, the suggested zigzag structure is only a model for the most thermodynamically stable elemental arrangement and thus, the relative energy of the actual arrangement should be even lower than that calculated for zigzag structure [134].

Geometric structure of the system:

Structural parameters of PdZn arranged in zigzags are significantly different from those of PdZn with row structure (see Fig. 3-47). The interatomic distances in the alloy with row structure are within 273-278 pm in the absence of CO and in the range of 274-283 pm at a coverage of $\theta(\text{CO}) = \frac{1}{2}$ ML. The longest distances are calculated between Pd and Zn atoms, while interatomic Pd-Pd and Zn-Zn distance stay close to 275 pm, the value for Pd(111). The slight elongation of the average bond length at high CO coverage accompanied with negligible lateral displacements is due to substantial increase of surface corrugation. The latter is measured as average difference between vertical coordinates of Pd and Zn atoms located on the surface, $\langle z(\text{Pd}) \rangle - \langle z(\text{Zn}) \rangle$. In line with previous DFT and LEIS studies [200, 203, 205, 208], in this work, surface corrugation of PdZn/Pd(111) is calculated to be 15, -28, and -19 pm for monolayer, bilayer, and multilayer surface alloys, respectively. As could be expected, CO molecules upon adsorption pull out Pd atoms with the strongest effect at high CO coverage. In the case of 4 layers PdZn surface alloy adsorption of CO at $\theta(\text{CO}) = \frac{1}{2}$ ML (CO molecules occupy every surface Pd atom) inverts the surface corrugation, that is, Pd atoms become located above Zn atoms like in monolayer PdZn surface alloy. Corrugation increases to 58, 49, and 46 pm on one-, two-, and four-layer-thick alloys, respectively, and becomes of Pd-out/Zn-in type for any alloy thickness [134].

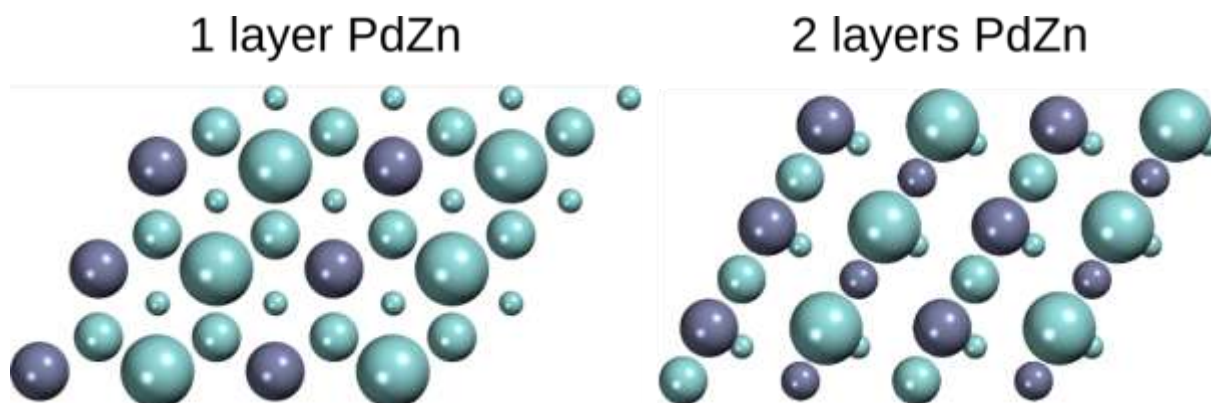


Fig. 3-46: Stacking of layers for PdZn surface alloys with 1 and 2 layer thickness. Pd atoms are displayed as cyan balls, Zn atoms as violet balls. Big balls represent atoms of the first layer, middle sized balls represent atoms of the second layer, small balls – third layer [239].

The distribution of bond lengths is much wider in PdZn surface alloys with the zigzag structure. The lateral reconstruction makes possible elongation of Pd-Pd (284-300 pm) and Zn-Zn (281-297 pm) distances and simultaneous contraction of the majority of Pd-Zn bonds (262-282 pm). These changes in bond lengths, not possible in the highly symmetric row

structure, are in line with elongation of Pd-Pd and Zn-Zn bonds (289 pm) and contraction of Pd-Zn bonds (264 pm) measured in PdZn bulk [240] in comparison with interatomic distance in Pd bulk (275 pm). Adsorption of mutually repulsing *CO* molecules at high coverage drives Pd atoms apart from each other and results in increased Pd-Pd distances of 290-315 pm. This in turn increases distances between adjacent Zn atoms (280-308 pm) and contracts or expands Pd-Zn bonds (259-290 pm). In the absence of *CO*, the corrugation of PdZn with zigzag structure is not much different from corrugation of respective alloys arranged in rows, with deviations up to 7 pm. However, the corrugation of PdZn with zigzag structure in the presence of *CO* is ~40 pm for monolayer and ~25 pm for multilayer alloy. As in the case of PdZn/Pd(111) arranged in rows, Pd-out/Zn-in type corrugation takes place in all cases, but the amplitude of corrugation is ~20 pm smaller in the case of laterally reconstructed surface [134].

Tab. 3-2: Structural properties of PdZn surface alloy configurations in the absence of *CO*. Vertical atomic displacements, Δz , separations between *i*-th and *j*-th layers calculated for atoms of type *X*, $d_{ij}(X)$, as well as minimum and maximum bond distances, *r*, are given in pm. Indexes after atom types denote surface layers, where these atoms are located [134].

	R1	Z1	R2	Z2	R4	Z4
corrugation	15	16	-28	-23	-19	-12
$\Delta z(\text{Pd}1)$	2	4	-30	-20	-46	-38
$\Delta z(\text{Zn}1)$	-13	-13	-2	3	-27	-26
$\Delta z(\text{Pd}2)$	4	4	10	10	-21	-24
$\Delta z(\text{Zn}2)$	--	--	-18	-16	-31	-28
$d_{12}(\text{Pd})$	234	236	197	207	211	222
$d_{12}(\text{Zn})$	--	--	254	256	240	239
$d_{23}(\text{Pd})$	238	238	242	242	236	232
$d_{23}(\text{Zn})$	--	--	--	--	214	219
$r(\text{Pd}1\text{-Pd}1)$	275	284-293	275	283-300	275	281-295
$r(\text{Pd}1\text{-Zn}1)$	275	262-280	275-278	260-280	273-278	263-282
$r(\text{Zn}1\text{-Zn}1)$	275	281-290	275	284-297	275	278-296
$r(\text{Pd}1\text{-Pd}2)$	283	278-293	304-314	278-313	292-346	281-341
$r(\text{Pd}1\text{-Zn}2)$	--	--	264	261-277	263-264	261-286
$r(\text{Zn}1\text{-Pd}2)$	270-271	266-278	264	263-269	271	273-290

Tab. 3-3: Structural properties of PdZn surface alloy configurations at high CO coverage $\theta(\text{CO}) = 0.5 \text{ ML}$. Vertical atomic displacements, Δz , separations between i-th and j-th layers calculated for atoms of type X, $d_{ij}(\text{X})$, as well as minimum and maximum bond distances, r, are given in pm. Indexes after atom types denote surface layers, where these atoms are located. The most stable adsorption modes of CO, i.e. bridge sites for rows and on-top sites for zigzags, were considered [134].

	R1	Z1	R2	Z2	R4	Z4
corrugation	58	38	49	23	46	24
$\Delta z(\text{Pd1})$	30	15	22	4	-1	-17
$\Delta z(\text{Zn1})$	-28	-23	-26	-19	-48	-41
$\Delta z(\text{Pd2})$	2	3	3	8	-26	-22
$\Delta z(\text{Zn2})$	--	--	-14	-14	-22	-26
$d_{12}(\text{Pd})$	261	247	256	233	261	241
$d_{12}(\text{Zn})$	--	--	224	232	211	221
$d_{23}(\text{Pd})$	239	238	235	240	228	233
$d_{23}(\text{Zn})$	--	--	--	--	241	243
$r(\text{Pd1-Pd1})$	275	291-303	274-276	292-315	274-275	290-303
$r(\text{Pd1-Zn1})$	281	260-290	275-283	259-286	276-281	259-286
$r(\text{Zn1-Zn1})$	275	280-296	274-277	286-308	275	279-305
$r(\text{Pd1-Pd2})$	301-311	286-313	303-310	289-303	311-312	286-298
$r(\text{Pd1-Zn2})$	--	--	306-318	279-316	299	278-300
$r(\text{Zn1-Pd2})$	259-261	258-273	255-262	257-259	263-264	258-277

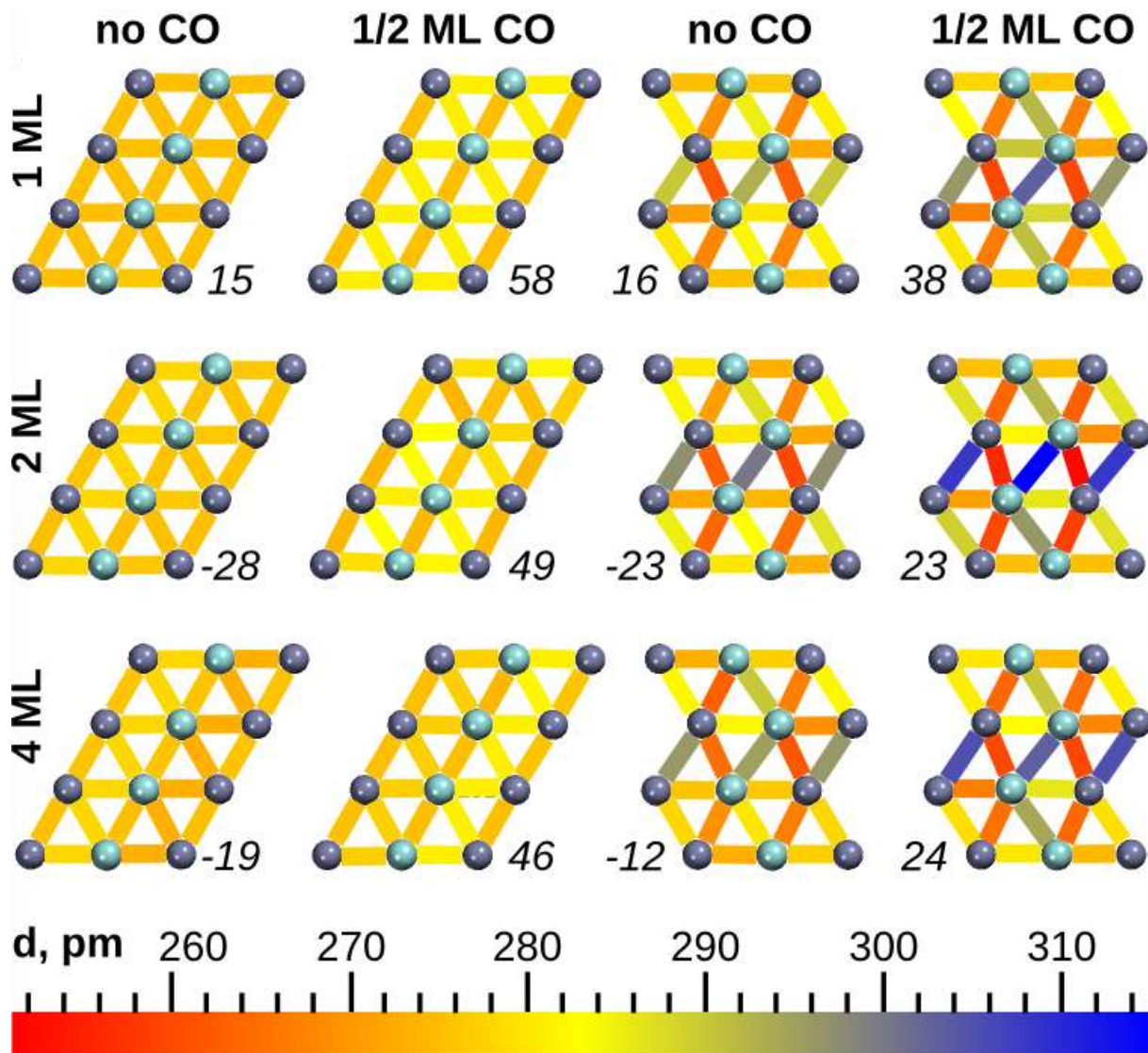


Fig. 3-47: Color coded interatomic distances between atoms on the surface of 1, 2, and 4 layer thick PdZn surface alloys on Pd(111) with row and zigzag structure, in the absence of CO and at $\theta(\text{CO})=1/2$ ML. Numbers in italic indicate surface corrugation in pm, positive values correspond to Pd-out/Zn-in type of corrugation [134].

Significant differences between interatomic distances on the surface and surface corrugation of the PdZn alloys arranged in rows and zigzags will affect adsorptive properties of the system. Here, this statement is exemplified by considering adsorption of *CO*, a ubiquitous probe molecule. However, one should note here that on metal surfaces *CO* usually adsorbs on top, bridge, or 3-fold hollow sites. These sites may be sensitive only to very short-range structural changes and largely insensitive to changes in second and farther coordination spheres of adjacent metal atoms. Also, the considered modification of component arrangement does not introduce new types of the mentioned sites, that is, 3-fold hollow sites made exclusively of Pd or Zn atoms. Thus, one can speculate that adsorption of bigger

molecules that interact with higher number of metal atoms on the surface will be much more strongly affected by structural changes induced by the rearrangement of components.

Electronic structure:

The electronic structure of PdZn/Pd(111) with zigzag arrangement is very similar to that of the alloy arranged in rows as shown in Fig. 3-48, although structural changes of the surface are significant. The DOS of the monolayer alloys is markedly different from that of the multilayer alloys, being closer to DOS of Pd(111).

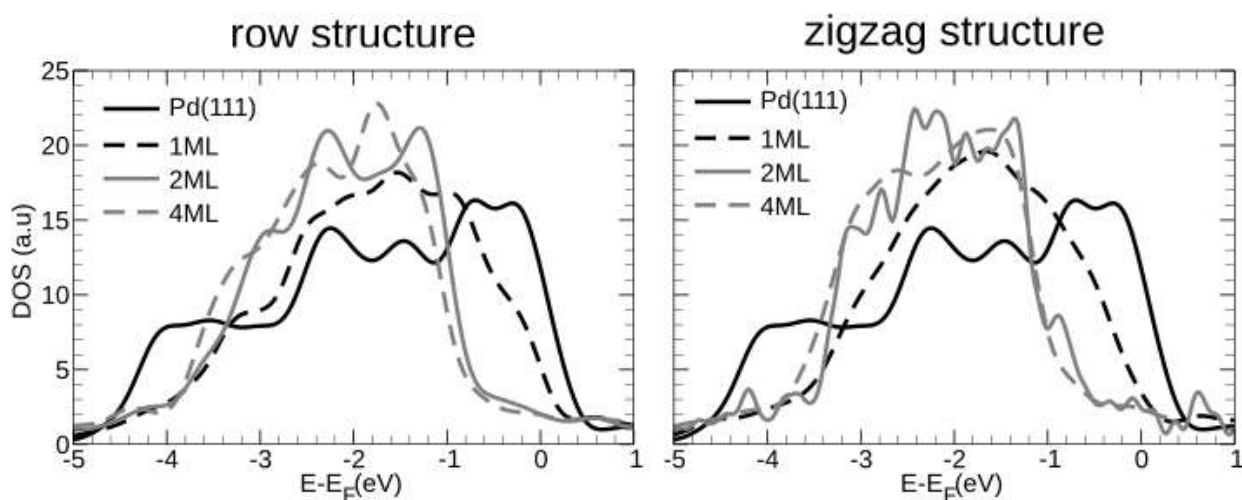


Fig. 3-48: Calculated DOS of 1, 2, and 4 layers thick PdZn surface alloys on Pd(111) in the absence of CO projected on Pd atoms located on the surface [134].

Calculated Bader charges [241] reveal that, irrespective of the elemental arrangement, the PdZn surface alloys on Pd(111) have peculiar intermetallic nature in agreement with results calculated for bulk ($\text{Pd}^{-0.4}\text{Zn}^{+0.4}$) [240]. That is, charges of (+0.34) - (+0.43) (herein charges are given in electron units) are induced on the majority of Zn atoms; atoms on the interface of multilayer PdZn and Pd(111) bear charges of (+0.46) - (+0.5). In turn, the charges on most Pd atoms are (-0.4) - (-0.37), and on those located on the interface with Pd substrate, (-0.29) - (-0.21). Thus, calculated charges on Pd atoms located on the surface of monolayer PdZn/Pd(111) are almost 2 times smaller in magnitude than those located on the multilayer alloys, which is again in line with their different catalytic properties [206]. The difference between electronic properties of surface Pd atoms in monolayer and in multilayer alloys may be rationalized by different numbers of adjacent Zn atoms (4 and 6, respectively). The fewer number of Zn neighbors and higher number of Pd neighbors renders Pd atoms in the monolayer PdZn/Pd with DOS and Bader charges closer to those of pristine Pd(111). This

explains the phenomenon of subsurface controlled selectivity, that is, reported dependency of PdZn/ Pd(111) catalyst properties on the surface alloy thickness [134].

PM-IRAS studies:

As already mentioned, the modification of elemental arrangement also changes the relative stability of the available adsorption sites. Because *CO* does not adsorb on Zn atoms (at least for temperatures ≥ 200 K) [205, 206, 213], there are only two types of adsorption sites available on the surface: on top of Pd atoms and on Pd–Pd bridge sites. In general, three conclusions can be drawn from calculated adsorption energies of *CO* on PdZn/Pd(111) summarized in Tab. 3-4:

- On the >4 ML surface alloy, *CO* adsorbs by 0.2 - 0.4 eV more weakly than on the monolayer alloy, illustrating the importance of subsurface layers composition on properties of PdZn catalysts.
- The adsorption energies of *CO* on top and on bridge sites are different by up to 0.14 eV at low *CO* coverage and by up to 0.23 eV at high coverage.
- Theoretical data show that on monolayer and bilayer PdZn arranged in rows, *CO* adsorption on bridge sites is preferred, whereas on PdZn arranged in zigzags, on-top sites are clearly preferred at high *CO* coverage.

On the alloy arranged in rows, bridge sites are more stable than on-top sites by 0.11 - 0.16 eV for monolayer and bilayer structures but only by 0.02 - 0.07 eV for a four-layer-thick alloy. On the contrary, on the reconstructed alloys with zigzag structure, on-top sites are significantly more stable than bridge sites by ~ 0.2 eV at high *CO* coverage. At the low coverage of 1/12 ML the adsorption sites have essentially the same stability. Also, on the bilayer alloys with zigzag structure, bridge sites are not stable at all, because the energy difference between adjacent top and bridge sites is sufficient to overcome the diffusion barrier between them. One can also note that at high *CO* coverage the adsorption is always stronger on the reconstructed surface [134].

Tab. 3-4: Adsorption Energies and Vibrational Frequencies of the *CO* Stretching Mode for *CO* Adsorbed on PdZn Surface Alloys of Various Thickness and Structure on Pd(111) at $\theta(\text{CO}) = 1/12$ and $1/2$ ML. ^a Bridge sites are not stable for these structures; *CO* moves from bridge to top sites during geometry optimization [134].

	top		bridge	
	$1/12$ ML	$1/2$ ML	$1/12$ ML	$1/2$ ML
	<i>Rows, 1 ML PdZn</i>			
Adsorption energies [eV]	1.11	0.71	1.25	0.87
Vibrational frequencies [cm^{-1}]	2035	2083	1893	1995
	<i>Rows, 2 ML PdZn</i>			
Adsorption energies [eV]	0.81	0.36	0.95	0.47
Vibrational frequencies [cm^{-1}]	2027	2068	1884	1970
	<i>Rows, 4 ML PdZn</i>			
Adsorption energies [eV]	0.81	0.48	0.88	0.5
Vibrational frequencies [cm^{-1}]	2024	2059	1894	1971
	<i>Zigzags, 1 ML PdZn</i>			
Adsorption energies [eV]	1.11	0.95	1.13	0.73
Vibrational frequencies [cm^{-1}]	2035	2072	1883	1966
	<i>Zigzags, 2 ML PdZn</i>			
Adsorption energies [eV]	0.94	0.64	a	a
Vibrational frequencies [cm^{-1}]	2031	2066	a	a
	<i>Zigzags, 4 ML PdZn</i>			
Adsorption energies [eV]	0.91	0.67	0.89	0.44
Vibrational frequencies [cm^{-1}]	2034	2067	1889	1967

Preference of bridge sites for *CO* adsorption on unreconstructed surface can be understood in analogy with *CO* adsorption on pristine Pd(111). Indeed, at low coverage *CO* is known to adsorb on 3-fold hollow sites on Pd(111) [242] and shows a clear preference for sites with higher coordination by Pd atoms [243]. On the defect-free PdZn surface alloys, 3-fold hollow sites entirely made of Pd atoms are not present; thus the sites with the highest possible coordination are Pd-Pd bridge sites, and *CO* prefers to adsorb on them. At high coverage a

similar reasoning would apply to *CO* adsorption on the alloy with row structure, because in this case distance between *CO* molecules does not depend on the type of occupied adsorption sites. However, on the reconstructed zigzag alloy the distance between coadsorbates at high coverage depends on where they adsorb, being 317-327 pm for on-top sites and only 279-294 pm for bridge sites on a four-layer-thick alloy. Thus, it is not surprising that on-top sites are most stable in this case at high coverage, allowing reduction of the lateral repulsion between *CO* adsorbates, while at low coverage the stability of the sites is similar [134].

The adsorption energies of *CO* on top and on bridge sites are different by less than 0.15 eV at low *CO* coverage. On PdZn arranged in rows, bridge site is slightly preferred (by more than 0.1 eV for monolayer and bilayer PdZn surface alloys) and on PdZn arranged in zigzags bridge sites and top sites are close in energy at low *CO* coverage. However bridge site is more destabilized than top site at high *CO* coverage, due to smaller distance between some of the coadsorbates (see Fig. 3-49 and Fig. 3-50).

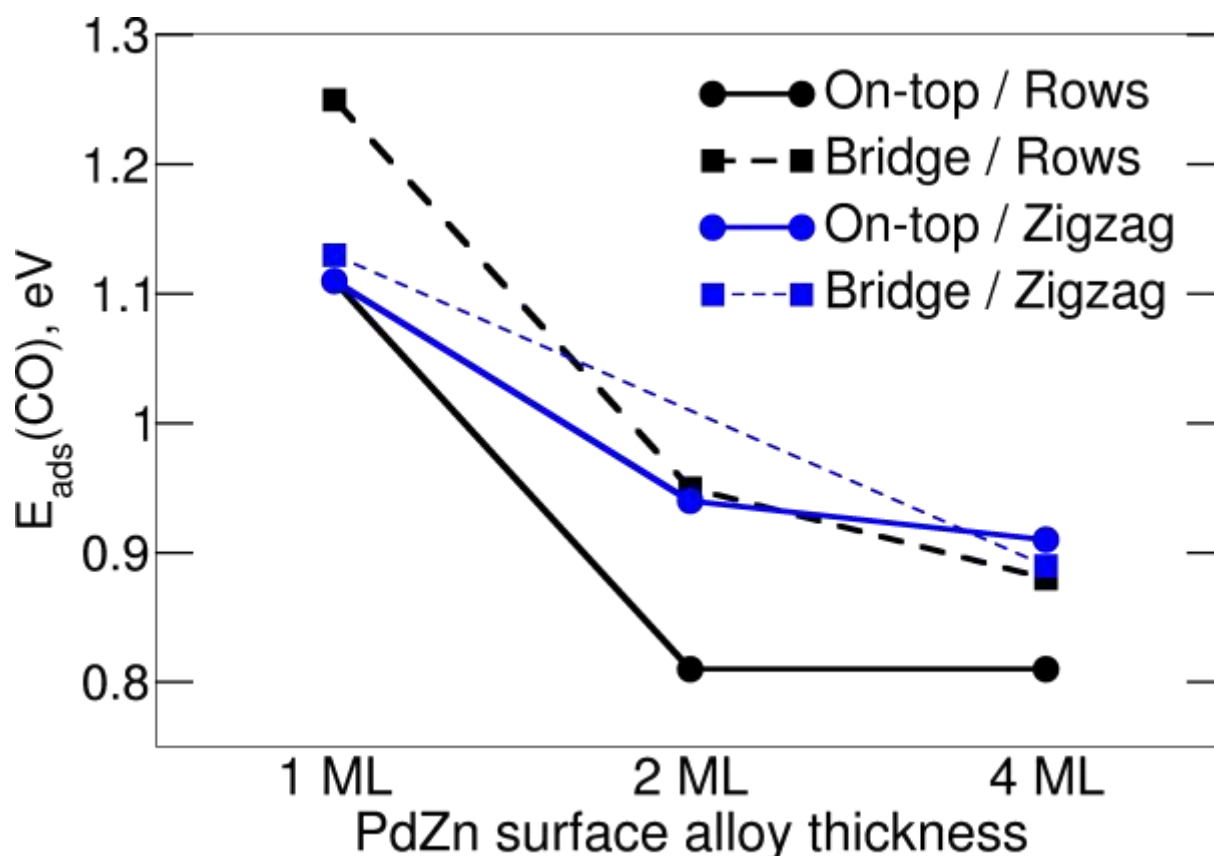


Fig. 3-49: Adsorption energies of *CO* on surface alloys with various structure at coverage of 1/12 [239].

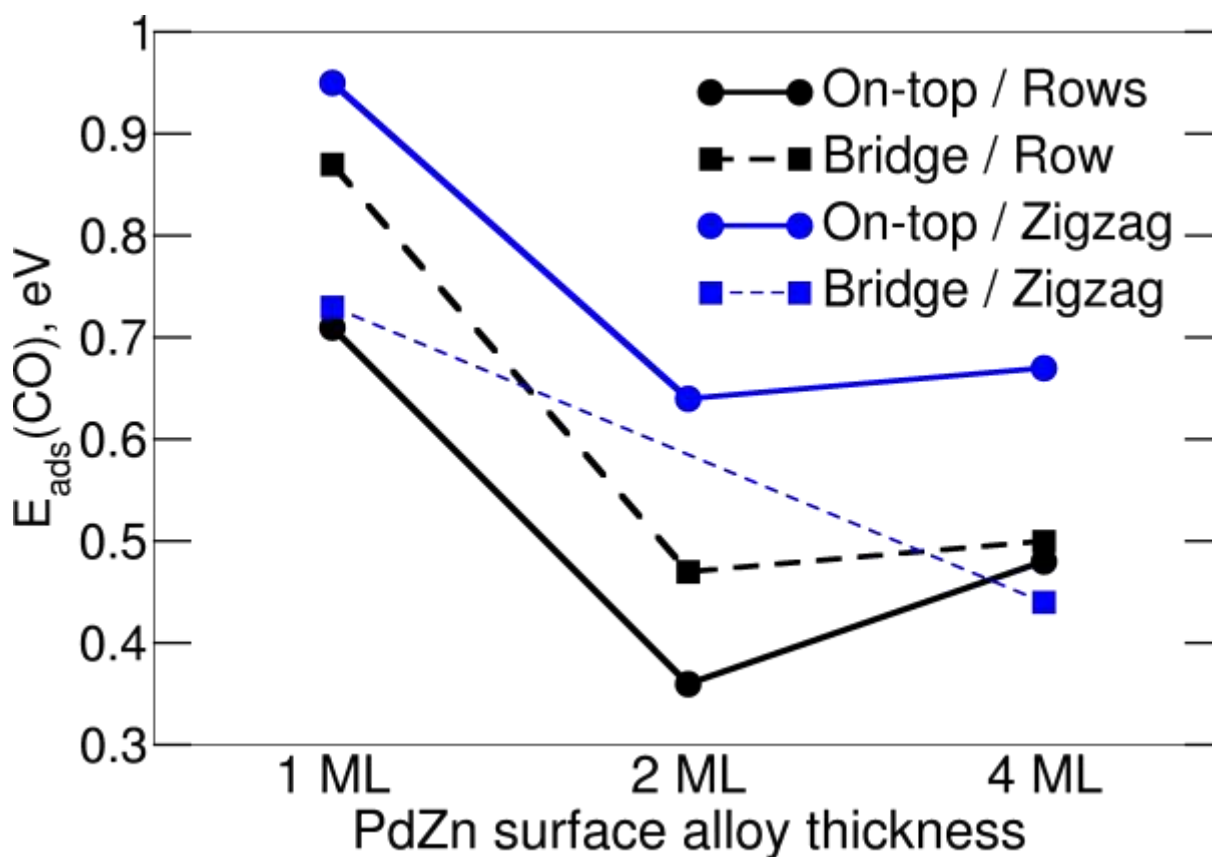


Fig. 3-50: Adsorption energies of *CO* on surface alloys with various structure at coverage $\frac{1}{2}$ [239].

By use of PM-IRAS, it could be shown [205, 206, 213] that on well-defined PdZn/Pd(111) surface alloys exclusively on-top sites were occupied by adsorbed *CO* molecules, irrespective of alloy thickness (2-6 PdZn layers). PdZn surface alloys could be characterized by a sharp, characteristic band at $\approx 2070 \text{ cm}^{-1}$ (on-top *CO*) in IR experiments performed in a *CO* atmosphere, that is, at high *CO* coverage. Similar spectra are obtained on oxide-supported PdZn nanoparticles [166, 244]. Only upon annealing of such alloys to temperatures above 623 K were multiple bound *CO* species observed by PM-IRAS. At this temperature partial alloy decomposition starts. DFT-calculated stretching frequencies of *CO* on top of Pd atoms are $2024\text{-}2035 \text{ cm}^{-1}$ at $\theta(\text{CO}) = 1/12 \text{ ML}$ and $2059\text{-}2083 \text{ cm}^{-1}$ at $\theta(\text{CO}) = 1/2 \text{ ML}$ (as shown in Tab. 3-4) and support the assignment of experimentally observed $\approx 2070 \text{ cm}^{-1}$ peak. In contrast, *CO* adsorbed on bridge sites was calculated to vibrate with frequencies of $1883\text{-}1894 \text{ cm}^{-1}$ at low coverage and $1966\text{-}1995 \text{ cm}^{-1}$ at high *CO* coverage and was experimentally observed only at high temperatures, when decomposition of the alloy took place. Notably, calculated *CO* stretching frequencies do not significantly depend on the alloy thickness. Taking into account that some bridge-adsorbed species should be observed on the unreconstructed surface - because of their calculated higher stability, one can conclude that PM-IRAS studies provide evidence for the suggested surface reconstruction.

In chapter 3.5.1 coverage dependent IR spectra were presented (Fig. 3-29, *CO* on 4 ML PdZn). At low dosage a broad band at 2048 cm^{-1} and a sharper, less intense band at 2068 cm^{-1} could be observed. Increasing the dosage leads to an increase in the intensity of the band at 2068 cm^{-1} , whereas the band at 2048 cm^{-1} decreases and is finally vanished after a dosage of 10 L *CO*.

As already mentioned in chapter 3.5.1, the appearance of two IR bands corresponds to two different *CO* species on the surface. The band at 2048 cm^{-1} can be assigned to “isolated” *CO* (low coverage) and the band at 2068 cm^{-1} can be assigned to “neighboring” *CO* (higher coverage).

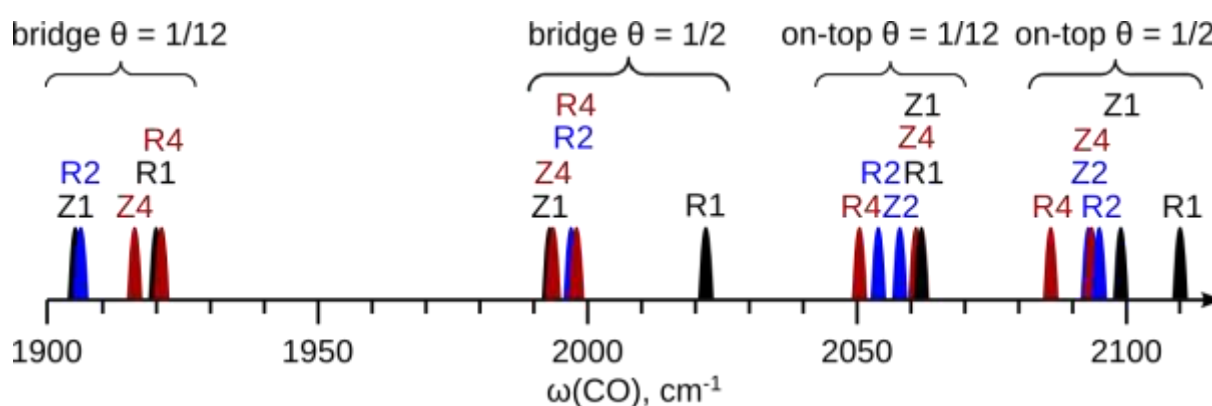


Fig. 3-51: Shifted harmonic frequencies of *CO* molecules adsorbed on PdZn/Pd(111) surface alloys of various structure. The surface alloy of *N* layers arranged in rows (zigzags) is denoted as RN (ZN) [239].

The position of the IR-Bands from experiment are in good agreement with calculated frequencies of *CO* adsorbed on the 4 ML alloy with zigzag structure (2034 and 2067 cm^{-1} , respectively, see Tab. 3-4 and Fig. 3-51). The calculated frequencies of *CO* adsorbed on top sites of the unreconstructed PdZn with 4 ML thickness (2024 and 2059 cm^{-1} , respectively) were somewhat further away from the experimental band positions. One can see, that the vibrational frequencies depend mostly on the nature of adsorption site (on-top or bridge) and then on the surface coverage. In most cases *CO* vibrational frequencies are not sensitive to surface alloy structure (except row structure for 1 ML alloy at high *CO* coverage). It should be noted that accuracy of the calculations is in the range of $\sim 10\text{ cm}^{-1}$.

Differential adsorption energies:

To model TPD spectra we have calculated differential adsorption energies (E_{diff}) of CO . These are energies required for only one CO molecule to desorb at a given coverage, $\theta = N/12$, where N is the number of molecules in the supercell, using the definition in (1.1.46):

$$E_{\text{diff}} \theta = E[CO_{N-1}/PdZn/Pd] + E[CO_{\text{gas}}] - E[CO_N/PdZn/Pd] \quad (1.1.46)$$

E_{diff} was calculated for CO adsorbed on the on top sites of the alloys with zigzag structure and both on top and bridge sites on the alloys with row structure at $\theta=1/2$ ML ($N = 6$), see Fig. 3-52. On non-reconstructed surfaces arranged in rows CO is highly stable only up to coverage of $\theta \leq 0.33$ ML, with a sharp decrease of stability at higher coverage. This makes full coverage of the surface Pd atoms by CO molecules strongly unfavorable at room temperature (and also at 100 K, the starting temperature for TPD) for the row structure. At the same time differential adsorption energies of CO on the reconstructed surface alloy are positive and higher than 0.34 eV even at $\theta(CO) = 1/2$ ML.

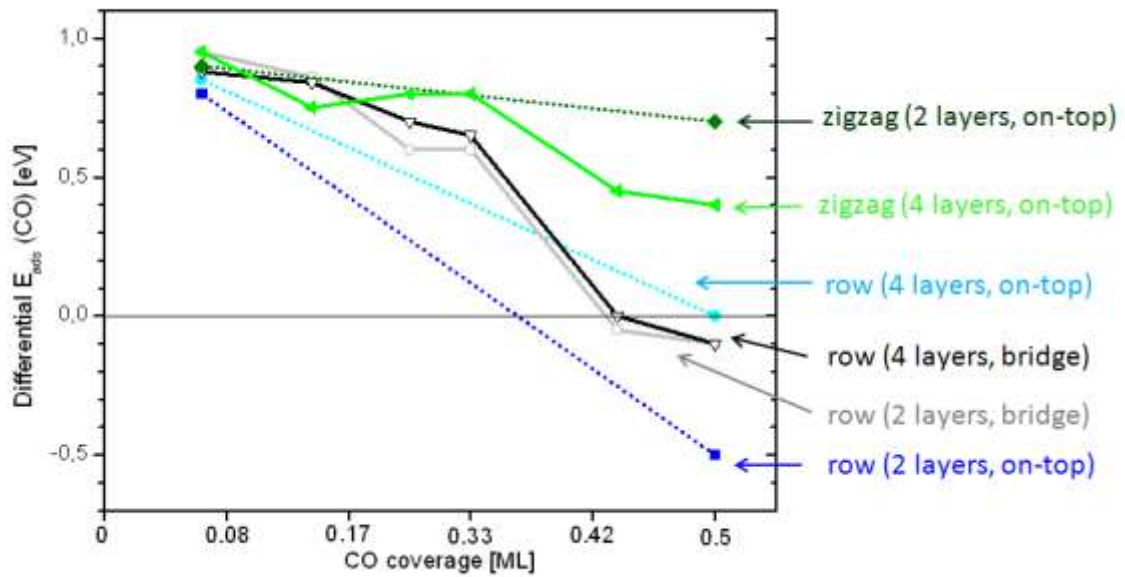


Fig. 3-52: Differential adsorption energy of CO molecule versus their coverage on $PdZn/Pd(111)$ surface alloys with different structure.

The saturation CO coverage on $PdZn/Pd(111)$ was experimentally investigated by TPD measurements as described in chapter 3.5.2. The TPD spectra are summarized in Fig. 3-30 and Fig. 3-31. The deduced coverage from these measurements is presented in Fig. 3-32 and

Fig. 3-33. Experimentally observed coverage of 0.50 ± 0.02 ML for a 2 ML alloy and 0.47 ± 0.02 ML for the 4 ML alloy, respectively are a strong indication for the presence of a reconstructed zigzag structure. Bearing in mind that the Pd:Zn ratio is 1:1 in a PdZn alloy surface layer, these values indicate that every surface Pd atom is occupied by a CO molecule. Along the Pd rows/zigzags the CO molecules are even more densely packed than in the (2×2) CO super structure on Pd(111), which could represent a possible driving force for rearrangement of the surface [134].

Desorption energies, estimated from TPD are in very good agreement with calculated values from CO adsorption energy for CO adsorption on the reconstructed surface. This may also be taken as a hint toward CO-induced surface reconstruction, although it should be emphasized that the experimental numbers change if another pre-exponential factor is chosen (see also 3.2.5).

Tab. 3-5: Estimated desorption energies for “ideal” PdZn/Pd(111) surfaces from TPD experiments compared to desorption energies calculated from DFT, see Tab. 3-4.

Surface alloy	Desorption temperature [K]	Desorption energy [eV]	Calculated desorption energy [eV]
2 ML PdZn/Pd(111)	212	0.66	0.64
>4 ML PdZn/Pd(111)	207	0.64	0.67

In addition, dosage dependent TPD spectra were performed (see Fig. 3-34 and Fig. 3-35 in chapter 3.5.2). Again, the desorption energy from these spectra were estimated using the temperature peak maximum by applying the Redhead equation. See Tab. 3-6 for a comparison between DFT values and values estimated from experiment.

Tab. 3-6: CO Desorption maxima and respective desorption energies for 2 and >4 ML PdZn surface alloys from TPD spectra in Fig. 3-34 and Fig. 3-35.

CO dose [L]	2 ML PdZn/Pd(111)		>4 ML PdZn/Pd(111)	
	T_{des} [K]	E_{TPD} [eV]	T_{des} [K]	E_{TPD} [eV]
0.5	295	0.92	256	0.80
1	285	0.89	236	0.74
2	185/227	0.58/0.70	194/231	0.60/0.72
5	183/226	0.57/0.70	193/218	0.60/0.68
sat.	183/224	0.57/0.69	180/213	0.56/0.67

The experimentally measured values of desorption energy from TPD obtained after low dose fit quite well the DFT numbers (see Tab. 3-4). However, because calculated CO adsorption energies on PdZn with row and zigzag structures are very similar at low coverage, it is not possible to differentiate the two structures on the basis of these experimental results. At higher CO dosage, the main peaks at 210-230 K seem to be reproduced well by average adsorption energy of CO on top sites of the respective alloys with zigzag structure (see Tab. 3-4). The adsorption energies derived from TPD experiments favor the modification of elemental arrangement in the surface layer [134].

STM simulation:

These simulations were done by Sergey Kozlov using the Tersoff-Hamann approach, which is a very good approximation to simulate the "perfect" STM tip and so to obtain STM images with unrealistically high resolution. The model of Tersoff and Hamann is widely used for interpretation of the STM images. Since the tip is modeled as locally spherical potential and the actual microscopic geometry of the tip might be quite different, the interpretation of the experimental results hampers to a larger extent by the insufficient knowledge of technical details of the measurements than by inadequacies of the theory [245].

For calculations in this chapter the *PAW method* (Projector augmented-wave method) was used to simulate core electrons, which is also one of the best methods available on the market⁸. This method generalizes both the pseudopotential method and the linear augmented-plane-wave method. The augmentation procedure is generalized by partial-wave expansions and not determined by the value and the derivative of the envelope function, but rather by the overlap with localized projector functions. [142, 246]. In variation, *FLAPW* (full-potential linearized augmented plane wave) [247] is a method to simulate properties of core electrons, which are not so important for STM images. The latter are sensitive only to very few valence states in the vicinity of the Fermi level and almost do not feel core electrons [248].

In Fig. 3-53 and Fig. 3-54 simulated STM images of monolayer thick film of ZnPd on Pd(111) with row and zigzag arrangements in the absence of any adsorbates are shown (using $V_t=371$ mV and high tunneling current; similar parameters were also used for some of the measurements). Due to the necessarily high computation time only a few calculation were

⁸ But, basically for STM images it does not really matter, which method to use.

done at this time. Pd atoms are bright in these conditions, while Zn atoms remain dark. The apparent corrugation of the row structure is 407 pm, while the corrugation of zigzag structure is 448 pm, significantly higher than that of the row structure. (Probably in experiments lower corrugations will be measured due to a lower tunneling current and maybe a lack of subatomic resolution).

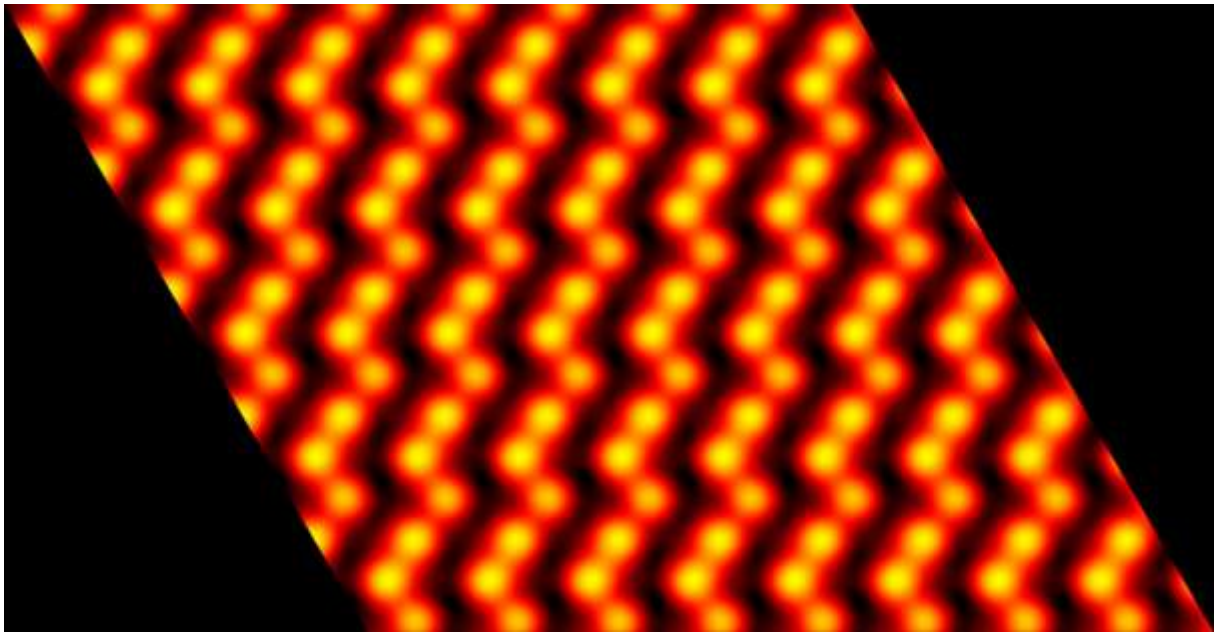


Fig. 3-53: Simulated STM image of the proposed zigzag structure correspond to a voltage of 371 mV and high tunneling current.

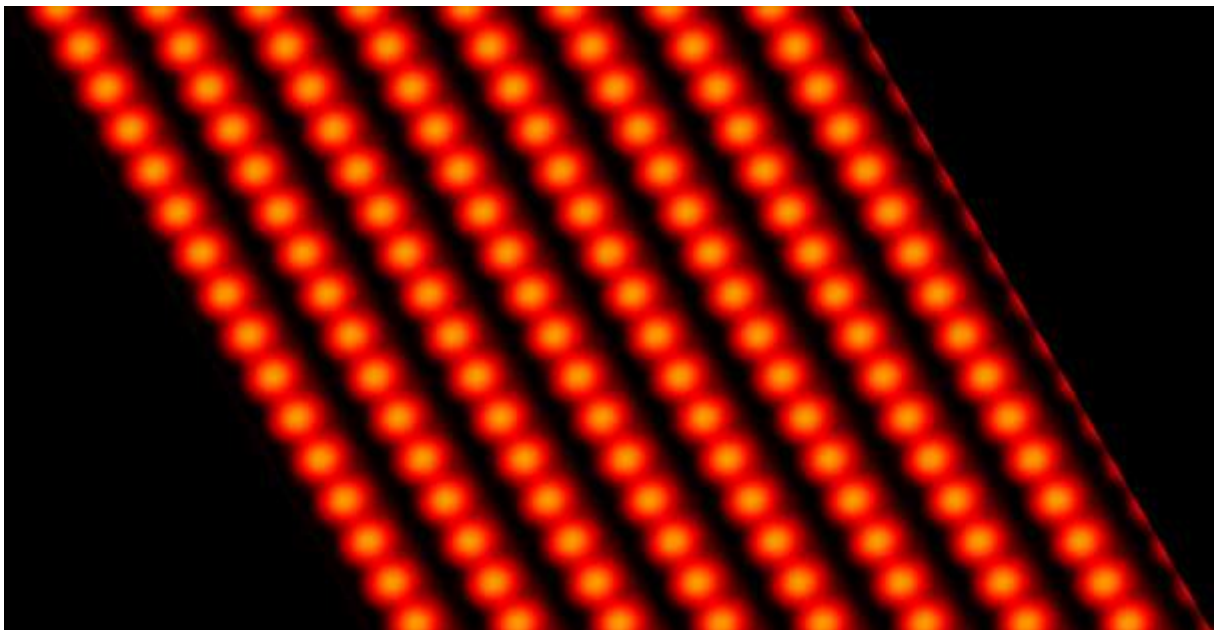


Fig. 3-54: Simulated STM image of the row structure correspond to a voltage of 371 mV and high tunneling current.

The geometric corrugations of row and zigzag structures are both ~ 15 pm only. The difference in the STM corrugations comes from electronic effects. Also, the reason for STM corrugations being much higher than geometric corrugations is the absence of almost any tunneling through Zn atoms, which renders them very dark [248, 249].

3.8 Methanol dehydrogenation on PdZn/Pd(111)

As PdZn alloys have been identified as promising catalysts for use in industrial methanol steam reforming applications (see chapter 1 and Tab. 1-1), the interaction of CH_3OH/D_2O with the PdZn/Pd(111) surface alloy model system has been investigated.

3.8.1 TPD measurements

Fig. 3-55 shows the TPD spectrum obtained after the dosage of 10 L methanol (considering a gas correction factor of 1.9 for the ion gauge) at 90 K on a clean PdZn/Pd(111) surface alloy prepared by deposition of 1 ML Zn at 300 K, followed by annealing for 5 Min at 573 K (=2 ML alloy). An exposure of 10 L is sufficient to cover the surface of the single crystal with a multilayer of methanol [36]. As for the TPD measurements before, 90 K per minute was used as heating rate. The desorption temperature of methanol (M32) from PdZn/Pd(111) was found to be 165 K (the M30 and M28 signals at this temperature are fragments of MS-ionization) and additionally two small “bumps” at ~360 K and ~480 K are visible. The latter were reproducible but their origin is unclear (tentatively attributed to recombinative MeOH desorption). Unfortunately, it was not possible to resolve multilayer and monolayer MeOH desorption. In contrast to the methanol desorption on Pd(111) (under the same conditions; see Fig. 3-9) no CO desorption could be observed. Obviously, methanol was significantly dehydrogenated to CO on Pd(111) whereas this pathway was apparently not available on PdZn. This is in agreement with the higher energy barriers for methanol dehydrogenation on PdZn surfaces, as calculated by Chen et al. [250]. For both surfaces desorption of formaldehyde (M30), being a likely intermediate during methanol decomposition, was not observed [30].

D₂O desorption (upon dosing D₂O alone) from PdZn/Pd(111) yielded one single TPD peak at 173 K (not shown), this is slightly higher than on Pd(111), where D₂O desorbs at 166 K (see Fig. 3-11). The stronger bonding of water on PdZn is in good accordance with DFT calculations for adsorption energies of water from Neyman et al. [209]

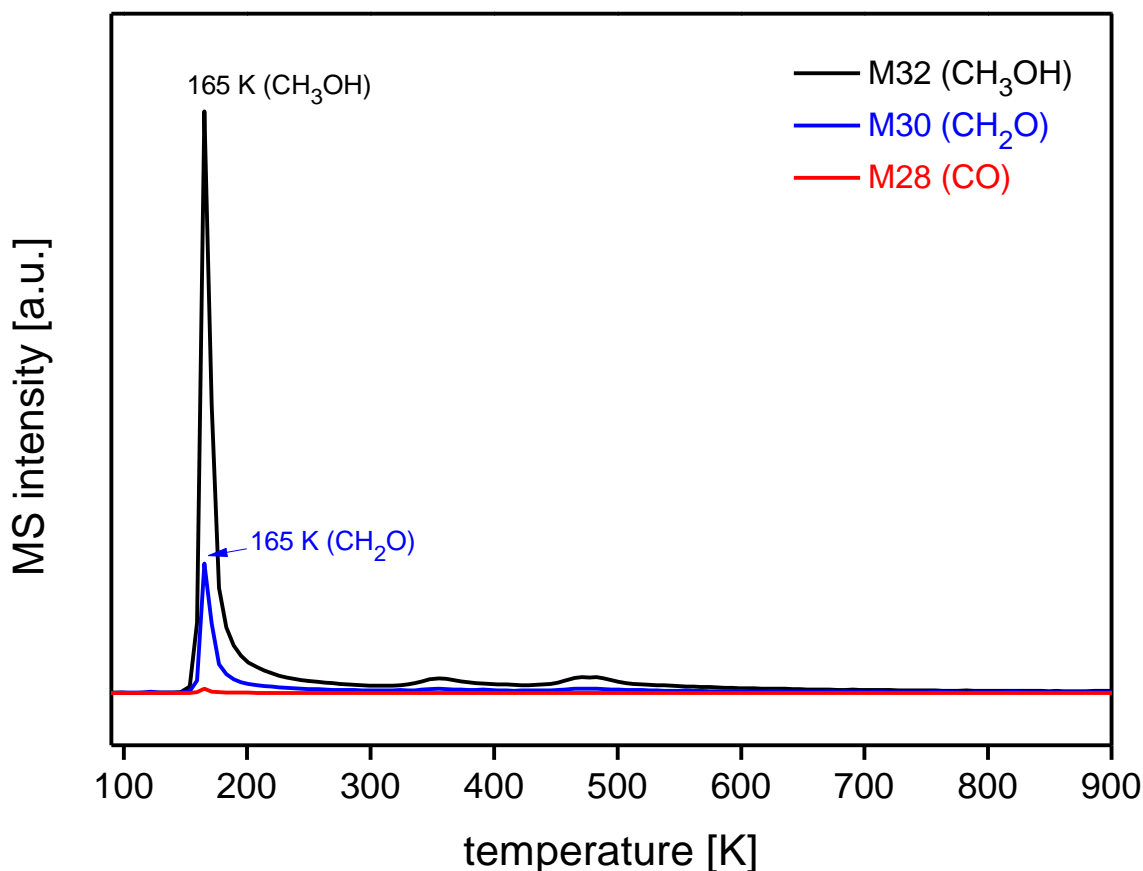


Fig. 3-55: TPD spectra for CO , CH_2O , CH_3OH after dosing of 10 ML methanol at 90 K on 2 ML PdZn/Pd(111) prior annealed to 573 K. Methanol desorbs at 165 K (the M30 and M28 signals at this temperature are fragments of MS-ionization) and additionally two small “bumps” at ~ 360 K and ~ 480 K of chemisorbed methanol are visible.

As already described in chapter 3.3 we have dosed a “mixture” of methanol (first) and D_2O (second) to mimic the process of methanol steam reforming [176-178]. The corresponding desorption features were about 10 K lower as compared to methanol dosage alone (see Fig. 3-56). No significant amounts of CO have been found for the decomposition of methanol on PdZn in agreement with our measurements with methanol only. Under the same conditions CO desorption was observed on Pd(111) (see Fig. 3-10 in chapter 3.3.1). One would expect a bigger effect of the co-dosage of D_2O than the small shift in desorption temperature for PdZn but D_2O desorbs already at 162 K. For a further reaction of intermediates/MeOH to CO_2 the water has to be activated/split on the surface as shown in reference [206]. The low temperatures are probably a reason why the water is yet not activated and so no further products were detected.

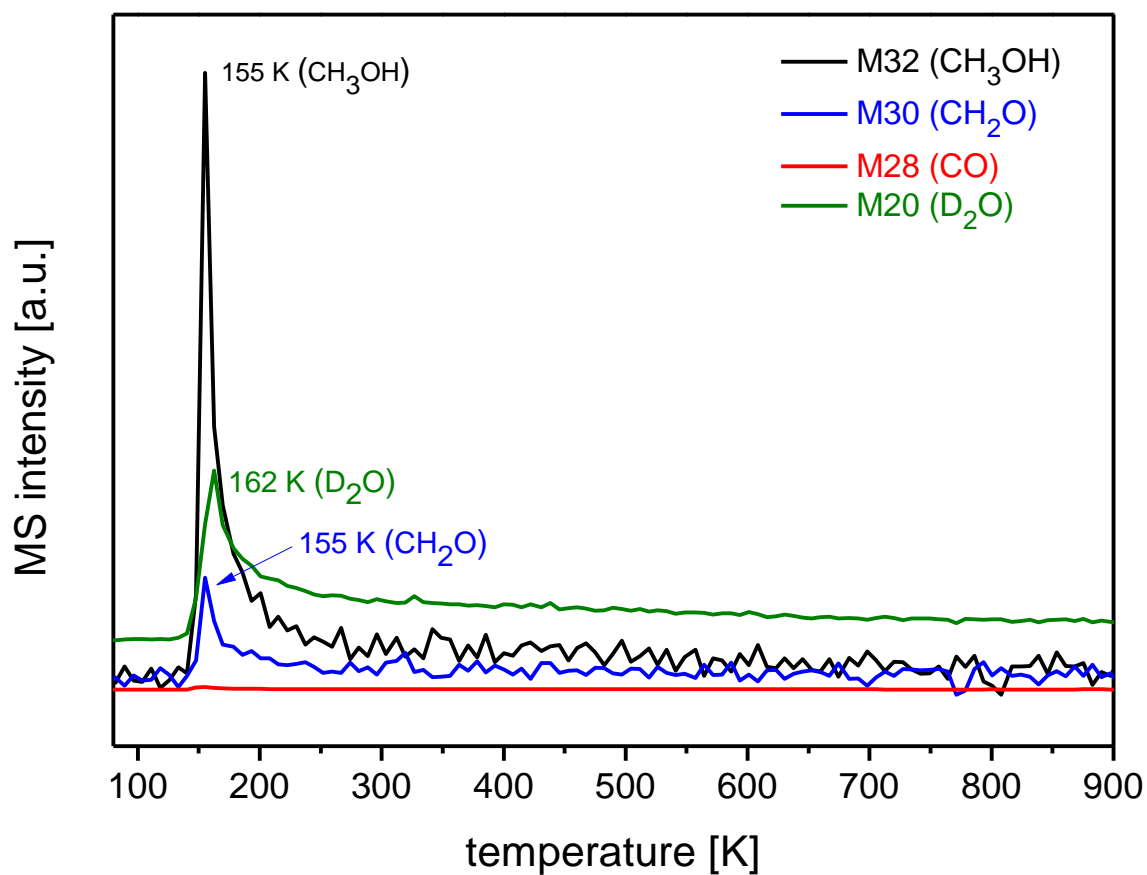


Fig. 3-56: TPD spectra for CO , CH_2O , CH_3OH , and D_2O after dosing of 10 ML methanol and D_2O at 90 K on 2 ML PdZn/Pd(111) prior annealed to 573 K. Methanol desorbs at about 10 K lower as compared to methanol dosage alone (Fig. 3-55).

3.8.2 PM-IRAS measurements

To further investigate the dehydrogenation mechanism and identify possible reaction intermediates, the decomposition of methanol was monitored in situ by PM-IRAS at a pressure of 5 mbar methanol at room temperature (~ 295 K).

Fig. 3-57 shows the PM-IRAS surface spectra and Fig. 3-58 shows the PM-IRAS gas phase spectra, obtained from Pd(111) and 2 ML PdZn/Pd(111) surface alloy. The spectra shown were acquired (in the reaction gas) after 2 hours of methanol exposure. In the surface spectrum (Fig. 3-57) of Pd(111) an IR band of CO adsorbed on 3-fold hollow sites was visible at ~ 1870 cm^{-1} , whereas the surface of the PdZn alloy was basically free from adsorbate species. On both surfaces, no intermediate species such as adsorbed formaldehyde or formyl could be detected by PM-IRAS.

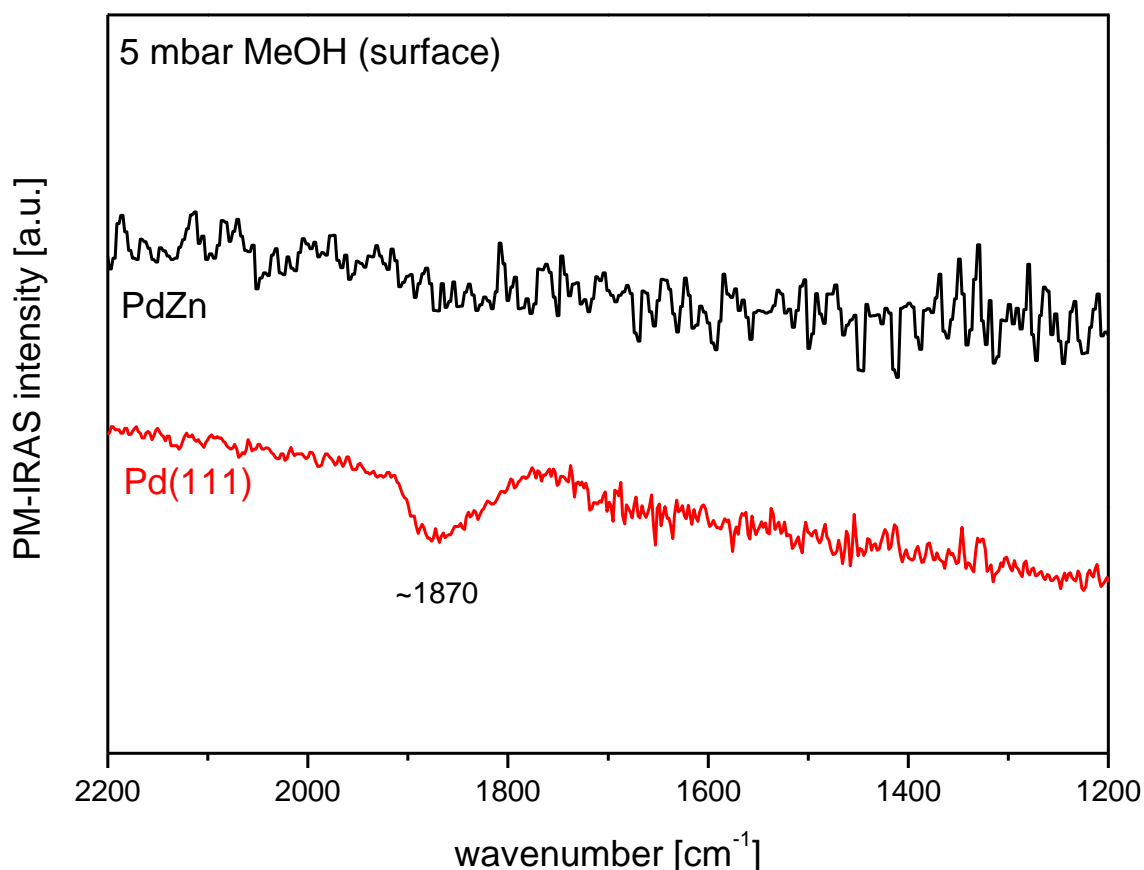


Fig. 3-57: PM-IRAS spectra (surface) during methanol decomposition on Pd(111) (red) and 2 ML PdZn/Pd(111) (black). Acquired after 2 hours in 5 mbar MeOH at room temperature. On Pd(111) an IR band at ~ 1870 cm^{-1} is clearly visible. This can be assigned to CO , adsorbed on 3-fold hollow sites.

The gas phase spectra (Fig. 3-58) show a strong band at 1033 cm^{-1} of methanol. No IR signals for the decomposition products CO (2143 cm^{-1}) or formaldehyde (1750 cm^{-1}), were observed, i.e. significant methanol decomposition does not take place on Pd(111) and PdZn/Pd(111) at this temperature. This agrees with previous PM-IRAS results reported for methanol dehydrogenation on Pd(111) [173]. The Pd(111) surface is basically poisoned by adsorbed CO at room temperature and therefore not active for further methanol decomposition. On PdZn, no detectable CO was produced from methanol. The absence of reaction products of methanol decomposition in the gas phase for the PdZn surface alloy may be explained by the low reaction temperature of $\sim 300\text{ K}$, which is too low to produce formaldehyde. This is in line with theory and XPS (see Fig. 3-63) indicating that full dehydrogenation of methanol to CO does not occur on the alloy surface (CO would be clearly visible in PM-IRAS under these conditions).

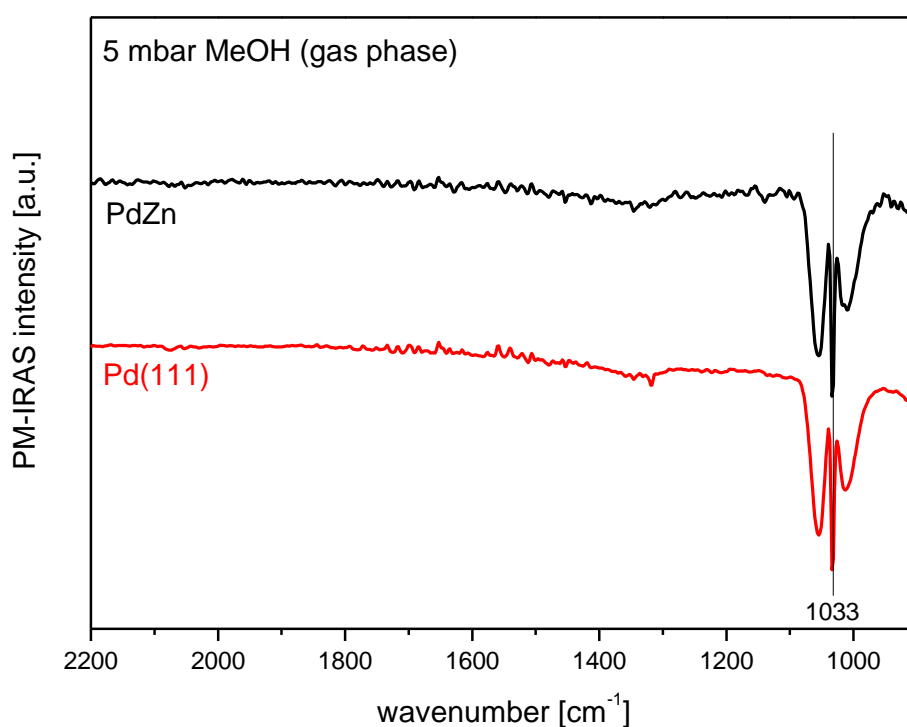


Fig. 3-58: PM-IRAS spectra of methanol (gas phase) during methanol decomposition on Pd(111) (red) and 2 ML PdZn/Pd(111) (black). Acquired after 2 hours in 5 mbar MeOH at room temperature. The strong band at 1033 cm^{-1} can be assigned to $\nu(\text{CO})$ of methanol.

Methanol decomposition performed on a 2 ML PdZn/Pd(111) alloy at different reaction temperatures is shown in Fig. 3-59. At 473 K and 523 K, no decomposition products could be detected in the gas phase. Increasing the temperature to 573 K and 623 K resulted in the

formation of CO , but no formaldehyde was detected. This is probably due the decomposition of CH_2O on PdZn. At these temperatures, multiple-bound CO was also detected in the PM-IRAS surface spectra (see Fig. 3-59), giving rise to a broad band in the range of 1870 cm^{-1} . When the reaction mixture is cooled from 623 K to room temperature, IR bands for on-top CO at 2071 cm^{-1} and multiple-bound CO at 1920 cm^{-1} were detected on the PdZn surface, this indicates a rearrangement of the surface at temperatures higher than 623 K [30].

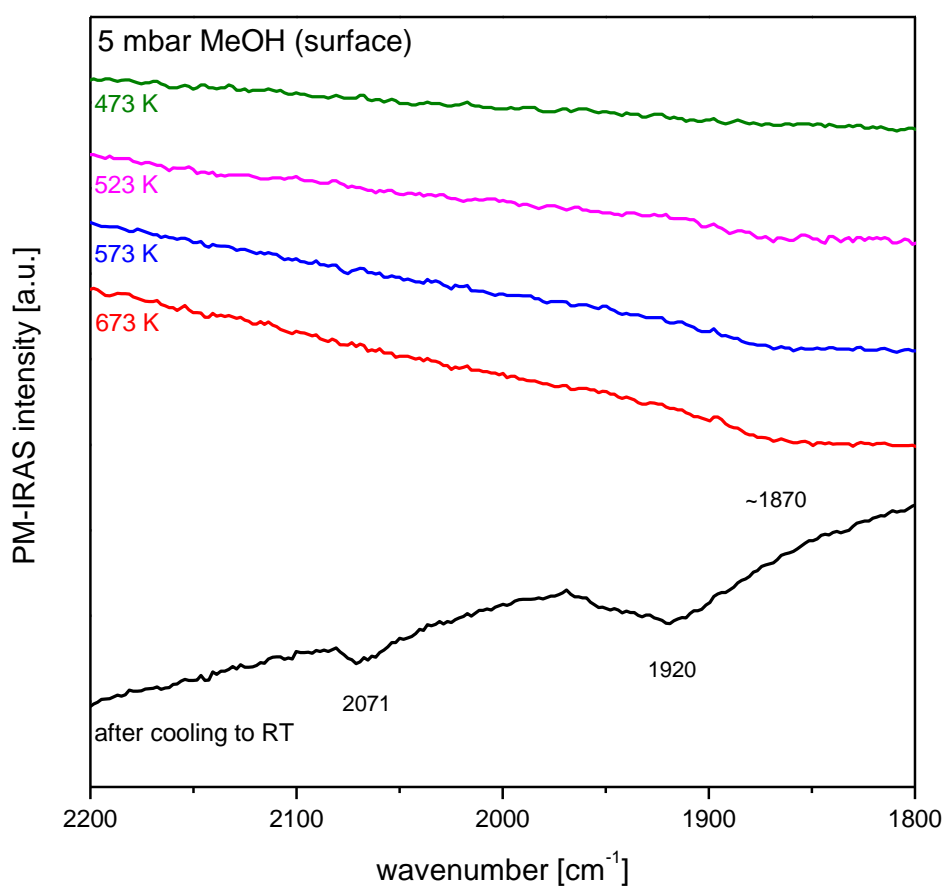


Fig. 3-59: PM-IRAS spectra (surface) acquired on 2 ML PdZn/Pd(111) in 5 mbar CH_3OH at different temperatures. The IR band at 2071 cm^{-1} indicates on-top CO . IR bands at 1920 and 1870 cm^{-1} can be assigned to multiple-bound CO .

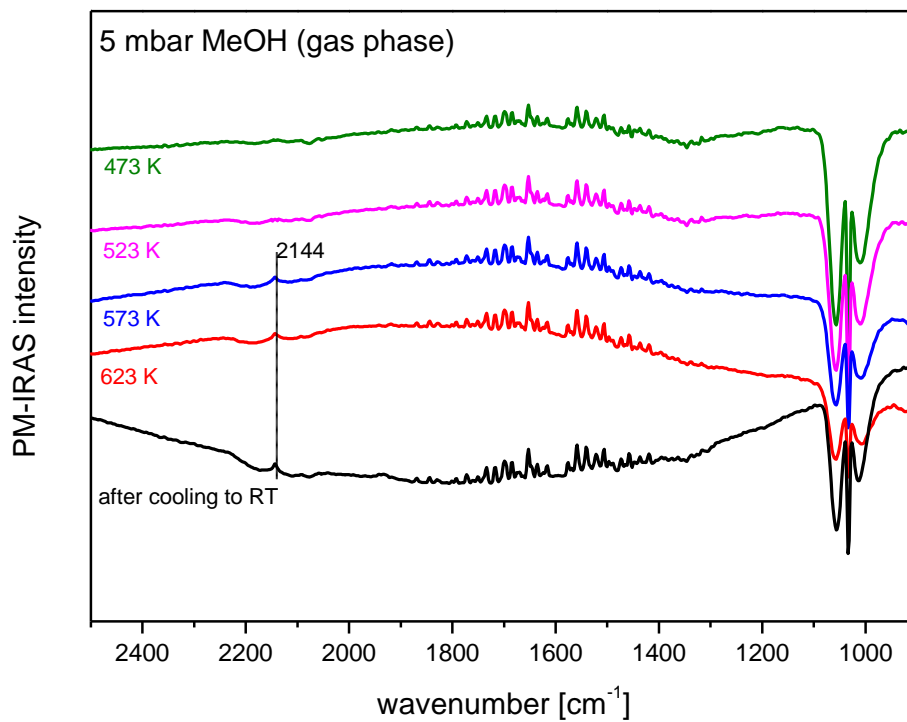


Fig. 3-60: PM-IRAS spectra (gas phase) acquired on 2 ML PdZn/Pd(111) in 5 mbar CH_3OH at different temperatures. Methanol is observed at $\sim 1033 \text{ cm}^{-1}$. The small band at 2143 cm^{-1} can be assigned to CO .

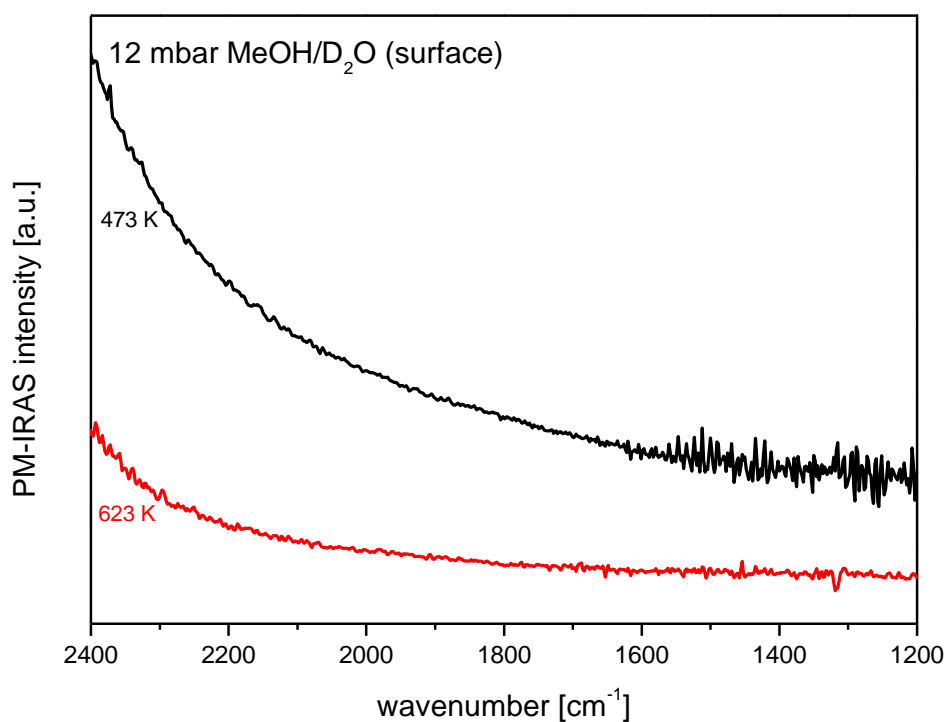


Fig. 3-61: PM-IRAS spectra (surface) acquired on 2 ML PdZn/Pd(111) in 12 mbar $\text{CH}_3\text{OH}/\text{D}_2\text{O}$ each at 473 K and 623 K.

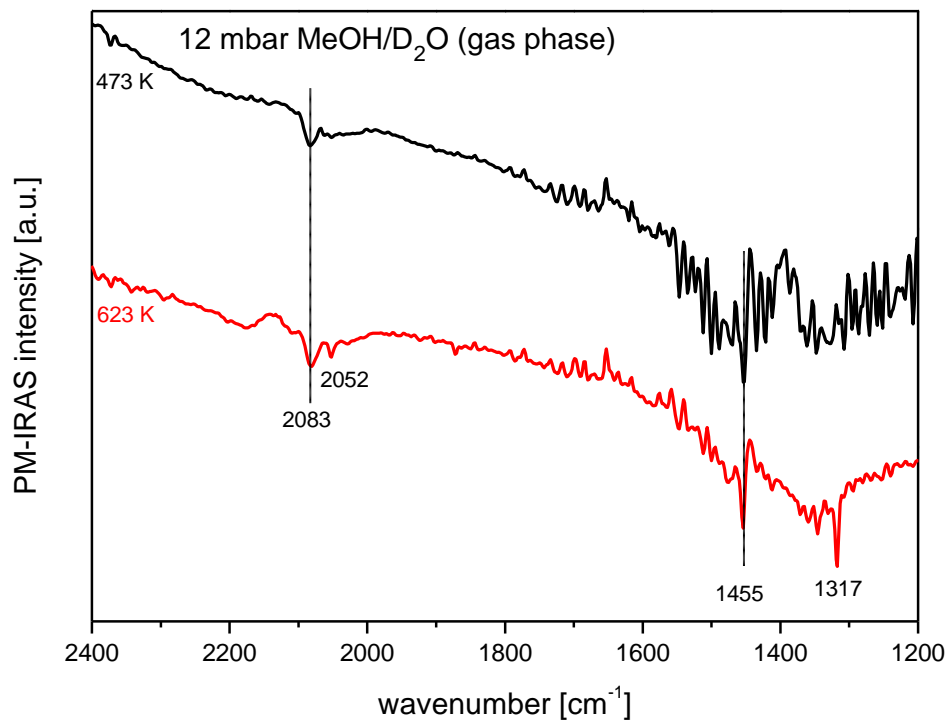


Fig. 3-62: PM-IRAS spectra (gas phase) acquired on 2 ML PdZn/Pd(111) in 12 mbar CH_3OH/D_2O each at 473 K and 623 K.

3.8.3 XPS measurements

Methanol decomposition was also studied by XPS (see Fig. 3-63) by following the evolution of the C 1s signal with time (carbon coverage was quantified from the C 1s peak area as described in chapter 3.3.3), upon exposing the two different surfaces to $3 \cdot 10^{-8}$ mbar methanol background pressure at 300 K and 450 K. The formation of CH_x species ($x=0-3$; C 1s signal at ~ 284.5 eV) is shown in Fig. 3-63 a); on a Pd(111) surface a rapid formation of carbonaceous species was observed at 300 K, and was even more pronounced at 450 K. In contrast, on a 2 ML PdZn/Pd(111) surface alloy basically no carbonaceous species were produced under the same conditions, even after 510 min methanol exposure. Fig. 3-63 b) shows the CO formation by XPS (C 1s signal at ~ 286 eV). At 300 K, the CO coverage decreased at first, due to progressive poisoning of the surface with CH_x , but then remained more or less constant after 200 min of methanol exposure. At 450 K, the CO coverage on Pd(111) decreased to less than 0.1 ML, which was attributed to the larger extent of surface poisoning by CH_x , and to the fact that 450 K is close to the desorption temperature of CO on Pd(111). On the contrary, on the PdZn surface alloy adsorbed CO was not detected at all by XPS (red trace of Fig. 3-63 b). The absence of adsorbed CO on PdZn at 300 K does not rule out the possibility of CO formation on this surface, since it was shown by PM-IRAS (Fig. 3-57 and Fig. 3-58) and TPD (Fig. 3-55 and Fig. 3-56) that at these conditions CO already desorbs from the alloy surface [30].

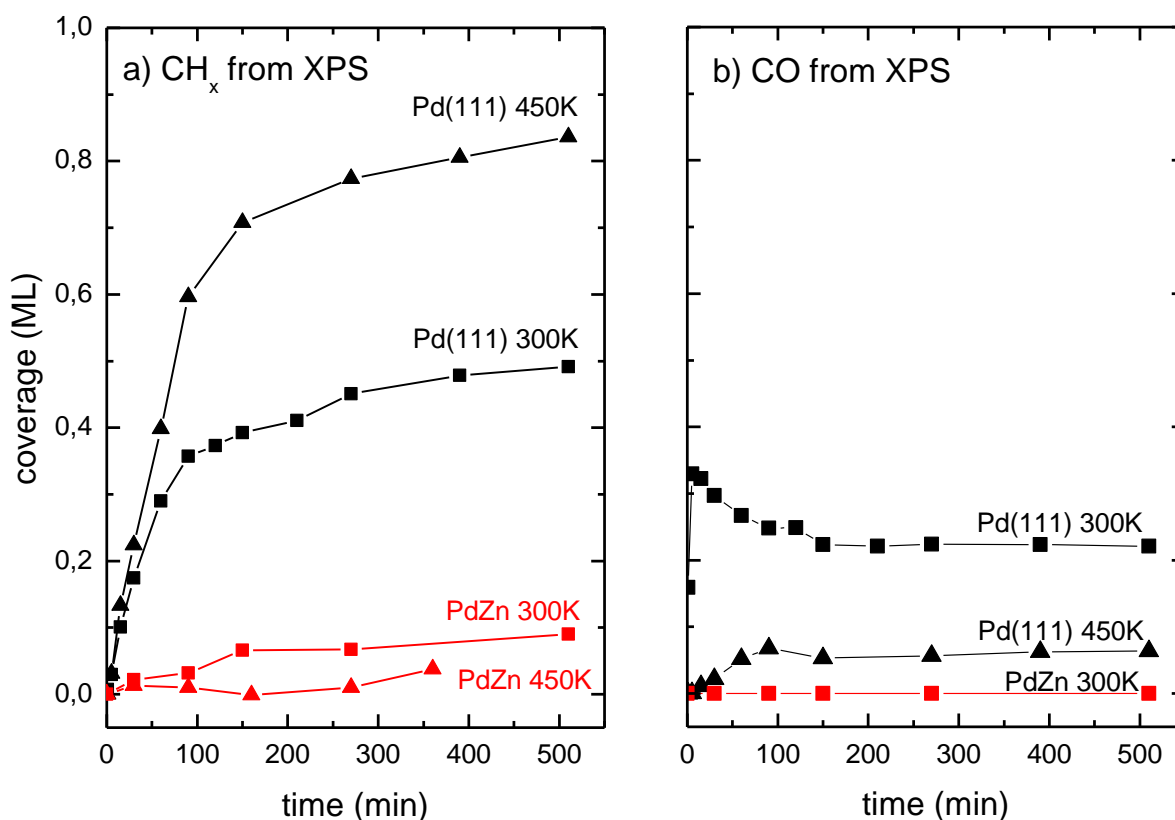


Fig. 3-63: Methanol decomposition: evolution of CH_x and CO coverage on Pd(111) and PdZn/Pd(111) with time at a background pressure of $3 \cdot 10^{-8}$ mbar methanol. a) CH_x coverage deduced from the XPS C 1s signal at 284.5 eV; b) CO coverage deduced from the XPS C 1s signal at 286 eV.

TPD and XPS results indicate that, in contrast to Pd(111), methanol dehydrogenated to CO did not substantially occur on the PdZn/Pd(111) surface alloys. CH_x formation due to cleavage of the methanolic $C-O$ bond did also not take place to a significant amount on PdZn/Pd(111). Chen et al. have calculated the energetics for methanol decomposition and dehydrogenation. $C-O$ bond cleavage is clearly endothermic (+60 kJ/mol) on PdZn with a high activation barrier, whereas it is only slightly endothermic (+5 kJ/mol) on Pd(111) with a reduced barrier [251, 252]. Moreover, full dehydrogenation of adsorbed methoxy species is exothermic on Pd(111) by -233 kJ/mol. Although the overall dehydrogenation of methoxy to CO on the PdZn(111) surface is still exothermic by -14 kJ/mol, full dehydrogenation to CO is unlikely to occur on the PdZn/Pd(111) surface because it is a highly activated process (CH_2O to CO) due to the high reaction barriers and endothermic intermediate species (Fig. 3-64).

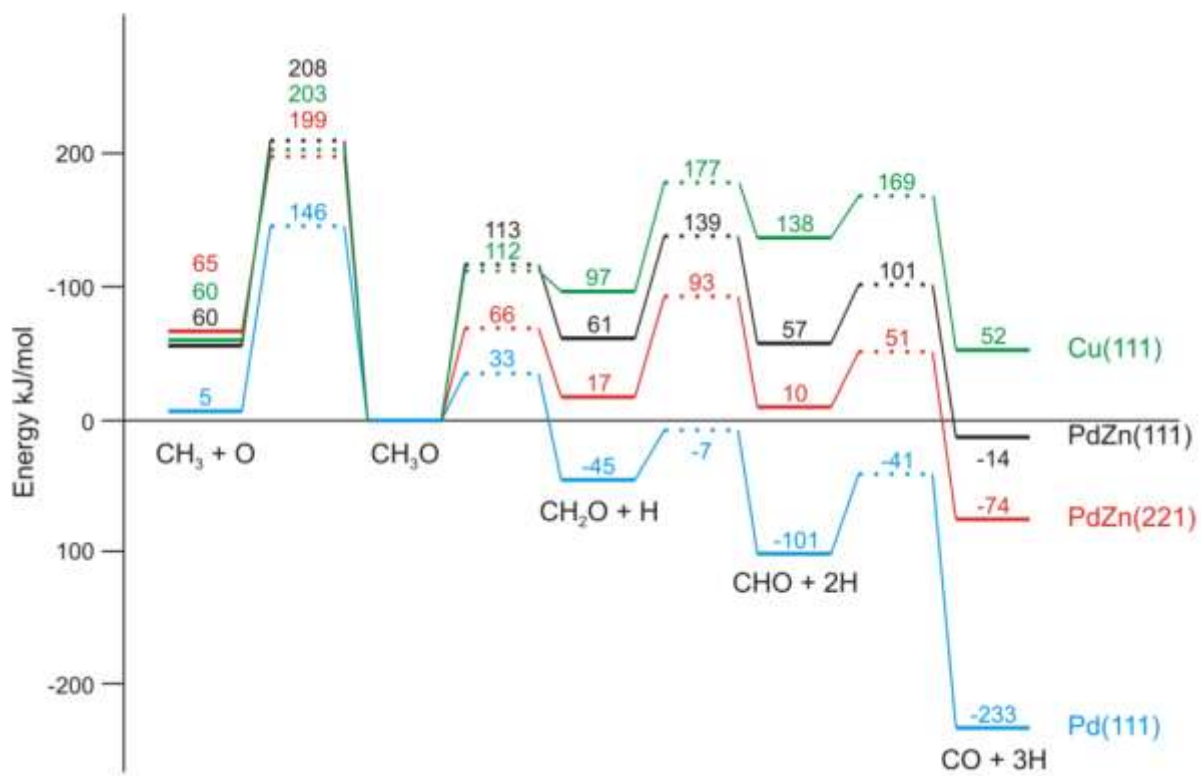


Fig. 3-64: Calculated energies during dehydrogenation of methoxy adsorbed on various surfaces [39].

3.9 Methanol decomposition and oxidation on Pd(111) by HP-XPS

3.9.1 Introduction

Chemical reactions of catalysts observed under UHV conditions are not necessarily the same as under ambient (=more realistic) pressures. XPS investigations are usually limited to high vacuum conditions. To perform measurements at higher pressures of the adsorbate (gas or gas mixtures) it is necessary to use special equipment (differentially pumped chambers, see chapter 2.3.4). At the moment the pressure limit is in the range of a few mbars [253].

We (Christian Weilach and me) had the opportunity for a beamtime at the Maxlab synchrotron at beamline I511-1 in Lund (see chapter 2.3.4) with a high pressure XPS endstation. The main objectives of this project were:

- Identification of a possible Pd_xC_y phase during methanol decomposition on Pd(111) at different temperatures by in situ ambient pressure XPS for a detailed understanding of this process including identification and quantification of relevant CH_x species
- Quantification of the extent of Pd_xC_y formation by depth profiling
- Elucidation of the influence of O_2 on Pd_xC_y formation and catalytic properties

In a previous combined Sum-Frequency-Generation (SFG) and XPS study [254] it was shown that coking plays only a minor role at low pressures and temperatures ($1 \cdot 10^{-6}$ mbar, 300 K) but becomes dominant close to ambient pressure (0.1 mbar) and 450 K. However, Gabasch et al. [255] demonstrated that at even higher temperatures, the carbon deposits produced during ethene oxidation can dissolve in the Pd bulk forming a Pd_xC_y phase, which is stable between 480 and 660 K. The formation and stability of this phase was identified by the Pd 3d XPS signal at a binding energy of 335.34 eV and the presence of this phase could in fact be correlated with catalytic activity.

Similar to ethene oxidation, the formation of a dissolved carbon phase may strongly influence the catalytic properties of Pd(111) for methanol decomposition. Instead of catalyst poisoning via coking, the formation of Pd_xC_y may even be beneficial for the reaction. Using Polarization Modulation Infrared Reflection Absorption Spectroscopy (PM-IRAS) and GC, Borasio et al. [38] showed that when low amounts of carbonaceous deposits were present on the surface (i.e. initial deactivation), the catalytic selectivity was actually steered towards formaldehyde, a

valuable product. This was attributed to site blocking or electronic alterations of Pd which prevent further dehydrogenation of formaldehyde, two effects which may as well result from the formation of Pd_xC_y. Consequently, the catalytic properties at high temperature may strongly differ from those observed around 300 K.

By applying ambient pressure photoelectron spectroscopy we aim at a detailed understanding of this process including identification and quantification of relevant CH_x species. Depth profiling, by variation of the incident photoelectron energy, was performed to study the thickness and extent of Pd_xC_y phase formation. The influence of the Pd_xC_y phase on the catalytic properties such as activity, stability and selectivity was studied by correlating the spectroscopic results with mass spectrometric measurements of products. Thus, it was possible to obtain detailed knowledge on a fundamental basis of possible structure(phase)-activity relationships during methanol decomposition on Pd(111).

Another part of the project was to investigate the influence of O₂ on the methanol/Pd(111) system. Addition of gas phase oxygen to the reaction mixture may again change its properties. The formation of the Pd_xC_y phase may be hindered due to oxidation of the CH_x species. Instead Pd(111) may itself become oxidized under this conditions [255] or complete dehydrogenation of methanol to CO may be reduced by increased oxidation of intermediate species to formaldehyde.

The identification of the Pd_xC_y phase necessarily requires synchrotron based XPS operating at (almost) ambient pressure, as the formation of the Pd_xC_y phase requires substantial amounts of C-O bond cleavage, i.e. elevated reactant pressure and a high energy resolution is mandatory to enable discrimination between the different Pd signals related to Pd_xC_y and the underlying Pd(111) bulk (~0.4 eV). Depth profiling experiments were performed by varying the primary photon energy. Corresponding valence band spectra were acquired for calibration of the binding energy scale. When oxygen was present in the gas phase, we had additionally acquire O1s photoelectron spectra in the range between 525-540 eV. It has to be mentioned, that in this spectral region there is a significant overlap between the Pd 3p and O 1s signal.

3.9.2 Setup and sample preparation

Unfortunately we lost a lot of time due to connection problems from the sample plate to the sample holder. It seems that the manufacturer provided a sample plate which is not properly designed for this system. The recorded temperature differed dramatically from the supposed temperature on the sample. These problems could be fixed by some skilful tinkering and we could record reliable temperatures during the measurements. The sample plate design is similar to the one we use in our STM system except of the thermocouple connection to the sample holder. The sample has to be attached to the plate with two screwed tantalum clamps from the front side. See Fig. 3-65 for details.



Fig. 3-65: Sample plate and transfer holder of the HP-XPS system. The transfer holder is used to move the sample from the load lock to the UHV chamber. Due to the arrangement of the vacuum chamber, transfer steps cannot be observed through a viewport, but could be observed by a camera.

After optimizing the cleaning procedure it was possible to get a carbon-free Pd(111) surface, confirmed by XPS and LEED under UHV conditions. The procedure was similar to that we used in the XPS system in Vienna. This should not have any influences to the final properties of the surface. See appendix 7.2 for more detailed drawings of the experimental setup and beam information.

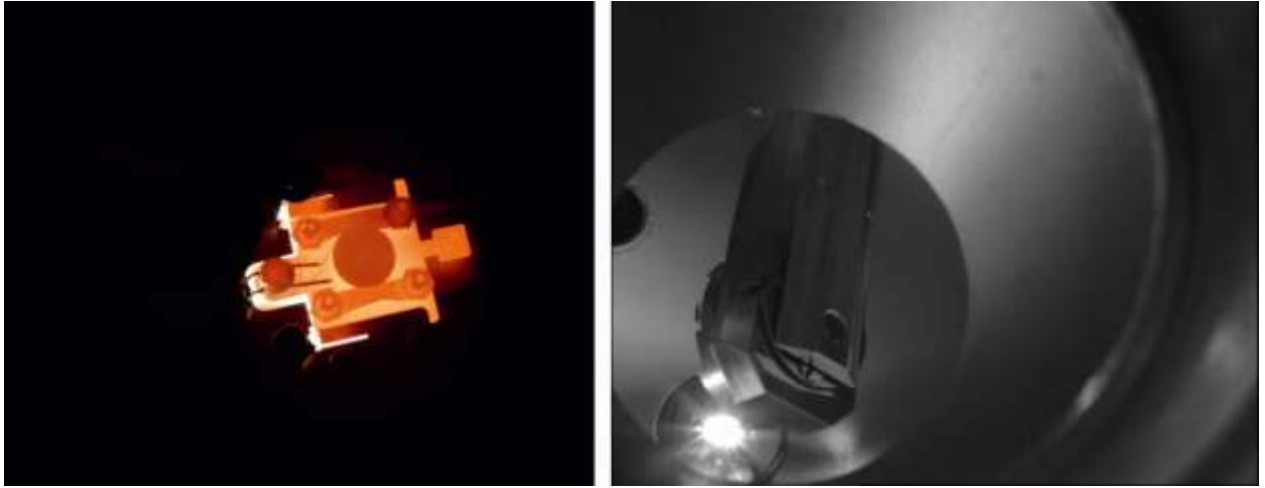


Fig. 3-66: Sample heating (left) and sputtering (right). The view of the sputter gun was only accessible by a greyscale camera which was also used observing the sample transfer.

3.9.3 Measurement plan

The measurements were performed at varying MeOH and MeOH/O₂ pressures, different temperatures, and for depth profiling, at different photon energies (to ensure equal information depth for all spectral regions); the spectra XP-spectra were also recorded directly after transfer to the reaction chamber.

The clean Pd(111) was first measured under UHV conditions after transferring it to the high pressure cell. Then, XP spectra were recorded in 0.5 mbar MeOH at 400 K and 600 K. The experiment was repeated in a mixture of 0.5 mbar MeOH and 0.1 mbar O₂ at 400 K and 600 K (see Tab. 3-7). The methanol ($\geq 99.9\%$) in the gasline was cleaned by repeated freeze-thaw cycles. The base pressure in the gasline for oxygen (5.0) was $\sim 8 \cdot 10^{-9}$ mbar (which is extremely good for a gasline). The base pressure in the main UHV chamber was $\sim 9 \cdot 10^{-11}$ mbar. Depth profiling experiments were performed by varying the primary photon energy. Acquiring with different primary x-ray energy results in equal inelastic mean free path lengths (IMFP) of the photoelectrons, calculated after [256, 257].

Tab. 3-7: Spectra collection, beam energies [eV] at different reaction conditions used in this chapter.

	0.5 mbar MeOH			0.5 mbar MeOH + 0.1 mbar O ₂				
T [K]	RT Transfer	400K	600K	RT Transfer	400K	450K	500K	600K
Pd	x	480	480	480	480	480	480	480
	720	720	720	720	720	x	x	720
	x	1120	1120	1120	1120	x	x	1120
C	x	420	420	420	420	420	420	420
	660	660	660	660	660	x	x	660
	x	1060	1060	1060	1060	x	x	1060
O	x	x	x	670	670	670	670	670
	x	x	x	910	910	x	x	910
	x	x	x	1310	1310	x	x	1310

3.9.4 Summary

As discussed in chapter 2.3 in a synchrotron system, sample and X-Ray source are not on the same potential. Therefore the Fermi edge has to be measured to correct the binding energy. See appendix 7.2 for more information of the beamline setup and specifications.

Fig. 3-67 shows C 1s and Pd 3d spectra acquired in situ during methanol decomposition/oxidation at mbar pressure and elevated temperatures.

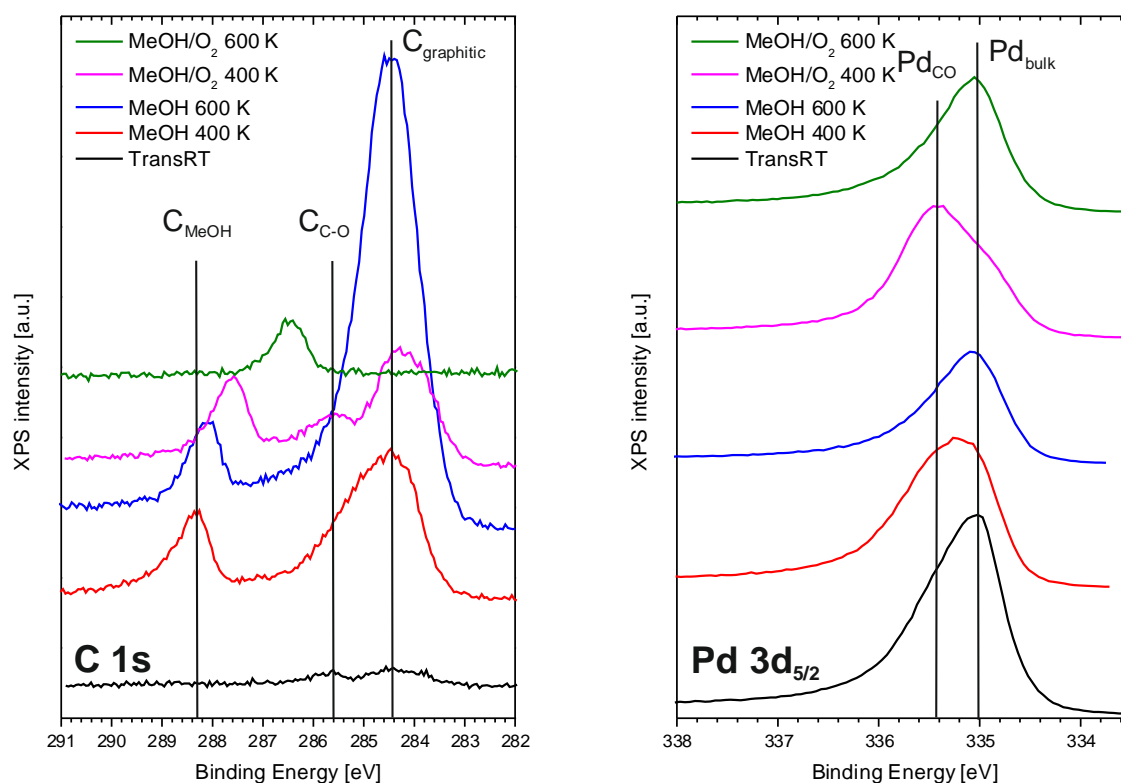


Fig. 3-67: Overview of collected C 1s and Pd 3d_{5/2} spectra under different reaction conditions. TransRT: in vacuum after sample transfer to HP cell; MeOH 400 K/600 K: in 0.5 mbar MeOH at 400/600 K; MeOH/O₂ 400/600 K: in reaction mixture of 0.5 mbar MeOH and 0.1 mbar O₂ at 400/600 K.

Despite a high binding energy peak attributed to gas phase Methanol (C_{MeOH}) two other features are visible in the C 1s region, one at 284.5 eV assigned to elemental carbon ($C_{\text{graphitic}}$) and another for Carbon at approximately 285.5 eV ($C_{\text{C-O}}$) bound to oxygen in methoxy or CO species. The peak at 286.5 eV, only visible in the MeOH/O₂ mixture at 600 K, belongs most probably to formaldehydic carbon. CO species are a product of full methanol dehydrogenation. Carbon species are a result of C-O bond scission.

From HREELS studies [191] one can suppose that methanol reforming and partial oxidation proceeds on Pd via methoxy as the first intermediate. The CH_x formation occurs as subsequent reactions:



In our system in Vienna, PM-IRAS measurements also have shown that formyl species on the surface developed with time (1255 and 1305 cm^{-1} , see 3.3).

Highly dehydrogenated carbon species and carbon are bonded to hollow sites, whereas CO is mainly bonded to bridge sites [254].

It is obvious that the graphitic carbon is the dominant species in pure MeOH atmosphere, most pronounced at 600 K due to intensive formation of carbonaceous species (CH_x , where $x=0-3$) via C-O bond cleavage. These carbonaceous species effectively block the Pd surface. In the presence of oxygen, the amount of carbonaceous species is significantly removed at 400 K reaction temperature and they are fully removed by oxidation at 600 K. In former studies it was shown that CO oxidation on Pd starts even at 200 K [258].

The Pd3d region is dominated by the XPS signal from the Pd(111) substrate at 335.0 eV (Pd_{bulk}). Only at lower reaction temperature (before the formation of the Pd_xC_y phase should occur) a second feature is visible, shifted by 0.25 eV towards a higher binding energy (Pd_{CO}). The latter we attribute to Pd atoms, which have CO or methoxy species adsorbed retracting electron density from the Pd atoms. At elevated temperature this species disappears again from the spectrum due to CO desorption, but no indications for the presence of a Pd_xC_y phase were found.

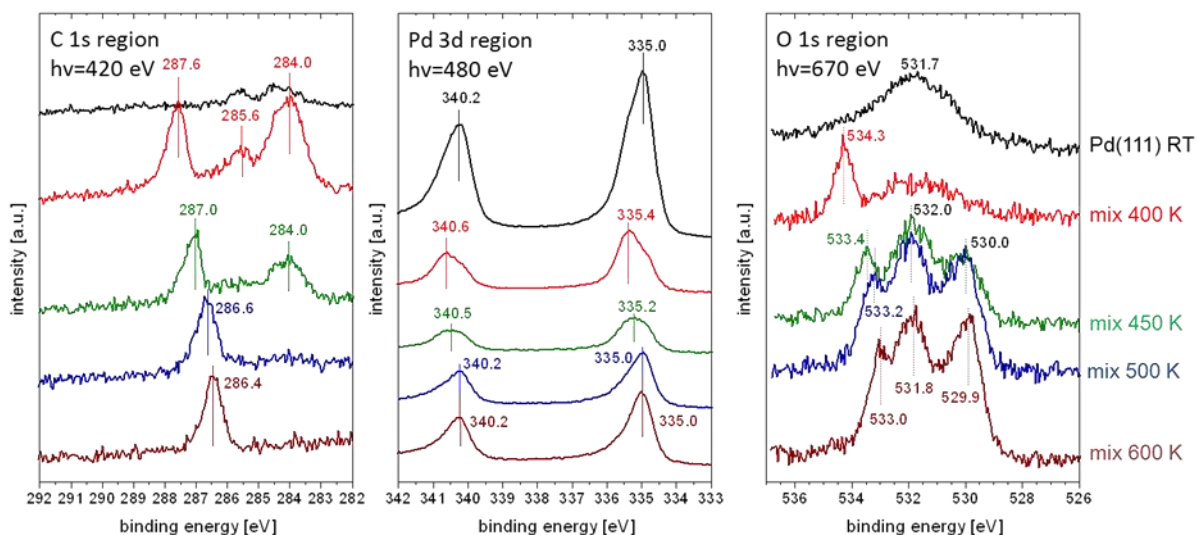


Fig. 3-68: Pd 3d, C 1s, and O 1s XP-spectra at different reaction conditions (see Tab. 3-7).

The absence of a Pd_xC_y phase was also corroborated by evaluation of the Pd to C ratio upon variation of the incident photon energy during spectra acquisition (see Fig. 3-69). The Pd to C ratio was almost linearly increasing with increasing photon energy (i.e. increasing probing depth), showing accumulation of carbon in subsurface layers.

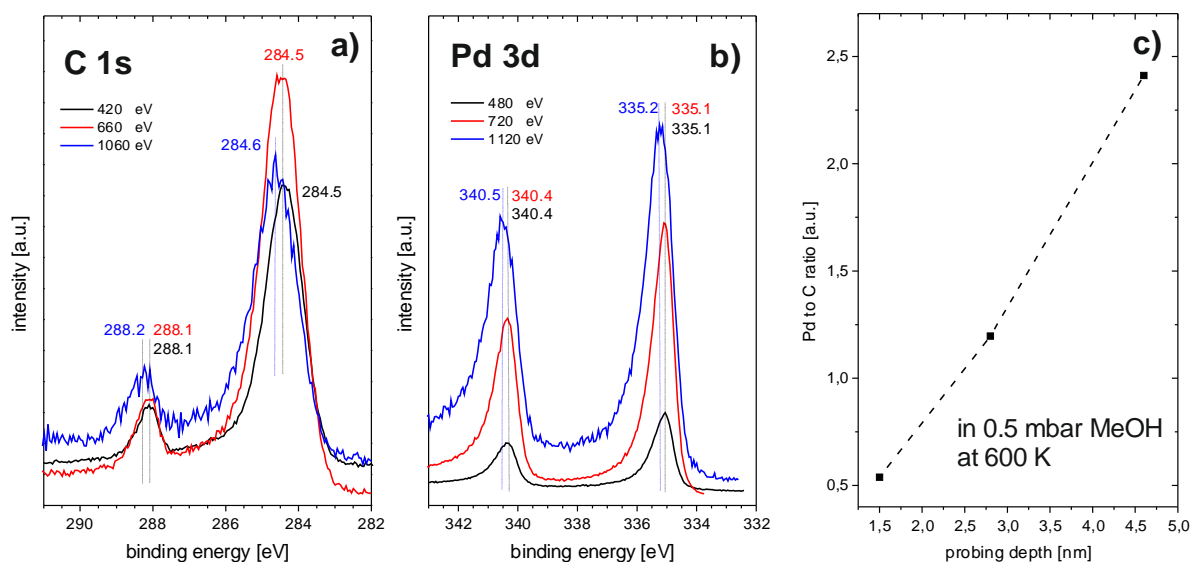


Fig. 3-69: C 1s (a) and Pd 3d (b) XP-spectra and depth profiling of Pd(111) (c) in 0.5 mbar MeOH at 600 K by varying incident photon energies (see Tab. 3-7).

O 1s spectra may be another way to differentiate between adsorbed CO and CH_3O . Unfortunately, due to overlapping of O1s and Pd3p XPS signals, a clear interpretation of the

data was not possible (Fig. 3-68) and are difficult to be used for calculating elemental ratios. At 600 K the O 1s signal from the methyl group (~534 eV) vanishes but some oxygen species are remaining on the Pd(111) surface. At higher photon energies the Pd 3p signal is dominating (see Fig. 3-77). The different surface orientation of *CO* (carbon bounded on the surface) and *CH₃O* (oxygen bounded) may also influence the oxygen KLL Auger peaks (see methanol on Pd and PdZn at low pressures, chapter 3.3). Former studies of Pd(111) oxidation reported chemisorbed oxygen in the p(2x2) structure at about 529.2 eV [259] while oxygen features from Pd₅O₄ (“2-dimensional oxide”), were observed at about 529.5 eV [260].

The oxygen-free sample after transfer shows a signal in the O1s region at 532.1 eV which belongs to Pd 3p. Using a beam energy of 670 eV, the sample at 400 K in MeOH/O₂ shows signals at a binding energy of 532.3 and 534.3 eV and at 600 K binding energy signals of 530.1 and 532.0 eV. Using a beam energy of 910 eV, the sample at 400 K shows binding energy signals at 532.0 and 534.3 eV and at 600 K two signals at 530.1 and 531.9 eV. Finally at a beam energy of 1310 eV, one can see only one feature at a binding energy of 532.1 eV for the oxygen-free sample after transfer and also in reaction mixture (CH₃OH/O₂) at 400 and 600 K which belongs to Pd (bulk).

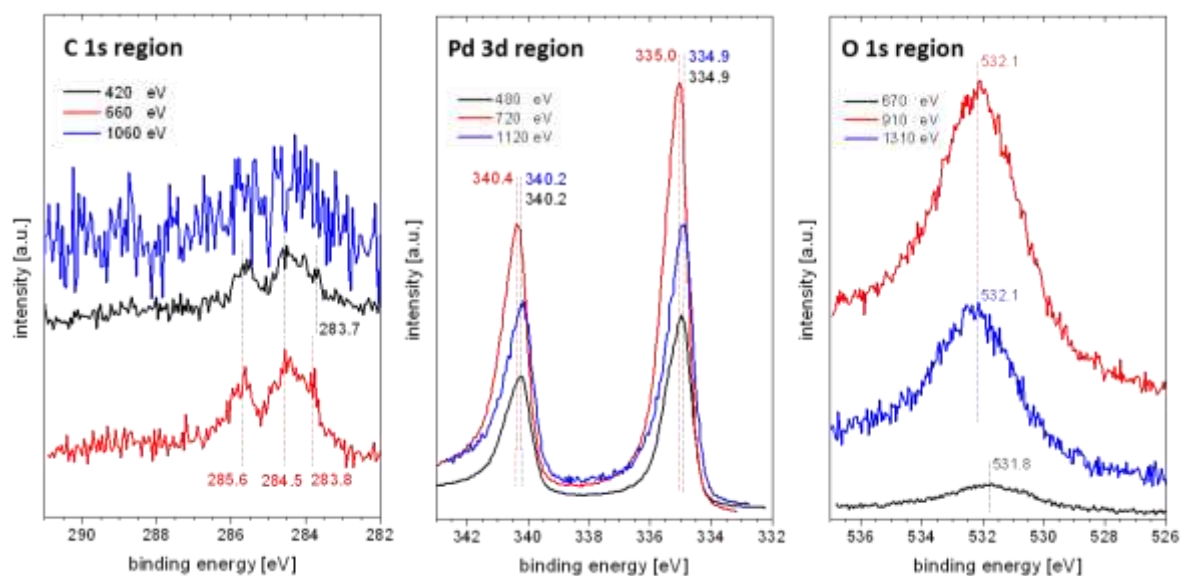


Fig. 3-70: Pd(111) after transfer at room temperature in UHV at varying photon energies for C 1s, Pd 3d, and O 1s (see Tab. 3-7).

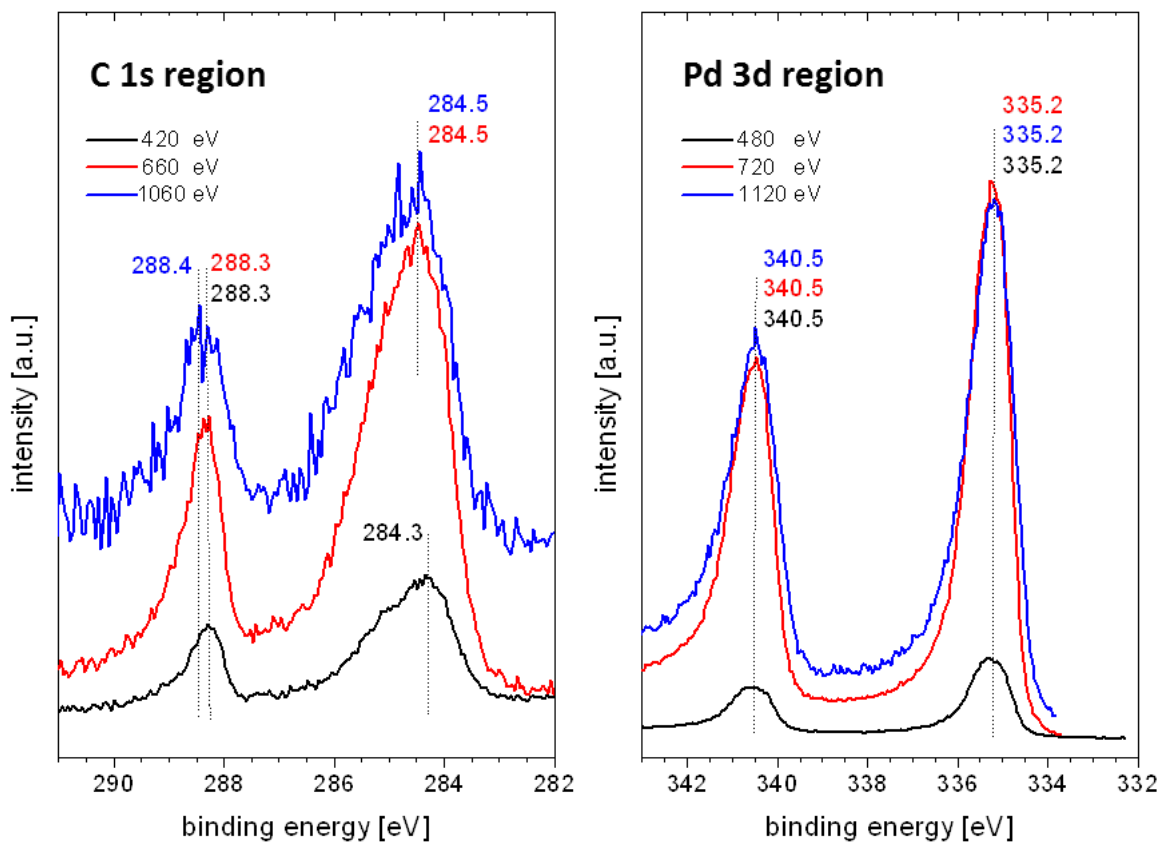


Fig. 3-71: Pd(111) at 400 K in 0.5 mbar MeOH and with different photon energies for C 1s and Pd 3d (see Tab. 3-7).

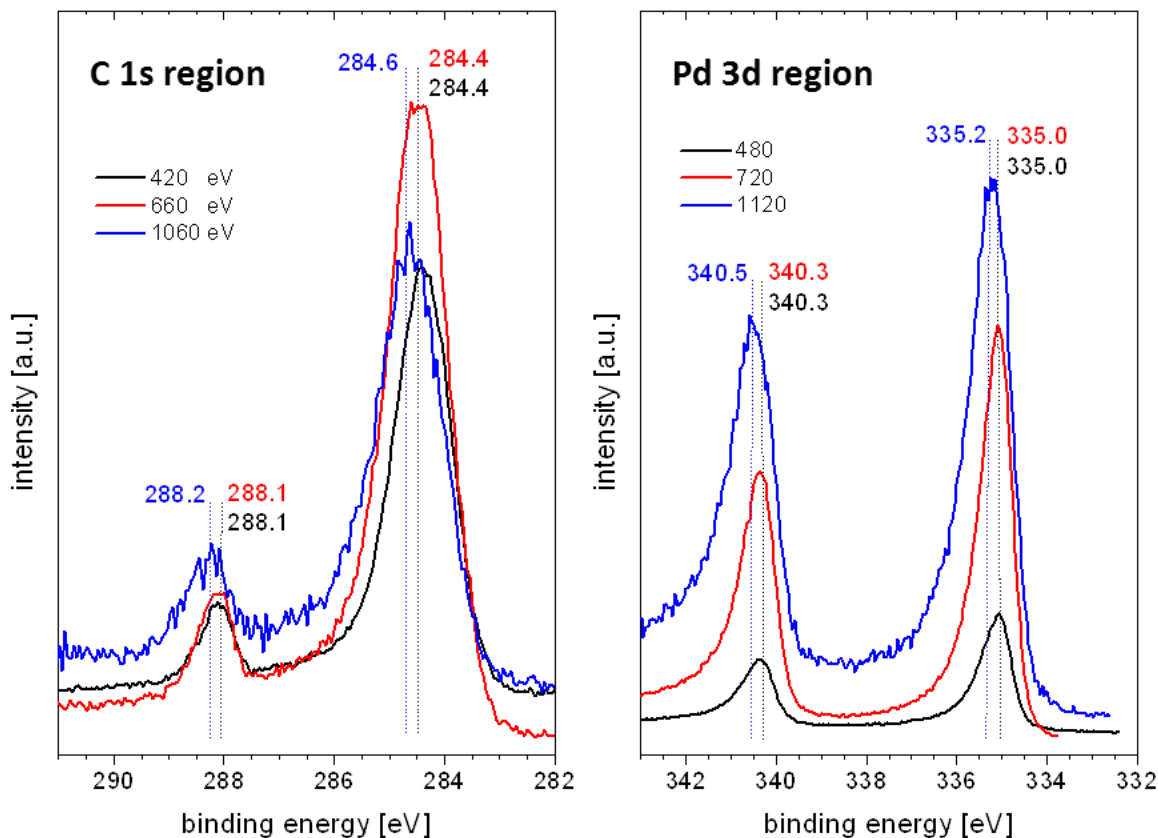


Fig. 3-72: Pd(111) at 600 K in 0.5 mbar MeOH recorded with different photon energies for C 1s and Pd 3d (see Tab. 3-7).

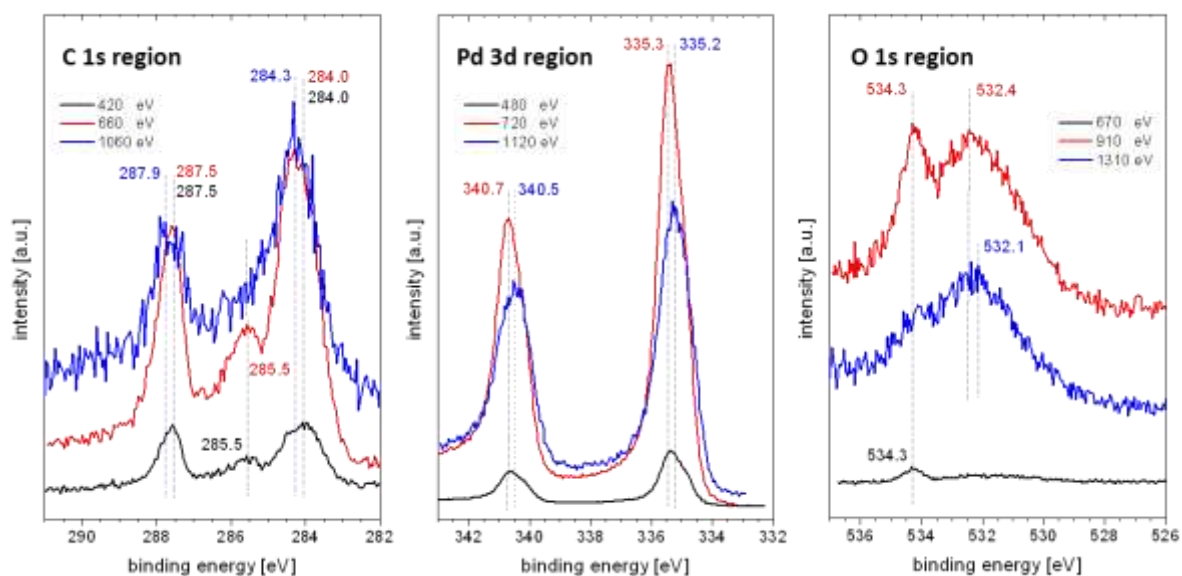


Fig. 3-73: Pd(111) at 400 K in 0.5 mbar MeOH and 0.1 mbar O₂ recorded with different photon energies for C 1s, Pd 3d, and O 1s (see Tab. 3-7).

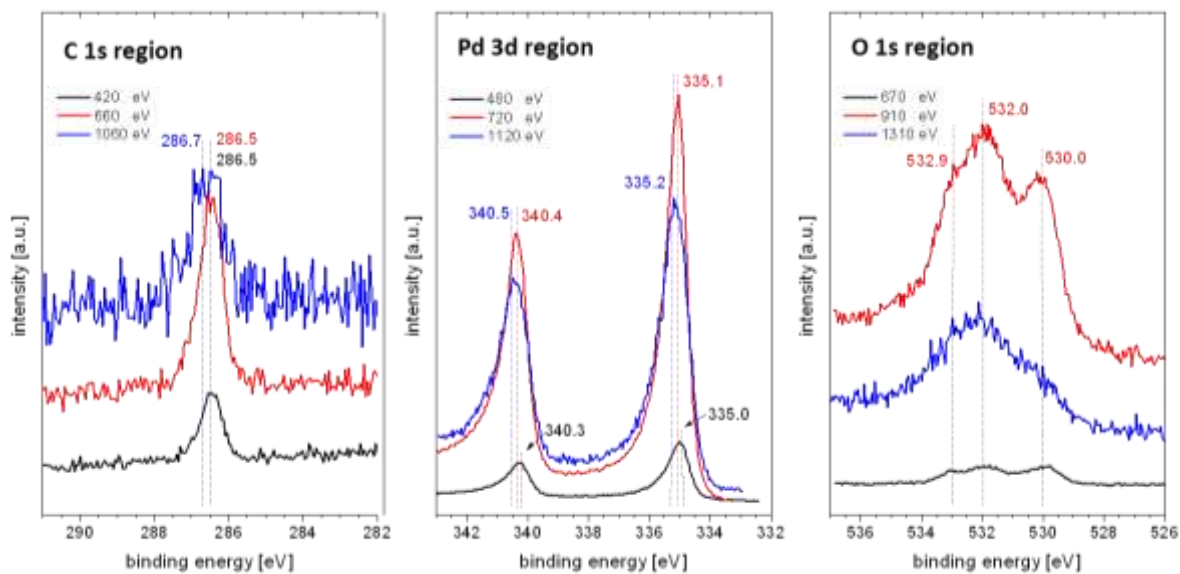


Fig. 3-74: Pd(111) at 600 K in 0.5 mbar MeOH and 0.1 mbar O₂ recorded with different photon energies for C 1s, Pd 3d, and O 1s (see Tab. 3-7).

In Fig. 3-75 - Fig. 3-77 energy dependent Pd/C/O XP spectra are shown. In the C 1s spectrum one can see the accumulation of carbon in subsurface layers with increasing information depth. The O 1s signal overlaps with the Pd 3p signal. Pd/O species are visible in surface sensitive spectra (low beam energy).

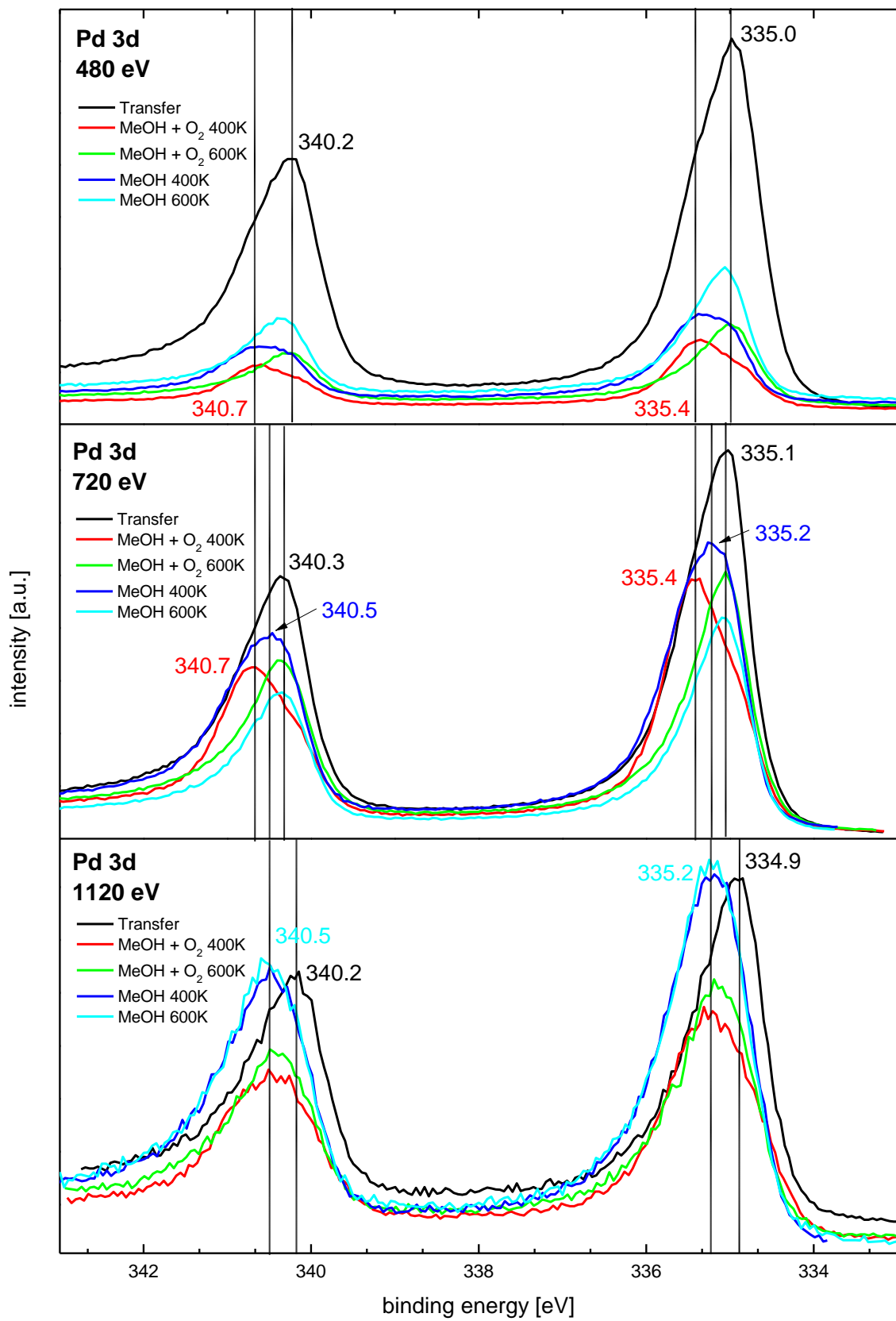


Fig. 3-75: Overview of energy dependent Pd 3d XP-spectra at varying reaction conditions.

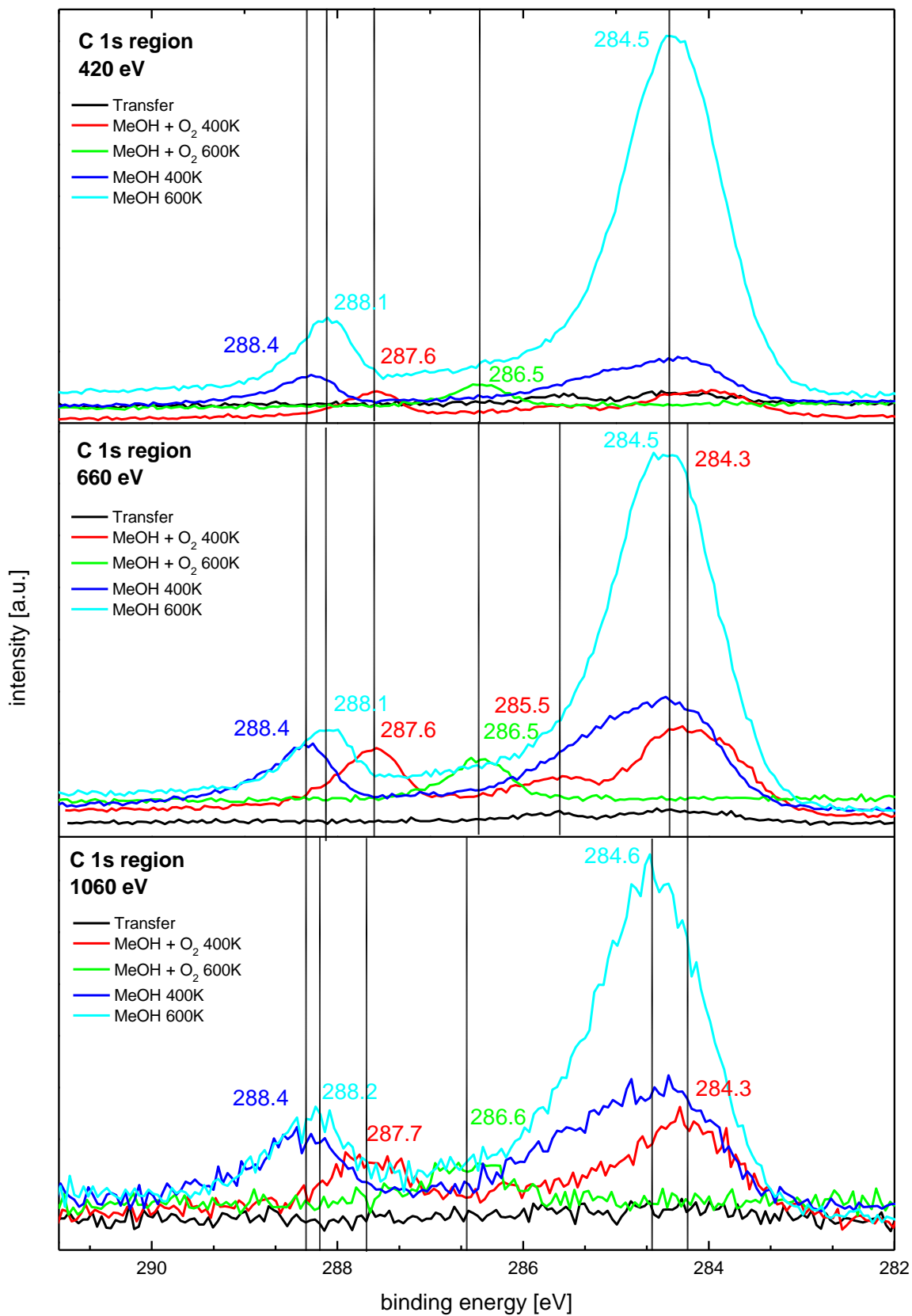


Fig. 3-76: Overview of energy dependent C 1s XP-spectra at varying reaction conditions.

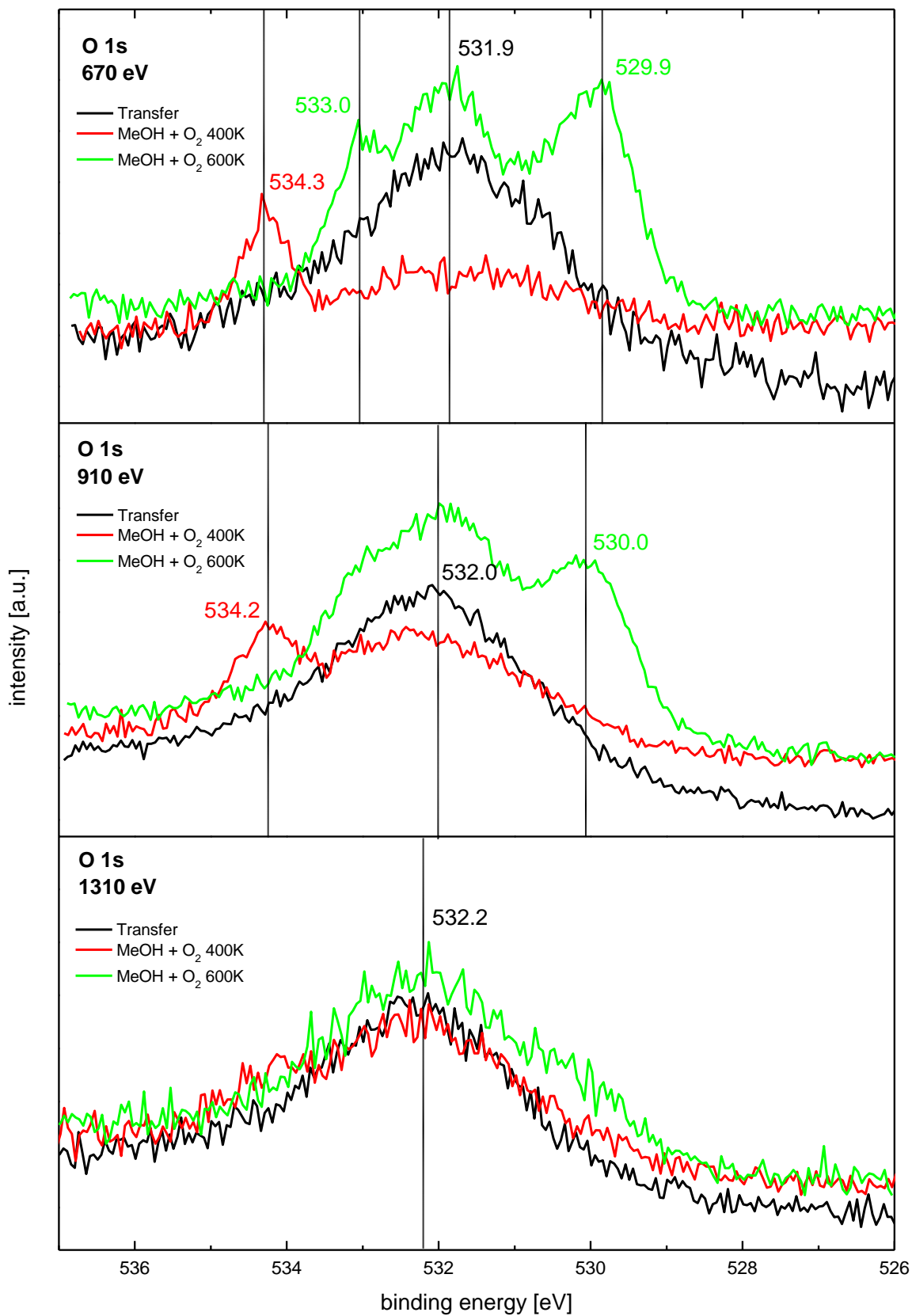


Fig. 3-77: Overview of energy dependent O 1s XP-spectra at varying reaction conditions. The O 1s signal overlaps with the Pd 3p signal.

Overall, it can be shown that instead of the formation of a selective palladium-carbon phase at elevated temperature, the Pd(111) catalyst was significantly covered (poisoned) by an overlayer of carbonaceous species during methanol decomposition. The amount of poisoning could be drastically removed upon adding O₂ to the reaction feed. Due to the absence of an MS possible changes in product distribution could not be detected. At 600 K the surface was actually completely free from carbon. As presented in Fig. 3-67 and Fig. 3-69, we could demonstrate that ambient pressure XPS is a valuable tool to study catalytic reactions, e.g. it allows to follow the presence/absence of species depending on reaction conditions, their quantification and depth profiling via photon energy variation.

4 ZnPd Bulk Intermetallics

4.1 Introduction

Although valuable insight to the catalytic reactivity could be gained and interesting properties were revealed on the model systems, the model may not satisfactorily represent the real catalyst. To identify possible differences between the surface alloy “models” and “real” system, comparative study between the adsorption properties of well-defined PdZn/Pd(111) surface alloys and bulk intermetallic ZnPd (also called “PdZn”) sinter „single“ crystals were performed. As integration of the electron density reveals charge transfer from Zn to Pd, in accordance with their electronegativities, it is suggested to describe (following the IUPAC nomenclature) the intermetallic phase “ZnPd” instead of “PdZn” (see also Fig. 4-3). *CO* was used as a probe molecule and its adsorption/desorption properties on intermetallic ZnPd were studied by XPS, TPD, and PM-IRAS [24, 26, 240, 261].

An “intermetallic compound” is composed of two (or more) metallic elements and possesses a crystal structure which is different from the involved elements and at least partly ordered. The term “compound” implies that it is single phase, this is not in contradiction to the often broad homogeneity ranges of intermetallic compounds. In contrast, the more common term “alloy” corresponds to a mixture of metals, intermetallic compounds, and/or nonmetals, and can consist of more than one phase [24, 262, 263].

In Fig. 4-1 one can see the consequences of an ordered intermetallic compound on the electronic structure of Pd and intermetallic ZnPd, which crystallizes in the ordered “AuCu-type” of crystal structure (see Tab. 4-1 and Fig. 4-2).

The phase present from 0 to ~10 atom% Zn is referred to as “ α -Pd”, a solid solution of Pd and Zn with Zn incorporated into the fcc Pd structure. The selectivity of this phase was shown as unfavorable for MSR [264, 265].

The region from nominally 37 to 56 atom% Zn is tetragonal β_1 -PdZn, the main part of investigation in this chapter. It was shown that this phase has a proper selectivity for MSR [266].

Since the Pd₂Zn is between the α -phase (selective to *CO*), and the β_1 -phase (selective to *CO*₂), the performance of this phase is of general interest. A Pd₂Zn structure was published by

Stadlmaier in 1963 [267] and is similar to the structure of Co_2Si . Armbrüster et al. described the Pd_2Ga phase recently also with the same Co_2Si structure [268].

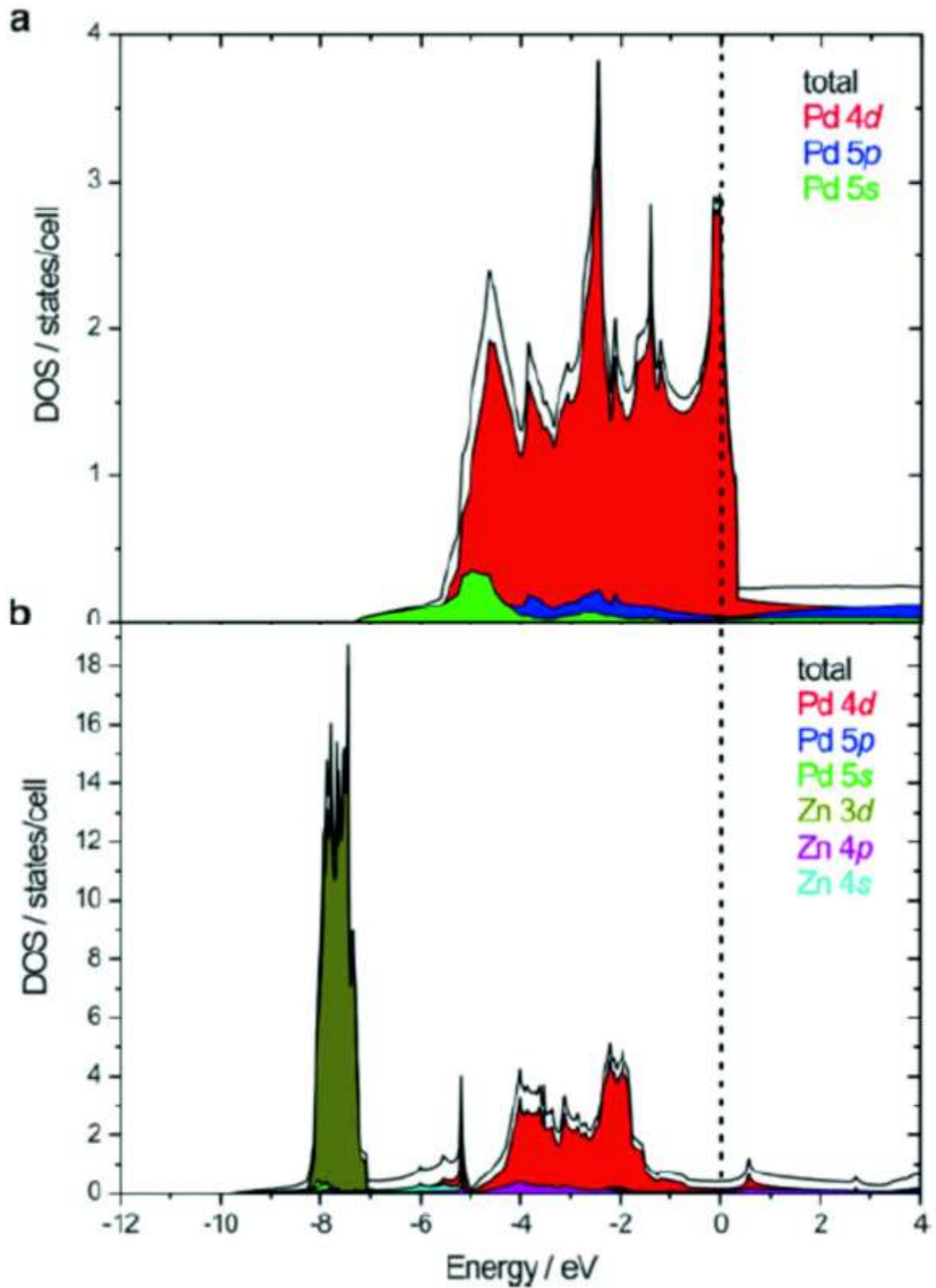


Fig. 4-1: Density of states (DOS) of Pd metal (a) and PdZn intermetallic compound (b), respectively. Huge differences can be observed at the Fermi level and in the width of the Pd d-bands [24].

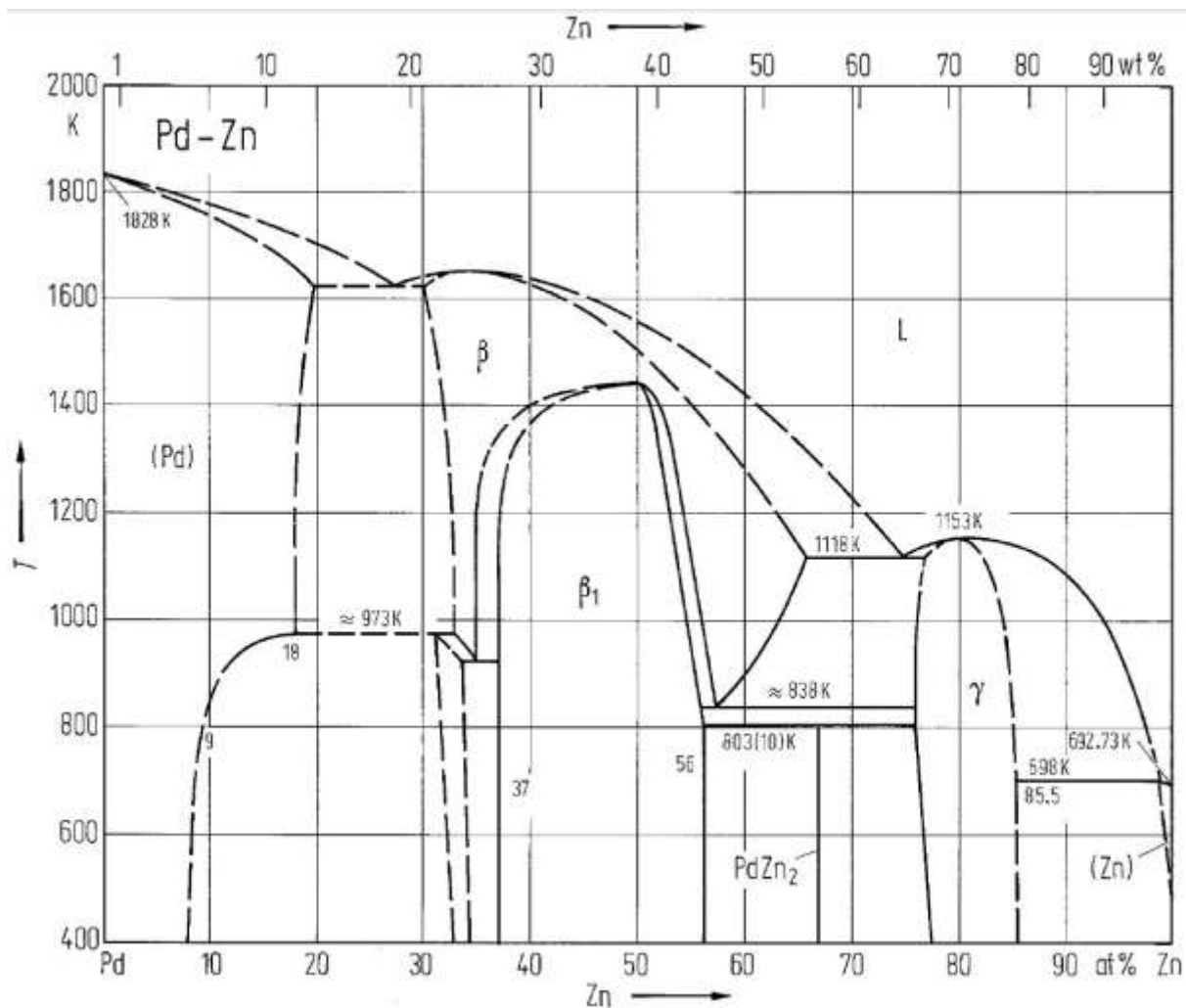


Fig. 4-2: Phase diagram of the system Pd-Zn [269].

Tab. 4-1: Crystal structure and lattice parameters of Pd/Zn intermediate phases [269].

Phase	Structure	Type	a [nm]	b [nm]	c [nm]
Pd ₄ Zn	cub	Cu	0.3868		
Pd ₂ Zn	cub	CsCl	0.3055		
PdZn	tetr	AuCu	0.4100		0.3346
Pd ₂ Zn ₃	cub	CsCl	0.3049		
PdZn ₂	orth	PdZn ₂	0.7525	0.7363	1.2307
Pd ₂ Zn ₉	cub	Cu ₇ Zn ₈	0.91022		

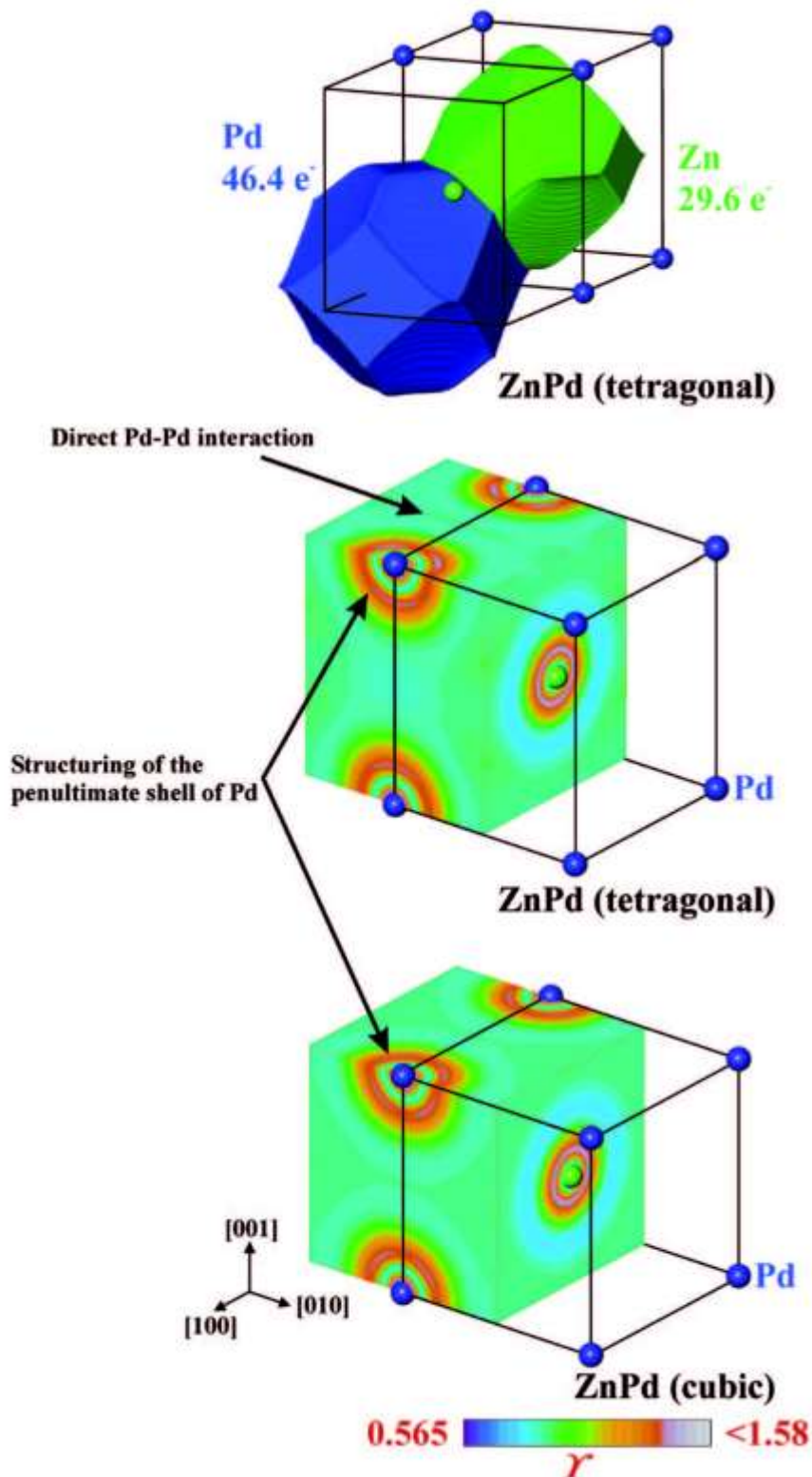


Fig. 4-3: Chemical bonding in ZnPd: (top) QTAIM (Quantum Theory of Atoms in Molecules) basins of palladium (blue) and zinc (green) in tetragonal ZnPd with the according electronic populations revealing the charge transfer from zinc to palladium. (middle) Electron localizability indicators (ELI-D) distribution in the (100), (010) and (001) planes in tetragonal ZnPd shows strong structuring of the penultimate shell of palladium in the (001) plane as well as small ELI-D maxima between palladium atoms along (100). (bottom) ELI-D distribution in the (100), (010) and (001) planes in cubic ZnPd shows weaker structuring of the penultimate shell of palladium in all three planes [240].

4.2 Tetragonal ZnPd

4.2.1 Preparation

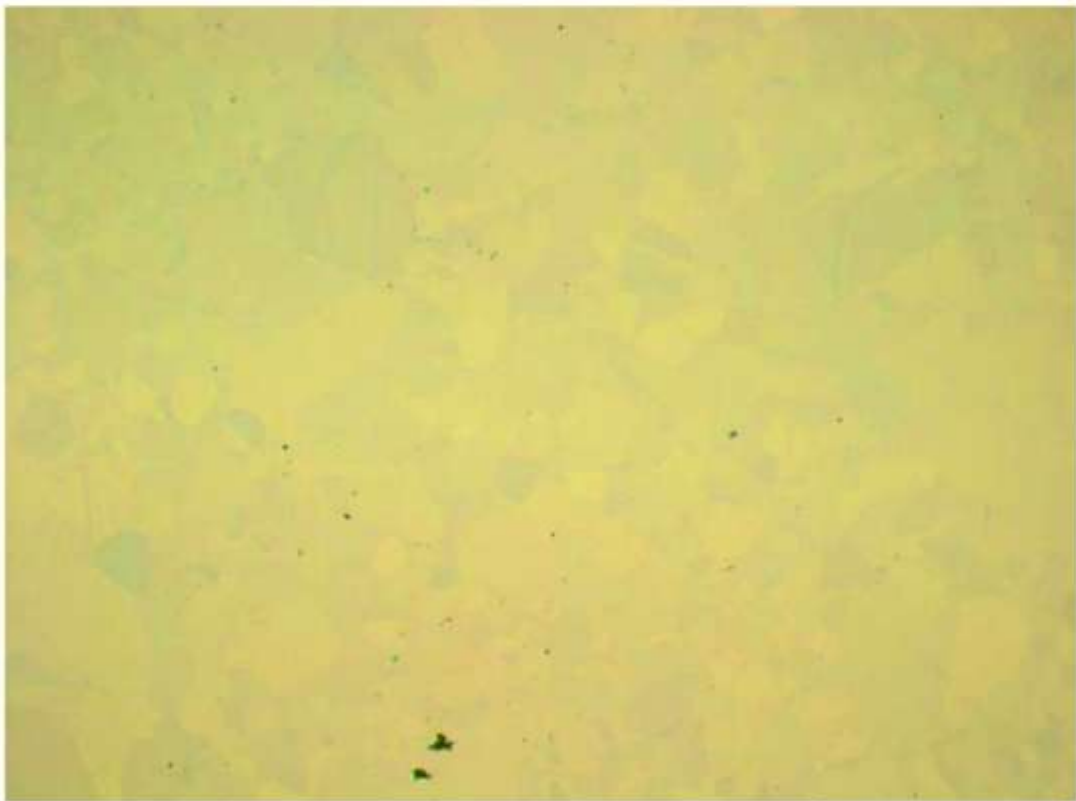
The intermetallic ZnPd bulk material was prepared by powder metallurgical means and subsequent spark-plasma-sintering by Marc Armbrüster at the “Max-Planck-Institut für Chemische Physik fester Stoffe” in Dresden. Elemental Pd (99.9% powder, ChemPur) and Zn (99.9999% powder, ChemPur) were filled in a quartz glass ampoule in an Ar-atmosphere glove box (H_2O and O_2 concentration below 0.1 ppm). After evacuating the ampoule, the mixture was heated up to 1123 K and annealed for 6 days. The phase purity was then verified by X-ray powder diffraction and a single-phase tetragonal AuCu type was confirmed [26, 240]. After the sintering process the sample was polished in an aqueous suspension, finished with 0.25 μm diamond [270].

The metallographic check-up (Fig. 4-4, Fig. 4-5, and Fig. 4-6) was done in at the “Max-Planck-Institut für Chemische Physik fester Stoffe” in Dresden.



28,7 : 1

1mm



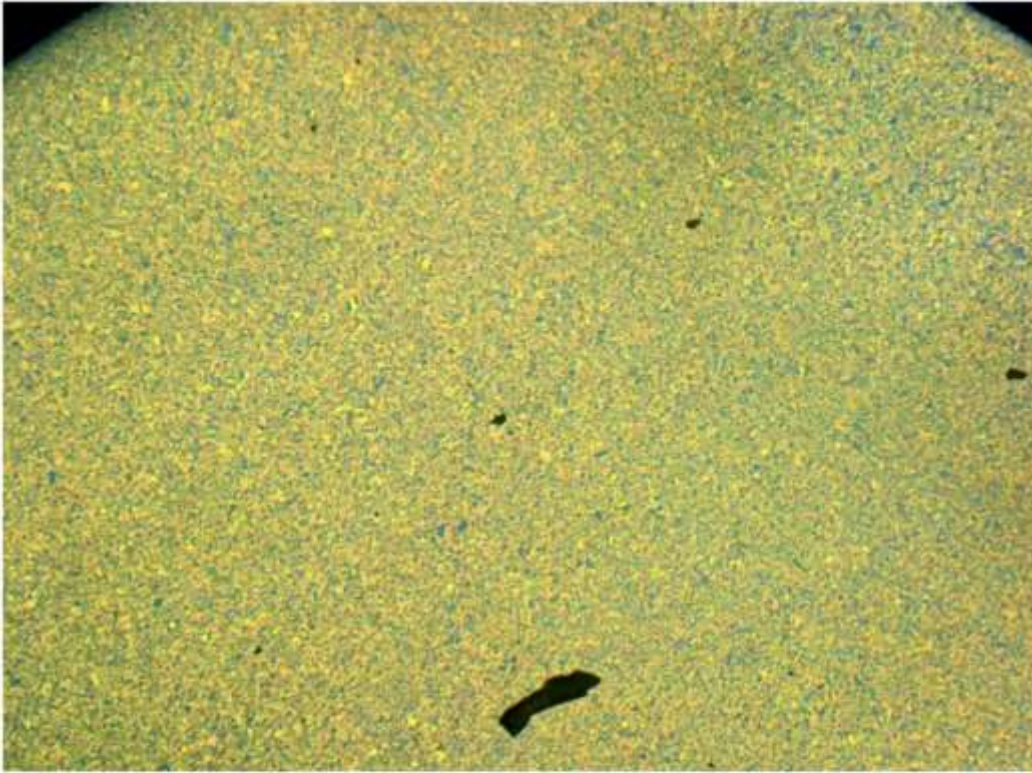
573 : 1

50µm

Abb. : MA760034-09

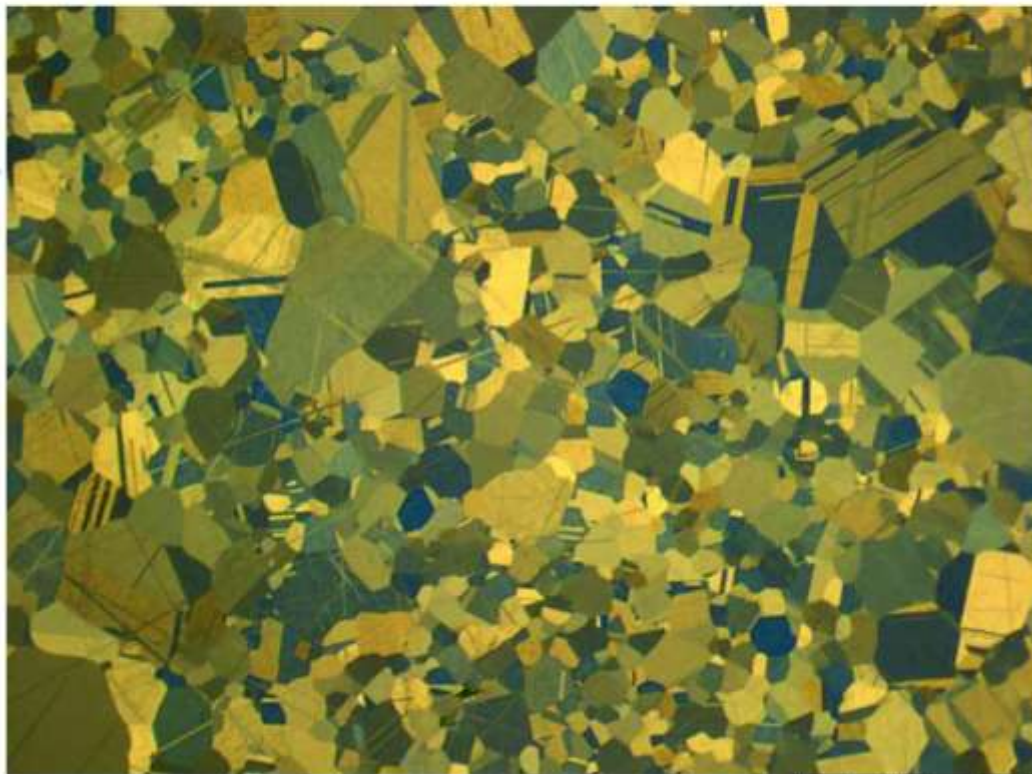
Hellfeld

Fig. 4-4: Bright field microscopic pictures of the ZnPd bulk sample used for this work at different magnifications.



28,7 : 1

1mm



573 : 1

50μm

Abb. : MA760034-10

polarisiertes Licht

Fig. 4-5: Petrographic microscope pictures of the ZnPd bulk sample used for this work at different magnifications.

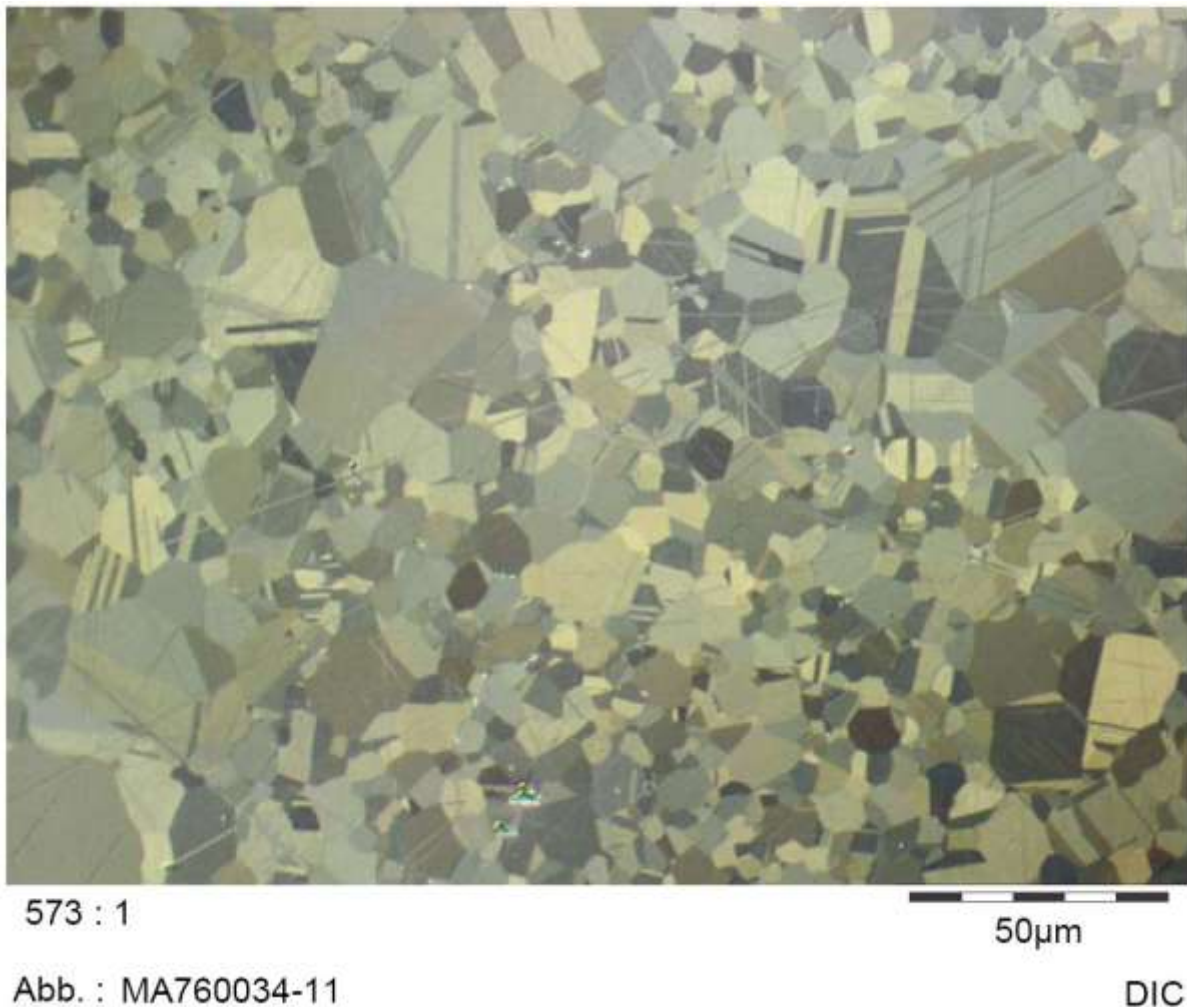


Fig. 4-6: Differential interference contrast (DIC) picture of the ZnPd bulk sample used for this thesis.

Before PM-IRAS and TPD measurements were performed at the IMC, the pellet was cleaned by annealing and a mild surface oxidation/reduction cycle. The sample was not sputtered due to preferential (Zn) sputtering. An oxidation cycle at $1 \cdot 10^{-5}$ mbar O_2 at 700 K for 10 min leads to a Zn-enrichment, but could be returned to the previous condition using some runs with $2 \cdot 10^{-6}$ mbar H_2 at 825 K for 10 min. Treatment at $5 \cdot 10^{-7}$ mbar O_2 to 825 K for 10 min did not alter the sample but decreases the carbon on the surface significantly. Zn was not detectable with MS during this procedure.

At first view the following procedure were figured out as the optimum cleaning procedure: heating up in $5 \cdot 10^{-7}$ mbar O_2 to 825 K for 10 min, cooling down to room temperature and then heating up in $2 \cdot 10^{-6}$ mbar H_2 to 700 K for 10 min. This cycle has to be repeated until the sample is carbon-free in XPS (usually ~5-10 times). An x-ray diffractometric analysis (the sample was sent back to the Max-Planck-Institut in Dresden) of the surface revealed that the diffraction pattern corresponds to a cubic CsCl structure with a lattice constant of 0.32 nm

(the bulk remains unaltered). Fortunately we successfully tried to restore the surface to the tetragonal structure by heating in 10^{-6} mbar He for 2 hours at 600 K. This treatment was finally used for the measurements presented in this thesis.

In Fig. 4-8 XP spectra of a cleaning cycle are shown. It is clearly visible that the amount of carbon species on the surface decreases and a small shift (0.3 eV) towards lower binding energies can be observed. Estimated from the Zn 3d signal (9.4 eV; not shown), ~20% ZnO_x was present on the surface. After reduction, ~6% ZnO_x was present on the surface and the Zn 3d signal was slightly increasing. Pd 3d was observed as a symmetric peak at 335.5 eV and no changes could be observed during cleaning the sample.

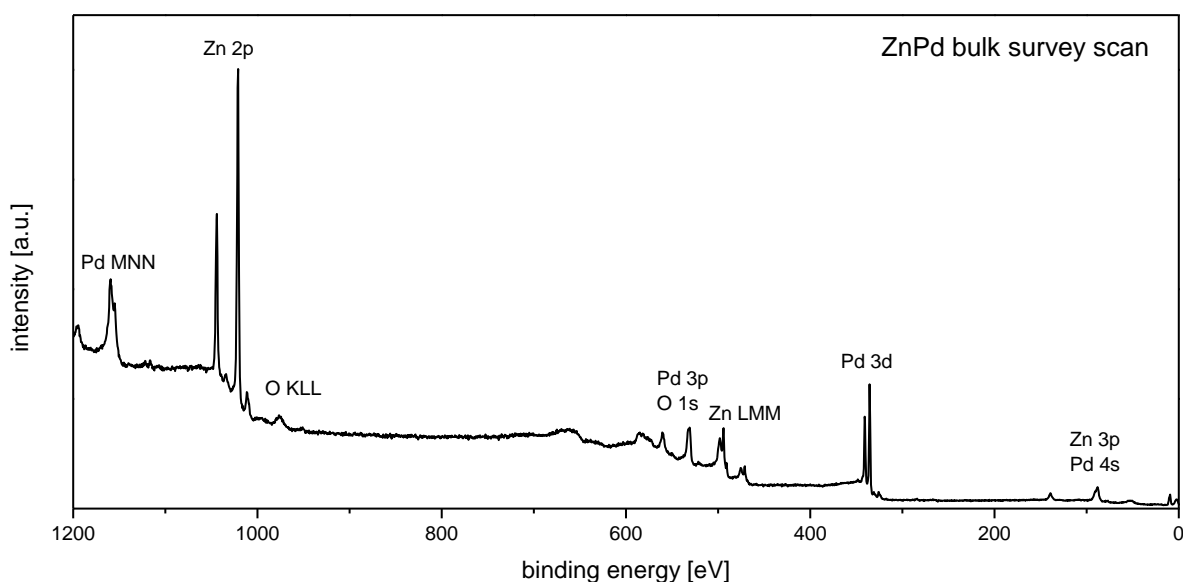


Fig. 4-7: XPS survey scan of the cleaned ZnPd sample (Al anode). The main XP and Auger peaks are labelled in the figure.

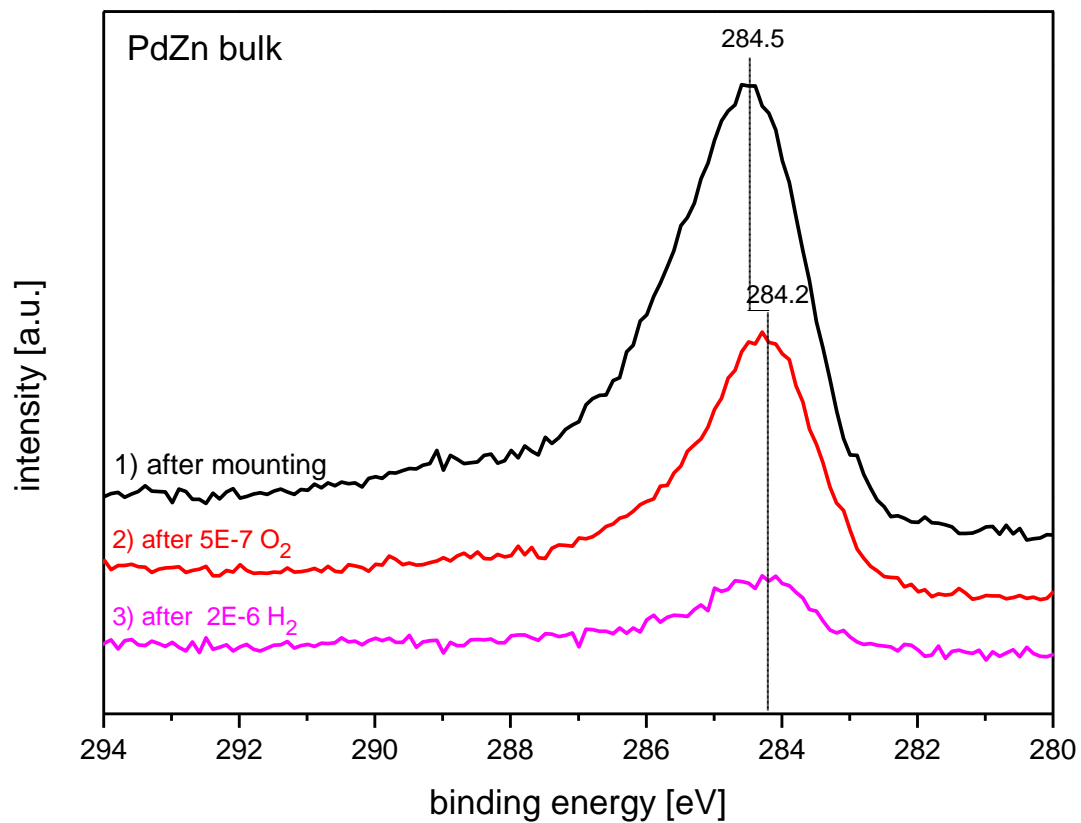


Fig. 4-8: XP C 1s signal after mounting the ZnPd bulk pellet, after oxidation in $5 \cdot 10^{-7}$ mbar O₂ at 825 K for 10 min, cooling down and then heating up in $2 \cdot 10^{-6}$ mbar H₂ to 700 K for 10 min.

4.2.2 CO and D₂O adsorption on ZnPd bulk sinter crystals

TPD and PM-IRAS measurements were performed utilizing CO as a probe molecule to study the adsorption sites available on the ZnPd bulk sinter crystal. CO-coverage dependent measurements were performed in the same way done as for PdZn/Pd(111). 0.5, 1, and 2 L dosage were used. To saturate the surface the sample was cooled down in $5 \cdot 10^{-6}$ CO from 600 K to 90 K.

Upon low CO doses (0.5 L), two overlapping desorption peaks (303 K and 325 K) are observed which do not appear in the CO TPDs from the surface alloys (see Fig. 3-34 and Fig. 3-35). These peaks also do not correlate with CO adsorbed on clean Pd ($T_{\text{des}} \geq 450$ K). Increasing the dosage (1 L) leads to a broad, asymmetric desorption peak at 280 K. Only after high or saturation dosage multiple CO desorption peaks are detected (138/212/276 K for 2 L dosage and 135/218/275 K on a saturated surface).

After this TPD cycle (see above) XPS reveals that the sample was slightly oxidized (~4% ZnO_x). It seems that the CO on the surface was partly decomposed to some carbonaceous species (~50% of the total carbon on the surface).

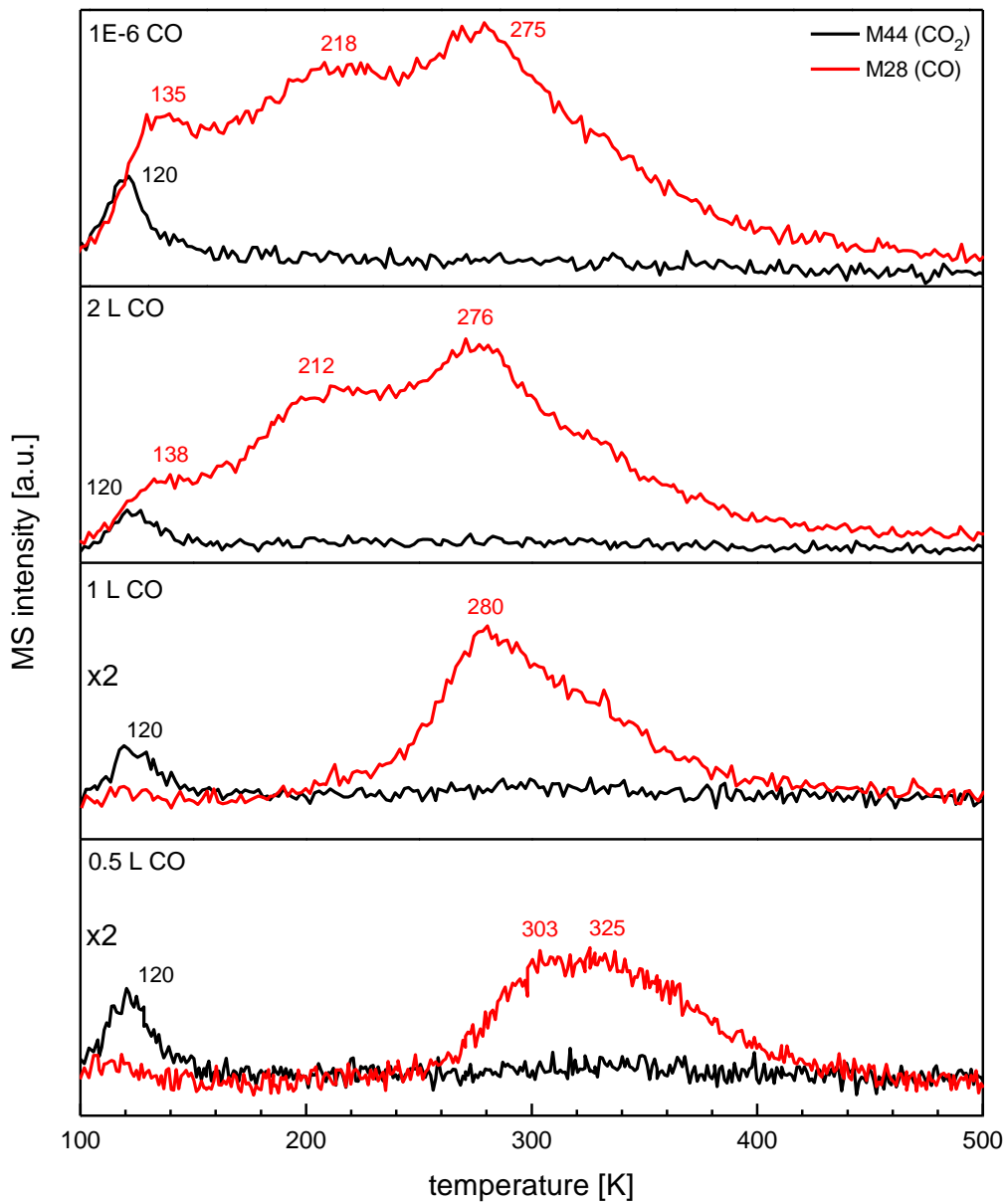


Fig. 4-9: CO/CO_2 TPD spectra after different CO exposure on the ZnPd bulk sample. For a better overview, the intensities for the spectra of 0.5 L and 1 L are magnified by the factor of 2.

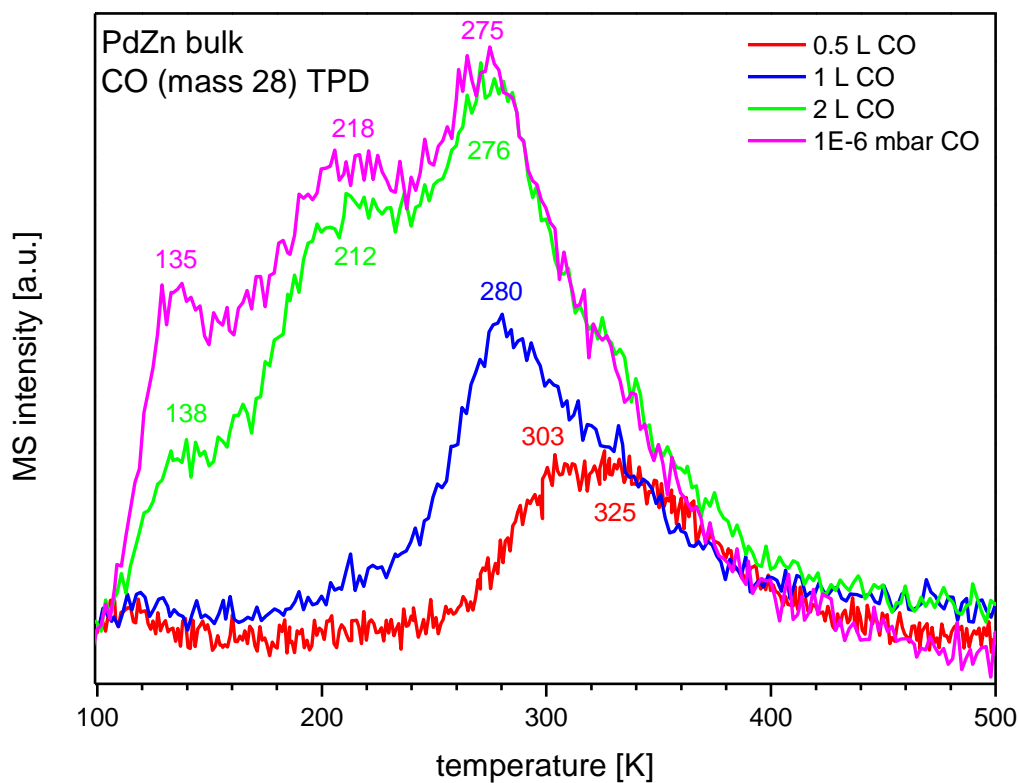


Fig. 4-10: Summarized CO TPD spectra after different CO exposures on ZnPd bulk.

The CO (mass 28) area was estimated from TPD spectra using the saturation coverage (cooling down in $5 \cdot 10^{-6}$ mbar CO) as 100%. At low dosage (up to 1 L) only about 10% of the surface is covered. Further increasing the dosage leads to a rapid increase of the coverage, at 2 L the coverage is ~90% of the saturation coverage (see Fig. 4-11).

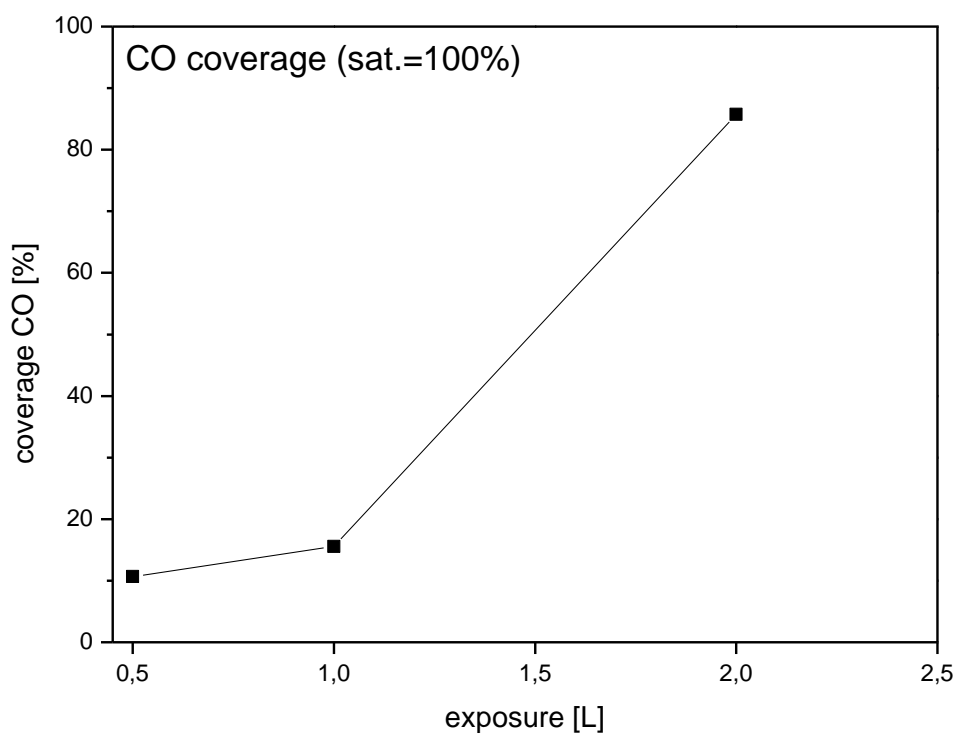


Fig. 4-11: *CO* coverage as deduced from the TPD spectra versus exposure. The saturation coverage was defined as the coverage on a sample cooled down in $5 \cdot 10^{-6}$ mbar *CO*.

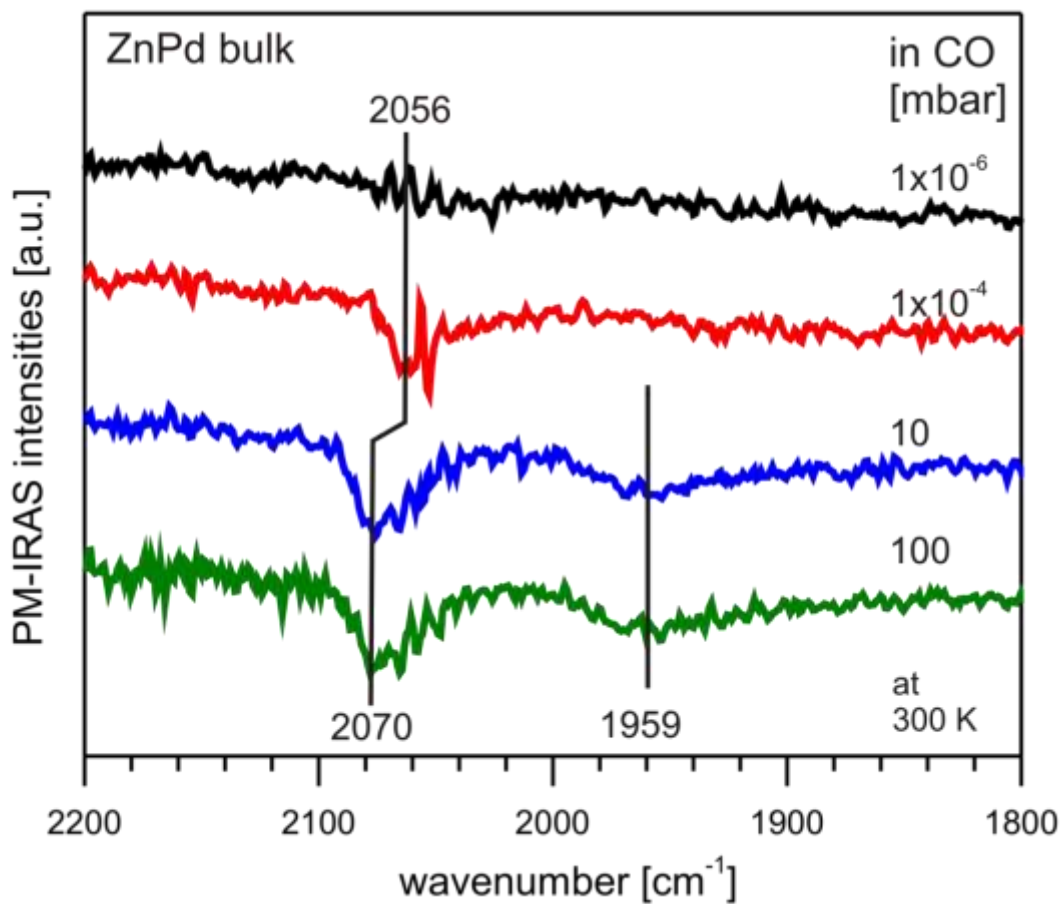


Fig. 4-12: *CO* adsorption on ZnPd observed by PM-IRAS in *CO* atmosphere. On-top *CO* can be observed at 2056-2070 cm⁻¹ and multiple-bond *CO* at 1959 cm⁻¹.

The ZnPd bulk material shows the same characteristic IR band at 2070 cm⁻¹ for *CO* on ZnPd like the surface alloys. Further multiple bound *CO* species are detected at 1959 cm⁻¹ indicating the presence of additional adsorption sites (Pd ensembles, mixed ZnPd sites?) populated only at high coverage.

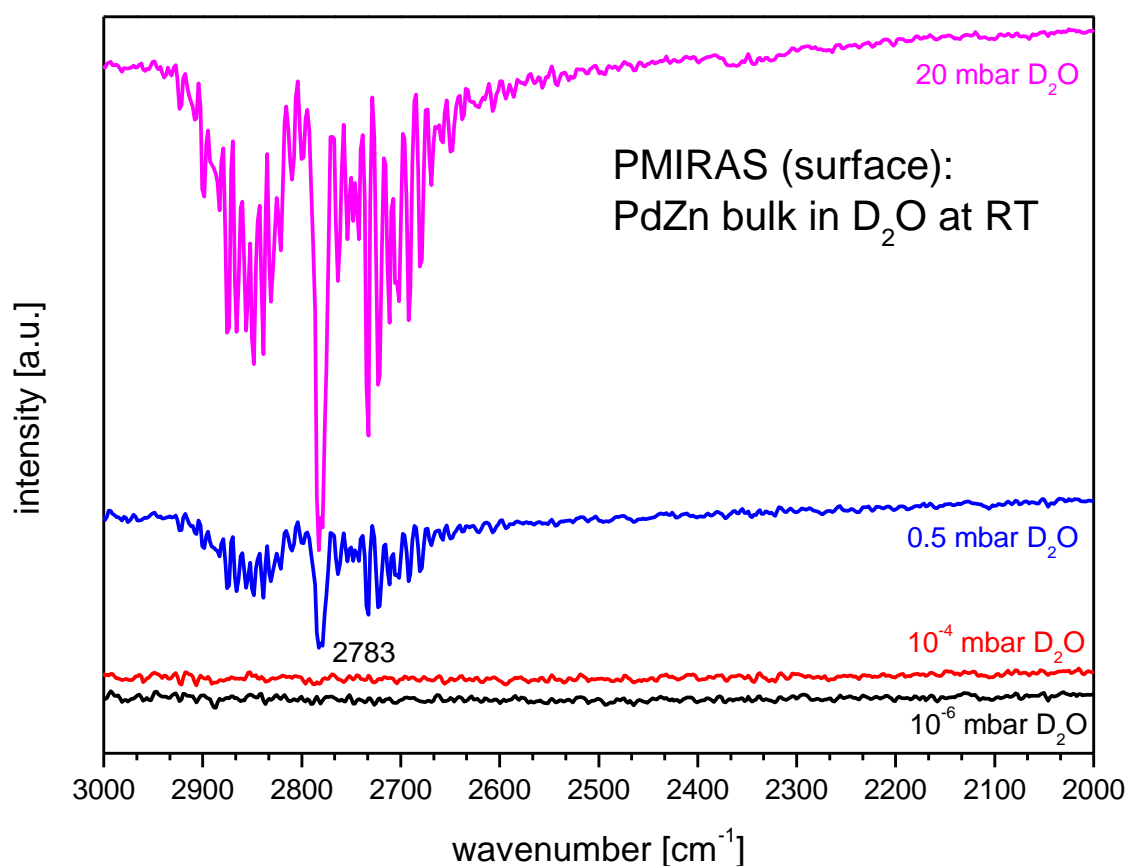


Fig. 4-13: Adsorption of D_2O on ZnPd observed by PM-IRAS in D_2O atmosphere. The broad band at $\sim 2780\text{ cm}^{-1}$, observed at high coverages is assigned to $\nu_{\text{asym}}(D_2O)$. The surface alters significantly under these conditions.

As shown in Fig. 4-13, adsorption of D_2O could not be observed by PM-IRAS at pressures below 0.5 mbar. The high carbon content after IR measurements comes probably from a contamination of the high pressure cell. The sample surface was observed through the UVH viewport a little bit “rougher” than before. With TPD no significant D_2O adsorption was observed (except a small peak after 100 L coverage). Unfortunately under these conditions the tetragonal ZnPd surface alters dramatically. These changes could be clearly seen by optical microscopy, the surface looked very rough and not “mirror-like”. These changes were also observed by XPS, this will be discussed later.

Reactions/changes on the surface of the sample as deduced from XP-spectra: a brief overview of experiments on this sample is given in Tab. 4-2 and in Fig. 4-14 – Fig. 4-16. As mounted (1) without any further treatment the sample was significantly oxidized and covered with carbonaceous species. After a couple of cleaning cycles (2), see chapter 4.2 for details, the surface was oxide- and carbon-free. After CO-TPD experiments (3) the surface was slightly oxidized (Zn 3d; valence band slightly shifted) and almost carbon-free. The CO on the surface was partly (~50%) decomposed to some carbonaceous species. After cleaning again (4), the sample looks like in (2). After PM-IRAS experiments with CO as adsorbate, the sample is oxide-free but significantly covered with carbon (again it seems that CO is decomposed to ~50% carbonaceous species). PM-IRAS experiments with D₂O at 20 mbars increased the roughness of the surface, but no ZnO was observed on the surface (6). After this step the sample had to be remounted due to a detached thermocouple wire. During the next experiments and cleaning cycles (7, 8, 9, 10), the surface was significantly oxidized, as deduced from the Zn 3d signal.

Tab. 4-2: Overview of XPS measurements after TPD/IR series. The numbers are also used for Fig. 4-14 – Fig. 4-16

No.	Note	ZnO	Zn 3d	Pd 3d _{5/2}	C
1	as mounted	20%	9.4 eV	335.5 eV	30%
2	cleaned	0%	9.2 eV	335.4 eV	2%
3	after CO TPD	4%	9.3 eV	335.5 eV	3%
4	cleaned	0%	9.2 eV	335.4 eV	2%
5	after CO IR	0%	9.2 eV	335.4 eV	16%
6	after D ₂ O IR	0%	9.2 eV	335.4 eV	30%
7	cleaned	9%	9.2 eV	335.3 eV	6%
8	after D ₂ O TPD	15%	9.4 eV	335.6 eV	6%
9	cleaned	10%	9.2 eV	335.4 eV	5%
10	after D ₂ O TPD	14%	9.4 eV	335.5 eV	5%

In Fig. 4-14 – Fig. 4-16 the evolution of the Zn 3d, Pd 3d and C 1s signals during the experiments are presented.

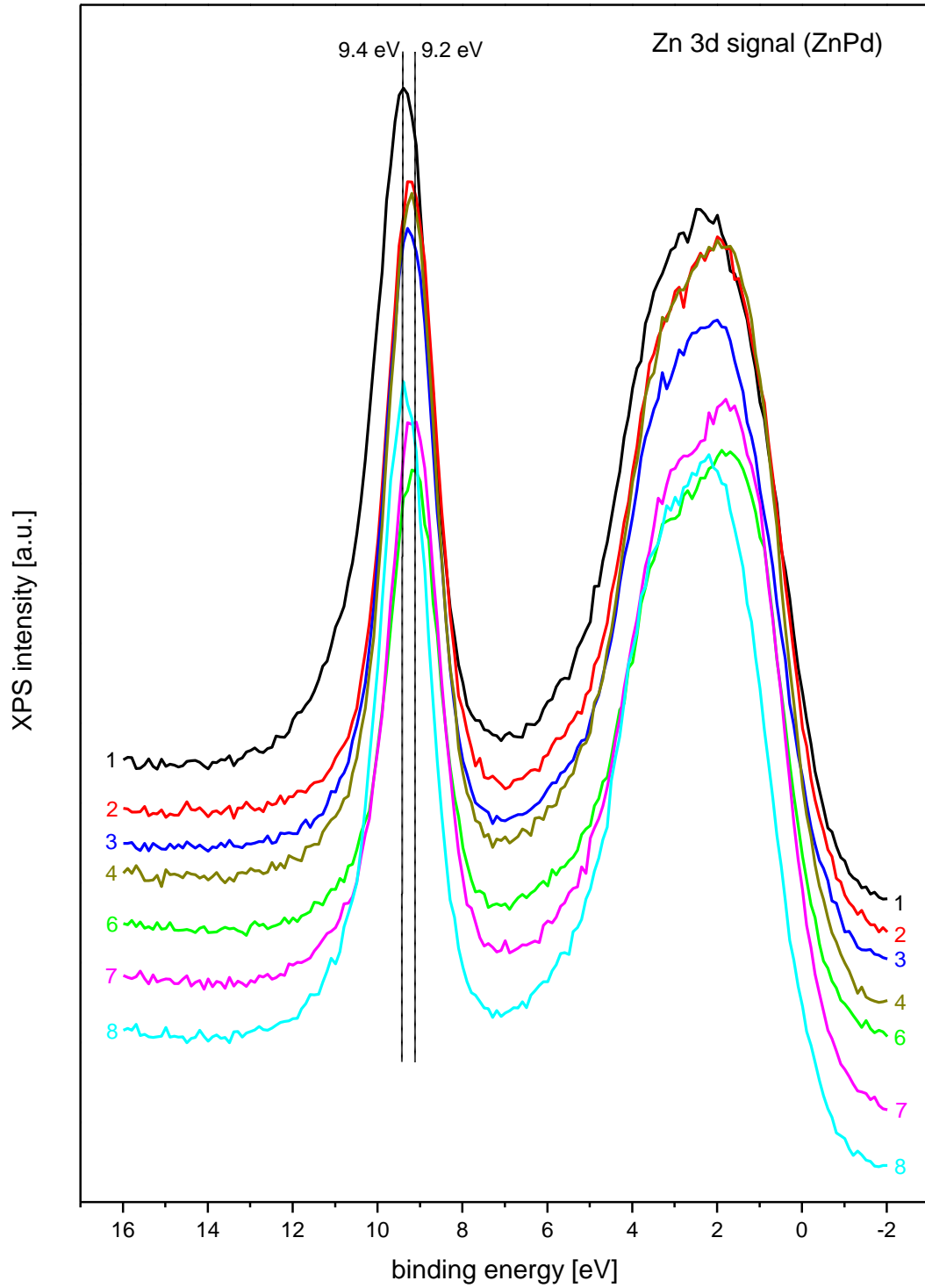


Fig. 4-14: Evolution of the Zn 3d signal during measurements on ZnPd. The numbers for labelling the spectra are taken from Tab. 4-2.

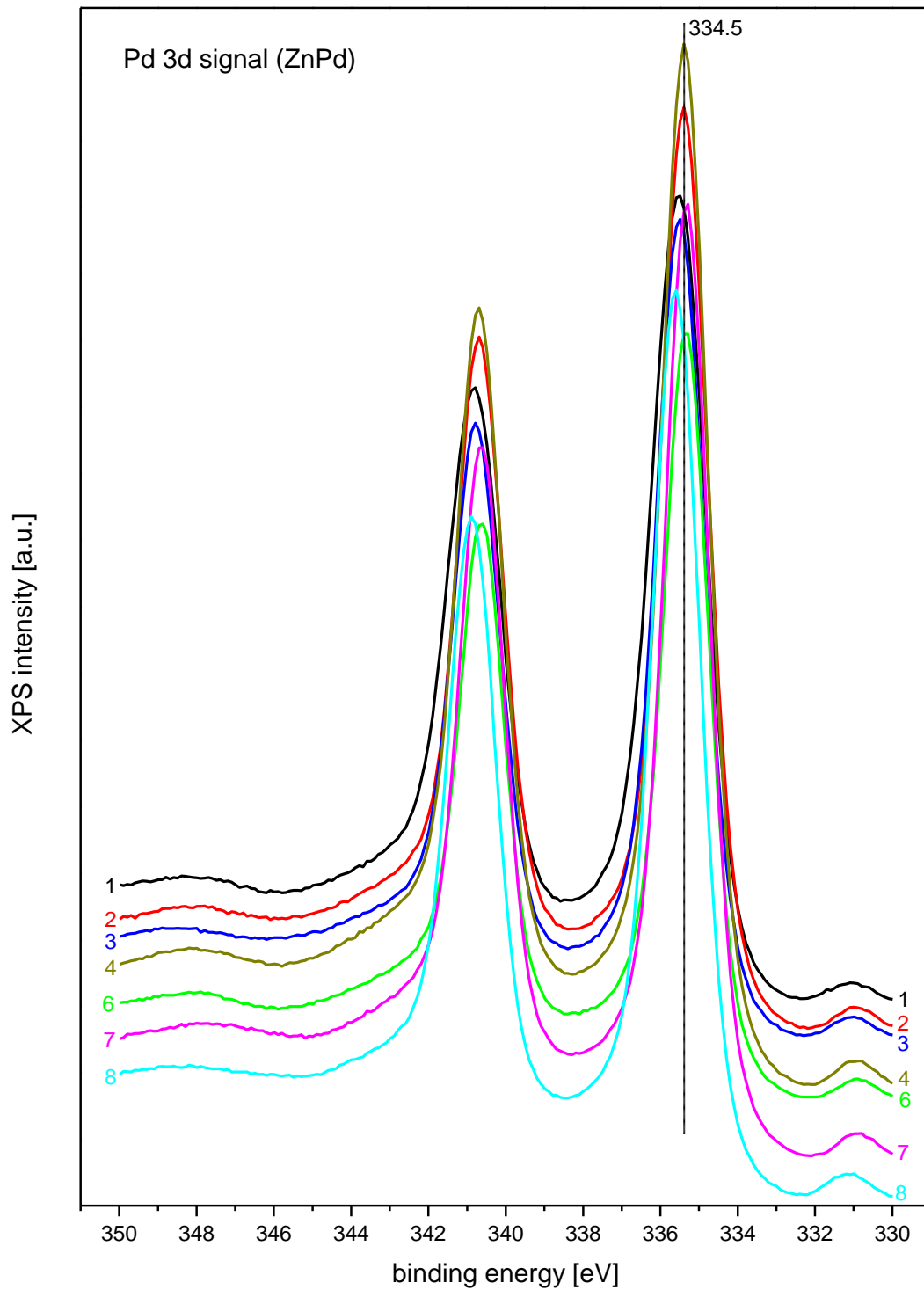


Fig. 4-15: Evolution of the Pd 3d signal during measurements on ZnPd. The numbers for labelling the spectra are taken from Tab. 4-2.

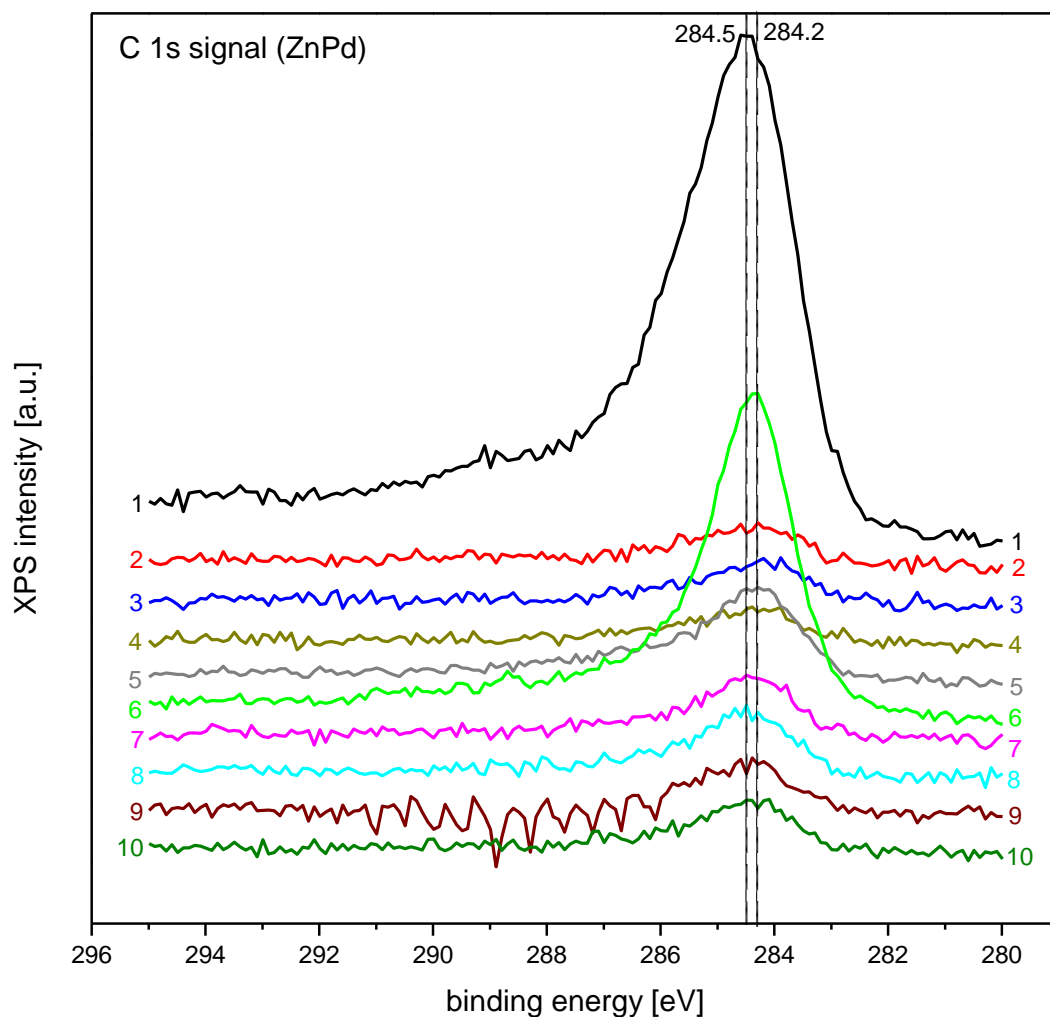
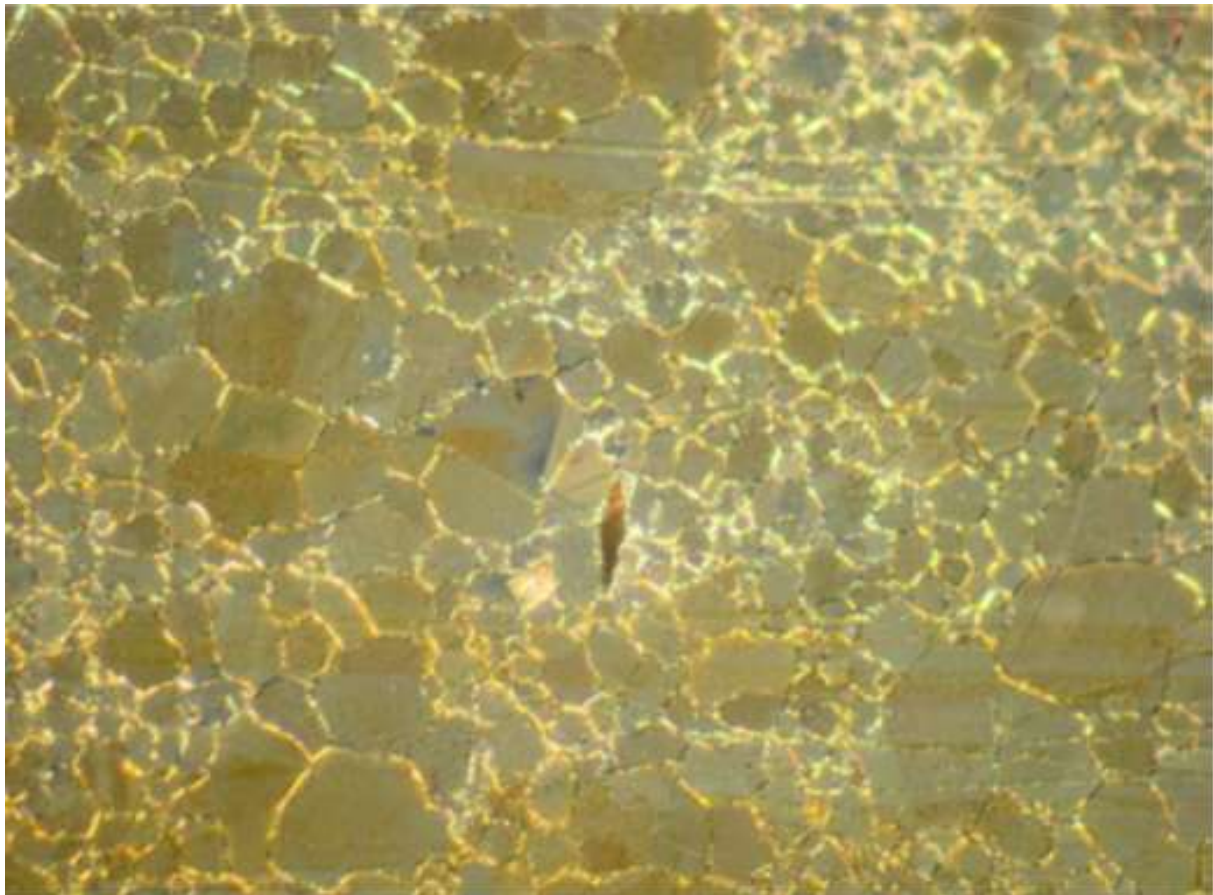


Fig. 4-16: Evolution of the C 1s signal during measurements on ZnPd. The numbers for labelling the spectra are taken from Tab. 4-2. The most intense signals were observed for the sample as mounted (1), after CO IR (5) and after D₂O IR (6).

The sample was sent back to the “Max-Planck-Institut für Chemische Physik fester Stoffe” in Dresden for further metallographic analysis. These measurements lead to the conclusion that the surface is no longer in an intermetallic state. Bright field microscopic pictures show that the grain boundaries are more pronounced and the surface of the grains look rough. With polarized light (Fig. 4-13) the grains are clearly visible. The colorization, originated from polarization as seen in Fig. 4-5, correlates with the orientation of the separate grains. After the D₂O treatment no uniform polarization colors of the grains are visible, only several greyscales were observed (Fig. 4-18).



Fig. 4-17: Reflected-light microscopic picture (magnification 200x) of the ZnPd bulk sample after D₂O adsorption at the IMC. The glass splinter (dark area) is probably a residue from the preparation process, the size is about 19x78 μm.



573 : 1

50µm

Abb. : MA760034-07

polarisiertes Licht

Fig. 4-18: Petrographic microscope pictures of the ZnPd bulk sample after D_2O adsorption (the sample was sent back to Dresden for microscopic analysis). The surface altered significantly.

Differential interference contrast (DIC) and scanning electron microscope SEM (Fig. 4-19) reveals a formation of walls around the grain boundaries. The oxygen content (oxygen is the small not labeled peak at low energy in the EDX spectra) could not be quantified but it is clearly visible that the surface is strongly oxidized and enriched with palladium (Fig. 4-20 – Fig. 4-24). This leads to the conclusion that the surface structure changed due to a combination of adsorbates and reaction temperature.

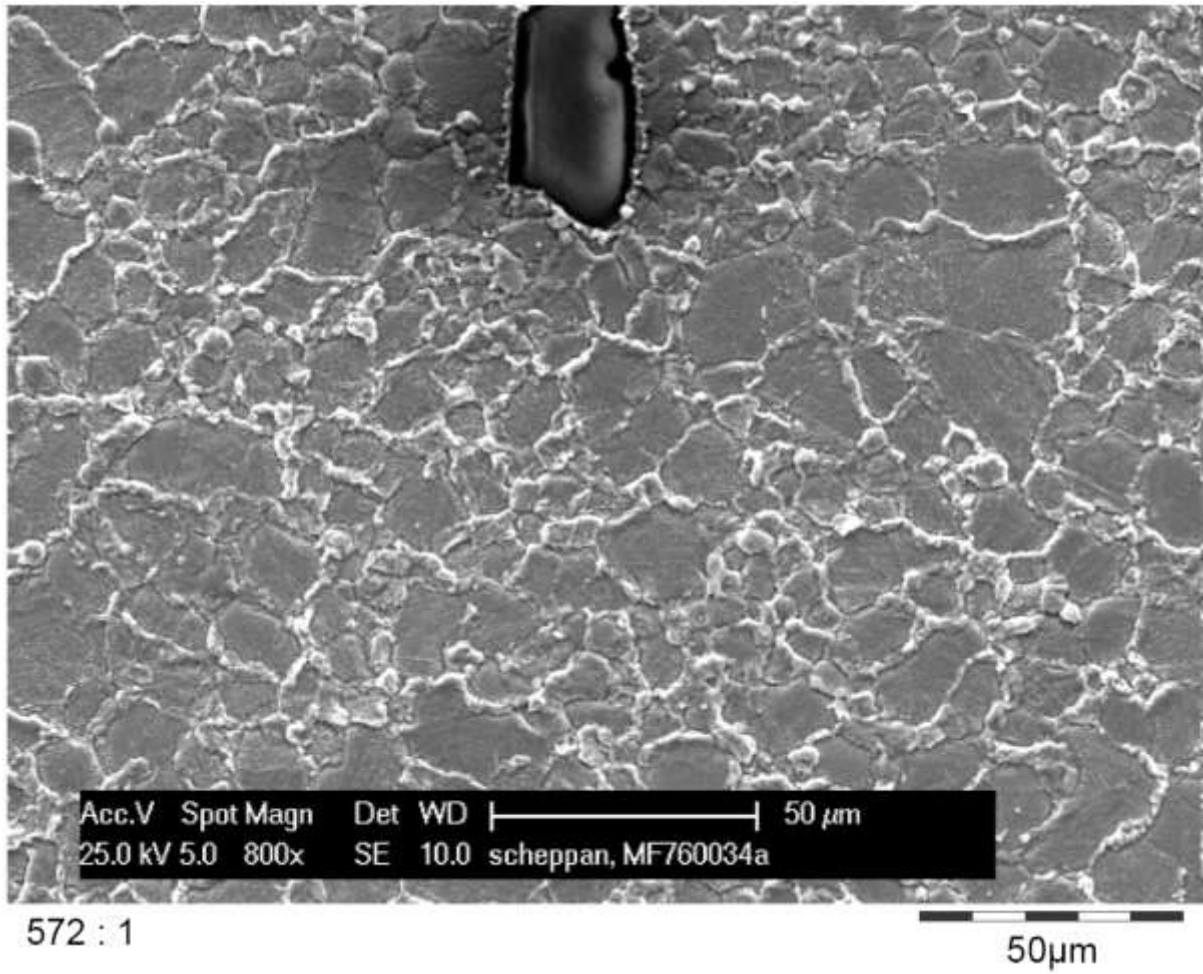


Fig. 4-19: Scanning electron microscope (SEM) analysis with secondary electrons (SE) of the ZnPd bulk sample after D_2O adsorption (the sample was sent back to Dresden for microscopic analysis). The surface altered significantly.

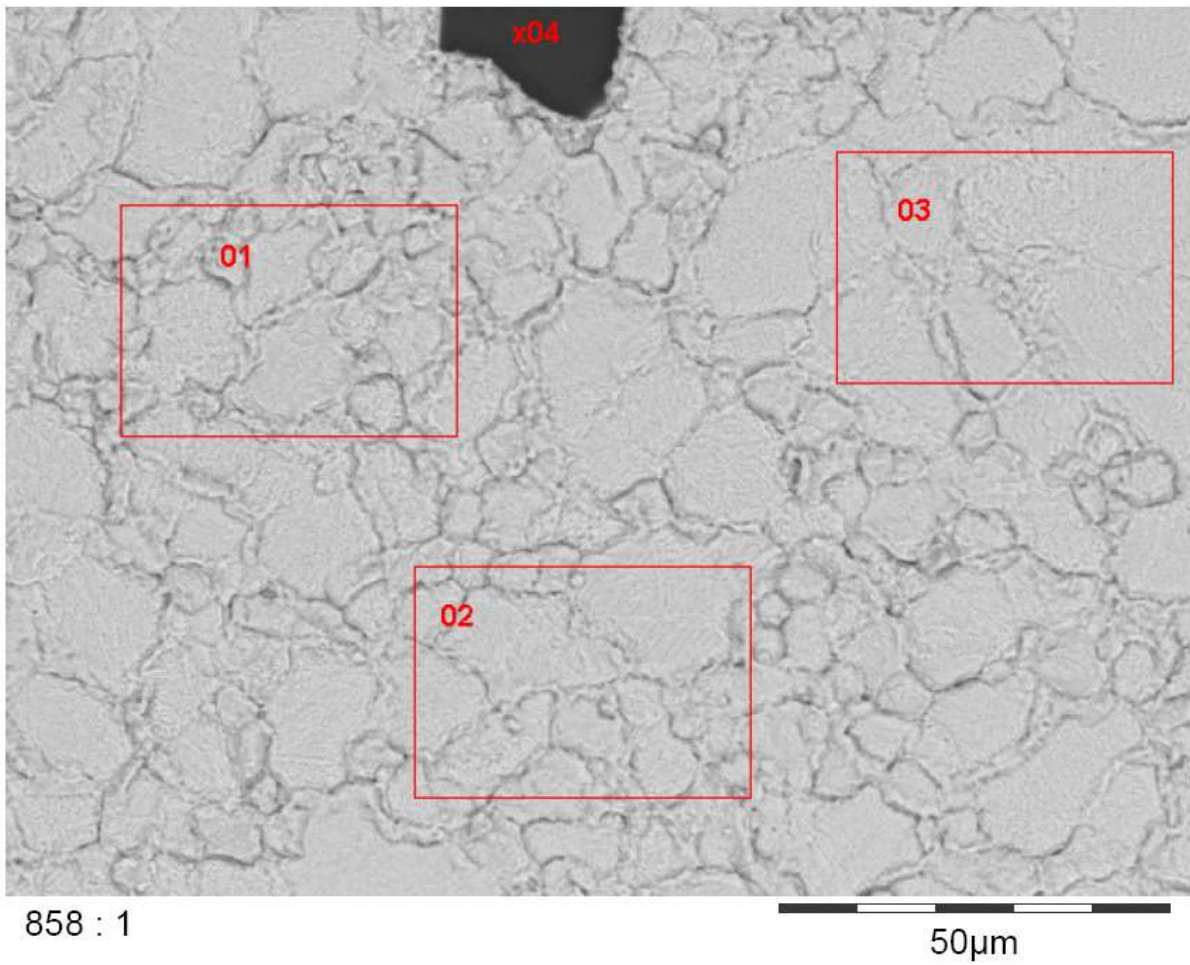
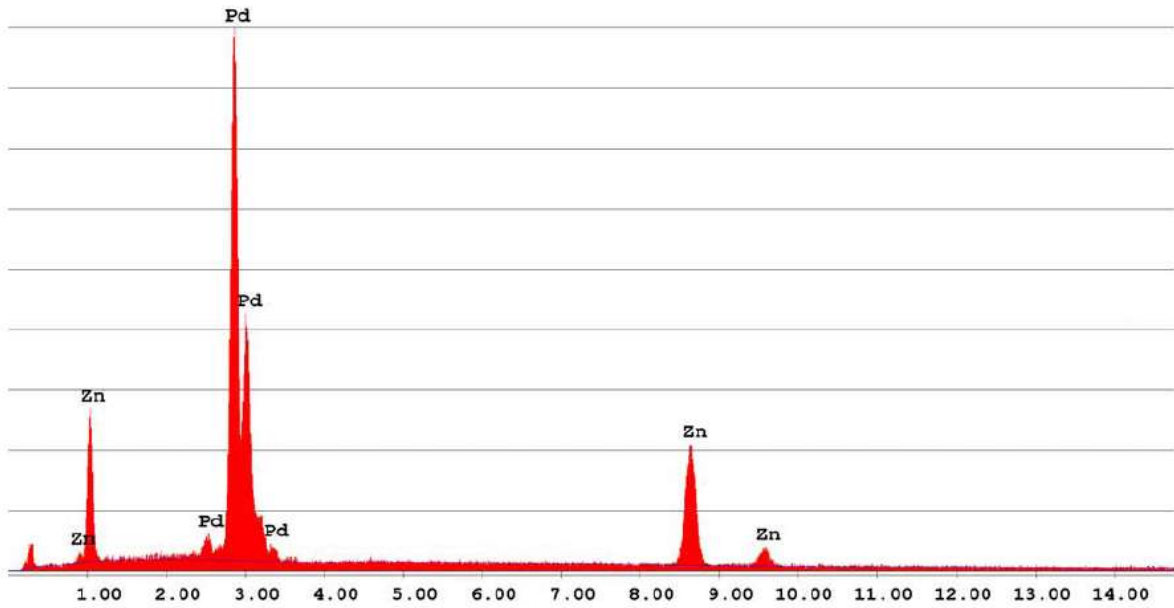


Fig. 4-20: Scanning electron microscope (SEM) analysis with back-scattered electrons (BSE) of the ZnPd bulk sample after D_2O adsorption (the sample was sent back to Dresden for microscopic analysis). The surface altered significantly.

kV:25.0 Tilt:1.5 Take-off:36.1 Det Type:SUTW+ Res:128 Tc:50

FS : 3373 Lsec : 60

2-Nov-2012 10:24:09



EDAX ZAF Quantification (Standardless)

Element Normalized

SEC Table : Default

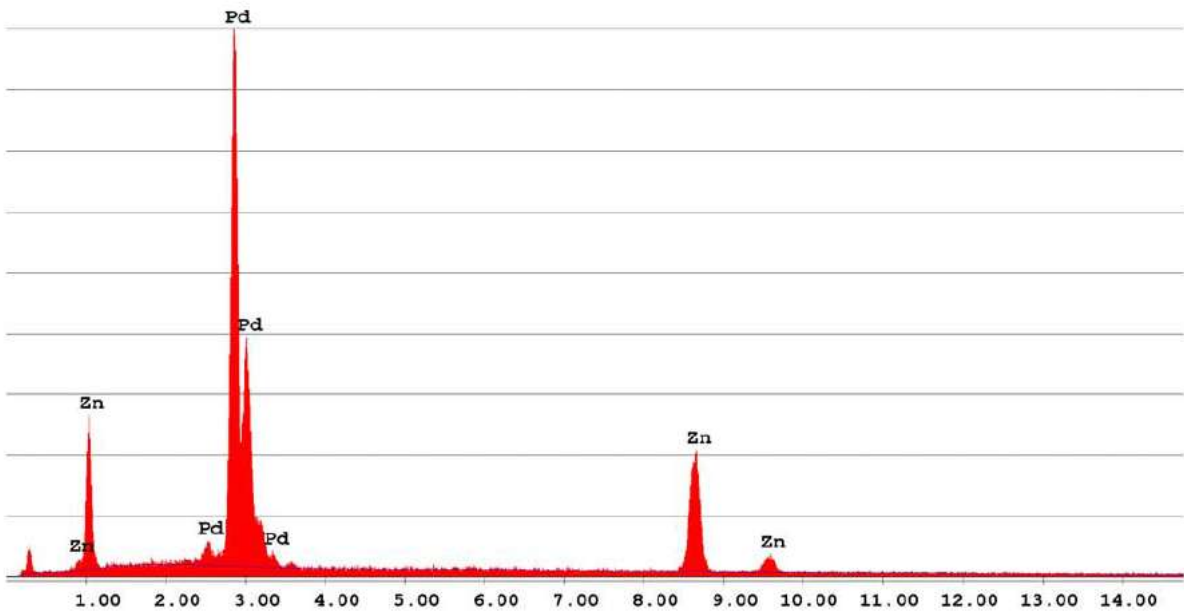
Element	Wt %	At %	K-Ratio	Z	A	F
PdL	67.34	55.89	0.5909	0.9687	0.9058	1.0000
ZnK	32.66	44.11	0.3299	1.0590	0.9541	1.0000
Total	100.00	100.00				

Element	Net Inte.	Bkgd Inte.	Inte. Error	P/B
PdL	392.82	9.23	0.67	42.54
ZnK	139.67	6.90	1.15	20.24

Fig. 4-21: Energy-dispersive X-ray spectroscopy (EDX) analysis from area 01 (see Fig. 4-20) of the of the ZnPd bulk sample after D_2O adsorption (the sample was sent back to Dresden for microscopic analysis). The surface was oxidized (especially on the grain boundaries) and enriched with Pd.

kV:25.0 Tilt:1.5 Take-off:36.1 Det Type:SUTW+ Res:128 Tc:50
 FS : 3601 Lsec : 60

2-Nov-2012 10:27:06



EDAX ZAF Quantification (Standardless)
 Element Normalized
 SEC Table : Default

Element	Wt %	At %	K-Ratio	Z	A	F
PdL	67.54	56.10	0.5931	0.9689	0.9063	1.0000
ZnK	32.46	43.90	0.3280	1.0592	0.9540	1.0000
Total	100.00	100.00				

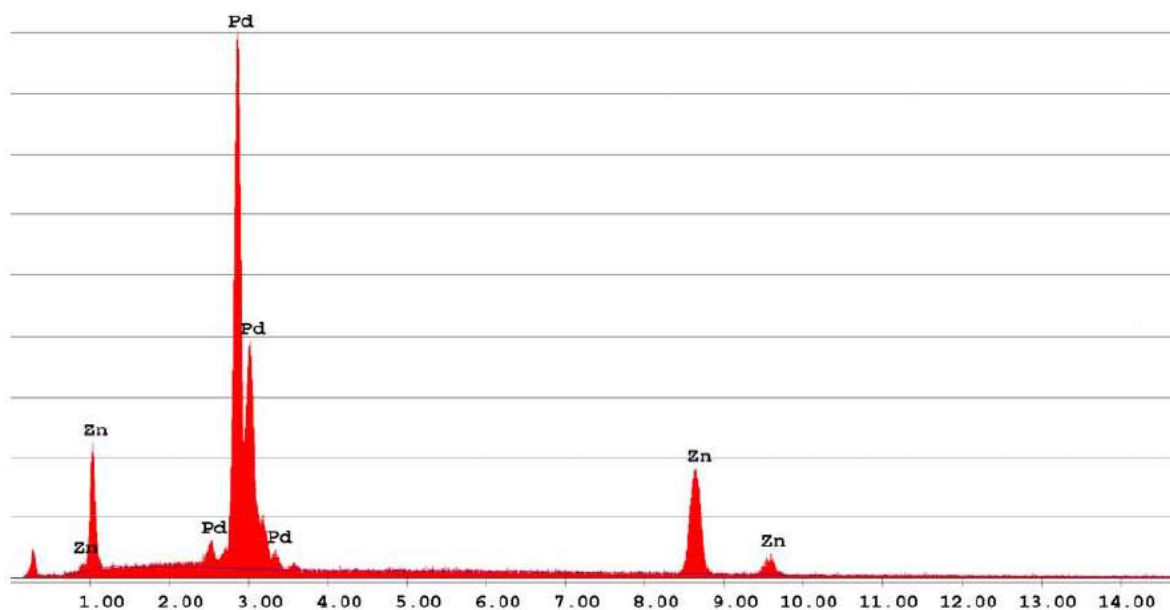
Element	Net Inte.	Bkgd Inte.	Inte. Error	P/B
PdL	414.58	10.42	0.65	39.80
ZnK	146.02	6.67	1.12	21.90

Fig. 4-22: Energy-dispersive X-ray spectroscopy (EDX) analysis from area 02 (see Fig. 4-20) of the ZnPd bulk sample after D_2O adsorption (the sample was sent back to Dresden for microscopic analysis). The surface was oxidized (especially on the grain boundaries) and enriched with Pd.

kV:25.0 Tilt:1.5 Take-off:36.1 Det Type:SUTW+ Res:128 Tc:50

FS : 3966 Lsec : 60

2-Nov-2012 10:30:19



EDAX ZAF Quantification (Standardless)

Element Normalized

SEC Table : Default

Element	Wt %	At %	K-Ratio	Z	A	F
PdL	69.66	58.52	0.6169	0.9708	0.9121	1.0000
ZnK	30.34	41.48	0.3067	1.0612	0.9526	1.0000
Total	100.00	100.00				

Element	Net Inte.	Bkgd Inte.	Inte. Error	P/B
PdL	457.93	10.37	0.62	44.17
ZnK	145.00	8.17	1.13	17.76

Fig. 4-23: Energy-dispersive X-ray spectroscopy (EDX) analysis from area 03 (see Fig. 4-20) of the of the ZnPd bulk sample after D_2O adsorption (the sample was sent back to Dresden for microscopic analysis). The surface was oxidized (especially on the grain boundaries) and enriched with Pd.

kV:25.0 Tilt:1.5 Take-off:36.1 Det Type:SUTW+ Res:128 Tc:50

FS : 6606 Lsec : 51

2-Nov-2012 10:41:50

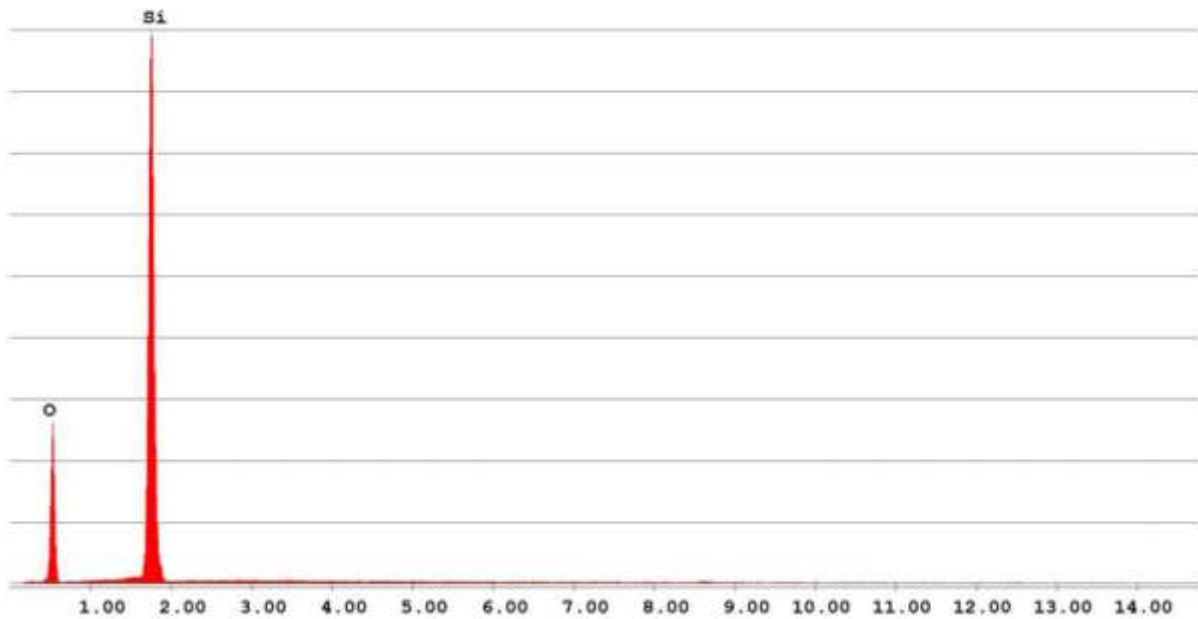


Fig. 4-24: Energy-dispersive X-ray spectroscopy (EDX) analysis from area x04 (see Fig. 4-20) of the of the ZnPd bulk sample after D_2O adsorption (the sample was sent back to Dresden for microscopic analysis). The SiO_2 grain is most probably originated from the manufacturing process.

4.2.3 MeOH desorption on ZnPd

Fig. 4-25 and Fig. 4-26 shows TPD spectra of desorption of methanol on ZnPd after dosing 1 L, 2 L, 5 L, 10 L of methanol (a correction factor of 1.9, according to the manual, was considered for the ion gauge). In addition the sample was cooled down from 500 K to 90 K in 10^{-7} mbar *MeOH* to definitely saturate the surface and a TPD was recorded. A heating rate of 90 K per minute (as also used for the CO-TPD's in this work) was used. A pronounced sharp desorption peak for *CH₃OH* was found at 157 K (the M28 and M30 peaks at this temperature are fragments of the MS ionization process). For low dosage (1 L and 2 L) a weak and very broad desorption peak of *CO* desorption was found in the range of 270 to 400 K (see Fig. 4-25). At higher dosage and on the saturated surface this feature was not observed. An explanation is (coverage dependent) reactions on the “new adsorption sites” which were observed with *CO* as probe molecule. Another explanation is possible interactions with background water, adsorbed on the surface. At higher dosages and on the methanol saturated surface (the sample was cooled down from a temperature above the desorption temperature of water) less water is available on the surface. The desorption temperature of water was recorded with a peak at 163 K (not shown). This is slightly lower than on Pd(111) with 166 K and higher than on PdZn/Pd(111) (155 K). The peak shape of MeOH desorption is similar to the TPDs recorded for Pd(111) and PdZn/Pd(111). The desorption temperature of methanol is 157 K for 1 L – 10 L dosed on the surface and slightly higher on the saturated surface (161 K). This is similar to the desorption temperatures recorded for Pd(111) (150 K) and PdZn/Pd(111) (165 K). In contrast to the Pd(111) system the pronounced CO peak at ~461 K was not observed.

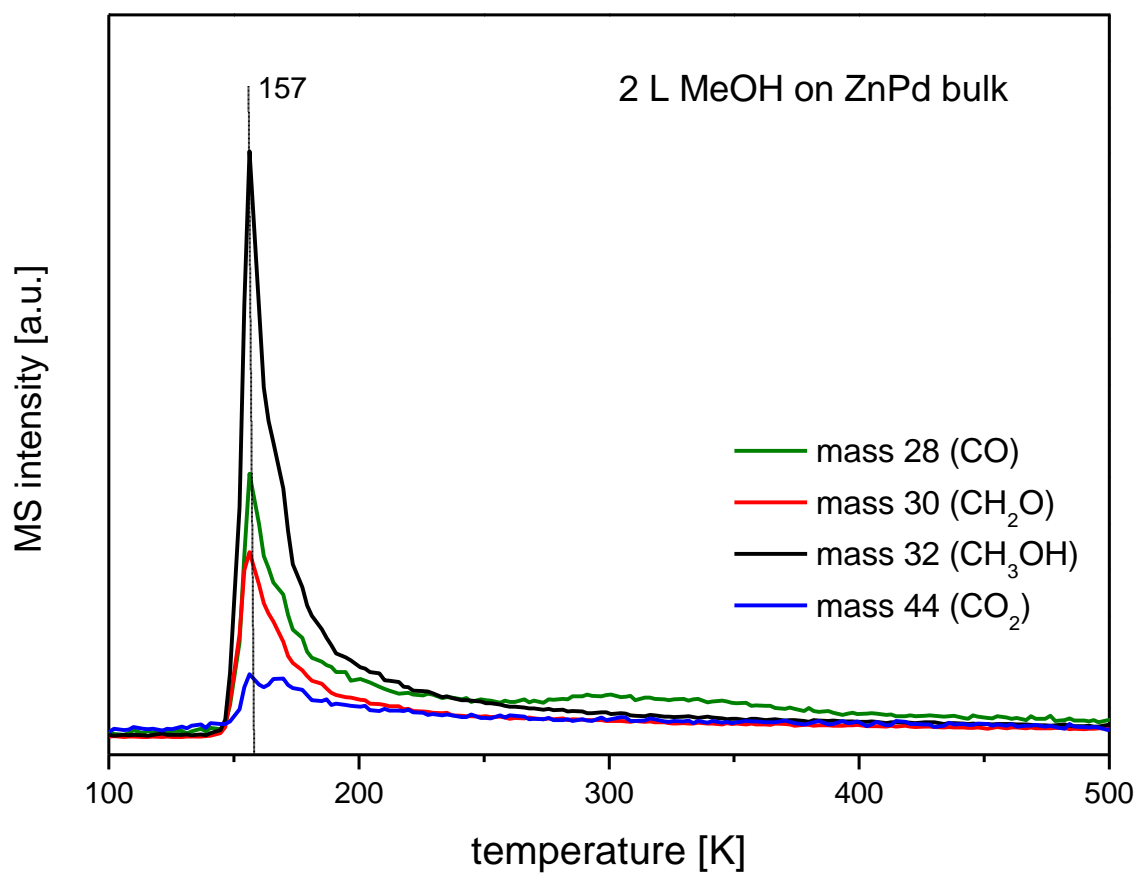


Fig. 4-25: TPD spectra for CO , CH_2O , CH_3OH , and CO_2 after dosing of 2 L methanol at 90 K on ZnPd bulk.

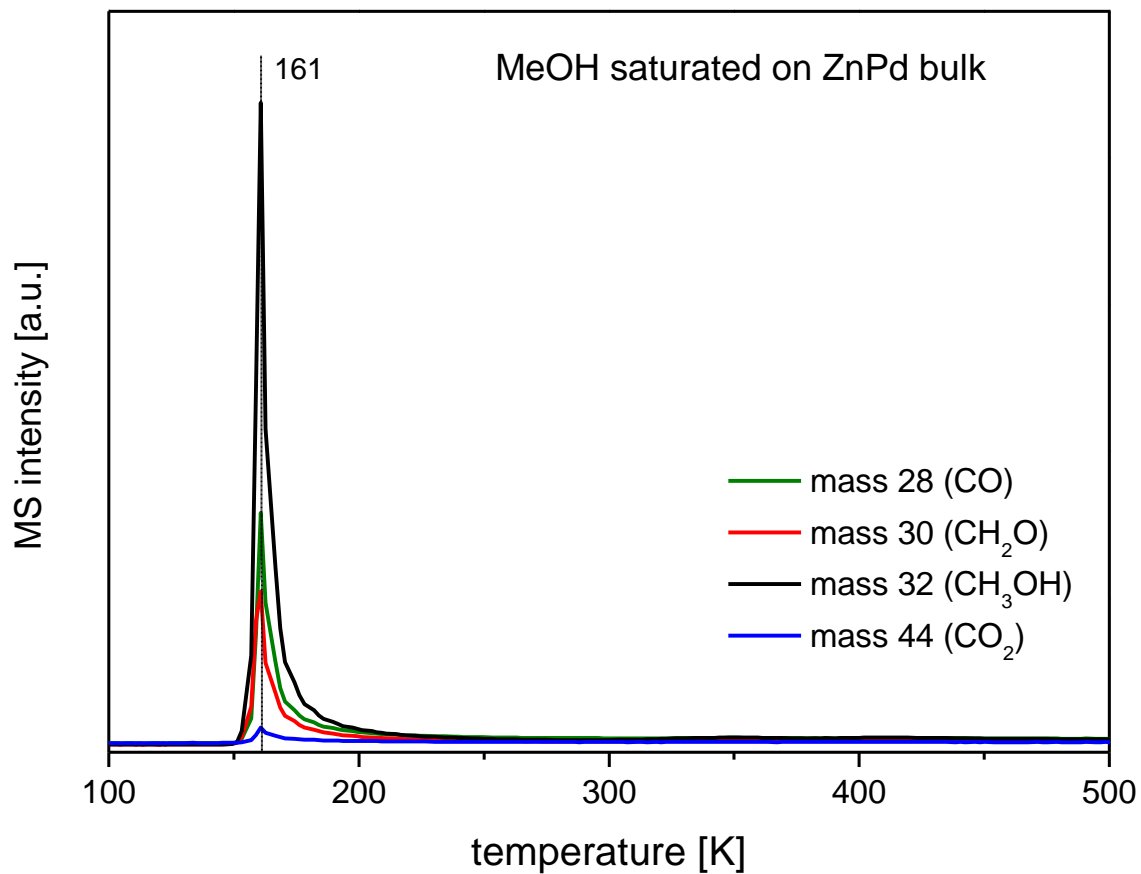


Fig. 4-26: TPD spectra for CO , CH_2O , CH_3OH , and CO_2 on a methanol saturated PdZn bulk surface (sample was cooled down in $1E-7$ mbar MeOH from 500 K to 90 K).

4.3 Pd₂Zn

The group of A. Datye [271] prepared a Pd-Zn system with an oxide (enclosed in a quartz capillary) using a Zn(NO₃)₂ solution as precursor and progressively heated it from room temperature to 600°C in H₂-flow. From XRD data they deduced it to a Pd₂Zn phase. Unfortunately the provided sample was not regularly shaped which makes it difficult to mount it to our system. The other problem was that the pellets were not polished, the surface was very rough with some enclaves (see Fig. 4-27 and Fig. 4-28).



Fig. 4-27: Picture of the Pd₂Zn pellet. The surface is rough and non-uniform, also some contaminations/enclaves in the bulk can be seen.

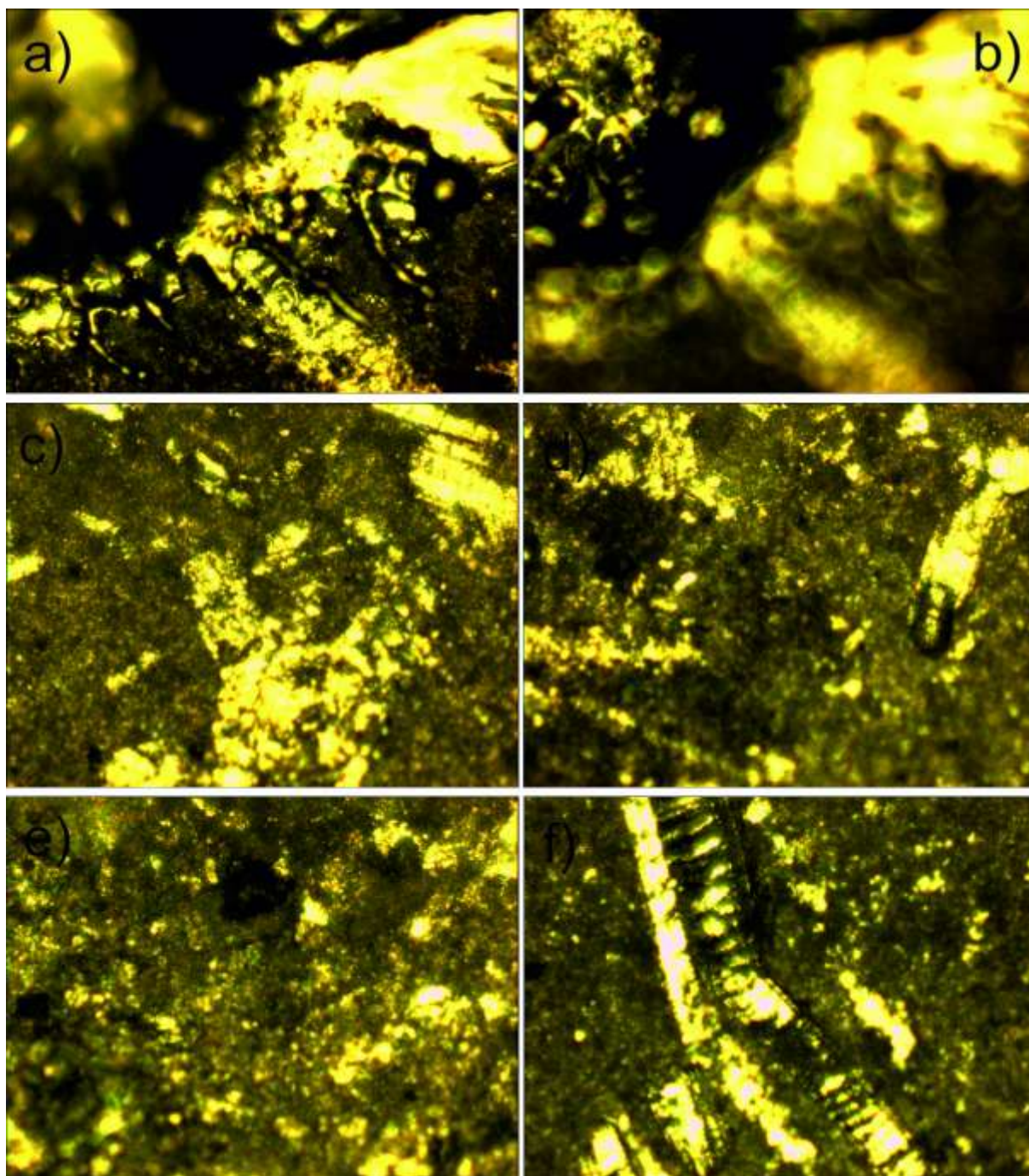


Fig. 4-28: Microscopic image (magnification 200x) of the Pd₂Zn surface. Picture a) and b) shows the boundary of the big enclave (elliptical shaped region with high reflectivity shown in Fig. 4-27). Pictures c) – f) shows different regions of the surface where no enclaves are visible to the naked eye.

This makes it difficult to compare the measurements with well polished surface alloys or bulk crystals. Since the pellets were too thin and brittle for mechanical treatment (making a groove to mount it in the usual way for the XPS system) a workaround was used. It was possible to attach a pellet on a small tantalum foil which was then mounted with tantalum wires to the Mo rods. The main problem was to get a good thermal contact. Therefore the TPD heating ramp was not that linear as for regular samples in our system. Also due to the

nonuniform thickness distance of the nozzle of the MS to the sample surface was bigger than for all other samples used in this thesis. Anyway *CO* and *MeOH* TPD series were measured and are shown in Fig. 4-31 and Fig. 4-32.

Furthermore it was not possible to use this sample pellets for our PM-IRAS setup.

From XPS measurements (see Fig. 4-29 and Fig. 4-30), the elemental Pd:Zn ratio is 2.1:1 which fits well to the sample specifications. As mentioned in chapter 4.2 the sample needs to be cleaned without sputtering by oxidation/reduction cycles and the same treatment was chosen. Even after 30 cleaning cycles it was not possible to get a completely carbon-free surface. It is to be assumed that the source of carbon is in the bulk (probably from the preparation process) and cannot be removed in that way. But the sample was considered that the sample clean enough for TPD experiments described later in this chapter. In the carbon region (Fig. 4-30) a peak at 284.0 eV (elemental carbon) and a less intense peak at 292.5 eV (probably carbonates) is visible. The Pd 3d_{5/2} peak at 335.1 eV, which is in good agreement of the measured peak position of the PdZn sample described in chapter 4.2.

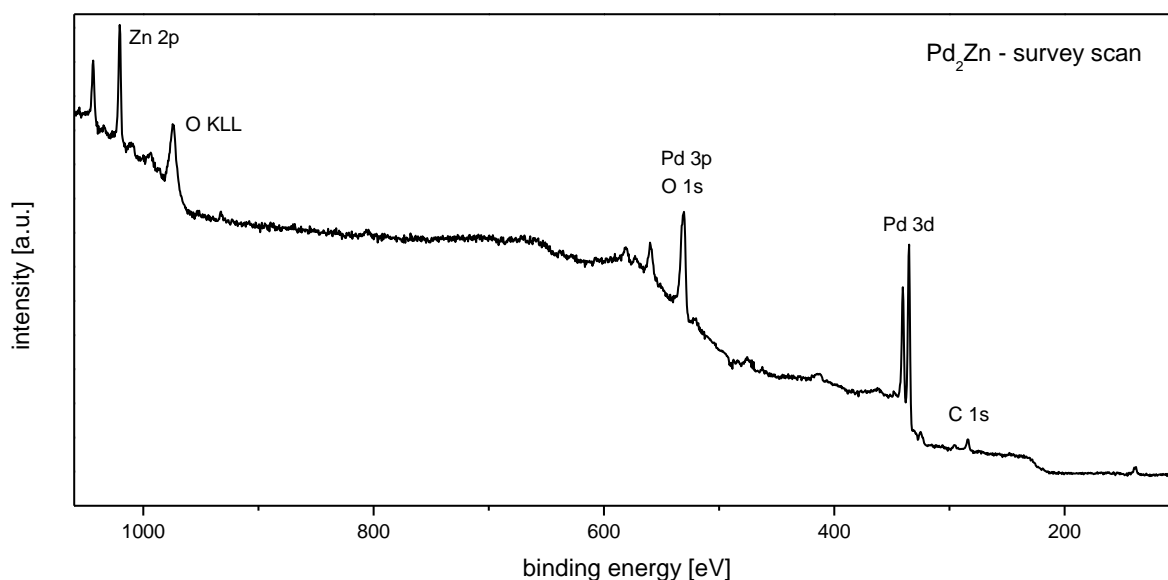


Fig. 4-29: XPS survey scan of the cleaned Pd₂Zn sample.

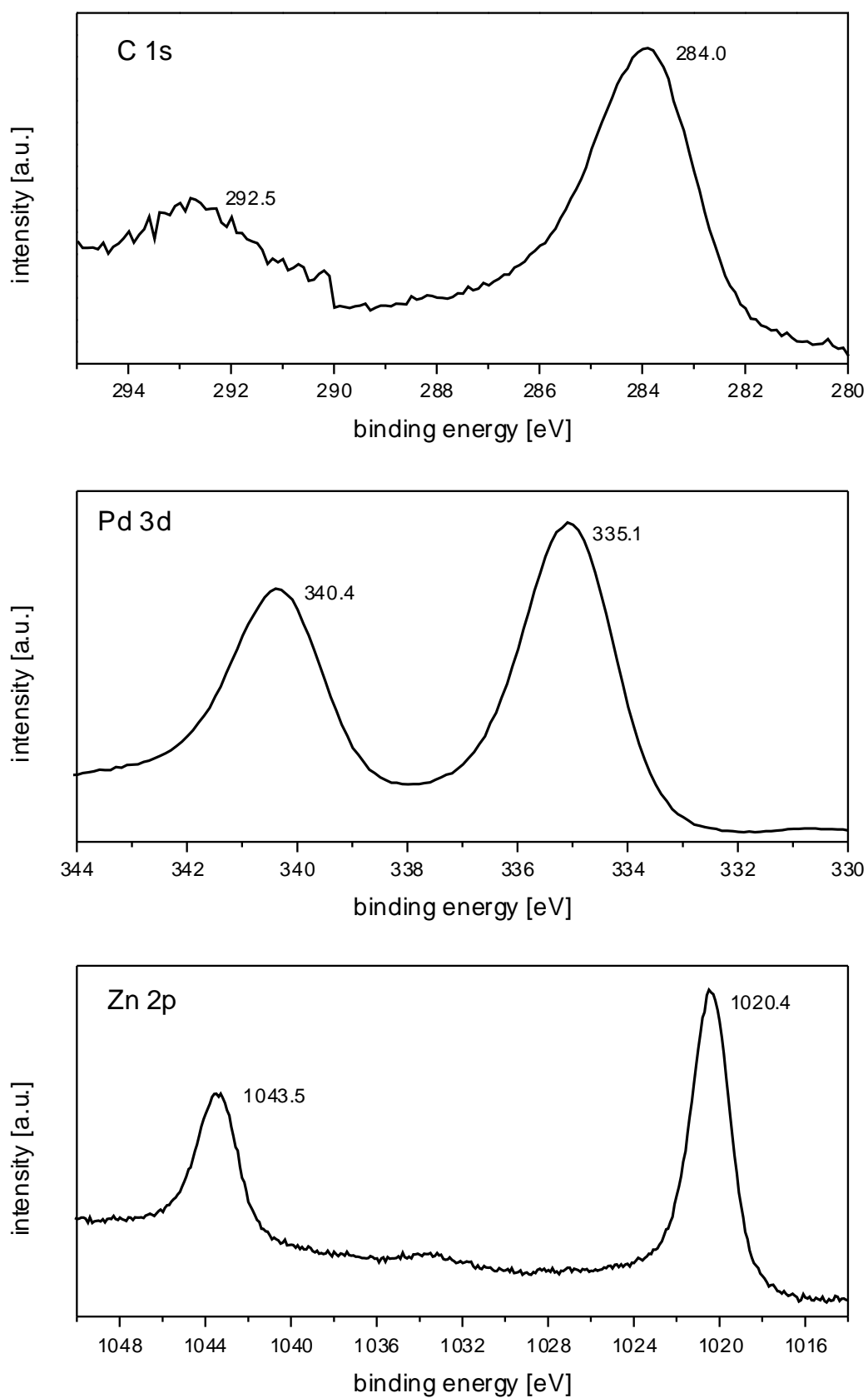


Fig. 4-30: C 1s, Pd 3d, and Zn 2p XPS regions of the Pd₂Zn sample.

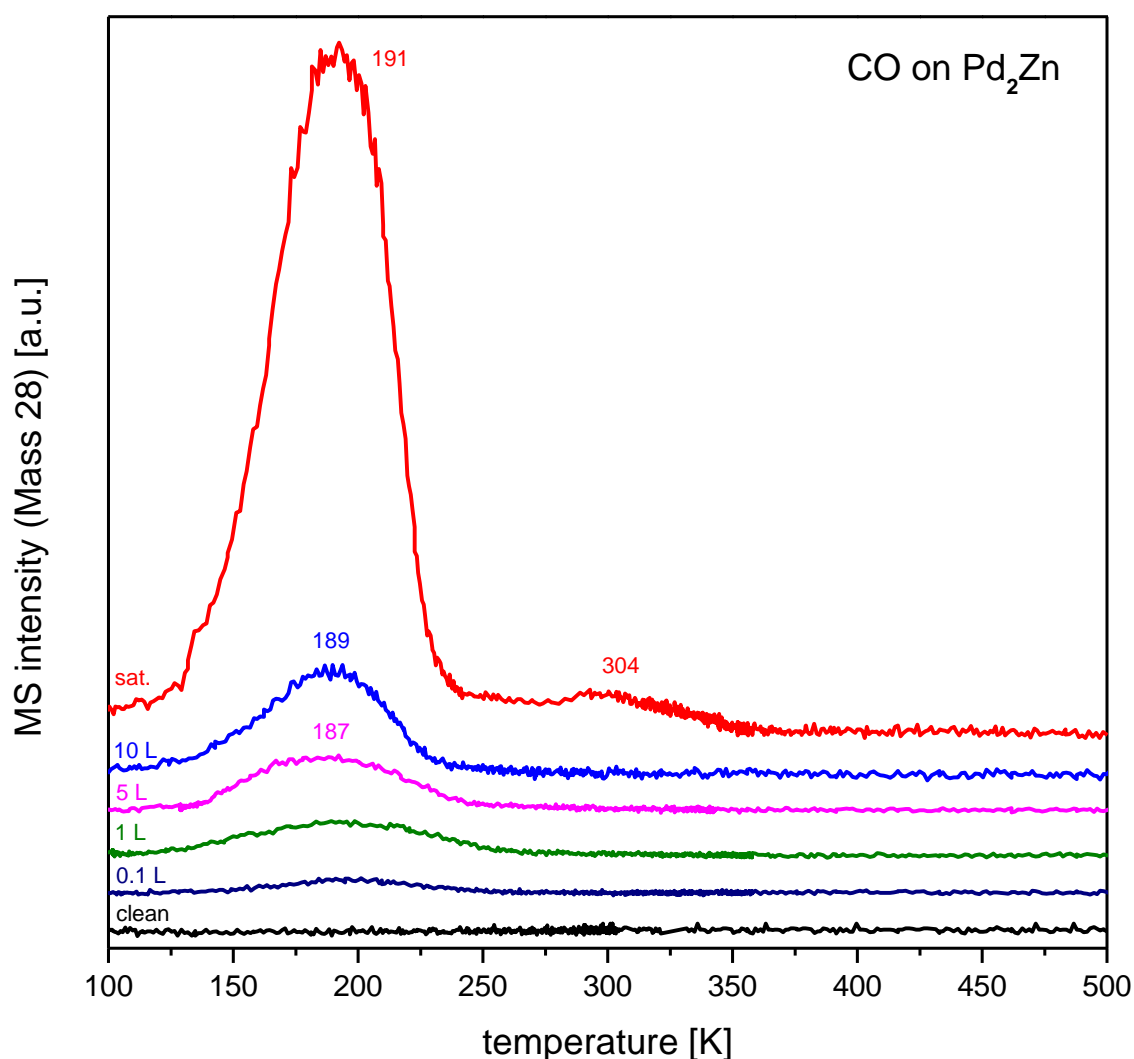


Fig. 4-31: CO TPD on a (non-polished) Pd₂Zn pellet. Sample surface, shape and mounting conditions differs from polished Pd(111) and ZnPd discs. The saturated CO adsorption (“sat.”) was prepared by cooling down the sample in 10E-6 mbar CO from 500 K to 100 K.

The big tailing in TPD spectra in general is probably a reason of the bad thermal contact as mentioned before. The CO TPD (Fig. 4-31) differs from the TPD of ZnPd bulk and surface alloy. The desorption temperature is higher than on PdZn/Pd(111) and ZnPd bulk. Only in the TPD of saturated CO a second feature was observed. Probably some features are unresolved and some adsorption sites are blocked by residual carbon or background water. The desorption temperature of methanol (Fig. 4-32) is 158 K which is comparable to the desorption temperature of the ZnPd bulk crystal and the surface alloy. Also a significant CO feature at ~351 K is observable but is probably a result of the metallic enclaves in the sample pellet. Therefore the catalytic properties remain unclear with this combination of sample shape and experimental setup.

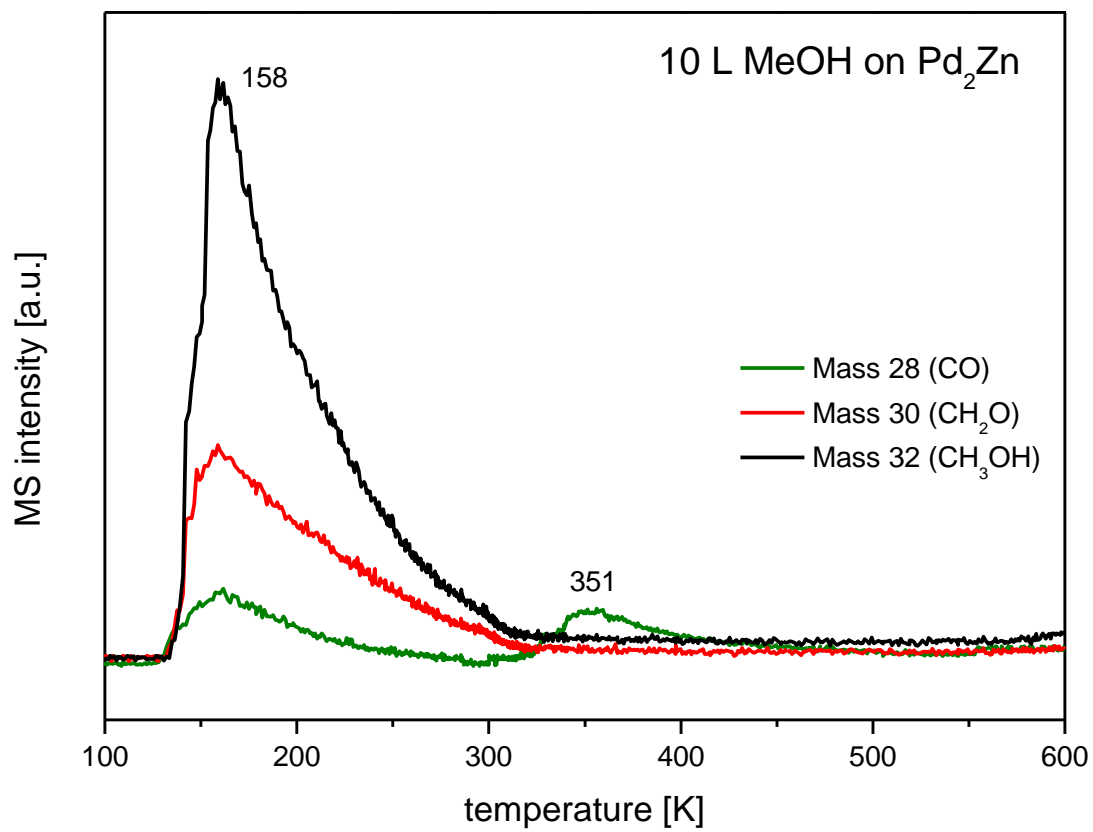


Fig. 4-32: 10 L MeOH TPD on a (non-polished) Pd₂Zn pellet.

4.3.1 Summary

In this summary only the ZnPd sinter crystal provided by Marc Armbrüster will be discussed as other Pd₂Zn materials described in chapter 0 were not suitable for our system and the results are not reasonably comparable. The Pd₂Zn in the condition we received could be probably more interesting to be compared with powder samples.

ZnPd surface alloys could be characterized by a sharp, characteristic IR band of linear adsorbed CO at $\approx 2070\text{ cm}^{-1}$ and a corresponding CO-TPD desorption peak around 200 K with a shoulder at 170 K. The same features could also be identified in the spectra obtained from the bulk ZnPd crystal, indicating the presence of the same kind of adsorption sites on both systems. However, on the ZnPd bulk materials additional features were observed, i.e. IR bands of multiple bound CO species at 1959 cm^{-1} appearing at mbar CO pressure and extra TPD peaks at 300 and 350 K. From comparison with reference spectra from CO adsorbed on Pd(111) the multiple bound CO bands and the high temperature desorption peak indicate that some fraction of the surface area of the bulk ZnPd crystal was made from pure Pd patches. Nevertheless the TPD peak at 300 K also suggested the presence of a new kind of adsorption sites on the bulk ZnPd which was not observed on the surface alloys.

5 Other Surface Science and Catalysis Projects

5.1 Carbon Nanotubes

Carbon nanotubes become highly in the focus of industry and research. The use of the possibilities of nanotechnology (nanoscale particles and fibers) are important for the development of ambitious materials. Multi-walled carbon nanotubes (MWNT) consist of multiple rolled layers (concentric tubes) of graphene. Nanostructured metal functionalized nanotubes can modify semiconductor properties (e.g. to increase sensing response for hydrogen sensors or for the enhancement of photocatalytic activity). The XPS measurements in this chapter were done in cooperation with Timo Bohnenberger (Fakultät für Elektrotechnik und Informationstechnik, TU Wien) who used a part of the shown measurements for his PhD thesis about functionalized multiwalled carbon nanotubes [272].

5.1.1 Sample preparation for XPS

Pt doped multiwalled carbon nanotubes (MWNT) are characterized by XPS (only this measurement method was accessible for this type of sample in our chamber). In order to understand the effect of substrate the measurements are repeated on Al and Cu, respectively. In addition, a non-doped MWNT sample was tested as reference. The samples (powder) were pressed on alumina or copper foils with 3 bar using an IR-press. To prevent the sample sticking on the piston a non-sticking baking paper was used between sample and piston. The amount of sample has to be sufficient to cover the part of foil (~ spatula point). Higher amounts are reducing the “background” of the foil, but tend to crumble off. The optimum amount depends on the sample material and substrate and has to be tested by trial and error. The foil was then attached on a sample plate which transferred to the XPS position in the chamber via a load-lock using a wobble stick.

Tab. 5-1: Detailed descriptions of four repeated measurements.

Measurement	Sample/Substrate
MWNT 1	MWNT-COOH-Pt supported by Al foil
MWNT 2	Higher amount of MWNT-COOH-Pt supported by Al foil
MWNT 3	MWNT-COOH-Pt supported by Cu foil
MWNT 4	MWNT-COOH supported by Al foil

5.1.1.1 XP Spectra of C 1s

In Fig. 5-1, Fig. 5-2, Fig. 5-3, and Fig. 5-4 the peak fitting results of C 1s peak are shown. The C 1s were fitted spectra with four components (C-C, C=O, O-C=O, and carbide).

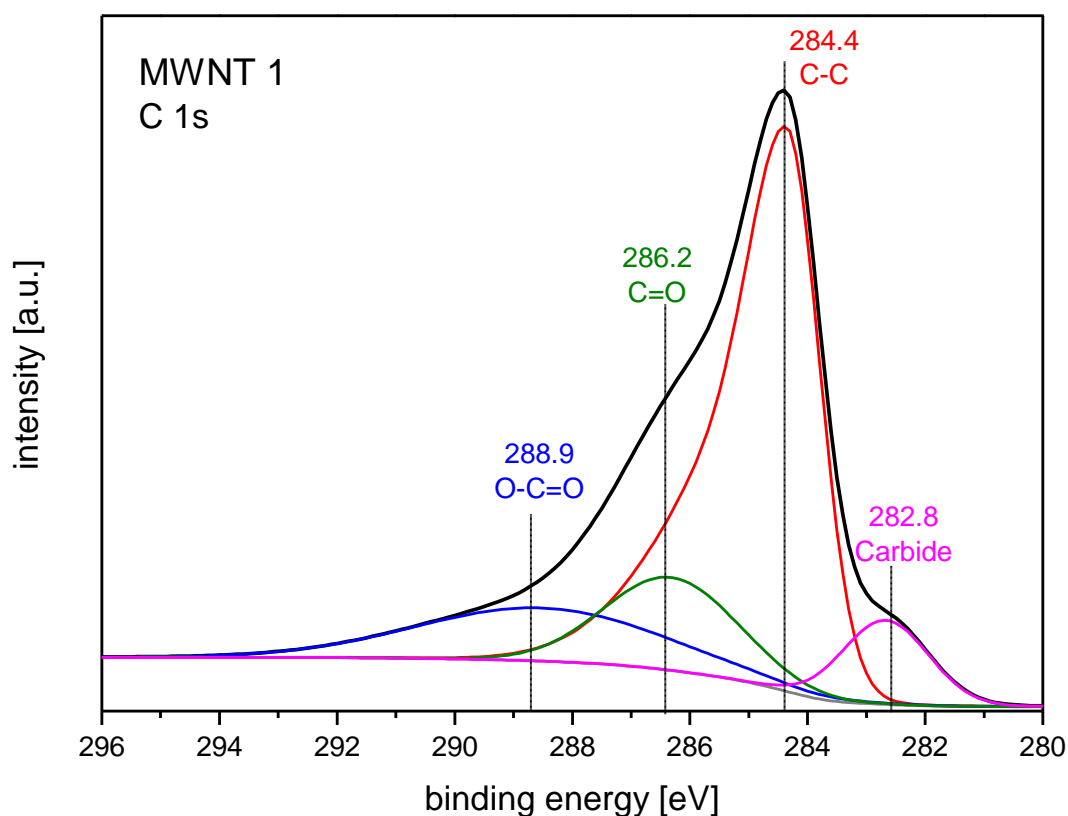


Fig. 5-1: XP spectra of C 1s for C-C, C=O, O-C=O, and carbide (MWNT 1: first measurement MWNT-COOH-Pt supported by Al foil).

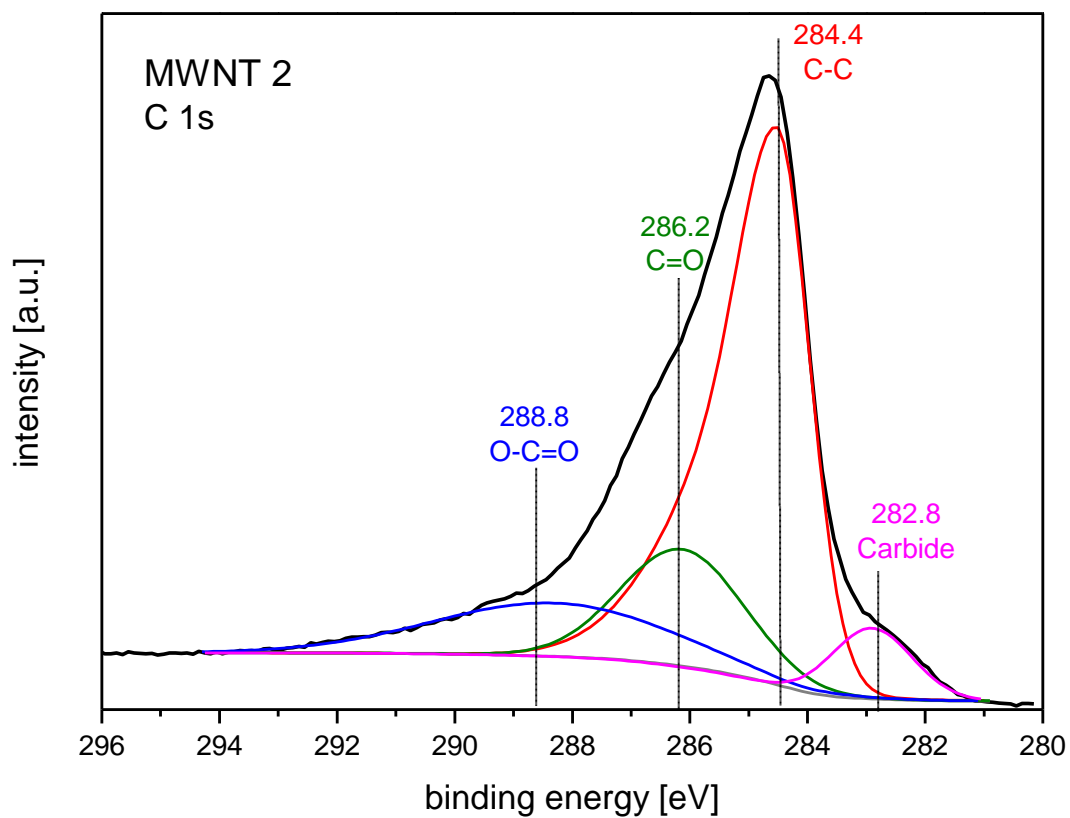


Fig. 5-2: XP spectra of C 1s for C-C, C=O, O-C=O, and carbide (MWNT 2: higher amount of MWNT-COOH-*Pt* supported by Al foil).

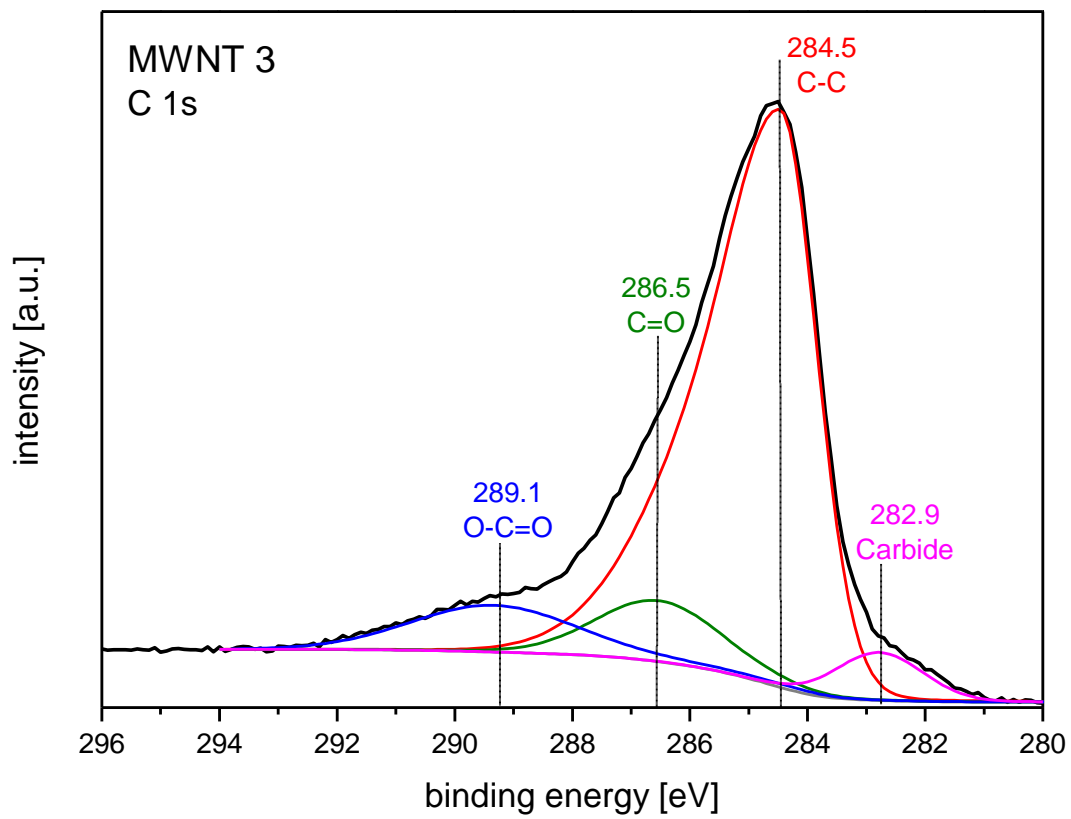


Fig. 5-3: XP spectra of C 1s for C-C, C=O, O-C=O, and carbide (MWNT 3: MWNT-COOH-Pt supported by Cu foil).

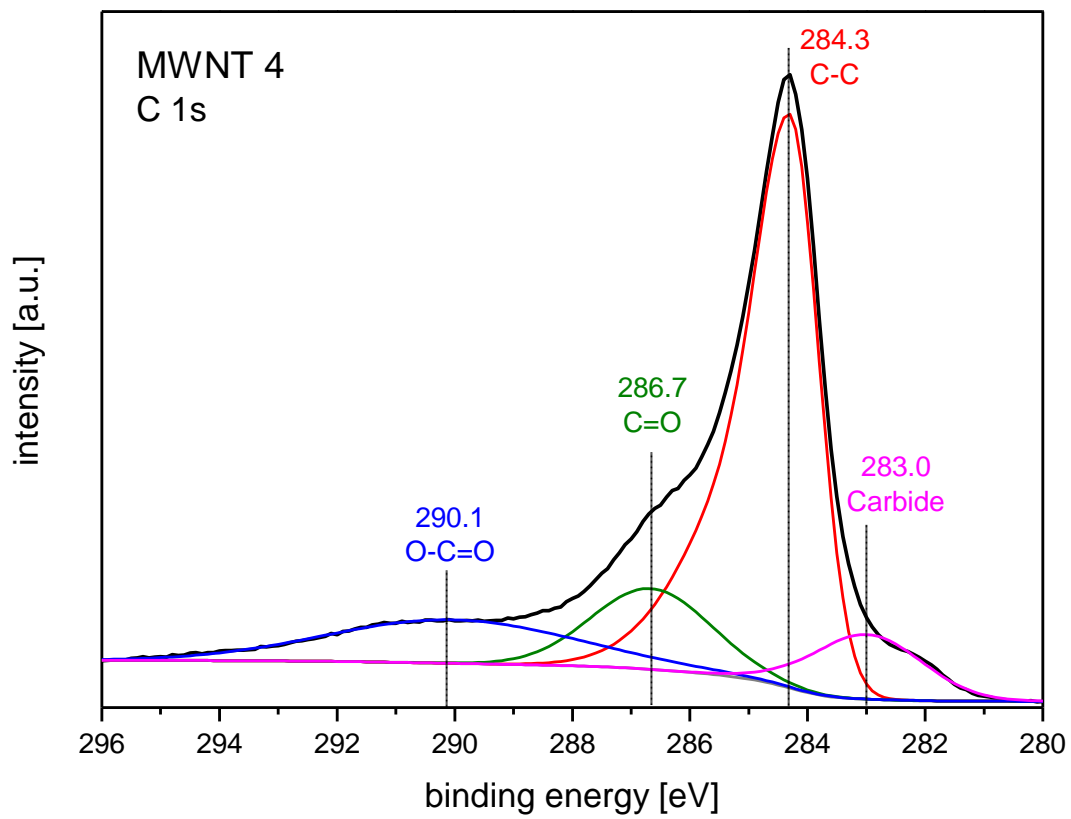


Fig. 5-4: XP spectra of C 1s for C-C, C=O, O-C=O, and carbide (MWNT 4: reference sample MWNT-COOH supported by Al foil).

5.1.1.2 XP Spectra of Al

Fig. 5-5 and Fig. 5-6 show the peak fitting results for the Al 2p peak. The spectra were fitted with three components Al 2p (AlO_x , Al, and satellite). The Pt 4f peak can not be resolved under our measuring conditions, the theoretical position of this peak is also marked in Fig. 5-5. It is also not possible to resolve the Pt 4f signal if a Cu foil is used as support due to the Cu 3p peak at a similar binding energy (not shown).

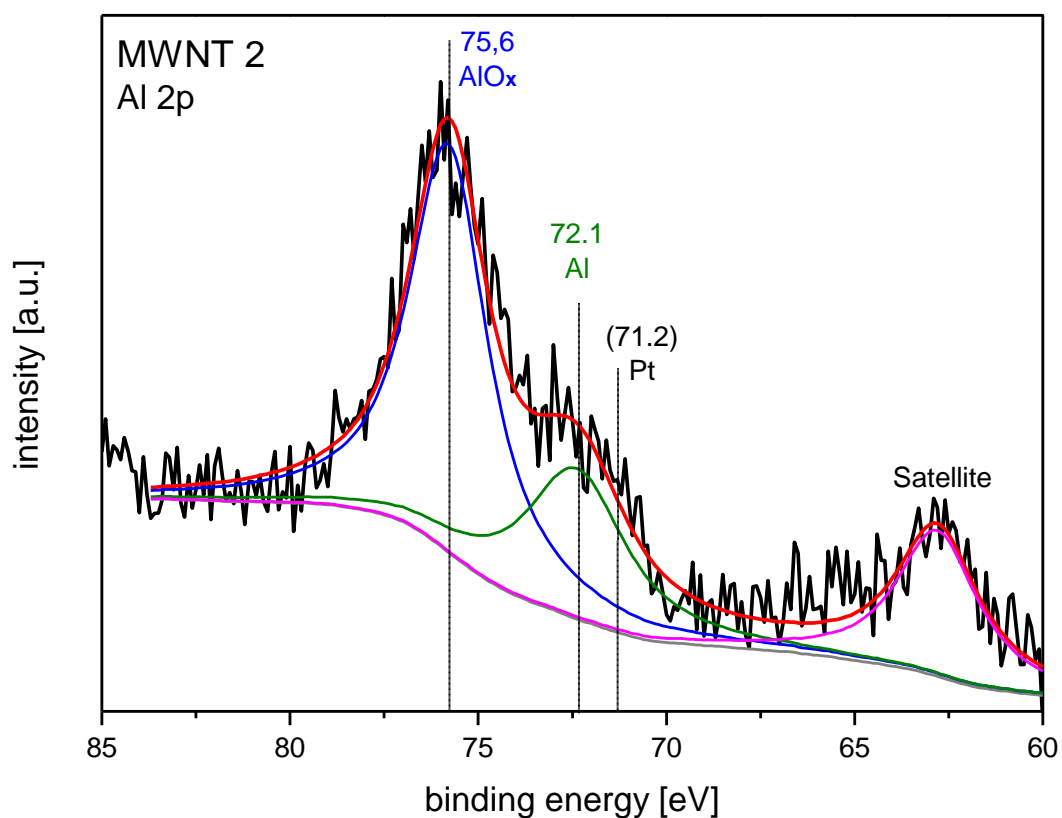


Fig. 5-5: XP spectra of Al 2p (MWNT 2: higher amount of MWNT-COOH-Pt supported by Al foil).

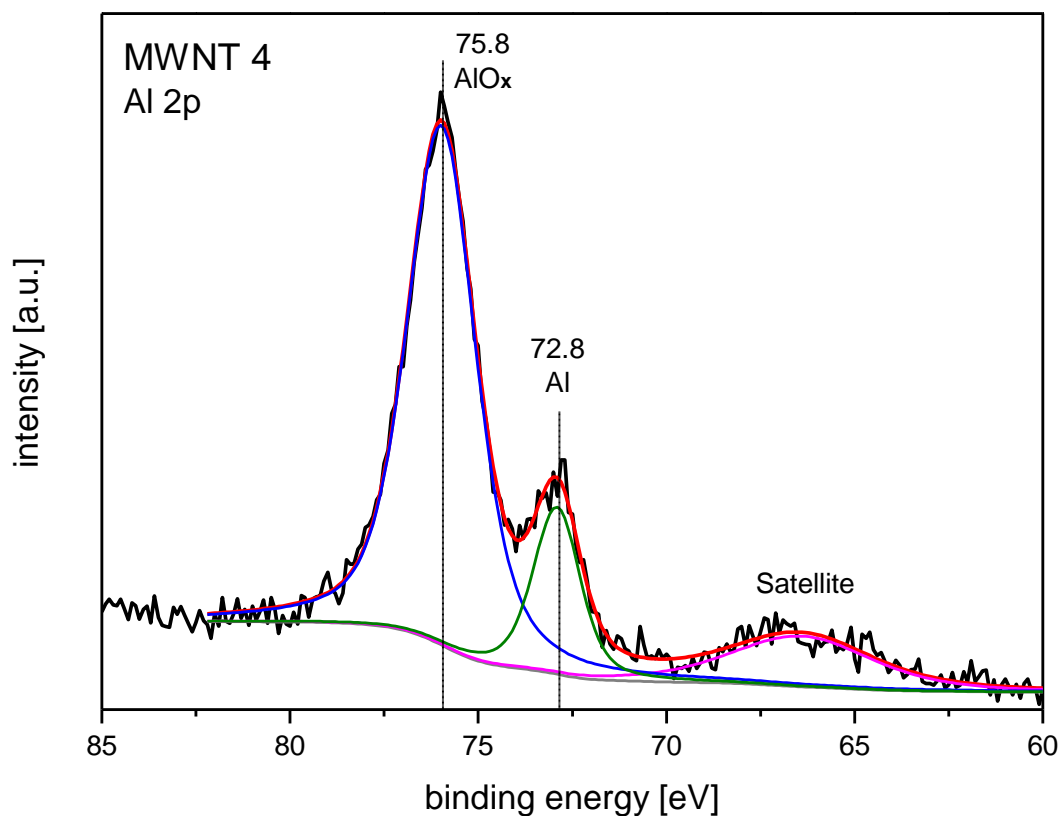


Fig. 5-6: XP spectra of Al 2p (MWNT 4: MWNT-COOH supported by Al foil).

5.1.1.3 XPS binding energies

The following binding energies for C 1s, Al 2p, and Pt 4f are used for this work. The binding energies for C 1s were taken from former studies about acidified carbon nanotubes (s. Tab. 5-2).

Tab. 5-2: Typical C 1s binding energies for organic samples [273, 274].

C-C/C=C (eV)	C=O (eV)	COOH (eV)
284.4 - 284.7	286.1 – 286.8	288.6 - 289.9

Tab. 5-3: Typical Al 2p and Pt 4f binding energies [80].

Al 2p (eV)	Pt 4f 5/2 (eV)	4f 7/2 (eV)
73.0	74.5	71.2

5.1.1.4 Discussion

According to the results of peak fitting, the percentages of different carbon species together with corresponding binding energies are given in Tab. 5-4. The peak positions of same species are relatively constant, and the slight shift of peak positions can be attributed to experiment error. Significant higher amount of *C-C* groups in MWNT 3 might be caused of the copper substrate, which was cleaned by toluene prior to the measurement. However, this also effects the calculated percentage of *C=O* and *O-C=O* in MWNT 3.

Tab. 5-4: Calculated percentages of different carbon species and corresponding binding energies.

	MWNT 1		MWNT 2		MWNT 3		MWNT 4	
	[%]	BE [eV]						
<i>C-C</i>	70.4	284.4	67.9	284.4	82.6	284.5	69.3	284.3
<i>C=O</i>	11.2	286.2	13.9	286.2	6.7	286.5	10.8	286.7
<i>O-C=O</i>	11.9	288.9	12.6	288.8	6.9	289.1	12.1	290.1
<i>Carbide</i>	6.5	282.8	5.5	282.8	3.8	282.9	7.9	283.0

It is possible to detect, but not possible to resolve the Pt 4f signal due to the overlap with the Al 2p signal when using alumina foil as substrate. We attempted to use copper foil as substrate as well, there is, however, still an overlap between Cu 3p and Pt 4f peaks (not shown) and furthermore the sample powder sticks better on the Al-foil. Therefore, to detect the Pt peak, another material should be selected as appropriate substrate in order to avoid an overlap of the XPS regions of substrate and Pt 4f.

6 Conclusions

The aim of this thesis was to study the properties and catalytic behavior of well-defined heterogeneous model catalysts under conditions relevant for real catalysis. PdZn/Pd(111) surface alloys have been prepared and characterized under the well-defined conditions of ultrahigh vacuum. Such 2-dimensional surface alloys serve as model system for the active PdZn alloy phase that has been identified to be formed during methanol steam reforming (MSR) on Pd/ZnO catalysts.

In the beginning of the thesis the experimental setup was transferred from the old location of the Institute of Materials Chemistry (“VetMed”) to the new location (“Getreidemarkt”) in Vienna. The System had been reassembled with some improvements. Using the example of CO adsorption on Pd(111) and PdZn/Pd(111), it was assured that the UHV setup was successfully rebuilt. In agreement with earlier data, XPS, PM-IRAS and TPD spectra could be measured with the same high resolution and high sensitivity.

The formation, stability, and structure of Pd(111) and PdZn/Pd(111) surface alloys and their interaction with CO, methanol and D₂O were studied by applying a combination of complementary techniques such as TPD, XPS, PM-IRAS, LEED, and STM. PdZn surface alloys represent well-suited model systems for modern MSR catalysts. PM-IRAS is a surface sensitive method which can be applied from UHV up to atmospheric pressure. It allows simultaneous monitoring of reaction intermediates adsorbed on the catalyst surface and of products in the gas phase. Thus, PM-IRAS is well-suited as an in situ method to study catalytic reactions. XPS, LEED, and STM have been applied for characterization of the model systems in UHV before and after reaction.

In line with earlier studies, PdZn/Pd(111) alloys have been prepared by deposition of Zn onto a Pd(111) single crystal substrate at 90 K or room temperature, followed by thermal annealing at 573 K. Using this procedure surface alloys with a Pd:Zn 1:1 composition were obtained. Alloy formation could be monitored by the observation of a characteristic (2x2) LEED pattern and the appearance of two characteristic signals in the XP spectrum, i.e. a Zn2p_{3/2} peak at 1020.9 eV and a Pd3d_{5/2} peak at 335.6 eV. It was shown by PM-IRAS that even at mbar pressure CO adsorbed exclusively on-top of the Pd atoms in the alloy layer, giving rise to a

characteristic IR band at 2070 cm^{-1} . PM-IRAS also proved that the surface alloy was structurally very homogeneous.

A thermal stability window for the PdZn alloy in a temperature range between $\sim 500\text{ K}$ and $\sim 600\text{ K}$ was deduced from XPS, TPD and PM-IRAS results. At lower temperatures, Zn was present in the form of non-interacting layer(s), as deduced from the absence of CO adsorption in PM-IRAS and the observation of only minor changes in the LEED pattern and the Pd 3d XPS signal. The occurrence of IR bands of multiple-bound CO upon annealing to 623 K was taken as an indication for the onset of alloy degradation by Zn depletion into the Pd bulk. The original Pd(111) surface was restored at temperatures above 900 K .

The CO saturation coverage was found to be $\frac{1}{2}\text{ ML}$ by TPD. To the contrary, on a surface with conventional, bulk-like geometric arrangement of Pd and Zn atoms in rows, CO adsorption on bridge sites with saturation coverage of $\sim \frac{1}{3}\text{ ML}$ was predicted by DFT calculations. The experiments presented in this work are supporting a suggested reconstruction of PdZn/Pd(111) to a “zigzag” rearrangement of the atomic components on the surface in the presence of CO. According to our DFT calculations, the suggested “zigzag” structure is the most thermodynamically stable elemental arrangement. This investigation sheds light on a new degree of complexity of bimetallic systems, e.g. changes of component arrangement on the surface in the presence of an adsorbate, which is not accompanied by surface segregation. This can have a remarkably influence on the properties of a bimetallic catalyst.

The STM was expected to prove our model of PdZn zigzag reconstruction but without localizing and eliminating the sources for the noises which are responsible for the stability problems it is a game of luck to get a well ordered sample, low adsorbates and a stable system at the same day. At least for sample preparations at lower temperatures the heating and temperature reading procedure needs some more improvement. At this time we are close to get a proof (or disprove) with STM and hopefully this can be finished very soon.

TPD and PM-IRAS spectra reveal that methanol was decomposing to a significant amount on Pd(111), yielding CO and CH_x , which did not happen on the PdZn surface alloys (i.e. methanol desorbed molecularly). No carbonaceous deposits were detectable with XPS, which is in great contrast to pure Pd where rapid carbon formation was observed. This difference is of great relevance in explaining the improved catalytic properties of PdZn catalysts for MSR.

One explanation might be the lack of adsorption sites for bridge bound formaldehyde species which are a likely precursor for C-O bond cleavage.

To identify possible differences between the surface alloy “models” and “real” system, a comparative study between the adsorption properties of well-defined PdZn/Pd(111) surface alloys and bulk intermetallic ZnPd sinter „single“ crystals were performed. The corresponding intermetallic ZnPd bulk material was prepared by powder metallurgical means and subsequent spark-plasma-sintering. Preferential sputtering of Zn made it impossible to clean the sample surface by sputtering. It was necessary to perform extended cleaning cycles using O₂ and H₂ at high temperatures alternately. It was figured out that an additional treatment in an inert gas was required to ensure a uniform tetragonal AuCu single phase, which was the relevant modification. The adsorption/desorption properties of CO as probe molecule on intermetallic ZnPd were studied by XPS, TPD, and PM-IRAS. For TPD, the same desorption features as observed on PdZn/Pd(111) could be identified in the spectra as obtained from the bulk PdZn crystal. This indicates the presence of the same kind of adsorption sites on both systems. However, on the PdZn bulk crystals additional desorption features were observed in TPD spectra. In PM-IRAS additional bands of multiple bound CO species were observed. This suggests the presence of a new kind of adsorption sites on the bulk PdZn crystal which was not observed on the surface alloys.

7 Appendix

Unless otherwise stated, all drawings were taken from our laboratory documentation and manuals. Not all drawings were available as high quality CAD documents and some labels are in German language. This part is prepared to give an overview about the whole system and its parts. If available, detailed technical drawings are given.

7.1 XPS/PM-IRAS System

7.1.1 Overview

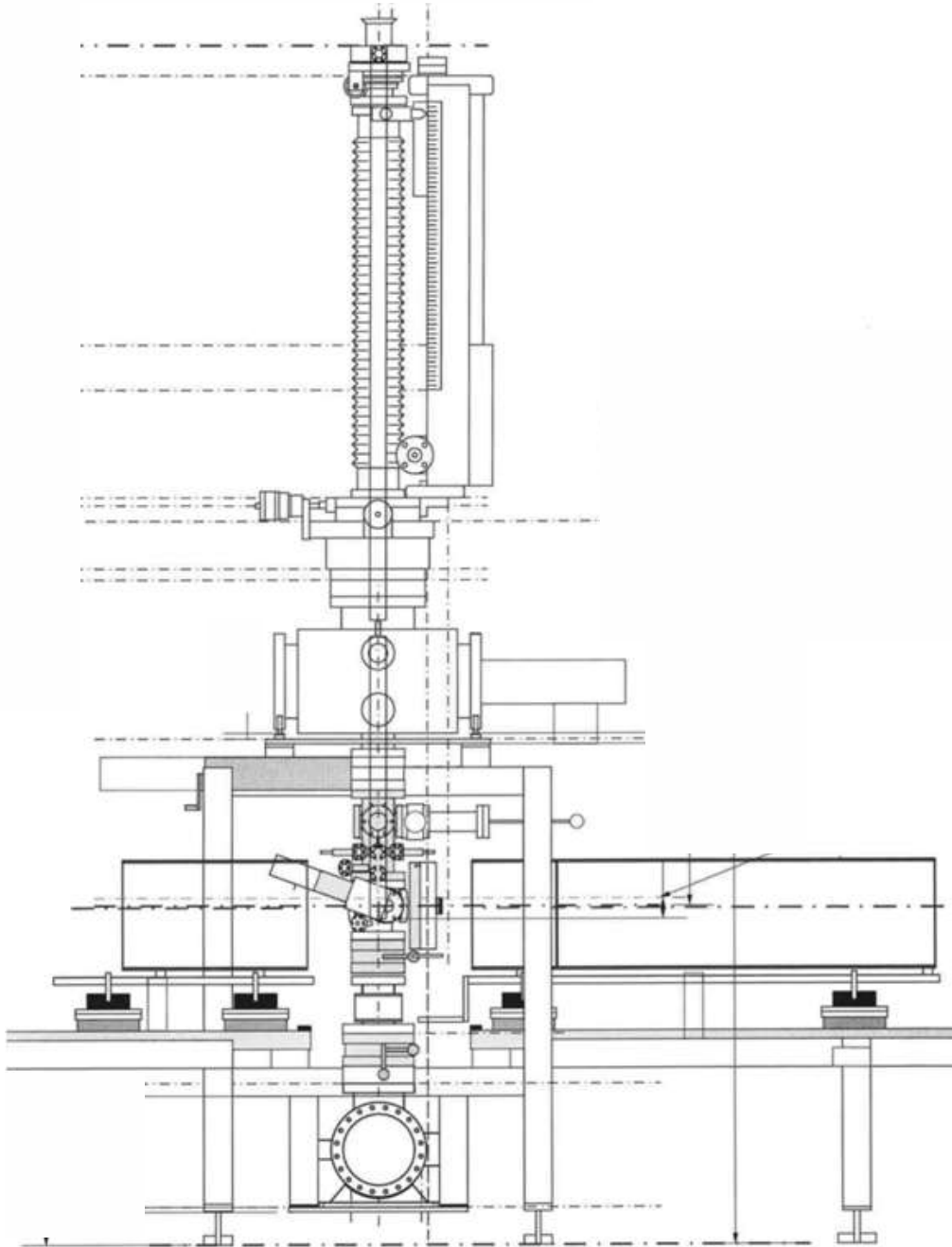


Fig. 7-1: Overview of the XPS system. Upper part: manipulator; in the middle: preparation chamber and XPS; on the bottom: high pressure cell and PM-IRAS and below turbomolecular pump and titan sublimation pump.

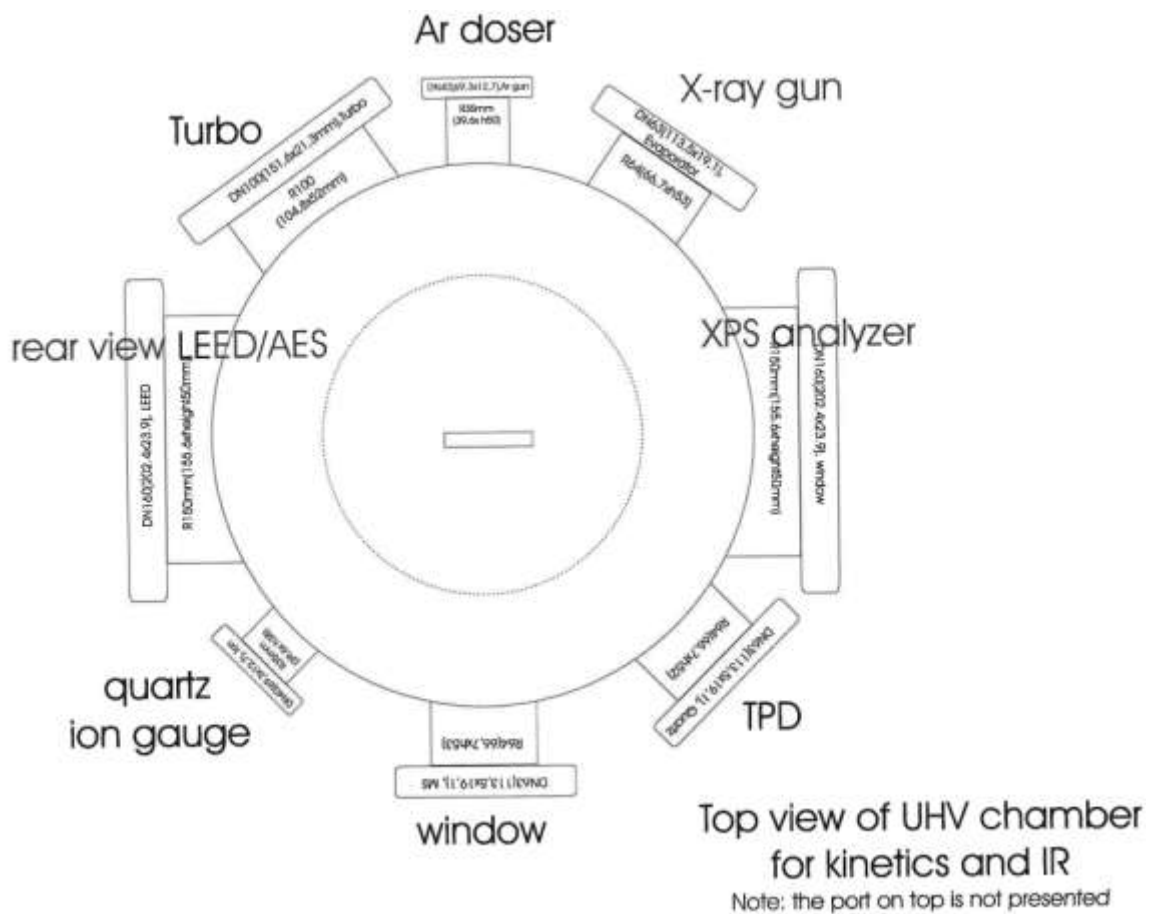


Fig. 7-2: XPS chamber.

7.1.2 Manipulator

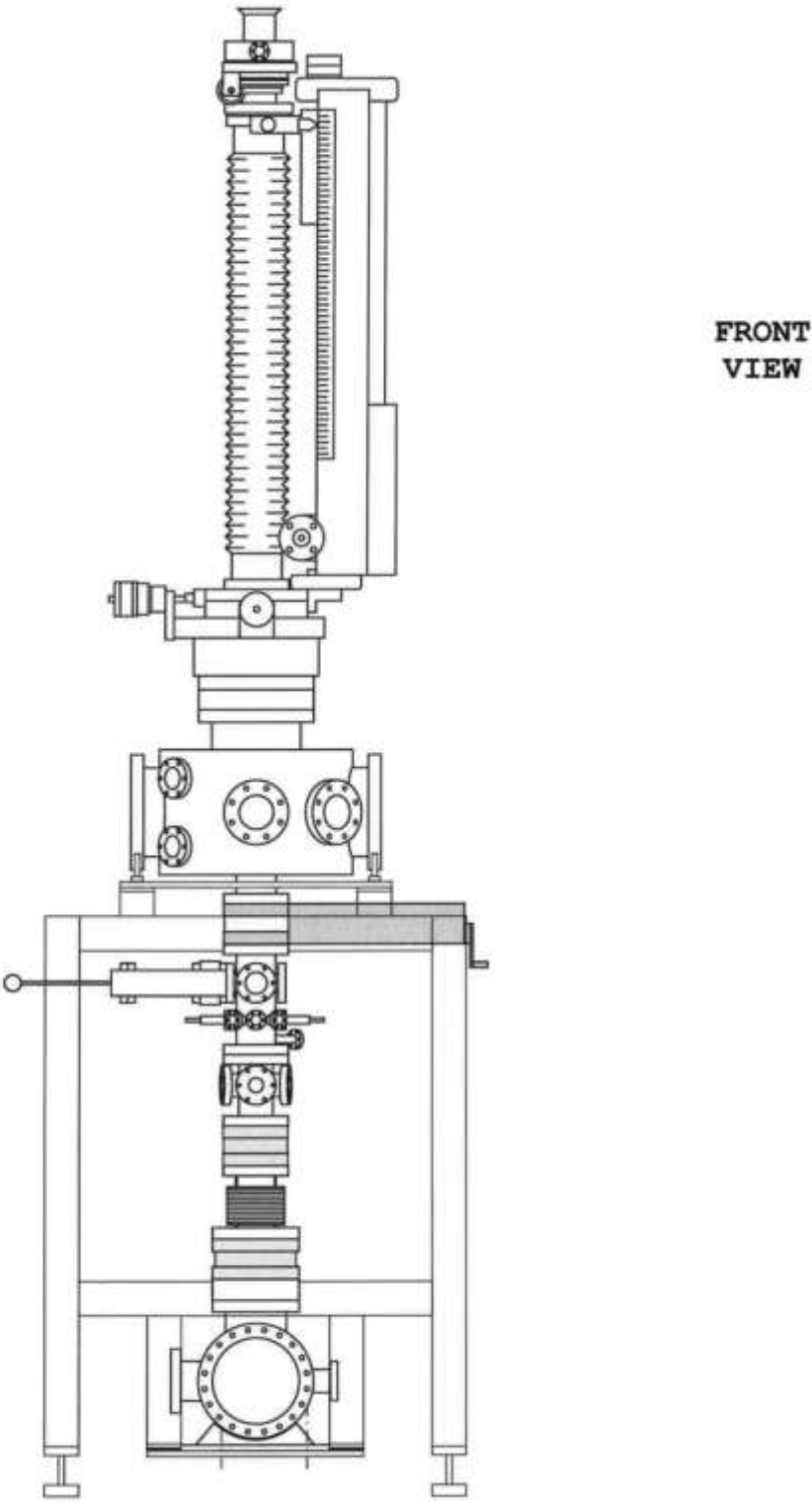


Fig. 7-3: 8-3: Manipulator front view.

7.1.3 X-Ray source

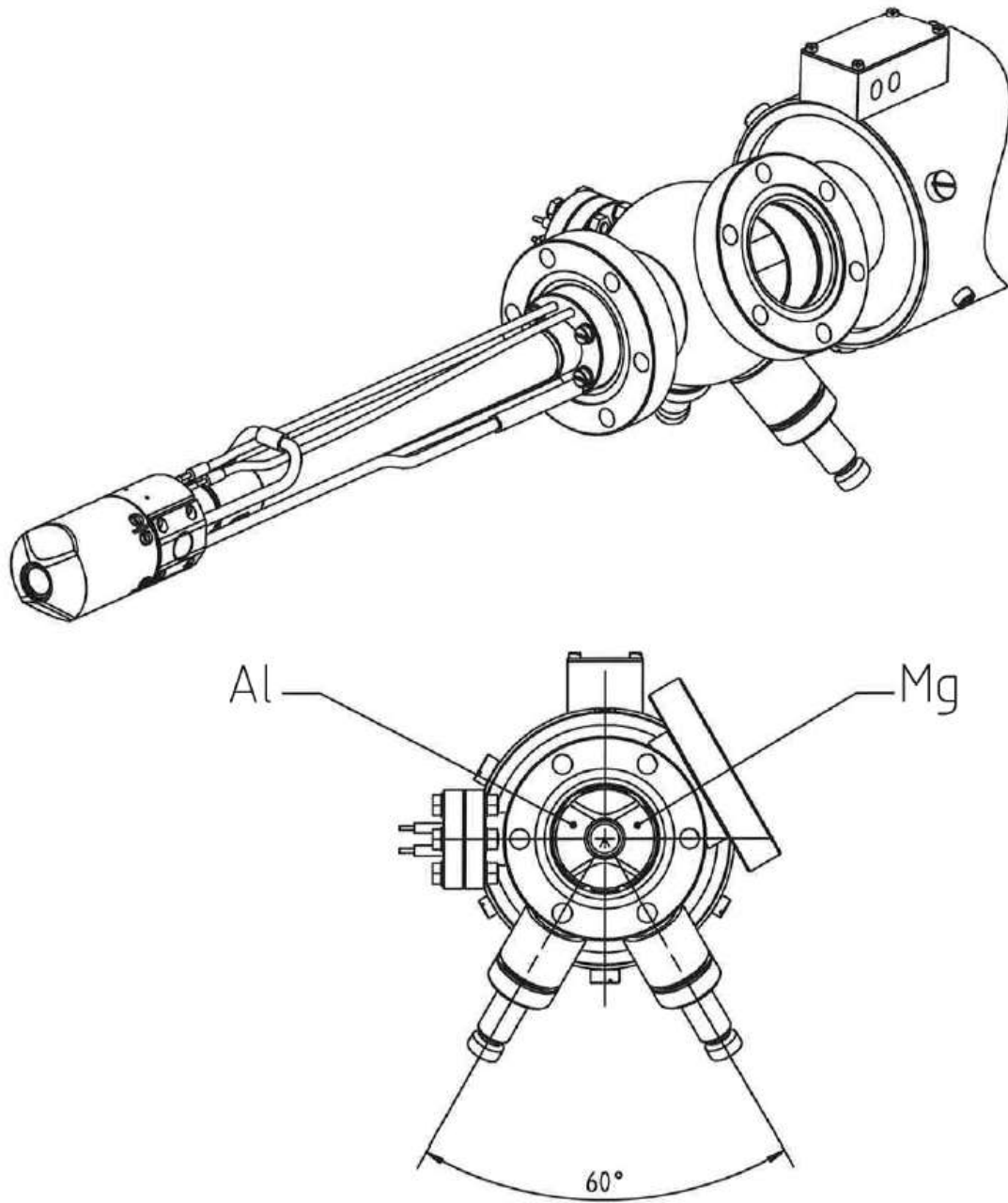


Fig. 7-4: Drawing of X-Ray source XR-50 [Specs].

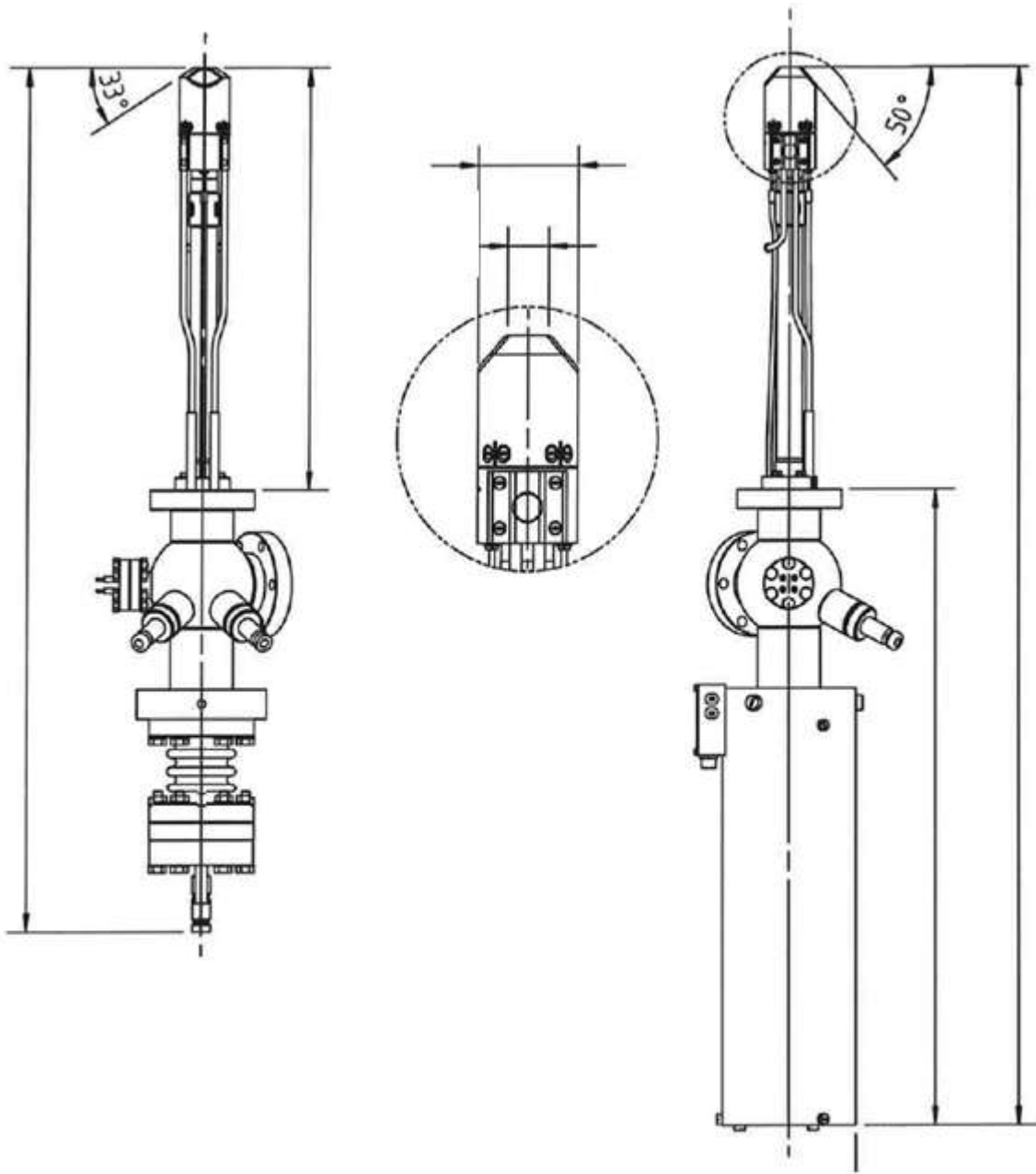


Fig. 7-5: Schematic drawing of X-Ray source XR-50 [Specs manual].

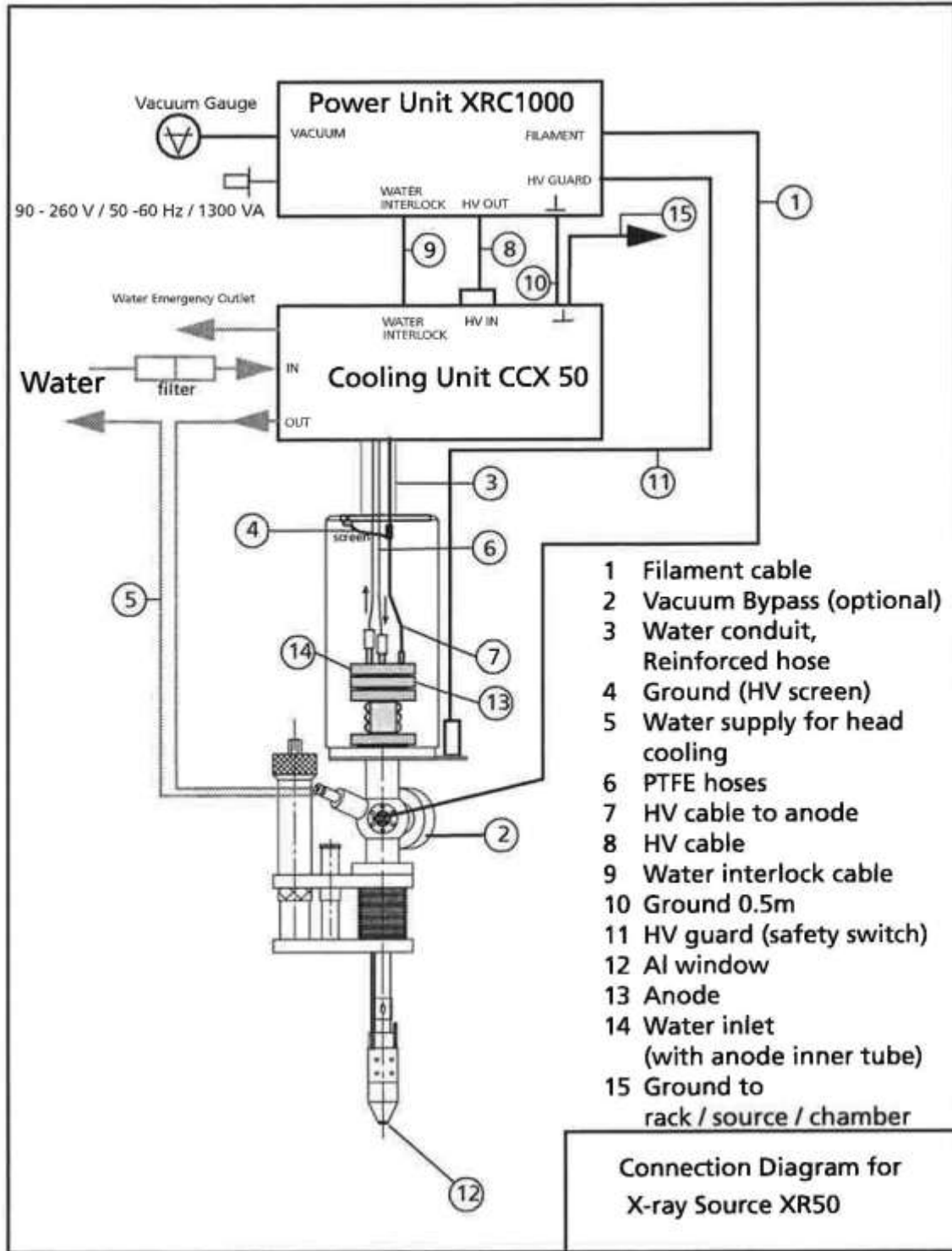


Fig. 7-6: Connection diagram for XR-500 [Specs manual].

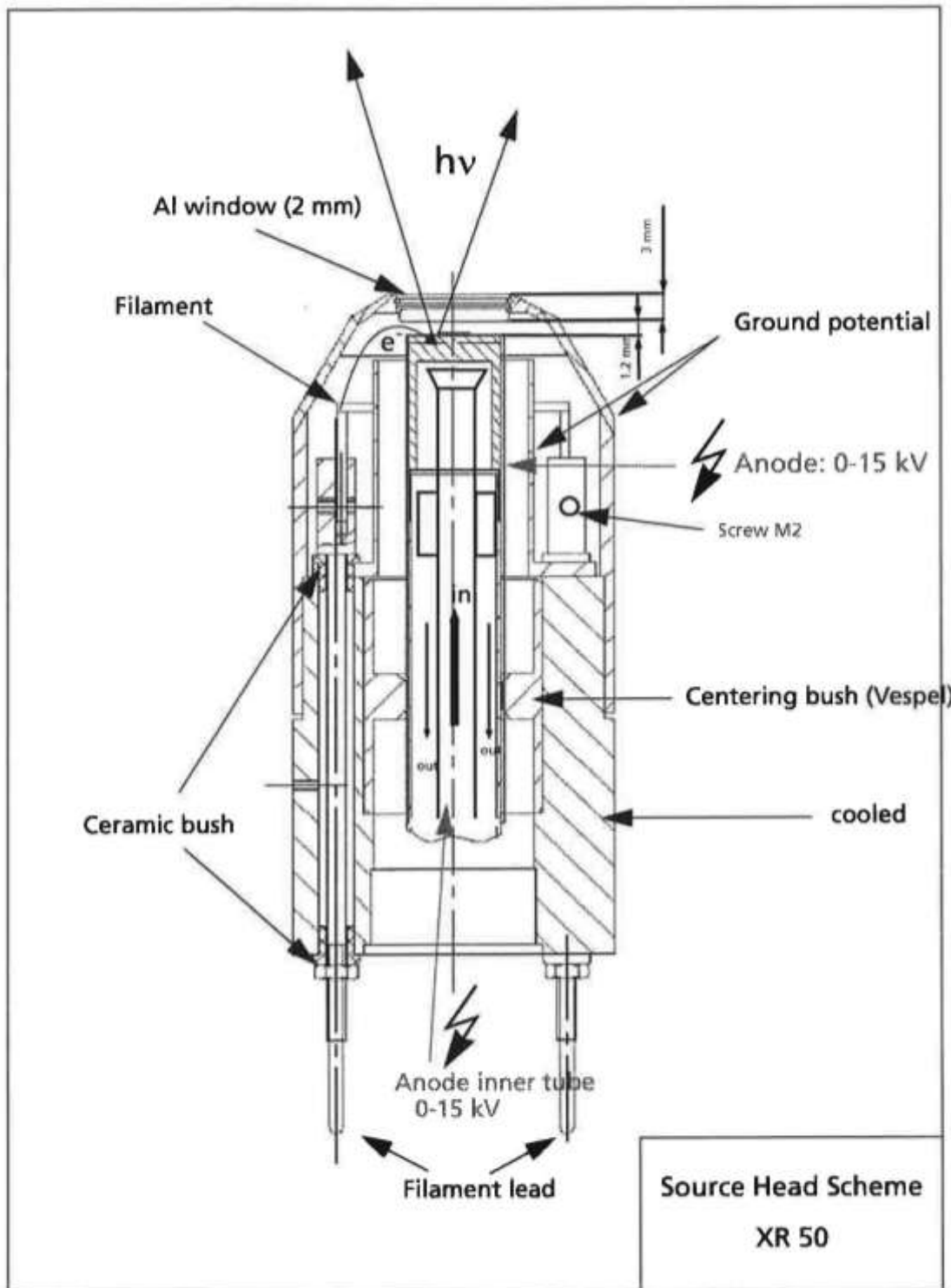


Fig. 7-7: Drawing of source head XR-50 [Specs manual].

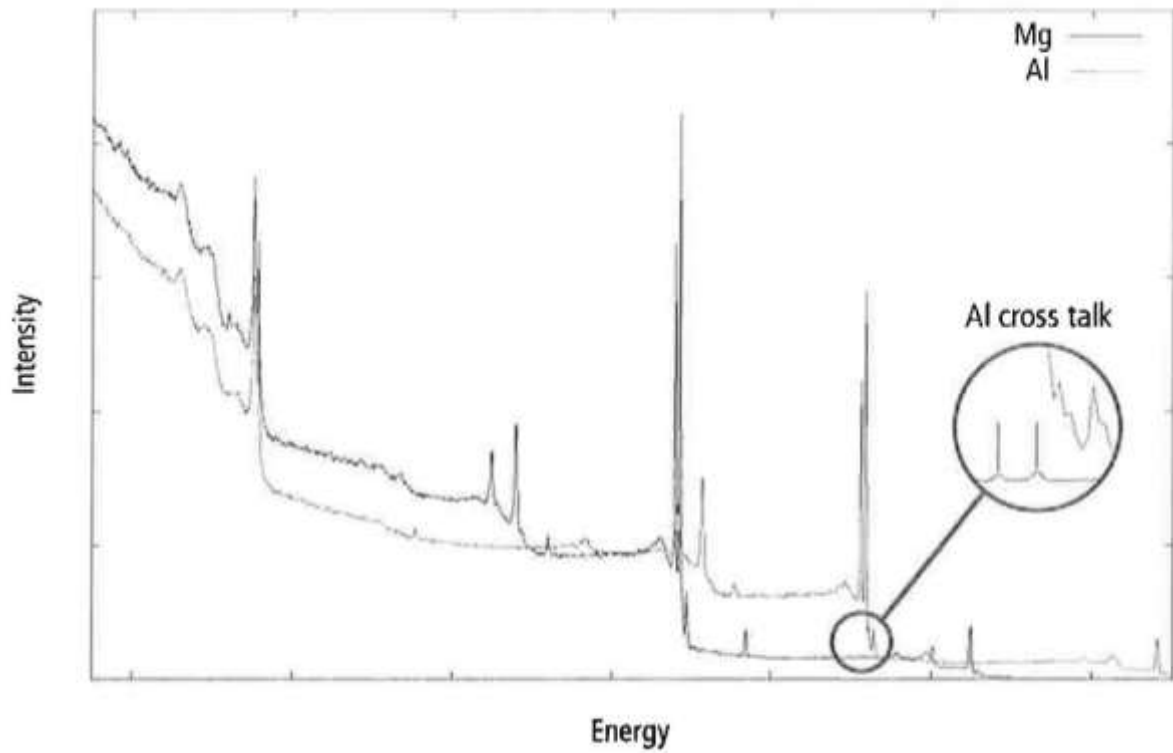


Fig. 7-8: Cross talk in the XR-50 gun. Just behind the aluminum window is a small rod to reduce Al/Mg cross talk (cross contamination). The rod separates the two anode sides from each other [Specs manual].

SPECS GmbH · Voltairestraße 5 · 13355 Berlin

X-Ray Source Specification XR50 061-2002

not sputtered Ag compact sample (still contamination on surface)

Base pressure:	5.0×10^{-9} mbar
He leak check after bake out	no leakage
Used system:	EA10 Standard Analyzer
Analyzer mode:	$E_{pass} = 60\text{eV}/100\text{ eV}$ $U_{Multiplier} = 3.6\text{kV}$
X-ray source was tested in front of the specification with	4 h 300 Watt for Mg and 4 h 300 Watt for Al 4 h 400 Watt for Al
Sample current (not biased, 30mm sample distance)	Mg 300 W: 87 nA Al 300 W: 77 nA Al 400 W: 103 nA

No.	Active side	Power (W)	Mode	Region (eV)	Intensity (cps)
1	Mg	300	dE = 30	870 - 905	32000
2	Mg	300	dE = 30	1100 - 1135	130
3	Mg	300	dE = 30	665 - 700	6200
4	Mg	300	dE = 30	0 - 1300	
5	Al	300	dE = 30	0 - 1500	
6	Al	300	dE = 30	1100 - 1135	24800
7	Al	300	dE = 30	665 - 700	<20

Al - cross talk	Int.2 / Int. 1 x 100%	< 0.41 %
Mg - cross talk	Int.7 / Int.3 x 100%	< 0,31 %*

*Please note: Mg crosstalk is difficult to estimate because of superposition of other peaks.

Tested by: D.Loof
Date of test: Berlin, 28. October 2002

Dateiname: xr50-061-2002.fm4
Revisionsstand: 01

Fig. 7-9: Specification of the X-Ray source, tested by Specs [Specs test report].

7.1.4 Analyzer

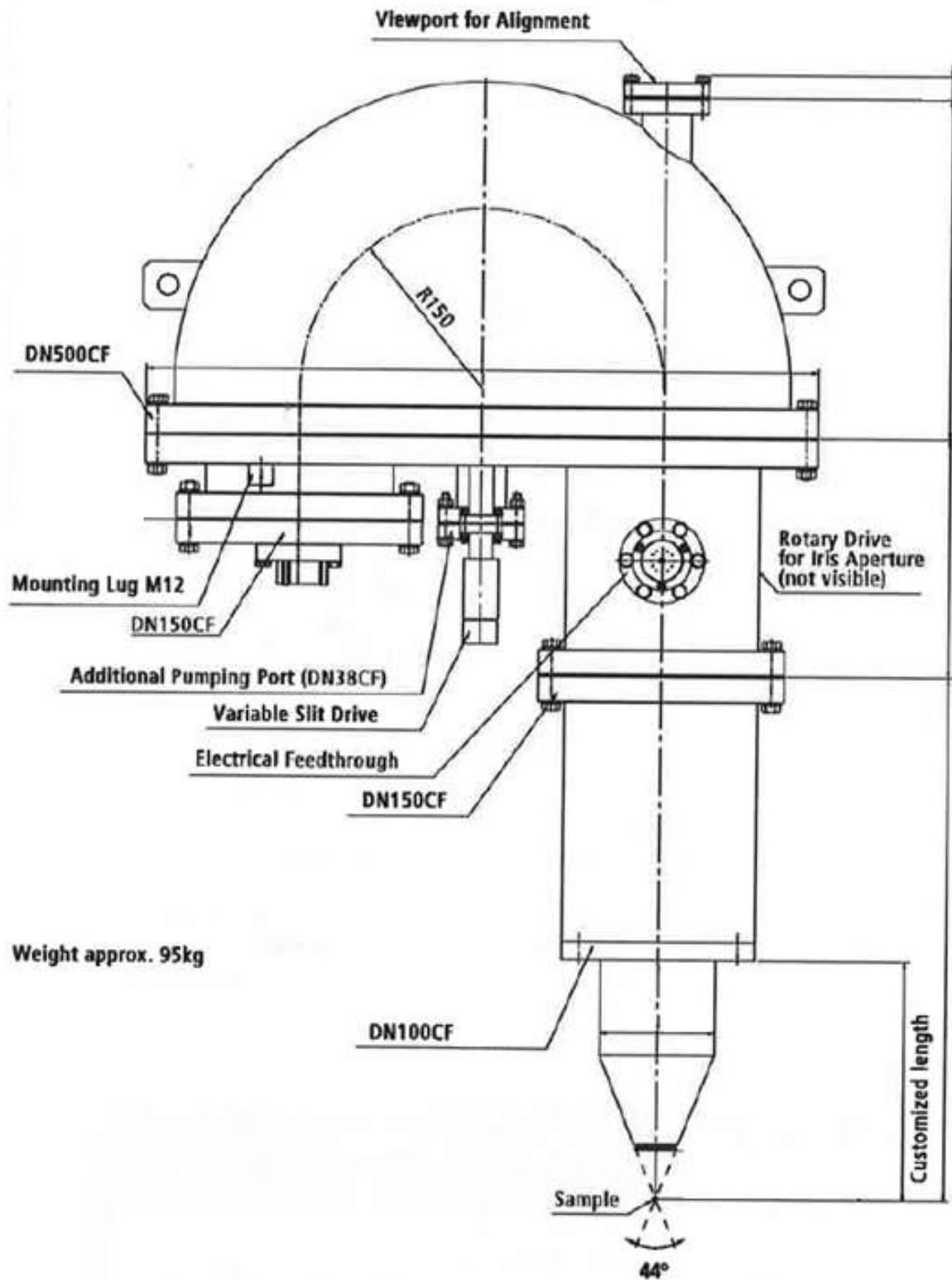


Fig. 7-10: Drawing Analyzer [Specs manual].

7.1.5 Triple Evaporator

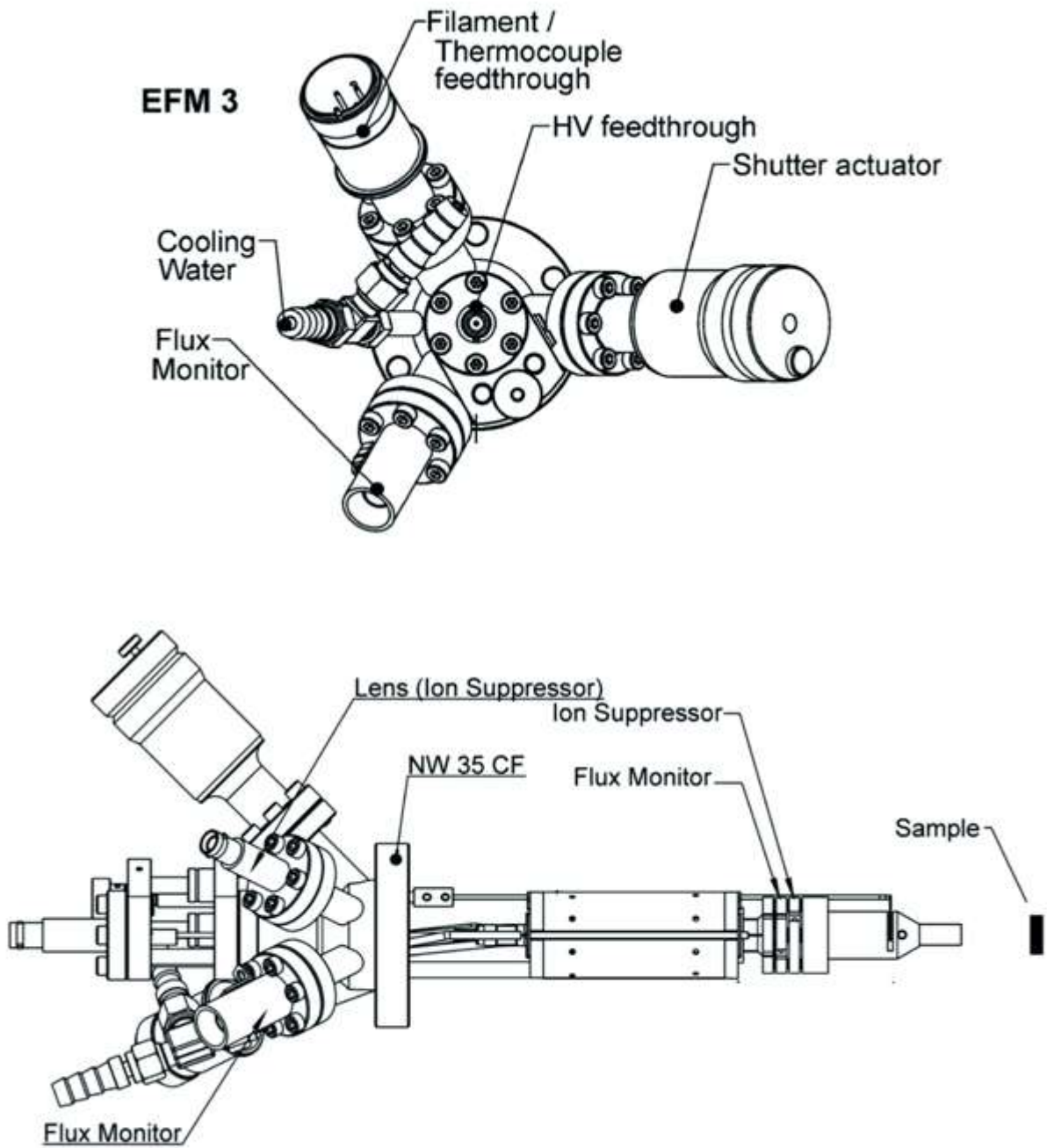


Fig. 7-11: Sketch of the Omicron EFM 3 evaporator as used in our lab [Omicron manual].

7.1.6 Auger-LEED unit

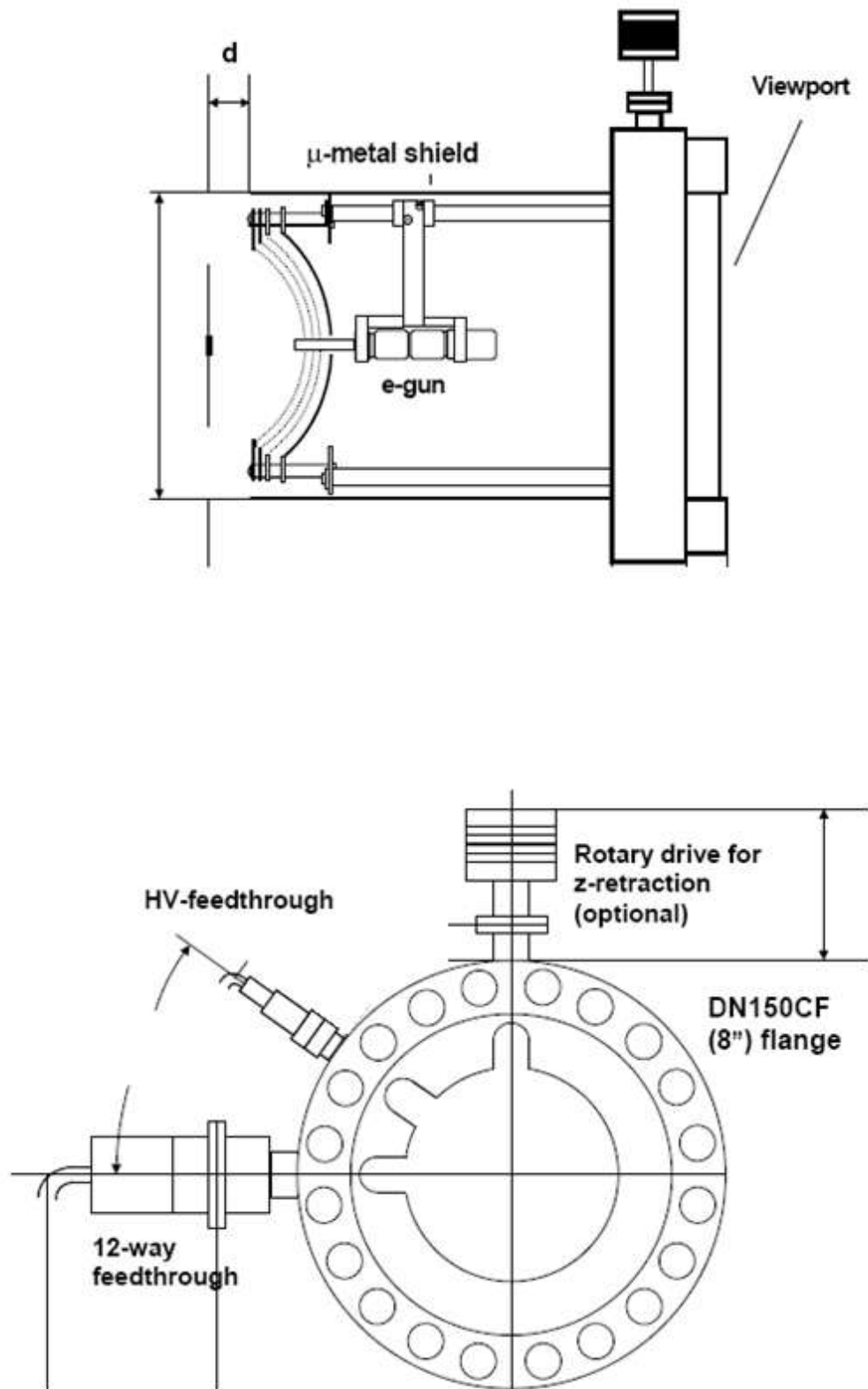


Fig. 7-12: Basic principle of the combined LEED/Auger system taken from the manufacturers (Specs) user manual [Specs manual].

7.1.7 STM-System

7.1.8 System overview

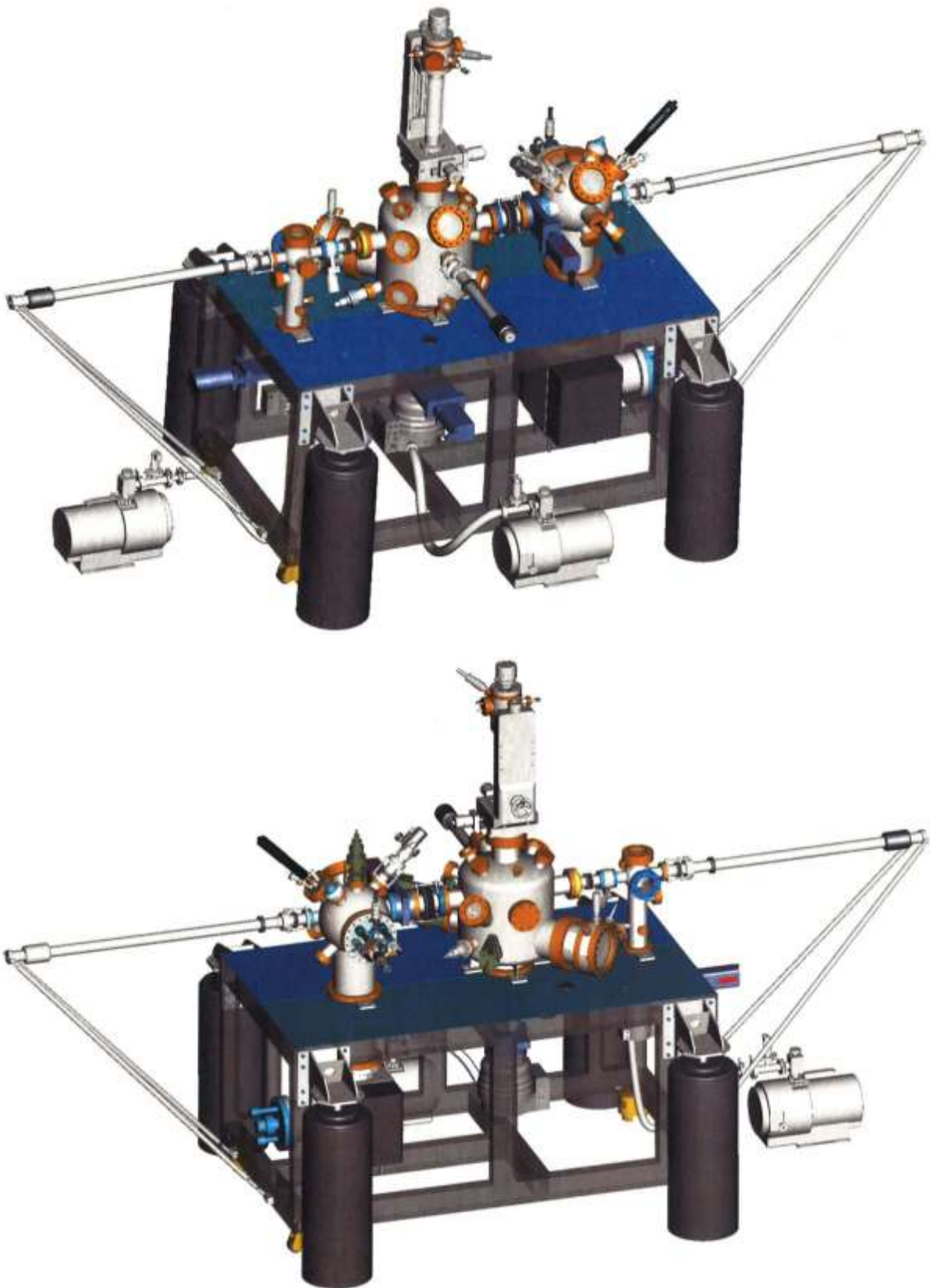


Fig. 7-13: 3-D sketch (front and back view) of the STM system.

7.1.10 STM unit

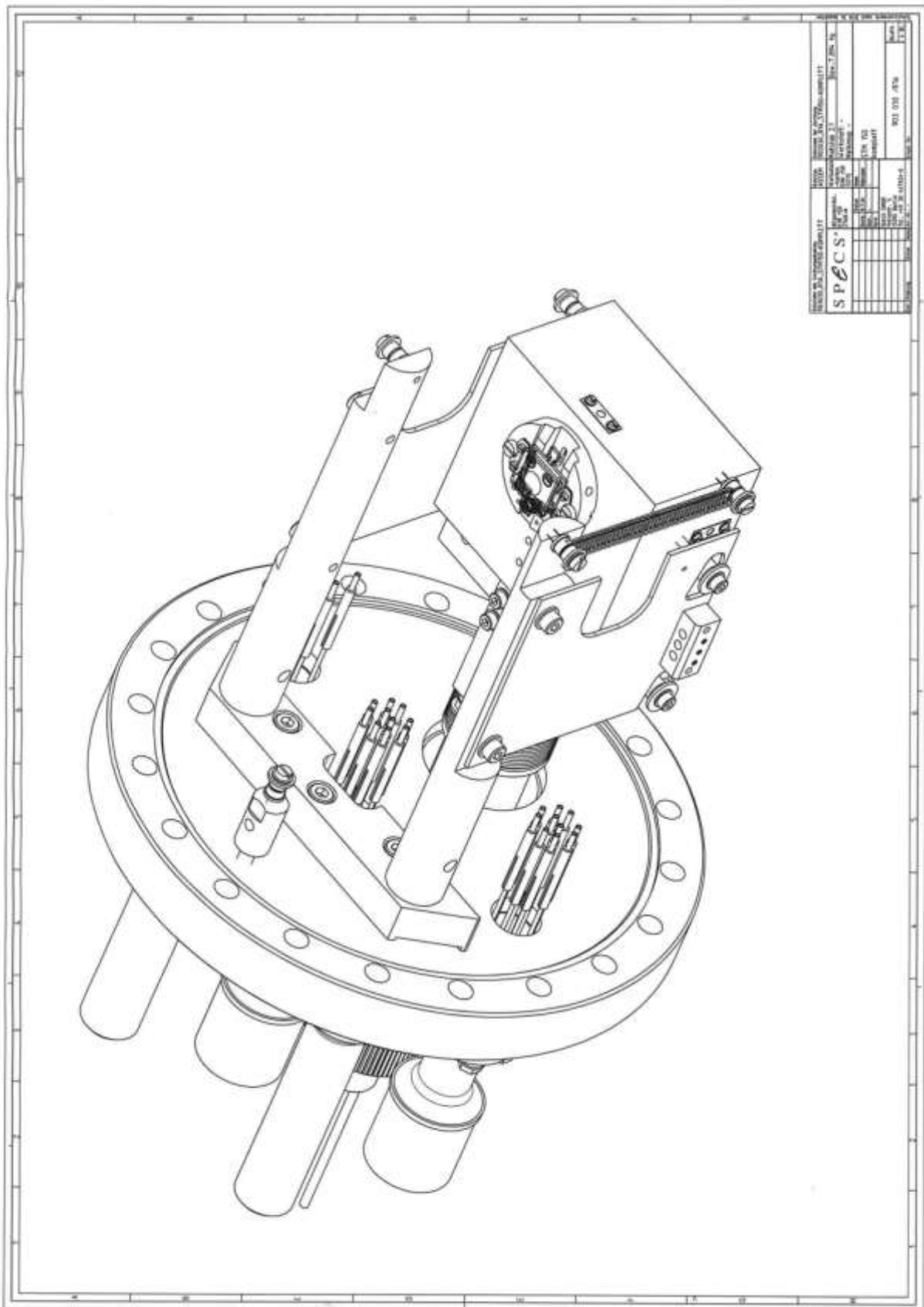


Fig. 7-15: STM, 3D view [Specs manual].

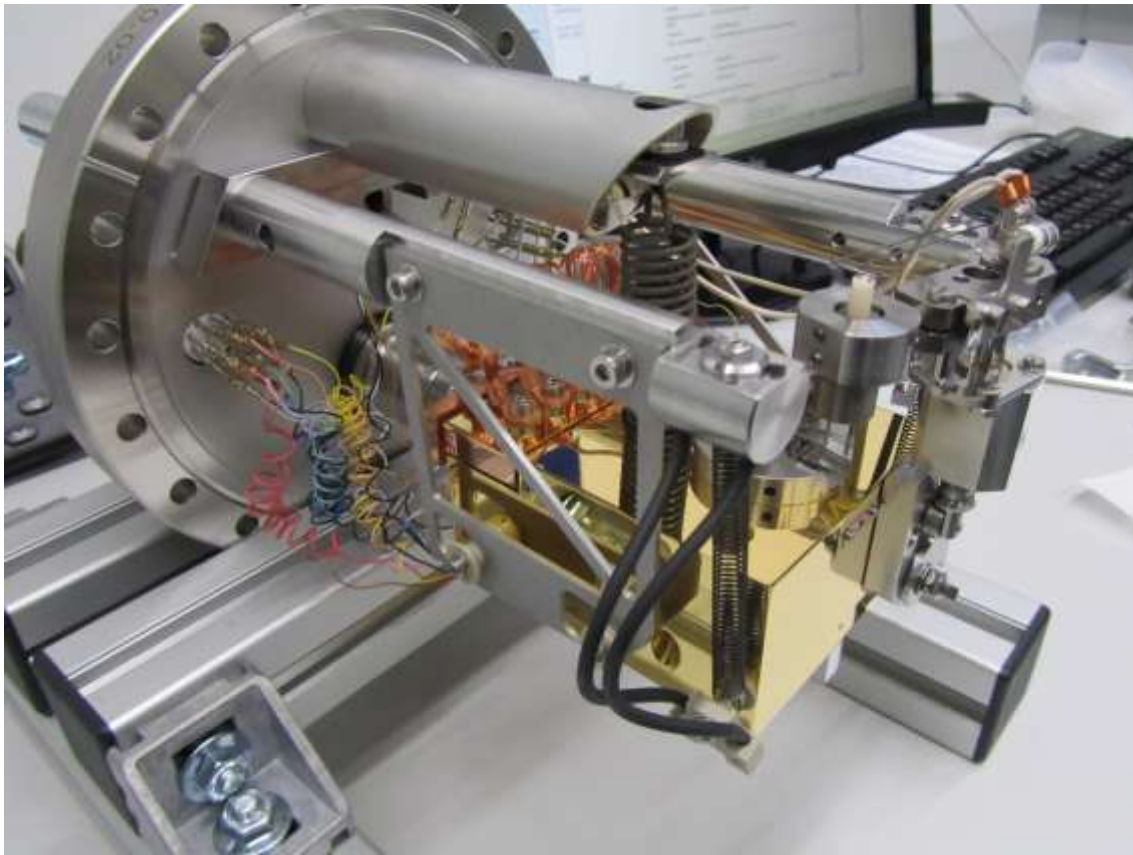


Fig. 7-16: Picture of the STM unit outside the vacuum chamber (before installation).

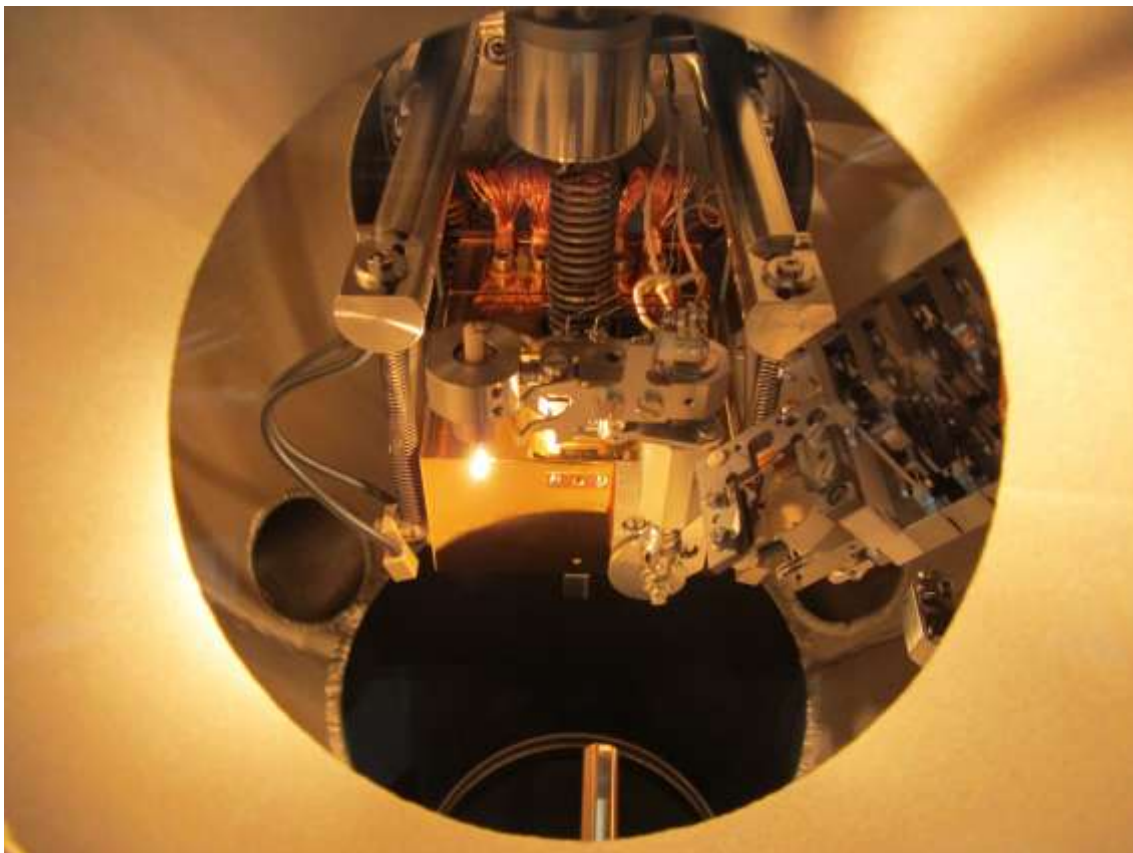


Fig. 7-17: Picture of the STM unit mounted in the vacuum chamber. The filament tower (glowing filament) can be used for sample heating during measurement. Small sapphire balls are used for thermal insulation between sample holder and STM electronics.

7.2 Maxlab-synchrotron data

7.2.1 Overview

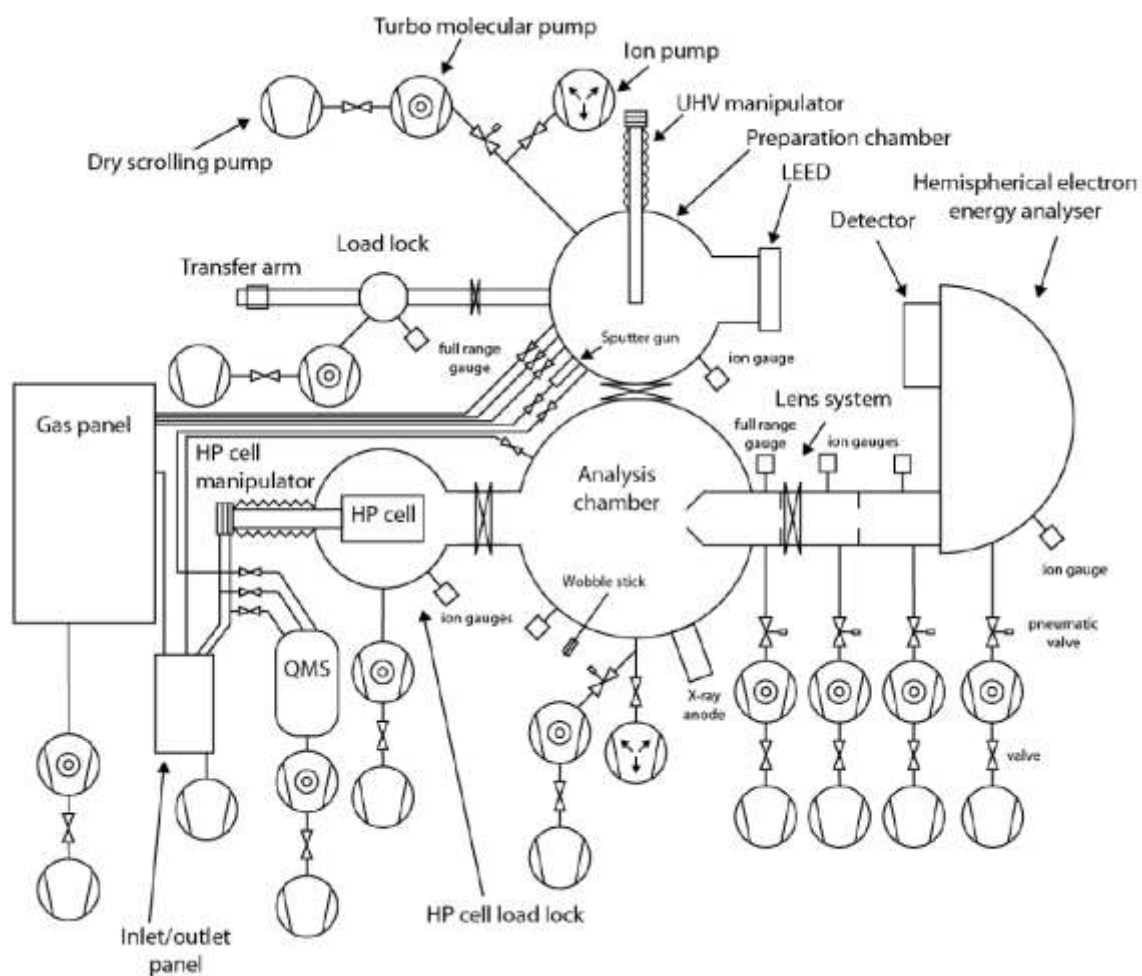


Fig. 7-18: Scheme of the Maxlab HP XPS system. The system consist of 8 different sections (4 chambers; load lock; analysis, preparation and reaction load lock), each pumped with a turbomolecular pump and a scroll pump. The QMS was not working at this beam time [79].

7.2.2 Technical data

Tab. 7-1: Technical data of beamline I511 taken from Maxlab website [79].

Source	Undulator, period = 52 mm, 49 periods, $K_{\max} = 2.7$.
Pre-focusing optics	Horizontally focusing spherical mirror.
Monochromator	Modified SX-700 with 250 l/mm and 1220 l/mm gratings, a spherical focusing mirror and movable exit slit. This allows a high flexibility concerning the interplay between photon flux, resolving power and higher order suppression.
Energy range	50 - ~1500 eV.
Energy resolution	$E/dE = 5 \times 10^3 - 2 \times 10^4$, with the 1220 l/mm grating.
Re-focusing optics	K-B mounted mirrors, one system for each branch line.
Photon flux on sample	$10^{11} - 10^{13}$ ph/s for the 1220 l/mm grating.
Experimental stations	<p>The radiation can be fed alternately into two experimental stations using a flip-mirror placed immediately after the exit slit.</p> <p>I511-1 (HP-XPS) is designed for surface science experiments from UHV up to near ambient pressure and is equipped with a SPECS Phoibos 150 NAP electron analyser for HP-XPS. HP-XAS can be carried out in Auger-yield mode.</p> <p>I511-3 (RIXS) is designed for XES and XAS on both gas phase, and solid phase systems as well as on liquids not requiring UHV.</p>

7.2.3 Sample mounting

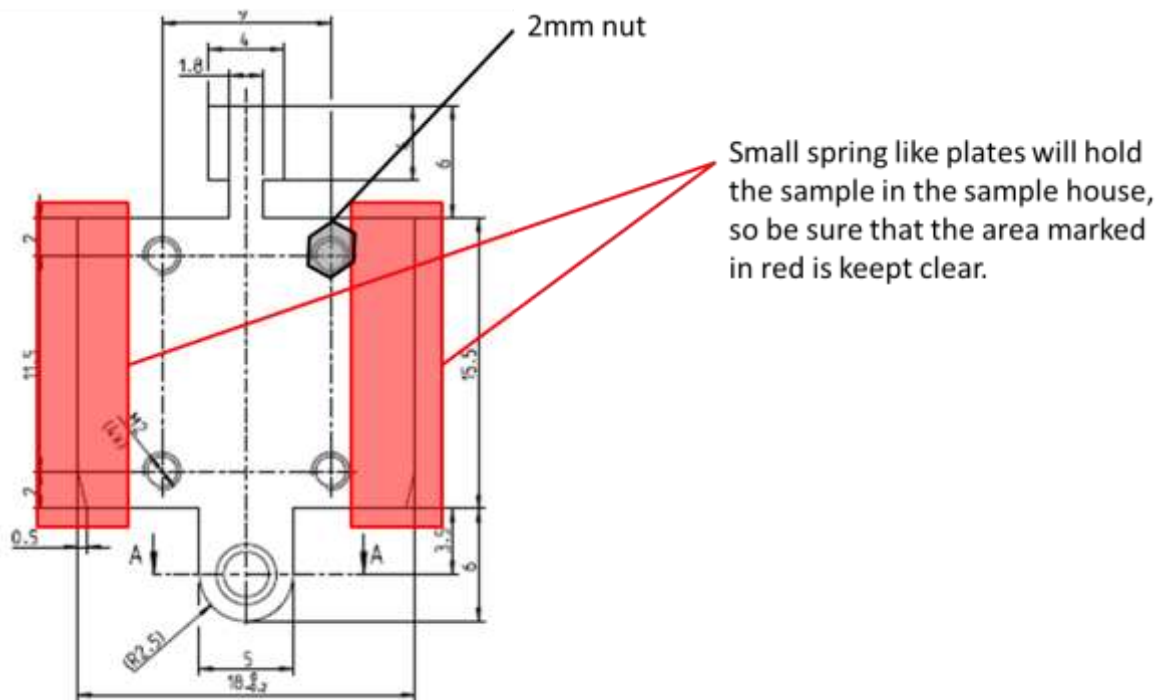


Fig. 7-19: Drawing and dimensions of the sample holder.

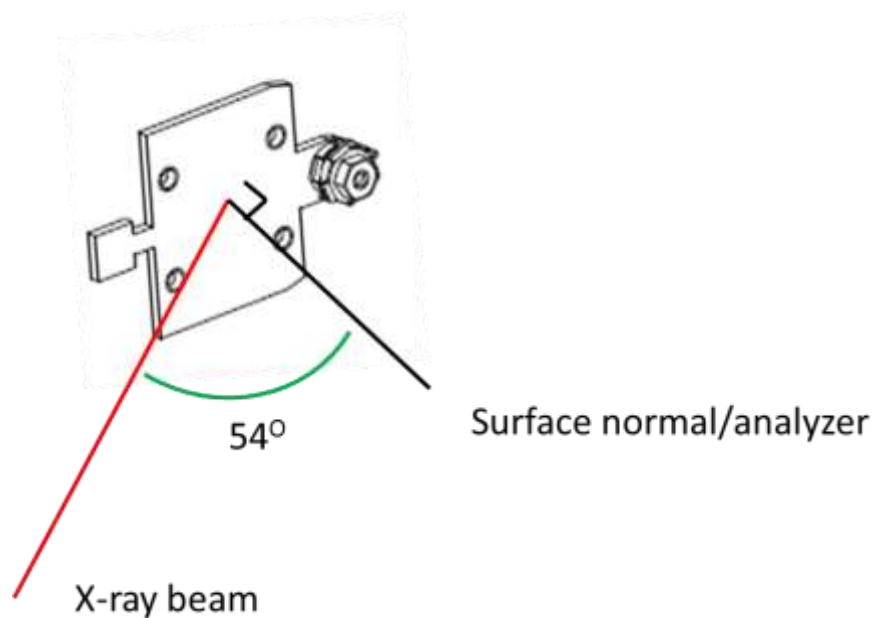


Fig. 7-20: Orientation of the sample during experiment.

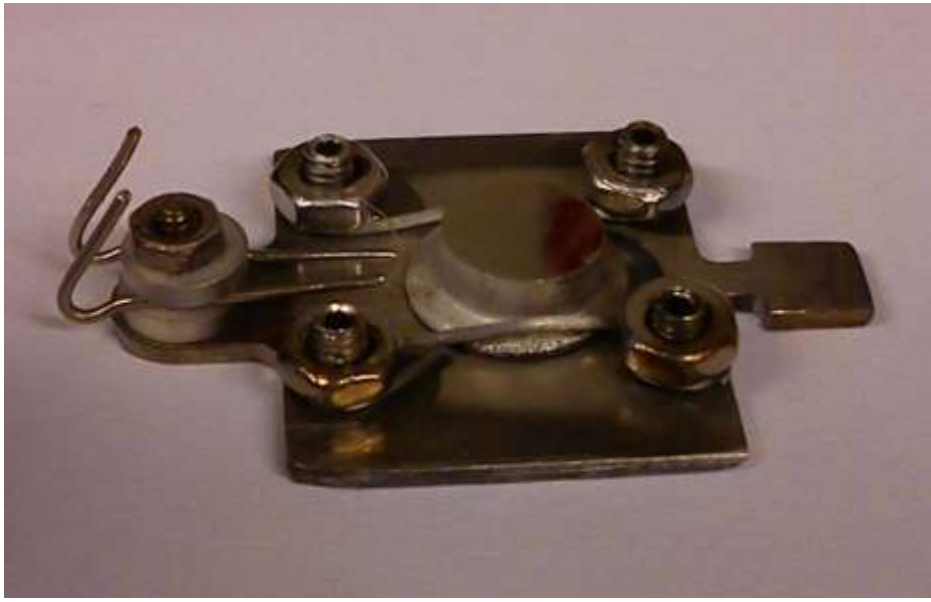


Fig. 7-21: Sample holder with bended alumel/chromel thermocouple wires.

7.2.4 Pressure monitoring

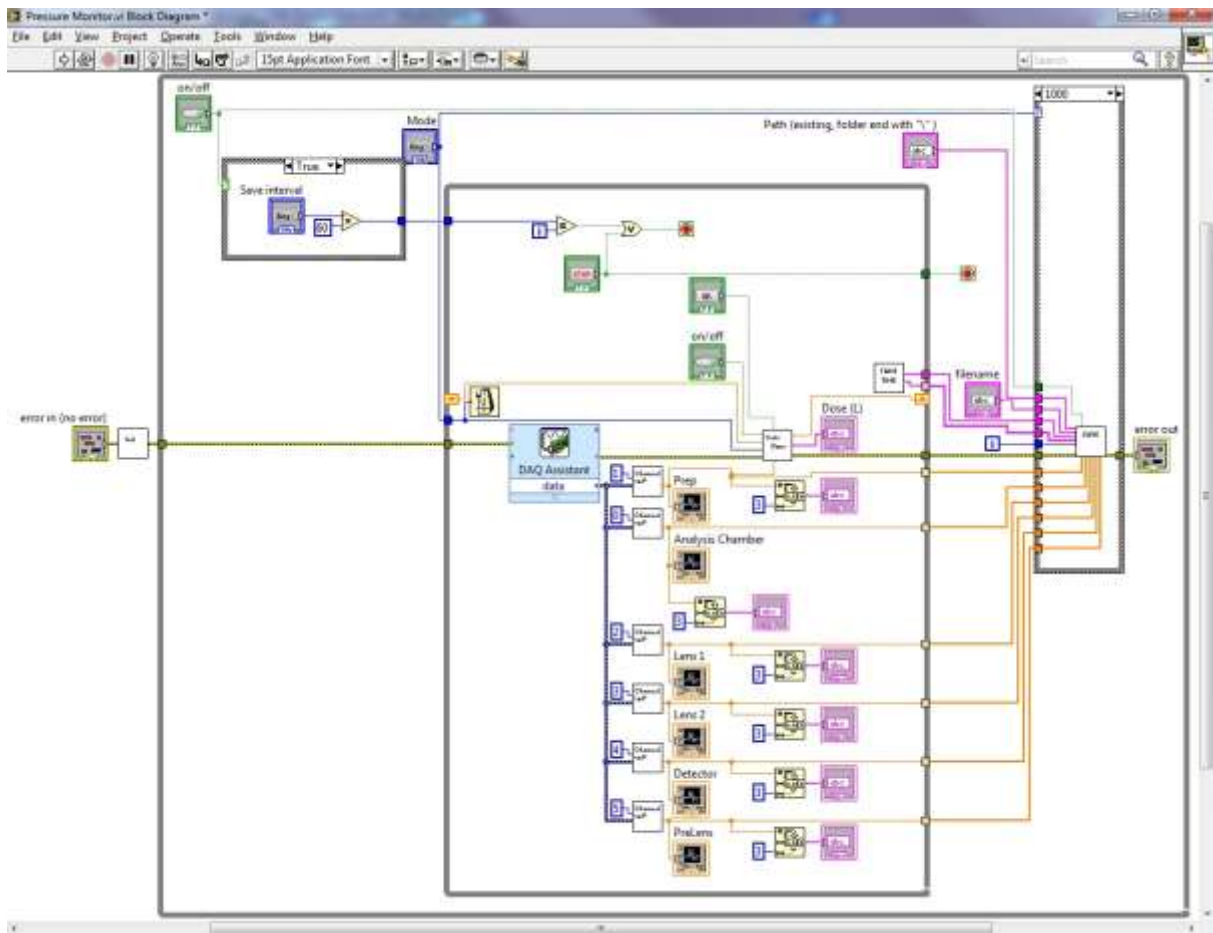


Fig. 7-22: Scheme of the pressure measurement system. All vacuum gauges are each connected to a control unit that continuously monitors and displays the pressure using a LabView script.

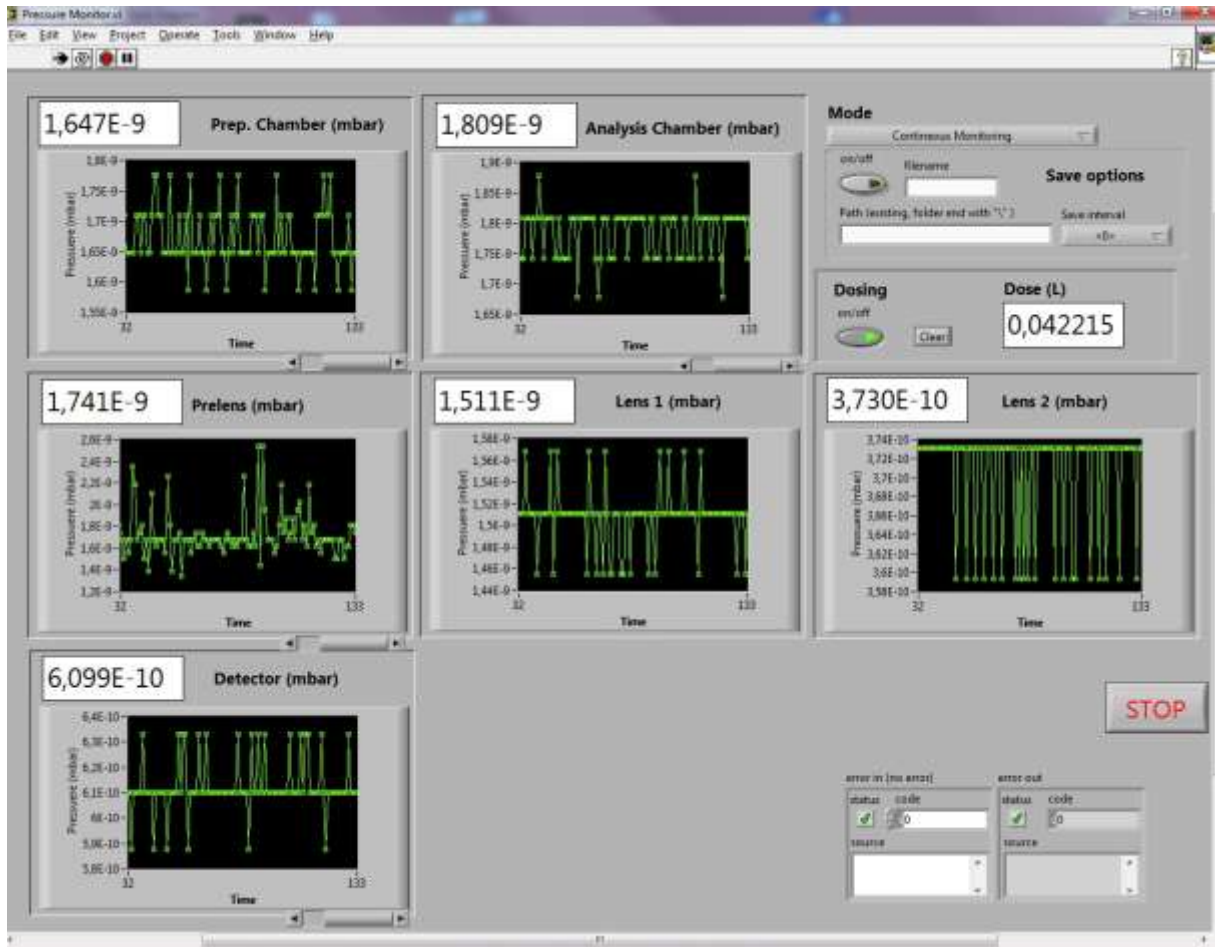


Fig. 7-23: Front panel of the pressure control system.

7.2.5 Beam flux calibration

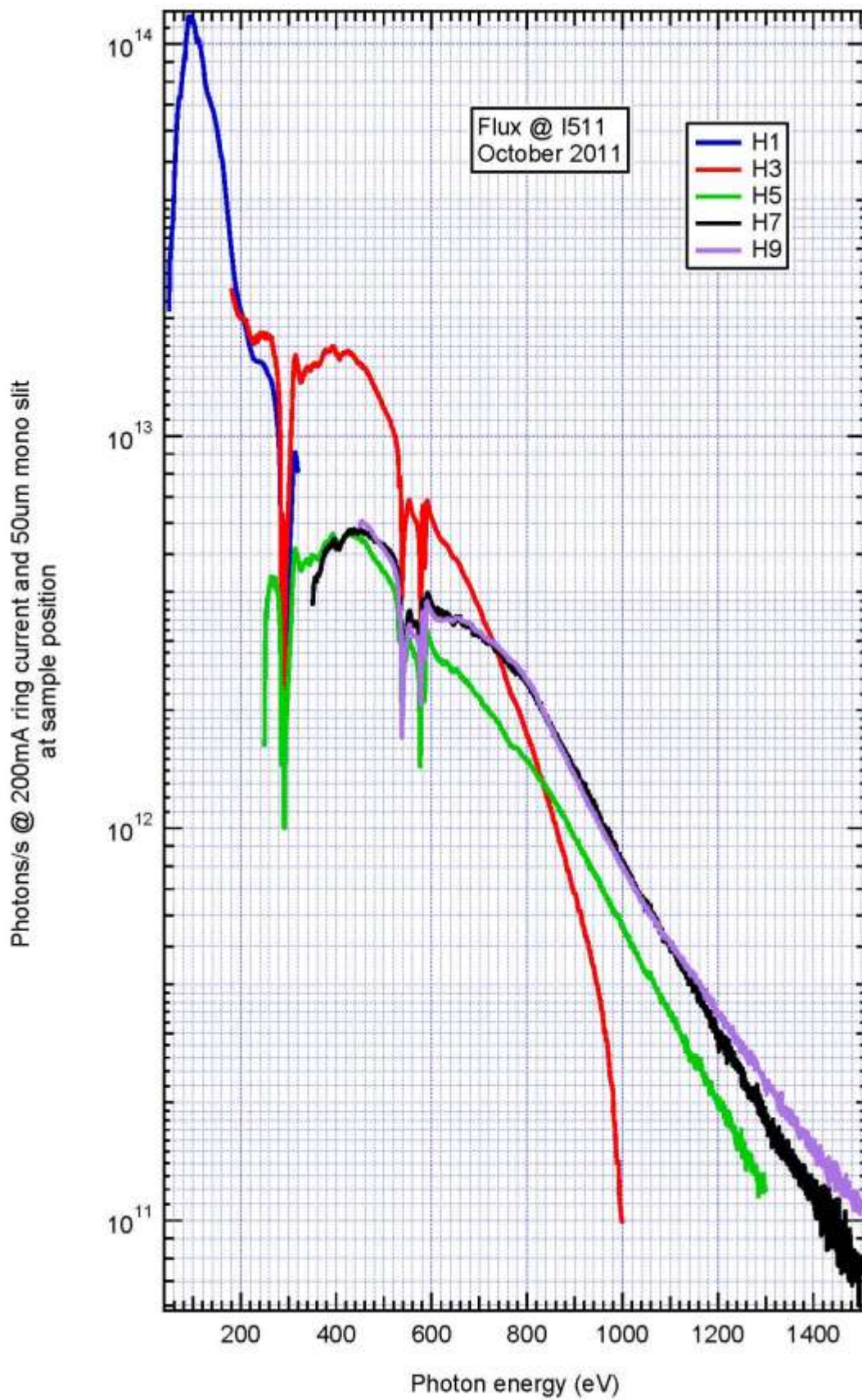


Fig. 7-24: Beam flux calibration for Maxlab I511 beamline during beamtime.

SX700 Resolution, 1220 l/mm, C=4.5, M3 50%

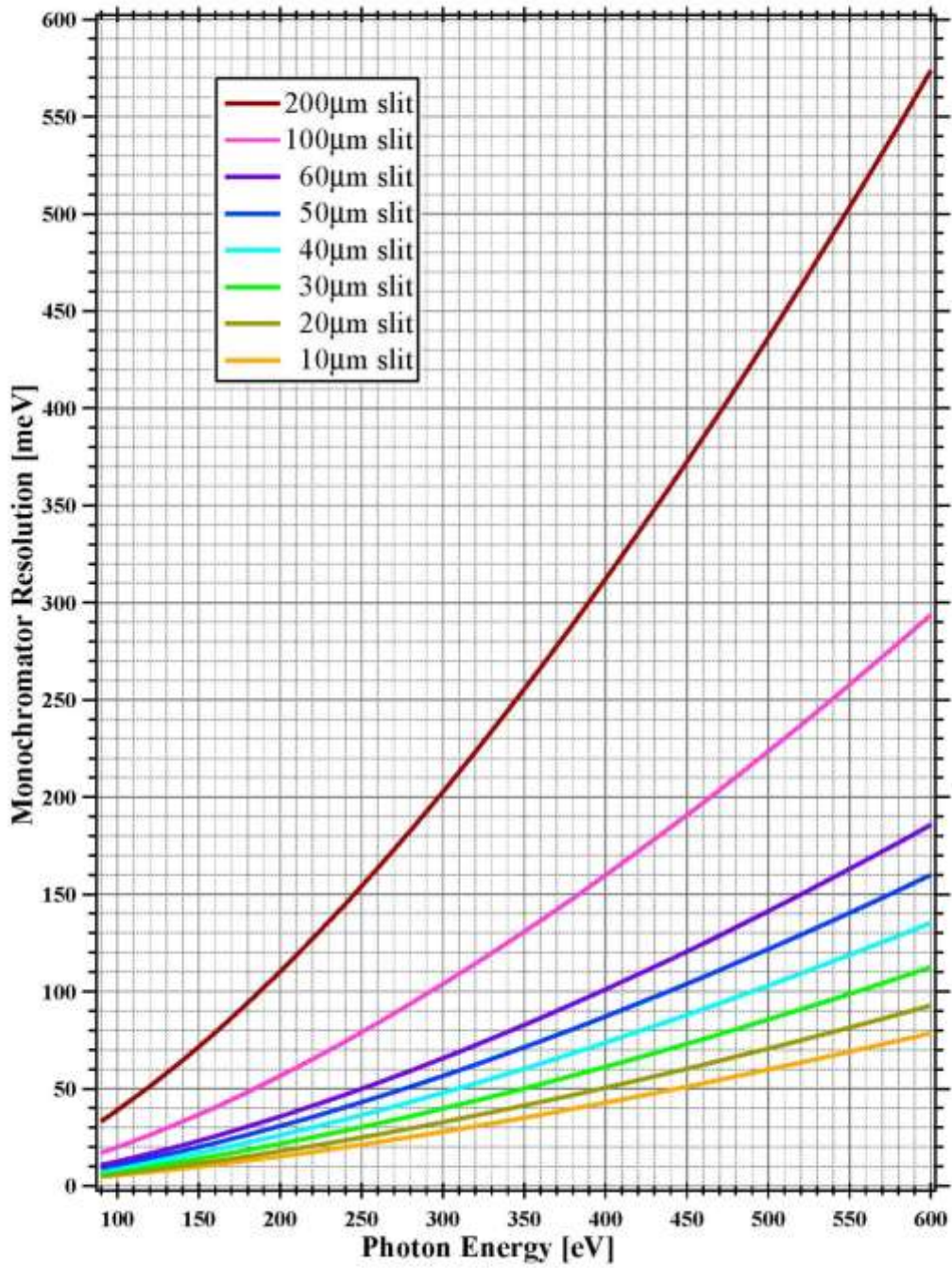


Fig. 7-25: Monochromator resolution 90 – 600 eV during beamtime.

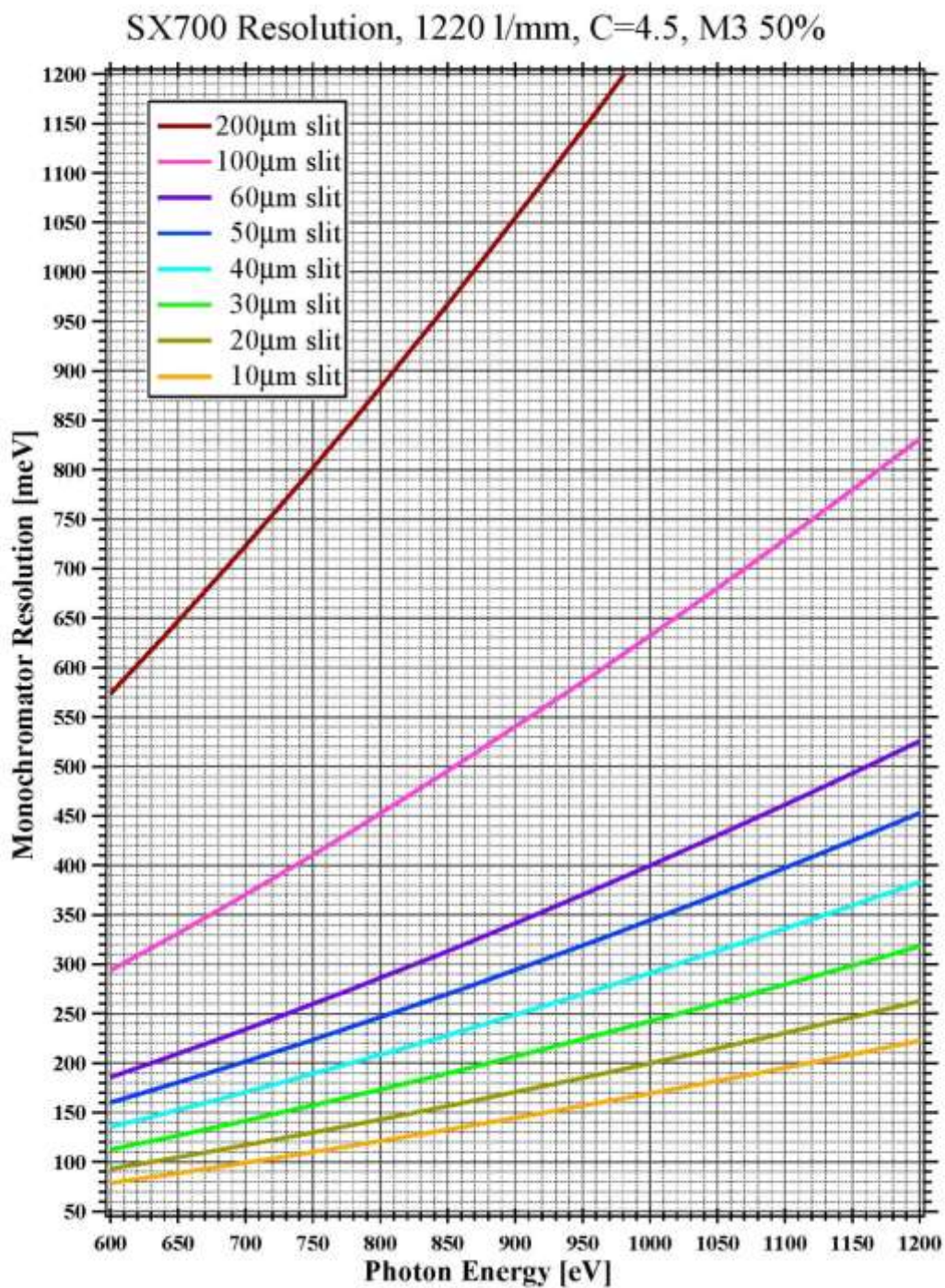


Fig. 7-26: Monochromator resolution 600 – 1200 eV during beamtime.

7.3 Mean free path

The following diagrams were provided by the National Institute for Materials Science (NIMS). More details about Penn algorithm, Bethe equation and TPP-2M equation can be found in [85, 275-279].

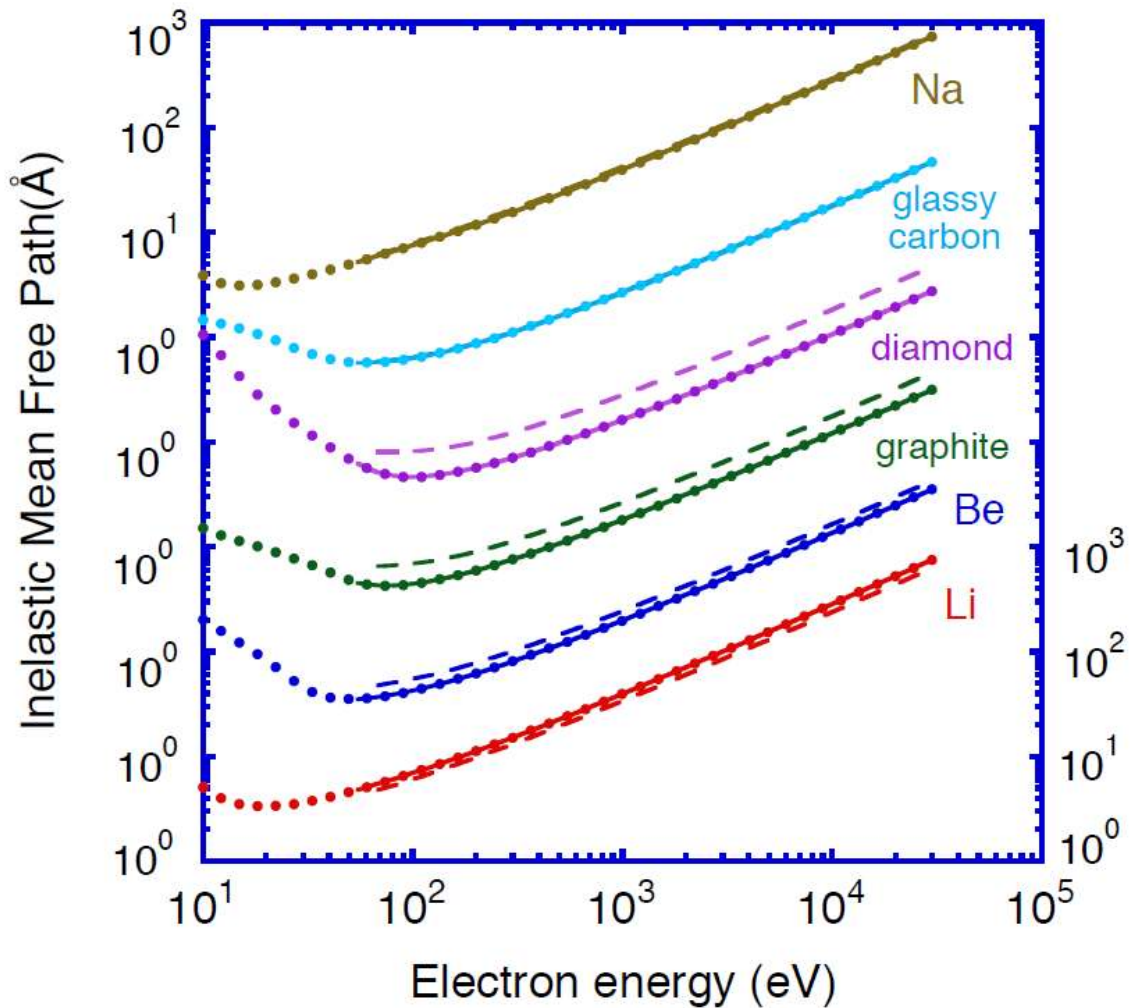


Fig. 7-27: Plots of electron inelastic mean free paths as a function of electron energy. Solid circles are showing calculated IMFPs from the Penn algorithm, solid lines are showing fits to these IMFPs with the modified Bethe equation and long-dashed lines indicate IMFPs calculated from the TPP-2M equation. Successive plots have been displaced vertically for clarity, and the ordinate scale at the left indicates these displacements [275].

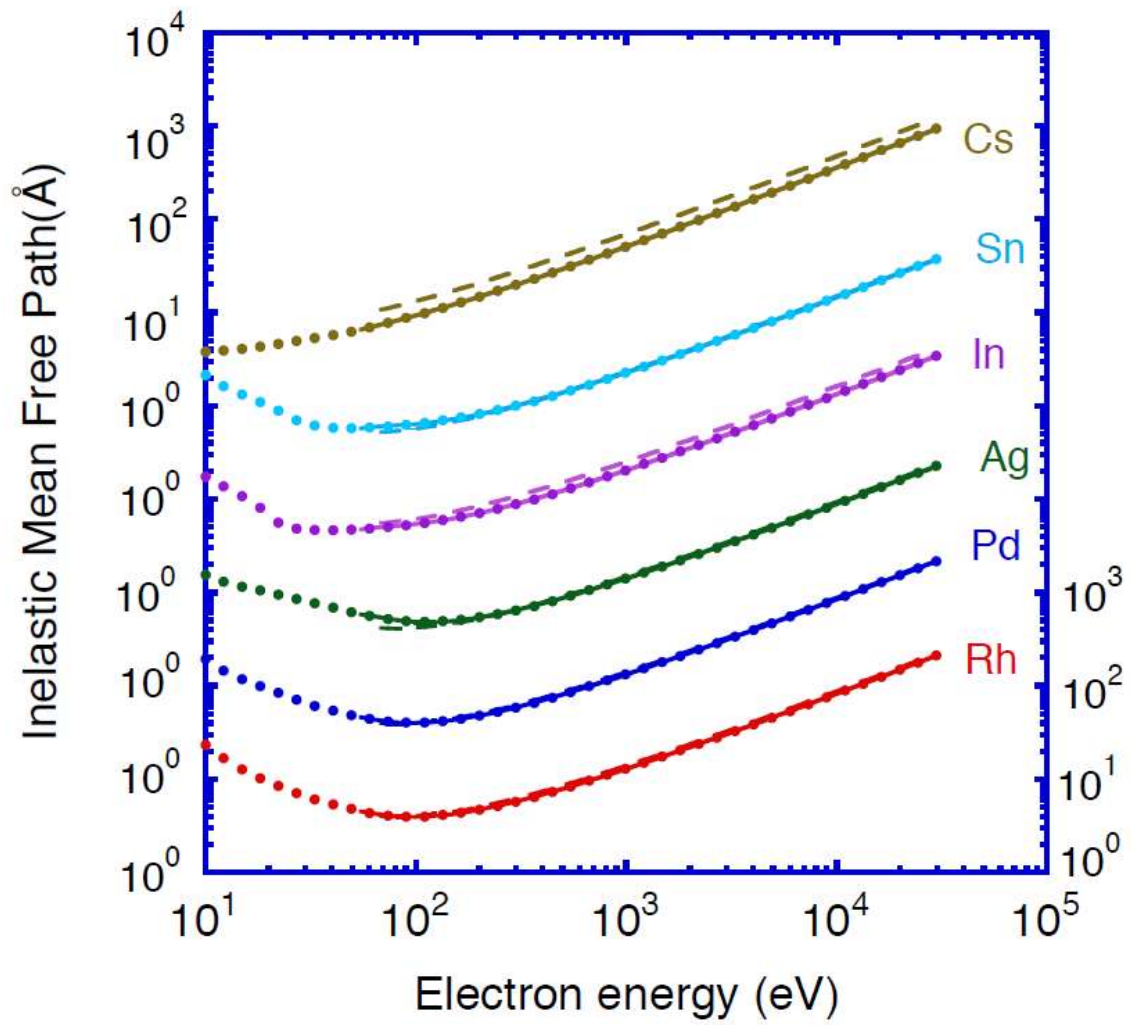
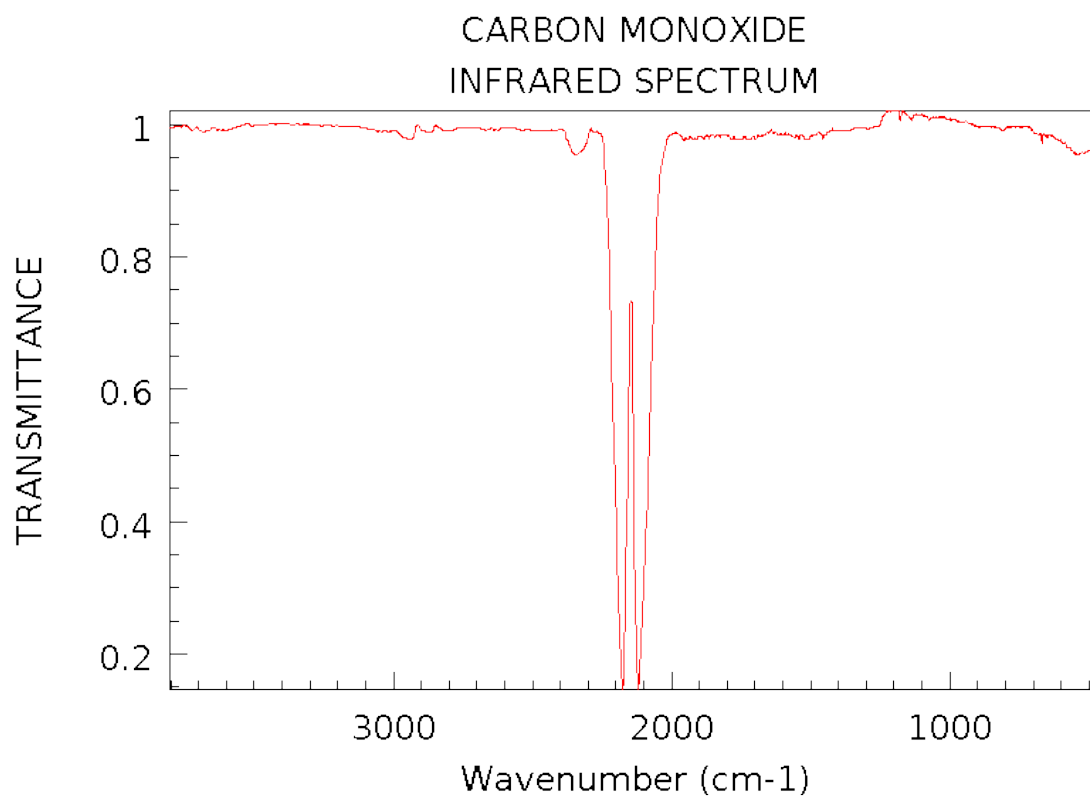


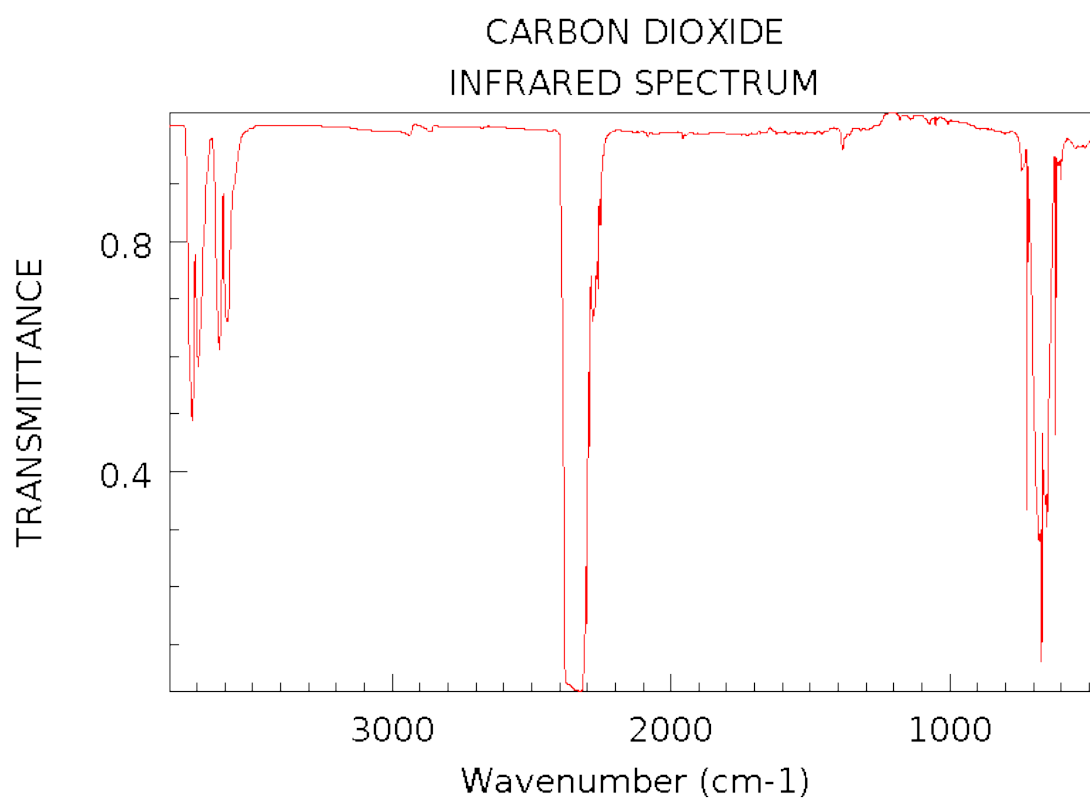
Fig. 7-28: Plots of electron inelastic mean free paths. See caption to Fig. 8-27 [275].

7.4 Infrared spectra in gas phase



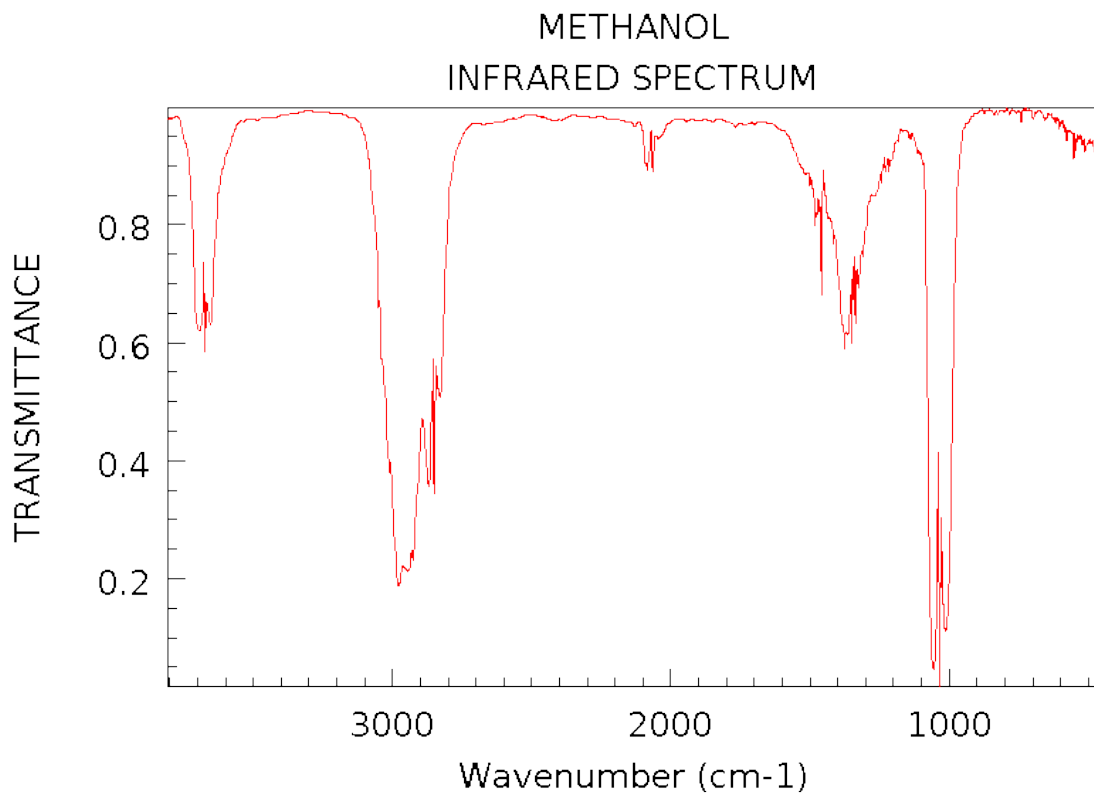
NIST Chemistry WebBook (<http://webbook.nist.gov/chemistry>)

Fig. 7-29: Gas phase IR spectrum of CO . Reprinted from [280].



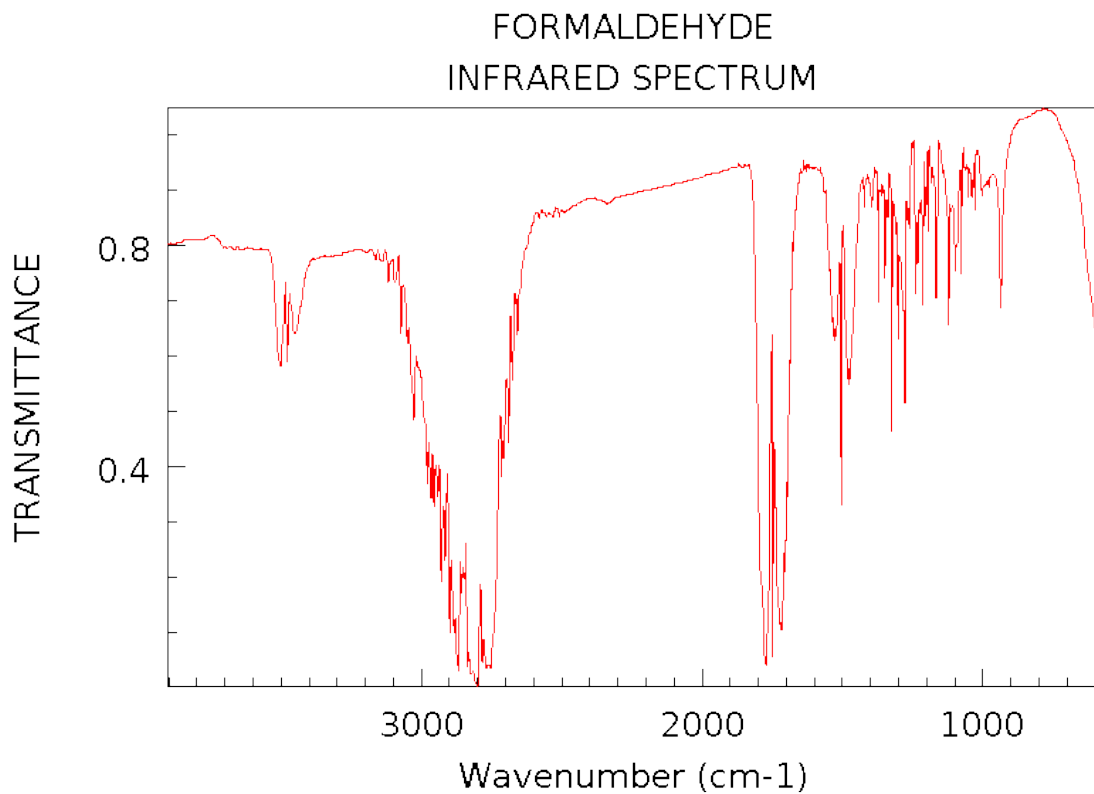
NIST Chemistry WebBook (<http://webbook.nist.gov/chemistry>)

Fig. 7-30: Gas phase IR spectrum of CO_2 . Reprinted from [280].



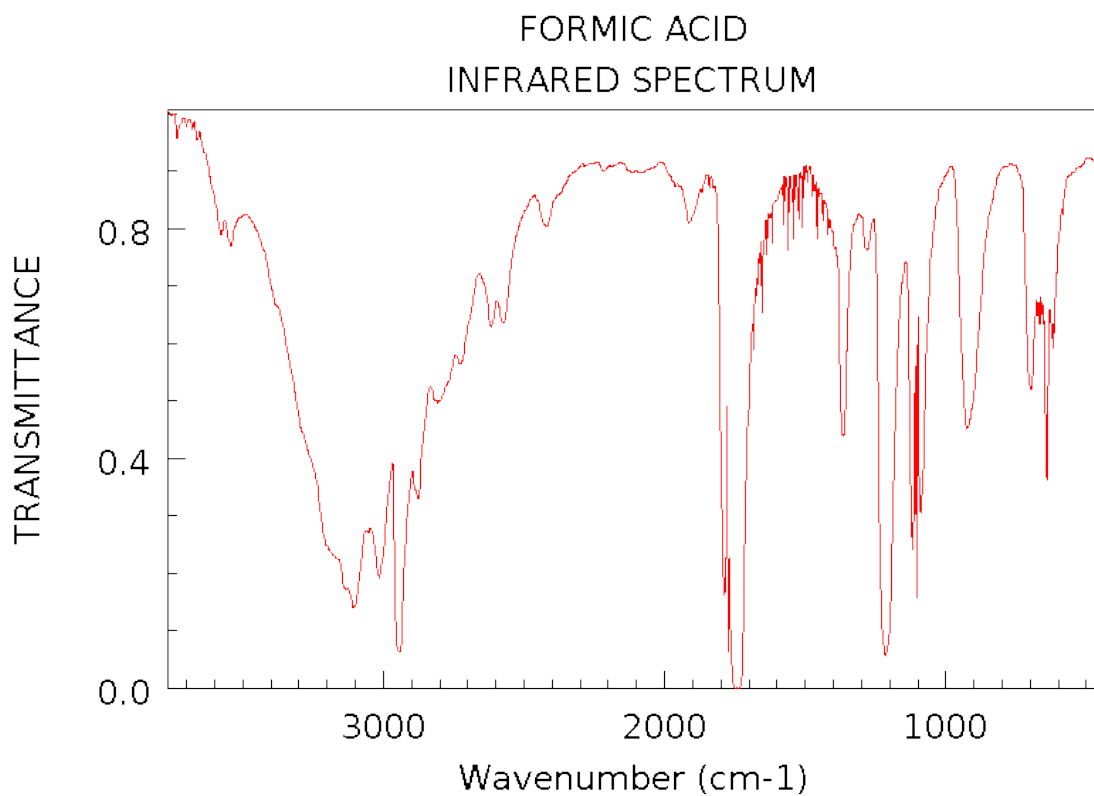
NIST Chemistry WebBook (<http://webbook.nist.gov/chemistry>)

Fig. 7-31: Gas phase IR spectrum of methanol. Reprinted from [280].



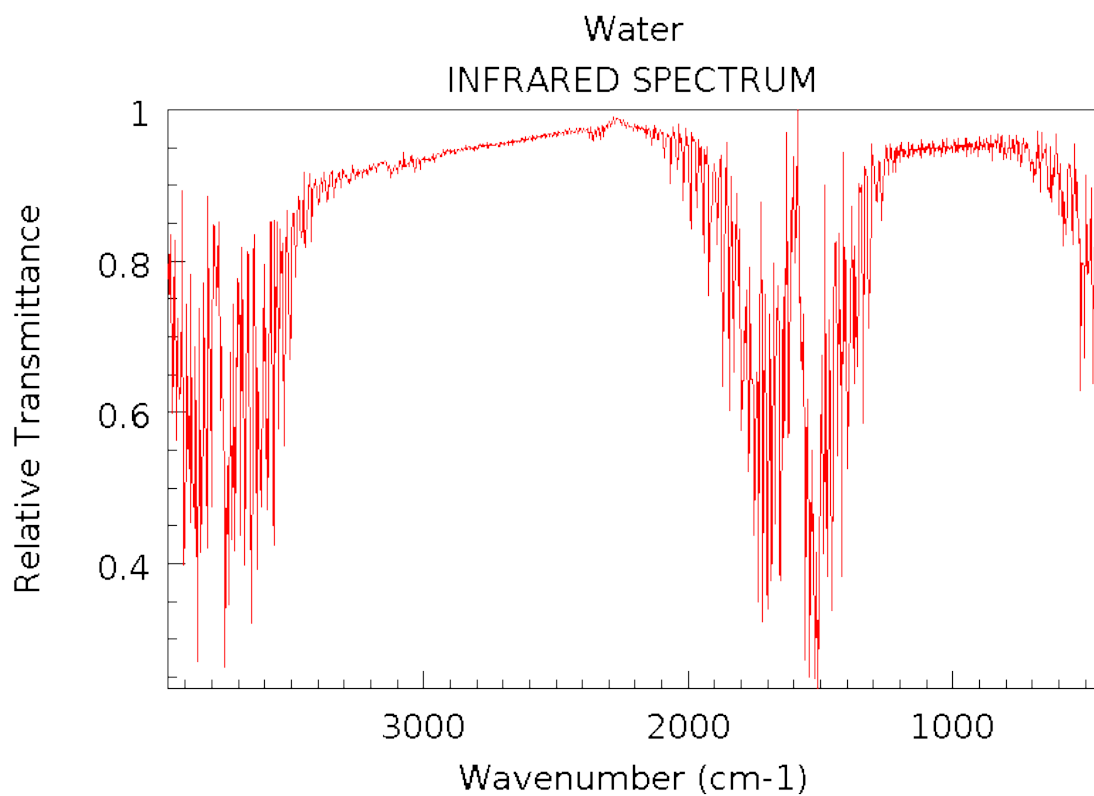
NIST Chemistry WebBook (<http://webbook.nist.gov/chemistry>)

Fig. 7-32: Gas phase IR spectrum of formaldehyde. Reprinted from [280].



NIST Chemistry WebBook (<http://webbook.nist.gov/chemistry>)

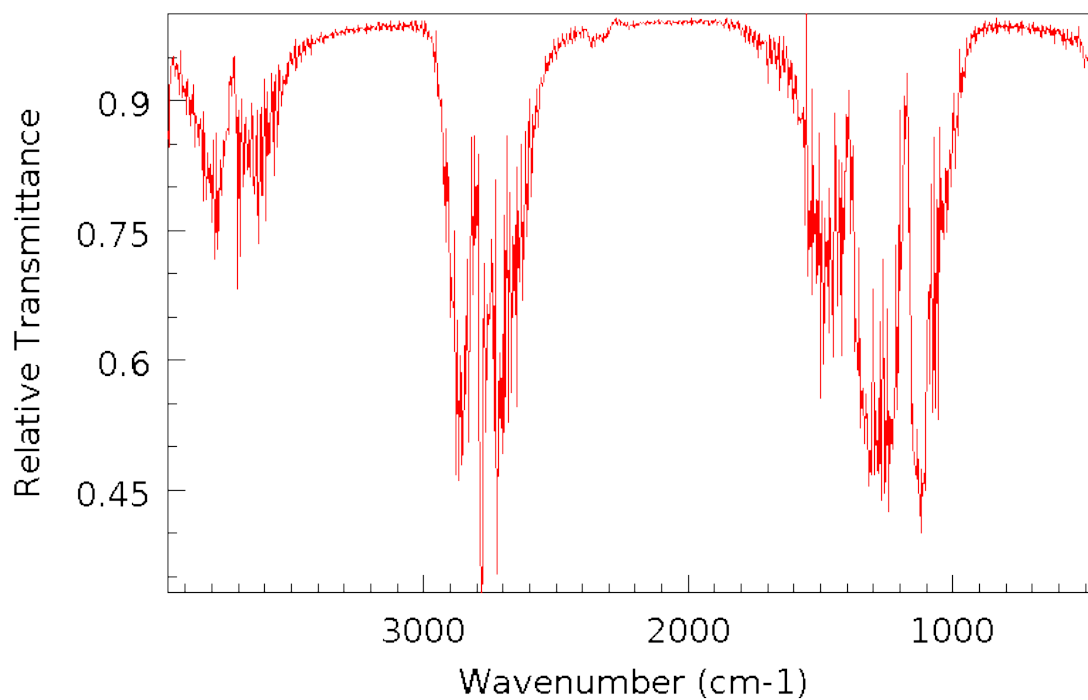
Fig. 7-33: Gas phase IR spectrum of formic acid. Reprinted from [280].



NIST Chemistry WebBook (<http://webbook.nist.gov/chemistry>)

Fig. 7-34: Gas phase IR spectrum of water. Reprinted from [280].

Deuterium oxide
INFRARED SPECTRUM



NIST Chemistry WebBook (<http://webbook.nist.gov/chemistry>)

Fig. 7-35: Gas phase IR spectrum of D_2O . Reprinted from [280].

7.5 Infrared spectra on a Pd(111) surface

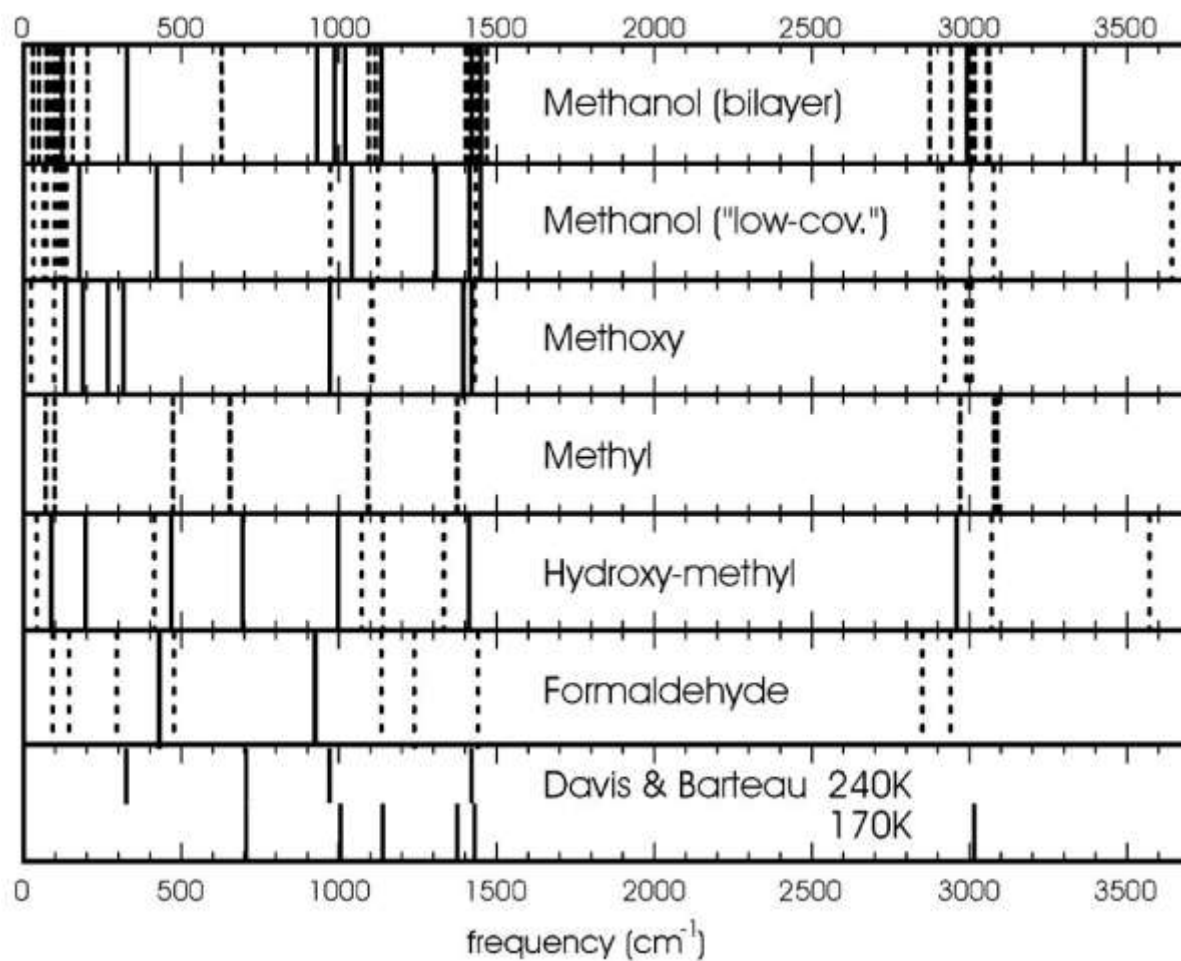
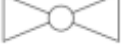
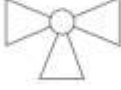


Fig. 7-36: Calculated IR frequencies on Pd(111) for methanol and possible decomposition intermediates. Full lines: modes with a large dynamic dipole moment; dashed lines: modes with a small dynamic dipole moment. The experimental EELS results are shown in the bottom panel for comparison at 170 K (lower half) and 240 K (upper half). Reprinted from [281].

7.6 Vacuum symbols

Common vacuum symbols for pumps, valves, and measurement used for this work [129].

Tab. 7-2: Common vacuum symbols.

	Vacuum pump, general		Cooling trap
	positive displacement vacuum pump, rotating		Vacuum chamber
	Rotary vane pump		Valve, general
	Turbopump, general		Angle valve
	Turbomolecular pump		Straight-way cock
	Scroll pump		Three way valve
	Getter pump		Gate valve
	Adsorption pump		Linear transfer feedthrough with flange
	Flange connection, general		Vacuum label ⁹
	Flange connection, screwed		Vacuum gauge head ⁷
	Klein flange connection (KF)		Flow measurement

⁹ Only approvable in shown position (with cone end downward).

7.7 List of symbols

The following list contains all symbols used in this work:

A	Area	S	Sensitivity constant
a	Lattice vector	$S_{(E_{kin})}$	Spectrometer sensitivity
e	Elementary electric charge	\vec{S}	Total spin
E_0	Kinetic energy of peak position	T	Temperature
E_0	Pass energy	U	Direct voltage
E_B	Binding energy	$u(t)$	Time varying voltage
E_{des}	Desorption energy	U_x	Voltage applied to x drive (STM)
E_{fermi}	Fermi level	U_y	Voltage applied to y drive (STM)
E_{kin}	Kinetic Energy	U_z	Voltage applied to z drive (STM)
E_p	Electric field (p-polarized)	V	Alternating current voltage
E_s	Electric field (s-polarized)	v	Velocity vector
F_x	X-Ray flux	\bar{v}	Velocity magnitude
$fwhm$	Full width at half maximum	$\overline{v^2}$	Mean value of velocity square
h	Planck constant	V_m	Modulation voltage
I	Tunneling current (STM)	v_{rms}	Mean root square
I_0	Ion current	$V(z)$	Potential barrier
i_A	Auger electron current	w	Thickness potential barrier (STM)
i_p	Primary electron current	$w(v)$	Probability (velocity distribution)
I_p	Light intensity (p-polarized)	Y	Probability of Auger decay
I_s	Light intensity (s-polarized)	z	Probing depth
j	Total momentum (orbital)	z	Direction of tunneling current
J_2	Second order Bessel function	β	Heating rate (TPD)
\vec{J}	Total angular momentum	ε	Electric field
J_N	Flux	ε_0	Permittivity of free space
k	Boltzmann constant	γ	Angle between two base vectors
l	Orbital angular momentum	γ	Vibrational frequency
\vec{L}	Total orbital angular momentum	Θ	Take-off angle
m	Magnetic quantum number	Λ	Mean free path
m_0	Mass of one particle	λ	Inelastic mean free path of the Auger electron
N	Number of particles	λ	Wavelength
N	Electrons colliding with gas particles	ϑ	Angle of incidence
n	Number density of molecules	Φ	Particles per area
n	Principal quantum number	Φ	Work function
$n_{(z)}$	Concentration in z	$\psi(z)$	Wave function (STM)
p	Pressure	Ψ_e	Penetrating wave (STM)
Q	Ionization probability	ψ_a	Transmitted wave (STM)
R	Background scattering factor	σ	Cross section
R	Reflectance (PM-IRAS)	$\sigma_{(E_{kin})}$	Effective cross section of photoemission
R	Relative resolution (XPS)	ν	Wave number
r	Distance between two particles	ω	Frequency
r_1, r_2	Collision radii		
s	Spin quantum number		

7.8 List of abbreviations

AES	Auger Electron Spectroscopy
AFM	Atomic Force Microscopy
BSE	Back-scattered Electrons
CAE	Constant Analyzer Energy
CF	ConFlat (Flange)
DIC	Differential Interference Contrast (Microscopy)
DFT	Density Functional Theory
DMFC	Direct Methanol Fuel Cell
DOS	Density of States
EDX	Energy Dispersive X-Ray Spectroscopy
EELS	Electron Energy Loss Spectroscopy
EXAFS	Extended X-Ray Absorption Fine Structure
FAT	Fixed Analyser Transmission
FWHM	Full Width at Half Maximum
HOPG	Highly Ordered Pyrolytic Graphite
HP-XPS	High Pressure X-Ray Photoelectron Spectroscopy
HSA	Hemispherical Analyzer
HREELS	High Resolution Electron Energy Loss Spectroscopy
KF	Klein Flange
LEED	Low Energy Electron Diffraction
MCT	Mercury Cadmium Telluride (HgCdTe)
ML	Monolayer
MSR	Methanol Steam Reforming
MWNT	Multi-walled Nanotubes
NEXAFS	Near Edge X-Ray Absorption Fine Structure
PAW	Projector Augmented-Wave Method
PED	Photoelectron Diffraction
PM-IRAS	Polarization-Modulation Infrared Reflection Absorption
QCM	Quartz Crystal Microbalance
QMS	Quadrupole Mass Analyzer
QTAIM	Quantum Theory of Atoms in Molecules

RPBE	Revised Perdew-Burke-Ernzerhof Functionals
SEM	Scanning Electron Microscope
SEXAFS	Surface-extended X-Ray Absorption Fine Structure
SFG	Sum Frequency Generation
SPS	Spark Plasma Sintering
STM	Scanning Tunneling Microscope
TCU	Thermal Control Unit
TEM	Transmission Electron Microscopy
TPD	Thermal Desorption Spectroscopy
UHV	Ultra-high Vacuum
UPS	Ultraviolet Photoelectron Spectroscopy
VASP	Vienna Ab initio Simulation Package
VOC	Volatile Organic Compound
XANES	X-Ray Absorption Near Edge Structure
XPS	X-Ray Photoelectron Spectroscopy
XRD	X-Ray Diffraction
XRF	X-Ray Fluorescence

7.9 List of figures

Fig. 1-1: The comparison of loss of reactivity over time between a conventional Cu catalyst (BASF F13456) and Pd/ZnO/Al ₂ O ₃ . The Cu-based catalyst suffers from fast deactivation, whereas the Pd-based catalyst deactivates to a lesser extent. Reprinted from [23]	14
Fig. 1-2: Activity (solid symbols) and CO selectivity (open symbols) of Pd/ZnO (circles) and an industrial Cu/ZnO catalyst (triangles). Reprinted from [24].....	15
Fig. 2-1: Overview of the XPS/PM-IRAS system and its components.	20
Fig. 2-2: Cold finger with a mounted single crystal (attached on Mo rods). The Alumel/Chromel wires are spot welded on the backside of the sample and connected to the thermocouple rods.	21
Fig. 2-3: Picture of the XPS and PM-IRAS setup located at VetMed (left side) and scheme of the components (right side).....	23
Fig. 2-4: New XPS and PM-IRAS setup located at Getreidemarkt/Lehartrakt after relocation.	24
Fig. 2-5: General scheme of the STM system before the preparation chamber was changed for the installation of a X-Ray source [44].....	25
Fig. 2-6: Assembling parts of the original sample plate for thick head-shaped crystals. The sample is clamped with a “spider” (picture on the right side). The mold for sample plate assembling (picture in the middle) is a self-made design by our technician. .	27
Fig. 2-7: Original sample plate for thick head-shaped crystals. The missing thermal/electrical insulation of the sample to the sample plate makes it impossible to reach stable high temperatures, as needed for sample preparation.	27
Fig. 2-8: New design of the K type thermocouple contact (sample holder to stage).	27
Fig. 2-9: Custom made ceramic plate (Al ₂ O ₃) to cover and insulate the single crystal in the sample holder.	28
Fig. 2-10: Scheme of CO bonding (on-top, bridge, three-fold hollow) on Pd (left) with the corresponding IRAS spectrum (right).....	29
Fig. 2-11: Dipoles of a bi-atomic molecule.....	31
Fig. 2-12: Reflection of an IR beam on a metal surface. a) Polarization planes and angle of incidence. b) Phase shift upon reflection. c) Surface Electric field and Intensity of p-polarized light vs. angle of incidence [39, 48].	31
Fig. 2-13: Principle of polarization modulation with a PEM a) relaxed and b) half-wave retardation respectively.....	32
Fig. 2-14: Polarizer and ZnSe-photoelastic modulator used for PM-IRAS.	33
Fig. 2-15: Sketch of the PM-IRAS setup in our lab.	33
Fig. 2-16: Data processing in PM-IRAS using CO adsorption on Pd(111) as example: a) average spectrum, b) modulated difference spectrum, c) differential reflectance spectrum (to the spectrum of the clean Pd(111) surface) and d) final PM-IRAS spectrum after normalizing. The inserts show magnifications of the range between 2300 cm ⁻¹ and 1700 cm ⁻¹ . The black curves in the inserts represent the corresponding background spectra of the empty surface.....	34
Fig. 2-17: PM-IRAS setup (left side: IR modulator, middle: high pressure chamber, right side: detector).	35
Fig. 2-18: PM-IRAS Setup. Detailed view of the high pressure cell.	36
Fig. 2-19: Scheme of the energy levels in XPS. The ejection of an electron requires more energy than the work function of the material.	39
Fig. 2-20: Photoemission for XPS and secondary processes (X-Ray fluorescence and Auger electron spectroscopy).	40

Fig. 2-21: Scheme of available stationary states (not to scale). These starts to merge with increasing n , that is, as E_{Fermi} is approached. Spectroscopic notation is describing these levels is shown above and X-ray notation is shown in brackets.	41
Fig. 2-22: XPS survey scan of a Pd(111) sample evaporated with 3 ML Zn. XPS and Auger signals are visible.....	43
Fig. 2-23: Sketch and basic principle of a hemispherical analyzer (HSA).	48
Fig. 2-24: Sketch of a channeltron detector (left) and microchannel plate detector (right).....	50
Fig. 2-25: Overview of the whole Maxlab hall and beamlines (including I511), from Maxlab information folder.	52
Fig. 2-26: Maxlab III storage ring (left) and beamline I511 (right).	53
Fig. 2-27: Maxlab III HP-XPS endstation (beamline I511)	54
Fig. 2-28: HP-XPS cell. On the left side with open bayonet coupling to the analyzer, in the middle open sample inlet and on the right side ready for measurement.....	55
Fig. 2-29: Screenshot of the programm XPSpeak processing a Pd3d peak as example.	58
Fig. 2-30: Scheme of an KLM Auger process. A core electron can be removed by an photon or electron beam, leaving behind a hole. This core hole is then filled by an outer shell electron. The loss of energy is equal to the difference in orbital energies. This energy is coupled to a second outer shell electron, that will be emitted from the atom.	60
Fig. 2-31: Screenshot of RFA-PC recording a Pd(111) sample. This software is used for AES measurement and for the LEED settings.	62
Fig. 2-32: Comparison of low energy electron diffraction (LEED), backscattering photoelectron diffraction (PED), and surface extended X-ray absorption fine structure (SEXAFS).	63
Fig. 2-33: Schematic representation of a rectangular surface lattice and the corresponding LEED pattern. In the lower picture, a primitive 2x2 overlayer of e.g. adsorbate molecules is superimposed on the surface principal lattice [39].	65
Fig. 2-34: Scheme and principle of a LEED system.	66
Fig. 2-35: LEED pattern of a Pd(111) single crystal surface at 100 eV.	67
Fig. 2-36: Schematic TPD setup. TCU=Temperature Control Unit; QMS=Quadrupole Mass Spectrometer.	69
Fig. 2-37: Basic principle of a Quadrupole Mass Spectrometer for filtering sample ions, based on their mass/charge ratio.	71
Fig. 2-38: STM piezomotor controlled tip movement over a solid surface.	73
Fig. 2-39: Sketch of the Aarhus STM system. 1=sample, 2=holder, 3=quartz balls, 4=tip, 5=macor [®] holder, 6=scanner tube, 7=rod, 8=macor ring, 9=piezo tube [103].	74
Fig. 2-40: Tunneling through a potential wall. The energy of the tunneled particle ($E < V_0$) is the same but the amplitude is lower, proportional to the tunneling probability. Ψ_e =penetrating wave, Ψ_a =transmitted wave.	75
Fig. 2-41: Test pictures of HOPG with a Pt/Ir tip on air.	80
Fig. 2-42: Test pictures of a Si(111) 7x7 reconstructed surface in UHV (W-tip).	80
Fig. 2-43: Working principle of a clamping-type piezo motor (inchworm).	81
Fig. 2-44: Constant current mode. U_z =Voltage applied to the piezo drive for z movement (height).	83
Fig. 2-45: Constant height mode. Large structures can cause a tip crash.	84
Fig. 2-46: Active anti-vibration system (air buffer) in our STM system.	85
Fig. 2-47: Screenshot of "SPECsProbeUSB".	86
Fig. 2-48: Screenshot of WSxM software processing Pd(111) STM data.	87
Fig. 2-49: Picture of an Omicron EFM 3 evaporator as used in our lab. The instrument is designed for high precision sub-mono-layer up to multi-layer deposition of a wide variety of evaporants including highly refractory materials.	89

Fig. 2-50: Scheme of an Inficon microbalance as was used in our UHV-system.....	90
Fig. 2-51: E-beam heater of the STM system. Left: filament; right: glowing filament with sample.	92
Fig. 2-52: Scheme of spot welding. A high current melts the metal and forms the weld.	93
Fig. 2-53: Scheme of spark plasma sintering.	94
Fig. 2-54: Velocity distribution.	97
Fig. 2-55: Swagelok® fitting for connecting gasline tubes [Swagelok product catalogue]...	103
Fig. 2-56: Scheme of a Kleinflange (KF). 1=Kleinflange, 2=centering ring, 3=clamping ring.	104
Fig. 2-57: Scheme of a CF flange. Aa knife edge cuts into the copper gasket (black), providing an extremely leak-tight, metal-to-metal seal.	104
Fig. 2-58: Principle of a rotary vane pump, 1=rotor; 2=vanes; 3=pushrod/spring [128].	107
Fig. 2-59: Mechanism of a scroll pump	108
Fig. 2-60: Scroll pump orbiting (left side) and Teflon sealing (right side).	108
Fig. 2-61: 3D model of a turbomolecular pump [131].	110
Fig. 2-62: Momentum transfer in a turbopump.	111
Fig. 2-63: Scheme of a titanium sublimation pump.	112
Fig. 2-64: Getter pump: schematic drawing of the pumping effect of an adsorption pump. <i>K1</i> , <i>K2</i> getter cathode plates (Ti); <i>A</i> anode cylinder; <i>B</i> magnetic field; on <i>A</i> and outlying area of <i>K1</i> and <i>K2</i> gas particles covered with getter material (Ti); implanted gas particles in the inner area of <i>K1</i> and <i>K2</i> [125].	113
Fig. 2-65: Baratron gauge. 1=housing; 2=membrane; 3=feedthrough capacitor ring, 4=capacitor ring; 5=gas inlet (reference pressure p_2); 6=connection to vacuum chamber with pressure p_1 to be measured; 7=membrane zero position, Δs =membrane displacement [125].	116
Fig. 2-66: Scheme of a Pirani gauge. R_F =electrical resistance of the filament, R_C =compensation, R_1, R_2 =resistance of the branches, <i>D</i> =detector.	117
Fig. 2-67: Ion gauge. U_H =Filament voltage; U_A = Anode potential (acceleration voltage); I_H = Filament current of glow anode; I^- =Electron current to anode; i^+ =Electron current to collector; <i>K</i> =Cathode; <i>A</i> =Anode; <i>C</i> =Collector.	118
Fig. 2-68: Ion gauge. U_A = Anode potential, acceleration voltage; <i>K</i> =Cathode; <i>A</i> =Anode; <i>C</i> =Collector.....	118
Fig. 2-69: Schematic drawing. 1=Ionization of a gas particle by an electron and following emission of a secondary electron due to collision of the ion with the collector; 2=electron stimulated ion desorption; 3=X-ray effect; inverse X-ray effect (electron emission from the wall). When electrons are hitting the grid, there is a probability for the emission of photoelectrons which are producing photoelectric interferences in the ion collector. This limits the range of ion gauges but can be prevented with improved configuration of collector and cathode. The inverse X-ray effect is generated by X-ray stimulated photoelectrons from the gauge casing in the opposite direction but less intense. [122, 125].	120
Fig. 2-70: Scheme of CO molecular orbitals.....	122
Fig. 3-1: AlK α XP spectra of a clean Pd(111) surface.....	126
Fig. 3-2: Pd(111) hexagonal surface generated using BALSAC (web application) [157]. ...	128
Fig. 3-3: LEED of a hexagonal Pd(111) surface at 100 eV (left) and 225 eV (right), respectively.	128
Fig. 3-4: Lattice model of CO on Pd(111) at saturation coverage (0.75 ML) [39].	129
Fig. 3-5: LEED of CO on Pd(111). Low CO coverage (left) and saturation coverage (right), respectively.	130
Fig. 3-6: Carbon monoxide adsorbed on Pd(111) at saturation coverage (285.5 eV).....	131

Fig. 3-7: PM-IRAS spectra of CO on Pd(111) recorded at 200 K in 10^{-6} mbar CO. Three different adsorption sites (on-top, bridge, hollow bonded) are clearly visible.	132
Fig. 3-8: CO TPD of a saturated Pd(111) surface. A sharp peak at 146 K and a broad peak with an absolute maximum at 448 K and a shoulder at about 350 K can be observed. The broad band probably indicates heterogeneity of surface sites [28].	133
Fig. 3-9: TPD spectra for CO, CH ₂ O, and CH ₃ OH after dosing 10 L MeOH at 90 K on Pd(111). At 150 K a pronounced sharp desorption peak for CH ₃ OH can be detected (the M28 and M30 peaks at this temperature are fragments of the MS ionization process). A pronounced tailing desorption peak of CO desorption was found at 458 K.	136
Fig. 3-10: TPD spectra for D ₂ O (159 K), CO (461 K), CH ₂ O (155 K), and CH ₃ OH (156 K) after dosing each 10 L MeOH and D ₂ O at 90 K on Pd(111).	137
Fig. 3-11: TPD spectrum for D ₂ O after dosing 10 L D ₂ O at 90 K on Pd(111). D ₂ O desorbs at 166 K, slightly higher than with methanol co-dosing.	138
Fig. 3-12: PM-IRAS surface spectra measured after dosing 10 L methanol on Pd(111) at different temperatures. Range 1600 – 900 cm ⁻¹ . The IR band at ~1034 cm ⁻¹ can be assigned to $\nu(\text{CO})$	139
Fig. 3-13: PM-IRAS surface spectra measured after dosing 10 L methanol on Pd(111) at different temperatures. Range 2600 – 1600 cm ⁻¹ . The weak band at ~1700 cm ⁻¹ can be assigned to $\nu(\text{CO})$ from H ₂ CO.	140
Fig. 3-14: PM-IRAS surface spectra measured after dosing 10 L methanol on Pd(111) at different temperatures. Range 4000 – 2600 cm ⁻¹ . The broad band at ~3300 cm ⁻¹ can be assigned to $\nu(\text{OH})$ for high coverage MeOH and the narrow band at ~3550 cm ⁻¹ to low coverage MeOH.	140
Fig. 3-15: PM-IRAS surface spectra, MeOH on Pd(111) depending on the pressure (at RT). The IR bands at 1226 cm ⁻¹ and 1319 cm ⁻¹ can be assigned to formaldehyde and at ~1900 cm ⁻¹ to CO.	141
Fig. 3-16: XPS C1s spectra: evolution of carbonaceous species on Pd(111) after 10L MeOH exposure with increasing temperatures from 100-600K. The C 1s signal shifts from 286.8 eV (100 K) to 285.5 eV (400 K) and vanishes at 600 K completely.	142
Fig. 3-17: XPS Pd 3d spectra: evolution of the Pd 3d signal after 10L MeOH exposure with increasing temperatures from 100-600K. The Pd 3d _{3/2} shifts slightly from 340.4 eV (100 K) to 340.2 eV (600 K). The Pd 3d _{5/2} signal shifts from 335.1 eV (100 K) to 334.9 eV (600 K). At 100 and 125 K a thick methanol overlayer dampens the Pd 3d signal almost completely.	143
Fig. 3-18: XPS C1s spectra of different methanol exposures on Pd(111) at 100 and 300 K. After exposure of >1 L methanol at 100 K a clear C 1s signal at ~286 eV is present.	145
Fig. 3-19: C1s XP spectra measured during 10 ⁻⁶ mbar methanol exposure on Pd(111) at 300 K. The C 1s signal at 285.8 eV can be assigned to CO and the signal at ~284.0 eV can be assigned to carbonaceous species.	146
Fig. 3-20: C1s XP spectra measured during 10 ⁻⁶ mbar methanol exposure on Pd(111) at 450 K. The CH _x formation rate (~284.5 eV) is faster than at 300 K.	148
Fig. 3-21: Evolution with time of carbon species. Relative amounts of CO and CH _x species (estimated by comparing XPS C1s to Pd 3d peak area using the well-known (2x2)CO saturation coverage as reference).	149
Fig. 3-22: Evolution of the binding energy of the carbonaceous species (XPS C1s spectra). At 300 K, the binding energy shifts from initially 383.6 eV to 284.1 eV. At 450 K, the CH _x formation is very fast and finally reaches a constant value around 284.4 eV	150

Fig. 3-23: Evolution of the binding energy of the carbonaceous species on Pd(111) at 300 K and a pressure of 10^{-6} mbar CH_3OH/O_2 . The CH_x signal (~ 284 eV) increased during reaction.	151
Fig. 3-24: Reaction mechanism of the methanol decomposition on Pd(111) [39].	152
Fig. 3-25: Preparation of a PdZn surface alloy with corresponding LEED pictures. The surface is covered with a Zn-layer after evaporation. Annealing leads to the formation of a Pd:Zn 1:1 surface alloy [39, 203].	154
Fig. 3-26: XPS Pd 3d region: a) Evolution of the Pd signal during alloy formation with 3 ML Zn initially deposited on Pd(111) at room temperature. b) Peak fit of the Pd 3d region after annealing 550 K (i.e. of red trace in a)).	155
Fig. 3-27: XPS Zn 2p region: Evolution of the Zn signal during alloy formation with 3 ML Zn initially deposited on Pd(111) at room temperature (grey trace) and after annealing 550 K (red trace).	155
Fig. 3-28: PM-IRAS spectra characterizing the PdZn/Pd(111) alloy formation (1 ML Zn evaporated) at successively higher annealing temperatures (spectra acquired after cooling to 90 K after annealing in $1 \cdot 10^{-6}$ mbar CO). The signal at ~ 2070 cm^{-1} can be assigned to on-top CO . After decomposition of the surface alloy (900 K) two IR bands at 2087 cm^{-1} (on-top CO) and at 1954 cm^{-1} (bridge-bonded CO) can be observed.	159
Fig. 3-29: Coverage-dependent PM-IRAS spectra of CO adsorption on >4 ML PdZn/Pd(111) at 100 K. Two types of CO can be observed. CO that does not have other CO molecules at adjacent adsorption sites (low coverage) and those that have CO neighbors (high coverage). These two species can be distinguished by IR. The band at 2068 cm^{-1} (increasing with coverage) can be assigned to neighboring CO	161
Fig. 3-30: CO TPD spectra from a 2 ML PdZn/Pd(111) alloy depending on annealing temperature. After an annealing temperature of 473 K a clear CO desorption peak at 199 K appeared. The desorption peak reached its maximum intensity ("ideal" PdZn alloy) after an annealing temperature of 573 K. Multiple desorption peaks after an annealing temperature of 623 K are an indication for alloy decomposition.	163
Fig. 3-31: CO TPD spectra from a >4 ML PdZn/Pd(111) alloy depending on annealing temperature. After an annealing temperature of 473 K a clear CO desorption peak at 185 K appeared. The desorption peak reached its maximum intensity ("ideal" PdZn alloy) after an annealing temperature of 573 K. Multiple desorption peaks after an annealing temperature of 623 K are an indication for alloy decomposition.	164
Fig. 3-32: CO coverage as deduced from the TPD spectra versus annealing temperature. The dashed line indicates saturation coverage on the "perfect" alloy. Error bars were derived from three repeated measurements. The saturation coverage of CO on Pd(111) is 0.75 ML.	166
Fig. 3-33: CO coverage as deduced from the TPD spectra versus annealing temperature. The dashed line indicates saturation coverage on the "perfect" alloy. Error bars were derived from three repeated measurements. The saturation coverage of CO on Pd(111) is 0.75 ML.	167
Fig. 3-34: Coverage-dependent CO TPD spectra for 2 ML Zn/Pd(111). For each series the CO dose at 90 K was subsequently increased from 0.5 to 5 Langmuir. Saturation coverage (sat.) was achieved by cooling the system in $1 \cdot 10^{-6}$ mbar CO to 90 K... 168	
Fig. 3-35: Coverage-dependent CO TPD spectra for >4 ML Zn/Pd(111). For each series the CO dose at 90 K was subsequently increased from 0.5 to 5 Langmuir. Saturation coverage (sat.) was achieved by cooling the system in $1 \cdot 10^{-6}$ mbar CO to 90 K... 169	

Fig. 3-36: Atomic resolution on a Pd(111) surface (15x15 ÅxÅ, tunneling current I_t : 0.440 nA, tunneling voltage V_t : 371.7 mV).	172
Fig. 3-37: Steps on a clean Pd(111) surface (large area scan; 2000x2000 ÅxÅ, I_t : 0.370 nA, V_t : 441.9 mV).	173
Fig. 3-38: 3D visualization of the steps on Pd(111) shown in Fig. 3-37.	174
Fig. 3-39: 3D visualization of adsorbates on Pd(111) (.500x500 ÅxÅ, I_t : 0.760 nA, V_t : 1486.5 mV). The adsorbate in the left lower corner is about 100x40 ÅxÅ and 3 Å in height.	175
Fig. 3-40: STM image of a Pd(111) surface (V_t =371 mV; I_t =0.530 nA; 100x100 ÅxÅ) prepared for evaporating with Zn.	176
Fig. 3-41: STM image after evaporating 3 ML Zn and alloying at 573 K in $5 \cdot 10^{-6}$ mbar CO (V_t =371 mV; I_t =5.170 nA; 100x100 ÅxÅ). A Pd(111) patch can be seen in the middle. In the surrounding no atomic resolution was possible.....	178
Fig. 3-42: Not identified bother noises at the STM system, probably due to construction work near the building recorded as Hz/A spectrum. The noise at 300 Hz is much higher than noises after installation.	179
Fig. 3-43: PdZn surface alloy on Pd(111) with row structure and reconstructed zigzag structure. Pd atoms are displayed in cyan, Zn atoms are displayed in grey [134].	182
Fig. 3-44: 3D model of PdZn surface alloy on Pd(111) with row structure (left) and reconstructed zigzag structure (right). Pd atoms are displayed in cyan, Zn atoms are displayed in grey [239].	182
Fig. 3-45: Relative stability (eV) of reconstructed zigzag structure of PdZn/Pd(111) with respect to row structure depending on number of layers arranged in zigzag fashion and CO coverage. Values are calculated for p(4x3) supercell that has 12 atoms in each layer [134].	183
Fig. 3-46: Stacking of layers for PdZn surface alloys with 1 and 2 layer thickness. Pd atoms are displayed as cyan balls, Zn atoms as violet balls. Big balls represent atoms of the first layer, middle sized balls represent atoms of the second layer, small balls – third layer [239].	184
Fig. 3-47: Color coded interatomic distances between atoms on the surface of 1, 2, and 4 layer thick PdZn surface alloys on Pd(111) with row and zigzag structure, in the absence of CO and at $\theta(\text{CO})=1/2$ ML. Numbers in italic indicate surface corrugation in pm, positive values correspond to Pd-out/Zn-in type of corrugation [134]......	187
Fig. 3-48: Calculated DOS of 1, 2, and 4 layers thick PdZn surface alloys on Pd(111) in the absence of CO projected on Pd atoms located on the surface [134]......	188
Fig. 3-49: Adsorption energies of CO on surface alloys with various structure at coverage of 1/12 [239]......	191
Fig. 3-50: Adsorption energies of CO on surface alloys with various structure at coverage $1/2$ [239]......	192
Fig. 3-51: Shifted harmonic frequencies of CO molecules adsorbed on PdZn/Pd(111) surface alloys of various structure. The surface alloy of N layers arranged in rows (zigzags) is denoted as RN (ZN) [239]......	193
Fig. 3-52: Differential adsorption energy of CO molecule versus their coverage on PdZn/Pd(111) surface alloys with different structure.....	194
Fig. 3-53: Simulated STM image of the proposed zigzag structure correspond to a voltage of 371 mV and high tunneling current.	197
Fig. 3-54: Simulated STM image of the row structure correspond to a voltage of 371 mV and high tunneling current.	197
Fig. 3-55: TPD spectra for CO, CH ₂ O, CH ₃ OH after dosing of 10 ML methanol at 90 K on 2 ML PdZn/Pd(111) prior annealed to 573 K. Methanol desorbs at 165 K (the M30 and M28 signals at this temperature are fragments of MS-ionization) and	

additionally two small “bumps” at ~360 K and ~480 K of chemisorbed methanol are visible.....	200
Fig. 3-56: TPD spectra for <i>CO</i> , <i>CH₂O</i> , <i>CH₃OH</i> , and <i>D₂O</i> after dosing of 10 ML methanol and <i>D₂O</i> at 90 K on 2 ML PdZn/Pd(111) prior annealed to 573 K. Methanol desorbs at about 10 K lower as compared to methanol dosage alone (Fig. 3-55).	201
Fig. 3-57: PM-IRAS spectra (surface) during methanol decomposition on Pd(111) (red) and 2 ML PdZn/Pd(111) (black). Acquired after 2 hours in 5 mbar MeOH at room temperature. On Pd(111) an IR band at ~1870 cm ⁻¹ is clearly visible. This can be assigned to <i>CO</i> , adsorbed on 3-fold hollow sites.....	202
Fig. 3-58: PM-IRAS spectra of methanol (gas phase) during methanol decomposition on Pd(111) (red) and 2 ML PdZn/Pd(111) (black). Acquired after 2 hours in 5 mbar MeOH at room temperature. The strong band at 1033 cm ⁻¹ can be assigned to $\nu(\text{CO})$ of methanol.	203
Fig. 3-59: PM-IRAS spectra (surface) acquired on 2 ML PdZn/Pd(111) in 5 mbar <i>CH₃OH</i> at different temperatures. The IR band at 2071 cm ⁻¹ indicates on-top <i>CO</i> . IR bands at 1920 and 1870 cm ⁻¹ can be assigned to multiple-bond <i>CO</i>	204
Fig. 3-60: PM-IRAS spectra (gas phase) acquired on 2 ML PdZn/Pd(111) in 5 mbar <i>CH₃OH</i> at different temperatures. Methanol is observed at ~1033 cm ⁻¹ . The small band at 2143 cm ⁻¹ can be assigned to <i>CO</i>	205
Fig. 3-61: PM-IRAS spectra (surface) acquired on 2 ML PdZn/Pd(111) in 12 mbar <i>CH₃OH/D₂O</i> each at 473 K and 623 K.....	205
Fig. 3-62: PM-IRAS spectra (gas phase) acquired on 2 ML PdZn/Pd(111) in 12 mbar <i>CH₃OH/D₂O</i> each at 473 K and 623 K.....	206
Fig. 3-63: Methanol decomposition: evolution of <i>CH_x</i> and <i>CO</i> coverage on Pd(111) and PdZn/Pd(111) with time at a background pressure of 3·10 ⁻⁸ mbar methanol. a) <i>CH_x</i> coverage deduced from the XPS C 1s signal at 284.5 eV; b) <i>CO</i> coverage deduced from the XPS C 1s signal at 286 eV.	208
Fig. 3-64: Calculated energies during dehydrogenation of methoxy adsorbed on various surfaces [39].....	209
Fig. 3-65: Sample plate and transfer holder of the HP-XPS system. The transfer holder is used to move the sample from the load lock to the UHV chamber. Due to the arrangement of the vacuum chamber, transfer steps cannot be observed through a viewport, but could be observed by a camera.....	212
Fig. 3-66: Sample heating (left) and sputtering (right). The view of the sputter gun was only accessible by a greyscale camera which was also used observing the sample transfer.	213
Fig. 3-67: Overview of collected C 1s and Pd 3d _{5/2} spectra under different reaction conditions. TransRT: in vacuum after sample transfer to HP cell; MeOH 400 K/600 K: in 0.5 mbar MeOH at 400/600 K; MeOH/O ₂ 400/600 K: in reaction mixture of 0.5 mbar MeOH and 0.1 mbar O ₂ at 400/600 K.	215
Fig. 3-68: Pd 3d, C 1s, and O 1s XP-spectra at different reaction conditions (see Tab. 3-7).217	
Fig. 3-69: C 1s (a) and Pd 3d (b) XP-spectra and depth profiling of Pd(111) (c) in 0.5 mbar MeOH at 600 K by varying incident photon energies (see Tab. 3-7).....	217
Fig. 3-70: Pd(111) after transfer at room temperature in UHV at varying photon energies for C 1s, Pd 3d, and O 1s (see Tab. 3-7).	218
Fig. 3-71: Pd(111) at 400 K in 0.5 mbar MeOH and with different photon energies for C 1s and Pd 3d (see Tab. 3-7).	219
Fig. 3-72: Pd(111) at 600 K in 0.5 mbar MeOH recorded with different photon energies for C 1s and Pd 3d (see Tab. 3-7).....	220
Fig. 3-73: Pd(111) at 400 K in 0.5 mbar MeOH and 0.1 mbar O ₂ recorded with different photon energies for C 1s, Pd 3d, and O 1s (see Tab. 3-7).	220

Fig. 3-74: Pd(111) at 600 K in 0.5 mbar MeOH and 0.1 mbar O ₂ recorded with different photon energies for C 1s, Pd 3d, and O 1s (see Tab. 3-7).	221
Fig. 3-75: Overview of energy dependent Pd 3d XP-spectra at varying reaction conditions.	222
Fig. 3-76: Overview of energy dependent C 1s XP-spectra at varying reaction conditions. .	223
Fig. 3-77: Overview of energy dependent O 1s XP-spectra at varying reaction conditions. The O 1s signal overlaps with the Pd 3p signal.	224
Fig. 4-1: Density of states (DOS) of Pd metal (a) and PdZn intermetallic compound (b), respectively. Huge differences can be observed at the Fermi level and in the width of the Pd d-bands [24].....	227
Fig. 4-2: Phase diagram of the system Pd-Zn [269].....	228
Fig. 4-3: Chemical bonding in ZnPd: (top) QTAIM (Quantum Theory of Atoms in Molecules) basins of palladium (blue) and zinc (green) in tetragonal ZnPd with the according electronic populations revealing the charge transfer from zinc to palladium. (middle) Electron localizability indicators (ELI-D) distribution in the (100), (010) and (001) planes in tetragonal ZnPd shows strong structuring of the penultimate shell of palladium in the (001) plane as well as small ELI-D maxima between palladium atoms along (100). (bottom) ELI-D distribution in the (100), (010) and (001) planes in cubic ZnPd shows weaker structuring of the penultimate shell of palladium in all three planes [240].	229
Fig. 4-4: Bright field microscopic pictures of the ZnPd bulk sample used for this work at different magnifications.....	231
Fig. 4-5: Petrographic microscope pictures of the ZnPd bulk sample used for this work at different magnifications.....	232
Fig. 4-6: Differential interference contrast (DIC) picture of the ZnPd bulk sample used for this thesis.	233
Fig. 4-7: XPS survey scan of the cleaned ZnPd sample (Al anode). The main XP and Auger peaks are labelled in the figure.	234
Fig. 4-8: XP C 1s signal after mounting the ZnPd bulk pellet, after oxidation in $5 \cdot 10^{-7}$ mbar O ₂ at 825 K for 10 min, cooling down and then heating up in $2 \cdot 10^{-6}$ mbar H ₂ to 700 K for 10 min.....	235
Fig. 4-9: CO/CO ₂ TPD spectra after different CO exposure on the ZnPd bulk sample. For a better overview, the intensities for the spectra of 0.5 L and 1 L are magnified by the factor of 2.....	237
Fig. 4-10: Summarized CO TPD spectra after different CO exposures on ZnPd bulk.	238
Fig. 4-11: CO coverage as deduced from the TPD spectra versus exposure. The saturation coverage was defined as the coverage on a sample cooled down in $5 \cdot 10^{-6}$ mbar CO.	239
Fig. 4-12: CO adsorption on ZnPd observed by PM-IRAS in CO atmosphere. On-top CO can be observed at 2056-2070 cm ⁻¹ and multiple-bond CO at 1959 cm ⁻¹	240
Fig. 4-13: Adsorption of D ₂ O on ZnPd observed by PM-IRAS in D ₂ O atmosphere. The broad band at ~2780 cm ⁻¹ , observed at high coverage is assigned to ν_{asym} (D ₂ O). The surface alters significantly under these conditions.	241
Fig. 4-14: Evolution of the Zn 3d signal during measurements on ZnPd. The numbers for labelling the spectra are taken from Tab. 4-2.	243
Fig. 4-15: Evolution of the Pd 3d signal during measurements on ZnPd. The numbers for labelling the spectra are taken from Tab. 4-2.	244
Fig. 4-16: Evolution of the C 1s signal during measurements on ZnPd. The numbers for labelling the spectra are taken from Tab. 4-2. The most intense signals were observed for the sample as mounted (1), after CO IR (5) and after D ₂ O IR (6)....	245

Fig. 4-17: Reflected-light microscopic picture (magnification 200x) of the ZnPd bulk sample after D ₂ O adsorption at the IMC. The glass splinter (dark area) is probably a residue from the preparation process, the size is about 19x78 μm.	246
Fig. 4-18: Petrographic microscope pictures of the ZnPd bulk sample after D ₂ O adsorption (the sample was sent back to Dresden for microscopic analysis). The surface altered significantly.	247
Fig. 4-19: Scanning electron microscope (SEM) analysis with secondary electrons (SE) of the ZnPd bulk sample after D ₂ O adsorption (the sample was sent back to Dresden for microscopic analysis). The surface altered significantly.	248
Fig. 4-20: Scanning electron microscope (SEM) analysis with back-scattered electrons (BSE) of the ZnPd bulk sample after D ₂ O adsorption (the sample was sent back to Dresden for microscopic analysis). The surface altered significantly.	249
Fig. 4-21: Energy-dispersive X-ray spectroscopy (EDX) analysis from area 01 (see Fig. 4-20) of the of the ZnPd bulk sample after D ₂ O adsorption (the sample was sent back to Dresden for microscopic analysis). The surface was oxidized (especially on the grain boundaries) and enriched with Pd.	250
Fig. 4-22: Energy-dispersive X-ray spectroscopy (EDX) analysis from area 02 (see Fig. 4-20) of the of the ZnPd bulk sample after D ₂ O adsorption (the sample was sent back to Dresden for microscopic analysis). The surface was oxidized (especially on the grain boundaries) and enriched with Pd.	251
Fig. 4-23: Energy-dispersive X-ray spectroscopy (EDX) analysis from area 03 (see Fig. 4-20) of the of the ZnPd bulk sample after D ₂ O adsorption (the sample was sent back to Dresden for microscopic analysis). The surface was oxidized (especially on the grain boundaries) and enriched with Pd.	252
Fig. 4-24: Energy-dispersive X-ray spectroscopy (EDX) analysis from area x04 (see Fig. 4-20) of the of the ZnPd bulk sample after D ₂ O adsorption (the sample was sent back to Dresden for microscopic analysis). The SiO ₂ grain is most probably originated from the manufacturing process.	253
Fig. 4-25: TPD spectra for CO, CH ₂ O, CH ₃ OH, and CO ₂ after dosing of 2 L methanol at 90 K on ZnPd bulk.....	255
Fig. 4-26: TPD spectra for CO, CH ₂ O, CH ₃ OH, and CO ₂ on a methanol saturated PdZn bulk surface (sample was cooled down in 1E-7 mbar MeOH from 500 K to 90 K).	256
Fig. 4-27: Picture of the Pd ₂ Zn pellet. The surface is rough and non-uniform, also some contaminations/enclaves in the bulk can be seen.....	257
Fig. 4-28: Microscopic image (magnification 200x) of the Pd ₂ Zn surface. Picture a) and b) shows the boundary of the big enclave (elliptical shaped region with high reflectivity shown in Fig. 4-27). Pictures c) – f) shows different regions of the surface where no enclaves are visible to the naked eye.....	258
Fig. 4-29: XPS survey scan of the cleaned Pd ₂ Zn sample.	259
Fig. 4-30: C 1s, Pd 3d, and Zn 2p XPS regions of the Pd ₂ Zn sample.....	260
Fig. 4-31: CO TPD on a (non-polished) Pd ₂ Zn pellet. Sample surface, shape and mounting conditions differs from polished Pd(111) and ZnPd discs. The saturated CO adsorption (“sat.”) was prepared by cooling down the sample in 10E-6 mbar CO from 500 K to 100 K.....	261
Fig. 4-32: 10 L MeOH TPD on a (non-polished) Pd ₂ Zn pellet.....	262
Fig. 5-1: XP spectra of C 1s for C-C, C=O, O-C=O, and carbide (MWNT 1: first measurement MWNT-COOH-Pt supported by Al foil).	265
Fig. 5-2: XP spectra of C 1s for C-C, C=O, O-C=O, and carbide (MWNT 2: higher amount of MWNT-COOH-Pt supported by Al foil).....	266
Fig. 5-3: XP spectra of C 1s for C-C, C=O, O-C=O, and carbide (MWNT 3: MWNT-COOH-Pt supported by Cu foil).....	267

Fig. 5-4: XP spectra of C 1s for C-C, C=O, O-C=O, and carbide (MWNT 4: reference sample MWNT-COOH supported by Al foil).	268
Fig. 5-5: XP spectra of Al 2p (MWNT 2: higher amount of MWNT-COOH-Pt supported by Al foil).....	269
Fig. 5-6: XP spectra of Al 2p (MWNT 4: MWNT-COOH supported by Al foil).	270
Fig. 7-1: Overview of the XPS system. Upper part: manipulator; in the middle: preparation chamber and XPS; on the bottom: high pressure cell and PM-IRAS and below turbomolecular pump and titan sublimation pump.	276
Fig. 7-2: XPS chamber.	277
Fig. 7-3: 8-3: Manipulator front view.	278
Fig. 7-4: Drawing of X-Ray source XR-50 [Specs].....	279
Fig. 7-5: Schematic drawing of X-Ray source XR-50 [Specs manual].	280
Fig. 7-6: Connection diagram for XR-500 [Specs manual].	281
Fig. 7-7: Drawing of source head XR-50 [Specs manual].	282
Fig. 7-8: Cross talk in the XR-50 gun. Just behind the aluminum window is a small rod to reduce Al/Mg cross talk (cross contamination). The rod separates the two anode sides from each other [Specs manual].	283
Fig. 7-9: Specification of the X-Ray source, tested by Specs [Specs test report].	284
Fig. 7-10: Drawing Analyzer [Specs manual].	285
Fig. 7-11: Sketch of then Omicron EFM 3 evaporator as used in our lab [Omicron manual].	286
Fig. 7-12: Basic principle of the combined LEED/Auger system taken from the manufacturers (Specs) user manual [Specs manual].	287
Fig. 7-13: 3-D sketch (front and back view) of the STM system.....	288
Fig. 7-14: Manipulator, side view [Specs manual].	289
Fig. 7-15: STM, 3D view [Specs manual].	290
Fig. 7-16: Picture of the STM unit outside the vacuum chamber (before installation).....	291
Fig. 7-17: Picture of the STM unit mounted in the vacuum chamber. The filament tower (glowing filament) can be used for sample heating during measurement. Small sapphire balls are used for thermal insulation between sample holder and STM electronics.	291
Fig. 7-18: Scheme of the Maxlab HP XPS system. The system consist of 8 different sections (4 chambers; load lock; analysis, preparation and reaction load lock), each pumped with a turbomolecular pump and a scroll pump. The QMS was not working at this beam time [79].	292
Fig. 7-19: Drawing and dimensions of the sample holder.	294
Fig. 7-20: Orientation of the sample during experiment.	294
Fig. 7-21: Sample holder with bended alumel/chromel thermocouple wires.....	295
Fig. 7-22: Scheme of the pressure measurement system. All vacuum gauges are each connected to a control unit that continuously monitors and displays the pressure using a LabView script.	296
Fig. 7-23: Front panel of the pressure control system.	297
Fig. 7-24: Beam flux calibration for Maxlab I511 beamline during beamtime.	298
Fig. 7-25: Monochromator resolution 90 – 600 eV during beamtime.	299
Fig. 7-26: Monochromator resolution 600 – 1200 eV during beamtime.	300
Fig. 7-27: Plots of electron inelastic mean free paths as a function of electron energy. Solid circles are showing calculated IMFPs from the Penn algorithm, solid lines are showing fits to these IMFPs with the modified Bethe equation and long-dashed lines indicate IMFPs calculated from the TPP-2M equation. Successive plots have been displaced vertically for clarity, and the ordinate scale at the left indicates these displacements [275].	301

Fig. 7-28: Plots of electron inelastic mean free paths. See caption to Fig. 8-27 [275].	302
Fig. 7-29: Gas phase IR spectrum of CO . Reprinted from [280].	303
Fig. 7-30: Gas phase IR spectrum of CO_2 . Reprinted from [280].	303
Fig. 7-31: Gas phase IR spectrum of methanol. Reprinted from [280].	304
Fig. 7-32: Gas phase IR spectrum of formaldehyde. Reprinted from [280].	304
Fig. 7-33: Gas phase IR spectrum of formic acid. Reprinted from [280].	305
Fig. 7-34: Gas phase IR spectrum of water. Reprinted from [280].	305
Fig. 7-35: Gas phase IR spectrum of D_2O . Reprinted from [280].	306
Fig. 7-36: Calculated IR frequencies on Pd(111) for methanol and possible decomposition intermediates. Full lines: modes with a large dynamic dipole moment; dashed lines: modes with a small dynamic dipole moment. The experimental EELS results are shown in the bottom panel for comparison at 170 K (lower half) and 240 K (upper half). Reprinted from [281].	307

7.10 List of tables

Tab. 1-1: Steam reforming of methanol over various supported Pd catalysts. Reprinted from [22].	13
Tab. 2-1: Molecular orbital description of CO-bonding.	30
Tab. 2-2: X-Ray satellites for Al and Mg sources: separation from main peak ($K\alpha_{1,2}$) and relative intensity.	45
Tab. 2-3: Technical data of Max II, from Maxlab webpage [79].	52
Tab. 2-4: Mean velocities of gases at room temperature [122].	98
Tab. 2-5: Overview of properties in different ranges of vacuum [124, 125].	101
Tab. 2-6: Overview of vacuum in industry and nature [124, 125].	102
Tab. 2-7: Short overview of vacuum pumps [124].	106
Tab. 2-8: Measured TSP pumping speeds for some gases (in $\text{l s}^{-1}\text{cm}^{-2}$) [113].	112
Tab. 3-1: CO Desorption maxima for the <300 K regime for 2 and >4 ML PdZn/Pd(111) surface layers at different CO dosage. See also Fig. 3-34 and Fig. 3-35.	170
Tab. 3-2: Structural properties of PdZn surface alloy configurations in the absence of CO. Vertical atomic displacements, Δz , separations between i -th and j -th layers calculated for atoms of type X, $d_{ij}(X)$, as well as minimum and maximum bond distances, r , are given in pm. Indexes after atom types denote surface layers, where these atoms are located [134].	185
Tab. 3-3: Structural properties of PdZn surface alloy configurations at high CO coverage $\theta(\text{CO}) = 0.5$ ML. Vertical atomic displacements, Δz , separations between i -th and j -th layers calculated for atoms of type X, $d_{ij}(X)$, as well as minimum and maximum bond distances, r , are given in pm. Indexes after atom types denote surface layers, where these atoms are located. The most stable adsorption modes of CO, i.e. bridge sites for rows and on-top sites for zigzags, were considered [134].	186
Tab. 3-4: Adsorption Energies and Vibrational Frequencies of the CO Stretching Mode for CO Adsorbed on PdZn Surface Alloys of Various Thickness and Structure on Pd(111) at $\theta(\text{CO}) = 1/12$ and $1/2$ ML. ^a Bridge sites are not stable for these structures; CO moves from bridge to top sites during geometry optimization [134].	190
Tab. 3-5: Estimated desorption energies for “ideal” PdZn/Pd(111) surfaces from TPD experiments compared to desorption energies calculated from DFT, see Tab. 3-4.	195
Tab. 3-6: CO Desorption maxima and respective desorption energies for 2 and >4 ML PdZn surface alloys from TPD spectra in Fig. 3-34 and Fig. 3-35.	195
Tab. 3-7: Spectra collection, beam energies [eV] at different reaction conditions used in this chapter.	214
Tab. 4-1: Crystal structure and lattice parameters of Pd/Zn intermediate phases [269].	228
Tab. 4-2: Overview of XPS measurements after TPD/IR series. The numbers are also used for Fig. 4-14 – Fig. 4-16	242
Tab. 5-1: Detailed descriptions of four repeated measurements.	265
Tab. 5-2: Typical C 1s binding energies for organic samples [273, 274].	270
Tab. 5-3: Typical Al 2p and Pt 4f binding energies [80].	270
Tab. 5-4: Calculated percentages of different carbon species and corresponding binding energies.	271
Tab. 7-1: Technical data of beamline I511 taken from Maxlab website [79].	293
Tab. 7-2: Common vacuum symbols.	308

8 Publications

Bücher und Buch-Herausgaben

H. Holzapfel (Hrg.): *"Zeolites in Chemical Engineering"*; ProcessEng Engineering GmbH, Wien, 2011, ISBN: 978-3902655080; 500 S.

H. Holzapfel, M. Lackner, T. Suchy, P. Szentannai, F. Winter (Hrg.): *"Glossary of Combustion"*; ProcessEng Engineering GmbH, Wien, 2009, ISBN: 978-3-902655-01-1; 235 S.

Zeitschriftenartikel

H. Holzapfel, A. Wolfbeisser, Ch. Rameshan, C. Weilach, G. Rupprechter: *"PdZn surface alloys as models of methanol steam reforming catalysts: Molecular studies by LEED, XPS, TPD and PM-IRAS"*; Topics in Catalysis, 57 (2014), S. 1218 - 1228.

C. Weilach, S. Kozlov, H. Holzapfel, K. Föttinger, K. M. Neyman, G. Rupprechter: *"Geometric arrangement of components in bimetallic PdZn/Pd(111) surfaces modified by CO adsorption: a combined DFT, PM-IRAS, and TPD study"*; Journal of Physical Chemistry C, 116 (2012), 35; S. 18768 - 18778.

Vorträge und Posterpräsentationen (mit Tagungsband-Eintrag)

K. Föttinger, A. Haghofer, H. Holzapfel, Y. Suchorski, C. Weilach, K. Zorn, G. Rupprechter: *"Surface chemistry at ambient pressure: catalysis on UHV-based model systems and technological catalysts"*; Vortrag: 5th International Workshop on Surface Physics, Satellite Workshop to ECOSS-28, Ladek-Zdrój, Poland; 02.09.2011 - 05.09.2011; in: "Nanostructures and Surfaces, Uniwersytet Wroclawski", (2011), S. 36.

K. Föttinger, C. Weilach, A. Haghofer, H. Holzapfel, G. Rupprechter: *"The surface structure and catalytic properties of Pd-Zn and Pd-Ga nanoparticles"*; Vortrag: 15. Österreichische Chemietage 2013, TU-Graz, Graz, Österreich; 23.09.2013 - 26.09.2013; in: "15. Österreichische Chemietage - Programm", (2013), S. 63.

H. Holzapfel, M. Lackner, F. Winter: *"Untersuchung von Flammen mittels Laser Doppler Anemometrie (LDA) und Tunable Diode Laser Absorption Spectroscopy (TDLAS)"*;

Poster: 56. Jahrestagung der Österreichischen Physikalischen Gesellschaft, Graz; 18.09.2006 - 21.09.2006; in: "56. Jahrestagung der Österreichischen Physikalischen Gesellschaft", (2006).

H. Holzapfel, Ch. Rameshan, C. Weilach, S. Kozlov, K. M. Neyman, G. Rupprechter: *"Reconstruction of Bimetallic PdZn/Pd(111) Surface Alloys induced by CO?"*; Vortrag: 15th Austrian Chemistry Days (Chemietage), Graz; 23.09.2013 - 26.09.2013; in: "15th Austrian Chemistry Days, Graz University of Technology", (2013).

H. Holzapfel, Ch. Rameshan, C. Weilach, G. Rupprechter: *"In situ HP-XPS during methanol decomposition and oxidation on Pd(111)"*; Poster: Research at European Neutron and Synchrotron facilities by Austrian researchers, Vienna; 11.11.2013 - 12.11.2013; in: "Abstract Booklet "Research at European Neutron and Synchrotron facilities by Austrian researchers"", (2013), S. 66.

H. Holzapfel, C. Weilach, K. Föttinger, S. Kozlov, K. M. Neyman, G. Rupprechter: *"Adsorption induced rearrangement of PdZn surface alloys?"*; Vortrag: 11th Pannonian International Symposium on Catalysis, Obergurgl; 03.09.2012 - 07.09.2012; in: "11th Pannonian International Symposium on Catalysis", (2012), S. 55 - 56.

H. Holzapfel, C. Weilach, G. Rupprechter: *"Catalytic properties and structure of PdZn/Pd(111) surface alloys"*; Poster: 15th International Congress on Catalysis, München, Deutschland; 01.07.2012 - 06.07.2012; in: "15th International Congress on Catalysis", (2012), S. 1.

H. Holzapfel, C. Weilach, G. Rupprechter: *"Oberflächenkatalytische Untersuchungen auf PdZn-Legierungen mittels LEED, XPS, TPD und PM-IRAS"*; Poster: 16. Tagung Festkörperanalytik, Wien; 04.07.2011 - 06.07.2011; in: "16. Tagung Festkörperanalytik", Springer, (2011), S. P 25.

H. Holzapfel, C. Weilach, G. Rupprechter: *"Surface catalytic measurements on PdZn(111)-alloys"*; Vortrag: 14. Österreichische Chemietage 2011, Linz; 26.09.2011 - 29.09.2011; in: "GÖCH 14. Österreichische Chemietage 2011", (2011), 12 S.

H. Holzapfel, C. Weilach, G. Rupprechter: *"XPS and TPD measurements of the adsorption and desorption of CO, MeOH and D2O on PdZn(111) surface alloys"*; Poster: 10th Pannonian International Symposium on Catalysis, Krakau, Polen; 29.08.2010 - 02.09.2010; in: "Proceedings of the 10th International Symposium on Catalysis", (2010), ISBN: 978-83-929430-4-4; S. 97 - 98.

H. Holzapfel, C. Weilach, G. Rupprechter, K. M. Neyman, S. Kozlov: *"Adsorption induced arrangement of atoms in bimetallic PdZn/Pd(111) surface alloys"*; Poster: COST Action CM1104 "Reducible oxide chemistry, structure and functions" Working Groups Meeting, Vienna, Austria; 18.04.2013 - 19.04.2013; in: "COST Action CM1104 Reducible oxide chemistry, structure and functions", (2013), 64 S.

C. Weilach, H. Holzapfel, K. Föttinger, S. Kozlov, K. M. Neyman, G. Rupprechter: *"Co induced reconstruction of PdZn/Pd(111) surface alloys?"*; Poster: 15th International Congress on Catalysis, München, Deutschland; 01.07.2012 - 06.07.2012; in: "15th International Congress on Catalysis", (2012), S. 1.

C. Weilach, H. Holzapfel, K. Föttinger, S. Kozlov, K. M. Neyman, G. Rupprechter: *"PdZn surface alloys for hydrogen generation: In situ studies on model and technological catalysts"*; Vortrag: European Conference on Surface Science 28, Wroclaw, Poland; 28.08.2011 - 02.09.2011; in: "European Conference on Surface Science - ECOSS 28", (2011), S. 61 - 62.

Vorträge und Posterpräsentationen (ohne Tagungsband-Eintrag)

H. Holzapfel, Ch. Rameshan, C. Weilach, S. Kozlov, K. M. Neyman, G. Rupprechter:

"Rearrangement of atoms in bimetallic PdZn/Pd(111) surface alloys";

Poster: 2nd Annual Symposium of SFB F45 Functional Oxide Surfaces and Interfaces (FOXSI), Conference Center Burg Schlaining, Stadtschlaining, Austria; 18.09.2013 - 20.09.2013.

H. Holzapfel, C. Weilach, K. Föttinger, S. Kozlov, K. M. Neyman, G. Rupprechter:

"Adsorption induced rearrangement of PdZn surface alloys?"; Poster: COST CM1104 General Meeting 2012, Prague, Czech Republic; 26.09.2012 - 28.09.2012.

H. Holzapfel, C. Weilach, S. Kozlov, K. M. Neyman, G. Rupprechter: *"Adsorption induced rearrangement of PdZn surface alloys"*; Vortrag: IAP Seminar of U.Diebold, Freihaus (eingeladen); 12.10.2012.

H. Holzapfel, C. Weilach, G. Rupprechter: *"Surface Analysis of PdZn and Pd model catalysts"*; Vortrag: Workshop *"In situ Spectroscopy and Model Catalysis"*, Andechs, Deutschland; 07.07.2012.

S. Kozlov, C. Weilach, H. Holzapfel, K. Föttinger, G. Rupprechter, K. M. Neyman: *"Theoretical studies of CO adsorption on PdZn surface alloys and induced structural modifications of the substrate"*; Poster: European COST Action MP0903 Joint Working Group Meetings, Barcelona, Spanien; 14.04.2011 - 16.04.2011.

H. Li, K. Anic, H. Holzapfel, C. Weilach, Ch. Rameshan, G. Rupprechter: *"Preparation and characterization of Pd particles grown on ZrO₂ ultra thin film"*; Poster: 2nd Annual Symposium of SFB F45 Functional Oxide Surfaces and Interfaces (FOXSI), Conference Center Burg Schlaining, Göstling/Ybbs; 18.03.2013 - 21.03.2013.

C. Weilach, H. Holzapfel, K. Föttinger, S. Kozlov, K. M. Neyman, G. Rupprechter: *"CO induced rearrangement of atoms in PdZn/Pd(111) surface alloys?"*; Vortrag: Workshop *"In situ Spectroscopy and Model Catalysis"*, Andechs, Deutschland; 07.07.2012.

C. Weilach, H. Holzapfel, K. Föttinger, S. Kozlov, K. M. Neyman, G. Rupprechter: "*PdZn nanoalloys for methanol steam reforming: PM-IRAS, XPS and DFT studies*"; Poster: European COST Action MP0903 Joint Working Group Meetings, Barcelona, Spanien; 14.04.2011 - 16.04.2011.

C. Weilach, H. Holzapfel, K. Föttinger, S. Kozlov, K. M. Neyman, G. Rupprechter: "*Surface science and technological catalysis on PdZn nanoalloys*"; Vortrag: European COST Action MP0903 Joint Working Group Meetings, Barcelona, Spanien; 14.04.2011 - 16.04.2011.

C. Weilach, S. Kozlov, H. Holzapfel, K. Föttinger, K. M. Neyman, G. Rupprechter: "*Arrangement of components in PdZn surface nanoalloy films on Pd(111) modified by CO adsorption*"; Poster: First International Training School on NanoAlloys (ISNA), Tirrenia, Italy; 20.05.2012 - 26.05.2012.

9 Curriculum Vitae

Personal information

Name & Surname: Harald Helmuth Holzapfel

Title: Dipl.-Ing.

Gender: male

Date of birth: 13.12. 1975

Birthplace: Vienna

Address: Jörgerstraße 3/39, 1170 Vienna, Austria, Europe

Mobile phone: +43 680 2057402

Phone (TU Vienna): 0043-(0)1/58801-165120

E-mail: harald.holzapfel@tuwien.ac.at

h.holzapfel@gmx.at

Citizenship: Austria

Education

Primary school

Secondary school

HBLVA für chem. Industrie Rosensteingasse (Federal Secondary College of Engineering)

→ Graduation: Matura (general qualification for university entrance)

University of Technology, Vienna

→ 2008: Graduation Diplomingenieur (Master of Science) passed with distinction

Skills

Languages: German (mother tongue), English

Scientific

2007-2008 Diploma thesis: H. Holzapfel: “*Investigation of Gas Phase Combustion Chemistry*”, Supervisors: F. Winter, M. Lackner (Institute of Chemical Engineering, University of Technology Vienna); First examiner: F. Winter (Institute of Chemical Engineering, University of Technology Vienna). Second examiners: K. Schwarz (Institute of Materials Chemistry TU Vienna) and H. Hutter (Institute of Chemical Technologies and Analytics TU Vienna). Final examination: 31.03. 2008.

Since 2010 Univ.-Ass. Institute of Materials Chemistry, TU Vienna
Ph.D. studies in technical chemistry, Vienna University of Technology, Austria
Supervisor: Prof. G. Rupprechter

Prizes and awards:

2003 Innovationspreis “Genius” des Landes Niederösterreich, together with M. Lackner, B. Klatzer, W. Stelzer

10 References

- [1] G. Ertl, Reactions at surfaces: From atoms to complexity (Nobel lecture), *Angew. Chem. Int. Ed.*, 47 (2008) 3524-3535.
- [2] G.A. Somorjai, *Chemistry in two dimensions: surfaces*, Cornell University Press, 1981.
- [3] G.A. Somorjai, Y. Li, *Introduction to Surface Chemistry and Catalysis*, John Wiley & Sons, 2010.
- [4] G. Ertl, H. Knözinger, F. Schüth, J. Weitkamp, *Handbook of Heterogeneous Catalysis*, 8 Volumes, Wiley, 2008.
- [5] D.W. Goodman, Model studies in catalysis using surface science probes, *Chem. Rev.*, 95 (1995) 523-536.
- [6] J.A. Rodriguez, Interactions in Bimetallic Bonding: Electronic and Chemical Properties of PdZn Surfaces, *The Journal of Physical Chemistry*, 98 (1994) 5758-5764.
- [7] J. Barth, H. Brune, G. Ertl, R. Behm, Scanning tunneling microscopy observations on the reconstructed Au (111) surface: Atomic structure, long-range superstructure, rotational domains, and surface defects, *Phys. Rev. B*, 42 (1990) 9307.
- [8] T. Fink, J.-P. Dath, R. Imbihl, G. Ertl, Kinetic oscillations in the NO+ CO reaction on Pt (100): Experiments and mathematical modeling, *The Journal of chemical physics*, 95 (1991) 2109.
- [9] M. Berdau, G.G. Yelenin, A. Karpowicz, M. Ehsasi, K. Christmann, J.H. Block, Macroscopic and mesoscopic characterization of a bistable reaction system: CO oxidation on Pt (111) surface, *J. Chem. Phys.*, 110 (1999) 11551-11573.
- [10] H. Brune, J. Wintterlin, J. Trost, G. Ertl, J. Wiechers, R. Behm, Interaction of oxygen with Al (111) studied by scanning tunneling microscopy, *The Journal of chemical physics*, 99 (1993) 2128.
- [11] R. Behm, K. Christmann, G. Ertl, M. Van Hove, Adsorption of CO on Pd (100), *The Journal of Chemical Physics*, 73 (1980) 2984.
- [12] K. Christmann, R. Behm, G. Ertl, M. Van Hove, W. Weinberg, Chemisorption geometry of hydrogen on Ni (111): Order and disorder, *The Journal of Chemical Physics*, 70 (1979) 4168.
- [13] R. Behm, K. Christmann, G. Ertl, Adsorption of hydrogen on Pd (100), *Surf. Sci.*, 99 (1980) 320-340.
- [14] G.A. Olah, A. Goepfert, G.S. Prakash, *Beyond oil and gas: the methanol economy*, John Wiley & Sons, 2009.

- [15] W. Gu, J.-P. Shen, C. Song, Hydrogen Production From Integrated Methanol Reforming Over Cu-ZnO/Al₂O₃ and Pt/Al₂O₃ Catalysts For PEM Fuel Cells, Prepr. Pap.-Am. Chem. Soc., Div. Fuel Chem, 48 (2003) 804.
- [16] M.L. Cubeiro, J.L.G. Fierro, Partial oxidation of methanol over supported palladium catalysts, Appl. Catal., A, 168 (1998) 307 - 322.
- [17] M. Cubeiro, J. Fierro, Selective production of hydrogen by partial oxidation of methanol over ZnO-supported palladium catalysts, J. Catal., 179 (1998) 150-162.
- [18] K. Sun, W. Lu, M. Wang, X. Xu, Characterization and catalytic performances of La doped Pd/CeO₂ catalysts for methanol decomposition, Appl. Catal., A, 268 (2004) 107-113.
- [19] Y. Usami, K. Kagawa, M. Kawazoe, Y. Matsumura, H. Sakurai, M. Haruta, Catalytic methanol decomposition at low temperatures over palladium supported on metal oxides, Appl. Catal., A, 171 (1998) 123 - 130.
- [20] R. Ubago-Perez, F. Carrasco-Marin, C. Moreno-Castilla, Methanol partial oxidation on carbon-supported Pt and Pd catalysts, Catal. Today, 123 (2007) 158-163.
- [21] N. Iwasa, S. Kudo, H. Takahashi, S. Masuda, N. Takezawa, Highly Selective Supported Pd Catalysts for Steam Reforming of Methanol, Catal. Lett., 19 (1993) 211-216.
- [22] N. Iwasa, N. Takezawa, New Supported Pd and Pt Alloy Catalysts for Steam Reforming and Dehydrogenation of Methanol, Top. Catal., 22 (2003) 215-224.
- [23] T. Conant, A.M. Karim, V. Lebarbier, Y. Wang, F. Girgsdies, R. Schlögl, A. Datye, Stability of bimetallic Pd-Zn catalysts for the steam reforming of methanol, J. Catal., 257 (2008) 64 - 70.
- [24] M. Behrens, M. Armbrüster, Methanol steam reforming, in: Catalysis for Alternative Energy Generation, Springer, 2012, pp. 175-235.
- [25] E. Arendt, E.M. Gaigneaux, Taking advantage of a priori unwanted catalysts modifications, Appl. Catal., A.
- [26] M. Friedrich, D. Teschner, A. Knop-Gericke, M. Armbrüster, Influence of bulk composition of the intermetallic compound ZnPd on surface composition and methanol steam reforming properties, J. Catal., 285 (2012) 41-47.
- [27] M. Friedrich, M. Armbrüster, Die intermetallische Verbindung PdZn in der Methanoldampfreformierung, Z. Anorg. Allg. Chem., 636 (2010) 2044-2044.
- [28] M. Armbrüster, M. Behrens, K. Föttinger, M. Friedrich, É. Gaudry, S.K. Matam, H.R. Sharma, The Intermetallic Compound ZnPd and Its Role in Methanol Steam Reforming, Catalysis Reviews, 55 (2013) 289-367.

- [29] M. Kratzer, A. Tamtögl, J. Killmann, R. Schennach, A. Winkler, Preparation and calibration of ultrathin Zn layers on Pd(111), *Applied Surface Science*, 255 (2009) 5755-5759.
- [30] H.H. Holzapfel, A. Wolfbeisser, C. Rameshan, C. Weilach, G. Rupprechter, PdZn Surface Alloys as Models of Methanol Steam Reforming Catalysts: Molecular Studies by LEED, XPS, TPD and PM-IRAS, *Top. Catal.*, 57 (2014) 1218-1228.
- [31] H. Marquardt, S.G. Schäfer, *Lehrbuch der Toxikologie*, Wiss. Verlag-Ges., 2004.
- [32] 253. Verordnung des Bundesministers für Wirtschaft und Arbeit über Grenzwerte für Arbeitsstoffe und über krebserzeugende Arbeitsstoffe (Grenzwerteverordnung 2001 – GKV 2001), in: *Bundesgesetzblatt, Austria*, 2001, pp. 1469 - 1533.
- [33] G. Rupprechter, Sum Frequency Generation and Polarization-Modulation Infrared Reflection Absorption Spectroscopy of Functioning Model Catalysts from Ultrahigh Vacuum to Ambient Pressure, *Adv. Catal.*, 51 (2007) 133-263.
- [34] G. Rupprechter, Surface vibrational spectroscopy on noble metal catalysts from ultrahigh vacuum to atmospheric pressure, *Annu. Rep. Prog. Chem. Sect. C: Phys. Chem.*, 100 (2004) 237-311.
- [35] G. Rupprechter, T. Dellwig, H. Unterhalt, H.J. Freund, CO adsorption on Ni(100) and Pt(111) studied by infrared-visible sum frequency generation spectroscopy: design and application of an SFG-compatible UHV-high-pressure reaction cell, *Top. Catal.*, 15 (2001) 19-26.
- [36] O.R. de la Fuente, M. Borasio, P. Galletto, G. Rupprechter, H.J. Freund, The influence of surface defects on methanol decomposition on Pd(1 1 1) studied by XPS and PM-IRAS, *Surf. Sci.*, 566-568 (2004) 740 - 745.
- [37] M. Borasio, Polarization Modulation Infrared Reflection Absorption Spectroscopy on Pd Model Catalysts at Elevated Pressure, in, *Freie Universität Berlin*, 2006.
- [38] M. Borasio, O.R. de la Fuente, G. Rupprechter, H.J. Freund, In situ studies of methanol decomposition and oxidation on Pd(111) by PM-IRAS and XPS spectroscopy, *J. Phys. Chem. B*, 109 (2005) 17791-17794.
- [39] C. Weilach, Surface Science Investigations of Mono- and Bimetallic Catalytic Nanostructures by PM-IRAS and XPS Spectroscopy, in, *Technische Universität Wien*, 2009.
- [40] G. Rupprechter, Surface vibrational spectroscopy from ultrahigh vacuum to atmospheric pressure: adsorption and reactions on single crystals and nanoparticle model catalysts monitored by sum frequency generation spectroscopy, *Phys. Chem. Chem. Phys.*, 3 (2001) 4621-4632.

- [41] G. Rupprechter, C. Weilach, Mind the gap! Spectroscopy of catalytically active phases, *Nano Today*, 2 (2007) 20 - 29.
- [42] G. Rupprechter, C. Weilach, Spectroscopic studies of surface-gas interactions and catalyst restructuring at ambient pressure: mind the gap!, *Journal of Physics-Condensed Matter*, 20 (2008).
- [43] M. Borasio, O. Rodriguez de la Fuente, G. Rupprechter, H.-J. Freund, In Situ Studies of Methanol Decomposition and Oxidation on Pd(111) by PM-IRAS and XPS Spectroscopy, *J. Phys. Chem. B*, 109 (2005) 17791-17794.
- [44] K. Anic, Personal communication, 2013.
- [45] B. Schrader, *Infrared and Raman spectroscopy*, Wiley. com, 2008.
- [46] K.W. Kolasinski, *Surface science foundations of catalysis and nanoscience*, accessed:
- [47] H. Ibach, D.L. Mills, H. Ibach, *Electron energy loss spectroscopy and surface vibrations*, Academic Press New York, 1982.
- [48] F.M. Hoffmann, Infrared reflection-absorption spectroscopy of adsorbed molecules, *Surf. Sci. Rep.*, 3 (1983) 107-192.
- [49] R.G. Greenler, *Infrared Study of Adsorbed Molecules on Metal Surfaces by Reflection Techniques*, AIP, 1966.
- [50] J.W. Niemantsverdriet, *Spectroscopy in Catalysis*, 2 ed., Wiley, 2000.
- [51] P. Hollins, J. Pritchard, A. Bell, M. Hair, Vibrational spectroscopies for adsorbed species, in: *ACS Symp. Ser.*, 1980, pp. 51.
- [52] B.J. Barner, M.J. Green, E.I. Saez, R.M. Corn, Polarization Modulation Fourier-Transform Infrared Reflectance measurements of thin-films and monolayers at metal-surfaces utilizing real-time sampling electronics, *Anal. Chem.*, 63 (1991) 55-60.
- [53] K. Hipps, G. Crosby, Applications of the photoelastic modulator to polarization spectroscopy, *J. Phys. Chem.*, 83 (1979) 555-562.
- [54] W. Demtroder, F.K. Tittel, *Laser spectroscopy: basic concepts and instrumentation*, *Optical Engineering*, 35 (1996) 3361-3362.
- [55] O. Instruments, *The book of photon tools, Light collection and system throughput*, (2002).
- [56] H. Hertz, Ueber einen Einfluss des ultravioletten Lichtes auf die electrische Entladung, *Annalen der Physik*, 267 (1887) 983-1000.
- [57] W. Hallwachs, Ueber den Einfluss des Lichtes auf electrostatisch geladene Körper, *Annalen der Physik*, 269 (1888) 301-312.

- [58] A. Einstein, Fundamental ideas and problems of the theory of relativity, Les Prix Nobel 1922, (1923) 482-490.
- [59] A. Einstein, Über einen die Erzeugung und Verwandlung des Lichtes betreffenden heuristischen Gesichtspunkt, Annalen der Physik, 322 (1905) 132-148.
- [60] S. Hagström, C. Nordling, K. Siegbahn, Electron spectroscopy for chemical analyses, Physics Letters, 9 (1964) 235-236.
- [61] A. Fahlman, K. Hamrin, J. Hedman, R. Nordberg, C. Nordling, K. Siegbahn, Electron spectroscopy and chemical binding, Nature, 210 (1966) 4-8.
- [62] K. Siegbahn, Electron spectroscopy for atoms, molecules, and condensed matter, Science (Washington, DC);(United States), 217 (1982).
- [63] C.C. Chusuei, D.W. Goodman, X-Ray photoelectron spectroscopy, Encyclopedia of Physical Science and Technology, 17 (2002) 921-938.
- [64] T.A. Carlson, X-ray photoelectron spectroscopy, Dowden, Hutchinson & Ross, 1978.
- [65] P. van der Heide, X-ray Photoelectron Spectroscopy: An introduction to Principles and Practices, Wiley, 2011.
- [66] G. Friedbacher, H. Bubert, Surface and Thin Film Analysis: A Compendium of Principles, Instrumentation, and Applications, Wiley, 2011.
- [67] I.U.o. Pure, A. Chemistry, IUPAC Gold Book, IUPAC, 2006.
- [68] H. Fellner-Feldegg, U. Gelius, B. Wannberg, A.G. Nilsson, E. Basilier, K. Siegbahn, New developments in ESCA-instrumentation, J. Electron. Spectrosc. Relat. Phenom., 5 (1974) 643-689.
- [69] S. Hofmann, Auger- and X-Ray Photoelectron Spectroscopy in Materials Science: A User-Oriented Guide, Springer, 2012.
- [70] J.F. Moulder, W.F. Stickle, P.E. Sobol, K.D. Bomben, Handbook of X-ray Photoelectron Spectroscopy, Physical Electronics, Inc., 1995.
- [71] C. Powell, A. Jablonski, A. Naumkin, A. Kraut-Vass, J. Conny, J. Rumble Jr, NIST data resources for surface analysis by X-ray photoelectron spectroscopy and Auger electron spectroscopy, J. Electron. Spectrosc. Relat. Phenom., 114 (2001) 1097-1102.
- [72] U. Gelius, P. Heden, J. Hedman, B. Lindberg, R. Manne, R. Nordberg, C. Nordling, K. Siegbahn, Molecular spectroscopy by means of ESCA III. Carbon compounds, Phys. Scr., 2 (1970) 70.
- [73] J.M. Wagner, X-Ray Photoelectron Spectroscopy, Nova Science Publishers, Incorporated, 2011.

- [74] M.P. Seah, Quantitative AES and XPS: convergence between theory and experimental databases, *J. Electron. Spectrosc. Relat. Phenom.*, 100 (1999) 55-73.
- [75] G. Lutz, *Seimiconductor Radiation Detectors: Device Physics*, Springer, 1999.
- [76] G. Ertl, J. Küppers, *Low Energy Electrons and Surface Chemistry*, VCH, 1985.
- [77] R. Denecke, P. Väterlein, M. Bässler, N. Wassdahl, S. Butorin, A. Nilsson, J.E. Rubensson, J. Nordgren, N. Mårtensson, R. Nyholm, Beamline I511 at MAX II, capabilities and performance, *J. Electron. Spectrosc. Relat. Phenom.*, 101–103 (1999) 971-977.
- [78] J. Schnadt, J. Knudsen, J.N. Andersen, H. Siegbahn, A. Pietzsch, F. Hennies, N. Johansson, N. Martensson, G. Ohrwall, S. Bahr, The new ambient-pressure X-ray photoelectron spectroscopy instrument at MAX-lab, *Journal of Synchrotron Radiation*, 19 (2012) 0-0.
- [79] MAXIV-Lab, www.maxlab.lu.se/node/277, accessed: 11 05 2014.2014
- [80] J.F. Moulder, J. Chastain, R.C. King, *Handbook of X-ray photoelectron spectroscopy: a reference book of standard spectra for identification and interpretation of XPS data*, Physical Electronics Eden Prairie, MN, 1995.
- [81] S. Hofmann, Quantitative Auger electron spectroscopy in thin film depth profiling, *Vacuum*, 48 (1997) 607-612.
- [82] L. Meitner, Über dieβ-Strahl-Spektren und ihren Zusammenhang mit der γ-Strahlung, *Zeitschrift für Physik*, 11 (1922) 35-54.
- [83] P. Auger, Sur l'effet photoélectrique composé, *J. Phys. Radium*, 6 205-208.
- [84] I.S. Tilinin, A. Jablonski, W.S.M. Werner, Quantitative surface analysis by Auger and x-ray photoelectron spectroscopy, *Prog. Surf. Sci.*, 52 (1996) 193-335.
- [85] C. Powell, A. Jablonski, I. Tilinin, S. Tanuma, D. Penn, Surface sensitivity of Auger-electron spectroscopy and X-ray photoelectron spectroscopy, *J. Electron. Spectrosc. Relat. Phenom.*, 98 (1999) 1-15.
- [86] T.A. Carlson, *Photoelectron and Auger spectroscopy*, Plenum Press, 1975.
- [87] A. Jablonski, Universal quantification of elastic scattering effects in AES and XPS, *Surf. Sci.*, 364 (1996) 380-395.
- [88] CasaSoftware, *CasaXPS Manual*, accessed: 08.09.2014
- [89] C. Davisson, L.H. Germer, Diffraction of Electrons by a Crystal of Nickel, *Physical Review*, 30 (1927) 705-740.

- [90] H. Viefhaus, Low-energy electron diffraction. Von M. A. Van Hove, W. H. Weinberg und C.-M. Chn. Springer-Verlag Berlin - Heidelberg - New York -London -Paris -Tokyo 1986. XVII, 603 S., 213 Abb., DM 124,-.ISBN 3-540-16262-3, Mater. Corros., 38 (1987) 404-404.
- [91] A. Nilsson, L.G.M. Pettersson, J. Norskov, Chemical Bonding at Surfaces and Interfaces, Elsevier Science, 2011.
- [92] D.R. Palo, R.A. Dagle, J.D. Holladay, Methanol steam reforming for hydrogen production, Chem. Rev., 107 (2007) 3992-4021.
- [93] P.J. Estrup, E.G. McRae, Surface studies by electron diffraction, Surf. Sci., 25 (1971) 1-52.
- [94] D.W. Dorninger, W.B. Müller, Allgemeine Algebra und Anwendungen, Teubner, 1984.
- [95] J.L. Falconer, J.A. Schwarz, Temperature-Programmed Desorption and Reaction: Applications to Supported Catalysts, Catalysis Reviews, 25 (1983) 141-227.
- [96] D.A. King, Thermal desorption from metal surfaces: A review, Surf. Sci., 47 (1975) 384-402.
- [97] P.A. Redhead, Thermal desorption of gases, Vacuum, 12 (1962) 203 - 211.
- [98] P. Redhead, Effects of re-adsorption on outgassing rate measurements, Vacuum, 47 (1996) 317 - 317.
- [99] D.A. Skoog, J.J. Leary, D. Brendel, S. Hoffstetter-Kuhn, Instrumentelle Analytik: Grundlagen - Geräte - Anwendungen, Springer, 1996.
- [100] NobelMedia, Press Release: The 1986 Nobel Prize in Physics, accessed: 13. Aug.2013
- [101] C. Bai, Scanning tunneling microscopy and its applications, Springer, 2000.
- [102] D.P. Woodruff, Is seeing believing?: Atomic-scale imaging of surface structures using scanning tunnelling microscopy, Curr. Opin. Solid State Mater. Sci., 7 (2003) 75-81.
- [103] AarhusUniversity, Scanning tunneling microscopy, <http://inano.au.dk/research/research-platforms/nanoanalysis/scanning-tunneling-microscopy/>, accessed: 19.12.2013
- [104] P. Jelínek, M. Švec, P. Pou, R. Perez, V. Cháb, Tip-induced reduction of the resonant tunneling current on semiconductor surfaces, Phys. Rev. Lett., 101 (2008) 176101.
- [105] W. Nolting, Grundkurs Theoretische Physik 5/1, Springer, 2004.
- [106] F. Schwabl, Quantenmechanik (QM I), Springer, 2002.
- [107] J. Bardeen, Tunnelling from a many-particle point of view, Phys. Rev. Letters, 6 (1961).
- [108] J. Tersoff, Theory of the Scanning Tunneling Microscope, in: M. Hove, S.Y. Tong (Eds.) The Structure of Surfaces, Springer Berlin Heidelberg, 1985, pp. 54-54.

- [109] R. Wiesendanger, Scanning Probe Microscopy and Spectroscopy, Cambridge University Press, 1994.
- [110] P. Eckle, M. Smolarski, P. Schlup, J. Biegert, A. Staudte, M. Schoffler, H.G. Muller, R. Dorner, U. Keller, Attosecond angular streaking, *Nat Phys*, 4 (2008) 565-570.
- [111] I. Horcas, R. Fernandez, J. Gomez-Rodriguez, J. Colchero, J. Gómez-Herrero, A. Baro, WSXM: a software for scanning probe microscopy and a tool for nanotechnology, *Rev. Sci. Instrum.*, 78 (2007) 013705.
- [112] P. Klapetek, <http://gwyddion.net/>, accessed: 08.09.2014
- [113] A. Chambers, Modern Vacuum Physics, CRC PressINC, 2005.
- [114] J.E. Mahan, Physical Vapor Deposition of Thin Films, Wiley, 2000.
- [115] G. Sauerbrey, Verwendung von Schwingquarzen zur Wägung dünner Schichten und zur Mikrowägung, *Zeitschrift für Physik*, 155 (1959) 206-222.
- [116] R.J. Schwankner, A. Bettermann, J. Dorner, C. Feigl, R. Laubinger, F. Vilser, Aus Bildung und Wissenschaft-Zwei Anwendungen von Thorium, *Mathematische und Naturwissenschaftliche Unterricht*, 53 (2000) 295-302.
- [117] P.-T. Emitters, Tungsten, Thoriated-Tungsten, and Thoria Emitters, in: *Electron tube design*, 1962, pp. 90.
- [118] W.E. Karnaugh, Carburized thoriated tungsten, in, Google Patents, 1958.
- [119] W.E. Harbaugh, Process of Carburizing, in, Google Patents, 1953.
- [120] M. Suárez, A. Fernández, J.L. Menéndez, R. Torrecillas, H.U. Kessel, J. Hennicke, R. Kirchner, T. Kessel, Challenges and Opportunities for Spark Plasma Sintering: A Key Technology for a New Generation of Materials, 2013.
- [121] T. Hungría, J. Galy, A. Castro, Spark Plasma Sintering as a Useful Technique to the Nanostructuring of Piezo-Ferroelectric Materials, *Adv. Eng. Mater.*, 11 (2009) 615-631.
- [122] C. Edelmann, *Vakuumphysik*, Spektrum-Akademischer Vlg, 1998.
- [123] E. Wiberg, A.F. Holleman, N. Wiberg, *Lehrbuch Der Anorganischen Chemie*, Gruyter, Walter de GmbH, 2007.
- [124] Pfeiffer-Vacuum, Vacuum Technology Know How, in, www.pfeiffer-vacuum.de.
- [125] K. Jousten, W. Jitschin, F. Sharipov, R. Lachenmann, *Wutz Handbuch Vakuumtechnik*, Vieweg+Teubner Verlag, 2009.
- [126] E. Westrum Jr, C. Chou, D. Osborne, H. Flotow, Specific heat of apiezon T grease from 1 to 350° K, *Cryogenics*, 7 (1967) 43-44.
- [127] S.V. Pepper, Effect of test environment on lifetime of a vacuum lubricant, in: *World Tribology Congress III*, American Society of Mechanical Engineers, 2005, pp. 943-944.

- [128] M. Henzler, W. Göpel, Oberflächenphysik des Festkörpers, Vieweg+Teubner Verlag, 1994.
- [129] OerlikonLeyboldVacuum, Grundlagen der Vakuumtechnik, 2007.
- [130] A. Chambers, Basic Vacuum Technology, 2nd edition, Taylor & Francis, 2010.
- [131] Wikipedia, http://en.wikipedia.org/wiki/File:Cut_through_turbomolecular_pump.jpg, accessed: 26.06.2013
- [132] B.R. Holsteina, The van der Waals interaction, (2001).
- [133] R. Hoffmann, Solids and Surfaces: A Chemist's View of Bonding in Extended Structures, Wiley, 1989.
- [134] C. Weilach, S.M. Kozlov, H.H. Holzapfel, K. Föttinger, K.M. Neyman, G. Rupprechter, Geometric Arrangement of Components in Bimetallic PdZn/Pd(111) Surfaces Modified by CO Adsorption: A Combined Study by Density Functional Calculations, Polarization-Modulated Infrared Reflection Absorption Spectroscopy, and Temperature-Programmed Desorption, J. Phys. Chem. C, (2012).
- [135] W. Oed, H. Lindner, U. Starke, K. Heinz, K. Müller, Adsorbate-induced relaxation and reconstruction of $c(2 \times 2)$ O/Ni (100): A reinvestigation by leed structure analysis, Surf. Sci., 224 (1989) 179-194.
- [136] W. Oed, H. Lindner, U. Starke, K. Heinz, K. Müller, D. Saldin, P. de Andres, J. Pendry, Adsorbate induced reconstruction phase $p(2 \times 2)$ O/Ni (100), Surf. Sci., 225 (1990) 242-248.
- [137] G. Kresse, J. Furthmüller, Efficient iterative schemes for ab initio total-energy calculations using a plane-wave basis set, Phys. Rev. B, 54 (1996) 11169.
- [138] B. Hammer, L.B. Hansen, J.K. Nørskov, Improved adsorption energetics within density-functional theory using revised Perdew-Burke-Ernzerhof functionals, Phys. Rev. B, 59 (1999) 7413.
- [139] J.P. Perdew, K. Burke, M. Ernzerhof, Generalized gradient approximation made simple, Phys. Rev. Lett., 77 (1996) 3865.
- [140] I.V. Yudanov, R. Sahnoun, K.M. Neyman, N. Rösch, Metal nanoparticles as models of single crystal surfaces and supported catalysts: Density functional study of size effects for CO/Pd (111), The Journal of chemical physics, 117 (2002) 9887-9896.
- [141] X. Guo, J.T. Yates, Dependence of effective desorption kinetic parameters on surface coverage and adsorption temperature: CO on Pd(111), 90 (1989) 6761-6766.
- [142] G. Kresse, D. Joubert, From ultrasoft pseudopotentials to the projector augmented-wave method, Phys. Rev. B, 59 (1999) 1758.

- [143] H.J. Monkhorst, J.D. Pack, Special points for Brillouin-zone integrations, *Phys. Rev. B*, 13 (1976) 5188-5192.
- [144] M. Methfessel, A. Paxton, High-precision sampling for Brillouin-zone integration in metals, *Phys. Rev. B*, 40 (1989) 3616.
- [145] R.G. Parr, R.G.P.W. Yang, *Density-Functional Theory of Atoms and Molecules*, Oxford University Press, USA, 1989.
- [146] X. Xu, W.A. Goddard III, The extended Perdew-Burke-Ernzerhof functional with improved accuracy for thermodynamic and electronic properties of molecular systems, *The Journal of chemical physics*, 121 (2004) 4068-4082.
- [147] J. Paier, R. Hirschl, M. Marsman, G. Kresse, The Perdew–Burke–Ernzerhof exchange-correlation functional applied to the G2-1 test set using a plane-wave basis set, *The Journal of chemical physics*, 122 (2005) 234102.
- [148] R. Dronskowski, R. Hoffmann, *Computational Chemistry of Solid State Materials: A Guide for Materials Scientists, Chemists, Physicists and others*, Wiley, 2008.
- [149] M. Kalff, G. Comsa, T. Michely, Temperature dependent morphological evolution of Pt (111) by ion erosion: destabilization, phase coexistence and coarsening, *Surf. Sci.*, 486 (2001) 103-135.
- [150] W.K. Kuhn, J. Szanyi, D.W. Goodman, CO adsorption on Pd (111): the effects of temperature and pressure, *Surf. Sci.*, 274 (1992) L611-L618.
- [151] M. Rose, T. Mitsui, J. Dunphy, A. Borg, D. Ogletree, M. Salmeron, P. Sautet, Ordered structures of CO on Pd (111) studied by STM, *Surf. Sci.*, 512 (2002) 48-60.
- [152] H. Ohtani, M.V. Hove, G. Somorjai, Leed intensity analysis of the surface structures of Pd (111) and of CO adsorbed on Pd (111) in a ($\sqrt{3} \times \sqrt{3}$) R30° arrangement, *Surf. Sci.*, 187 (1987) 372-386.
- [153] P. Galletto, H. Unterhalt, G. Rupprechter, The molecular orientation of CO on Pd(1 1 1): a polarization-dependent SFG study, *Chem. Phys. Lett.*, 367 (2003) 785 - 790.
- [154] T. Engel, G. Ertl, Elementary steps in the catalytic oxidation of carbon monoxide on platinum metals, *Adv. Catal.*, 28 (1979) 1-78.
- [155] G. Blyholder, Molecular orbital view of chemisorbed carbon monoxide, *The Journal of Physical Chemistry*, 68 (1964) 2772-2777.
- [156] G. Blyholder, CNDO model of carbon monoxide chemisorbed on nickel, *The Journal of Physical Chemistry*, 79 (1975) 756-761.
- [157] K. Hermann, BALSAC (Build and Analyze Lattices, Surfaces, And Clusters), accessed: 2014

- [158] M. Morkel, G. Rupprechter, H.-J. Freund, Ultrahigh vacuum and high-pressure coadsorption of CO and H₂ on Pd(111): A combined SFG, TDS, and LEED study, 119 (2003) 10853-10866.
- [159] M. Tüshaus, W. Berndt, H. Conrad, A. Bradshaw, B. Persson, Understanding the structure of high coverage CO adlayers, *Appl. Phys. A*, 51 (1990) 91-98.
- [160] G. Rupprechter, H. Unterhalt, M. Morkel, P. Galletto, L. Hu, H.-J. Freund, Sum frequency generation vibrational spectroscopy at solid-gas interfaces: CO adsorption on Pd model catalysts at ambient pressure, *Surf. Sci.*, 502 (2002) 109-122.
- [161] L. Hanley, X. Guo, J.T. Yates Jr, Photolysis of chemisorbed dioxygen on Pd (111): Dependence on photon energy, *The Journal of Chemical Physics*, 91 (1989) 7220-7227.
- [162] D. Loffreda, D. Simon, P. Sautet, Vibrational frequency and chemisorption site: a DFT-periodic study of NO on Pd (111) and Rh (111) surfaces, *Chem. Phys. Lett.*, 291 (1998) 15-23.
- [163] M. Beutl, J. Lesnik, The influence of subsurface vanadium on the adsorption of hydrogen and carbon monoxide on Pd (111), *Vacuum*, 61 (2001) 113-117.
- [164] M. Mavrikakis, M.A. Barteau, Oxygenate reaction pathways on transition metal surfaces, *J. Mol. Catal. A: Chem.*, 131 (1998) 135-147.
- [165] J.J. Chen, Z.C. Jiang, Y. Zhou, B.R. Chakraborty, N. Winograd, Spectroscopic studies of methanol decomposition on Pd[111], *Surf. Sci.*, 328 (1995) 248 - 262.
- [166] Q. Zhang, R.J. Farrauto, A PdZn catalyst supported on stabilized ceria for stoichiometric methanol steam reforming and hydrogen production, *Appl. Catal., A*, 395 (2011) 64 - 70.
- [167] R. Schennach, A. Eichler, K.D. Rendulic, Adsorption and Desorption of Methanol on Pd (111) and on a Pd/V Surface Alloy, *J. Phys. Chem. B*, 107 (2003) 2552-2558.
- [168] M. Rebholz, N. Kruse, Mechanisms of methanol decomposition on Pd {111}, *The Journal of chemical physics*, 95 (1991) 7745-7759.
- [169] Y. Matsumura, M. Okumura, Y. Usami, K. Kagawa, H. Yamashita, M. Anpo, M. Haruta, Low-temperature decomposition of methanol to carbon monoxide and hydrogen with low activation energy over Pd/ZrO₂ catalyst, *Catal. Lett.*, 44 (1997) 189-191.
- [170] D. Wickham, B. Logsdon, S. Cowley, C. Butler, A TPD and XPS investigation of palladium on modified alumina supports used for the catalytic decomposition of methanol, *J. Catal.*, 128 (1991) 198-209.

- [171] R. Shiozaki, T. Hayakawa, Y.-y. Liu, T. Ishii, M. Kumagai, S. Hamakawa, K. Suzuki, T. Itoh, T. Shishido, K. Takehira, Methanol decomposition to synthesis gas over supported Pd catalysts prepared from synthetic anionic clays, *Catal. Lett.*, 58 (1999) 131-140.
- [172] E.M. Cordi, J.L. Falconer, Oxidation of Volatile Organic Compounds on Al₂O₃, Pd/Al₂O₃, and PdO/Al₂O₃ Catalysts, *J. Catal.*, 162 (1996) 104-117.
- [173] M. Borasio, O. Rodríguez de la Fuente, G. Rupprechter, H.-J. Freund, In situ studies of methanol decomposition and oxidation on Pd (111) by PM-IRAS and XPS spectroscopy, *J. Phys. Chem. B*, 109 (2005) 17791-17794.
- [174] M. Baeumer, J. Libuda, K.M. Neyman, N. Roesch, G. Rupprechter, H.J. Freund, Adsorption and reaction of methanol on supported palladium catalysts: microscopic-level studies from ultrahigh vacuum to ambient pressure conditions, *PCCP*, 9 (2007) 3541-3558.
- [175] E. Demirci, A. Winkler, Quantitative determination of reaction products by in-line thermal desorption spectroscopy: The system methanol/Pd(111), *J Vac Sci Technol A*, 26 (2008) 78-82.
- [176] S. Liu, K. Takahashi, M. Ayabe, Hydrogen production by oxidative methanol reforming on Pd/ZnO catalyst: effects of Pd loading, *Catal. Today*, 87 (2003) 247-253.
- [177] R.A. Dagle, A. Platon, D.R. Palo, A.K. Datye, J.M. Vohs, Y. Wang, PdZnAl catalysts for the reactions of water-gas-shift, methanol steam reforming, and reverse-water-gas-shift, *Appl. Catal., A*, 342 (2008) 63 - 68.
- [178] Y. Kawamura, T. Yahata, A. Igarashi, Improvement of performance of palladium-based catalyst for small methanol reformer, *Chem. Eng. Sci.*, 65 (2010) 201 - 207.
- [179] R.J. Levis, J. Zhicheng, N. Winograd, Thermal decomposition of methanol adsorbed on palladium {111}. A new reaction pathway involving methyl formation, *J. Am. Chem. Soc.*, 111 (1989) 4605-4612.
- [180] E. Martono, J.M. Vohs, Reaction of CO, CH₂O, CH₃OH on Zn-Modified Pt(111) Surfaces, *J. Phys. Chem. C*, 117 (2013) 6692-6701.
- [181] R.B. Barros, A.R. Garcia, L.M. Ilharco, The decomposition pathways of methanol on clean Ru (0001), studied by reflection-absorption infrared spectroscopy (RAIRS), *J. Phys. Chem. B*, 105 (2001) 11186-11193.
- [182] J.-J. Chen, Z.-C. Jiang, Y. Zhou, B. Chakraborty, N. Winograd, Spectroscopic studies of methanol decomposition on Pd [lcub] 111 [rcub], *Surf. Sci.*, 328 (1995) 248-262.
- [183] K. Christmann, J. Demuth, The adsorption and reaction of methanol on Pd (100). I. Chemisorption and condensation, *The Journal of Chemical Physics*, 76 (1982) 6308-6317.

- [184] K. Christmann, J. Demuth, The adsorption and reaction of methanol on Pd (100). II. Thermal desorption and decomposition, *The Journal of Chemical Physics*, 76 (1982) 6318-6327.
- [185] A.K. Bhattacharya, M.A. Chesters, M.E. Pemble, N. Sheppard, The decomposition of methanol on Pd(110) as studied by electron energy loss spectroscopy: Evidence for the formation of CH₃O and HCO surface species, *Surf. Sci.*, 206 (1988) L845 - L850.
- [186] J.A. Gates, L.L. Kesmodel, Methanol adsorption and decomposition on clean and oxygen precovered palladium (111), *J. Catal.*, 83 (1983) 437 - 445.
- [187] N.M. Rodriguez, P.E. Anderson, A. Wootsch, U. Wild, R. Schlögl, Z. Paál, XPS, EM, and Catalytic Studies of the Accumulation of Carbon on Pt Black, *J. Catal.*, 197 (2001) 365 - 377.
- [188] G. Kok, A. Noordermeer, B. Nieuwenhuys, Decomposition of methanol and the interaction of coadsorbed hydrogen and carbon monoxide on a Pd (111) surface, *Surf. Sci.*, 135 (1983) 65-80.
- [189] J. Hoffmann, S. Schaueremann, V. Johánek, J. Hartmann, J. Libuda, The kinetics of methanol oxidation on a supported Pd model catalyst: molecular beam and TR-IRAS experiments, *J. Catal.*, 213 (2003) 176 - 190.
- [190] X. Guo, L. Hanley, J. Yates Jr, Thermal stability of the carbon-oxygen bond of methanol on the palladium (111) surface: an isotopic mixing study, *J. Am. Chem. Soc.*, 111 (1989) 3155-3157.
- [191] J. Davis, M. Barteau, Spectroscopic identification of alkoxide, aldehyde, and acyl intermediates in alcohol decomposition on Pd (111), *Surf. Sci.*, 235 (1990) 235-248.
- [192] J. Davis, M. Barteau, Decarbonylation and decomposition pathways of alcohol's on Pd (111), *Surf. Sci.*, 187 (1987) 387-406.
- [193] S.M. Francis, J. Corneille, D.W. Goodman, M. Bowker, The adsorption and oxidation of methanol on thin palladium films, *Surf. Sci.*, 364 (1996) 30 - 38.
- [194] M. Rebholz, V. Matolin, R. Prins, N. Kruse, Methanol decomposition on oxygen precovered and atomically clean Pd(111) single crystal surfaces, *Surf. Sci.*, 251-252 (1991) 1117 - 1122.
- [195] S. Schaueremann, J. Hoffmann, V. Johánek, J. Hartmann, J. Libuda, H.J. Freund, Catalytic activity and poisoning of specific sites on supported metal nanoparticles, *Angew. Chem. Int. Ed.*, 41 (2002) 2532-2535.

- [196] V.V. Kaichev, M. Morkel, H. Unterhalt, I.P. Prosvirin, V.I. Bukhtiyarov, G. Rupprechter, H.J. Freund, C-O bond scission on defect-rich and perfect Pd(111)?, *Surf. Sci.*, 566-568 (2004) 1024 - 1029.
- [197] H. Luth, G.W. Rubloff, W.D. Grobman, Chemisorption and decomposition reactions of oxygen-containing organic molecules on clean Pd surfaces studied by UV photoemission, *Surf. Sci.*, 63 (1977) 325 - 338.
- [198] F. Solymosi, A. Berkó, Z. Tóth, Adsorption and dissociation of CH₃OH on clean and K-promoted Pd(100) surfaces, *Surf. Sci.*, 285 (1993) 197 - 208.
- [199] M. Kratzer, A. Tamtögl, J. Killmann, R. Schennach, A. Winkler, Preparation and calibration of ultrathin Zn layers on Pd(1 1 1), *Appl. Surf. Sci.*, 255 (2009) 5755 - 5759.
- [200] G. Weirum, M. Kratzer, H.P. Koch, A. Tamtögl, J. Killmann, I. Bako, A. Winkler, S. Surnev, F.P. Netzer, R. Schennach, Growth and desorption kinetics of ultrathin Zn layers on Pd(111), *J. Phys. Chem. C*, 113 (2009) 9788-9796.
- [201] X. He, Y. Huang, Z.-X. Chen, Zinc coverage dependent structure of PdZn surface alloy, *Phys. Chem. Chem. Phys.*, 13 (2011) 107-109.
- [202] A. Bayer, K. Flechtner, R. Denecke, H.P. Steinruck, K.M. Neyman, N. Rosch, Electronic properties of thin Zn layers on Pd(111) during growth and alloying, *Surf. Sci.*, 600 (2006) 78-94.
- [203] W. Stadlmayr, S. Penner, B. Klötzer, N. Memmel, Growth, thermal stability and structure of ultrathin Zn-layers on Pd(1 1 1), *Surf. Sci.*, 603 (2009) 251-255.
- [204] H.P. Koch, I. Bako, G. Weirum, M. Kratzer, R. Schennach, A theoretical study of Zn adsorption and desorption on a Pd(111) substrate, *Surf. Sci.*, 604 (2010) 926-931.
- [205] W. Stadlmayr, C. Rameshan, C. Weilach, H. Lorenz, M. Hävecker, R. Blume, T. Rocha, D. Teschner, A. Knop-Gericke, D. Zemlyanov, S. Penner, R. Schlögl, G. Rupprechter, B. Klötzer, N. Memmel, Temperature-Induced Modifications of PdZn Layers on Pd(111), *J. Phys. Chem. C*, 114 (2010) 10850-10856.
- [206] C. Rameshan, W. Stadlmayr, C. Weilach, S. Penner, H. Lorenz, M. Hävecker, R. Blume, T. Rocha, D. Teschner, A. Knop-Gericke, R. Schlögl, N. Memmel, D. Zemlyanov, G. Rupprechter, B. Klötzer, Subsurface-gesteuerte CO₂-Selektivität von PdZn-Oberflächenlegierungen in der H₂-Erzeugung durch Methanoldampfreformierung, *Angew. Chem.*, 122 (2010) 3292-3296.

- [207] C. Rameshan, W. Stadlmayr, C. Weilach, S. Penner, H. Lorenz, M. Hävecker, R. Blume, T. Rocha, D. Teschner, A. Knop-Gericke, R. Schlögl, N. Memmel, D. Zemlyanov, G. Rupprechter, B. Klötzer, Subsurface-Controlled CO₂ Selectivity of PdZn Near-Surface Alloys in H₂ Generation by Methanol Steam Reforming, *Angew. Chem., Int. Ed.*, 49 (2010) 3224-3227.
- [208] Z.X. Chen, K.M. Neyman, A.B. Gordienko, N. Rösch, Surface structure and stability of PdZn and PtZn alloys: Density-functional slab model studies, *Phys. Rev. B*, 68 (2003) 075417.
- [209] K.M. Neyman, K.H. Lim, Z.-X. Chen, L.V. Moskaleva, A. Bayer, A. Reindl, D. Borgmann, R. Denecke, H.-P. Steinruck, N. Rosch, Microscopic models of PdZn alloy catalysts: structure and reactivity in methanol decomposition, *PCCP*, 9 (2007) 3470-3482.
- [210] J. Lipton-Duffin, J. MacLeod, M. Vondráček, K. Prince, R. Rosei, F. Rosei, Thermal evolution of the submonolayer near-surface alloy of ZnPd on Pd (111), *PCCP*, 16 (2014) 4764-4770.
- [211] Y. Huang, W. Ding, Z.-X. Chen, Effect of Zn on the adsorption of CO on Pd(111), *The Journal of Chemical Physics*, 133 (2010) 214702.
- [212] J.A. Rodriguez, Physical and chemical properties of bimetallic surfaces, *Surf. Sci. Rep.*, 24 (1996) 225-287.
- [213] C. Rameshan, C. Weilach, W. Stadlmayr, S. Penner, H. Lorenz, M. Hävecker, R. Blume, T. Rocha, D. Teschner, A. Knop-Gericke, R. Schlögl, D. Zemlyanov, N. Memmel, G. Rupprechter, B. Klötzer, Steam reforming of methanol on PdZn near-surface alloys on Pd(1 1 1) and Pd foil studied by in-situ XPS, LEIS and PM-IRAS, *J. Catal.*, 276 (2010) 101 - 113.
- [214] K. Föttinger, J.A. van Bokhoven, M. Nachtegaal, G.n. Rupprechter, Dynamic Structure of a Working Methanol Steam Reforming Catalyst: In Situ Quick-EXAFS on Pd/ZnO Nanoparticles, *J. Phys. Chem. Lett.*, 2 (2011) 428-433.
- [215] H. Gabasch, A. Knop-Gericke, R. Schlögl, S. Penner, B. Jenewein, K. Hayek, B. Klötzer, Zn adsorption on Pd(111): ZnO and PdZn alloy formation, *J. Phys. Chem. B*, 110 (2006) 11391-11398.
- [216] E. Jeroro, V. Lebarbler, A. Datye, Y. Wang, J.M. Vohs, Interaction of CO with surface PdZn alloys, *Surf. Sci.*, 601 (2007) 5546-5554.
- [217] E. Jeroro, M.P. Hyman, J.M. Vohs, Ensemble vs. electronic effects on the reactivity of two-dimensional Pd alloys: a comparison of CO and CH₃OH adsorption on Zn/Pd(111) and Cu/Pd(111), *Phys. Chem. Chem. Phys.*, 11 (2009) 10457-10465.

- [218] A. Tamtogl, M. Kratzer, J. Killman, A. Winkler, Adsorption/desorption of H₂ and CO on Zn-modified Pd(111), *J. Chem. Phys.*, 129 (2008) 224706.
- [219] C. Dupont, F. Delbecq, D. Loffreda, Y. Jugnet, Preferential CO oxidation in a large excess of hydrogen on Pt₃Sn surfaces, *J. Catal.*, 278 (2011) 239-245.
- [220] R.M. Lambert, F.J. Williams, R.L. Cropley, A. Palermo, Heterogeneous alkene epoxidation: past, present and future, *J. Mol. Catal. A: Chem.*, 228 (2005) 27-33.
- [221] P. Maetz, R. Touroude, Modification of surface reactivity by adsorbed species on supported palladium and platinum catalysts during the selective hydrogenation of but-1-yne, *Appl. Catal., A*, 149 (1997) 189-206.
- [222] G. Somorjai, The experimental evidence of the role of surface restructuring during catalytic reactions, *Catal. Lett.*, 12 (1992) 17-34.
- [223] L.C. Grabow, A.A. Gokhale, S.T. Evans, J.A. Dumesic, M. Mavrikakis, Mechanism of the water gas shift reaction on Pt: First principles, experiments, and microkinetic modeling, *J. Phys. Chem. C*, 112 (2008) 4608-4617.
- [224] A.A. Gokhale, J.A. Dumesic, M. Mavrikakis, On the mechanism of low-temperature water gas shift reaction on copper, *J. Am. Chem. Soc.*, 130 (2008) 1402-1414.
- [225] S. Gonzalez, K.M. Neyman, S. Shaikhutdinov, H.-J. Freund, F. Illas, On the promoting role of Ag in selective hydrogenation reactions over Pd-Ag bimetallic catalysts: A theoretical study, *J. Phys. Chem. C*, 111 (2007) 6852-6856.
- [226] V.R. Stamenkovic, B.S. Mun, M. Arenz, K.J. Mayrhofer, C.A. Lucas, G. Wang, P.N. Ross, N.M. Markovic, Trends in electrocatalysis on extended and nanoscale Pt-bimetallic alloy surfaces, *Nature materials*, 6 (2007) 241-247.
- [227] L. Rygh, C. Nielsen, Infrared Study of CO Adsorbed on a Co/Re/ γ -Al₂O₃-Based Fischer-Tropsch Catalyst, *J. Catal.*, 194 (2000) 401-409.
- [228] D. Cheng, I. Atanasov, M. Hou, Influence of the environment on equilibrium properties of Au-Pd clusters, *The European Physical Journal D*, 64 (2011) 37-44.
- [229] Y. Dai, L. Ou, W. Liang, F. Yang, Y. Liu, S. Chen, Efficient and Superiorly Durable Pt-Lean Electrocatalysts of Pt-W Alloys for the Oxygen Reduction Reaction, *J. Phys. Chem. C*, 115 (2011) 2162-2168.
- [230] B.N. Wanjala, J. Luo, B. Fang, D. Mott, C.-J. Zhong, Gold-platinum nanoparticles: alloying and phase segregation, *J. Mater. Chem.*, 21 (2011) 4012-4020.
- [231] R. Ferrando, J. Jellinek, R.L. Johnston, Nanoalloys: from theory to applications of alloy clusters and nanoparticles, *Chem. Rev.*, 108 (2008) 845-910.

- [232] I.V. Yudanov, K.M. Neyman, Stabilization of Au at edges of bimetallic PdAu nanocrystallites, *PCCP*, 12 (2010) 5094-5100.
- [233] E. Demirci, C. Carbogno, A. Groß, A. Winkler, Adsorption of CO on Ni/Cu (110) bimetallic surfaces, *Phys. Rev. B*, 80 (2009) 085421.
- [234] J.A. Stephens, H.C. Ham, G.S. Hwang, Atomic Arrangements of AuPt/Pt (111) and AuPd/Pd (111) Surface Alloys: A Combined Density Functional Theory and Monte Carlo Study, *J. Phys. Chem. C*, 114 (2010) 21516-21523.
- [235] F. Maroun, F. Ozanam, O. Magnussen, R. Behm, The role of atomic ensembles in the reactivity of bimetallic electrocatalysts, *Science*, 293 (2001) 1811-1814.
- [236] J. Yuhara, M. Schmid, P. Varga, Two-dimensional alloy of immiscible metals: Single and binary monolayer films of Pb and Sn on Rh (111), *Phys. Rev. B*, 67 (2003) 195407.
- [237] M. Haé, R. Blume, T. Rocha, D. Teschner, A. Knop-Gericke, R. Schloé, N. Memmel, D. Zemlyanov, G. Rupprechter, Theoretical Studies of CO Adsorption on PdZn Surface Alloys and Induced Structural Modifications of the Substrate.
- [238] K.-P. Huber, G. Herzberg, *Molecular spectra and molecular structure*, Vol. 4, Constants of diatomic molecules Van Nostrand Reinhold, New York, (1979) 158.
- [239] S. Kozlov, Personal communication, 2012.
- [240] M. Friedrich, A. Ormeci, Y. Grin, M. Armbruster, PdZn or ZnPd: Charge Transfer and Pd-Pd Bonding as the Driving Force for the Tetragonal Distortion of the Cubic Crystal Structure, *Z. Anorg. Allg. Chem.*, 636 (2010) 1735-1739.
- [241] R.F. Bader, *Atoms in molecules*, Wiley Online Library, 1990.
- [242] M.K. Rose, T. Mitsui, J. Dunphy, A. Borg, D.F. Ogletree, M. Salmeron, P. Sautet, Ordered structures of CO on Pd(1 1 1) studied by STM, *Surf. Sci.*, 512 (2002) 48 - 60.
- [243] D. Loffreda, D. Simon, P. Sautet, Dependence of stretching frequency on surface coverage and adsorbate-adsorbate interactions: a density-functional theory approach of CO on Pd (111), *Surf. Sci.*, 425 (1999) 68-80.
- [244] V. Lebarbier, R. Dagle, T. Conant, J.M. Vohs, A.K. Datye, Y. Wang, CO/FTIR Spectroscopic Characterization of Pd/ZnO/Al₂O₃ Catalysts for Methanol Steam Reforming, *Catal. Lett.*, 122 (2008) 223-227.
- [245] J. Tersoff, D. Hamann, Theory of the scanning tunneling microscope, in: *Scanning Tunneling Microscopy*, Springer, 1993, pp. 59-67.
- [246] P.E. Blöchl, Projector augmented-wave method, *Phys. Rev. B*, 50 (1994) 17953-17979.
- [247] M. Weinert, G. Schneider, R. Podloucky, J. Redinger, FLAPW: applications and implementations, *J. Phys.: Condens. Matter*, 21 (2009) 084201.

- [248] S. Kozlov, Personal communication, 2014.
- [249] W. Hofer, G. Ritz, W. Hebenstreit, M. Schmid, P. Varga, J. Redinger, R. Podlucky, Scanning tunneling microscopy of binary-alloy surfaces: is chemical contrast a consequence of alloying?, *Surf. Sci.*, 405 (1998) L514-L519.
- [250] Z.-X. Chen, K.M. Neyman, K.H. Lim, N. Rösch, CH₃O Decomposition on PdZn(111), Pd(111), and Cu(111). A Theoretical Study, *Langmuir*, 20 (2004) 8068-8077.
- [251] M. Chen, Y. Cai, Z. Yan, K. Gath, S. Axnanda, D.W. Goodman, Highly active surfaces for CO oxidation on Rh, Pd, and Pt, *Surf. Sci.*, 601 (2007) 5326-5331.
- [252] Z.X. Chen, K.M. Neyman, K.H. Lim, N. Rösch, CH₃O decomposition on PdZn(111), Pd(111), and Cu(111). A theoretical study, *Langmuir*, 20 (2004) 8068-8077.
- [253] H. Bluhm, M. Hävecker, A. Knop-Gericke, M. Kiskinova, R. Schloegl, M. Salmeron, In situ x-ray photoelectron spectroscopy studies of gas-solid interfaces at near-ambient conditions, *MRS Bull.*, 32 (2007) 1022-1030.
- [254] M. Morkel, V.V. Kaichev, G. Rupprechter, H.J. Freund, I.P. Prosvirin, V.I. Bukhtiyarov, Methanol dehydrogenation and formation of carbonaceous overlayers on Pd(111) studied by high-pressure SFG and XPS spectroscopy, *J. Phys. Chem. B*, 108 (2004) 12955-12961.
- [255] H. Gabasch, W. Unterberger, K. Hayek, B. Klötzer, E. Kleimenov, D. Teschner, S. Zafeirotos, M. Hävecker, A. Knop-Gericke, R. Schlögl, J. Han, F.H. Ribeiro, B. Aszalos-Kiss, T. Curtin, D. Zemlyanov, In situ XPS study of Pd(1 1 1) oxidation at elevated pressure, Part 2: Palladium oxidation in the 10-1 mbar range, *Surf. Sci.*, 600 (2006) 2980 - 2989.
- [256] S. Tanuma, C.J. Powell, D.R. Penn, Calculations of electron inelastic mean free paths. II. Data for 27 elements over the 50–2000 eV range, *Surf. Interface Anal.*, 17 (1991) 911-926.
- [257] S. Tanuma, C. Powell, D. Penn, Calculations of electron inelastic mean free paths, *Surf. Interface Anal.*, 37 (2005) 1-14.
- [258] H. Gabasch, A. Knop-Gericke, R. Schloegl, M. Borasio, C. Weilach, G. Rupprechter, S. Penner, B. Jenewein, K. Hayek, B. Kloetzer, Comparison of the reactivity of different Pd-O species in CO oxidation, *PCCP*, 9 (2007) 533-540.
- [259] F. Leisenberger, G. Koller, M. Sock, S. Surnev, M. Ramsey, F. Netzer, B. Klötzer, K. Hayek, Surface and subsurface oxygen on Pd (111), *Surf. Sci.*, 445 (2000) 380-393.
- [260] E. Lundgren, G. Kresse, C. Klein, M. Borg, J.N. Andersen, M. De Santis, Y. Gauthier, C. Konvicka, M. Schmid, P. Varga, Two-dimensional oxide on Pd (111), *Phys. Rev. Lett.*, 88 (2002) 246103.

- [261] A. Ota, E.L. Kunkes, I. Kasatkin, E. Groppo, D. Ferri, B. Poceiro, R.M. Navarro Yerga, M. Behrens, Comparative study of hydrotalcite-derived supported Pd₂Ga and PdZn intermetallic nanoparticles as methanol synthesis and methanol steam reforming catalysts, *J. Catal.*, 293 (2012) 27-38.
- [262] K. Kovnir, M. Armbrüster, D. Teschner, T. Venkov, F. Jentoft, A. Knop-Gericke, Y. Grin, R. Schlögl, A new approach to well-defined, stable and site-isolated catalysts, *Science and Technology of Advanced Materials*, 8 (2007) 420-427.
- [263] H. Kohlmann, R. Meyers, Metal hydrides, *Encyclopedia of physical science and technology*, 9 (2002) 441-458.
- [264] B. Halevi, E.J. Peterson, A. Roy, A. DeLariva, E. Jeroro, F. Gao, Y. Wang, J.M. Vohs, B. Kiefer, E. Kunkes, M. Hävecker, M. Behrens, R. Schlögl, A.K. Datye, Catalytic reactivity of face centered cubic PdZn α for the steam reforming of methanol, *J. Catal.*, 291 (2012) 44-54.
- [265] D.J. Childers, N.M. Schweitzer, S.M.K. Shahari, R.M. Rioux, J.T. Miller, R.J. Meyer, Modifying structure-sensitive reactions by addition of Zn to Pd, *J. Catal.*, 318 (2014) 75-84.
- [266] B. Halevi, E.J. Peterson, A. DeLaRiva, E. Jeroro, V.M. Lebarbier, Y. Wang, J.M. Vohs, B. Kiefer, E. Kunkes, M. Havecker, Aerosol-Derived Bimetallic Alloy Powders: Bridging the Gap \dagger , *J. Phys. Chem. C*, 114 (2010) 17181-17190.
- [267] H. Stadelmaier, W. Hardy, Ternaere Kohlenstofflegierungen von Palladium und Platin mit Magnesium, Aluminium, Zink, Gallium, Germanium, Kadmium, Indium, Zinn, Quecksilber, Thallium und Blei, *Zeitschrift fuer Metallkunde*, 52 (1961) 391-396.
- [268] M. Armbrüster, K. Kovnir, M. Behrens, D. Teschner, Y. Grin, R. Schlögl, Pd– Ga Intermetallic Compounds as Highly Selective Semihydrogenation Catalysts, *J. Am. Chem. Soc.*, 132 (2010) 14745-14747.
- [269] B. Predel, Pd-Zn (Palladium-Zinc), in: O. Madelung (Ed.) *SpringerMaterials - The Landolt-Börnstein Database*
- [270] M. Armbrüster, personal communication, 2014.
- [271] Z. Wei, J. Sun, Y. Li, A.K. Datye, Y. Wang, Bimetallic catalysts for hydrogen generation, *Chem. Soc. Rev.*, 41 (2012) 7994-8008.
- [272] T. Bohnenberger, Funktionale Schichten aus Kohlenstoffnanoröhrchen und ihre Anwendung in elektrochemischen Doppelschichtkondensatoren, in: Fakultät für Elektrotechnik und Informationstechnik; Fakultät für Technische Chemie, Technische Universität Wien, Wien, 2013.

- [273] M. Li, M. Boggs, T.P. Beebe, C. Huang, Oxidation of single-walled carbon nanotubes in dilute aqueous solutions by ozone as affected by ultrasound, *Carbon*, 46 (2008) 466-475.
- [274] H. Wang, A. Zhou, F. Peng, H. Yu, J. Yang, Mechanism study on adsorption of acidified multiwalled carbon nanotubes to Pb (II), *J. Colloid Interface Sci.*, 316 (2007) 277-283.
- [275] National Institute for Materials Science (NIMS) | 1-2-1 Sengen Tsukuba-city Ibaraki 305-0047 Japan; Database of electron inelastic mean free path for elemental solids, accessed: 20.01.2014
- [276] C. Powell, A. Jablonski, The NIST electron effective-attenuation-length database, *Journal of surface analysis*, 9 (2002) 322-325.
- [277] H. Bethe, Zur theorie des durchgangs schneller korpuskularstrahlen durch materie, *Annalen der Physik*, 397 (1930) 325-400.
- [278] D.R. Penn, Electron mean-free-path calculations using a model dielectric function, *Phys. Rev. B*, 35 (1987) 482-486.
- [279] S. Tanuma, C.J. Powell, D.R. Penn, Calculations of electron inelastic mean free paths. V. Data for 14 organic compounds over the 50–2000 eV range, *Surf. Interface Anal.*, 21 (1994) 165-176.
- [280] NIST, Chemistry WebBook - Standard Reference Database Number 69, accessed: 2014
- [281] R. Schennach, A. Eichler, K. Rendulic, Adsorption and desorption of methanol on Pd (111) and on a Pd/V surface alloy, *J. Phys. Chem. B*, 107 (2003) 2552-2558.

Hiermit erkläre ich an Eides statt, dass ich die vorliegende Arbeit selbstständig verfasst und keine anderen als die angegebenen Quellen und Hilfsmittel verwendet habe.